FEDERAL UNIVERSITY OF SANTA CATARINA

DEPARTMENT OF MECHANICAL ENGINEERING

DEVELOPMENT OF THERMAL REGENERATORS FOR MAGNETIC COOLING APPLICATIONS

Paulo Vinicius Trevizoli

Florianópolis, SC

2015

Paulo Vinicius Trevizoli

DESENVOLVIMENTO DE REGENERADORES TÉRMICOS PARA APLICAÇÕES EM SISTEMAS DE REFRIGERAÇÃO MAGNÉTICA

Tese submetida ao Programa de Pós-Graduação em Engenharia Mecânica da Universidade Federal de Santa Catarina para a obtenção do título de Doutor em Engenharia Mecânica.

Orientador:
Prof. Jader R. Barbosa Jr., Ph.D.

Florianópolis, SC

2015

Ficha de identificação da obra elaborada pelo autor,
através do Programa de Geração Automática da Biblioteca Universitária da UFSC.

Trevizoli, Paulo Vinicius
Desenvolvimento de regeneradores térmicos para aplicações em sistemas de refrigeração magnética / Paulo Vinicius Trevizoli ; orientador, Jader Riso Barbosa Jr. - Florianópolis, SC, 2015.
380 p.

Tese (doutorado) - Universidade Federal de Santa Catarina, Centro Tecnológico. Programa de Pós-Graduação em Engenharia Mecânica.

Inclui referências

1. Engenharia Mecânica. 2. Regeneradores térmicos. 3. Regeneradores magnético-ativos. 4. Refrigeração magnética. 5. Otimização. I. Barbosa Jr., Jader Riso . II. Universidade Federal de Santa Catarina. Programa de Pós-Graduação em Engenharia Mecânica. III. Título.

UNIVERSIDADE FEDERAL DE SANTA CATARINA
PROGRAMA DE PÓS-GRADUAÇÃO EM ENGENHARIA MECÂNICA

DESENVOLVIMENTO DE REGENERADORES TÉRMICOS PARA APLICAÇÕES EM SISTEMAS DE REFRIGERAÇÃO MAGNÉTICA

PAULO VINICIUS TREVIZOLI

Esta Tese foi julgada adequada para obtenção do Título de "Doutor em Engenharia Mecânica", e aprovada em sua forma final pelo Programa de Pós-Graduação em Engenharia Mecânica da Universidade Federal de Santa Catarina.

27 de Agosto de 2015

Prof. Jader Riso Barbosa Jr., Ph.D – Orientador

Prof. Armando Albertazzi Gonçalves. Jr., Dr.Eng – Coordenador do Curso

BANCA EXAMINADORA

Prof. Jader Riso Barbosa Jr., Ph.D – Presidente

Prof. Renato Machado Cotta, Ph.D – Relator

Prof. Leandro Alcoforado Sphaier, Ph.D

Prof. Rogério Tadeu da Silva Ferreira, Ph.D

Prof. Alvaro Toubes Prata, Ph.D

Prof. Amir Antônio Martins de Oliveira Jr., Ph.D

Prof. Alexandre Kupka da Silva, Ph.D

"Cooling breeze from a summer day
Hearing echoes from your heart
Learning how to recompose the words
Let time just fly
Joyful sea-gulls roaming on the shore
Not a single note will sound
Raise my head after I dry my face
Let time just fly
Recalling, retreating
Returning, retrieving
A small talk your missing
More clever but older now
A leader, a learner
A lawful beginner
A lodger of lunacy
So lucid in the jungle
A helper, a sinner
A scarecrow's agonizing smile
Oh! Minutes go round and round
Inside my head
Oh! My chest will now explode
Falling into pieces
Rain breaks on the ground
One minute forever
A sinner regretting
My vulgar misery ends
Ride the winds of a brand new day
High where mountain's stand
Found my hope and pride again
Rebirth of a man
Time to fly."
(Rebirth, Angra)

To my lovely wife, Dayane
to my parents Edemir and Alcidinéa,
to my brother Edermir Jr. and sister Claudia.
You are my example of courage, determination and dedication.

Acknowledgments

I would like to express my sincere gratitude to my advisor Prof. Jader Riso Barbosa Jr. for the continuous support of my doctoral research, for his patience, motivation and knowledge. His guidance helped me in all the time of research and writing of this thesis.

My sincere thanks go to Prof. Andrew Rowe to welcomed me to his research group. It was a really fruitful experience, fundamental to my growth as a researcher. Also, I am very thankful to the IESVic Team: Prof. Armando Tura, Daniel Arnold, Tom Burdyny, Alex Ruebsaat-Trott, Oliver Campbell and Yifeng Liu.

Besides, I would like to thank the committee: Prof. Renato M. Cotta, Prof. Leandro A. Sphaier, Prof. Rogério T. S. Ferreira, Prof. Alvaro T. Prata, Prof. Amir A. M. de Oliveira and Prof. Alexandre Kupka da Silva, for their comments and contributions to this thesis.

I would like to express my gratitude to the financial support of the CNPq, the Instituto Nacional em Ciência e Tecnologia (INCT) em Refrigeração e Termofísica and Embraco. I am thankful also to the Programa de Pós-Graduação em Engenharia Mecânica.

My thanks also go to Dr. Lian Zang (BASF) for his collaboration with the characterization the magnetocaloric properties of our gadolinium samples and to Dr. Kurt Engelbrecht and Dr. Christian Bahl (Risoe-Denmark), who kindly share with us their gadolinium properties data-set. Also to Mr. Roberto Horn (Coca-Cola), who kindly provided the 3D prototyping parts.

Many thanks to Polo's staff and technicians, especially Mr. Rafael V. Lima, Mr. Pedro O. Cardoso and Mr. Jorge Luiz S. Lubas, who provided valuable assistance by sharing their own expertise.

I am thankful to the Emerging Technologies Team: Jaime A. Lozano, Matheus S. Capovilla, Diego P. Alcalde, Fabio Canesin. A especial sincere thanks go to the students, Guilherme F. Peixer and Alan T.

Nakashima: your assistance and friendship was fundamental to finish this thesis.

I am thankful to my friends. Firstly, to my best friend Gibbs to always cheering me up. To my great friends Fernando F. Czubinski, Pablo A. de Oliveira, Dalton Bertoldi, Moisés Marcelino Neto, Daniel Hense, Pedro M. de Oliveira, Paulo Sedrez, Igor A. Maia, Alvaro N. de Carvalho, Gustavo G. Ribeiro, Luigi Passos, Michele F. Lazzari, Bruno Schaefer, Fabiana Maronezi, Rafael B. Schipfer, and others friends that, somehow, helped in the development of this thesis, with technical support and for all the fun we have had in the last years. Thanks also to my friends from Universidade Estadual de Maringá: Prof. Cleber Santiago Alves, Prof. Flávio Colman and Prof. Jean R. Bocca. Also to Prof. Alexandre Magnus G. Carvalho.

I would like also to express my sincere gratitude to my family. Firstly, to my parents, Edemir Trevizoli and Alcidinéa M. V. Trevizoli. To my brother, Edemir Trevizoli Jr., and sister, Claudia D. Trevizoli. To my parents-in-law, Aparecido Mezuram and Elza Mezuram. To my sisters and brothers-in-law, Aline P. Trevizoli and Elaine M. Previatti, Fernando T. do Nascimento and Rodrigo C. Previatti. Also, to my nephews and nieces, Gabriel M. Previatti, Matheus P. Trevizoli, Bárbara M. Previatti, Isabela T. do Nascimento and Eduarda P. Trevizoli. Your support, motivation and encouragement were fundamental to the development of this thesis.

Last but not the least, I would like to thank my beautiful wife, Dayane, for your love, dedication and comprehension. She was always there cheering me up and stood by me through the good times and bad.

I would never have been able to finish this thesis without the guidance of my supervisor, help from friends, and support and love from my family and wife.

Contents

List of Figures **xxi**

List of Tables **xxxix**

Nomenclature **xlv**

Abstract **li**

Resumo **liii**

1 Introduction **1**

1.1 Objectives and Contributions 5

1.2 Outline of the Thesis 7

2 Fundamentals and State of the Art of Thermal Regenerators **9**

2.1 Applications of Thermal Regenerators 10

2.2 Types of Regenerators 11

2.3 Merits of Regenerators 13

2.4 Thermal Fluids Used in Regenerators 14

2.4.1 Gases 14

2.4.2 Liquids 16

2.5 The Ideal Regenerator 18

2.6 Regenerator Design and Performance Parameters 20

2.7 The Magnetocaloric Effect 24
2.7.1 Thermodynamics of the MCE 26
2.7.2 The Reversibility of the MCE 28
2.7.3 Magnetocaloric Materials 30
2.8 Active Magnetic Regenerators 34
2.8.1 The AMR Cycle 34
2.8.2 Numerical Modeling of AMRs 36
2.9 Design and Optimization of Thermal Regenerators . . . 38
2.10 Magnetic Cooling Systems 41

3 Experimental Apparatus 45
3.1 Description 46
3.1.1 Passive Regenerator Apparatus 46
3.1.2 Active Magnetic Regenerator Apparatus 51
3.2 Sub-systems of the Apparatus 55
3.2.1 Magnetic Circuit 55
3.2.2 Pumping System 62
3.2.3 Transmission System 64
3.2.4 Magnetic and Fluid Flow Synchronization 66
3.3 Passive Regenerators Matrices 66
3.3.1 Packed Beds of Spheres 68
3.3.2 Void Volume and Entrance Effects 70
3.3.3 Parallel Plates and Pin Arrays 72
3.4 AMR Matrices 74
3.5 Thermal Insulation 76
3.6 Instrumentation and Data Acquisition 79
3.7 Details of the Final Assembly 81

4 Problem Formulation and Solution Method 87

4.1 Regenerative Porous Matrix Modeling 87

4.1.1 Momentum Equation 88

4.1.2 Energy Equations 90

4.1.2.1 Fluid Phase Energy Equation 91

4.1.2.2 Solid Phase Energy Equation 92

4.2 Losses Modeling 93

4.2.1 Void Volume Modeling 93

4.2.2 Casing Heat Transfer Modeling 95

4.3 Closure Relationships 98

4.3.1 Particle Diameter and Surface Area Density . . . 98

4.3.2 Permeability and Ergun Constant 99

4.3.3 Interstitial Heat Transfer Coefficient 100

4.3.4 Effective Thermal Conductivity 101

4.3.4.1 Fluid Phase Effective Thermal Conductivity 101

4.3.4.2 Solid Phase Effective Thermal Conductivity 102

4.3.5 Longitudinal Dispersion 102

4.3.6 Wall Heat Transfer Coefficient 103

4.4 Magnetic Properties and their Implementation 104

4.4.1 Implementation of the Magnetocaloric Effect . . 104

4.4.2 Magnetic Losses due to Demagnetizing Effects . 106

4.4.3 Experimental Thermo-Magnetic Properties . . . 108

4.5 Numerical Implementation 109

4.5.1 Momentum Equation 112

4.5.2 Energy Equations 115

4.5.3 Void Volume 119
4.5.4 Casing Heat Transfer 123
4.5.5 Complete Regenerator Simulation Routine 126
4.6 Numerical Mesh and Convergence Evaluation 128
4.7 Initial Model Verification 133
4.7.1 Ideal Passive Regenerator Model 133
4.7.2 Validation of the MCE Implementation 137
4.8 RegSim Development 139

5 Passive Thermal Regenerators 141

5.1 Time-Dependent Measurements 141
5.1.1 Temperature Measurements 141
5.1.2 Mass Flow Rate Measurement 149
5.1.3 Pressure Drop Measurements 152
5.2 Performance Metrics and Data Regression 154
5.2.1 Uncertainty Analysis 157
5.3 Experimental Results 159
5.3.1 Reproducibility of the Experimental Results . . . 159
5.3.2 Effectiveness Imbalance 161
5.3.3 Packed Bed Regenerator 163
5.3.3.1 Pressure Drop and Pumping Power . . 163
5.3.3.2 Effectiveness: Effect of the Sphere Diameter 165
5.3.3.3 Effectiveness: Effect of Regenerator Housing Dimensions 171
5.3.3.4 General Conclusions About the Packed Bed Regenerators 174

5.3.4 Pins, Plates and Spheres: A Regenerative Matrix Comparison 175

5.4 Numerical Results 178

5.4.1 Packed Bed Regenerator 178

5.4.2 Pin, Plate and Sphere Matrices 196

5.5 Void Volume and Inlet Flow Maldistribution 201

6 Active Magnetic Regenerators 209

6.1 Preliminary Tests 209

6.2 Time-Dependent Measurements 213

6.2.1 Temperature Measurements 213

6.2.2 Torque Measurements 215

6.2.3 Influence of the Oscillating Torque on the Pressure Drop and Mass Flow Rate 217

6.3 Performance Metrics and Data Regression 219

6.3.1 Uncertainty Analysis 224

6.4 Reproducibility of the Experimental Results 226

6.5 Spheres Packed Bed Regenerator 228

6.5.1 Experimental Results 228

6.5.1.1 Characteristic Curves 228

6.5.1.2 Total Power (Work) Analysis 230

6.5.1.3 AMR Performance Analysis 234

6.5.2 Numerical Results and Losses Analyses 244

6.6 Performance Assessment of Different Matrix Geometries 259

7 Optimization of Thermal Regenerators 277

7.1 Entropy Generation Model 278

7.2 Optimization of Passive Oscillating-Flow Regenerators 281

7.2.1 Performance Evaluation Criteria for Passive Regenerators 281

7.2.2 PEC Numerical Implementation 284

7.2.3 Entropy Generation-Effectiveness Contour Maps 285

7.2.4 Individual Contributions to the Total Entropy Generation 288

7.2.5 Variable Geometry (**VG**) Evaluation Criteria . . 290

7.2.5.1 Fixed Frequency 290

7.2.5.2 Fixed Mass Flow Rate 295

7.2.6 Fixed Face Area (**FA**) Evaluation Criteria 298

7.2.6.1 Fixed Frequency 298

7.2.6.2 Fixed Mass Flow Rate 301

7.3 Optimization of Active Magnetic Regenerators 303

7.3.1 Performance Evaluation Criteria for AMRs . . . 303

7.3.2 Entropy Generation Cycle-Average Cooling Capacity Contour Maps 304

7.3.3 Variable Geometry (**VG**) Evaluation Criteria . . 308

7.3.3.1 Fixed Frequency 308

7.3.3.2 Fixed Mass Flow Rate 313

7.3.4 Fixed Face Area (**FA**) Evaluation Criteria 317

7.3.4.1 Fixed Frequency 317

7.3.4.2 Fixed Mass Flow Rate 320

8 Final Considerations **325**

8.1 Recommendations to Future Works 327

References **329**

Appendix A Nested Halbach Cylinder Design **347**

A.1 Modeling 347

A.1.1 Analytical Modeling 347

A.1.1.1 Basic Equations 347

A.1.1.2 Parameters and Constraints 348

A.1.1.3 Design Procedure 350

A.1.2 COMSOL Multiphysics Modeling 352

A.2 Experimental Analysis 352

A.3 Results and Discussions 353

A.3.1 Design Procedure Results 353

A.3.2 Magnetization Reversal and Energy Product (BH) Analysis 357

A.3.3 Nested Halbach Cylinder Final Design 363

A.3.4 Experimental Results 366

Appendix B Assembly of the Regenerative Matrices **373**

B.1 Assembly of Packed Bed Matrices 373

B.2 Assembly of Parallel-Plate and Pin Array Matrices . . . 375

Appendix C Nusselt Number Correlation for Packed Beds of Spheres **379**

List of Figures

Figure 1.1 – Carnot cycle comparison between vapor compression and magnetic refrigeration. Adapted from Russek and Zimm (2006). 3

Figure 2.1 – Regenerator types: (a) Single fixed-bed; (b) Multiple fixed-bed; (c) Rotary. Adapted from Nellis and Klein (2009). 12

Figure 2.2 – Schematic Stirling cryocooler and corresponding T-S diagram. Adapted from Kreith (2000). 15

Figure 2.3 – Effectiveness as a function of NTU and utilization (defined as U in the figure), solution for balanced and symmetric regenerators. Adapted from Nellis and Klein (2009). 24

Figure 2.4 – Illustration of the isothermal and adiabatic magnetization processes in a T-s diagram. Adapted from Pecharsky and Gschneidner Jr. (1999). 25

Figure 2.5 – (a) ΔT_{ad} and (b) c_{H} as a function of the temperature and magnetic flux density. Adapted from Siddikov *et al.* (2005). 28

Figure 2.6 – Experimental demonstration of the reversibility of the MCE in Gd. The change in magnetic flux density was approximately 1.65 T. Adapted from Trevizoli *et al.* (2012). 29

Figure 2.7 – Direct measurement results of the ΔT_{ad} under adiabatic magnetization and demagnetization as a function of the temperature, for a magnetic flux density variation of approximately 1.65 T. The demagnetization curve shows the absolute value ($|\Delta T_{\mathrm{ad}}|$). Adapted from Trevizoli *et al.* (2012). 30

Figure 2.8 – (a) Isothermal entropy change; (b) Adiabatic temperature change for different magnetocaloric materials. Adapted from Gschneidner Jr. *et al.* (2005). 31

Figure 2.9 – (a) Single-material; (b) Multi-material active magnetic regenerator. 33

Figure 2.10 –Specific heat capacity at constant magnetic flux density for Gd. Adapted from Siddikov *et al.* (2005). . . 33

Figure 2.11 –Schematic description of the processes in a thermo-magnetic regenerative Brayton cycle. 35

Figure 2.12 –Schematic T-S diagram of the thermo-magnetic regenerative Brayton cycle. 36

Figure 2.13 –State-of-the-art magnetic cooling prototypes: (a) Tura and Rowe (2011); (b) Engelbrecht *et al.* (2012); (c) Jacobs *et al.* (2014); (d) Arnold *et al.* (2014); (e) Eriksen *et al.* (2015); (f) Lozano *et al.* (2015). 44

Figure 3.1 – Passive and active magnetic regenerators experimental apparatus. 47

Figure 3.2 – Schematic diagram of the experimental passive regenerator apparatus. 48

Figure 3.3 – Passive regenerator test apparatus: (a) Frontal view showing the pumping system, gear boxes, check valves and mass flow meters; (b) Top view showing the regenerator housing, heat exchangers, temperature probes and pressure transducers. 49

Figure 3.4 – Schematic diagram of the experimental active magnetic regenerator apparatus. 52

Figure 3.5 – Active magnetic regenerator test apparatus: (a) Frontal view showing the pumping system, gear boxes and mass flow meters; (b) Isometric view showing the magnet, heat exchangers, temperature probes, pressure transducers and the heater. 53

Figure 3.6 – Nested Halbach cylinders: (a) At the maximum magnetic field position; (b) At the minimum magnetic field position. The black arrows indicate the remanent flux density of the permanent magnet segments, while the red arrows indicate $\vec{B}$ in the magnetic gap. 55

Figure 3.7 – Illustration of the NHC magnetic field variation: (a) Rotation of the internal magnet with a static external magnet; (b) Counter rotation of the internal and external magnets. The black arrows indicate the remanent flux density of the permanent magnet segments, while the red arrows indicate $\vec{B}$ in the magnetic gap. 58

Figure 3.8 – Nested Halbach Cylinder magnetic circuit built according to the dimensions obtained from the proposed design procedure. 59

Figure 3.9 – y-z cutaway view of the NHC design showing the bearing structure to enable the counter rotation of the external and internal magnets. Dimensions in mm. . . . 59

Figure 3.10 – Experimental resultant magnetic flux density measurements at different positions along the z axis as a function of the rotating angle of the inner magnet. . . 60

Figure 3.11 – Magnitude of the components, resultant and direction of the magnetic flux density at the maximum field position along the z-axis. 61

Figure 3.12 – Axial variation of the maximum magnetic flux density. 62

Figure 3.13 – Pumping system: (a) Double effect pumps; (b) Check valves; (c) Crank disc. 64

Figure 3.14 – Transmission system to counter rotate the NHC while keeping the phasing with the pumping system: (a) Overall design; (b) Transmission relations between the shafts. 65

Figure 3.15 – Magnetic and fluid flow waveforms synchronization. 67

Figure 3.16 – Stainless steel spheres for the packed bed regenerative matrices. 69

Figure 3.17 –Regenerator casings: (a) Frontal view of Casings #1, #2 and #3; (b) Top view of Casings #1, #2 and #3; (c) Isometric view of Casings #3 and #4; (d) Top view of Casings #3 and #4. 70

Figure 3.18 – R-T adapters: (a) Design details; (b) Built R-T adapters. 71

Figure 3.19 –Casing #7 - Zero void volume regenerator design: (a) Isometric view detailing the entrance and exiting passages; (b) Top view of the rectangular cross sectional area. 72

Figure 3.20 – Parallel plate and square pin arrays: (a) Detail of square pins; (b) Detail of parallel plates; (c) Scale of the pin array piece; (d) Scale of the parallel plate piece. 73

Figure 3.21 – Parallel plate and pin array regenerators: (a) Combination of the five pieces into a 100-mm long matrix; (b) Digital ABS housing; (c) Assembling the matrix in the ABS housing; (d) ABS housing inside the G10 casing. 75

Figure 3.22 –R-T adapters for the parallel plate and pin array matrices. 75

Figure 3.23 –Steps of the application of the thermal insulation on the passive regenerators. 77

Figure 3.24 – AMR insulation: (a) Casing #3; (b) Casing #5 (parallel plates) and Casing #6 (pin array). Casing #4 is similar to (b) but with a round cross sectional area. . 78

Figure 3.25 – Packed bed regenerators: (a) Casing #3 final assembly; (b) Internal temperature probe positioning; (c) Ends temperature probe positioning. 82

Figure 3.26 – Parallel plate and pin array regenerator: (a) Casing #5 and #6 final assembly; (b) Ends temperature probe positioning. 82

Figure 3.27 – Zero void volume regenerator: (a) Casing #7 final assembly; (b) Positioning of end temperature probes. 83

Figure 3.28 – AMR beds: (a) Final assembly; (b) Positioning of the end temperature probes; (c) Final assembly with the temperature probes and bearing housings. 84

Figure 3.29 – Positions of the pressure transducers. The red arrows indicate the hot blow and the blue arrows the cold blow. 85

Figure 3.30 –Final design and details of the passive and active regenerator experimental setup. 86

Figure 4.1 – Basic geometry of the 1-D fluid flow and heat transfer model of a regenerative porous matrix. 88

Figure 4.2 – Basic geometry of the 1-D fluid flow and heat transfer model including the void volumes. 94

Figure 4.3 – Basic geometry of the 1-D fluid flow and heat transfer model including the void volumes and the adjacent domains (wall, air gap and magnet). 96

Figure 4.4 – Interpolated thermo-magnetic properties of the gadolinium samples used in this thesis as a function of temperature and magnetic flux density: (a) T-s diagram; (b) ΔT_{ad}; (c) Specific heat capacity; (d) Specific magnetization. 109

Figure 4.5 – Basic Cartesian grid for: (a) 1-D domain; (b) 2-D domain. 111

Figure 4.6 – Solver routine for the momentum equation. . . . 114

Figure 4.7 – Solver routine for the energy equations. 120

Figure 4.8 – Passive and active magnetic regenerator final solver routine. 127

Figure 4.9 – Mesh evaluation for passive regenerators and comparison with the ideal regenerator solution. 130

Figure 4.10 – Effectiveness vs. NTU for spheres packed bed matrix with different particle sizes. Comparison of numerical modeling results with the Dragutinovic and Baclic (1998) solution for ideal passive regenerators. 134

Figure 4.11 – Effectiveness vs. NTU for spheres packed bed matrix with different operating frequencies. Comparison of numerical modeling results with the Dragutinovic and Baclic (1998) solution for ideal passive regenerators. . . 135

Figure 4.12 – Effectiveness vs. *NTU* for parallel plates matrix with different plate thickness. Comparison of numerical modeling results with the Dragutinovic and Baclic (1998) solution for ideal passive regenerators. 136

Figure 4.13 – Effectiveness vs. *NTU* for parallel plates matrix with different porosities. Comparison of numerical modeling results with the Dragutinovic and Baclic (1998) solution for ideal passive regenerators. 137

Figure 4.14 – Comparison between the discrete and built-in implementation of the MCE. 138

Figure 4.15 – *RegSim - Regenerator Simulator* interface. . . . 140

Figure 5.1 – Time-dependent temperature evolution in the passive experimental tests. 142

Figure 5.2 – Time-dependent temperature measurements: (a) Test#1; (b) Test#2; (c) Test#3; (d) Test#4. 145

Figure 5.3 – Axial temperature profiles after the hot blow (open symbols) and after the cold blow (solid symbols). Conditions are presented in Table 5.1. 146

Figure 5.4 – Time-dependent temperature behavior at the hot end: (a) Constant utilization (≈ 0.62) and variable frequency; (b) Constant frequency (0.5 Hz) and variable utilization. 147

Figure 5.5 – Axial temperature profiles after the hot blow (open symbols) and after the cold blow (solid symbols): (a) Constant utilization (≈ 0.31) and variable frequency; (b) Constant frequency (0.5 Hz) and variable utilization. 148

Figure 5.6 – Time-dependent mass flow rate measurements: (a) Constant utilization (≈ 0.62) and variable frequency; (b) Constant frequency (0.25 Hz) and variable utilization; (c) Detail of the no flow period. 151

Figure 5.7 – Experimental blow-averaged mass flow rate as a function of the reference mass flow rate. The solid symbols correspond to the cold blow and the open symbols are related to the hot blow measurements. 152

Figure 5.8 – Time-dependent total pressure drop measurements: (a) Constant utilization (≈ 0.62) and variable frequency; (b) Constant frequency (0.5 Hz) and variable utilization. 153

Figure 5.9 – Reproducibility tests: $\overline{\Delta P}$ as a function of Re_{dp} and comparison with the numerical model. 160

Figure 5.10 – Reproducibility tests: ϵ as a function of NTU. . 161

Figure 5.11 – Effectiveness imbalance as a function of NTU for Casing #3 with 0.5 and 1-mm stainless steel spheres. 162

Figure 5.12 – $\overline{\Delta P}$ for packed bed regenerators as a function of Re_{dp} for sphere sizes of 0.5, 0.8 and 1 mm: (a) Casing #1; (b) Casing #2; (c) Casing #3; (d) Casing #4. . . . 164

Figure 5.13 – $\overline{\dot{W}}_{\mathrm{pump}}$ for packed bed regenerators as a function of Re_{dp} for spheres sizes of 0.5, 0.8 and 1 mm: (a) Casing #1; (b) Casing #2; (c) Casing #3; (d) Casing #4. . . . 165

Figure 5.14 – Casing #1: ϵ as a function of NTU for different values of sphere size and utilization. 166

Figure 5.15 – Casing #2: ϵ as a function of NTU for different values of sphere size and utilization. 167

Figure 5.16 – Casing #3: ϵ as a function of NTU for different values of sphere size and utilization. 168

Figure 5.17 – Casing #4: ϵ as a function of NTU for different values of sphere size and utilization. 169

Figure 5.18 – $d_{\mathrm{p}} = 0.5$ mm: ϵ as a function of NTU for different regenerator casings. 171

Figure 5.19 – $d_{\mathrm{p}} = 0.8$ mm: ϵ as a function of NTU for different regenerator casings. 172

Figure 5.20 – $d_{\mathrm{p}} = 1$ mm: ϵ as a function of NTU for different regenerator casings. 173

Figure 5.21 – Viscous losses of the different matrix geometries: (a) $\overline{\Delta P}$ as a function of Re_{dp}; (b) $\overline{\dot{W}}_{\mathrm{pump}}$ as a function of Re_{dp}. 176

Figure 5.22 – ϵ as a function of NTU and utilization for different regenerator geometries. 177

Figure 5.23 – Comparison between the numerical results and the experimental data: $\overline{\Delta P}$ as a function of Re_{dp} for packed beds with spheres of different sizes: (a) Casing #1; (b) Casing #2; (c) Casing #3; (d) Casing #4. . . . 179

Figure 5.24 – Comparison between the numerical results and the experimental data: f_{D} as a function of Re_{dp} for packed beds of spheres. 180

Figure 5.25 – Comparison between the numerical results and the experimental data: ϵ as a function of NTU for Casing #1 and $d_{\mathrm{p}} = 0.5$ mm. 181

Figure 5.26 – Comparison between the numerical results and the experimental data: ϵ as a function of NTU for Casing #1 and $d_{\mathrm{p}} = 0.8$ mm. 182

Figure 5.27 – Comparison between the numerical results and the experimental data: ϵ as a function of NTU for Casing #1 and $d_{\mathrm{p}} = 1$ mm. 183

Figure 5.28 – Comparison between the numerical results and the experimental data: ϵ as a function of NTU for Casing #2 and $d_{\mathrm{p}} = 0.5$ mm. 184

Figure 5.29 – Comparison between the numerical results and the experimental data: ϵ as a function of NTU for Casing #2 and $d_{\mathrm{p}} = 0.8$ mm. 185

Figure 5.30 – Comparison between the numerical results and the experimental data: ϵ as a function of NTU for Casing #2 and $d_{\mathrm{p}} = 1$ mm. 186

Figure 5.31 – Comparison between the numerical results and the experimental data: ϵ as a function of NTU for Casing #3 and $d_{\mathrm{p}} = 0.5$ mm. 187

Figure 5.32 – Comparison between the numerical results and the experimental data: ϵ as a function of NTU for Casing #3 and $d_{\mathrm{p}} = 0.8$ mm. 188

Figure 5.33 – Comparison between the numerical results and the experimental data: ϵ as a function of NTU for Casing #3 and $d_p = 1$ mm. 189

Figure 5.34 – Comparison of the experimental and numerical time-dependent temperatures with ($\vartheta \neq 0$) and without ($\vartheta = 0$) the void volumes for Casing #3, $d_p = 0.8$ mm, $\phi \approx 0.467$ and different operating frequencies; at the hot end (top) and at the cold end (bottom). 191

Figure 5.35 – Prediction of the time-dependent experimental temperature by the numerical model (continuous lines) considering the void volume for Casing #3, $d_p = 0.8$ mm, $f = 0.5$ Hz and different values of utilization. . . . 192

Figure 5.36 – Experimental and numerical temperature profiles for Casing #1, $f = 0.5$ Hz and $d_p = 0.8$ mm. 193

Figure 5.37 – Experimental and numerical temperature profiles for Casing #2, $f = 0.5$ Hz and $d_p = 0.8$ mm. 194

Figure 5.38 – Experimental and numerical temperature profiles for Casing #3, $f = 0.5$ Hz and $d_p = 0.5$ mm. 194

Figure 5.39 – Experimental and numerical temperature profiles for Casing #3, $f = 0.5$ Hz and $d_p = 0.8$ mm. 195

Figure 5.40 – Experimental and numerical temperature profiles for Casing #3, $f = 0.5$ Hz and $d_p = 1$ mm. 195

Figure 5.41 – Comparison between the numerical results and the experimental data: $\overline{\Delta P}$ as a function of Re_{dp} for different matrix geometries. 196

Figure 5.42 – Comparison between the numerical results and the experimental data: f_D as a function of Re_{dp} to different matrix geometries. 197

Figure 5.43 – Comparison between the numerical results and the experimental data: ϵ as a function of NTU for the packed bed regenerator - Casing #4 and $d_p = 0.8$ mm. . 198

Figure 5.44 – Comparison between the numerical results and the experimental data: ϵ as a function of NTU for the parallel plate regenerator. 199

Figure 5.45 – Comparison between the numerical results and the experimental data: ϵ as a function of NTU for the pin array regenerator. 200

Figure 5.46 – Numerical results for ϵ as a function of NTU for Casing #1 with 1-mm spheres and different void volume fractions. 202

Figure 5.47 – Casing #1 experimental results for ϵ as a function of NTU for different void volume sizes. 202

Figure 5.48 – Casing #2 experimental results for ϵ as a function of NTU for different void volume sizes. 203

Figure 5.49 – Casing #3 experimental results for ϵ as a function of NTU for different void volume sizes. 203

Figure 5.50 – Experimental data and numerical results for ϵ as a function of NTU for the zero void volume regenerator: Casing #7 with 0.5-mm spheres. 205

Figure 5.51 – Experimental data and numerical results for ϵ as a function of NTU for the zero void volume regenerator: Casing #7 with 1-mm spheres. 206

Figure 5.52 – Experimental data and numerical results for $\overline{\Delta P}$ as a function of Re_{dp} for the zero void volume regenerator. 207

Figure 6.1 – Typical time-dependent temperature evolution during the AMR preliminary tests. 210

Figure 6.2 – ΔT_{Reg} as a function of T_{H}: (a) $f = 0.25$ Hz; (b) $f = 1$ Hz. 211

Figure 6.3 – Time-dependent temperature measurements at the periodically developed regime for different thermal loads at the operating condition of $f = 0.5$ Hz and $\phi \approx 0.41$ for Spheres#3 geometry (Casing #3 and $d_{\mathrm{p}} = 0.55$ mm). 214

Figure 6.4 – Time-dependent total torque measurements: (a) Variable ΔT_{Hex} for $f = 0.5$ Hz and $\phi \approx 0.41$; (b) Variable utilization for $f = 0.5$ Hz and $\Delta T_{\mathrm{Hex}} = 0$. 216

Figure 6.5 – Oscillating torque influences on the: (a) Instantaneous mass flow rate for PP#122.5 and s_k = 10 mm; (b) Instantaneous total pressure drop for PP#122.5 and s_k = 10 and 20 mm. 218

Figure 6.6 – Schematic representation of the main variables of a generic magnetic refrigerator. 220

Figure 6.7 – Time-dependent measurements of T_H, T_C, T_{HE} and T_{CE}: (a) Intermediate thermal load test; (b) Maximum thermal load test. 222

Figure 6.8 – Reproducibility tests for $\overline{\dot{Q}}_C$ as a function of ΔT_{Hex}. 227

Figure 6.9 – $\overline{\dot{Q}}_C$ as a function of ΔT_{Hex} for T_H = 300 K and a range of utilization factors: (a) f = 0.25 Hz; (b) f = 0.5 Hz; (c) f = 1 Hz. 230

Figure 6.10 – $\overline{\dot{Q}}_C$ as a function of ΔT_{Hex} and ΔT_{Reg}, for $\phi \approx$ 0.38 and different frequencies (0.25, 0.5 and 1 Hz). . . . 231

Figure 6.11 – $\overline{\dot{W}}$ as a function of T_C for different utilization factors (0.28, 0.38 and 0.58) and frequencies (0.5 and 1 Hz). 232

Figure 6.12 – $\overline{\dot{Q}}_C$ as a function of ϕ for T_H = 300 K and different ΔT_{Hex}: (a) f = 0.25 Hz; (b) f = 0.5 Hz; (c) f = 1 Hz. 236

Figure 6.13 – COP as a function of ϕ for T_H = 300 K and different ΔT_{Hex}: (a) f = 0.25 Hz; (b) f = 0.5 Hz; (c) f = 1 Hz. 238

Figure 6.14 – η_{2nd} as a function of ϕ for T_H = 300 K and different ΔT_C: (a) f = 0.25 Hz; (b) f = 0.5 Hz; (c) f = 1 Hz. 240

Figure 6.15 – Maximum ΔT_{Hex} as a function of ϕ for T_H = 300 K and different operating frequencies. 242

Figure 6.16 – Maximum $\overline{\dot{Q}}_C$ as a function of ϕ for T_H = 300 K and different operating frequencies. 243

Figure 6.17 – Comparison between the numerical model and experimental data for $\overline{\dot{Q}}_{\mathrm{C}}$ as a function of ΔT_{Hex} for different values of utilization and frequency, considering different types of losses. 246

Figure 6.18 – Cycle average casing heat gain at different regenerator positions (finite volumes) for: (a) Different ΔT_{Hex} for $\phi \approx 0.38$ and $f = 0.25$ Hz; (b) Different operating frequencies for $\phi \approx 0.38$ and $\Delta T_{\mathrm{Hex}} = 25$ K; (c) Different utilization factors for $f = 0.25$ Hz and $\Delta T_{\mathrm{Hex}} = 25$ K. . 250

Figure 6.19 – Comparison between the numerical results and experimental data for the time-dependent temperatures at different operating conditions: (a) Different ΔT_{Hex}; (b) $\Delta T_{\mathrm{Hex}} \approx 0$. 253

Figure 6.20 – Numerical results (solid lines) and experimental data (open symbols) for $\overline{\dot{Q}}_{\mathrm{C}}$ as a function of ϕ for $T_{\mathrm{H}} = 300$ K and different ΔT_{Hex}: (a) $f = 0.25$ Hz; (b) $f = 0.5$ Hz; (c) $f = 1$ Hz. 256

Figure 6.21 – Numerical results (solid lines) and experimental data (symbols) for ΔT_{Hex} as a function of ϕ for $T_{\mathrm{H}} = 300$ K: (a) $f = 0.25$ Hz; (b) $f = 0.5$ Hz; (c) $f = 1$ Hz. . 259

Figure 6.22 – $\overline{\dot{Q}}_{\mathrm{C}}$ as a function of ϕ for the three matrix geometries: $f = 0.25$ Hz, $T_{\mathrm{H}} = 300$ K and different ΔT_{Hex}. 263

Figure 6.23 – $\overline{\dot{Q}}_{\mathrm{C}}$ as a function of ϕ for the three matrix geometries: $f = 0.5$ Hz, $T_{\mathrm{H}} = 300$ K and different ΔT_{Hex}. 264

Figure 6.24 – $\overline{\dot{Q}}_{\mathrm{C}}$ as a function of ϕ for the three matrix geometries: $f = 1$ Hz, $T_{\mathrm{H}} = 300$ K and different ΔT_{Hex}. . 265

Figure 6.25 – COP as a function of ϕ for the three matrix geometries: $f = 0.25$ Hz, $T_{\mathrm{H}} = 300$ K and different ΔT_{Hex}. 266

Figure 6.26 – COP as a function of ϕ for the three matrix geometries: $f = 0.5$ Hz, $T_{\mathrm{H}} = 300$ K and different ΔT_{Hex}. 267

Figure 6.27 – COP as a function of ϕ for the three matrix geometries: $f = 1$ Hz, $T_{\mathrm{H}} = 300$ K and different ΔT_{Hex}. 268

Figure 6.28 – $\eta_{2\mathrm{nd}}$ as a function of ϕ for the three matrix geometries: $f = 0.25$ Hz, $T_{\mathrm{H}} = 300$ K and different ΔT_{Hex}. 269

Figure 6.29 – η_{2nd} as a function of ϕ for the three matrix geometries: $f = 0.5$ Hz, $T_H = 300$ K and different ΔT_{Hex}. 270

Figure 6.30 – η_{2nd} as a function of ϕ for the three matrix geometries: $f = 1$ Hz, $T_H = 300$ K and different ΔT_{Hex}. . 271

Figure 6.31 – Comparison of the maximum ΔT_{Hex} as a function of ϕ for each AMR regenerator geometry and $T_H = 300$ K: (a) $f = 0.25$ Hz; (b) $f = 0.5$ Hz; (c) $f = 1$ Hz. . 274

Figure 6.32 – Comparison of the maximum $\overline{\dot{Q}}_C$ as a function of ϕ for each AMR regenerator geometry and $T_H = 300$ K: (a) $f = 0.25$ Hz; (b) $f = 0.5$ Hz; (c) $f = 1$ Hz. 276

Figure 7.1 – Entropy generation model. 278

Figure 7.2 – Flow chart of the various scenarios evaluated in the simulations for the passive regenerator optimization. 282

Figure 7.3 – Lines of constant effectiveness (blue lines) and S_g (red lines) as a function of d_p and $D_{h,Reg}$ for the **VG** PEC for $\dot{m} = 60$ kg/h and frequencies of (a) 1 Hz; (b) 3 Hz. 286

Figure 7.4 – Lines of constant effectiveness (blue lines) and S_g (red lines) as a function of d_p and ζ for the **FA** PEC for $\dot{m} = 250$ kg/h and frequencies of (a) 1 Hz; (b) 3 Hz. 287

Figure 7.5 – Effectiveness as a function of the particle diameter for Cases 1 and 2 at 60 kg/h and 1 Hz. 288

Figure 7.6 – Entropy generation due to each contribution: (a) Case 1: $D_h = 12.5$ mm and $\zeta = 16$; (b) Case 2: $D_h = 75$ mm and $\zeta = 0.074$. 289

Figure 7.7 – Entropy generation in the **VG** PEC, for a mass flow rate of 60 kg/h and $f = 1$ Hz, at a constant effectiveness of 95%. 291

Figure 7.8 – Minimum entropy analysis for the **VG** PEC for $\epsilon = 95\%$, frequency of 1 Hz and variable flow rates in the range of 40-100 kg/h: (a) S_g as a function of d_p; (b) S_g as a function of $D_{h,Reg}$; (c) S_g as a function of ζ. . . 294

Figure 7.9 – Minimum entropy analysis for the **VG** PEC for $\epsilon = 95\%$, fixed mass flow rate of 60 kg/h and variable frequencies in the range of 1-4 Hz: (a) S_g as a function of d_p; (b) S_g as a function of $D_{h,Reg}$; (c) S_g as a function of ζ. 297

Figure 7.10 – Minimum entropy analysis for the **FA** PEC for $\epsilon = 95\%$, fixed frequency of 1 Hz and variable mass flow rates in the range of 100-300 kg/h: (a) S_g as a function of d_p; (b) S_g as a function of ζ. 300

Figure 7.11 – Minimum entropy analysis for the **FA** PEC for $\epsilon = 95\%$, fixed mass flow rate of 250 kg/h and variable frequencies in the range of 1-4 Hz: (a) S_g as a function of d_p; (b) S_g as a function of ζ. 302

Figure 7.12 – Lines of constant $\overline{\dot{Q}}_c$ (blue lines) and S_g (red lines) as a function of d_p and $D_{h,Reg}$ for the **VG** PEC with $\dot{m} = 60$ kg/h and frequencies of (a) 1 Hz; (b) 4 Hz. 306

Figure 7.13 – Lines of constant $\overline{\dot{Q}}_c$ (blue lines) and S_g (red lines) as a function of d_p and ζ for the **FA** PEC with $\dot{m} = 200$ kg/h and frequencies of (a) 1 Hz; (b) 4 Hz. . . 307

Figure 7.14 – Minimum entropy analysis for the **VG** PEC for $\overline{\dot{Q}}_c = 20$ W per regenerator and $\Delta T_{Hex} = 15$ K, at a frequency of 1 Hz and variable flow rates in the range of 40-100 kg/h: (a) S_g as a function of d_p; (b) S_g as a function of $D_{h,Reg}$; (c) S_g as a function of ζ. 310

Figure 7.15 – Individual contributions to the total entropy at the minimum, $S_{g,min}$, for the **VG** PEC for $\overline{\dot{Q}}_c = 20$ W per regenerator and $\Delta T_{Hex} = 15$ K, at a fixed frequency of 1 Hz and flow rates between 40 and 100 kg/h. 311

Figure 7.16 – Minimum entropy analysis for the **VG** PEC for $\overline{\dot{Q}}_c = 20$ W per regenerator at $\Delta T_{Hex} = 15$ K, fixed mass flow rate of 60 kg/h and variable frequencies in the range of 1-4 Hz: (a) S_g as a function of d_p; (b) S_g as a function of $D_{h,Reg}$; (c) S_g as a function of ζ. 315

Figure 7.17 – Individual contributions to the total entropy at the minimum, $S_{g,min}$, for the **VG** PEC for $\overline{\dot{Q}}_c = 20$ W per regenerator at $\Delta T_{Hex} = 15$ K, at a fixed mass flow rate of 60 kg/h and frequencies between 1 and 4 Hz. . . 316

Figure 7.18 – Minimum entropy analysis for the **FA** PEC for $\overline{\dot{Q}}_c = 20$ W per regenerator at $\Delta T_{Hex} = 15$ K, fixed frequency of 1 Hz and variable mass flow rates in the range of 50-200 kg/h: (a) S_g as a function of d_p; (b) S_g as a function of ζ. 318

Figure 7.19 – Individual contributions to the total entropy at the minimum, $S_{g,min}$, for the **FA** PEC for $\overline{\dot{Q}}_c = 20$ W per regenerator at $\Delta T_{Hex} = 15$ K, fixed frequency of 1 Hz and variable mass flow rates in the range of 50-200 kg/h. 319

Figure 7.20 – Minimum entropy analysis for the **FA** PEC for $\overline{\dot{Q}}_c = 20$ W per regenerator at $\Delta T_{Hex} = 15$ K, fixed mass flow rate of 200 kg/h and variable frequencies in the range of 1-4 Hz: (a) S_g as a function of d_p; (b) S_g as a function of ζ. 322

Figure 7.21 – Individual contributions to the total entropy at the minimum, $S_{g,min}$, for the **FA** PEC for $\overline{\dot{Q}}_c = 20$ W per regenerator at $\Delta T_{Hex} = 15$ K, at a fixed mass flow rate of 200 kg/h and variable frequency between 1 and 4 Hz. 323

Figure A.1 – Illustration of the probe position to measure magnetic flux density components: (a) Measurement of the B_x component. (b) Measurement of the B_y component. 353

Figure A.2 – Magnetic flux density distribution in the x-y plane at the center of the magnet array ($z = 0$): (a) Maximum flux density magnet position; (b) Minimum flux density magnet position. 356

Figure A.3 – Magnetic flux density at the maximum position along the axial z-direction for different values of the internal magnet length. 358

Figure A.4 – Magnetization reversal analysis: (a) Maximum magnetic field position; (b) Minimum magnetic field position. The gray arrows represent the remanent flux density orientation of each segment. 360

Figure A.5 – Energy product of the permanent magnet array: (a) Maximum magnetic flux density magnet position; (b) Minimum magnetic magnetic flux density magnet position. The black arrows indicate the remanent flux density of each segment. 361

Figure A.6 – Energy product analysis of the internal magnet: (a) Maximum magnetic field position; (b) Minimum magnetic field position. The black arrows indicate the remanent flux density of each segment. 364

Figure A.7 – Nested Halbach Cylinder magnetic circuit built according to the dimensions obtained from the proposed design procedure. 365

Figure A.8 – $y - z$ cutaway view of the NHC design showing the bearing structure to enable the counter rotation of the external and internal magnets. Dimensions in mm. . 365

Figure A.9 – Motion system designed and constructed to counter rotate the magnets in the NHC array. 366

Figure A.10 –Experimental magnetic flux density vector measurements at different positions along the z axis as a function of the rotating angle of the inner magnet. (a) y-component; (b) x-component; (c) Resultant; (d) Angle of the resultant with the vertical direction. The legend presented in figure (b) is the same for the other figures. 368

Figure A.11 –Magnitude of the components, resultant and direction of the magnetic flux density at the maximum field position along the z-axis. 370

Figure A.12 –Comparison between the 3-D COMSOL simulation results and the experimental data for the magnetic flux density: (a) As a function of the rotating angle for different axial positions; (b) Axial variation of the maximum magnetic flux density. 371

Figure A.13 –Torque measurements: (a) Torque as a function of the rotating angle at different frequencies; (b) Average cycle torque as a function of the operating frequency. . . 372

Figure B.1 – Steps of the assembly of the packed bed matrix. 374

Figure B.2 – Steps of the assembly of the parallel plate and pin array matrices. 376

Figure B.3 – (a) Detail in the alignment of the parallel plates geometry; (b) Detail in the alignment of the pins array geometry. 377

Figure C.1 – Effectiveness as a function of frequency for Casing #3: (a) $d_p = 0.5$ mm; (b) $d_p = 0.8$ mm. 380

List of Tables

Table 2.1 – Promissing magnetocaloric materials properties and characteristics compared with Gd. Fonte: Adapted from Gschneidner Jr. *et al.* (2005). 32

Table 2.2 – State of the art magnetic cooling prototypes. . . 43

Table 3.1 – Passive regenerator test conditions. 50

Table 3.2 – Active magentic regenerator test conditions. . . . 51

Table 3.3 – Dimensions of the NHC array obtained from the analytical design procedure. 58

Table 3.4 – Displaced volume (V_{pump}) [cm^3] used in the experiments. 63

Table 3.5 – Packed bed of spheres passive regenerators. . . . 69

Table 3.6 – Void volume fractions for different casings and sizes of R-T adapters. 70

Table 3.7 – Casing #7 - zero void volume regenerator design. 72

Table 3.8 – Characteristics of the passive regenerators. 74

Table 3.9 – Characteristics of the AMR regenerators. 76

Table 3.10 – Summary of the instrumentation. 79

Table 3.11 – Main components of the National Instruments data acquisition system. 79

Table 4.1 – Variables in the momentum equation. 112

Table 4.2 – Variables in the energy equations. 115

Table 4.3 – Variables in the void volume model. 119

Table 4.4 – Variables in the casing heat transfer model. . . . 124

Table 4.5 – Porous medium heat transfer model meshes. . . . 129

Table 4.6 – Simulations cases used in the mesh evaluation. . 129

Table 4.7 – Mesh evaluation for passive regenerators. 129

Table 4.8 – Mesh evaluation for AMRs. 131

Table 4.9 – Mesh evaluation of the void volume model. . . . 132

Table 4.10 – Mesh evaluation to wall heat transfer model. . . 132

Table 4.11 – Operating conditions of the simulated cases to compare the different MCE implementations. 138

Table 5.1 – Geometry and operating conditions of the experimental tests to evaluate the time-dependent temperature measurements. 143

Table 5.2 – Reproducibility tests. 160

Table 6.1 – Impact of the casing heat gain on the cycle average cooling capacity for different values of ΔT_{Hex}, for $\phi \approx 0.38$ and $f = 0.25$ Hz. 248

Table 6.2 – Impact of the casing heat gain on the cycle average cooling capacity for different values of f, for $\phi \approx 0.38$ and ΔT_{Hex} of 25 K. 248

Table 6.3 – Impact of the casing heat gain on the cycle average cooling capacity for different values of ϕ, for $f = 0.25$ Hz and ΔT_{Hex} of 25 K. 251

Table 6.4 – Demagnetizing factors for the different AMR matrices. 260

Table 7.1 – Ranges of the geometric variables for each PEC of the passive regenerator optimization. 281

Table 7.2 – Constraints of the regenerator analysis for the **VG** and **FA** PEC for a fixed frequency and a variable mass flow rate in the passive regenerator optimization. . 283

Table 7.3 – Constraints of the regenerator analysis for the **VG** and **FA** PEC for a fixed mass flow rate and a variable frequency in the passive regenerator optimization. . . . 283

Table 7.4 – Parameters of the case study on the contributions to the total entropy generation. 288

Table 7.5 – Minimum S_g parameters for the **VG** PEC for $\epsilon = 95\%$, at a fixed frequency of 1 Hz and flow rates between 40 and 100 kg/h. 292

Table 7.6 – Individual contributions to the total entropy at the minimum, $S_{g,min}$, for the **VG** PEC for $\epsilon = 95\%$, at a fixed frequency of 1 Hz and flow rates between 40 and 100 kg/h. 292

Table 7.7 – Minimum S_g parameters for the **VG** PEC for $\epsilon = 95\%$, at a fixed mass flow rate of 60 kg/h and frequencies between 1 and 4 Hz. 295

Table 7.8 – Individual contributions to the total entropy at the minimum, $S_{g,min}$, for the **VG** PEC for $\epsilon = 95\%$, at a fixed mass flow rate of 60 kg/h and frequencies between 1 and 4 Hz. 295

Table 7.9 – Minimum S_g parameters for the **FA** PEC for $\epsilon = 95\%$, at a fixed frequency of 1 Hz and variable flow rates between 100 and 300 kg/h. 299

Table 7.10 – Individual contributions to the total entropy at the minimum, $S_{g,min}$, for the **FA** PEC for $\epsilon = 95\%$, at a fixed frequency of 1 Hz and variable flow rates between 100 and 300 kg/h. 299

Table 7.11 – Minimum S_g parameters for the **FA** PEC for $\epsilon = 95\%$, at a fixed mass flow rate of 250 kg/h and variable frequency between 1 and 4 Hz. 301

Table 7.12 – Individual contributions to the total entropy at the minimum, $S_{g,min}$, for the **FA** PEC for $\epsilon = 95\%$, at a fixed mass flow rate of 250 kg/h and variable frequency between 1 and 4 Hz. 301

Table 7.13 – Ranges of the geometric variables for each PEC in the AMR optimization. 304

Table 7.14 – Minimum S_g parameters for the **VG** PEC for $\overline{\dot{Q}}_c = 20$ W per regenerator and $\Delta T_{Hex} = 15$ K, at a fixed frequency of 1 Hz and flow rates between 40 and 100 kg/h. 308

Table 7.15 –Ideal Halbach cylinder dimensions considering the optimized parameters according to the **VG** PEC for a frequency of 1 Hz and flow rates between 40 and 100 kg/h.313

Table 7.16 – Minimum S_g parameters for the **VG** PEC for $\overline{\dot{Q}}_c = 20$ W per regenerator at $\Delta T_{Hex} = 15$ K, at a fixed mass flow rate of 60 kg/h and frequencies between 1 and 4 Hz. 313

Table 7.17 – Minimum S_g parameters for the **FA** PEC for $\overline{\dot{Q}}_c = 20$ W per regenerator at $\Delta T_{Hex} = 15$ K, at a fixed frequency of 1 Hz and variable flow rates between 50 and 200 kg/h. 317

Table 7.18 –Minimum S_g parameters for the **FA** PEC for $\overline{\dot{Q}}_c = 20$ W per regenerator at $\Delta T_{Hex} = 15$ K, at a fixed mass flow rate of 200 kg/h and variable frequency between 1 and 4 Hz. 321

Table A.1 – $Nd_2Fe_{14}B$ sintered magnet grade properties (BAKKER-MAGNETICS, 2014). 354

Table A.2 – Dimensions of the NHC array obtained from the analytical design procedure. 355

Table A.3 – Magnetic flux densities and Λ_{cool} results for the NHC array obtained from the analytical design procedure.355

Table A.4 – Analytical and 3D COMSOL Multiphysics results for the center of the NHC magnet array. 355

Table A.5 – Results of the design procedure for different lengths of the internal magnet. 359

Table A.6 – Energy product BH (in kJ/m^3) calculated from the 2-D COMSOL simulations of the external and internal magnet arrays. 362

Table A.7 – Comparison of the analytical, 3-D COMSOL simulation and experimental results for the magnetic flux density and figure of merit at the center of the magnet for the constructed NHC system. 369

Nomenclature

Symbols

A	Area	m^2
A_c	Cross sectional area	m^2
A_t	Amplitude of the fluid flow waveform	m/s^2
B	Magnetic flux density	T
Bi	Biot number	-
Br	Brinkman number	-
c	Specific heat capacity	J/kg-K
c_E	Ergun constant	-
C	Thermal capacity	W/K
COP	Coefficient of Performance	-
d	Porous media characteristic diameters	m, mm
D	Diameter	m, mm
$D_{\|\|}$	Longitudinal thermal dispersion	m^2/s
Da	Darcy number	-
e	Thickness	m ,mm
f	Frequency	Hz
f_D	Friction factor	-
F	Forchheimer Number	-
Fo	Fourier number	-

h	Convection heat transfer coefficient	W/m^2-K
H	Magnetic field	A/m
H	Height	m, mm
k	Thermal conductivity	W/m-K
K	Porous media permeability	m^2
ℓ_c	Characteristic length of the porous medium	m
L	Length	m, mm
m	Mass	kg
M	Magnetization	A/m
N_D	Demagnetization factor	-
NTU	Number of heat transfer units	-
NTU_o	Modified number of heat transfer units	-
Nu	Nusselt number	-
P	Pressure	kPa, bar
Pe	Peclet number	-
Pr	Prandtl number	-
$\dot{q}$	Energy rate per unit volume	W/m^3
q''	Heat Flux	W/m^2
Q	Heat	J
$\dot{Q}_C$	Cooling capacity	W
$\Re^*$	Thermal capacity ratio	-
Re	Reynolds number	-
Re_ω	Kinetic Reynolds number	-
s	Specific entropy	J/kg-K
s_k	Piston stroke	mm

S	Entropy	J/K
S_{g}	Entropy generation	J/K
S_{v}	Specific surface area based on the solid volume	1/m
t	time	s
T	Temperature	K
u	Superficial or Darcian velocity	m/s
$u_{\mathrm{D,max}}$	Maximum velocity via Darcy Equation	m/s
U	Overall convective heat transfer coefficient	W/m^2-K
$\vec{v}$	Vector velocity	m/s
V	Volume	m^3
V_{pump}	Displaced volume	cm^3
$\dot{W}$	Power	W
W	Width	m, mm
z	z or axial direction	-

Greek

α	Thermal diffusivity	m^2/s
β	Surface area density of the porous medium	m^2/m^3
β_ϵ	Effectiveness imbalance	-
ϵ	Effectiveness	-
η_{2nd}	Second-Law Efficiency	-
κ^{eff}	Effective thermal conductivity	W/m-K
μ	Dynamic viscosity	Pa-s
ν	Kinematic viscosity	m^2/s
ω	Angular frequency	rad/s
ϕ	Utilization factor	-

ρ	Density	kg/m^3
σ	Specific magnetization	Am^2/kg
θ	Dimensionless temperature	-
Γ	Torque	Nm
ε	Porosity	-
ϑ	Void volume	cm^3
ϑ^*	Void volume fraction	-
ζ	Aspect ratio [-]	

Composed Symbols

ΔP	Pressure difference or Pressure drop	kPa
Δs_{mag}	Magnetic entropy variation	J/kg-K
ΔT	Temperature difference or span	K
ΔT_{ad}	Adiabatic temperature change	T
Δz	Increment of volume length	m, mm
$g(t^*)$	Dimensionless function	-
T_{Curie}	Curie Temperature	K

Constants

μ_0	Magnetic permeability	$4\pi\times10^{-7}$ N/A^2

Abreviations

AMR	Active Magnetic Regenerator
CHG	Casing Heat Gain
DAQ	Data Acquisition
EGM	Entropy Generation Minimization
FA	Fixed Face Area PEC
FG	Fixed Geometry PEC

MCE	Magnetocaloric Effect
MF	Non-uniformity of the magnetic field
MFM	Mass Flow Meter
NHC	Nested Halbach Cylinders
PEC	Performance Evaluation Criteria
VG	Variable Geometry PEC
VV	Void Volume

Sub and Super-Scripts

$*$	Represents non-dimensional variables
$\bar{x}$	Average value
$''$	Indicates fluxes
air	Air layer variables
apl	Applied
blow	One blow period
C	Cold variables
CB	Cold blow period
CE	Cold end
csg	Casing
cyl	cylinder
d_h	Variable based on the hydraulic diameter
d_p	Variable based on the particle diameter
demag	Demagnetization process
eff	Effective
ele	electronic
f	Fluid phase

FAC	Fluid axial heat conduction
geo	Geometry
H	Hot variables
h	hydraulic
HB	Hot blow period
HE	Hot end
HT	Interstitial heat transfer
lat	lattice
mag	Magnetization process
mag	Magnetic
max	Maximum
min	Minimum
p	Particle
Reg	Regenerator bed variables
s	Solid phase
SAC	Solid axial heat conduction
sht	shaft
tot	Total
tub	Tube
VD	Viscous dissipation
vv	Void volume variables
wall	Regenerator housing wall layer variables

Abstract

The research on alternative technologies aims at the development of environmentally-friendly thermal systems with a lower energy consumption. In this context, magnetic refrigeration at near-room temperature stands out as a promising alternative technology for the development of refrigeration systems.

The present thesis advances theoretical and experimental analyses of passive and active magnetic regenerators aiming at applications in refrigeration systems. The study of passive regenerators will provide the basis for the assessment of the active matrices. Therefore, the thesis work was carried out along two research fronts. The first is concerned with the study of the thermal-hydraulic performance of passive regenerators through an evaluation of their effectiveness and viscous losses. The second front is dedicated to the evaluation of active magnetic regenerators as part of a refrigeration cycle, by means of an analysis of the system cooling capacity, temperature difference between the thermal reservoirs and coefficient of performance.

Both fronts have experimental and numerical approaches. In the experimental part, an apparatus for the evaluation of passive and active magnetic regenerators was designed and built. Different matrix geometries (parallel plates, pin arrays and packed beds of spheres) were evaluated in terms of their thermal performances. In the numerical analysis, a mathematical model based on the finite volume method was developed to solve the transient one-dimensional forms of the momentum equation for the fluid flow through the porous matrix and the energy equations for the fluid and solid phases. Different types of losses were included in the model, such as the internal demagnetizing field, heat transfer to the surroundings, axial heat conduction and void volume losses. Finally, a methodology to optimize passive and active regenerators based on the Entropy Generation Minimization theory was proposed and implemented in the numerical model.

Resumo

A pesquisa por tecnologias alternativas busca o desenvolvimento de sistemas térmicos com menor consumo energético e ambientalmente amigáveis. Neste contexto, a refrigeração magnética, baseada no efeito magnetocalórico, se destaca como uma tecnologia alternativa promissora para o desenvolvimento de sistemas de refrigeração.

O presente trabalho de doutoramento tem por objetivo fazer uma análise teórico-experimental de regeneradores passivos e magnético-ativos para aplicações em sistemas de refrigeração. O estudo de matrizes regenerativas passivas servirá de base para a avaliação das matrizes ativas. Logo, o trabalho desenrola-se em duas frentes de pesquisa. A primeira tem como objetivo estudar o desempenho térmico e hidrodinâmico de regeneradores passivos por meio da avaliação da efetividade e perdas viscosas. A segunda frente tem como objetivo avaliar regeneradores magnético-ativos quanto a sua aplicação em um ciclo de refrigeração, sendo extraídas informações acerca da capacidade de refrigeração, da diferença de temperaturas entre os reservatórios térmicos do sistema e do coeficiente de performance.

Ambas as frentes de pesquisa terão abordagem experimental e numérica. Na primeira, foi projetado e construído um aparato para a avaliação de regeneradores passivos e magnético-ativos, além da fabricação de diferentes geometrias de matrizes (placas paralelas, banco de pinos e leito de esferas) para a avaliação e comparação de seus respectivos desempenhos térmicos. Já na abordagem numérica, foi desenvolvido um modelo unidimensional e transiente, baseado em volumes finitos, o qual resolve a equação da quantidade de movimento para meios porosos e as equações da energia para as fases fluida e sólida de forma acoplada. Diferentes tipos de perdas como o campo desmagnetizante interno, além de perdas térmicas para o ambiente, condução axial e volume morto foram incluídas no modelo. Por fim, é proposta uma metodologia de otimização de regeneradores baseada na Teoria da Minimização da Entropia, implementada no modelo numérico.

1 Introduction

Refrigeration is concerned with the cooling of bodies or fluids to temperatures lower than those available in the surroundings at a particular time and place (GOSNEY, 1982). The development of cooling systems expanded the possibilities in food storage, transport, conservation and thermal comfort. Certainly, refrigerators and air-conditioning systems were fundamental to the evolution of the quality of life enjoyed in our society.

The most conventional cooling technology is based on the mechanical compression and expansion of a vapor. The first compressors and refrigerators were over-designed, heavy and inefficient. However, vapor compression technologies experienced numerous developments in the 20th century. As a result, the compressors used today in a range of domestic and commercial applications are small, inexpensive and efficient, thus making the mechanical compression of refrigerants the dominant technology for a host of cooling applications.

Over the last three decades or so, environmental and energy policies are being imposed to restrict the use of non-environmentally friendly substances and low efficiency conversion systems. As a result, the use of CFC and HCFC refrigerants that contribute to global warming and ozone layer depletion has been suspended in several countries (UNITED NATIONS, 2015).

Possible replacements of the non-environmentally friendly substances are the natural refrigerants, such as CO_2 (R-744) and hydrocarbons, but these may have some disadvantages in terms of energy efficiency (GIROTTO *et al.*, 2004) or undesired physical-chemical properties such as flammability. Therefore, new technologies that are not based on the use of harmful fluids and are capable of developing thermodynamic efficiencies at similar levels are being sought. In this scenario, magnetic

refrigeration is the one of the leading contenders among the so-called emerging technologies for the development of cooling and heat pumping systems.

Magnetic cooling does not rely on volatile refrigerants, as a magnetic solid material is used as the refrigerant and an aqueous solution is the heat transfer agent between the magnetic material and the thermal reservoirs. Magnetic coolers can operate at low absolute pressures, are conceptually simpler than vapor compression equipment, since they can be designed with fewer moving parts to generate less mechanical vibration and noise (YU *et al.*, 2003; PECHARSKY; GSCHNEIDNER JR., 2006; GSCHNEIDNER JR.; PECHARSKY, 2008). Magnets can, in principle, be recycled or reused in more advanced refrigerators, which constitutes an economic benefit compared to other technologies. Finally, and more importantly, magnetic refrigeration has the potential to be thermodynamically more efficient, since it is, in principle, easier to perform a reversible magnetization of a magnetic material than a reversible compression of a gas or vapor. As will be discussed later, the magnetocaloric effect is reversible.

Fig. 1.1 compares the Carnot cycles for gas compression and magnetic refrigeration. The gas compression system is based on the fundamental processes of isentropic compression, (0)-(1), and expansion, (2)-(3), between the hot and cold reservoirs. Heat is removed isothermally from a cold reservoir (at T_{C}), (3)-(0), and rejected isothermally at the hot reservoir (at T_{H}), (1)-(2). The difference between Q_H and Q_C is equal to the net mechanical work transferred to the system.

The magnetic cooling system is based on the fundamental process of adiabatic magnetization, (0)-(1), and demagnetization, (2)-(3). In this case, changes in magnetic flux density (ΔB) are responsible for establishing a temperature difference between the hot and cold reservoirs, at T_{H} and T_{C}, respectively. Similarly, the difference between Q_H and Q_C is equal to the net magnetic work transfer to the system (STEYERT, 1978; KITANOVSKI; EGOLF, 2006). The temperature variation of the solid magnetic material when the external magnetic flux density is changed under adiabatic conditions is called the Magnetocaloric Effect (MCE).

Vapor compression systems can generate temperature spans between the hot and cold reservoirs of the order of 40 to 70 K, which correspond to pressure changes between 10 and 20 bar for most refrigerants. These are typical operating conditions for the majority of compres-

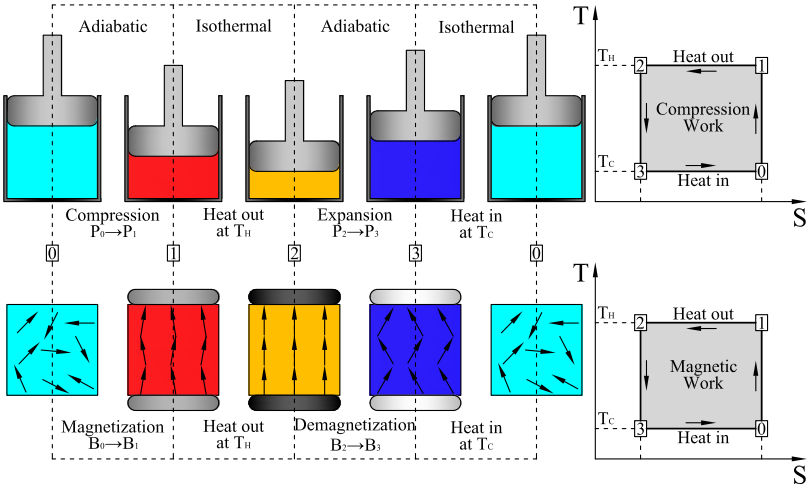

Figure 1.1 – Carnot cycle comparison between vapor compression and magnetic refrigeration. Adapted from Russek and Zimm (2006).

sors in vapor compression systems. On the other hand, the MCE is of the order of a few degrees Kelvin, even for large magnetic flux density variations. For example, the benchmark magnetocaloric material for near room temperature applications, gadolinium (Gd), has a peak MCE around 15 K for a ΔB of 7.5 T (DAN´KOV *et al.*, 1998). At a more realistic operating condition, ΔB is expected to be around 1.0 T, for which the peak MCE is about 3.0 K (BAHL; NIELSEN, 2009). Therefore, even for large magnetic flux densities variations, the best known magnetocaloric materials are not capable of providing temperature differences compatible with those observed in gas or vapor compression technologies.

To overcome this thermodynamic limitation, magnetic cooling systems are based on regenerative cycles, in which the solid refrigerant is assembled as a regenerative matrix, and a heat transfer fluid is used as a thermal exchange medium between the refrigerant and the cold and hot reservoirs. As a result of the intermittent heat transfer between the solid matrix and the fluid during processes in an appropriate thermomagnetic cycle, such as the Brayton Cycle, the regenerator amplifies the temperature difference between the hot and cold reservoirs (temperature span). This type of regenerator is called the Active Magnetic Regenerator (AMR) (BARCLAY; STEYERT, 1982). Tura (2005) obtained

experimentally a temperature span of 50 K for a ΔB of 2.0 T in an AMR composed of Gd-alloys for which the peak MCE is approximately 6.0 K for the same ΔB (i.e., a gain factor of eight or so for the temperature span).

The use of thermal regenerators in magnetic cooling cycles brings about several technical challenges. The first one is the manufacture complexity of the magnetocaloric material in an appropriate geometry that can be used as a regenerative matrix, such as spheres, parallel plates, wire meshes or pin arrays. Secondly, the operational complexity is increased, as complex sealing and flow distribution systems are required to generate oscillating or bidirectional flows through the regenerative matrix (KUPPAN, 2000). Additionally, matrices are compact porous media which, when processing an aqueous heat transfer fluid, may cause a dramatic increase in viscous losses and pumping power.

Single-phase heat transfer between the process fluid (thermal agent) in the regenerator and in the heat exchangers connected to the thermal reservoirs increases the system irreversibilities due to sensible heat transfer with a finite temperature difference. Thus, bigger heat transfer surface areas are required in both, hot and cold, heat exchangers, which increases the geometric complexity and the viscous losses.

Other technical challenges are related to the magnetic field generation. Joule heating of the magnetic circuit together with restrictions to magnetic flux densities in excess of 2 T due to health and safety issues (e.g., in domestic applications) limit the range of possibilities for the magnetic field generation to rare earth permanent magnet circuits (KITANOVSKI *et al.*, 2015). Monfared *et al.* (2014) presented a comprehensive life cycle assessment of both magnetic and vapor-compression refrigerators. They concluded that the designation of environmentally friendly technology is questionable when considerable amounts of rare earth metals are required to build a magnetic refrigerator. Clearly, the high costs involved in the use of rare earth based permanent magnets and magnetocaloric materials is another important economic limitation.

The above discussion exposed some of the main limitations and challenges for the technological development of magnetic cooling systems. In this context, a specific research project on thermal regeneration can contribute significantly to the field of magnetic refrigeration. Parameters such as matrix (bed) geometry, casing geometry/dimensions, and the identification and minimization of different types of losses (thermal,

hydrodynamic and magnetic losses) must be investigated systematically in order to improve and optimize the existing magnetic cooling devices or design more efficient ones. A list of desirable characteristics in a thermal regenerator for magnetic cooling applications is as follows:

- High thermal effectiveness due to low heat transfer irreversibilities;
- Small viscous losses, resulting in simpler and smaller pumping systems;
- Small magnetic losses, resulting in a large MCE;
- Compactness, resulting in lower torques, less mechanical losses and smaller motors. As a result, lighter magnetic circuits can be employed, using smaller quantities of rare earth-based materials.

1.1 Objectives and Contributions

The objective of the present thesis is to investigate experimentally and numerically the behavior of active magnetic regenerators in order to optimize their performance, considering different matrix geometries.

To accomplish this objective, an evaluation of both, *passive* and *active*, matrices with identical geometries and operating at the same conditions was carried out. In passive regenerators, the magnetic field is not present, which facilitates the differentiation between losses that are common to both types of regenerators and those that are exclusive to active magnetic regenerators. This way, experiments with passive matrices may help to quantify the influence of the porous medium geometry on the thermal-hydraulic performance of the regenerator independently of losses taking place in the presence of a change in magnetic field (i.e., magnetic losses).

To enable the development of this research work, the following actions were pursued:

- Design and build a versatile experimental apparatus to evaluate passive and active magnetic regenerators, for a variety of operating conditions and matrix geometries;

- Develop a one-dimensional, transient finite volume-based numerical model to evaluate and optimize the performance of passive and active magnetic regenerators.

The project was divided in two stages. The first stage involved the study of the thermal-hydraulic aspects of oscillating-flow passive regenerators. The impact of the regenerative matrix geometry on the heat transfer and on the viscous and thermal losses were studied experimentally and numerically using conventional materials for the regenerator matrix (e.g., stainless steel). The following specific objectives have been defined for this part of the study:

- Perform experimental tests to determine the time-dependent temperature and pressure change behaviors in regenerators filled with different regenerative matrix geometries (packed spheres, pin arrays and parallel plates). The independent operating parameters are the mass flow rate and the frequency;
- Compare the experimental results for the different matrix geometries in terms of (i) the regenerator effectiveness as a function of the number of transfer units and (ii) the pressure drop as a function of the particle Reynolds number. Analysis such as these help to quantify the influence of thermal-hydraulic losses, such as axial conduction and viscous friction, on the regenerator performance;
- Perform numerical simulations in order to reproduce the experimental results;
- With the assistance of the numerical model, identify the appropriate closure relationships for fluid flow and heat transfer for each specific regenerative matrix geometry;
- Propose an optimization procedure for passive regenerators based on the Entropy Generation Minimization theory (BEJAN, 1995) combined with the Performance Evaluation Criteria of Webb and Kim (2005).

The second stage was concerned with the thermal-hydraulic and magnetic aspects of active magnetic regenerators, thus enabling a more in-depth analysis of the impact of the magnetic losses on the AMR performance. The specific objectives for this part of the study are as follows:

- Perform experimental tests to determine the time-dependent temperature and pressure change behaviors in active magnetic regenerators filled with different matrix geometries (packed spheres, pin arrays and parallel plates). The time-dependent torque required to rotate the magnet system is also evaluated experimentally. The independent operating parameters are the mass flow rate, frequency and the thermal load applied on the cold side;

- Incorporate the thermo-magnetic phenomena in the numerical model and perform numerical simulations to reproduce the experimental results;

- Compare the experimental results for the different matrix geometries in terms of the temperature span, cooling capacity, coefficient of performance and second-law efficiency. Analysis such as these help to quantify the influence of both, thermal-hydraulic and magnetic, losses on the AMR performance;

- Propose an optimization procedure for active magnetic regenerators based on the Entropy Generation Minimization theory (BEJAN, 1995) combined with the Performance Evaluation Criteria of Webb and Kim (2005).

1.2 Outline of the Thesis

The present thesis was divided into eight chapters as follows. In Chapter 2 - *Fundamentals and State of the Art of Thermal Regenerators* - the fundamentals and the state of the art of thermal regenerators are presented, from their basic operation as passive storage devices to their application in magnetic refrigeration. The thermodynamics of the magnetocaloric effect is also discussed. Additionally, a review about modeling and optimization of regenerators is presented. Chapter 3 - *Experimental Apparatus* - describes the design and construction of the laboratory apparatus, the experimental procedure and data processing for the passive and active magnetic regenerator experiments. Chapter 4 - *Problem Formulation and Solution Method* - describes the numerical modeling of passive and active magnetic regenerators, including the modeling of the thermo-magnetic phenomena and the different types of losses, i.e., the thermal-hydraulic and magnetic losses. Chapter 5 - *Passive Thermal Regenerators* - presents the experimental and numerical results for the passive regenerators, including a comparison between

the thermal performances of the different matrix geometries. A detailed accounting of the passive regenerator losses (e.g., void volume, entrance losses) is carried out. Chapter 6 - *Active Magnetic Regenerators* - presents the experimental data and numerical results for the active magnetic regenerators, including a comparison between different matrix geometries. As with the passive regenerators, the thermal and magnetic losses in the active regenerators are quantified and discussed. Chapter 7 - *Optimization of Thermal Regenerators* - describes the Entropy Generation Minimization-based method developed to design passive and active magnetic regenerators. Finally, Chapter 8 summarizes the final considerations and recommendations for future work.

2 Fundamentals and State of the Art of Thermal Regenerators

In 1816, Robert Stirling built the first regenerative hot air engine. Later, in 1834, it was suggested by John Herschel that regenerative engines could be used as refrigerators. More than 100 years later, in 1959, Gifford and McMahon developed a regenerative cryogenic refrigerator to cool infrared detectors and laser amplifiers (ACKERMANN, 1997). Nearly two decades later, Brown (1976) developed the first near room-temperature magnetic heat pump and, a few years after that, Barclay and Steyert (1982) patented the active magnetic regenerator. However, a greater interest in magnetic cooling near the room temperature emerged mainly after 1997 with the discovery of special alloys with the so-called 'giant' magnetocaloric effect by Pecharsky and Gschneidner Jr. (1997a). After that, several developments in magnetocaloric materials and magnetic cooling systems have been reported in the open literature (YU *et al.*, 2010; SMITH *et al.*, 2012; KITANOVSKI *et al.*, 2015).

This chapter reviews the fundamentals of thermal regeneration, with a special emphasis on the coupling of regenerator modeling with the magnetocaloric effect associated with the solid matrix. This combination results in a unique regenerator type, the active magnetic regenerator (AMR), which is one of the focal points of this thesis. After presenting the basics of the AMR cycle, some approaches to optimize AMRs are reviewed.

2.1 Applications of Thermal Regenerators

Regenerators are storage-type heat exchangers in which hot and cold fluid streams flow in alternating directions through a porous matrix, giving rise to intermittent heat transfer between the solid and the fluid. The regenerative matrix (or simply matrix) is the porous medium composed by solid material processed in a specified bed geometry (SCHMIDT; WILLMOTT, 1981; HAUSEN, 1983; ACKERMANN, 1997; KUPPAN, 2000; SHAH; SEKULIĆ, 2003; NELLIS; KLEIN, 2009). Thermal regenerators have several industrial applications, such as waste heat recovery in gas turbine or steam power plants and as internal heat exchangers in thermodynamic cycles (KUPPAN, 2000).

In cooling technologies, the applications of regenerative heat exchangers can be classified according to the temperature range and type of heat transfer fluid. Gases are much more common than liquids and are the thermal agents in a number of cryogenic and low-temperature cycles, such as the Stirling, pulse-tube, thermoacoustic, Gifford- McMahon and Vuillemier cycles (KUPPAN, 2000; SHAH; SEKULIĆ, 2003). Regenerators that use liquids as thermal fluids are encountered in near room-temperature conditions involving some magnetocaloric and electrocaloric cooling cycles (OZBOLT *et al.*, 2014; KITANOVSKI *et al.*, 2015).

During the hot-to-cold blow (or simply hot blow), the fluid at a higher temperature exchanges heat with the solid phase, warming up the matrix that stores thermal energy from the fluid phase. In the cold-to-hot blow (or simply cold blow), the matrix releases the stored energy as heat, warming up the fluid. As the matrix is alternately exposed to the hot and cold streams, its temperature and that of the fluid vary as a function of time. Thus, a so-called periodically developed condition is observed after a number of cycles, in which the variations of temperature with time (for the solid and fluid phases) are the same during successive cycles.

The duration of the time periods of the hot and cold blows should allow for heat transfer between the solid and the fluid at every position of the matrix. Thus, temperature, pressure, flow velocity and thermophysical properties are essentially both time and space dependent. This distinguishes regenerators from recuperators, where in the latter heat is transferred between two continual fluid streams across a fixed boundary. At steady state, the properties of both streams depend only on the spatial position (KUPPAN, 2000).

Due to the intermittent heat transfer and alternating flow condition, the following are desirable characteristics in a regenerator matrix (SHAH; SEKULIĆ, 2003; KUPPAN, 2000):

1. High volumetric heat capacity;
2. Compact, for minimum volume and reduction of the void space;
3. Large thermal conductance, which can be achieved with a large heat transfer area per unit of volume and/or a high convective (interstitial) heat transfer coefficient;
4. High permeability and non-obstructed porous media to minimize the viscous losses;
5. Axially discontinuous and/or highly thermally resistant in the flow direction to minimize axial heat conduction.

2.2 Types of Regenerators

There are two basic regenerator designs: the fixed-bed (or stationary) and the rotary, as presented in Fig. 2.1. To perform the alternating flow periods, in the fixed-bed the hot and cold streams must be continuously alternated by means of directional valves, such as rotary, linear or solenoid valves and check valves. On the other hand, in the case of a rotary regenerator the regenerative matrix must be rotated periodically into and out of the fixed streams (KUPPAN, 2000; SHAH; SEKULIĆ, 2003; NELLIS; KLEIN, 2009).

Fig. 2.1(a) illustrates the single matrix fixed-bed regenerator. In this case, the overall cycle is discontinuous, since the heat interactions with the thermal reservoirs occur only in a fraction of the total cycle period. The hot blow period takes a fraction of the total period, where the black lines represent the flow direction from the hot to the cold reservoir, passing through the regenerator. Next, the fluid exiting the regenerator interacts with the cold reservoir. The remaining period fraction is dedicated to the cold blow, where by means of switch (rotary, linear or solenoid) valves or a double effect pump, the flow direction is alternated (black lines), and the fluid exiting the regenerator now interacts with the hot reservoir. To have a continuous cycle in stationary regenerators, multiple beds can be employed in parallel. In this case, the

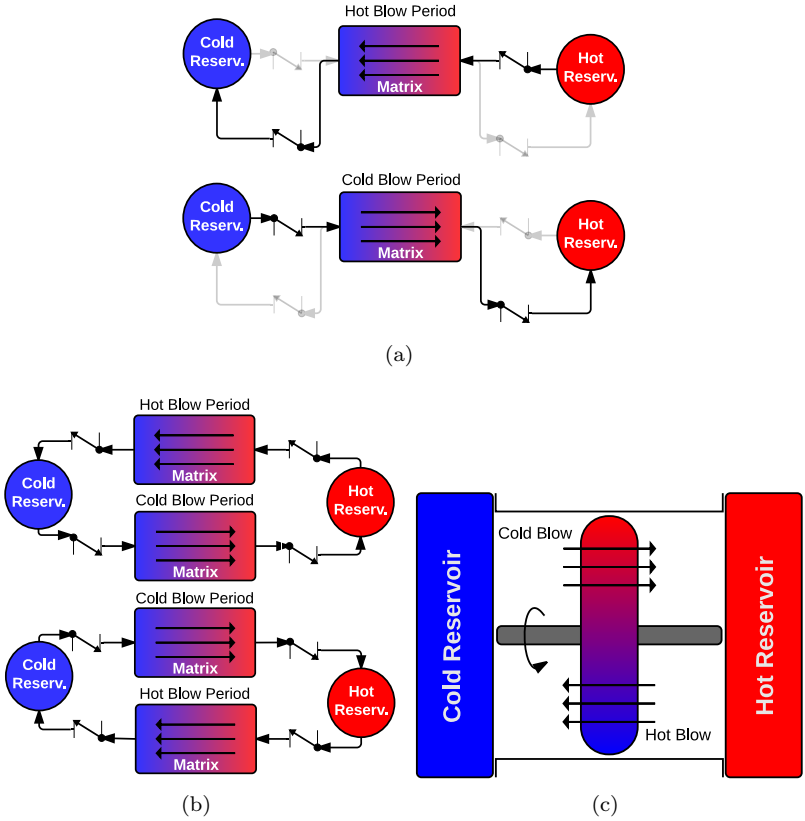

Figure 2.1 – Regenerator types: (a) Single fixed-bed; (b) Multiple fixed-bed; (c) Rotary. Adapted from Nellis and Klein (2009).

heat interactions with the cold and hot reservoirs are performed during the entire cycle. Fig. 2.1(b) illustrates the case of a multiple fixed-bed regenerator, where the alternating flow in the matrix is achieved by changing the position of a switch (rotary, linear or solenoid) valve or a double effect pump. The rotary type regenerator is presented in Fig. 2.1(c), where the hot and cold streams are generated by rotating the matrix, thus ensuring a continuous cycle. In this case, the heat interactions with the cold and hot reservoirs are performed during the whole cycle.

While fixed-bed regenerators are simpler to build and maintain, and

are less prone to leakages, they are usually less compact (smaller surface area per unit volume) and are more difficult to operate at high frequencies than rotary-type regenerators.

2.3 Merits of Regenerators

A discussion about the desirable characteristics and types of regenerators enables highlighting the advantages and disadvantages of regenerators compared to other kinds of heat exchangers, such as fluid-fluid heat exchangers (recuperators). The main advantages are follows: (KUPPAN, 2000; KREITH, 2000; NELLIS; KLEIN, 2009)

1. Simplicity: a regenerator matrix can be as simple as a bed of particles, eliminating the need for complex accessories, such as elaborated gaskets and headers;

2. Compactness: regenerators can be designed for a large heat transfer area per unit matrix volume;

3. Cost: it is possible to obtain a thermal effectiveness approaching unity using inexpensive solid materials in a compact arrangement;

In contrast, the following disadvantages can be listed:

1. Large matrix heat capacity: to achieve a high thermal effectiveness, the heat capacity of the solid matrix has to be larger than that of the working fluid. This is a special concern when the working fluid is an aqueous solution, which may result in a heavy regenerator;

2. Friction losses: highly compact regenerators (i.e., with a large surface area density) can produce high viscous losses;

3. Alternating flow: changes of flow direction (in fixed-bed units) result in additional flow irreversibilities, increasing the regenerator pressure drop;

4. Leakages: the performance of regenerators is very sensitive to leakages, which may result in undesired mixing of the streams (SHAH; SEKULIĆ, 2003). Pressure leakages are caused by pressure

differences between the hot and cold streams and are of special concern in gas regenerators. Carryover leakages in a gas regenerator are the transport of trapped fluid in the void spaces of the matrix to the other fluid side due to matrix rotation. In a fixed-bed regenerator, the carryover leakage corresponds to the fluid that changes its direction outside the regenerator, i.e., in the headers and/or in the spaces between each thermal reservoir and the nearest regenerator end (see Fig. 2.1(a)). Also known as void (or dead) volume losses, carryover losses in single fixed-bed regenerators impose a penalty on the regenerator thermal performance as they correspond to a fluid volume that has been displaced but does not interact thermally with the thermal reservoirs, thereby producing neither a cooling nor a heating effect at the reservoirs.

2.4 Thermal Fluids Used in Regenerators

2.4.1 Gases

As mentioned above, cryogenics is the main field of application of thermal regenerators that employ gases as heat transfer fluids. Ackermann (1997) presents a comprehensive discussion of the theory and design of regenerative heat exchangers for cryogenic applications. The Stirling cryocooler (piston-displacer configuration), illustrated in Fig. 2.2, is used in many cryogenic applications, including cooling of spacecraft instruments, infrared thermal imaging systems and superconducting elements. Ibrahim and Tew Jr (2012) reviewed the latest developments in regenerator research, from modeling and computational fluid dynamics (CFD) analyses to applications of Stirling regenerators.

Noble gases, such as helium (He), are the preferred thermal fluid in gas regenerators for their high specific heat capacity ratio. The Stirling cycle starts with the compression, (1)-(2), of the gas by the power piston, while heat, Q_{H}, is rejected to the external ambient to achieve a near isothermal compression, at T_{H}. Next, in process (2)-(3), the displacer piston moves the high-pressure gas through the regenerator where the hot gas releases heat to the matrix and is cooled to a lower operating temperature. This process occurs approximately at a constant volume. The cold high-pressure gas coming from the regenerator is expanded, in process (3)-(4), by the coupled motion of the power and displacer

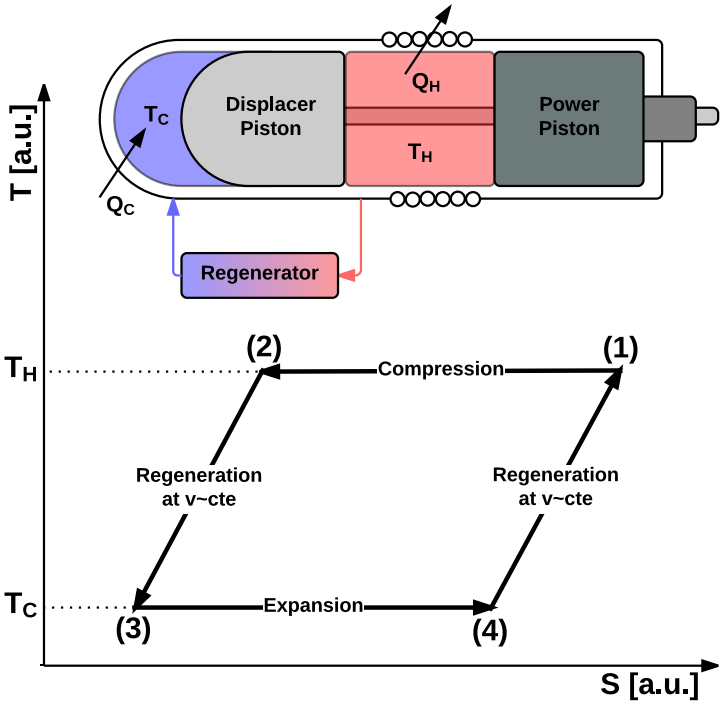

Figure 2.2 – Schematic Stirling cryocooler and corresponding T-S diagram. Adapted from Kreith (2000).

pistons, while the heat load, Q_C, is transferred to the gas from the low-temperature region at the cold end of the cylinder to achieve a near-isothermal expansion, at T_C. Finally, in process (4)-(1), the cold low-pressure gas flows back through the regenerator driven by the displacer piston. The gas receives heat from the matrix and is warmed up before returning to the initial condition (KREITH, 2000).

de Boer (1994, 1995) presented a thermodynamic analyses of pulse-tube refrigerators with and without regenerators. The results led to the conclusion that the use of a regenerator increases significantly the heat removal per cycle, the coefficient of performance and the refrigeration (i.e., second-law) efficiency. These results show the importance of the application of regenerators in thermodynamic cycles and can be extended to clarify the importance of optimized regenerators design.

A number of experimental and numerical approaches have been developed to study the fluid flow and heat transfer in passive regenerators working with gases under oscillating flow conditions (GEDEON; WOOD, 1996; JU *et al.*, 1998; LEE *et al.*, 1998; NAM; JEONG, 2005, 2006; CHEN *et al.*, 2007; CHA *et al.*, 2008; JU; SHEN, 2009). The general objectives of these works are to predict and correlate the friction factor and Nusselt number to overcome the inaccuracies of conventional models for steady state, which tend to fail at high oscillating frequencies (> 10 Hz). The prediction methods were developed for a range of different geometries, such as wire meshes, parallel wires, tubes and plates, and different porosities (generally higher than 0.6, which is usual for gas applications).

2.4.2 Liquids

The application of liquids as thermal fluids in regenerators gained more importance with the development of magneto and electrocaloric cooling systems (OZBOLT *et al.*, 2014; KITANOVSKI *et al.*, 2015). However, most models available in the literature are based on relationships for steady-state porous media, single blow or oscillating-flow regenerators that use low Prandtl-number fluids, i.e., gases.

Marconnet (2007) designed and built a single-blow regenerator test setup to study heat transfer in packed beds of spheres using water and water-glycol mixtures as heat transfer fluids. The proposed approach was to compare the experimental and the numerical time-dependent temperature data to adjust the A and B constants of the Nusselt number correlation of Wakao and Kaguei (1982)[1], given by,

$$Nu = A + BRe_{\mathrm{D}}^{3/5} Pr^{1/3} \tag{2.1}$$

Frischmann *et al.* (2008), Engelbrecht (2008) and Knauf *et al.* (2008) used the same apparatus as Marconnet (2007) to evaluate the performance of friction factor and Nusselt number correlations for packed spheres. The general conclusion was that the Wakao and Kaguei (1982) correlation overestimated the Nusselt number for aqueous solutions as

[1] Wakao and Kaguei (1982) derived their correlation from experimental results that used gases as heat transfer fluid. A more in-depth discussion about the validity of this correlation for aqueous fluids will be presented later in this thesis.

heat transfer fluids at low Reynolds numbers (< 100). On the other hand, the well established correlation of MacDonald *et al.* (1979) for the friction factor in packed bed porous media gave satisfactory results, with deviations of the order of the experimental uncertainties.

Schopfer (2010) investigated both experimentally and theoretically the thermal-hydraulic behavior of oscillating-flow regenerators using water as the heat transfer fluid. Two different matrix geometries were studied: packed beds of spheres and micro-channels. Schopfer (2010) proposed a new Nusselt number correlation for both geometries in terms of a dimensionless frequency known as the kinetic Reynolds number (SIMON; SEUME, 1988). The Nusselt number results for the packed bed of spheres exhibited different trends with respect to the single-blow experimental results of Engelbrecht (2008). On the other hand, the friction factor results showed a fair agreement with the model predictions, of the order of the experimental uncertainties.

Engelbrecht *et al.* (2011) investigated the effects of porosity, corrugation angle and the presence of dimples on the performance of parallel plate regenerators. The plates were made of aluminum with 0.4 mm thickness. The experimental analysis was carried out for a range of cycle periods and utilization values. The best performance was found for a 90° corrugated plate regenerator. Also, a decrease of the porosity by reducing the plate spacing did not result in a significant increase in performance, although the heat transfer coefficient was expected to increase with the plate spacing.

Scarpa *et al.* (2012) developed a Kalman filter-based inverse method and applied it to numerically simulated experiments to determine the interstitial convective heat transfer coefficient in regenerators using liquids. A one-dimensional model was used to describe the heat transfer in the regenerator. The identification (reconstruction) of the heat transfer coefficient was based on the inlet and outlet fluid temperatures. The authors demonstrated that there was an optimal operating frequency of the inlet fluid temperature at which the heat transfer coefficient could be determined with the greatest precision (minimum standard deviation). At the time of the study, the model had not been applied to real data and the influences of parameters such as mass flow rate and effective conductivities of both the fluid and solid matrix had not been quantified.

Trevizoli *et al.* (2013, 2014) performed experiments with passive regenerators using water as the thermal fluid. The study aimed at quanti-

fying the fluid pumping power and the regenerator heat transfer effectiveness as a function of operating parameters such as frequency and utilization factor. Three different packed beds were used: 1-mm diameter stainless steel spheres, 0.5-mm diameter lead spheres and 0.5-mm diameter gadolinium spheres. For equivalent ranges of utilization, all matrices presented a high effectiveness, with the lead matrix showing the highest effectiveness and the smallest pumping power, due to a combination of large surface area per unit volume (small particle diameter) and low mass flow rates (large NTU). However, due to the low fluid velocities, the lead matrix was more susceptible to axial conduction losses. The gadolinium matrix exhibited a large effectiveness imbalance between the cold and hot blows due to a strong variation of the solid specific heat capacity with temperature. The Gd matrix also exhibited the highest viscous losses due to the small particle size and high superficial velocities, for the same utilization ranges.

Although the number of studies on the performance of passive regenerators using liquids has increased in the past decade, a systematic study on the subject is still lacking. New data and improved models are therefore extremely valuable for the development of improved methods for active magnetocaloric regenerators. Without the need to deal with the magnetocaloric phenomena during the early stages of the development, the test regenerators can be manufactured with more conventional materials, at a much lower cost. This enables evaluating other promising regenerative matrix geometries for application in AMRs, such as parallel plates, packed beds of spheres or irregular particles, and pin arrays.

2.5 The Ideal Regenerator

In a perfectly insulated regenerator with an infinite heat transfer (interstitial) area, the fluid temperature exiting the cold end, $T_{\mathrm{f}}|_{\mathrm{CE}}$, will be equal to the temperature of the cold reservoir, T_{C}. Conversely, the fluid temperature exiting the hot end, $T_{\mathrm{f}}|_{\mathrm{HE}}$, will be equal to the temperature of the hot reservoir, T_{H}. In this externally reversible situation, the thermal effectiveness of the regenerator is 100%. However, this does not guarantee the internal reversibility. In order for a regenerator to be cast as ideal (internally reversible), the following hypotheses must be fulfilled:

1. Constant fluid and solid properties;
2. Constant flow velocity;
3. No fluid leakage;
4. Constant inlet fluid temperature;
5. Negligible thermal resistance in the transverse direction (normal to the flow);
6. Infinite heat conduction resistance in the streamwise direction;
7. Uniform interstitial heat transfer coefficient[2];
8. No losses to the surrounding and no mixing of streams;
9. Negligible thermal capacity of the fluid compared to that of the solid matrix.

The latter assumption translates into the following relationship:

$$\frac{(mc_{\mathrm{p}})|_{\mathrm{f}}}{(mc)|_{\mathrm{s}}} << 1 \tag{2.2}$$

where c and c_{p} are the specific heat capacities of the solid and fluid phases, respectively, and m is the mass of each phase. The subscripts 's' and 'f' stand for the solid and fluid phases, respectively.

Generally, for regenerators operating with gases, the thermal capacity ratio constraint presented in Eq. (2.2) is easily fulfilled. Important exceptions are the helium cryogenic regenerators, for which at 6 K the heat capacity of the fluid becomes one order of magnitude larger than that of the matrix (ACKERMANN, 1997). On the other hand, in passive and active magnetic regenerators using aqueous solutions as thermal agents, Eq. (2.2) is hardly ever valid. For AMRs, the thermal capacity ratio varies from 0.1 to much grater than 1 and, in general, the performance peaks is around 1. In the AMR literature, the thermal capacity ratio is commonly referred to as the utilization factor (or simply utilization) (NELLIS; KLEIN, 2009).

[2]Ideally, the convective heat transfer coefficient should approach infinity.

The heat transfer in an ideal regenerator is modeled mathematically by the following differential heat balances in the solid and fluid phases (SCHMIDT; WILLMOTT, 1981; ACKERMANN, 1997; NELLIS; KLEIN, 2009):

$$(mc)|_{\mathrm{s}} \frac{\partial T_{\mathrm{s}}}{\partial t} = h A_{\mathrm{HT}} (T_{\mathrm{s}} - T_{\mathrm{f}}) \tag{2.3}$$

$$0 = h \frac{A_{\mathrm{HT}}}{L} (T_{\mathrm{f}} - T_{\mathrm{s}}) + (\dot{m} c_{\mathrm{p}})|_{\mathrm{f}} \frac{\partial T_{\mathrm{f}}}{\partial z} \tag{2.4}$$

where h is the convective heat transfer coefficient, A_{HT} is the heat transfer area, L is the regenerator length, t is the time and $\dot{m}$ is the mass flow rate. Note that in the ideal regenerator the transient term in the fluid energy equation can be neglected since the thermal capacity of the fluid phase is small compared with the solid phase. The initial and boundary conditions for this model are as follows:

- At $t = 0$, $T_{\mathrm{s}} = T_{\mathrm{i}}$, where T_{i} is a given initial temperature;
- For the hot blow: $T_{\mathrm{f}}|_{\mathrm{HE}} = T_{\mathrm{H}}$ at $z = 0$;
- For the cold blow: $T_{\mathrm{f}}|_{\mathrm{CE}} = T_{\mathrm{C}}$ at $z = L$.

The exact solution of Eqs. (2.3) and (2.4) can be found in different references. Schmidt and Willmott (1981) p. 20, presented a classical solution based on the dimensionless time and length. In a different approach, Dragutinovic and Baclic (1998) solved analytically the same equation in terms of the NTU and utilization factor, which will be presented in the next section.

2.6 Regenerator Design and Performance Parameters

Regenerators are usually designed based on the following parameters (SCHMIDT; WILLMOTT, 1981; HAUSEN, 1983; ACKERMANN, 1997):

1. Overall thermal conductance, UA_{HT}, where U is the overall heat transfer coefficient;

2. Temperatures of the cold and hot inlet streams, $T_{\mathrm{C,in}}$ and $T_{\mathrm{H,in}}$;
3. Thermal capacity of the fluid during the hot and cold blows, C_{HB} and C_{CB}, where $C = \dot{m}c_{\mathrm{p}}$;
4. Thermal capacity of the matrix ($(mc)|_{\mathrm{s}}$);
5. Operating frequency;

The performance of a regenerator is evaluated based on the average outlet fluid temperatures at the cold and hot ends, $\overline{T}_{\mathrm{C,out}}$ and $\overline{T}_{\mathrm{H,out}}$. Undoubtedly, these outlet average temperatures are a function of the design parameters listed above. However, the regenerator performance is more commonly evaluated in terms of non-dimensional variables (SCHMIDT; WILLMOTT, 1981; HAUSEN, 1983; ACKERMANN, 1997; SHAH; SEKULIĆ, 2003; NELLIS; KLEIN, 2009).

Based on Eq. (2.2), the first dimensionless parameter to be defined is the utilization factor, ϕ, which for a fixed bed regenerator is given by,

$$\phi = \frac{\dot{m}c_{\mathrm{p}}\tau_{\mathrm{blow}}|_{\mathrm{f}}}{mc|_{\mathrm{s}}} \tag{2.5}$$

where τ_{blow} is the time period of one blow. The utilization is the ratio of the thermal capacity of the fluid phase flowing through the regenerator during one blow (hot or cold) and the thermal capacity of the regenerator solid matrix. As mentioned above, a good regenerator must have a large matrix heat capacity so that it can store energy from the fluid without changing temperature substantially (NELLIS; KLEIN, 2009).

The second dimensionless parameter is the number of heat transfer units, NTU, which can be intuitively related to the thermal size of the heat exchanger (SHAH; SEKULIĆ, 2003; NELLIS; KLEIN, 2009):

$$NTU = \left.\frac{UA_{\mathrm{HT}}}{C}\right|_{\mathrm{blow}} \tag{2.6}$$

In principle, as shown in Eq. (2.6), NTU can be evaluated separately for the cold and hot blows. Additionally, regenerators can be evaluated in terms of the modified number of transfer units, NTU_{o}, given by,

$$NTU_{\mathrm{o}} = \frac{U_{\mathrm{o}} A_{\mathrm{HT}}}{C_{\min}} \tag{2.7}$$

where

$$\frac{1}{U_{\mathrm{o}}} = \frac{1}{h}\bigg|_{\mathrm{HB}} + \frac{1}{h}\bigg|_{\mathrm{CB}} \tag{2.8}$$

Although Eq. (2.8) indicates that the two convection thermal resistances associated with each blow are connected in series, this is not true for a regenerator, since there is no direct heat transfer between the hot and cold streams. In the so-called balanced regenerator, the mass flow rates of the cold and hot blows are identical and the hot and cold blow periods are the same. Thus, the thermal capacity rates of the cold and hot streams are identical, $C_{\min} = C_{\mathrm{CB}} = C_{\mathrm{HB}}$, and the NTU is the same for both blows (SCHMIDT; WILLMOTT, 1981; ACKERMANN, 1997; NELLIS; KLEIN, 2009):

$$NTU_{\mathrm{o}} = \frac{NTU}{2} \tag{2.9}$$

In the present thesis, balanced flow conditions were used in all experiments. Thus, the results will be always evaluated in terms of NTU.

The third and last non-dimensional parameter is the thermal effectiveness, ϵ. The effectiveness is a measure of how good the real regenerator is when compared with a perfect regenerator subjected to the same temperature difference between the thermal reservoirs (SCHMIDT; WILLMOTT, 1981; ACKERMANN, 1997; SHAH; SEKULIĆ, 2003; NELLIS; KLEIN, 2009). Thus:

$$\epsilon = \frac{Q_{\mathrm{blow}}}{Q_{\max}} \tag{2.10}$$

where Q_{blow} is the actual amount of heat transferred from or to the matrix in a given blow (hot or cold) and $Q_{\max}$ is the maximum possible amount of heat transferred from or to the matrix in a perfect regenerator. Under balanced flow conditions, the thermal effectiveness can be expressed in terms of the average outlet temperatures as follows:

$$\epsilon_{CB} = \frac{\overline{T}_{H,out} - T_{C,in}}{T_{H,in} - T_{C,in}} \tag{2.11}$$

$$\epsilon_{HB} = 1 - \frac{\overline{T}_{C,out} - T_{C,in}}{T_{H,in} - T_{C,in}} \tag{2.12}$$

Dragutinovic and Baclic (1998) solved analytically and numerically the governing energy equations for ideal regenerators (Eqs. (2.3) and (2.4)). Fig. 2.3 presents the results for the effectiveness as a function of NTU and utilization for balanced and symmetric ideal regenerators. As can be seen, only regenerators with an utilization lower than unity are capable of reaching 100% effectiveness. This limit is reached earlier (i.e., smaller values of NTU) as the utilization approaches zero (negligible thermal capacity of the fluid stream). For an utilization factor higher than unity, the maximum achievable effectiveness is lower than 100%. Therefore, it is not possible to attain perfect regeneration when the thermal capacity of the fluid exceeds that of the matrix. Also, the maximum achievable effectiveness is reached earlier (i.e., smaller values of NTU) as the utilization factor increases above unity (ACKERMANN, 1997; NELLIS; KLEIN, 2009).

The ideal regenerator solution helps to understand the influence of the basic design parameters on the actual regenerator performance. However, any real regenerator design must incorporate real effects and losses in order to provide a true estimate of the performance of a real cooling system. The following is a list of phenomena that must be accounted for in the modeling of regenerators aiming at applications in magnetic cooling:

1. Thermal capacity of the fluid phase so as to deal with regenerators that use aqueous solutions as thermal agents;

2. Viscous dissipation, which may become significant in highly compact regenerators with a large heat transfer area per unit of volume and a low porosity;

3. Axial (streamwise) heat conduction in the fluid and solid phases;

4. Variable thermophysical properties of the solid and fluid phases with respect to temperature, pressure and magnetic flux density (in the case of an active magnetic regenerator);

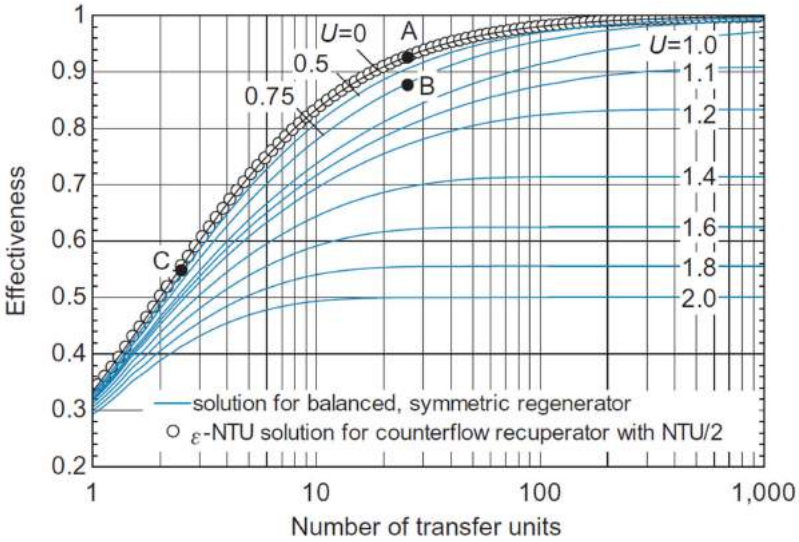

Figure 2.3 – Effectiveness as a function of NTU and utilization (defined as U in the figure), solution for balanced and symmetric regenerators. Adapted from Nellis and Klein (2009).

5. Effective properties of the porous medium (e.g., dispersion) as a function of the flow regime.

2.7 The Magnetocaloric Effect

The Magnetocaloric Effect (MCE) is the thermal response of a magnetic material when subjected to a changing magnetic field. The historical aspects of the MCE, including its discovery in 1917 by Weiss and Piccard are presented and discussed in the review article by Smith (2013).

Physically, the MCE is a manifestation of the entropy variation of the material due to the coupling of the magnetic moments in the material with the magnetic field. A suitable engineering approximation for the majority of magnetocaloric materials is to assume that the specific entropy of the solid material, s, is the sum of three main contributions: electronic, s_{ele}, lattice, s_{lat}, and magnetic, s_{mag}. s_{ele} and s_{lat} are as-

sumed to depend only on the temperature, while s_{mag} is a function of the temperature and the external magnetic flux density[3] (TISHIN; SPICHKIN, 2003; PECHARSKY; GSCHNEIDNER JR., 1999; PECHARSKY *et al.*, 2001; SMITH *et al.*, 2012):

$$s(T, B) = s_{\mathrm{mag}}(T, B) + s_{\mathrm{ele}}(T) + s_{\mathrm{lat}}(T) \tag{2.13}$$

When the external magnetic flux density on the solid magnetocaloric material is changed from B_0 to B_1, the resulting MCE can be quantified in terms of the two thermodynamic process presented in the temperature-specific entropy (T-s) diagram in Fig. 2.4.

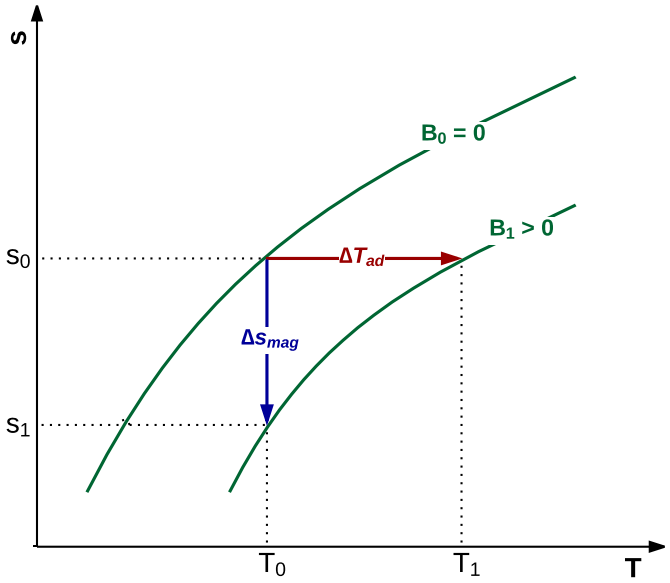

Figure 2.4 – Illustration of the isothermal and adiabatic magnetization processes in a T-s diagram. Adapted from Pecharsky and Gschneidner Jr. (1999).

[3] In general, the applied magnetic flux density, B, is represented by the applied magnetic field, H. These quantities are related by $B = \mu_0 H$, where μ_0 is the magnetic permeability of the vacuum and, essentially, represent the same quantity. To be consistent with the theoretical formalism, in the present thesis, the magnetic flux density will be used.

If the magnetic flux density is varied under isothermal conditions, the lattice and electronic contributions to the total entropy do not change, and the MCE is characterized by the total entropy variation from s_0 to s_1, which is proportional to the magnetic entropy variation as follows:

$$\Delta s_{\mathrm{mag}}(T, \Delta B) \approx \Delta s(T, \Delta B) = s_1(T, B) - s_0(T, B) \tag{2.14}$$

On the other hand, if the magnetic flux density is varied under adiabatic conditions, the total entropy remains constant. Thus, the resulting magnetic entropy variation is thermically compensated by the electronic and lattice entropies and, as a result, the temperature of the materials changes from T_0 to T_1:

$$-\Delta s_{\mathrm{mag}}(T, B) = \Delta s_{\mathrm{ele}}(T) + \Delta s_{\mathrm{lat}}(T) \tag{2.15}$$

2.7.1 Thermodynamics of the MCE

The isothermal entropy variation, also referred in the literature as the magnetic entropy variation, $\Delta s_{\mathrm{mag}}(T, \Delta B)$, can be evaluated by the following Maxwell relationship that relates entropy and the specific magnetization, σ, which are both functions of temperature and magnetic flux density:

$$\left(\frac{\partial s}{\partial B}\right)_{\mathrm{T}} = \left(\frac{\partial \sigma}{\partial T}\right)_{\mathrm{B}} \tag{2.16}$$

Integration of Eq. (2.16) leads to:

$$\Delta s(T, \Delta B) = \int_{B_0}^{B_1} \left(\frac{\partial \sigma(T, B)}{\partial T}\right) dB \tag{2.17}$$

The entropy can also be related to the specific heat capacity (c) by:

$$\left(\frac{\partial s}{\partial T}\right)_{\mathrm{B}} = \frac{c(T, B)}{T} \tag{2.18}$$

Eq. (2.18) can be integrated to determine the entropy change if the specific heat capacity as a function of temperature and magnetic flux density is known. Thus:

$$\Delta s(T, \Delta B) = \int_0^T \frac{1}{T}\Big[c(B_1, T) - c(B_0, T)\Big]dT \tag{2.19}$$

At constant pressure, volume and composition, the entropy can be written in terms of temperature and magnetic flux density as follows:

$$ds = \left(\frac{\partial s}{\partial T}\right)_{\mathrm{B}} dT + \left(\frac{\partial s}{\partial B}\right)_{\mathrm{T}} dB \tag{2.20}$$

For a reversible adiabatic (i.e., isentropic) process, substituting Eqs. (2.16) and (2.18) in Eq. (2.20) gives:

$$dT = -\frac{T}{c(T, B)}\left(\frac{\partial \sigma}{\partial T}\right)_{\mathrm{B}} dB \tag{2.21}$$

Integration of Eq. (2.21) results in the adiabatic temperature variation, ΔT_{ad}, which is formally defined as:

$$\Delta T_{\mathrm{ad}}(T, \Delta B) = T_1(s_0(T_1, B_1)) - T_0(s_0(T_0, B_0)) \tag{2.22}$$

Thus, upon integration one has:

$$\Delta T_{\mathrm{ad}}(T, \Delta B) = -\int_{B_0}^{B_1} \left(\frac{T}{c(T, B)}\right)\left(\frac{\partial \sigma(T, B)}{\partial T}\right) dB \tag{2.23}$$

Since the MCE depends on the temperature and on the intensity of the magnetic flux density variation, it presents a single peak around the transition temperature where $\left(\frac{\partial \sigma}{\partial T}\right)$ is maximum. This temperature transition is called the Curie Temperature, T_{Curie} (TISHIN; SPICHKIN, 2003; PECHARSKY; GSCHNEIDNER JR., 1999; PECHARSKY *et al.*, 2001; SMITH *et al.*, 2012). Fig. 2.5 illustrates the behavior of ΔT_{ad} and c_{H} (the specific heat capacity at constant magnetic field) of gadolinium (SID-

DIKOV *et al.*, 2005), for which T_{Curie} was about 295 K in that particular set of experiments. For gadolinium, at low magnetic flux densities, the Curie Temperature has been reported within the range of 290 to 297 K (BAHL; NIELSEN, 2009), which largely depends on the level of purity of the sample.

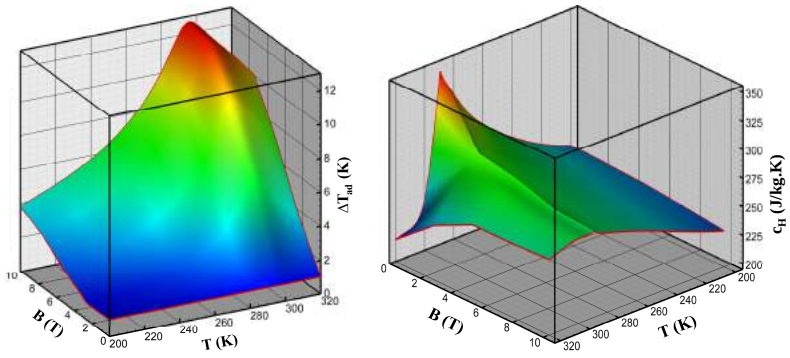

(a) (b)

Figure 2.5 – (a) ΔT_{ad} and (b) c_{H} as a function of the temperature and magnetic flux density. Adapted from Siddikov *et al.* (2005).

2.7.2 The Reversibility of the MCE

Magnetocaloric materials with a continuous magnetic phase transition at the Curie Temperature exhibit a reversible magnetocaloric effect (NIELSEN *et al.*, 2010). The reversibility of the MCE has been demonstrated experimentally based on direct measurements of ΔT_{ad} in Gd samples (BAHL; NIELSEN, 2009; TREVIZOLI *et al.*, 2012). Fig. 2.6 shows the sample temperature when it is initially magnetized and then demagnetized a few moments later.

Starting with the sample at zero external magnetic flux density, and the initial temperature T_0 around 293.15 K, the sample is magnetized adiabatically and its temperature increases to $T_1 = T_0 + \Delta T_{\text{ad}}(T_0, \Delta B)$. In the case illustrated in Fig. 2.6, T_1 is around 297 K and $\Delta T_{\text{ad,mag}}$ is about 3.8 K. After the adiabatic demagnetization, the temperature dropped to $T_2 = T_1 + \Delta T_{\text{ad}}(T_1, \Delta B)$. Experimentally, T_2 was observed to be very close to T_0, and $\Delta T_{\text{ad,demag}}$ was about -3.8 K. Thus, in simple mathematical terms (NIELSEN *et al.*, 2010):

$$\Delta T_{\mathrm{ad,mag}}(T_0, \Delta B) = -\Delta T_{\mathrm{ad,demag}}(T_0 + \Delta T_{\mathrm{ad,mag}}(T_0, \Delta B), \Delta B) \tag{2.24}$$

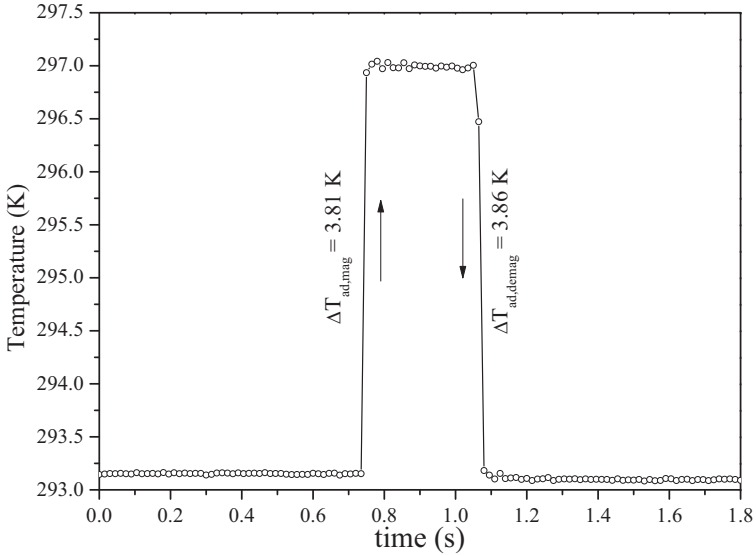

Figure 2.6 – Experimental demonstration of the reversibility of the MCE in Gd. The change in magnetic flux density was approximately 1.65 T. Adapted from Trevizoli *et al.* (2012).

The result described above can be explained on the grounds of the reversibility of MCE under conditions of zero heat transfer between the sample and the surroundings. Neglecting any kind of internal irreversibility (homogeneous material, uniform temperature variations), the system is expected to perform a cycle and return to the original state (i.e., zero total entropy variation) with zero entropy generation (TREVIZOLI *et al.*, 2012). As a result, a distinct temperature shift is observed when comparing the $\Delta T_{\mathrm{ad,mag}}$ and $\Delta T_{\mathrm{ad,demag}}$ curves as a function of temperature. Fig. 2.7 shows the direct measurement results of ΔT_{ad} under adiabatic magnetization and demagnetization. The experimental results for demagnetization are compared with the theoretical prediction using Eq. (2.24). This allows verification of the reversibility of the MCE, as distinct peaks are observed at around 293 K for

magnetization and 297 K for demagnetization.

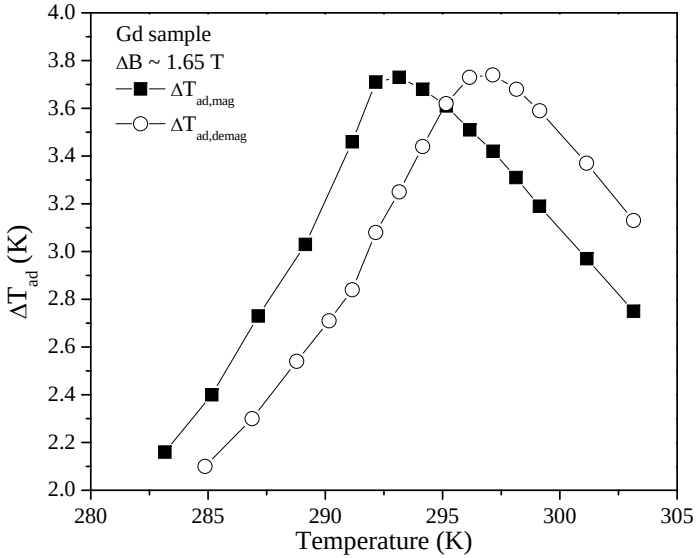

Figure 2.7 – Direct measurement results of the ΔT_{ad} under adiabatic magnetization and demagnetization as a function of the temperature, for a magnetic flux density variation of approximately 1.65 T. The demagnetization curve shows the absolute value ($|\Delta T_{\mathrm{ad}}|$). Adapted from Trevizoli *et al.* (2012).

2.7.3 Magnetocaloric Materials

The MCE is an intrinsic property of all magnetic materials, basically differing from each other with respect to the magnitudes of the entropy and temperature changes and the Curie temperature. Fig. 2.8 shows a comparison of the magnetocaloric properties of different materials applicable in low- and room-temperature cooling (GSCHNEIDNER JR. *et al.*, 2000, 2005).

According to Rowe *et al.* (2005b), for applications around room temperature, the ΔT_{ad} of magnetocaloric materials must be greater than 2 K/T. Nevertheless, other important properties should be considered, such as (YU *et al.*, 2003; TURA, 2005; GSCHNEIDNER JR.; PECHARSKY, 2008):

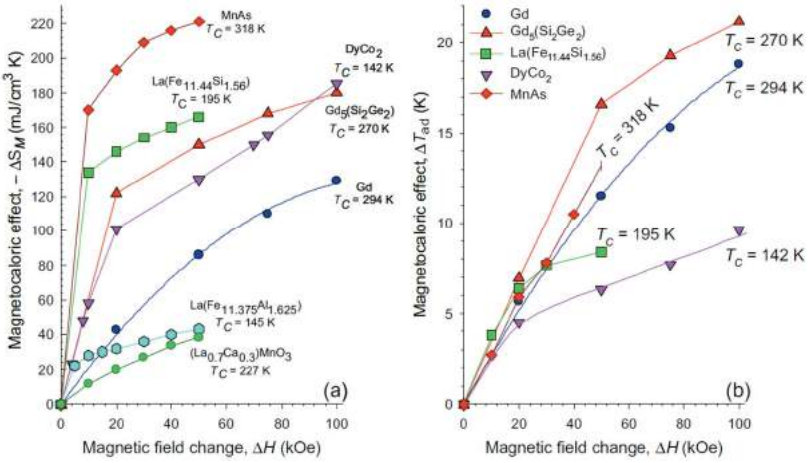

Figure 2.8 – (a) Isothermal entropy change; (b) Adiabatic temperature change for different magnetocaloric materials. Adapted from Gschneidner Jr. *et al.* (2005).

- MCE as large as possible over a broad temperature range, to maximize the cooling capacity and the temperature span;
- Minimum thermal and magnetic hysteresis;
- Large specific heat capacity to increase the thermal mass of the regenerative matrix;
- High thermal conductivity to improve the regenerator effectiveness;
- Chemical stability to avoid corrosion;
- Large electrical resistance to avoid eddy currents;
- Good mechanical properties to facilitate the manufacturing process;
- Low cost.

Gadolinium (Gd) is the benchmark material for applications around room temperature. Since the discovery of the 'giant' MCE in $Gd_5(Ge,Si)$ alloys (PECHARSKY; GSCHNEIDNER JR., 1997b), several different systems with large MCE have been reported, of which the most promising

ones are the La(Fe,Si) and MnFe-based alloys (BRÜCK *et al.*, 2008). Table 2.1 presents some important properties and characteristics of promising magnetocaloric materials compared with Gd.

Table 2.1 – Promissing magnetocaloric materials properties and characteristics compared with Gd. Fonte: Adapted from Gschneidner Jr. *et al.* (2005).

Property	Gd	Gd_5Tb_4	$RMnO_3$	LaFeSi	MnFe(P,As)	Ni_2MnGa
ΔS_M	0	+ +	-	+	+	+
ΔT_{ad}	0	+	-	-	0	-
Hysteresis	0	- -	0	-	-	- -
Preparation	0	-	- -	- -	- -	- -
Fabrication (sheet)	0	-	-	-	-	-
Corrosion	0	+ +	?	-	?	0
Raw Materials costs	0	-	+ +	+ +	+ +	+
Environmental concerns	0	0	0	0	-	0

One of the most complex characteristics of all magnetocaloric materials is the dependence of the MCE and the specific heat capacity with respect to temperature and magnetic field. Regarding the MCE dependence, it is highest at the Curie temperature and decreases as the temperature gradually deviates from T_{Curie}, as shown in Fig. 2.9. To illustrate this, an AMR operating with a hypothetical material with a temperature span of 70 K, where $T_C = 253$ K and $T_H = 323$ K, is shown in Fig. 2.9(a). The MCE at T_{Curie} is ≈6.5 K, and decreases to ≈2.5 K close to the cold end and to ≈1.5 K close to the hot end. To avoid this reduction of the MCE and achieve better performances, different magnetocaloric materials with different values of T_C can be combined sequentially in the regenerator in order to maintain locally a MCE as large as possible, as shown in Fig. 2.9(b). Several authors explored the concept of multi-material regenerators (HASHIMOTO *et al.*, 1987; SMAÏLI; CHAHINE, 1997; OKAMURA *et al.*, 2006; HIRANO *et al.*, 2010). Tura (2005) observed an increase of the maximum temperature span (zero thermal load) from ≈20 K using a single-layer Gd regenerator to ≈50 K for a multi-layer regenerator composed by layers of $Gd_{85}Er_{15}$, $Gd_{74}Tb_{26}$ and Gd. An identical magnetic field change was applied in the two situations.

Regarding the specific heat capacity, there is a strong dependence with respect to the applied magnetic flux density and temperature, as shown in Fig. 2.10 for gadolinium. The major complicating element associated

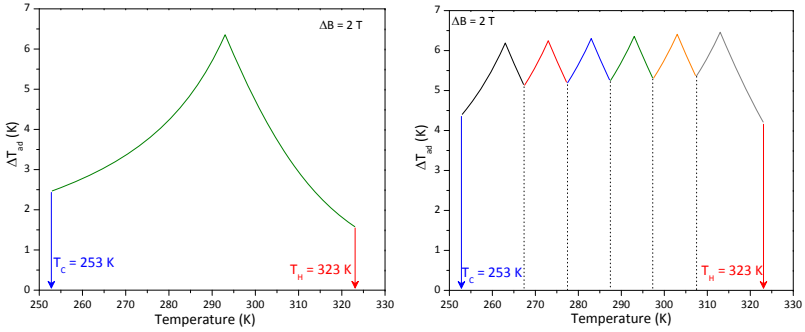

Figure 2.9 – (a) Single-material; (b) Multi-material active magnetic regenerator.

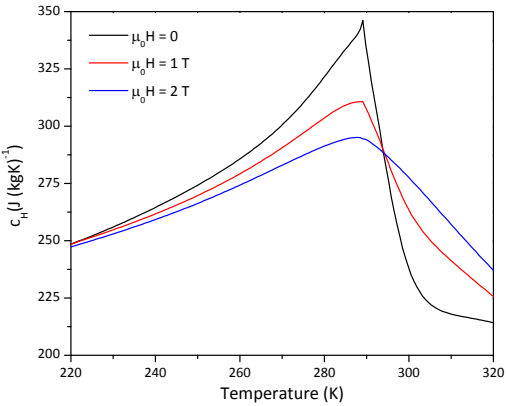

Figure 2.10 – Specific heat capacity at constant magnetic flux density for Gd. Adapted from Siddikov *et al.* (2005).

with this is the need to take the temperature and flux density dependence into account in the mathematical modeling of AMRs. As pointed out by several authors (NIELSEN *et al.*, 2011; TREVIZOLI *et al.*, 2014), the local heat transfer in the regenerative matrix can be severely influenced by changes in specific heat capacity, which has obvious consequences to the regenerator performance.

2.8 Active Magnetic Regenerators

2.8.1 The AMR Cycle

Magnetic refrigeration systems can be built according to different thermodynamic cycles, such as the Carnot, Ericsson, Stirling and Brayton cycles (KITANOVSKI; EGOLF, 2006; KITANOVSKI *et al.*, 2015). However, since the MCE is small, i.e., of the order of 3 K/T at low magnetic flux densities for the current magnetocaloric materials, large temperature spans cannot be achieved, unless some kind of thermal regeneration is used. In the active magnetic regenerator (AMR), the magnetocaloric material is employed as a solid regenerative matrix so as to amplify the temperature span by exchanging heat with a thermal agent (heat transfer fluid) (BARCLAY; STEYERT, 1982).

Regenerative cycles enable achieving large temperature spans and large cooling capacities. The Brayton cycle is the most common thermo-magnetic regenerative cooling cycle, and is schematically presented in Fig. 2.11. The following idealized steps, shown in a T-S diagram in Fig. 2.12, make up the idealized thermo-magnetic Brayton cooling cycle (ROWE *et al.*, 2005a):

1. *Adiabatic magnetization*: by changing adiabatically the magnetic field applied on the matrix, the total entropy of the magnetic solid remains constant. However, the decrease in magnetic entropy due to the magnetic field variation is compensated by an increase in the lattice and electronic entropies. As a result, the temperature of the magnetic material increases, which characterizes the magnetocaloric effect (MCE).

2. *Constant magnetic field cold blow*: after the adiabatic magnetization, cold fluid (at T_{C}) flows through the matrix, cools down the solid phase (which releases heat to the fluid) and rejects heat to a hot source at T_{H}.

3. *Adiabatic demagnetization*: similarly to the adiabatic magnetization, the demagnetization process reduces the temperature of the solid material, which undergoes an adiabatic temperature change.

4. *Constant magnetic field hot blow*: hot fluid (at T_{H}) returns through the matrix, and the solid phase removes heat from the fluid phase,

increasing the internal energy of the matrix. At the cold end, the fluid absorbs heat from a cold source at T_C.

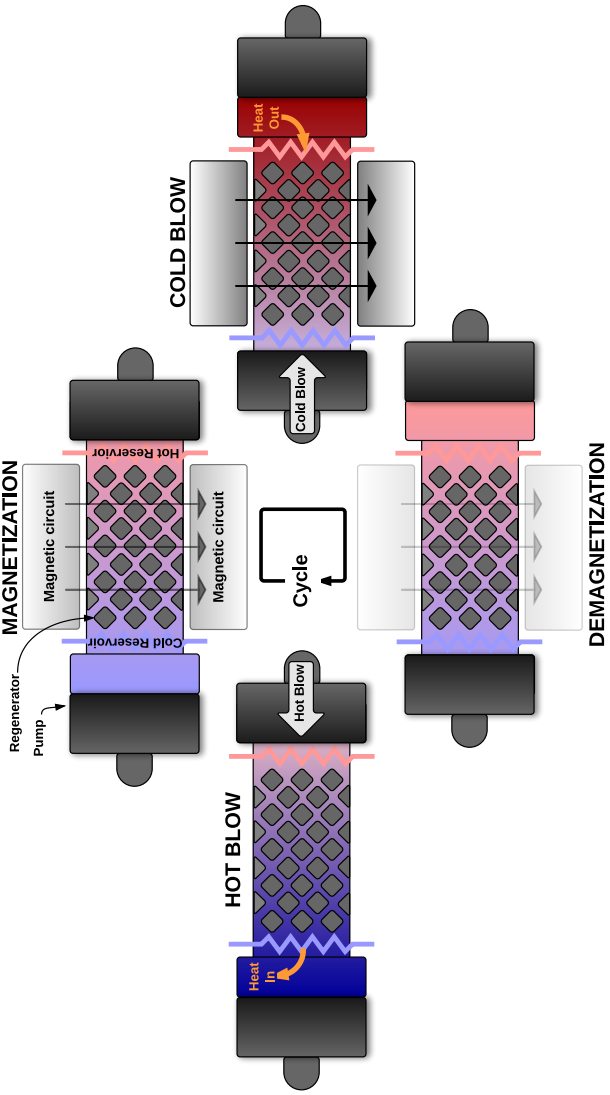

Figure 2.11 – Schematic description of the processes in a thermomagnetic regenerative Brayton cycle.

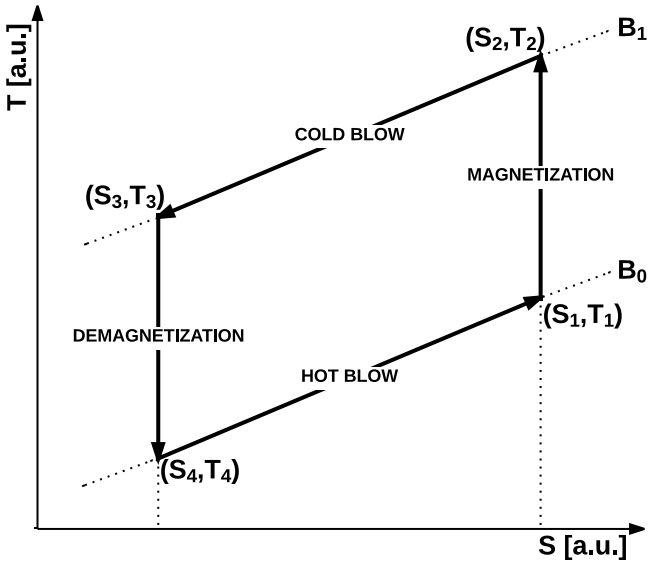

Figure 2.12 – Schematic T-S diagram of the thermo-magnetic regenerative Brayton cycle.

The efficiency of a magnetic active cooling system depends on the magnitude of the MCE (refrigerating effect) and on the effectiveness of the regenerative matrix. The MCE itself depends on the applied field change, i.e., the higher the magnetic flux density variation the higher the MCE, and on the magnetic properties of the magnetic material. The effectiveness, in turn, depends on the solid phase thermophysical properties, matrix geometry, thermal capacity, porosity and operating parameters, such as frequency and flow velocity (ROWE *et al.*, 2005a; TURA; ROWE, 2011; NIELSEN *et al.*, 2012; TREVIZOLI *et al.*, 2014).

2.8.2 Numerical Modeling of AMRs

The mathematical modeling of AMRs is a multidisciplinary task, since it involves the application of physical concepts in Thermodynamics, Heat Transfer, Fluid Dynamics, Solid-State Physics and Magnetism. The development of physically consistent models is fundamental to understand thermo-magnetic phenomena and to compute the regeneration

process in real AMRs prototypes. Mathematical models can also be applied in the optimization of regenerators, since there are several dependent parameters that can be evaluated to achieve the best regenerator performance, such as flow rate, frequency, magnetic field change and profile (waveform), heat transfer fluid, regenerator geometry and magnetocaloric material. According to several modeling studies of active magnetic regenerators, a complete mathematical model should include the following (NIELSEN *et al.*, 2011; TREVIZOLI *et al.*, 2012; KITANOVSKI *et al.*, 2015):

1. Detailed transient characteristics of the heat transfer, fluid flow and applied magnetic field;
2. A robust numerical solver to solve the time- and space-dependent energy equations, with acceptable convergence criteria;
3. Appropriate functions for the temperature and magnetic field dependence of the thermo-magnetic properties, such as the specific heat capacity and the adiabatic temperature change;
4. Appropriate models for estimating longitudinal heat conduction effects, thermal losses to the surroundings (e.g., casing, magnets and surrounding air) and viscous losses;
5. Flow maldistribution effects (e.g., by passing and channeling) and carryover (void volume) losses;
6. Appropriate models for computing magnetic losses, such as demagnetizing fields, magnetic hysteresis and eddy currents.

In general, most models published in the literature do not take into account all of the above losses. Nielsen *et al.* (2011) and Kitanovski *et al.* (2015) carried out extensive reviews of the state of the art in AMR modeling. Examples of models that are typical of the classes of models developed in the literature are discussed next.

Burdyny (2012) developed a simplified transient 1-D model based on the hypothesis of thermal equilibrium between the solid and fluid phases, which is a common approach in modeling of porous media. This assumption enables the combination of the energy equations of the two phases into a single medium, which reduces the computational cost (KAVIANY, 1995). External losses due to heat leaks and losses associated with eddy currents were implemented. The model reproduced the trends of the experimental data of Tura and Rowe (2011).

Engelbrecht (2008) developed a transient 1-D model, in which the regenerator was modeled as a porous medium and the energy equations for the fluid and solid phases were solved coupled. Engelbrecht (2008) used a progressive verification of the modeling approach. First, the model was used to predict the passive regenerator behavior, and was compared with the Dragutinovic and Baclic (1998) solution. After, the model was examined against experimental results and compared with the Petersen (2007) 2-D model for parallel plates, reproducing the results for temperature gradients, cooling capacity and COP. The agreement was better for small plate thickness (< 1 mm) because the 1-D model could not directly account for temperature gradients in the fluid or regenerator.

Petersen (2007), Nielsen (2010) and Oliveira *et al.* (2012) developed transient 2-D models for parallel plate AMRs. Nielsen (2010) included in his model different losses and compared the model against experimental data with good reproducibility of the trends obtained in the Risoe DTU test device. The model developed by Oliveira *et al.* (2012) aimed at studying the transient behavior of the oscillatory fluid flow and heat transfer in a parallel plate regenerator, in which an analytical solution was developed for the time-dependent fluid velocity. The energy equations for the fluid and the solid plates were solved via the finite volume method. The results showed that for kinetic Reynolds numbers above 50, a double-peak velocity profile was observed, which resulted in an intensification of the heat transfer coefficient. However, this limit corresponded to high operating frequencies, well above the frequencies encountered in AMR systems. The authors have concluded, therefore, that one-dimensional models based on interstitial heat transfer coefficients are sufficient for predicting the behavior of oscillating-flow regenerators.

2.9 Design and Optimization of Thermal Regenerators

In a heat exchanger, there must be good thermal contact between the fluid and solid phases, but the latter should offer a small resistance to the fluid flow. These conflicting requirements are often equalized using thermal optimization.

Thermal regenerator optimization models can be evaluated in terms of

several performance criteria. Among them, second-law based criteria have been used extensively. A concise review of applications of the method in the context of heat exchangers and storage systems was presented by Awad and Muzychka (2012). For passive regenerators, several optimization procedures were implemented as discussed below.

Krane (1987) evaluated the performance of regenerators using gases as working fluids and concluded that the storage and removal processes need to be analyzed together to determine the optimum characteristics of these devices, which were observed to be quite inefficient (i.e., 70-90% of the available exergy is destroyed by the end of a cycle). Das and Sahoo (1991) used the Entropy Generation Minimization (EGM) method in the thermodynamic optimization of regenerators under single blow operation. Their model disregarded the axial heat conduction and was valid only for low values of NTU. An optimum operating condition was identified in terms of the cycle time and NTU. In a subsequent work, Das and Sahoo (1999) included the time dependence and the axial conduction in the EGM analysis, thus extending the validity of their model to more densely packed regenerators operating at higher values of NTU.

de Waele *et al.* (1997) and Steijaert (1999) applied the EGM method to pulse-tube cryocoolers, taking into consideration the entropy production in every component (orifice, heat exchangers, regenerator, switching valves). The model was used to evaluate the thermodynamic performance of a cryocooler prototype. Based on the work of de Waele *et al.* (1997), Nam and Jeong (2006) employed the EGM method in the analysis of parallel-wire (segmented and unsegmented) mesh regenerators. They observed a better performance of the unsegmented parallel-wire configuration (in comparison to a screen mesh matrix) as a result of lower values of porosity and friction factor. However, axial heat conduction was identified as the main source of irreversibility in the parallel-wire case. To overcome this loss, a segmented parallel-wire geometry was used to decrease the axial conduction irreversibility and improve the thermodynamic performance of the parallel-wire regenerator.

In the context of AMR optimization, EGM analyses were conducted by Li *et al.* (2008) and Numazawa *et al.* (2012). Li *et al.* (2008) used a second-law analysis to find optimal regenerator dimensions and spheres diameters for a real apparatus. They correctly related the limitations regarding the regenerator housing diameter with the magnet circuit

size, where to keep the applied magnetic flux density constant and increase the housing diameter, the size of the magnetic circuit has to increase exponentially. Thus, for a fixed housing diameter, they carried out an optimization of the housing aspect ratio. As a result, Li *et al.* (2008) found an optimal coefficient of performance of 15.54 for a regenerator with an aspect ratio of 6.39 and spheres of 1.1 mm in diameter. However, in the work by Li *et al.* (2008), the COP was proposed as the objective function, which did not guarantee a fixed cycle-average heat transfer rate at the cold source, while the housing aspect ratio and the sphere size were changed. Numazawa *et al.* (2012) compared the performances of packed beds of spheres and parallel plates as regenerative geometries changing geometrical and operating parameters (plate thickness, sphere diameter, aspect ratio and frequency). However, as the cooling capacity was not taken as a constraint, it was difficult to quantify the effect of the geometric and operating parameters. Therefore, the combination of performance evaluation criteria (PEC) with the EGM theory to optimize the performance of regenerators is an original contribution of the present thesis.

In Entropy Generation Minimization methods, the total entropy generation can be used as the Objective function in an optimization procedure based on constraints, such as the performance evaluation criteria (PEC) established by Webb and Kim (2005). For a single-phase flow condition, a thermal device can be optimized according to fixed volume, fixed face area or variable geometry constraints, which may be useful in the context of regenerator design for both passive and active applications. An explanation of the PEC employed in this work is presented as follows:

- Variable Geometry (**VG**): this PEC enables varying the regenerator housing cross-section area and length, while keeping the total housing volume constant. The **VG** PEC may be useful when there is freedom in terms of the final aspect ratio of the regenerator. For a given mass (volume) of magnetocaloric material, this PEC can be combined with the design optimization procedure of the magnet system in order to achieve an optimal configuration of the AMR device;

- Fixed Face Area (**FA**): this PEC enables varying the regenerator housing length, while maintaining the cross-section area constant. The total mass of solid material is not constant in this PEC, since it changes with the housing length. In the context of magnetic

cooling, this PEC can be useful in the optimization of the regenerator to be fitted in an existing magnet gap. In this case, the regenerator length can be adjusted to satisfy a specific design constraint or metric, which generally do not take into account a performance assessment for the magnet, since its dimensions are already fixed. Conversely, the **FA** PEC can also be employed when neither the size of the magnet gap nor the mass of magnetocaloric material are constrained. In this case, both the magnet and the regenerator can be evaluated together in order to achieve the optimal applied magnetic flux density volume and the amount of magnetic raw material that satisfy a specific operating condition involving, say, the cooling capacity and temperature span;

- Fixed Geometry (**FG**): in this PEC, both the regenerator housing cross-section area and its length are kept constant. The **FG** PEC may be useful when the dimensions of the regenerator casing (and hence its total volume) cannot be changed. In a magnetic cooling apparatus, this is the case when the magnetic circuit is already designed and built, and there is a predefined volume to place the regenerator. In this case, only the bed characteristics (e.g., geometry, particle size) and the flow parameters (e.g., frequency, flow rate) can be varied. As will be seen later in this thesis, it is not possible to vary the flow parameters and maintain a fixed operating condition (cooling capacity and temperature span) while enforcing the **FG** PEC in magnetic regenerators.

In order to achieve an optimal set of geometric parameters and operating conditions that return the minimum entropy generation in the regenerator, additional constraints must be established. For passive regenerators, this additional constraint is imposed in terms of a target regenerator effectiveness, which must be met by the optimal geometry associated with each PEC. For active magnetic regenerators, the additional constraint is a fixed cooling capacity for a given temperature difference between the thermal reservoirs, which are the actual desired output of the cooling system.

2.10 Magnetic Cooling Systems

The first near-room-temperature magnetic heat pump was developed by Brown (1976), in which a temperature span of 47 K was achieved

applying Gd as refrigerant and a magnetic flux density of 7 T. However, only after 1997, with the increasing development of magnetocaloric materials, the research on magnetic cooling systems became more active. The magnetic cooling prototypes developed so far are described in review papers (PECHARSKY; GSCHNEIDNER JR., 2006; YU *et al.*, 2010) and books (KITANOVSKI *et al.*, 2015). Kitanovski *et al.* (2015) pointed out that approximately 60 prototypes for near-room-temperature refrigeration have been developed so far. A thorough description of these machines is beyond the scope of this thesis. However, as discussed earlier, in the AMR Brayton cycle the regenerator magnetization and demagnetization processes are performed in different periods of the cycle. The application and removal of the magnetic field can be performed in different ways:

- Reciprocating regenerator (Rec-Reg): in this configuration the regenerator moves back and forth into the stationary magnetic field. However, as far as the regenerator is concerned, it is still a stationary bed from the fluid flow point of view (BAHL *et al.*, 2008);
- Reciprocating magnet (Rec-Mag): in this configuration the regenerator is stationary and the magnet moves linearly. In general, these prototypes operate at low frequencies (< 1 Hz) due to the high inertial forces related to the motion of the magnet (TREVIZOLI *et al.*, 2011);
- Rotating regenerators (Rot-Reg): in this configuration the regenerator rotates to magnetize and demagnetize the regenerator synchronized with the fluid flow. These systems can operate at higher frequencies but add other complexities like flow distribution and leakages (ZIMM *et al.*, 2006; ENGELBRECHT *et al.*, 2012).
- Rotating magnet (Rot-Mag): in this configuration the regenerator bed is stationary and the magnet rotates to perform the magnetic field variation. This simplifies the flow distribution into and out of the regenerator beds but the operation at higher frequencies can be a limitation due to high torques. Nevertheless, some rotating magnets prototypes achieved frequencies of the order of 4 Hz (TURA; ROWE, 2011; LOZANO, 2015).

Table 2.2 presents some characteristics of the main state-of-the-art magnetic cooling prototypes presented in the literature, whose photographs are shown in Fig. 2.13.

Table 2.2 – State of the art magnetic cooling prototypes.

Ref.	Type	Magnetocaloric Material	Peak Field (T)	Mass (kg)	f (Hz)	Max. Span (K)	Operating Point
Tura and Rowe (2011)	Rot-Mag	Gd	1.45	0.11	4	29	50 W (455 W/kg) at 10 K (T_{H} = 295 K)
Engelbrecht *et al.* (2012)	Rot-Reg	Gd	1.24	2.80	2	25.4	280 W (100 W/kg) at 10 K (T_{H} = 301 K)
Jacobs *et al.* (2014)	Rot-Mag	LaFeSiH	1.44	1.52	4	18	2700 W (1776 W/kg) at 11 K (T_{H} = 317 K)
Arnold *et al.* (2014)	Rot-Mag	Gd	1.54	0.65	0.8	33	50 W (77 W/kg) at 15 K (T_{H} = 298 K)
Eriksen *et al.* (2015)	Rot-Mag	GdY	1.1	1.7	0.75	20	103 W (60.5 W/kg) at 10 K (T_{H} = 291 K)
Lozano *et al.* (2015)	Rot-Mag	Gd	1	1.7	0.8	12	80.4 W (47.3 W/kg) at 7.1 K (T_{H} = 294 K)

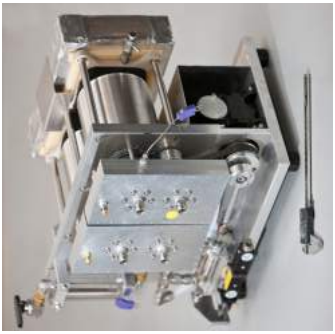

(a)

(b)

(c)

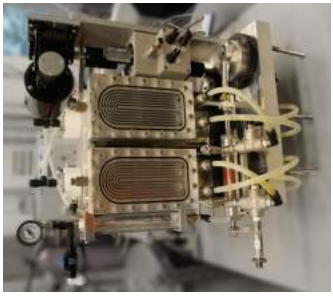

(d)

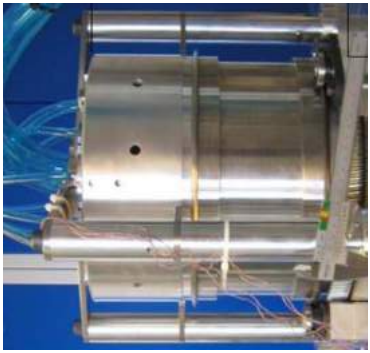

(e)

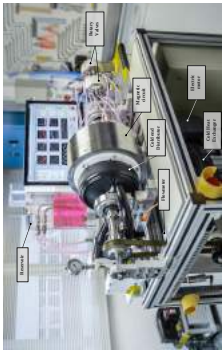

(f)

Figure 2.13 – State-of-the-art magnetic cooling prototypes: (a) Tura and Rowe (2011); (b) Engelbrecht *et al.* (2012); (c) Jacobs *et al.* (2014); (d) Arnold *et al.* (2014); (e) Eriksen *et al.* (2015); (f) Lozano *et al.* (2015).

3 Experimental Apparatus

Experimental analysis is the most straightforward way to evaluate the heat transfer and viscous losses in passive regenerators. It is also the simplest way to characterize the performance of active magnetic regenerators. To accomplish the objectives of the experimental research described in this thesis, a versatile infrastructure was built to enable studying passive and active magnetic regenerators in the same apparatus. This way, the passive regenerator tests with non-magnetocaloric materials were performed first, and the active magnetic regenerator were carried out next, using the same instrumentation and expertise accumulated with the passive tests. The following characteristics were pursued in the design of the experimental apparatus:

- Modularity, making it easy to maintain, assemble, disassemble and change the regenerator matrices;
- Simplicity, facilitating the variation of the operating parameters: utilization, frequency, heating power (thermal load) and temperatures;
- Robustness, particularly with respect to the instrumentation, as temperature, pressure, mass flow rate, frequency and torque transducers have been installed to perform a complete characterization;
- Versatility, enabling the application of different types of regenerators (passive and active magnetic) and pumping systems, such as positive displacement pumps and rotary valves.

This chapter presents the design of the experimental apparatus for testing passive and active magnetic regenerators. Next, the characteristics of the matrices evaluated experimentally will be discussed in detail.

3.1 Description

The passive and active magnetic regenerator apparatus is a laboratory scale set-up, designed to operate at different experimental conditions with different regenerator geometries and pumping systems. The following are more specific design aspects of the setup:

1. The regenerators are of the fixed-bed type;
2. The oscillatory fluid flow through the fixed bed is imposed by a double effect pumping system combined with check valves;
3. The change in magnetic flux density on the active magnetic regenerator is enforced by a magnetic circuit composed by nested rotating Halbach cylinders that allow operating frequencies up to 1 Hz.

The apparatus is divided in two parts, namely the main section and the motor section. The two parts are linked by elastic couplings to avoid vibration in the main section, where the principal components and instrumentation are located. In the main section, the electrical components are located at the lower level, the driving gears and pumping system are installed at the middle level and the regenerator, magnet, instrumentation and heat exchangers are placed at the top level. The motor section comprises the drive motor, secondary pump and torque meter. Fig. 3.1 presents the main section of the designed apparatus.

3.1.1 Passive Regenerator Apparatus

Fig. 3.2 shows the schematic diagram of the experimental passive regenerator apparatus, which is composed of a stationary regenerator bed, two brazed plate heat exchangers, check valves and a pumping system consisting of a double effect pump (or displacer), a crank disc and a stepper motor. Fig. 3.3 shows some images of the passive regenerator test apparatus.

Depending on the regenerator housing length and type of matrix, there are five to seven feed-through orifices along the regenerator to enable positioning of temperature probes in the matrix. The two main temperature probes (used in all matrix geometries) measure the time-dependent temperature at the hot and cold ends of the regenerator, T_{HE}

Figure 3.1 – Passive and active magnetic regenerators experimental apparatus.

and T_{CE}, which are used to calculate the thermal effectiveness of the regenerator. The remaining temperature probes (used only in sphere bed regenerators) measure the time-dependent temperature inside the matrix, T_{i1} up to T_{i5}. These are used to evaluate the temperature profile along the matrix and provide information about the amplitude of the temperature change at each position, which are useful in the evaluation of numerical models.

The temperatures at the hot and cold heat exchangers are controlled by two independent chillers (ThermoScientific - Neslab, models AC200-G50 and AC150-A25). The cold end was kept at a constant temperature, T_C, of 280 ± 0.2 K. The hot end was kept at a constant temperature, T_H, of 320 ± 0.2 K. The ambient temperature was kept at an intermediate temperature of 300 ± 2 K to balance the heat gain and heat loss at the regenerator cold and hot sides, respectively.

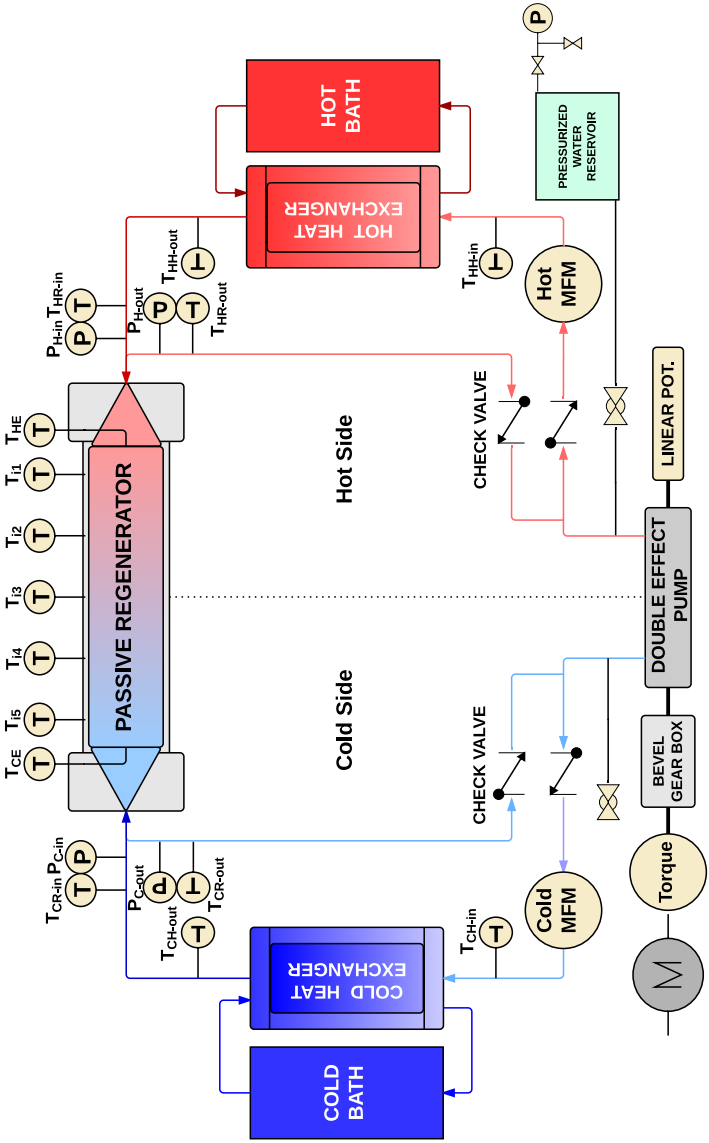

Figure 3.2 – Schematic diagram of the experimental passive regenerator apparatus.

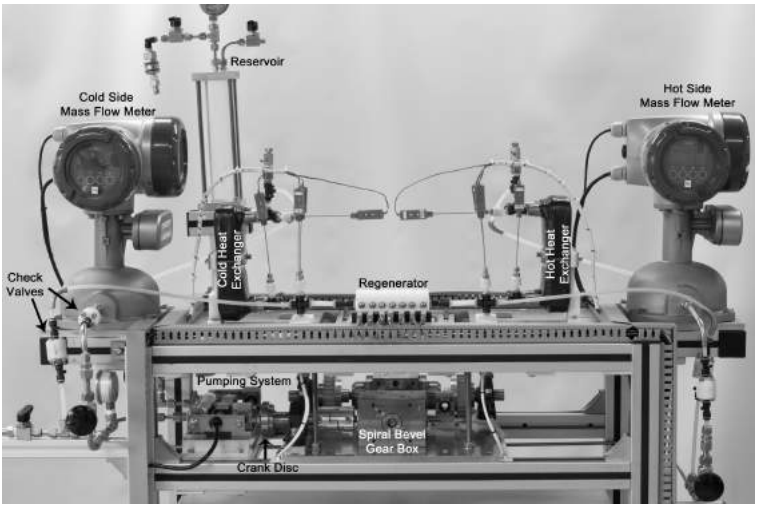

(a)

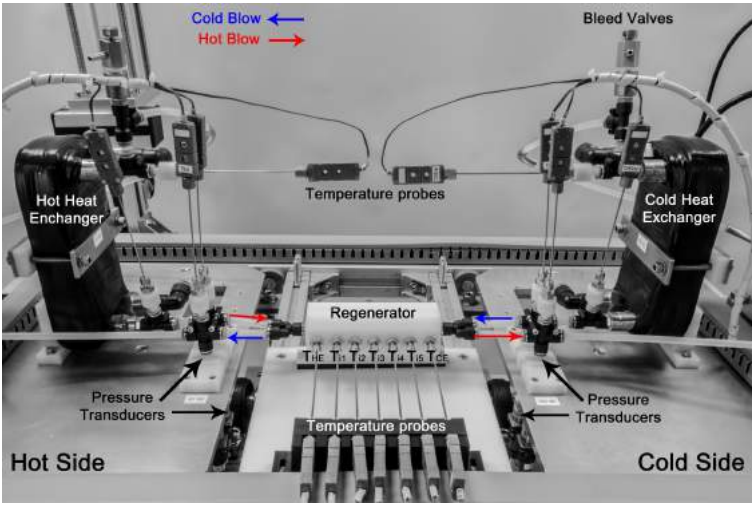

(b)

Figure 3.3 – Passive regenerator test apparatus: (a) Frontal view showing the pumping system, gear boxes, check valves and mass flow meters; (b) Top view showing the regenerator housing, heat exchangers, temperature probes and pressure transducers.

The pumping system delivers an oscillatory flow to the regenerator, whereby the flow velocity can be adjusted through the piston stroke (altering the crank disc position) and the frequency (changing the angular velocity of the motor). Check valves are used to guarantee unidirectional flow in the heat exchangers. The tests were performed using water as heat transfer fluid. Table 3.1 presents a summary of the conditions of the passive regenerator tests.

Table 3.1 – Passive regenerator test conditions.

Variable	Value or range	Units
T_{H}	320	K
T_{C}	280	K
ΔT_{span}	40	K
T_{amb}	300	K
f	0.25 - 2	Hz
ϕ	0.1 - 1.4	-
Fluid	Distilled water	-

The passive regenerator cycle starts with the hot blow, where the double effect pump driven by the stepper motor delivers a constant volume of fluid for a given period. The fluid passes through the mass flow meter (Hot MFM) and enters the hot heat exchanger where it is reconditioned to T_{H}. Then, the fluid exits the hot reservoir and enters the matrix at 320 K, after passing by the pressure transducer ($P_{\text{H-in}}$). Inside the regenerator, the end and internal temperatures are read, and the fluid exits the matrix returning to the pump, passing by the pressure transducer ($P_{\text{C-out}}$). Therefore, the effectiveness of the hot blow is calculated based on the time-dependent temperature of the fluid exiting the cold end, T_{CE}, and the pressure drop is the difference between $P_{\text{C-out}}$ and $P_{\text{H-in}}$.

In the remaining period of the cycle, the cold blow, the same volume of fluid is pumped back. The fluid passes through the mass flow meter (Cold MFM) and enters the cold heat exchanger, where it is reconditioned to T_{C}. Then, the fluid exits the cold reservoir and enters the matrix at 280 K, after passing by the pressure transducer ($P_{\text{C-in}}$). After flowing through the regenerator, the fluid exits the matrix returning to the pump, after flowing by the pressure transducer ($P_{\text{H-out}}$). Hence, the effectiveness of the cold blow is calculated based on the time-dependent temperature of the fluid exiting the hot end, T_{HE}, and the pressure drop is the difference between $P_{\text{H-out}}$ and $P_{\text{C-in}}$.

3.1.2 Active Magnetic Regenerator Apparatus

Fig. 3.4 shows the schematic diagram of the experimental active magnetic regenerator apparatus, which is composed by the same elements of the passive assembly plus the magnetic circuit and the electrical heater. The magnetic circuit is made up of two concentric (nested) Halbach cylinders. This configuration enables changing the applied magnetic flux density as the cylinders are rotated. The regenerator is placed in the magnetic gap, i.e., along the centerline of the internal hollow cylinder. A more detailed description of the magnetic circuit is presented in the following sections. The 100-mm long, 9.2-Ω electrical heater was assembled inside a 22.22-mm diameter fiberglass epoxy (G10) tube. In the AMR apparatus, there were no temperature probes positioned along the matrix. Fig. 3.5 shows some images of the magnetic active regenerator test apparatus.

The temperatures at the hot and cold heat exchangers are controlled by the same thermal baths used in the passive regenerator apparatus. The temperatures in both thermal reservoirs can be adjusted according to the experimental test condition. The fluid pumping system is also the same. Table 3.2 presents a summary of the experimental conditions in the AMR tests.

Table 3.2 – Active magentic regenerator test conditions.

Variable	Value or range	Units
T_{H}	290 to 315	K
T_{C}	varies according to the tests	K
ΔT_{Hex}	varies according to the tests	K
Cooling Capacity	varies according to the tests	W
T_{Amb}	293 and 300	K
f	0.25, 0.5 and 1.0	Hz
ϕ	0.16 - 3	-
Fluid	Distilled water 80% - ethylene glycol 20%	-

The AMR cycle is divided in two stages, namely the hot period and the cold period. The hot period starts with the magnetization process and, as the magnetic flux density in the regenerator changes, the cold blow is performed. As the fluid enters the matrix at T_{C}, heat is removed from the regenerator bed and the fluid leaves the regenerator at T_{H} to reject heat in the hot reservoir. As can be seen in Figs. 3.2 and 3.4, the apparatus was designed so that there is unidirectional flow through the hot and cold heat exchangers. This is accomplished by the two check

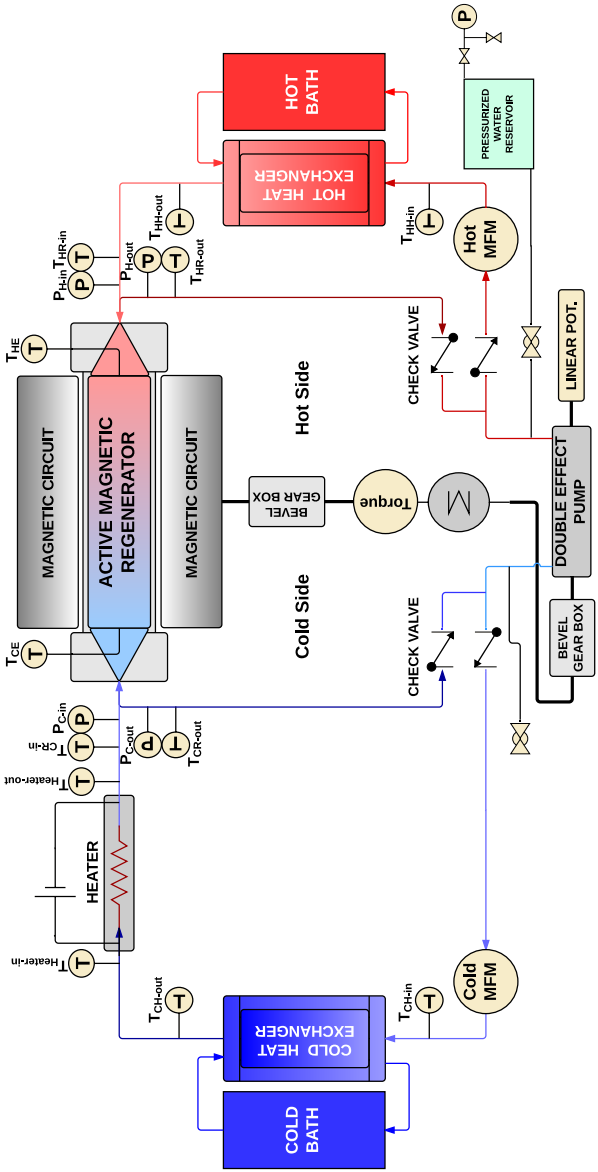

Figure 3.4 – Schematic diagram of the experimental active magnetic regenerator apparatus.

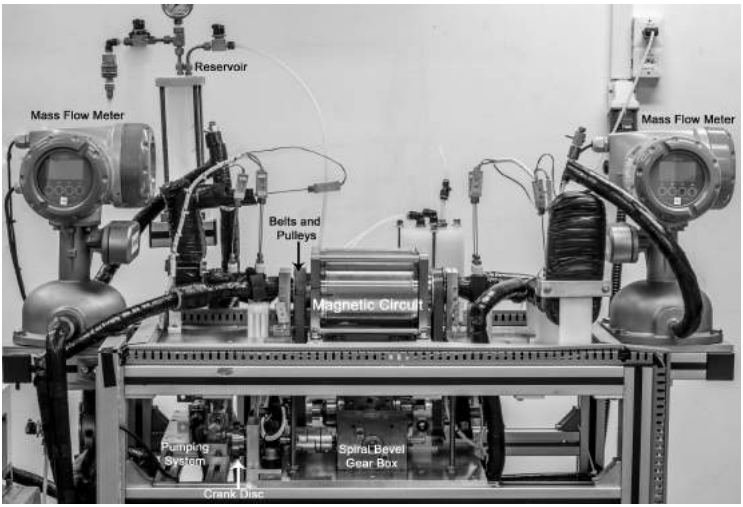

(a)

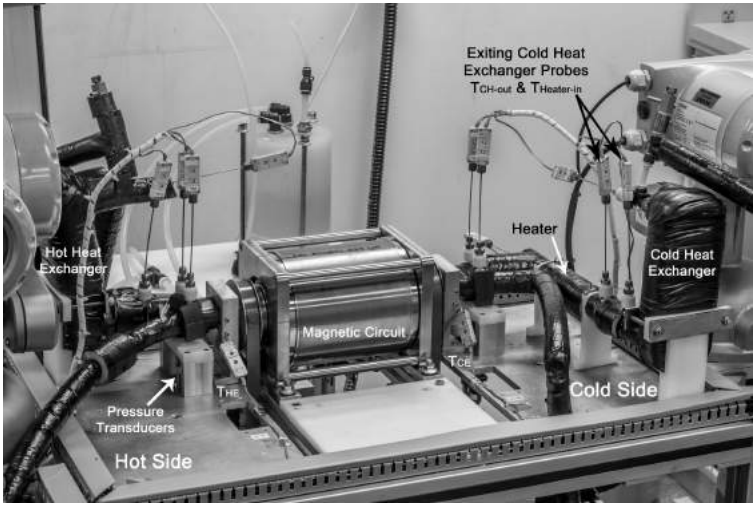

(b)

Figure 3.5 – Active magnetic regenerator test apparatus: (a) Frontal view showing the pumping system, gear boxes and mass flow meters; (b) Isometric view showing the magnet, heat exchangers, temperature probes, pressure transducers and the heater.

valves on each side of the apparatus. The cold blow mass flow rate is measured by the Cold MFM (mass flow meter) and the pressure drop is taken as the difference between $P_{\text{H-out}}$ and $P_{\text{C-in}}$.

During the cold period, the demagnetization process is performed as the fluid enters the matrix at T_{H} (hot blow), cools down as heat is transferred to the porous medium, and exits the regenerator at a temperature below T_{C}. The hot blow outlet temperature is represented by its time-average, $\overline{T}_{\text{CE}}$. Then, the fluid returns to the double effect pump and is pumped back to the regenerator through the Cold MFM. The fluid then flows through the cold heat exchanger and electrical heater, before returning to the regenerator. Note that in the hot blow the mass flow rate is measured by the Hot MFM and the pressure drop is taken as the difference between $P_{\text{C-out}}$ and $P_{\text{H-in}}$.

The thermal load is imposed by the electrical heater on the cold side. The temperature of the fluid entering the heater, $T_{\text{Heater-in}}$, is set equal to the time-average temperature of the fluid that exits the regenerator at the cold end during the hot blow, $\overline{T}_{\text{CE}}$. This is accomplished by the cold heat exchanger, which eliminates any heat gained along tubing and other elements on the cold side, including the instrumentation. Thus, there are two temperature probes to measure the heater inlet temperature (or the cold heat exchanger outlet temperature), $T_{\text{CH-out}}$ and $T_{\text{Heater-in}}$. The heater outlet temperature, $T_{\text{Heater-out}}$, is also measured. For practical purposes, this is taken as the cold reservoir temperature, i.e., $T_{\text{C}} = T_{\text{Heater-out}}$.

The cooling capacity is calculated based on the temperature difference between the regenerator inlet (cold blow) and outlet (hot blow) temperatures at the cold end, $\Delta T_{\text{CE}} = T_{\text{C}} - \overline{T}_{\text{CE}}$. A heat balance on the electrical heater can be used to check this calculation, where the heater temperature difference is given by $\Delta T_{\text{heater}} = T_{\text{C}} - T_{\text{Heater-in}}$. The cooling capacity calculation procedure will be explained in more detail in the AMR results chapter, together with some discussions about the uncertainties associated with the procedure.

3.2 Sub-systems of the Apparatus

3.2.1 Magnetic Circuit

Nested Halbach cylinders (NHC) were used recently in several AMR apparatuses (TURA; ROWE, 2011; ARNOLD *et al.*, 2014). The NHC configuration shown in Fig. 3.6 consists of two concentric Halbach cylinders so that each magnet array generates a magnetic field in its core. If the magnetic field contributions of each magnet are added, then the maximum magnetic flux density, $\vec{B}_{\max}$, of the NHC is observed at the core of the inner magnet, as shown in Fig. 3.6(a). Conversely, when the magnetic field contributions are subtracted, the minimum magnetic flux density, $\vec{B}_{\min}$, is obtained, as seen in Fig. 3.6(b). Thus, it follows that the NHC configuration is an alternating magnetic field source. By creating a relative motion between the cylinders, the magnetic field changes continuously between the maximum and the minimum flux density positions (COEY, 2002; BJØRK *et al.*, 2010d; TURA; ROWE, 2011).

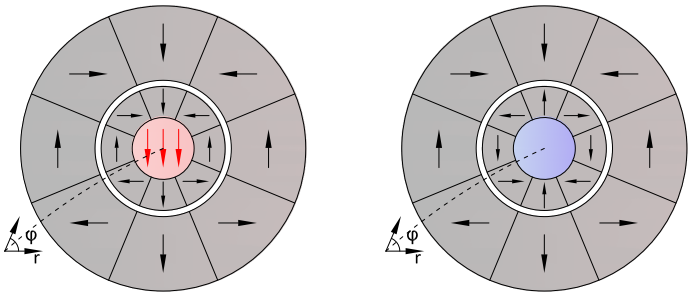

(a) (b)

Figure 3.6 – Nested Halbach cylinders: (a) At the maximum magnetic field position; (b) At the minimum magnetic field position. The black arrows indicate the remanent flux density of the permanent magnet segments, while the red arrows indicate $\vec{B}$ in the magnetic gap.

The NHC configuration was chosen as the magnetic field source for the present AMR test apparatus for the following reasons:

1. It can generate high magnetic flux densities of the order of 1.5 T;

2. It is compact and a reasonable mass of magnetocaloric material can be contained in the high magnetic field change region;

3. It can be easily assembled with a simple structure;

4. It creates a variable field simply by rotating the cylinders, thus enabling operating frequencies as high as 4 Hz (TURA; ROWE, 2011).

On the other hand, some drawbacks of NHCs can be listed as follows:

1. Only a single regenerator can be housed per core. Thus, for continuous cyclic operation, at least two NHCs are required;

2. Oscillating torques can be developed due to segmented magnets (ARNOLD *et al.*, 2014; MHÍOCHÁIN *et al.*, 1999);

3. Asymmetric magnetic field waveforms can be generated, which reduce the AMR performance by making the low field period shorter than the high field (TURA; ROWE, 2011; ARNOLD *et al.*, 2014; TREVIZOLI *et al.*, 2014);

4. A significant amount of permanent magnet raw material ($Nd_2Fe_{14}B$) is usually required to build NHCs, which leads to high unit costs.

Typically, NHC arrays have low values of the figure of merit Λ_{cool} when compared with other magnetic circuits (BJØRK *et al.*, 2010c)[1]. However, the ability to change the magnetic field at high frequencies with low inertial effects makes this configuration close to ideal for the present apparatus design. One of the main challenges of using NHC arrays as the variable magnetic field source in AMR test devices is the design of the motion system. Appropriate selection of components, such as gear boxes, pulleys, belts, driver and shaft couplings is crucial for achieving frequencies of the order of 1 Hz with low noise and small mechanical losses.

[1] Λ_{cool} can be used to quantify the potential of a magnetic circuit for magnetic refrigeration applications. An ideal magnet for an AMR prototype, with a high value of Λ_{cool}, should guarantee a large magnetic field variation (high magnetocaloric effect), a large volume of generated magnetic field (larger density of magnetocaloric material), must be used during most of the cycle time (ideally in a continuous cycle) and, equally important, use a small amount of permanent magnet (to reduce cost).

Rotating a single magnet or counter rotating the two magnets dictates how the magnetic field will change in the core of the NHC array, as illustrated in Fig. 3.7. Rotating the internal magnet (I) with a static external magnet (E), Fig. 3.7(a), results in the simplest and most compact magnet motion configuration, since the external magnet is usually the heaviest piece (TURA; ROWE, 2011). As illustrated in Fig. 3.7(a), rotating the inner array causes both the magnitude (modulus) and the orientation (direction) of the magnetic flux density vector to change continuously. At position [(E) at 0°; (I) at 0°], $\vec{B}$ is maximum with a downward direction, while at position [(E) at 0°; (I) at 45° or 135°], the modulus of $\vec{B}$ is smaller with the orientation always in phase with the angle of the inner array. The minimum field is observed at position [(E) at 0°; (I) at 180°]. The change in direction of $\vec{B}$ gives rise to a external magnetic force acting on the magnetocaloric regenerator positioned in the magnet core. This magnetic force tends to rotate the regenerator with the magnet, generating structural problems which are more serious when the regenerator matrix is composed by thin parallel plates or pins. Additionally, a rotating magnetic field direction in the magnetic gap increases the complexity of evaluating demagnetizing losses in AMRs (BAHL; NIELSEN, 2009; TREVIZOLI *et al.*, 2012).

Counter rotating the internal and external magnets, Fig. 3.7(b), requires a more complex magnet motion system. However, as the Halbach cylinders counter rotate, the modulus of $\vec{B}$ changes continuously, but the orientation is kept fixed. In Fig. 3.7(b), at position [(E) at 0°; (I) at 0°], $\vec{B}$ is maximum and points downward, while at position [(E) at -45°; (I) at 45°], the magnitude of $\vec{B}$ has decreased, maintaining the same direction. At position [(E) at -90°; (I) at 90°], $\vec{B}$ is minimum. Further counter rotation inverts the direction of $\vec{B}$. At position [(E) at -135°; (I) at 135°], the magnitude of $\vec{B}$ is larger, but it points upward. The maximum modulus is reached again at position [(E) at -180°; (I) at 180°], this time with an upward direction. For the counter rotating configuration, the frequency is twice that of the single magnet configuration.

The design of the NHC array built in this thesis was based on an analytical method to find the optimal NHC dimensions that guarantee high magnetic flux densities at the highest possible Λ_{cool}. The proposed method was validated with numerical simulations using COMSOL Multiphysics 3D and experimental measurements of the magnetic flux density in the magnet array (TREVIZOLI *et al.*, 2015). The NHC de-

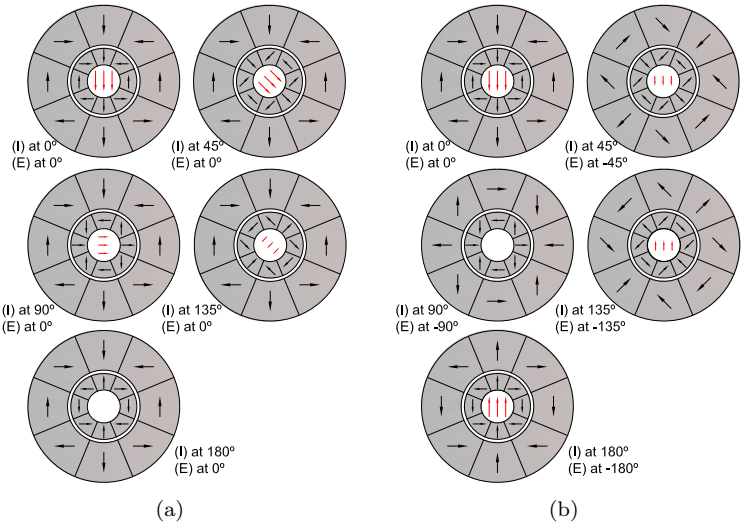

Figure 3.7 – Illustration of the NHC magnetic field variation: (a) Rotation of the internal magnet with a static external magnet; (b) Counter rotation of the internal and external magnets. The black arrows indicate the remanent flux density of the permanent magnet segments, while the red arrows indicate $\vec{B}$ in the magnetic gap.

sign and evaluation procedure is summarized in Appendix A. Sintered $Nd_2Fe_{14}B$ (BAKKER-MAGNETICS, 2014) was the magnet raw material used to manufacture the Halbach cylinders. To avoid the magnetization reversal effect (BLOCH *et al.*, 1998; BJØRK *et al.*, 2008), the N50M and N42UH magnet grades were used in the outer and inner cylinders, respectively. The final magnetic circuit dimensions are presented in Table 3.3.

Table 3.3 – Dimensions of the NHC array obtained from the analytical design procedure.

Internal Magnet			External Magnet		
$D_{i,I}$ (mm)	$D_{e,I}$ (mm)	L_I (mm)	$D_{i,E}$ (mm)	$D_{e,E}$ (mm)	L_E (mm)
27.0	58.0	115.0	64.0	135.0	130.0

A photograph of the final NHC design built according to the dimensions presented in Table 3.3 is shown in Fig. 3.8. Despite the more

complex bearing structure and motion system, the counter rotating configuration was preferred since one of the objectives of the AMR test apparatus is to evaluate experimentally regenerative geometries, such as parallel plates and staggered arrays of pins. Hence, a fixed direction of the magnetic flux density vector guarantees structural stability of the regenerator geometry. Fig. 3.9 presents a y-z cutaway view of the final magnet design, showing the bearing structure designed for the counter rotation of the magnets.

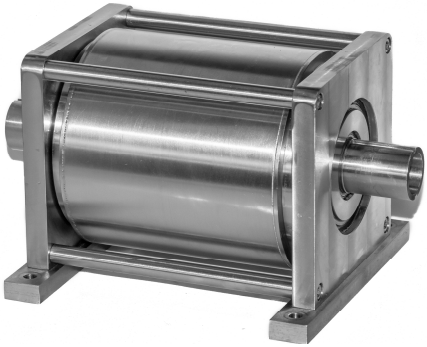

Figure 3.8 – Nested Halbach Cylinder magnetic circuit built according to the dimensions obtained from the proposed design procedure.

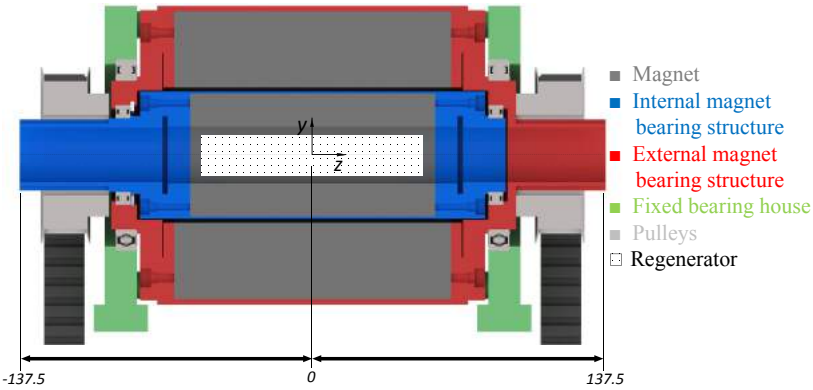

Figure 3.9 – y-z cutaway view of the NHC design showing the bearing structure to enable the counter rotation of the external and internal magnets. Dimensions in mm.

Fig. 3.10 presents the experimental results of the resultant magnetic

flux density along the center line ($x = y = 0$) of the NHC array (between $z = 0$ and 137.5 mm) as a function of the rotating angle of the internal cylinder. It should be noted that in the counter rotating configuration the two cylinders are dephased by 180°, so the rotating angle of the external cylinder has a negative sign. The solid lines represent the measurement stations inside the NHC array where the regenerator is located ($-50 \leq z \leq 50$ mm). The dotted lines correspond to stations outside the regenerator region surrounded by the bearing structure (see Fig. 3.9). This means that the NHC array has a maximum magnetic flux density (at 0 and 180°) of 1.69 T and a minimum flux density (at 90° and 270°) of about 0.04 T.

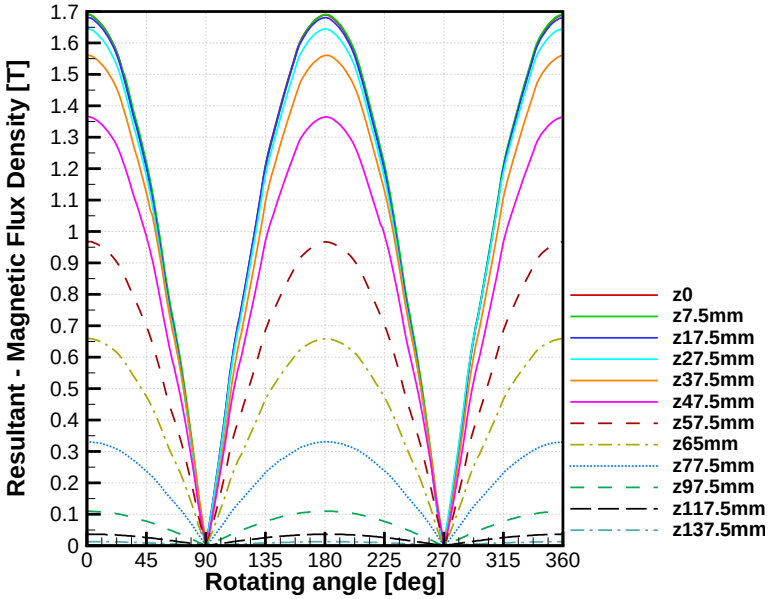

Figure 3.10 – Experimental resultant magnetic flux density measurements at different positions along the z axis as a function of the rotating angle of the inner magnet.

Fig. 3.11 shows the axial profiles of the maximum magnetic flux density components (x and y) and the resultant and the vector direction (θ). The dark gray region represents the external and internal cylinder arrays, and the light gray region the stainless steel support structure. In the regenerator region ($-50 \leq z \leq 50$ mm), the magnetic flux density is higher than 1.3 T. Regarding the vector direction, ideally, it should be

0°. However, the measured θ was approximately 2.5°. This indicates a small deviation of the $\vec{B}$ direction with respect to the vertical direction in the region occupied by the regenerator. Outside the cylinder arrays, the magnetic field decreases continuously to 0 T at $z = 137.5$ mm and the vector magnetic flux density changes its direction between $7.5 < \theta < 45^o$. As presented in the experimentally verified COMSOL simulation results, the radial distribution of the magnetic flux density is approximately uniform (see Fig. A.2). More information about the magnetic flux density characterization can be found in Appendix A.

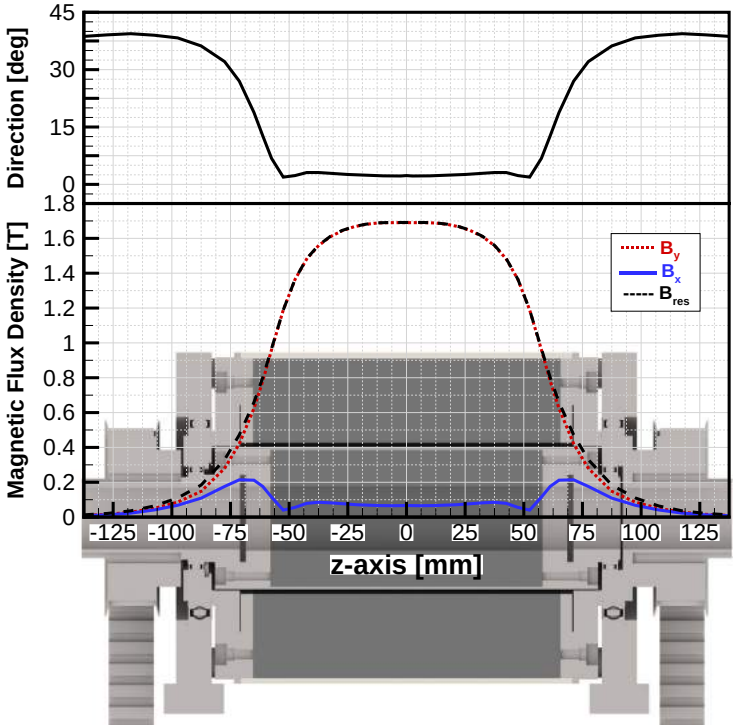

Figure 3.11 – Magnitude of the components, resultant and direction of the magnetic flux density at the maximum field position along the z-axis.

Fig. 3.12 shows the 3-D COMSOL simulations and the experimental results of the magnetic flux density as a function of the axial distance in the regenerator region ($-50 \leq z \leq 50$ mm). The experimental z-averaged magnetic flux density over the regenerator region was 1.61

T. A good agreement between COMSOL and the experimental data is observed. Deviations can be attributed mainly to the fabrication of the magnet. Therefore, the proposed design procedure, presented in Appendix A, can be used to develop NHC magnet systems for applications that require alternating magnetic field changes (TREVIZOLI *et al.*, 2015).

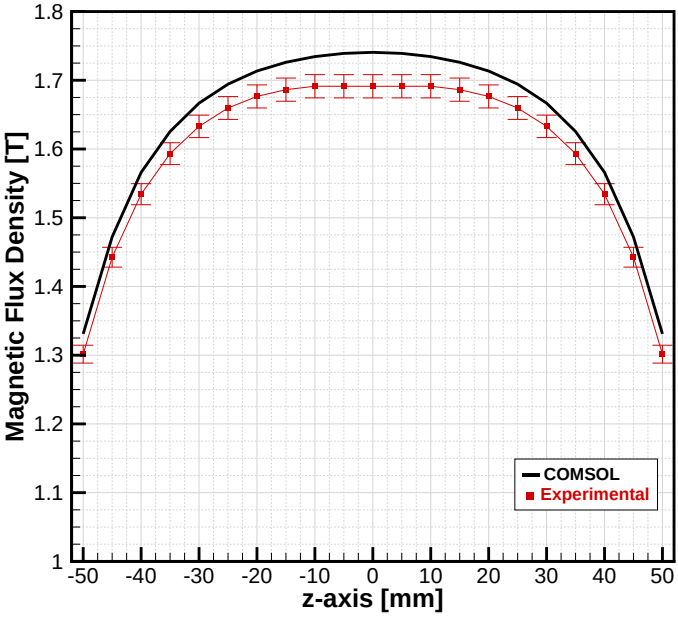

Figure 3.12 – Axial variation of the maximum magnetic flux density.

3.2.2 Pumping System

The pumping system of the passive and active magnetic regenerator apparatus is composed by a double effect pump and a crank disc coupled with the motor. The double effect pump was chosen as it presents the following advantages:

1. It can perform the cold and hot blows by simply rotating the crank disc and using only unidirectional check vales (Fig. 3.13(b));

2. For a given stroke adjusted in the crank disc, the volume of fluid

pumped per cycle is fixed. The mass flow rate (and hence the flow velocity) is adjusted simply by changing the operating frequency. This allows keeping a constant utilization factor while changing the mass flow rate (and hence the NTU), as was done to generate the ideal regenerator results presented in Fig. 2.3;

3. The pumping system is driven directly by the motor, which also drives the magnetic circuit. Thus, a single motor can be used, enabling an easier synchronization between the magnetic and fluid flow cycles. This also simplifies the analysis of the performance metrics, since the total motor work can be measured directly.

4. It is compact and easy to assemble, service and maintain.

Nevertheless, in terms of performance, the main disadvantage of double effect pumps is that they provide sinusoidal fluid flow waveforms, with a peak in flow velocity in the middle of the blow. As a consequence, peaks in pressure drop and pumping power are also observed. For instance, if the flow profile is perfectly sinusoidal with an average pressure drop of 100 kPa (1.0 bar), the peak pressure drop is about 157 kPa ($\pi/2 \times 100$ kPa), which can offer some restrictions to operating condition at high mass flow rates. As presented in Fig. 3.13(a) and in Table 3.4, three different pump sizes were used to cover a broad range of pumping volumes (and utilization factors). Table 3.4 also shows the pump dimensions and displaced volume as a function of the stroke that is adjusted at the crank disc, as presented in Fig. 3.13(c). Finally, the time-average ($\bar{\dot{m}}$) mass flow rate per blow is calculated by:

$$\overline{\dot{m}} = \rho_{\mathrm{f}} \omega \frac{s_{\mathrm{k}}}{4} (D_{\mathrm{cyl}}^2 - D_{\mathrm{shf}}^2) \tag{3.1}$$

where $\omega = 2\pi f$ is the angular frequency, s_{k} is the piston stroke, D_{cyl} is the pump cylinder diameter and D_{shf} is the shaft diameter.

Table 3.4 – Displaced volume (V_{pump}) [cm^3] used in the experiments.

Pump	Diameter [mm]		Stroke (s_{k}) [mm]				
	Cylinder	Shaft	10	15	20	25	30
PP42.5	19.05	6.35	2.53	3.80	5.07	6.33	-
PP92.5	27.00	7.92	5.23	7.84	10.45	13.07	-
PP122.5	31.75	11.10	6.95	10.42	13.90	17.37	20.85

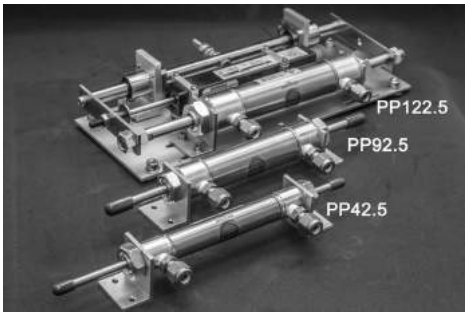

(a)

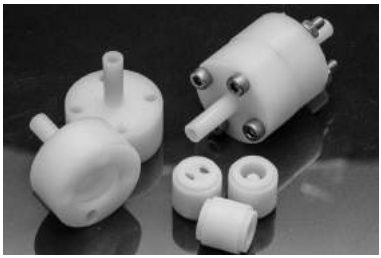

(b)

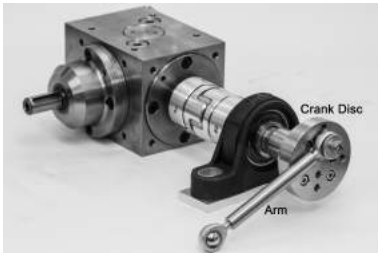

(c)

Figure 3.13 – Pumping system: (a) Double effect pumps; (b) Check valves; (c) Crank disc.

3.2.3 Transmission System

Fig. 3.14(a) shows the NHC and pumping motion system. A stepper motor (Kalatec Nema 34, model KML-HT34-487) coupled to a 15:1 reduction gearbox is employed to achieve high torques. The stepper motor is controlled by a driver (Applied Motion model ST10), which guarantees precise operating speed and frequency. The torque transducer is assembled between the reduction and the spiral bevel gearboxes. The spiral bevel gearbox (Tandler STD00-EA-III, 1:1) was found to be a suitable and compact solution to counter rotate the magnets, where the torque imposed by the stepper motor is transmitted by the bevel gears into two independent shafts that rotate in opposite directions. Two sets of pulleys and belts are used to connect the spiral bevel gearbox and the magnets.

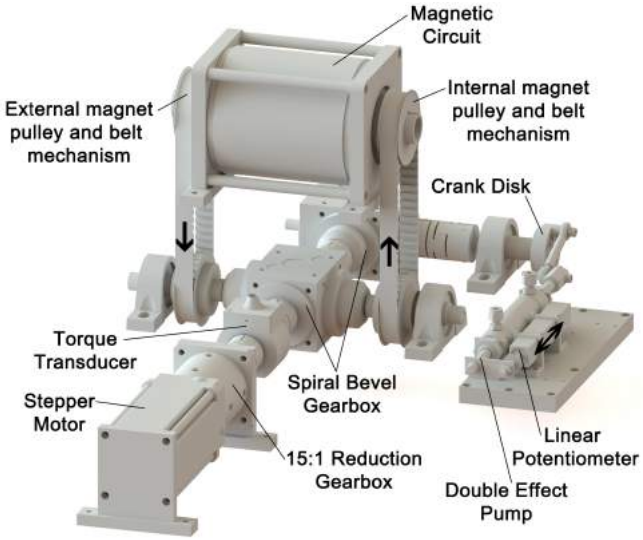

(a)

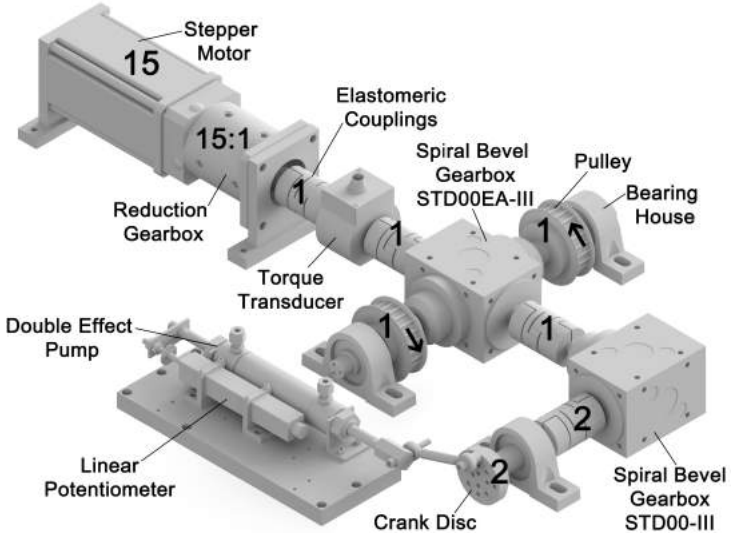

(b)

Figure 3.14 – Transmission system to counter rotate the NHC while keeping the phasing with the pumping system: (a) Overall design; (b) Transmission relations between the shafts.

A second spiral bevel gearbox (Tandler STD00-III, 1:2) was used to drive the double effect displacer. This gearbox was selected with a transmission relation of 1:2 to guarantee the phasing with the NHC since, for counter rotating magnets, the relation between the magnetic circuit and the motor driving shaft is 2:1. Thus, for a perfect synchronization, the pump also must have a relation of 2:1 with the driving shaft (two hot and two cold blows). Fig. 3.14(b) shows the transmission relations between all shafts of the system.

3.2.4 Magnetic and Fluid Flow Synchronization

Fig. 3.15 presents the magnetic and fluid flow waveforms of the AMR apparatus. The hot cycle takes place between 0 and 180°, during which the magnetic flux density increases from approximately 70% of its maximum at zero flow to 100% at a maximum flow velocity at 90°. Then, the magnetic flux density decreases to approximately 70% again and the flow reverses. In the remaining period, i.e., the cold cycle, the magnetic flux density reaches a minimum when the hot blow velocity reaches a maximum in the reverse direction. It is worth noting that the magnetic flux density waveform is a rectified sinusoidal profile, with a sharp minimum at around 270°. As shown in Trevizoli *et al.* (2013a, 2014), this results in a very short period of time at the minimum magnetic flux density, which has a negative impact on the performance of the magnetic cycle in comparison with the perfect sinusoidal and square waveforms.

3.3 Passive Regenerators Matrices

The passive regenerators matrices were built using different bed geometries to enable a comprehensive performance evaluation (e.g., losses) and model validation. The following matrix geometries were evaluated: packed beds of spheres, pin arrays and parallel plates. The resulting variety of geometric parameters, from porous media length scales to housing dimensions, are important to verify the sensitivity and generality of the experimental and numerical results. Additionally, the comparisons between different porous media matrices enabled analyzing the potential of each geometry in terms of their thermal performances and associated losses. All matrices used in the passive heat transfer analysis in this thesis were made from stainless steel AISI-304.

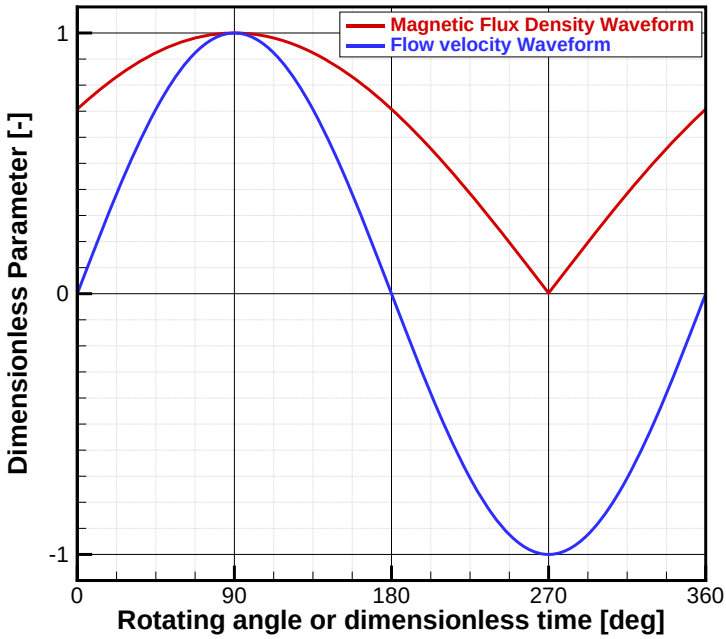

Figure 3.15 – Magnetic and fluid flow waveforms synchronization.

In the sphere packed bed regenerators, three different spherical particles and four different regenerator housing (casing) geometries were used. As will be seen, three casings have the same cross sectional area, $A_{c,Reg}$, and different lengths, L_{Reg}, while two share the same length but have different cross sectional areas. The porosity, ε, was approximately constant in all matrices. This allows a more precise performance comparison for different values of flow rate, superficial velocity and utilization, which is crucial for evaluating the sensitivity of the experimental apparatus, validating the numerical model and optimizing performance for a specified operating condition.

The void volume is another important parameter for evaluating the performance of regenerative matrices, especially when the total volume of the matrix is varied. As mentioned before, the void volume is defined as the volume of fluid between each regenerator end and its corresponding heat exchanger that changes direction outside the regenerator, without interacting thermally with it. The void volume fraction, ϑ^*, is defined as the ratio between the total void volume, ϑ, and the fluid volume in

the regenerator, $\varepsilon A_{c,Reg} L_{Reg}$:

$$\vartheta^* = \frac{\vartheta}{\epsilon A_{c,Reg} L_{Reg}} \tag{3.2}$$

To study the impact of the void volume on the thermal performance of passive regenerators, different regenerator-to-tube adapters (R-T adapters) were designed and fabricated with different void volume sizes, which can be combined with the different housing volumes to result in different values of ϑ^* for each case. The void volume size is approximately the internal volume of the R-T adapters.

Regarding the different bed geometries, the spheres, pins and plates were selected and/or fabricated to maintain approximately the same particle diameter. In porous media, the particle diameter is the ratio of the surface (interstitial heat transfer) area and the volume of the regenerator. Thus, for bed geometries with the same particle diameter and approximately the same porosity, the heat transfer surface area is approximately the same. As a result, by fixing the mass flow rate (constant utilization and frequency), housing cross sectional area and void volume fraction, what differentiates the surfaces with respect to their thermal performance are the magnitude of the interstitial heat transfer coefficient and the thermal losses, especially the axial heat conduction (since in passive regenerators the heat exchange with the ambient is negligible).

3.3.1 Packed Beds of Spheres

The packed bed matrices were composed by stainless steel spheres with particle diameters, d_p, of 0.5 mm, 0.8 mm and 1 mm, as shown in Fig. 3.16. The regenerator casings are presented in Fig. 3.17. Casings #1, #2 and #3 have the same cross sectional area but different lengths. Casings #3 and #4 have the same length but different cross sectional areas. Table 3.5 presents the dimensions and porosities associated with each matrix, where $D_{h,Reg}$ is the regenerator housing hydraulic diameter and $\zeta_{Reg} = L_{Reg}/D_{h,Reg}$ is the regenerator aspect ratio. The housing for the packed bed regenerators were made from acetal resin (POM). The R-T adapter #1 was used in the tests presented in this section for Casings #1, #2 and #3. For Casing #4 a specific R-T adapter was designed because of the smaller diameter

of this casing, as presented in Table 3.5. The different void volume fractions are also presented in Table 3.5.

The dimensional measurement uncertainties associated with the diameters and lengths were taken as the design tolerances used to machine the casings. The porosity was calculated using the casing volume and the total mass of the spheres, whose uncertainties involve the dimensional tolerance and the scale uncertainty. The maximum calculated uncertainty of the porosity was about ± 0.005. More details about the packed bed regenerator assembly can be found in Appendix B.

Table 3.5 – Packed bed of spheres passive regenerators.

Casing	Dimensions			Porosity ± 0.005 [-]			ϑ^* [%]
	$D_{h,Reg}$ [mm]	L_{Reg} [mm]	ζ_{Reg} [-]	d_p 0.5 mm	d_p 0.8 mm	d_p 1 mm	
#1	22.22	50	2.25	0.364	0.365	0.364	14.5
#2	22.22	75	3.375	0.363	0.365	0.364	9.67
#3	22.22	100	4.50	0.363	0.363	0.363	7.25
#4	14.70	100	6.80	0.369	0.370	0.368	14.4

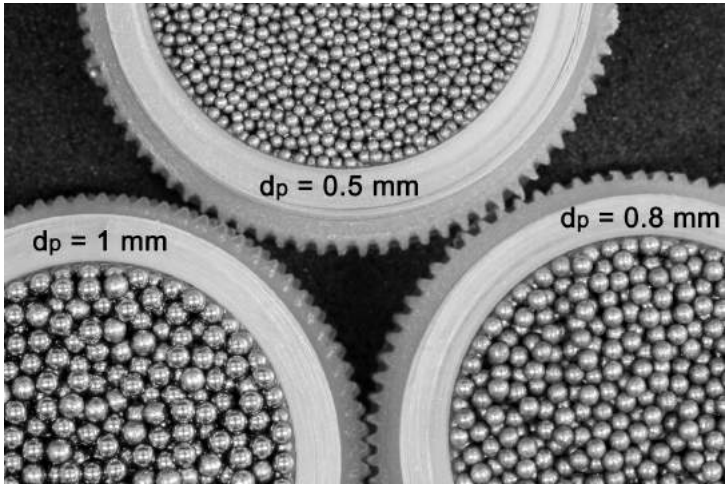

Figure 3.16 – Stainless steel spheres for the packed bed regenerative matrices.

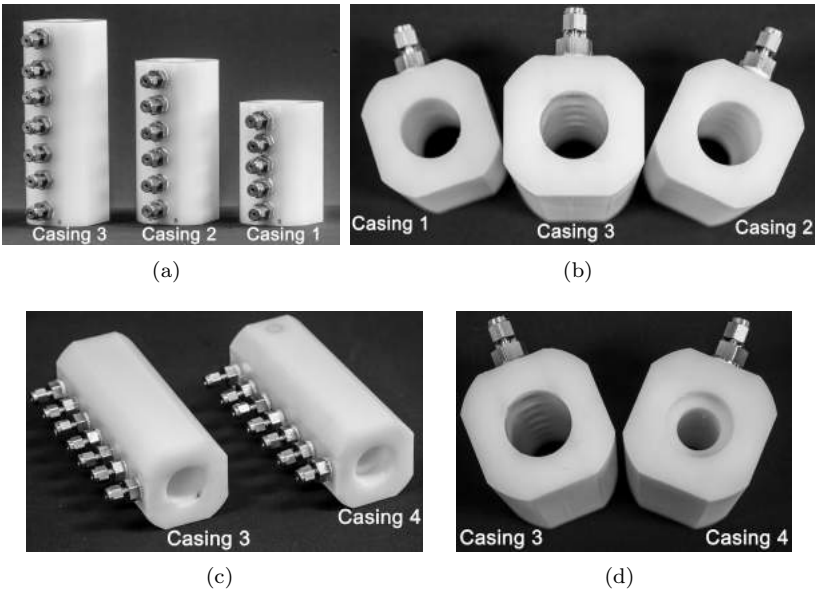

Figure 3.17 – Regenerator casings: (a) Frontal view of Casings #1, #2 and #3; (b) Top view of Casings #1, #2 and #3; (c) Isometric view of Casings #3 and #4; (d) Top view of Casings #3 and #4.

3.3.2 Void Volume and Entrance Effects

In the evaluation of the effect of the regenerator aspect ratio, it is important to maintain a fixed void volume fraction. Thus, different R-T adapters were fabricated in order to achieve a void volume fraction of about 7.5% in the regenerators with the same diameter and different lengths, as presented in the secondary diagonal of Table 3.6 and in Fig. 3.18.

Table 3.6 – Void volume fractions for different casings and sizes of R-T adapters.

Casing	d_p 1 mm Porosity	ϑ^*		
		R-T Adapter #1	R-T Adapter #2	R-T Adapter #3
#1	0.364	14.50%	9.67%	7.25%
#2	0.364	11.20%	7.44%	5.58%
#3	0.363	7.66%	5.10%	3.82%

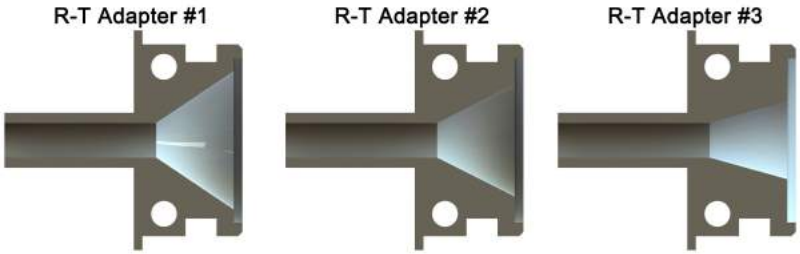

(a)

(b)

Figure 3.18 – R-T adapters: (a) Design details; (b) Built R-T adapters.

In theory, eliminating the void volumes improves the regenerator thermal performance, as these are directly related to the leakage losses (SHAH; SEKULIĆ, 2003). In order to systematically evaluate the impact of the void volumes on the performance of the passive regenerators developed here, the void volumes were decreased by reducing the diverging section of the R-T adapters. However, this reduction of the cross sectional area is known to increase the importance of two-dimensional flow entrance effects (i.e., mixing) inside the regenerator matrix, which can impact negatively on the regenerator effectiveness. Therefore, for a fixed regenerator geometry, changing the R-T adapter enables quantifying the balance between the impact of the void volume and the entrance effects on the thermal performance. Additionally, a zero void volume regenerator (Casing #7) was built based on the AMR geometry proposed by Lozano (2015). The zero void volume housing of Lozano (2015), presented in Fig. 3.19, had a round rectangular cross sectional area, with the flow streams entering and exiting the regenerator by the parallel ports on each side, flowing diagonally through the matrix. The

regenerator dimensions for Casing #7 are shown in Table 3.7, where W_{Reg} and H_{Reg} are the cross-section width and height, respectively. Two different spheres sizes were evaluated in this regenerator, namely 0.5 and 1 mm.

Table 3.7 – Casing #7 - zero void volume regenerator design.

Casing	Dimensions				Porosity ± 0.005 [-]		ϑ^*
	W_{Reg} [mm]	H_{Reg} [mm]	L_{Reg} [mm]	ζ_{Reg} [-]	d_{p} 0.5 mm	d_{p} 1 mm	
#7	27.85	10	80	5.44	0.373	0.365	-

(a) (b)

Figure 3.19 – Casing #7 - Zero void volume regenerator design: (a) Isometric view detailing the entrance and exiting passages; (b) Top view of the rectangular cross sectional area.

3.3.3 Parallel Plates and Pin Arrays

The parallel plate and staggered square pin array regenerators were machined by wire electrical discharge machining (WEDM). The mechanical design of the matrices took into account limitations such as the minimum wire diameter (0.14 mm) and maximum wire length (25 mm) (EDM-TECHNOLOGIES, 2013). A 1-mm thick base plate was used in the present design to guarantee the structural stability of the matrix.

Based on the above fabrication limitations and to guarantee an interstitial area equivalent to that of the 0.8-mm packed sphere regenerator, the pins and plates were designed to yield equivalent particle diameters and porosities of around 0.8 mm and 36%, respectively. This resulted in plates with a thickness of 0.25 mm and square pins with 0.53-mm

sides. Fig. 3.20 shows single pieces of a WEDM parallel plate and a square pin array matrix. For simplicity, the pin array and plate matrices have a square cross sectional area, while the cross section areas of the packed sphere matrices are round. The final regenerators were designed to have approximately the same cross sectional area and the same total matrix mass/volume. Therefore, given values of fluid flow rate and frequency will result in approximately the same utilization factor and fluid superficial velocity. Consequently, any differences in NTU or performance between the matrices can be regarded as due to differences in heat transfer coefficient and thermal losses. Table 3.8 shows the geometric characteristics of the matrices, where e_{g} denotes the thickness of the solid piece (plate or pin) and e_{ch} is the thickness of the flow channel or passage.

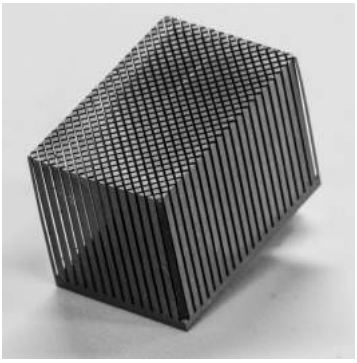

(a)

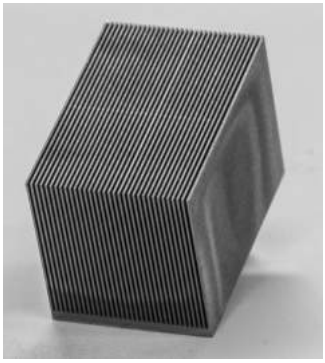

(b)

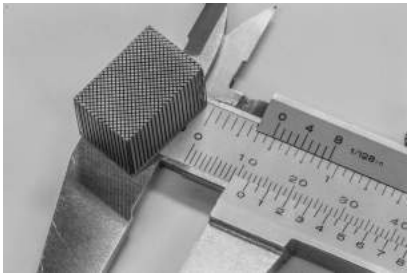

(c)

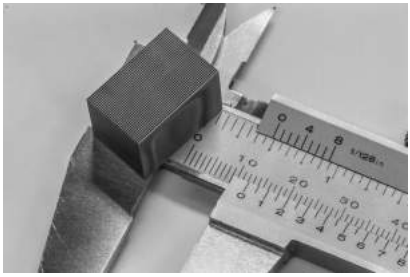

(d)

Figure 3.20 – Parallel plate and square pin arrays: (a) Detail of square pins; (b) Detail of parallel plates; (c) Scale of the pin array piece; (d) Scale of the parallel plate piece.

Table 3.8 – Characteristics of the passive regenerators.

Matrix	Geometry [mm]			ε [-]	Dimensions [mm]			ϑ^*[%]
	e_g	e_{ch}	d_p		W_{Reg}	H_{Reg}	L_{Reg}	
Spheres #4	-	-	0.8	0.370	14.7		100	14.4
Plates #5	0.25	0.14	0.75	0.359	13.12	13	100	15.8
Pins #6	0.53	0.14	0.795	0.374	13.27	13	100	15.0

To build the 100-mm long pin and plate regenerators, as presented in Fig. 3.21, five 20-mm long pieces were combined into a single regenerator matrix. The challenge in this assembly was to avoid obstructing the flow passages, as shown in Fig. 3.21(a). Next, the final matrix was inserted in a 3D-printed digital ABS (acrylonitrile butadiene styrene) housing, shown in Figs. 3.21(b) and (c). The matrices were kept fixed to the housing by epoxy resin to avoid flow channeling. Finally, the ABS housing was inserted into a G10 fiberglass resin casing to improve the mechanical resistance, as shown in Fig. 3.21(d). The mounting of the ABS piece into the G10 casing was designed with a tight tolerance to prevent external leakages. More details regarding the pin array and plate regenerators are presented in Appendix B.

New R-T adapters with a square sectional area were designed to minimize flow maldistributions in the parallel plate and pin array matrices. The void volume sizes of these adapters are the same as those made for Casing #4 (packed spheres). The square R-T adapters, shown in Fig. 3.22, were also 3D printed in digital ABS.

3.4 AMR Matrices

The AMR matrices were also built in the three different porous media geometries, i.e., packed beds of spheres, parallel plates and pin arrays. Also, as will be seen, the regenerator housing dimensions were kept constant. All the AMR matrices were made from commercial-grade gadolinium (Gd).

The first AMR matrix assembled and evaluated in this thesis (for this reason referred to as the Reference AMR) consists of a packed bed of Gd spheres with diameters in the range $0.5 \leq d_p \leq 0.6$ mm (0.55 mm average). The dimensions of the Reference AMR casing are 22.22 mm (ID of the G10 casing) and 100 mm (casing length), which are

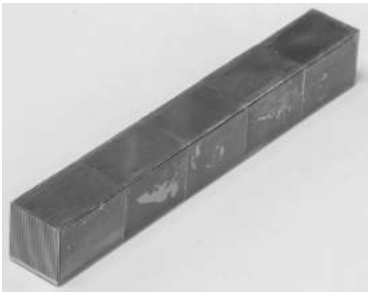

(a)

(b)

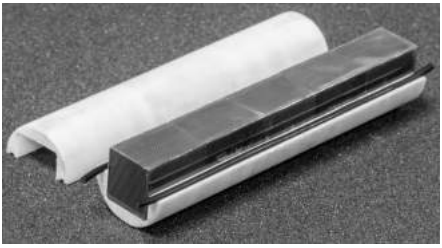

(c)

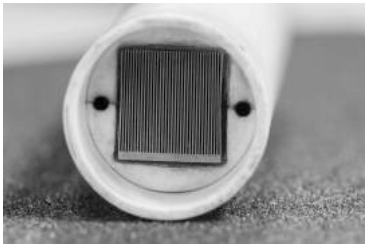

(d)

Figure 3.21 – Parallel plate and pin array regenerators: (a) Combination of the five pieces into a 100-mm long matrix; (b) Digital ABS housing; (c) Assembling the matrix in the ABS housing; (d) ABS housing inside the G10 casing.

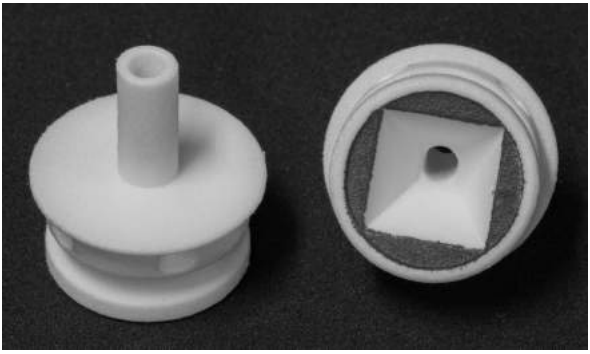

Figure 3.22 – R-T adapters for the parallel plate and pin array matrices.

the maximum housing dimensions that fit in the magnetic gap of the Halbach array.

Other AMR regenerators were built with the same dimensions of the passive regenerator matrices shown in Table 3.8. The housings and R-T adapters were also identical in their geometry and materials. The only slight difference between the passive and active regenerators lies in the sphere diameter range of the Gd packed bed regenerator. The Gd spheres were supplied with diameters in the range $0.71 \leq d_p \leq 0.85$ mm (0.78 mm average). Therefore, by evaluating the performances of the passive regenerators in the light of their thermal effectiveness, axial heat conduction and viscous losses, it will be possible to draw some conclusions about these losses in the AMR geometries and understand the impact of losses occurring only in active regenerators, i.e., the magnetic losses. Table 3.9 shows the geometric characteristics of the AMR regenerators.

Table 3.9 – Characteristics of the AMR regenerators.

Matrix	Geometry [mm]			ε [-]	Dimensions [mm]			ϑ^*[%]
	e_g	e_{ch}	d_p		W_{Reg}	H_{Reg}	L_{Reg}	
Spheres #3	-	-	0.55	0.362	22.22		100	7.25
Spheres #4	-	-	0.78	0.370	14.64		100	15.4
Plates #5	0.25	0.14	0.75	0.359	13.12	13	100	15.8
Pins #6	0.53	0.14	0.795	0.374	13.27	13	100	15.0

3.5 Thermal Insulation

Thermal insulation is a crucial aspect in regenerator design. The heat interactions between the regenerator and the surroundings have to be carefully considered when comparing experimental data and numerical results. A trustworthy comparison between numerical and experimental regenerator results can be performed in only two ways: (i) by making a good thermal insulation; (ii) by implementing a comprehensive model for the heat transfer with the surroundings.

In the passive regenerator experiments, the POM casings were designed with a minimum wall thickness of 11 mm. Additionally, there is enough space around the regenerator housing to put the thermal insulation, as can be seen in Fig. 3.23, where the red arrows indicate the steps of the insulation procedure. The ambient temperature was kept at 300

K during all experiments, as this is the average temperature between the reservoirs (i.e., 280 K at the cold and 320 K at the hot heat exchangers, respectively). All passive regenerator experimental tests were conducted at this condition so as to compensate the heat gained from and lost to the surroundings.

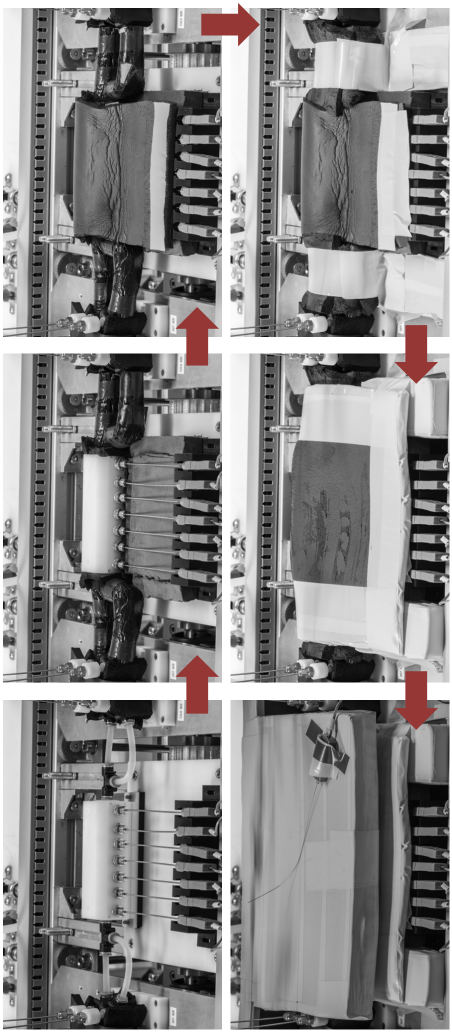

Figure 3.23 – Steps of the application of the thermal insulation on the passive regenerators.

On the other hand, in the AMR regenerators there is not sufficient space to put a good thermal insulation around the regenerator. Thus, there is a trade-off between how big the housing thickness can be and the total mass of magnetocaloric material to be placed in the regenerator. However, a thermal insulation as effective as the one used in the passive experiments is not possible. Fig. 3.24 shows cross-section views of the two types of AMRs inside the magnet gap. In Fig. 3.24(a), the Spheres #3 regenerator, the thermal insulation is performed only by the G10 casing. Conversely, in the parallel plate and pin array regenerators shown in Fig. 3.24(b) (Plates #5 and Pins #6), the thermal insulation is executed by the ABS and G10 layers. It should be noted that in the Spheres #4 geometry, the insulation is similar to that in the plate and pin array regenerators. The air gap between the regenerator casing and the inner magnet is 0.8-mm thick. Besides, the magnet has a much bigger thermal mass compared with that of the regenerator, thus, the heat transfer interaction between the regenerator and the magnet cannot be disregarded. As will be seen, special attention has been given to the modeling of the heat transfer to the casing and surroundings in the present thesis.

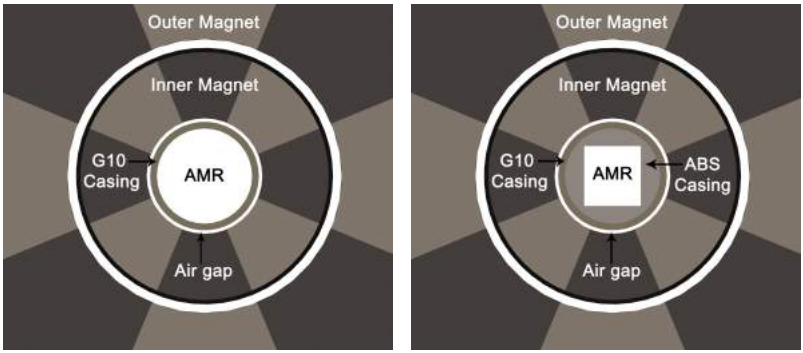

(a) (b)

Figure 3.24 – AMR insulation: (a) Casing #3; (b) Casing #5 (parallel plates) and Casing #6 (pin array). Casing #4 is similar to (b) but with a round cross sectional area.

3.6 Instrumentation and Data Acquisition

For an in-depth characterization of the thermal passive and active magnetic regenerator performances, different transducers were applied, as presented in Table 3.10. The instrumentation was positioned at different points of the experimental setup, as shown in Figs. 3.2 and 3.4 for the passive and AMR apparatuses, respectively. The readings were performed with a National Instruments data acquisition (DAQ) system connected to a computer equipped with Labview 2009. The time-dependent variables were measured, graphically evaluated and saved in data files for a subsequent data regression. Additional information about the main components of the DAQ are presented in Table 3.11.

Table 3.10 – Summary of the instrumentation.

Sensor	Comp.	Model	Uncertainty
Temperature probe	Omega	TMQSS-020G-6	0.15-0.2 K
Pressure transducer	Omega	PX613-200G5V	0.5 kPa
Linear potent.	Omega	LP802-50	-
Mass flow meter	Krone	Optimass 3300C-S04	1%
Torque Meter	HBM	T22/20Nm	0.5%
Torque Meter	HBM	T22/50Nm	0.5%
Scale	Shimadzu	UX4200H	0.02 g

Table 3.11 – Main components of the National Instruments data acquisition system.

Component	Model
Chassis	SCXI-1001 12 slots
Board	NI PCI-6289 18-bits
Temperate Module	SCXI-1112 8ch
Voltage Module	SCXI-1102B 32ch
Terminal Block	SCXI-1303 32ch

Grounded 0.5-mm diameter temperature probes (T-type thermocouples) were selected for the transient temperature measurements, due to their low inertia. The probes were calibrated using a standard thermometer with an uncertainty of 0.1 K. The probes and the standard thermometer were positioned in a thermal bath with a variable temperature between 263 and 333 K (intervals of 5 K). For every temperature, after stabilization, the readings were averaged over 2 minutes. The calculated uncertainty of the probes positioned at the regenerator ends, inside the matrix and the probes used to calculate the heater enthalpy

flux was 0.15 K. The uncertainty of the ambient temperature probes was 0.2 K.

The pressure transducers were calibrated using a DH Bundenberg 580-series dead-weight tester between 100 kPa and 1000 kPa. According to the calibration report, the maximum uncertainty of the pressure transducers was 0.5 kPa. The scale was calibrated using standard weights between 50 and 500 g, and the uncertainty was evaluated at 0.02 g.

The uncertainties of the remaining instruments were obtained from their respective catalog information. Two different torque meters were used, depending on the torque being measured. To measure the individual torques developed by the pumping system the low range transducer was applied due to the smaller uncertainties involved. However,to measure the total torque developed by the AMR (including pumping system and magnetic circuit), which can be as high as 30 Nm, a 50 Nm (full scale) torque meter was used. Coriolis mass flow meters were selected for their capability of reading pulsating flows with a relatively low uncertainty. The time constant of the present Coriolis flow meters was such that they were capable of reading flow rate transients at low frequencies (between 0.25 and 0.5 Hz). Average mass flow rates for frequencies between 0.75 and 2 Hz still can be measured with reasonable accuracy (to be discussed later). Nevertheless, due to the large time constant, the average mass flow can be slightly overestimated up to 15 kg/h for high mass flow rates (> 100 kg/h).

A linear potentiometer is positioned in phase with the double effect pump (see Figs. 3.13(a) and 3.14) and is used mainly to calculate the operating frequency to be used in the data regression. Based on the time-dependent potentiometer signal, the Labview Tone Measurement tool reads the sinusoidal waveform and converts it into a frequency value. An excellent correlation was verified between the stepper motor and the potentiometer frequency signal. Also, based on the potentiometer signal, it was possible to identify the points where the hot and cold blows start and end. This is the first step in the evaluation of the performance metrics, where no phasing is verified between the potentiometer and temperature probes, but a small phasing, less than 3% of the blow period, is corrected in the pressure transducers and torque meter readings. Only the mass flow meters presented a more noticeable phasing that can be attributed to the time constant.

For a precise time-average analysis, the data acquisition rate, f_{DAQ}, was selected according to the operating frequency as follows:

$$\frac{f_{\mathrm{DAQ}}}{f} = 300 \tag{3.3}$$

which means that, irrespective of the frequency, there are 150 data points in the cold and hot cycles, respectively.

3.7 Details of the Final Assembly

The calibration and positioning of the temperature probes are extremely important in the present experimental analysis, since the thermal effectiveness and temperature control of the cold end in AMR tests are based on the time-average temperatures at the ends of the regenerators. Fig. 3.25(a) presents the final assembly of Casing #3, where the internal and end temperature probes can be identified in Figs. 3.25(b) and (c). It should be noted that Casings #1, #2 and #4 are similar, but Casing #1 has 3 internal probes, Casing #2 has 4 internal probes and Casing #3 and #4 have 5 internal probes.

Fig. 3.26(a) shows a picture of the parallel plate (Plates #5) regenerator (identical to Pins #6), with the instrumentation at the regenerator ends. Fig. 3.26(b) shows an end temperature probe in detail. No internal probes were used in the plate and pin array geometries.

Fig. 3.27(a) shows a picture of Casing #7, with the instrumentation positioned at the regenerator ends. Fig. 3.27(b) shows the end temperature probes. For Casing #7, no internal temperature probes were used. As Casing #7 was designed and fabricated without void volumes, two different temperature probes were used on each side; one for the inlet and another for the outlet flow measurements. All other matrices used single probes positioned in the void volume at each regenerator end, allowing measurements of temperatures of the inlet and outlet streams.

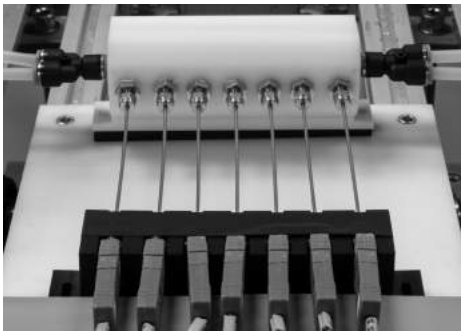

(a)

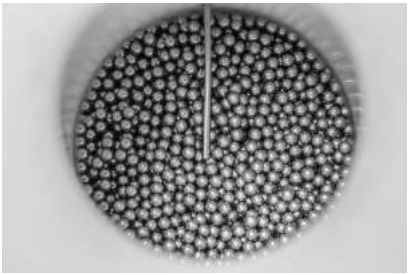

(b)

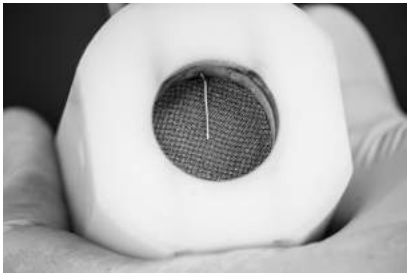

(c)

Figure 3.25 – Packed bed regenerators: (a) Casing #3 final assembly; (b) Internal temperature probe positioning; (c) Ends temperature probe positioning.

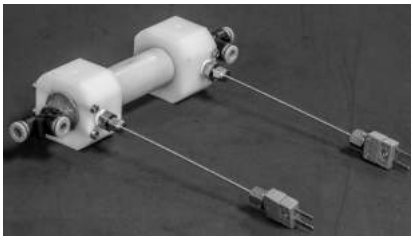

(a)

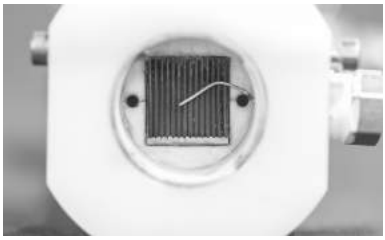

(b)

Figure 3.26 – Parallel plate and pin array regenerator: (a) Casing #5 and #6 final assembly; (b) Ends temperature probe positioning.

(a)

(b)

Figure 3.27 – Zero void volume regenerator: (a) Casing #7 final assembly; (b) Positioning of end temperature probes.

Regarding the AMR regenerators, all matrices had the same length and no internal temperature probes were used. Fig. 3.28(a) shows the final AMR assembly, where the regenerator region is at the middle part. The AMR length is 100 mm and, as presented in Fig. 3.9, the magnetic circuit is 275 mm in length. To increase the final housing length, the AMR is assembled between two G10 tube adapters. The G10 tube adapters are fitted to centering bearing housings, shown in Fig. 3.28(c), that are positioned at the ends of the magnetic circuit to guarantee the concentricity between the regenerator housing and the magnet cylinders. Since there is little room available around the matrix, the temperature probe is assembled axially and bent to ensure cross flow around the probe, as shown in Fig. 3.28(b).

(a)

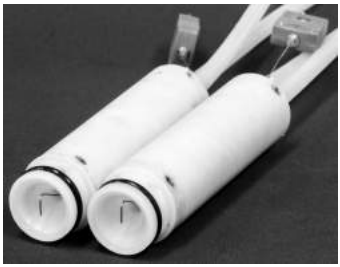

(b)

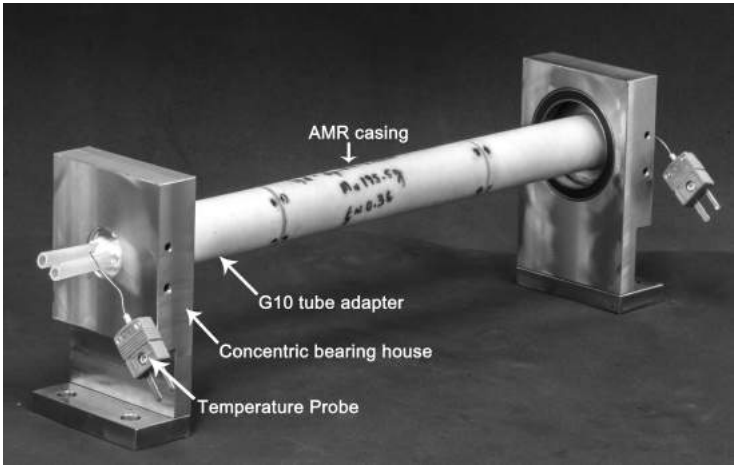

(c)

Figure 3.28 – AMR beds: (a) Final assembly; (b) Positioning of the end temperature probes; (c) Final assembly with the temperature probes and bearing housings.

Four transducers were used to measure the flow static pressure: two for the hot blow (indicated by the red arrows) and two for the cold blow (blue arrows), as presented in Fig. 3.29. This configuration was preferred to avoid oscillating flow on the pressure transducers, which simplifies the calculation of the time-average pressure drop, especially in terms of phasing between the temperature and pressure readings.

Fig. 3.30 shows cutaway views of the passive and active regenerator setup, showing in detail the position of the temperature probes and pressure transducers.

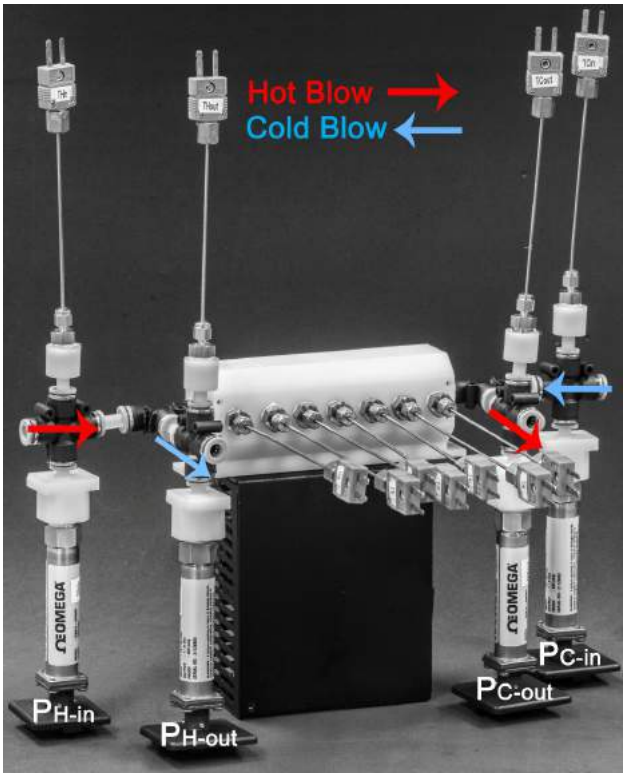

Figure 3.29 – Positions of the pressure transducers. The red arrows indicate the hot blow and the blue arrows the cold blow.

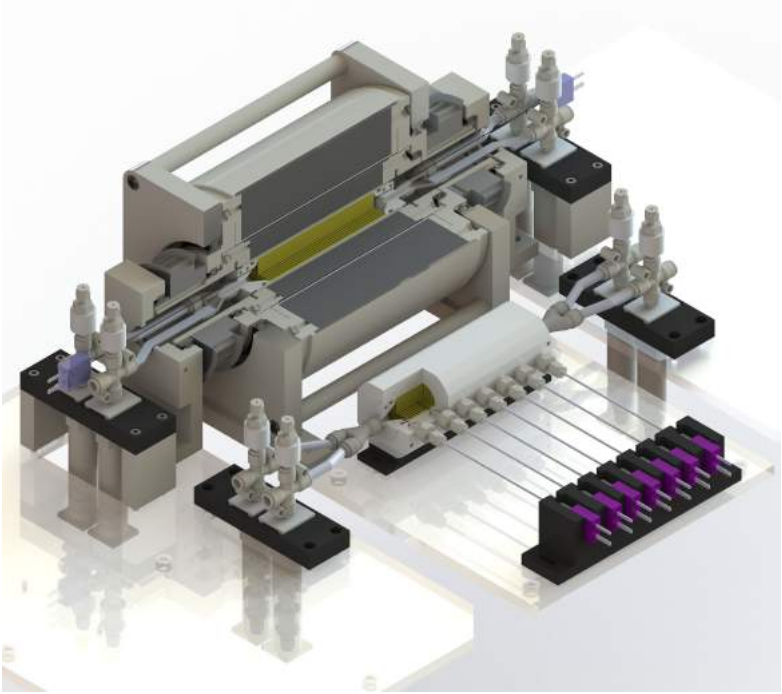

Figure 3.30 – Final design and details of the passive and active regenerator experimental setup.

4 Problem Formulation and Solution Method

This chapter describes the numerical model developed to study passive and active magnetic regenerators. The fluid flow and heat transfer in the porous medium are modeled using a one-dimensional, transient, thermal non-equilibrium approach. Besides the magnetic field dependent physical properties, the main difference between the passive and AMR thermal models lies in the presence of a source term in the solid energy equation, which is responsible for the magnetocaloric effect.

4.1 Regenerative Porous Matrix Modeling

The regenerator matrix is treated as a porous medium, with a void volume fraction (porosity), ε, occupied by the fluid phase. The solid phase fraction is $1-\varepsilon$. Thermal non-equilibrium is assumed between the phases, which have different temperatures (KAVIANY, 1995). A volume-average approach (QUINTARD; WHITAKER, 1993; KAVIANY, 1995) was adopted to avoid the computational costs involved in solving the transfer processes at the pore scale level. In the one-dimensional formulation, the heat transfer between the phases is modeled in terms of an interstitial heat transfer coefficient, evaluated based on correlations for the Nusselt number.

The passive regenerator model comprises the momentum equation, which is used to calculate the fluid flow through the porous matrix and conjugate energy equations for the fluid and solid phases. To extend this heat transfer model to the AMR case, a magnetic model is incorporated into the heat transfer calculation loop to compute the

magnetocaloric effect (MCE) and the demagnetization losses.

The mathematical model of the fluid flow and heat transfer in a regenerative porous matrix is described next. The basic geometry of the model is presented in Fig. 4.1. The following simplifying assumptions were made:

1. One dimensional flow;
2. Laminar, incompressible fluid flow;
3. Low porosity medium, i.e., $\varepsilon < 0.6$;
4. Absence of body forces.

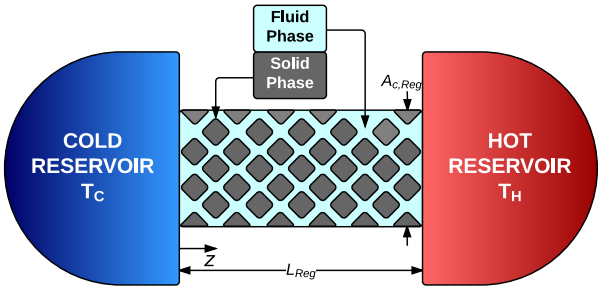

Figure 4.1 – Basic geometry of the 1-D fluid flow and heat transfer model of a regenerative porous matrix.

In the porous medium heat transfer model, initially, the thermal losses to the surroundings and the void volumes on each end of the matrix adjacent to the thermal reservoirs are disregarded. The fluid enters the regenerator at constant and uniform temperatures, i.e., $T_{\mathrm{CE}} = T_{\mathrm{C}}$ at the cold end and $T_{\mathrm{HE}} = T_{\mathrm{H}}$ at the hot end, where T_{C} and T_{H} are the temperatures of the cold and hot thermal reservoirs, respectively.

4.1.1 Momentum Equation

The macroscopic momentum equation, also known as Brinkman-Forchheimer equation, is given by (KAVIANY, 1995; NIELD; BEJAN, 2006):

$$\frac{\rho_{\mathrm{f}}}{\varepsilon}\left(\frac{\partial \vec{v}}{\partial t}+\vec{v}\cdot\nabla\vec{v}\right)=-\nabla P+\rho_{\mathrm{f}}\vec{\mathrm{f}}+\frac{\mu_{\mathrm{f}}}{\varepsilon}\nabla^2\vec{v}-\frac{\mu_{\mathrm{f}}}{K}\vec{v}-\frac{c_{\mathrm{E}}\rho_{\mathrm{f}}}{K^{1/2}}|\vec{v}|\vec{v} \quad (4.1)$$

where the term on the left is the macroscopic inertial force and those on the right are the pore pressure gradient, body force, macroscopic viscous shear stress (Brinkman viscous term), microscopic shear stress (Darcy term) and microscopic inertial force (Ergun inertial term), respectively. In the fluid flow model, the fluid properties were treated as constants obtained at an average fluid temperature. The solutions of the flow and temperature fields are, therefore, uncoupled. This simplifies the model and reduces significantly the convergence time, since it is not necessary to solve the pressure-velocity coupling to guarantee the mass conservation. Using the simplifying assumptions (2), (3) and (4), one can neglect $\vec{v}\cdot\nabla\vec{v}$, the Brinkman viscous term and the body force term, respectively. Therefore:

$$\frac{\rho_{\mathrm{f}}}{\varepsilon}\left(\frac{\partial u}{\partial t}\right)=-\frac{\partial P}{\partial z}-\frac{\mu_{\mathrm{f}}}{K}u-\frac{c_{\mathrm{E}}\rho_{\mathrm{f}}}{K^{1/2}}|u|u \quad (4.2)$$

where t is the time, u is the superficial (Darcian) flow velocity, ρ is the density, μ is the dynamic viscosity. Additionally, K is the permeability of the porous media and c_E is the Ergun constant, which depend on the geometry and porosity of the matrix and are evaluated based on a closure relationships that will be presented Section 4.3.

The non-dimensionalization of Eq. (4.2) is explained next. The dimensionless time is defined as $t^* = \omega t$, where $\omega = 2\pi f$ is the angular frequency and f the cycle frequency. To describe the oscillatory flow in the regenerator, the pressure gradient can be approximated by a time-dependent function, which contains a characteristic waveform (ZHAO; CHENG, 1996, 1998; OLIVEIRA *et al.*, 2012):

$$-\frac{\partial P}{\partial z}=\rho_{\mathrm{f}}A_{\mathrm{t}}g(t^*) \quad (4.3)$$

where A_{t} is the amplitude of the pressure drop waveform and $g(t^*)$ is the dimensionless mathematical function that describes the waveform. In the present thesis, since the fluid flow is generated by a double effect

displacer coupled to a rotating crank disc, the fluid flow has a sinusoidal waveform, hence $g(t^*) = \sin(\omega t)$. Thus, in Eq. (4.2), the dimensionless pressure gradient can be approximated directly by $-\frac{\partial P}{\partial z}\Big|^* = g(t^*)$.

The dimensionless velocity in the momentum equation is defined as $u_{\mathrm{D}}^* = u/u_{\mathrm{D,max}}$, where $u_{\mathrm{D,max}}$ is the maximum velocity calculated via the Darcy Equation, i.e., when the dimensionless pressure gradient is constant and maximum, $g(t^*) = 1$. As a result:

$$u_{\mathrm{D,max}} = -\frac{K}{\mu_{\mathrm{f}}}\frac{\partial P}{\partial z}\Big|_{max} = -\frac{K}{\nu_{\mathrm{f}}}A_{\mathrm{t}} \tag{4.4}$$

Therefore, when terms other than the microscopic shear stress are non-negligible, the actual maximum velocity in the porous medium, $u_{\max}$, is different from $u_{\mathrm{D,max}}$, which means that the value of $u_{\mathrm{D}}^* = u/u_{\mathrm{D,max}}$ is, in general, less than unity. In geometries such as parallel plates, the shear stress is small and, as a result, $u_{\mathrm{D,max}} = u_{\max}$. The dimensionless momentum equation in its final form is given by:

$$\frac{Re_\omega Da}{\varepsilon}\frac{\partial u_{\mathrm{D}}^*}{\partial t^*} = g(t^*) - u_{\mathrm{D}}^* - F|u_{\mathrm{D}}^*|u_{\mathrm{D}}^* \tag{4.5}$$

where the dimensionless groups are the kinetic Reynolds number $Re_\omega = \omega d_{\mathrm{h}}^2/\nu_{\mathrm{f}}$, the Darcy number $Da = K/d_{\mathrm{h}}^2$ and the Forchheimer number $F = c_{\mathrm{E}}A_{\mathrm{t}}K^{1.5}/\nu_{\mathrm{f}}^2$. In the above equations, ν_{f} is the kinematic viscosity, $d_{\mathrm{h}} = 4\varepsilon/\beta$ is the porous medium hydraulic diameter and β is the surface area density of the porous medium.

4.1.2 Energy Equations

The derivation of the energy equations for the fluid and solid phases considers the one-dimensional, laminar, incompressible fluid flow in the porous medium. The thermophysical properties of both phases depend on the temperature and, in the active magnetic regenerator case, the properties of the magnetocaloric material also depend on the magnetic flux density. Again, it is important to note that the momentum equation and the energy equations are solved uncoupled. Hence, the flow velocity is an input parameter in the energy solver.

4.1.2.1 Fluid Phase Energy Equation

The macroscopic energy balance for the fluid phase is given by,

$$\rho_{\mathrm{f}}(T)c_{\mathrm{p,f}}(T)\left(\varepsilon\frac{\partial T_{\mathrm{f}}}{\partial t}+u\frac{\partial T_{\mathrm{f}}}{\partial z}\right)=h(z)\beta(T_{\mathrm{s}}-T_{\mathrm{f}})+\left|u\frac{\partial P}{\partial z}\right|+$$
$$\varepsilon\left[\kappa_{\mathrm{f}}^{\mathrm{eff}}+\rho_{\mathrm{f}}(T)c_{\mathrm{p,f}}(T)D_{||}\right]\frac{\partial^2 T_{\mathrm{f}}}{\partial z^2}+\dot{q}_{\mathrm{csg}} \tag{4.6}$$

where the terms on the left are due to inertial (thermal capacity) effects and longitudinal advection, and those on the right are the interstitial heat transfer term calculated using a convective heat transfer coefficient, the viscous dissipation, the axial conduction and the casing heat transfer terms, respectively (KAVIANY, 1995; NIELD; BEJAN, 2006). T_{f} is the fluid temperature and T_{s} is the solid temperature, $c_{\mathrm{p,f}}$ is the fluid specific heat capacity, $\kappa_{\mathrm{f}}^{\mathrm{eff}}$ is the effective thermal conductivity of the fluid phase, $D_{||}$ is the longitudinal thermal dispersion and Pr is the Prandtl number based on the fluid properties. In dimensionless form, Eq. (4.6) is given by,

$$\frac{\partial\theta_{\mathrm{f}}}{\partial t^*}=Nu_{\mathrm{dh}}Fo_{\mathrm{f}}(\theta_{\mathrm{s}}-\theta_{\mathrm{f}})-\frac{Re_{\max}}{Re_{\omega}\zeta}u^*\frac{\partial\theta_{\mathrm{f}}}{\partial z^*}+\frac{Br}{Pr}\left|g(t^*)u^*\right|+$$
$$\frac{1}{PrRe_{\omega}\zeta^2}\left(\frac{k_{\mathrm{f}}^{\mathrm{eff}}}{k_{\mathrm{f}}(T)}+\frac{D_{||}}{\alpha_{\mathrm{f}}}\right)\frac{\partial^2\theta_{\mathrm{f}}}{\partial z^{*2}}+\dot{q}^*_{\mathrm{csg}} \tag{4.7}$$

where the dimensionless fluid and solid temperatures are given by $\theta_{\mathrm{f,s}}=(T_{\mathrm{f,s}}-T_{\mathrm{C}})/(T_{\mathrm{H}}-T_{\mathrm{C}})$, where T_{C} and T_{H} are the cold and hot reservoir temperatures, respectively. In the energy equation, the dimensionless superficial velocity is defined as $u^*=u/u_{\max}$, where u_{max} is the maximum instantaneous velocity in the oscillatory flow field already known from the momentum solution. $z^*=z/L_{\mathrm{Reg}}$ is the dimensionless axial distance, and L_{Reg} is the length of the regenerator bed. The aspect ratio based on the hydraulic diameter of the porous medium is defined as $\zeta=L_{\mathrm{Reg}}/d_{\mathrm{h}}$. Finally, $\alpha_{\mathrm{f}}=k_{\mathrm{f}}(T)/(\rho_{\mathrm{f}}(T)c_{\mathrm{p,f}}(T))$ is the thermal diffusivity of the fluid.

The dimensionless numbers in Eq. (4.7) are the Nusselt number based on the hydraulic diameter $Nu_{\mathrm{dh}}=h(z)d_{\mathrm{h}}/k_{\mathrm{f}}(T)$, the Fourier number

for the fluid phase $Fo_\mathrm{f} = \alpha_\mathrm{f}/\omega(d_\mathrm{h}/2)^2$, the Reynolds number based on the maximum velocity and on the hydraulic diameter $Re_\mathrm{max} = (u_\mathrm{max}/\varepsilon)d_\mathrm{h}/\nu_\mathrm{f}(T)$ and the Brinkman number $Br = \frac{\mu_\mathrm{f}(T)A_\mathrm{t}(u_\mathrm{max}/\varepsilon)}{k_\mathrm{f}(T)\omega(T_\mathrm{H}-T_\mathrm{C})}$. The variables $\kappa_\mathrm{f}^\mathrm{eff}$, $D_{||}$ and Nu_dh depend on the geometry of the porous media and are calculated using specific closure relationships that will be presented in Section 4.3. The dimensionless casing heat transfer term, $\dot{q}^*_\mathrm{csg}$, is defined in Section 4.2.2

The dependence of the fluid properties, namely ρ, c_p, k and μ, on the temperature was considered by means of interpolations from the EES (Engineering Equation Solver) database (KLEIN, 2013). In the passive regenerator modeling, the properties were those of distilled water, while in the AMR modeling the fluid was a mixture of distilled water and ethylene-glycol (80%/20% wt.).

4.1.2.2 Solid Phase Energy Equation

The macroscopic energy balance for the solid phase is given by:

$$\rho_\mathrm{s}(T)c_\mathrm{s}(T)(1-\varepsilon)\frac{\partial T_\mathrm{s}}{\partial t} = h(z)\beta(T_\mathrm{f}-T_\mathrm{s}) + (1-\varepsilon)k_\mathrm{s}^\mathrm{eff}\frac{\partial^2 T_\mathrm{s}}{\partial z^2} + \dot{q}_\mathrm{MCE} \quad (4.8)$$

where the term on the left accounts for thermal inertia in the solid, and those on the right are due to interstitial heat convection, axial heat conduction and the magnetocaloric effect source term (if applicable), respectively. ρ_s is the solid density, c_s is the solid specific heat capacity and $k_\mathrm{s}^\mathrm{eff}$ is the effective thermal conductivity of the solid (KAVIANY, 1995; NIELD; BEJAN, 2006).

Using the same dimensionless variables of the fluid energy equation, the dimensionless form of the solid phase energy equation is given by:

$$\frac{\partial \theta_\mathrm{s}}{\partial t^*} = BiFo_\mathrm{s}(\theta_\mathrm{f}-\theta_\mathrm{s}) + \frac{\kappa_\mathrm{s}^\mathrm{eff}/k_\mathrm{f}(T)}{PrRe_\omega\zeta^2}\Re^*\frac{\partial^2\theta_\mathrm{s}}{\partial z^{*2}} + \dot{q}^*_\mathrm{MCE} \quad (4.9)$$

where $Bi = h(z)\ell_\mathrm{c}/k_\mathrm{s}(T)$ is the Biot number and $Fo_\mathrm{s} = \alpha_\mathrm{s}/\omega\ell_\mathrm{c}^2$ is the Fourier number of the solid phase. $\alpha_\mathrm{s} = k_\mathrm{s}(T)/(\rho_\mathrm{s}(T)c_\mathrm{s}(T))$ is the thermal diffusivity of the solid, $\ell_\mathrm{c} = (1-\varepsilon)/\beta$ is the characteristic length of the porous medium and $\Re^* = \rho_\mathrm{f}(T)c_\mathrm{pf}(T)/\rho_\mathrm{s}(T)c_\mathrm{s}(T)$ is the

thermal capacity ratio. The effective thermal conductivity of the solid, κ_s^{eff}, depends on the geometry of the porous medium and is calculated using an appropriate closure relationship to be described in Section 4.3. The Biot number can be calculated based on the Nusselt number, $Bi = (\ell_c/d_h)(k_f(T)/k_s(T))Nu$. The dimensionless magnetocaloric term, $\dot{q}^*_{MCE}$, is defined in Section 4.4.1.

The dependence of the solid properties of the passive matrix, namely ρ, c and k, on the temperature were calculated via interpolations of the properties of stainless steel available in EES (KLEIN, 2013). In the modeling of active regenerators, the properties of Gd were estimated using a specific calculation procedure to be described in Section 4.4.3.

4.2 Losses Modeling

The modeling of different types of losses is necessary for a more precise comparison with the experimental data, which leads to more consistent evaluations of the physical phenomena involving heat transfer and fluid flow. Regarding the void volume losses, Jacobs and Zimm (2008) presented numerical results that showed a significant impact of the void volume size on the AMR cooling capacity. According to Nielsen *et al.* (2011), the heat interactions between the regenerator bed and its surroundings are disregarded in most AMR models, which assume a perfect insulation of the bed and ignore the thermal interactions with the regenerator housing. Thus, the present numerical model introduces a comprehensive modeling of thermal and void volume losses in order to better evaluate their impact on the thermal performance of passive and active magnetic regenerators.

4.2.1 Void Volume Modeling

The void volume modeling consists in evaluating the time-dependent temperature of the fluid in the space between each regenerator end and the adjacent heat exchanger. At the end of a given blow, a volume of fluid stops in the void volume and returns to the regenerator bed in the next blow. This fluid does not interact with the thermal reservoirs. Moreover, the fluid that returns to the regenerator does so at a temperature that is actually time dependent. The temperatures of the fluid entering the regenerator at the cold and hot ends (during the

cold and hot blows, respectively), coming from the void volumes, are termed here $T_f^{vv}(t)|_{CE}$ and $T_f^{vv}(t)|_{HE}$. These temperatures are calculated based on a solution of the energy equation for the cold and hot void volumes. Fig. 4.2 shows the basic geometry of the 1-D fluid flow and heat transfer model including the void volumes, which are modeled as an extension of the regenerator bed without the porous medium.

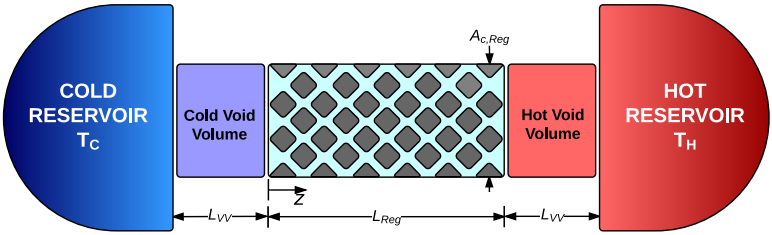

Figure 4.2 – Basic geometry of the 1-D fluid flow and heat transfer model including the void volumes.

The assumptions made in the derivation of the energy equation for the void volumes are as follows:

1. One dimensional, laminar and incompressible flow;
2. The void volumes have the same cross sectional area as the regenerator bed. Hence, the flow velocity in the void volumes is the same as the superficial velocity in the regenerator;
3. The heat transfer with the walls is negligible;
4. The hot and cold void volumes are identical;
5. The fluid properties depend only on the temperature.

The void volume length, L_{vv}, is calculated based on the void volume fraction, ϑ^*, defined in Eq. (3.2), where the size of the void volume is defined as $\vartheta = A_{c,Reg} L_{vv}$. Therefore:

$$L_{vv} = \varepsilon \vartheta^* L_{reg} \tag{4.10}$$

After the assumptions, the energy equation for the fluid in the void volume is given by:

$$\frac{\partial T_{\mathrm{f}}^{\mathrm{vv}}}{\partial t} = -u\frac{\partial T_{\mathrm{f}}^{\mathrm{vv}}}{\partial z} + \frac{k_{\mathrm{f}}}{\rho_{\mathrm{f}} c_{\mathrm{p,f}}}\frac{\partial^2 T_{\mathrm{f}}^{\mathrm{vv}}}{\partial z^2} \tag{4.11}$$

and in dimensionless form it becomes:

$$\frac{\partial \theta_{\mathrm{f}}^{\mathrm{vv}}}{\partial t^*} = -\frac{Re_{\mathrm{max}}^{\mathrm{vv}}}{Re_{\omega}^{\mathrm{vv}}\zeta^{\mathrm{vv}}}u^*\frac{\partial \theta_{\mathrm{f}}^{\mathrm{vv}}}{\partial z^*} + \frac{1}{PrRe_{\omega}^{\mathrm{vv}}\zeta^{\mathrm{vv}2}}\frac{\partial^2 \theta_{\mathrm{f}}^{\mathrm{vv}}}{\partial z^{*2}} \tag{4.12}$$

where the dimensionless groups are now based on the regenerator housing hydraulic diameter, $D_{\mathrm{h,Reg}}$, and on the void volume length, L_{vv}. Thus: $Re_{\mathrm{max}}^{\mathrm{vv}} = (u_{\mathrm{max}}/\varepsilon)D_{\mathrm{h,Reg}}/\nu_{\mathrm{f}}$; $Re_{\omega}^{\mathrm{vv}} = \omega D_{\mathrm{h,Reg}}^2/\nu_{\mathrm{f}}$; $z^* = z/L_{\mathrm{vv}}$ and $\zeta^{\mathrm{vv}} = L_{\mathrm{Reg}}/D_{\mathrm{h,Reg}}$. The other dimensionless variables have been defined as before.

4.2.2 Casing Heat Transfer Modeling

The casing heat transfer modeling consists in determining the heat transfer rate per unit volume through the regenerator casing wall, $\dot{q}_{\mathrm{csg}}$. This loss is more significant in the AMR simulation, because the thermal insulation around the passive regenerator is more effective. In the AMR experiments, there is little room for a good thermal insulation and, as a result, the heat gained from the external environment can deteriorate the performance of the AMR. Thus, $\dot{q}_{\mathrm{csg}}$ has been included as a source term in the fluid energy equation (Eq. (4.6)).

Fig. 4.3 shows the basic geometry of the 1-D fluid flow and heat transfer model including the void volumes and the adjacent domains. In addition to the casing wall and air gap (thicknesses e_{wall} and e_{air}, respectively), the magnetic circuit is also considered in the heat interactions.

The following assumptions are considered in the casing heat transfer modeling:

1. The heat transfer in the wall and air gap is two-dimensional, i.e., both the radial and longitudinal directions are considered;
2. The curvature of the regenerator wall is negligible so that a cartesian coordinate system can be used to describe the problem geometry;
3. The air properties depend only on the temperature;

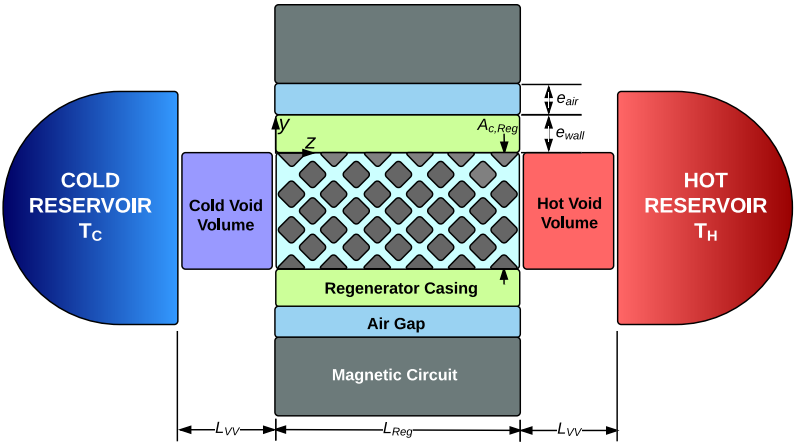

Figure 4.3 – Basic geometry of the 1-D fluid flow and heat transfer model including the void volumes and the adjacent domains (wall, air gap and magnet).

4. The wall properties are constant but, depending on the wall material, the transversal (i.e., radial) and longitudinal thermal conductivities can be different. Thus, specifically for the G10 casing $k_{\mathrm{wall,y}} \neq k_{\mathrm{wall,z}}$.

5. Since the thermal mass of the magnetic circuit is very large, the temperature of the magnet is assumed constant.

To calculate $\dot{q}_{\mathrm{csg}}$, the energy balances in the air gap and regenerator wall need to be evaluated. The energy equation for the air layer is given by:

$$\frac{\partial T_{\mathrm{air}}}{\partial t} = \frac{k}{\rho c_{\mathrm{p}}}\bigg|_{\mathrm{air}} \frac{\partial^2 T_{\mathrm{air}}}{\partial y^2} + \frac{k}{\rho c_{\mathrm{p}}}\bigg|_{\mathrm{air}} \frac{\partial^2 T_{\mathrm{air}}}{\partial z^2} + \frac{\dot{q}_{\mathrm{air}}}{\rho c_{\mathrm{p}}|_{\mathrm{air}}} \tag{4.13}$$

where $\dot{q}_{\mathrm{air}}$ is the viscous dissipation rate per unit volume, estimated assuming laminar Couette flow in the gap:

$$\dot{q}_{\mathrm{air}} = \mu_{\mathrm{air}} \left(\frac{\omega R_{\mathrm{i,I}}}{e_{\mathrm{air}}} \right)^2 \tag{4.14}$$

where $R_{\mathrm{i,I}}$ is the inner radius of the internal Halbach cylinder. The energy equation for the wall layer is:

$$\frac{\partial T_{\mathrm{wall}}}{\partial t} = \frac{k_{\mathrm{y}}}{\rho c}\Big|_{\mathrm{wall}} \frac{\partial^2 T_{\mathrm{wall}}}{\partial y^2} + \frac{k_{\mathrm{z}}}{\rho c}\Big|_{\mathrm{wall}} \frac{\partial^2 T_{\mathrm{wall}}}{\partial z^2} \tag{4.15}$$

In cases where the regenerator housing is composed by two different materials, such as in the parallel plates and pin arrays regenerators, Eq. (4.15) is solved for both layers of the casing. After solving the energy equations for the air gap and regenerator wall, $\dot{q}_{\mathrm{csg}}$ is calculated by:

$$\dot{q}_{\mathrm{csg}} = -h_{\mathrm{wall}} \frac{P_{\mathrm{c,Reg}}}{A_{\mathrm{c,Reg}}} (T_{\mathrm{f}} - T_{\mathrm{wall}}|_{(\mathrm{y}=0)}) \tag{4.16}$$

where $P_{\mathrm{c,Reg}}$ is the internal perimeter of the regenerator section and h_{wall} is the internal wall heat transfer coefficient (to be defined in Section 4.3.6). In dimensionless form, the energy equations for the air gap and regenerator wall are given by:

$$\frac{\partial \theta_{\mathrm{air}}}{\partial t^*} = \frac{\alpha_{\mathrm{air}}}{\omega e_{\mathrm{air}}^2} \frac{\partial^2 \theta_{\mathrm{air}}}{\partial y^{*2}} + \frac{\alpha_{\mathrm{air}}}{\omega L_{\mathrm{Reg}}^2} \frac{\partial^2 \theta_{\mathrm{air}}}{\partial z^{*2}} + \frac{\dot{q}_{\mathrm{air}}}{\rho c_{\mathrm{p}}|_{\mathrm{air}} \omega \Delta T_{\mathrm{Hex}}} \tag{4.17}$$

$$\frac{\partial \theta_{\mathrm{wall}}}{\partial t^*} = \frac{\alpha_{\mathrm{y,wall}}}{\omega e_{\mathrm{wall}}^2} \frac{\partial^2 \theta_{\mathrm{wall}}}{\partial y^{*2}} + \frac{\alpha_{\mathrm{z,wall}}}{\omega L_{\mathrm{Reg}}^2} \frac{\partial^2 \theta_{\mathrm{wall}}}{\partial z^{*2}} \tag{4.18}$$

where $y^* = y/e_{\mathrm{air}}$ or $y^* = y/e_{\mathrm{wall}}$, depending on the domain. It is important to notice that Eqs. (4.7), (4.17), (4.18) and (4.16) are solved coupled in the energy equation loop. The boundary conditions will be explained in detail in Section 4.5.

Additionally, the dimensionless $\dot{q}_{\mathrm{csg}}$ to include in the dimensionless form of the fluid phase energy equation (Eq. (4.7)) is given by:

$$\dot{q}_{\mathrm{csg}}^* = -Nu_{\mathrm{dh}}^{\mathrm{wall}} Fo_{\mathrm{f}} A^* (\theta_{\mathrm{f}} - \theta_{\mathrm{wall}}|_{(\mathrm{y}^*=0)}) \tag{4.19}$$

where $Nu_{\mathrm{wall}} = h_{\mathrm{wall}} d_{\mathrm{h}}/k_{\mathrm{f}}$ and $A^* = \frac{P_{\mathrm{c,Reg}} d_{\mathrm{h}}}{A_{\mathrm{c,Reg}}}$ is the dimensionless perimeter-area relation.

4.3 Closure Relationships

4.3.1 Particle Diameter and Surface Area Density

Before presenting the closure relationships, it is important to define the equivalent particle diameter, d_p, and the surface area density, β, of the porous medium. The surface area density is defined as the ratio of the interstitial area, A_HT, to the overall matrix volume, $V_s/(1-\varepsilon)$, where V_s is the volume of solid material in the matrix. Thus (KAVIANY, 1995):

$$\beta = (1-\varepsilon)S_\mathrm{v} \tag{4.20}$$

where $S_\mathrm{v} = A_\mathrm{HT}/V_s$ is the specific surface area, i.e., the interstitial area per unit solid volume. The equivalent particle diameter, in turn, is given by:

$$d_\mathrm{p} = \frac{6}{S_\mathrm{v}} \tag{4.21}$$

The geometry of the porous beds investigated in this thesis (i.e., packed bed of monodisperse spheres, parallel plates and square pin arrays) are simple enough so that the relationships that define their S_v and d_p are straightforward. Therefore, for each different matrix geometry, one has (KAVIANY, 1995):

$$S_\mathrm{v} = \frac{6}{d_\mathrm{sph}};\ d_\mathrm{p} = d_\mathrm{sph} \quad \text{(for bed of spheres)} \tag{4.22}$$

$$S_\mathrm{v} = \frac{4}{e_\mathrm{pin}};\ d_\mathrm{p} = \frac{3}{2}e_\mathrm{pin} \quad \text{(for pin arrays)} \tag{4.23}$$

$$S_\mathrm{v} \approx \frac{2}{e_\mathrm{PP}};\ d_\mathrm{p} = 3e_\mathrm{PP} \quad \text{(for parallel plates)} \tag{4.24}$$

where d_sph is the spherical particle diameter, e_pin is the square pin side length and e_PP is the parallel plate thickness.

4.3.2 Permeability and Ergun Constant

The momentum equation requires closure relationships for the porous medium permeability and Ergun constant. The permeability, K, can be written in the following form:

$$K = \frac{\varepsilon}{16 k_\mathrm{k}} d_\mathrm{h}^2 \tag{4.25}$$

where k_k is the Kozeny constant and d_h is related to the particle diameter by:

$$d_\mathrm{h} = \frac{2}{3} \frac{\varepsilon}{1-\varepsilon} d_\mathrm{p} \tag{4.26}$$

For parallel plates, the Kozeny constant can be determined from a solution of the Navier-Stokes equation for fully developed flow (KAVIANY, 1995). For packed spheres, the value suggested by Ergun (1952) was used, where $16k_\mathrm{k} = 150$. For pin arrays, there are several available correlations for the permeability (KAVIANY, 1995; NAKAYAMA; KUWAHARA, 2005; YAZDCHI *et al.*, 2011). However, none of them were found appropriate for the pin array geometry studied in the present work. Thus, k_k was calculated based on the tortuosity, τ, of the porous medium, as suggested by Kaviany (1995), p. 33, where $k_\mathrm{k} = k_\mathrm{o}\tau^2$. Assuming $k_\mathrm{o} = 2.5$ and $\tau = L_\mathrm{e}/L = 2^{1/2}$, where $L_\mathrm{e} = 2^{1/2}L$, results in $k_\mathrm{k} = 5$. Therefore:

$$k_\mathrm{k} = 9.375 \quad \text{(for packed beds of spheres (ERGUN, 1952))}$$

$$k_\mathrm{k} = 5 \quad \text{(for pin arrays)}$$

$$k_\mathrm{k} = 2 \quad \text{(for parallel plates (KAVIANY, 1995))}$$

The Ergun constant, c_E, can be generically written as follows:

$$c_\mathrm{E} = \frac{a}{(16 k_\mathrm{k} \varepsilon^3)^{1/2}} \tag{4.27}$$

where a is a constant proportional to the Ergun inertial term in the momentum equation. Hence, a is larger in geometries where the acceleration term is more important:

$$a = 1.75 \quad \text{(for packed beds of spheres (ERGUN, 1952))}$$

$$a = 2/3 \quad \text{(for pin arrays)}$$

$$a = 0 \quad \text{(for parallel plates)}$$

It is well known that for parallel plates the flow acceleration is nil. For packed beds of spheres, the value of a proposed by Ergun (1952) has been adopted. Finally, for pin arrays, the acceleration effect of the fluid is smaller when compared with the the bed of spheres. In the literature, there are different approaches to the modeling of c_{E} for pin arrays (KAVIANY, 1995; NAKAYAMA; KUWAHARA, 2005; NIELD; BEJAN, 2006; TERUEL; RIZWAN-UDDIN, 2009; TAMAYOL *et al.*, 2010). However, none of them reproduced well the present pin array porous media, due to different dimensions and ranges of operating conditions. Thus, the general procedure suggested on p. 67 of Kaviany (1995) was adopted here, which resulted in the constant a being equal to 2/3.

4.3.3 Interstitial Heat Transfer Coefficient

The interstitial heat transfer coefficient, h, was calculated using Nusselt number correlations written in terms of an appropriate characteristic length. For parallel plates, the correlation of Nickolay and Martin (2002) was used because it accounts for entrance effects on the parallel plate geometry, resulting in a Nusselt number, $Nu_{\mathrm{dh}}(z)$, that is a function of the longitudinal position, $0 \leq z \leq L_{Reg}$:

$$Nu_{\mathrm{dh}}(z) = \frac{h(z)d_{\mathrm{h}}}{k_{\mathrm{f}}} = Nu - \frac{Nu_2}{3}\left(\frac{Nu_2}{Nu}\right)^{\mathrm{n\text{-}1}} \tag{4.28}$$

where $Nu = (Nu_1^{\mathrm{n}} + Nu_2^{\mathrm{n}})^{1/\mathrm{n}}$, $Nu_1 = 7.541$, $Nu_2 = 1.841[Gz(z)]^{1/3}$ and $n = 3,592$. The Graetz number is defined as $Gz(z) = (d_{\mathrm{h}}/z)Pe$ and

$Pe = d_{\mathrm{h}}(u/\varepsilon)/\alpha_{\mathrm{f}}$. The hydraulic diameter in the parallel plate geometry is twice the channel thickness.

The interstitial convective heat transfer coefficient for packed bed of spheres and pin arrays was calculated using the particle diameter-based Nusselt number correlation proposed by (PALLARES; GRAU, 2010):

$$Nu_{\mathrm{dp}} = \frac{hd_{\mathrm{p}}}{k_{\mathrm{f}}} = 2\left(1 + \frac{4(1-\varepsilon)}{\varepsilon}\right) + (1-\varepsilon)^{1/2} Re_{\mathrm{dp}}^{0.6} Pr^{1/3} \tag{4.29}$$

where Re_{dp} is the Reynolds number based on the particle diameter. This correlation was preferred instead of more traditional ones for beds of spheres (WAKAO; KAGUEI, 1982; WHITAKER, 1983) because it is valid for porosities between 0.2 and 0.9 and for a wide range of Prandtl numbers and low Reynolds numbers ($Re_{dp} < 100$) (KUWAHARA *et al.*, 2001; PALLARES; GRAU, 2010). A more in-depth discussion regarding the Nusselt number correlation is presented in Appendix C.

4.3.4 Effective Thermal Conductivity

The effective thermal conductivity is the volume-averaged thermal conductivity used to evaluate the macroscopic heat transfer through a porous medium. In the non-equilibrium formulation, there is an effective thermal conductivity for each phase, as will be presented as follows.

4.3.4.1 Fluid Phase Effective Thermal Conductivity

The effective thermal conductivity of the fluid phase for parallel plates and packed spheres is evaluated by (KAVIANY, 1995):

$$\frac{k_{\mathrm{f}}^{\mathrm{eff}}}{k_{\mathrm{f}}} = \varepsilon \tag{4.30}$$

and for pin arrays the relationship is (KAVIANY, 1995):

$$\frac{k_{\mathrm{f}}^{\mathrm{eff}}}{k_{\mathrm{f}}} = 1 - (1-\varepsilon)^{1/2} \tag{4.31}$$

4.3.4.2 Solid Phase Effective Thermal Conductivity

The effective thermal conductivity of the solid phase for parallel plates is given by (KAVIANY, 1995):

$$\frac{k_{\mathrm{s}}^{\mathrm{eff}}}{k_{\mathrm{f}}} = (1-\varepsilon)\frac{k_{\mathrm{s}}}{k_{\mathrm{f}}} \tag{4.32}$$

For packed spheres, the Hadley (1986) correlation is recommended:

$$\frac{k_{\mathrm{s}}^{\mathrm{eff}}}{k_{\mathrm{f}}} = (1-\alpha_0)\frac{\varepsilon \mathrm{f}_0 + (1-\varepsilon \mathrm{f}_0)\frac{k_{\mathrm{s}}}{k_{\mathrm{f}}}}{1-\varepsilon(1-\mathrm{f}_0)+\frac{k_{\mathrm{s}}}{k_{\mathrm{f}}}\varepsilon(1-\mathrm{f}_0)} + \alpha_0\frac{2\left(\frac{k_{\mathrm{s}}}{k_{\mathrm{f}}}\right)^2(1-\varepsilon)+(1+2\varepsilon)\frac{k_{\mathrm{s}}}{k_{\mathrm{f}}}}{(2+\varepsilon)\frac{k_{\mathrm{s}}}{k_{\mathrm{f}}}+(1-\varepsilon)} \tag{4.33}$$

where $\mathrm{f}_0 = 0.8$ and $\log\alpha_0 = -1.084 - 6.778(\varepsilon - 0.298)$ are valid for $0.298 \leq \varepsilon \leq 0.58$. For pin arrays, $k_{\mathrm{s}}^{\mathrm{eff}}$ is defined as (KAVIANY, 1995):

$$\frac{k_{\mathrm{s}}^{\mathrm{eff}}}{k_{\mathrm{f}}} = \frac{(1-\varepsilon)^{1/2}\frac{k_{\mathrm{s}}}{k_{\mathrm{f}}}}{(1-(1-\varepsilon)^{1/2})\frac{k_{\mathrm{s}}}{k_{\mathrm{f}}}+(1-\varepsilon)^{1/2}} \tag{4.34}$$

4.3.5 Longitudinal Dispersion

In 1-D porous media modeling, the dispersion is due to fluid mixing along the bed, in the direction of flow. This way, the longitudinal dispersion, $D_{||}$, can be treated as an axial conduction term.

For parallel plates, $D_{||}$ is calculated by the following equation suggested by Engelbrecht (2008):

$$\frac{D_{||}}{\alpha_{\mathrm{f}}} = \frac{Pe_{\mathrm{dh}}^2}{210} \tag{4.35}$$

where the Peclet number based on the hydraulic diameter is $Pe_{\mathrm{dh}} = Pr(u/\varepsilon)d_{\mathrm{h}}/\nu_{\mathrm{f}}$.

For packed spheres, the well established correlation of Koch and Brady (1985) was used:

$$\frac{D_{||}}{\alpha_{\mathrm{f}}} = \frac{\sqrt{2}}{60}\frac{(Pe_{\mathrm{dp}}/2)^2}{(1-\varepsilon)^{1/2}} \quad \text{for} \quad \left(\frac{Pe_{\mathrm{dp}}}{2}\right)^2 << 1 \tag{4.36}$$

$$\frac{D_{||}}{\alpha_{\mathrm{f}}} = 0.75\frac{Pe_{\mathrm{dp}}}{2} \quad \text{for} \quad \frac{Pe_{\mathrm{dp}}}{2} > 1 \tag{4.37}$$

where the Peclet number based on the particle diameter is $Pe_{\mathrm{dp}} = Pr(ud_{\mathrm{p}})/\nu_{\mathrm{f}}$.

For pin arrays, $D_{||}$ is evaluated by the correlation proposed by DeGroot and Straatman (2012) for a staggered array of circular cylinders:

$$\frac{D_{||}}{\alpha_{\mathrm{f}}} = 0.0054Re_{\mathrm{d}}^{1.8}Pr^{1.7} \quad \text{for} \quad Pe_{\mathrm{d}} < 10 \tag{4.38}$$

$$\frac{D_{||}}{\alpha_{\mathrm{f}}} = 0.016Re_{\mathrm{d}}^{1.5}Pr^{1.1} \quad \text{for} \quad Pe_{\mathrm{d}} > 10 \tag{4.39}$$

where the Reynolds and Peclet numbers are based on the pin size, $d = e_{\mathrm{pin}}$. Thus, $Re_{\mathrm{d}} = ue_{\mathrm{pin}}/\nu_{\mathrm{f}}$ and $Pe_{\mathrm{d}} = Re_{\mathrm{d}}Pr$.

4.3.6 Wall Heat Transfer Coefficient

The heat transfer to the regenerator wall, h_{wall}, is evaluated via Nusselt number correlations based on the particle diameter, i.e., $Nu_{\mathrm{wall}} = h_{\mathrm{wall}}d_{\mathrm{p}}/k_{\mathrm{f}}(T)$. For packed beds of spheres, the use of the empirical correlation presented in Li and Finlayson (1977) is suggested. Thus (LI; FINLAYSON, 1977; WAKAO; KAGUEI, 1982):

$$Nu_{\mathrm{dp}}^{\mathrm{wall}} = 0.17Re_{\mathrm{dp}}^{0.79} \quad \text{for} \quad 20 \leq Re_{\mathrm{dp}} \leq 7600 \tag{4.40}$$

4.4 Magnetic Properties and their Implementation

The adiabatic temperature change, $\Delta T_{\mathrm{ad}}(\Delta B, T)$ is illustrated in Fig. 2.4. For a magnetic material at an equilibrium state specified by an initial temperature T_0 and magnetic field B_0, the total entropy is $s_0(B_0, T_0)$. If a variation in the applied field, $\Delta B = B_1 - B_0$, is performed adiabatically, the total entropy of the system remains constant, and $s_1 = s_0$. Therefore, a new equilibrium state is reached at $s_1(B_1, T_1)$. The difference between the initial and final temperatures is the adiabatic temperature change, i.e., $\Delta T_{\mathrm{ad}}(\Delta B, T) = T_1 - T_0$. If $\Delta B > 0$, then $\Delta T_{\mathrm{ad}}(\Delta B, T)$ is positive and, *reversibly*, when $\Delta B < 0$, $\Delta T_{\mathrm{ad}}(\Delta B, T)$ is negative. An extended discussion on the calculation of $\Delta T_{\mathrm{ad}}(\Delta B, T)$ for magnetization and demagnetization, and its impact on the regenerator performance is available in Bahl and Nielsen (2009), Nielsen *et al.* (2010), Trevizoli *et al.* (2012). The implementation of the MCE and of the demagnetizing losses on the AMR model are discussed next.

4.4.1 Implementation of the Magnetocaloric Effect

In AMR modeling, the MCE may be implemented in two different forms. The first is the so-called discrete approach, which is the simplest and most straightforward calculation method (NIELSEN *et al.*, 2011). It consists of a direct temperature increment (or reduction) during the magnetization (or demagnetization) step. Thus, for a one-dimensional domain:

$$T_{\mathrm{s}}(t + \Delta t, z) = T_{\mathrm{s}}(t, z) + \Delta T_{\mathrm{ad}}(\Delta B, T_{\mathrm{s}}(t, z)) \tag{4.41}$$

where $\Delta B = B(t + \Delta t, z) - B(t, z)$.

The second form is the so-called built-in approach, where the MCE is modeled as an instantaneous energy rate per unit volume, $\dot{q}_{\mathrm{MCE}}$, which is included as a source term in the solid energy equation (4.8) (NIELSEN *et al.*, 2011), where $\dot{q}_{\mathrm{MCE}}$ is given by (ENGELBRECHT, 2008; NIELSEN *et al.*, 2011):

$$\dot{q}_{\mathrm{MCE}}(t+\Delta t, z) = -\rho_{\mathrm{s}}(1-\varepsilon)T_{\mathrm{s}}(t,z)\frac{\partial s(B(t,z),T_{\mathrm{s}}(t,z))}{\partial B(t,z)}\frac{\partial B(t,z)}{\partial t} \quad (4.42)$$

According to Nielsen *et al.* (2011), the processes of magnetization and demagnetization can be simulated using both approaches, but the selection of the most appropriate one depends on the conditions of the simulation. When the magnetic flux density changes continuously with time, such as in the magnetic circuits used in the present AMR experimental apparatus, the built-in approach is the best. On the other hand, for a step change in the magnetic flux density, the simplest discrete approach is sufficient. However, it should be noted that step changes in magnetic flux density (magnetization and demagnetization) are very hard to implement in practice, so the vast majority of AMR apparatuses actually employ some type of continuous change in the magnetic flux density. A drawback of the built-in approach is that it requires somewhat refined data sets for the magnetocaloric properties and specific heat capacity as a function of temperature and magnetic flux density in order to calculate the entropy derivative. These may not be always available, especially for new materials that rely heavily on the experimental characterization of its parameters. As a result, when the required data are not available, the discrete method may be the only approach possible.

Both approaches to calculate the MCE were employed in the present model. In each case, ΔT_{ad} and $\partial s/\partial B$ were calculated based on the entropy lines in a $T-s$ diagram, as described earlier in Fig. 2.4. Evaluating the MCE from the $T-s$ diagram is the most advantageous because it takes the reversibility of the MCE directly into account. As will be seen in Section 4.7.2, if a refined magnetocaloric properties data set (e.g., $T-s$ lines) is available, even for a continuous magnetic flux density variation, both approaches give numerical results that are in good agreement.

In terms of dimensionless parameters, the discrete and built-in methods are given, respectively, by:

$$\theta_{\mathrm{s}}(t^*+\Delta t^*, z^*) = \theta_{\mathrm{s}}(t^*, z^*) + \frac{\Delta T_{\mathrm{ad}}(\Delta B, T_{\mathrm{s}}(t,z))}{\Delta T_{\mathrm{Hex}}} \quad (4.43)$$

$$\dot{q}^*_{\mathrm{MCE}}(t^*+\Delta t^*, z^*) = \frac{\frac{T_{\mathrm{s}}(t,z)}{c_{\mathrm{s}}(B,T_{\mathrm{s}}(t,z))}\frac{\partial s(B,T_{\mathrm{s}}(t,z))}{\partial B}\frac{\partial B}{\partial t}}{\omega \Delta T_{\mathrm{Hex}}} \tag{4.44}$$

where $\Delta T_{\mathrm{Hex}} = T_{\mathrm{H}} - T_{\mathrm{C}}$ is the temperature difference between the thermal reservoirs (i.e., hot and cold heat exchangers).

4.4.2 Magnetic Losses due to Demagnetizing Effects

When a magnetic material is subjected to a magnetic flux density, the resulting (effective) magnetic field vector, $\vec{H}_{\mathrm{eff}}$, is different from the applied magnetic field, $\vec{H}_{\mathrm{apl}}$. This is due to an internal demagnetizing field, $\vec{H}_{\mathrm{dem}}$, which is proportional to the demagnetizing tensor, $\overline{\overline{N}}_{\mathrm{D}}$, and to the magnetization, $\vec{M}(\vec{H}_{\mathrm{apl}}, T)$. Thus (BAHL *et al.*, 2008; SMITH *et al.*, 2010; TREVIZOLI *et al.*, 2012, 2013b):

$$\vec{H}_{\mathrm{eff}} = \vec{H}_{\mathrm{apl}} - \vec{H}_{\mathrm{dem}}(\vec{H}_{\mathrm{apl}}, T) \tag{4.45}$$

where

$$\vec{H}_{\mathrm{dem}}(\vec{H}_{\mathrm{apl}}, T) = \overline{\overline{N}}_{\mathrm{D}} \cdot \vec{M}(\vec{H}_{\mathrm{apl}}, T) \tag{4.46}$$

If the product between the demagnetization tensor and the magnetization is large, which is often the case when the material is in the ferromagnetic phase ($T < T_{\mathrm{Curie}}$), then $\vec{H}_{\mathrm{dem}}$ is also large, yielding values of $\vec{H}_{\mathrm{eff}}$ much smaller than $\vec{H}_{\mathrm{apl}}$. This constitutes a reduction in the adiabatic temperature change of the magnetocaloric material and a loss in terms of temperature span and cooling capacity. Thus, a properly designed regenerator should have, in principle, a small demagnetizing tensor (factor), which depends chiefly on the regenerator geometry and orientation with respect to the applied field.

At a constant (uniform) temperature, Eq. (4.45) can be simplified as the demagnetization tensor becomes a scalar. Thus, for a homogeneous temperature solid:

$$H_{\text{eff}} = H_{\text{apl}} - N_{\text{D}} M(H_{\text{apl}}, T) \tag{4.47}$$

where N_{D} is the demagnetization factor. Trevizoli *et al.* (2012) showed that, for the purpose of estimating losses due to internal demagnetization effects in a parallel plate geometry regenerator, the assumption of a constant (average) temperature gives values of $H_{\text{eff}}/H_{\text{apl}}$ which are in good agreement (less than 15% error in the worst case, less that 4% on average) with a more complex (i.e., vectorial) model that assumes a linear temperature profile along the plates (SMITH *et al.*, 2010).

Therefore, in the present model the effective magnetic field was calculated using a simplified method that consists of assuming a linear temperature profile (between T_C and T_H) along the regenerator bed and calculating an average temperature for each finite volume in the regenerator. Eq. (4.47) is used to calculate the local values of the effective magnetic field at each volume, which remain unchanged along the entire simulation. Numerically, Eq. (4.47) is implemented as:

$$H_{\text{eff}}(t,z) = H_{\text{apl}}(t,z) - N_{\text{D}} M(H_{\text{apl}}(t,z), T(t,z)) \tag{4.48}$$

and the effective magnetic flux density, $B_{\text{eff}}(t,z) = \mu_0 H_{\text{eff}}(t,z)$.

The total demagnetization factor of an AMR matrix, N_{D}, comprises the demagnetization factor of the matrix geometry, $N_{\text{D,geo}}$, and the demagnetizing factor of the casing geometry that surrounds the regenerative bed, $N_{\text{D,csg}}$. Hence, N_{D} was estimated using a correlation proposed for a packed bed of particles available in (COEY, 2010):

$$N_{\text{D}} = N_{\text{D,geo}} + (1-\varepsilon)(N_{\text{D,csg}} - N_{\text{D,geo}}) \tag{4.49}$$

where $N_{\text{D,csg}}$ can be estimated via relations for cylindrical and prismatic geometries proposed, respectively, by Sato and Ishii (1989) and Aharoni (1998). Eq. (4.49) is used for particle beds, such as spheres, where the demagnetization factor of a single sphere is $N_{\text{D,geo}} = 1/3$. For comparison purposes, in all the remaining geometries studied in the present thesis, the same equation will be used to evaluate N_{D}. $N_{\text{D,geo}}$ was calculated with the Sato and Ishii (1989) and Aharoni (1998) correlations for square pins and plates, respectively.

4.4.3 Experimental Thermo-Magnetic Properties

Although the thermo-magnetic properties of magnetocaloric materials can be evaluated by means of equations of state, such as the Weiss-Debye-Sommerfeld (WDS) theory for materials with a continuous magnetic transition (MORRISH, 1965; DINESEN, 2004), better accuracy can be achieved with interpolation curves derived from actual experimental data, as discussed by Nielsen *et al.* (2011).

The AMR modeling benefits from the development of T-s curves (diagram) as a function of the magnetic flux density to calculate ΔT_{ad} as function of B and T. The dependence of the specific heat capacity on B and T is also of fundamental importance, as is the characterization of the magnetization, M (or specific magnetization, σ), as a function of B and T to estimate the demagnetization losses. The Gd density and thermal conductivity were assumed equal to 7900 kg/m^3 and 10.5 W/m-K, respectively (PETERSEN *et al.*, 2008), and therefore, independent of the magnetic flux density and temperature.

The commercial-grade gadolinium used in this thesis (99% purity) was experimentally characterized in terms of its specific heat capacity and magnetic entropy change. The thermo-magnetic properties were measured at magnetic flux densities between 0 and 2 T in 0.1-T intervals, at temperatures ranging from 250 to 320 K, in steps of 1 K. The specific heat and magnetization measurements as a function of temperature and magnetic flux density were carried out by BASF. After processing the data, non-linear interpolations were performed to correlate the data as continuous functions of the magnetic flux density and temperature. All interpolating functions presented correlation coefficients $R^2 > 0.9999$.

In the AMR model, the physical properties of Gd are calculated via bi-linear interpolations of tabulated data generated through the non-linear interpolating functions described above. These tabulated data were generated with a resolution higher than that of the original data (i.e., 0.01 T and 0.1 K, for the 0-2 T and 255-310 K ranges) to guarantee high accuracy. Using the bi-linear interpolations instead of the continuous interpolating functions reduces the computational time. Numerical instabilities are also reduced in comparison with property estimation using bi-linear interpolations applied directly on the original experimental data.

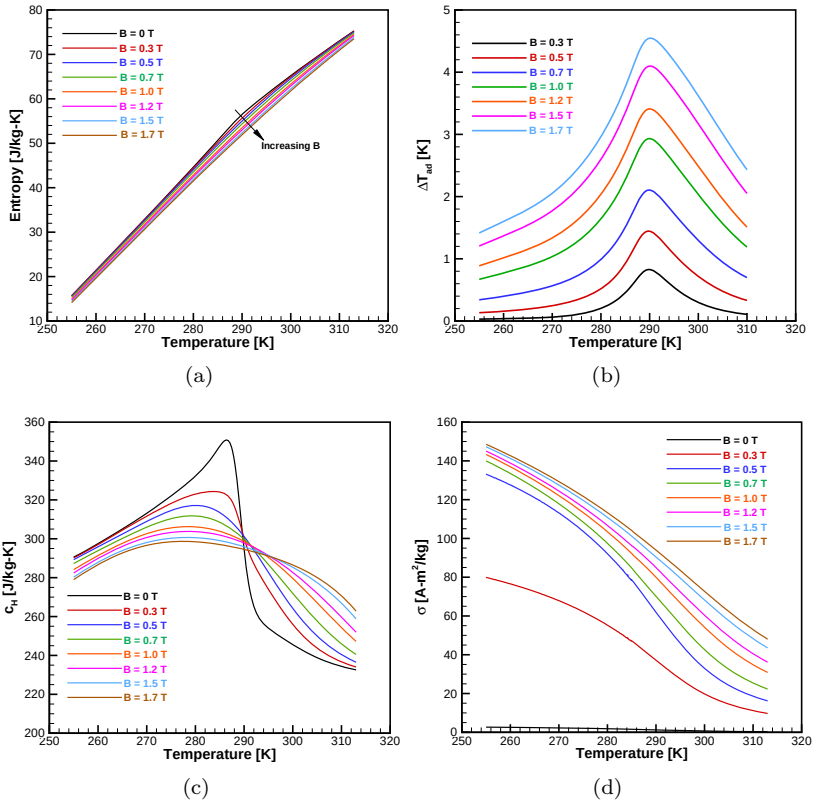

Figure 4.4 – Interpolated thermo-magnetic properties of the gadolinium samples used in this thesis as a function of temperature and magnetic flux density: (a) T-s diagram; (b) ΔT_{ad}; (c) Specific heat capacity; (d) Specific magnetization.

4.5 Numerical Implementation

The dimensionless governing equations, Eqs. (4.5), (4.7), (4.9), (4.12), (4.17) and (4.18), were solved using the finite volume method (FVM) (PATANKAR, 1980; MALISKA, 2004). In a generic form, the 1-D dimensionless equations, Eqs. (4.5), (4.7), (4.9) and (4.12), can be written as:

$$\frac{\partial}{\partial t^*}(\Gamma\varphi) = \frac{\partial}{\partial z^*}(-\Psi u^*\varphi) + \frac{\partial^2}{\partial z^{*2}}(\Lambda\varphi) + S \tag{4.50}$$

where φ is a generic variable for u^* or θ. Γ, Ψ and Λ represent the dimensionless parameters in the transient, advection and diffusion terms, respectively. $S = S_\mathrm{p}\varphi + S_\mathrm{c}$ is the source term.

For a cartesian grid in an 1-D domain, Fig. 4.5(a), the finite volume discretization is:

$$\int_{t^*}^{t^*+\Delta t^*}\int_\mathrm{w}^\mathrm{e}\frac{\partial}{\partial t^*}(\Gamma\varphi)dz^*dt^* =$$

$$\int_{t^*}^{t^*+\Delta t^*}\int_\mathrm{w}^\mathrm{e}\left(\frac{\partial}{\partial z^*}(-\Psi u^*\varphi) + \frac{\partial^2}{\partial z^{*2}}(\Lambda\varphi) + S_\mathrm{p}\varphi + S_\mathrm{c}\right)dz^*dt^* \tag{4.51}$$

$$\frac{\Delta z^*}{\Delta t^*}\Gamma_\mathrm{p}\varphi_\mathrm{p} = -\left(\Psi u^*\varphi\Big|_\mathrm{e} - \Psi u^*\varphi\Big|_\mathrm{w}\right) +$$

$$\left(\Lambda\frac{\partial\varphi}{\partial z^*}\bigg|_\mathrm{e} - \Lambda\frac{\partial\varphi}{\partial z^*}\bigg|_\mathrm{w}\right) + (S_\mathrm{p}\varphi_\mathrm{p} + S_\mathrm{c})\Delta z^* + \frac{\Delta z^*}{\Delta t^*}\Gamma_\mathrm{p}^\mathrm{o}\varphi_\mathrm{p}^\mathrm{o} \tag{4.52}$$

On the other hand, the 2-D dimensionless equations, Eqs. (4.17) and (4.18), can be rewritten in the following generic form:

$$\frac{\partial}{\partial t^*}(\Gamma\varphi) = \frac{\partial^2}{\partial y^{*2}}(\Lambda_{\mathrm{y}^*}\varphi) + \frac{\partial^2}{\partial z^{*2}}(\Lambda_{\mathrm{z}^*}\varphi) + S \tag{4.53}$$

For a cartesian grid in a 2-D domain, Fig. 4.5(b), the finite volume discretization is:

$$\int_{t^*}^{t^*+\Delta t^*}\int_\mathrm{w}^\mathrm{e}\int_\mathrm{s}^\mathrm{n}\frac{\partial}{\partial t^*}(\Gamma\varphi)dy^*dz^*dt^* =$$

$$\int_{t^*}^{t^*+\Delta t^*}\int_\mathrm{w}^\mathrm{e}\int_\mathrm{s}^\mathrm{n}\left(\frac{\partial^2}{\partial y^{*2}}(\Lambda_{\mathrm{y}^*}\varphi) + \frac{\partial^2}{\partial z^{*2}}(\Lambda_{\mathrm{z}^*}\varphi) + (S_\mathrm{p}\varphi + S_\mathrm{c})\right)dy^*dz^*dt^* \tag{4.54}$$

$$\frac{\Delta y^* \Delta z^*}{\Delta t^*}\varphi_\mathrm{p} = \frac{\Delta y^* \Delta z^*}{\Delta t^*}\varphi_\mathrm{p}^\mathrm{o} + (S_\mathrm{p}\varphi_\mathrm{p} + S_\mathrm{c})\Delta y^* \Delta z^* + \left(\Lambda_{\mathrm{y}^*}\frac{\partial \varphi}{\partial y^*}\bigg|_\mathrm{n} - \Lambda_{\mathrm{y}^*}\frac{\partial \varphi}{\partial y^*}\bigg|_\mathrm{s}\right)\Delta z^* + \left(\Lambda_{\mathrm{z}^*}\frac{\partial \varphi}{\partial z^*}\bigg|_\mathrm{e} - \Lambda_{\mathrm{z}^*}\frac{\partial \varphi}{\partial z^*}\bigg|_\mathrm{w}\right)\Delta y^* \quad (4.55)$$

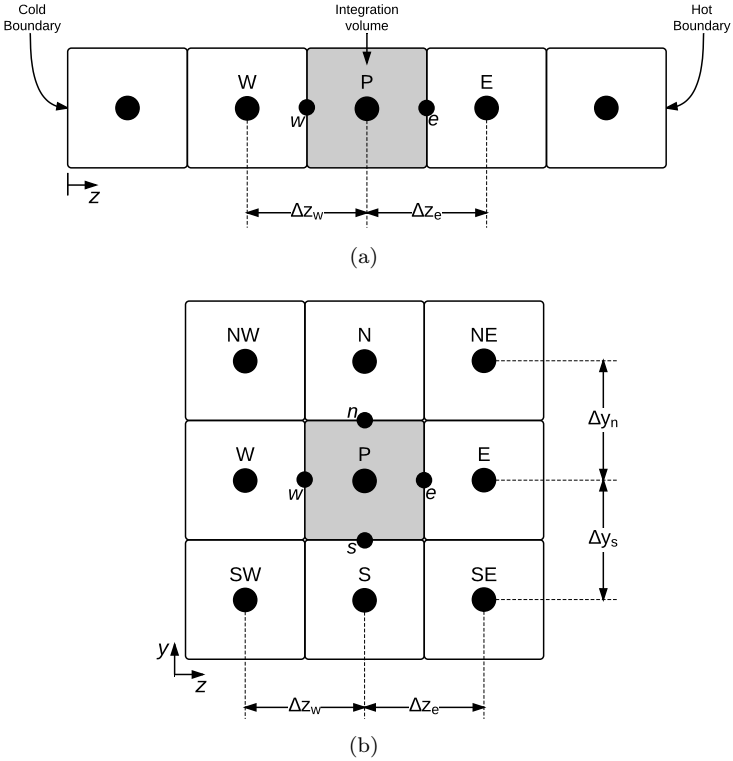

Figure 4.5 – Basic Cartesian grid for: (a) 1-D domain; (b) 2-D domain.

Based on the discretization equations for the 1-D and 2-D domains, the next sections will develop the final numerical forms of each macroscopic balance, using a discretization in the following form:

$$A_\mathrm{p}\varphi_\mathrm{p} = A_\mathrm{e}\varphi_\mathrm{E} + A_\mathrm{w}\varphi_\mathrm{W} + A_\mathrm{n}\varphi_\mathrm{N} + A_\mathrm{s}\varphi_\mathrm{S} + B_\mathrm{p} \quad (4.56)$$

where A_n and A_s are used only in the 2-D model.

4.5.1 Momentum Equation

The momentum equation, Eq. (4.5), is not position-dependent, since the pressure gradient is approximated by a harmonic function, enabling the adoption of a fully explicit discretization scheme, in which the right-hand side of Eq. (4.5) is incorporated into the source term (PATANKAR, 1980; MALISKA, 2004). Table 4.1 identifies the generic variables in the momentum equation.

Table 4.1 – Variables in the momentum equation.

φ	Γ	Ψ	Λ	$S = S_{\mathrm{P}}\varphi + S_{\mathrm{c}}$
u^*_{D}	$\frac{Re_\omega Da}{\varepsilon}$	0	0	$-(1 + G\lvert u^*_{\mathrm{D}}\rvert)u^*_{\mathrm{D}} + g(t^*)$

However, for the packed spheres and pin array geometries, for which $c_{\mathrm{E}} \neq 0$, the Ergun inertial term contains a strong non-linearity in $G|u^*_{\mathrm{D}}|u^*_{\mathrm{D}}$, which requires a procedure to linearize the source term and an iterative solution as follows (PATANKAR, 1980; MALISKA, 2004):

$$S = S^L + \left.\frac{dS}{du^*_{\mathrm{D}}}\right|_{\mathrm{P}}^{L} (u^*_{\mathrm{D,P}} - u^{*L}_{\mathrm{D}}) \tag{4.57}$$

$$S = -(1 \pm G u^{*L}_{\mathrm{D}})u^*_{\mathrm{D,P}} + g(t^*) \tag{4.58}$$

where the super script L refers to the linearization term. As a result, the final form of the discretized momentum equation is:

$$\left(\frac{1}{\Delta t^*}\frac{Re_\omega Da}{\varepsilon} + (1 \pm G u^{*L}_{\mathrm{D}})\right) u^*_{\mathrm{D,P}} = \left(\frac{1}{\Delta t^*}\frac{Re_\omega Da}{\varepsilon}\right) u^{*o}_{\mathrm{D,P}} + g(t^*) \tag{4.59}$$

where the coefficients A and B are:

$$A_{\mathrm{p}} = \left(\frac{1}{\Delta t^*}\frac{Re_\omega Da}{\varepsilon} + (1 \pm G u^{*L}_{\mathrm{D}})\right)$$

$$B_{\mathrm{p}} = \left(\frac{1}{\Delta t^*}\frac{Re_\omega Da}{\varepsilon}\right) u^{*o}_{\mathrm{D,P}} + g(t^*)$$

The initial condition of Eq. (4.59), is simply: $u_{\mathrm{D}}^{*} = 0$. Additionally, regarding the source term:

$$S_{\mathrm{p}} = (1 - G u_{\mathrm{D}}^{*L}) \quad \text{for the Cold Blow: } u^{*} > 0$$
$$S_{\mathrm{p}} = (1 + G u_{\mathrm{D}}^{*L}) \quad \text{for the Hot Blow: } u^{*} < 0$$

The solver routine for the momentum equation is presented in Fig. 4.6. The cold and hot blows are solved independently, and the total cycle period is $\tau_{\mathrm{cycle}}^{*} = \tau_{\mathrm{CB}}^{*} + \tau_{\mathrm{HB}}^{*} = \omega\tau_{\mathrm{cycle}}$. The cold blow starts at $t^{*} = 0$ and ends at $t^{*} = \tau_{\mathrm{CB}}^{*}$, while the hot blow starts at $t^{*} = \tau_{\mathrm{CB}}^{*}$ and ends at $t^{*} = \omega\tau_{\mathrm{cycle}}$. The model enables selecting different blow periods ($\tau_{\mathrm{CB}} \neq \tau_{\mathrm{HB}}$), but in all analyses presented in this thesis identical blow periods have been considered.

The solver starts with the input mass flow rate (MFR in the Fig. 4.6) and the cycle starts at $t^{*} = 0$. Based on the input mass flow rate, an initial value for the amplitude of the pressure drop waveform A_{t} is adjusted, and Eq. (4.59) is solved. If the matrix geometry is composed by packed spheres or pins, there is an internal loop to compute the source term linearization, for which the convergence criterion tolerance is 10^{-10}. If the parallel plate geometry is selected, u_{D}^{*} is solved directly. This procedure is repeated for all time steps until the end of the blow. When all time steps are solved, the cycle convergence is verified, which means comparing the values of $u_{\mathrm{D}}^{*}(t)$ corresponding to the current (ς) and the previous ($\varsigma - 1$) cycles. The convergence criterion is as follows:

$$\left| u_{\mathrm{D}}^{*}(t^{*})|_{\varsigma} - u_{\mathrm{D}}^{*}(t^{*})|_{\varsigma-1} \right| < 10^{-8} \tag{4.60}$$

where ς is the cycle count. The main loop is related to the convergence of the input mass flow rate, for which the convergence criterion tolerance is 10^{-10}. Based on the converged solution of the instantaneous superficial velocity, $u(t) = u_{\mathrm{D}}^{*} u_{\mathrm{D,max}}$ is calculated from the blow (hot and cold) average mass flow rate and compared with the input value, i.e.:

$$\left| \dot{m}_{\mathrm{input}} - \frac{1}{\tau_{\mathrm{blow}}} \int_{0}^{\tau_{blow}} \rho_{\mathrm{f}} A_{\mathrm{c,Reg}} u(t) dt \right| < 10^{-10} \tag{4.61}$$

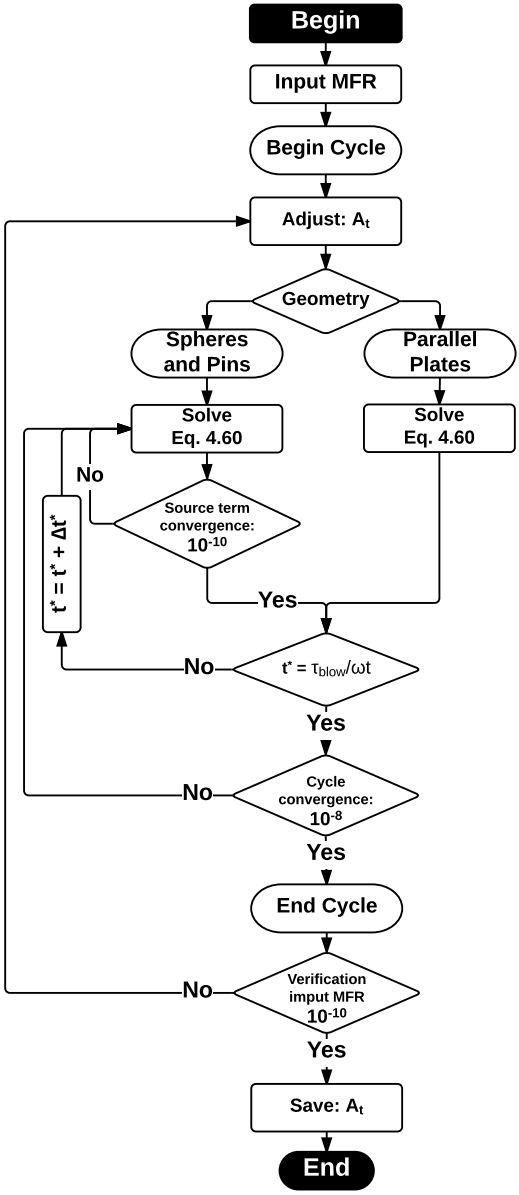

Figure 4.6 – Solver routine for the momentum equation.

If the convergence criterion is not satisfied, a new A_t is adjusted and the routine is repeated until the input mass flow rate convergence tolerance is respected.

4.5.2 Energy Equations

The energy equation for the fluid and solid phases, Eqs. (4.7) and (4.9), were implemented using a fully implicit scheme. Thus, a coupled solution of these equations is performed at a given time (PATANKAR, 1980; MALISKA, 2004). Table 4.2 identifies the generic variables for the energy equations.

Table 4.2 – Variables in the energy equations.

Phase	φ	Γ	Ψ	Λ	$S = S_p\varphi + S_c$
Fluid	θ_f	1	$\frac{Re_{max}}{Re_\omega \zeta}$	$\frac{1}{PrRe_\omega\zeta^2}\left(\frac{k_f^{eff}}{k_f} + \frac{D_{\|\|}}{\alpha_f}\right)$	$-Nu_{dh}Fo_f\theta_f + \dot{q}^*_{csg}$ $Nu_{dh}Fo_f\theta_s + \frac{Br}{Pr}\left\|g(t^*)u^*\right\|$
Solid	θ_s	1	0	$\frac{\kappa_s^{eff}/k_f}{PrRe_\omega\zeta^2}\Re^*$	$-BiFo_s\theta_s + BiFo_s\theta_f + \dot{q}^*_{MCE}$

where $\dot{q}^*_{csg}$ is only used when the wall heat transfer is considered and $\dot{q}^*_{MCE}$ is included when the built-in approach to simulate the MCE is selected. The final form of the discretized energy equation for the fluid is:

$$\frac{\Delta z^*}{\Delta t^*}\theta_{f,P} = -\left(\Psi_e u^*_e \theta_{f,e} - \Psi_w u^*_w \theta_{f,w}\right) + \left(\Lambda_e \frac{\partial\theta_f}{\partial z^*}\bigg|_e - \Lambda_w \frac{\partial\theta_f}{\partial z^*}\bigg|_w\right) + (S_p\theta_{f,P} + S_c)\Delta z^* + \frac{\Delta z^*}{\Delta t^*}\theta^o_{f,P} \tag{4.62}$$

The Weighted Upstream Differencing Scheme (WUDS) was used as the interpolation function for the advection and diffusion terms. In this interpolation scheme, α^i and β^i are weight coefficients for the advection and diffusion terms, respectively, which are both functions of the Peclet number (MALISKA, 2004). The numerical interpolations of the advective and diffusive terms are:

$$\theta_{\mathrm{f,e}} = (0.5 + \alpha^i_{\mathrm{e}})\theta_{\mathrm{f,P}} + (0.5 - \alpha^i_{\mathrm{e}})\theta_{\mathrm{f,E}} \tag{4.63}$$

$$\theta_{\mathrm{f,w}} = (0.5 + \alpha^i_{\mathrm{w}})\theta_{\mathrm{f,W}} + (0.5 - \alpha^i_{\mathrm{w}})\theta_{\mathrm{f,P}} \tag{4.64}$$

$$\left.\frac{\partial \theta_{\mathrm{f}}}{\partial z^*}\right|_{\mathrm{e}} = \beta^i_{\mathrm{e}} \left(\frac{\theta_{\mathrm{f,E}} - \theta_{\mathrm{f,P}}}{\Delta z^*} \right) \tag{4.65}$$

$$\left.\frac{\partial \theta_{\mathrm{f}}}{\partial z^*}\right|_{\mathrm{w}} = \beta^i_{\mathrm{w}} \left(\frac{\theta_{\mathrm{f,P}} - \theta_{\mathrm{f,W}}}{\Delta z^*} \right) \tag{4.66}$$

and α^i and β^i are given by:

$$\alpha^i_{\mathrm{e,w}} = 0.5 - \frac{\exp(Pe_{\mathrm{e,w}})/2 - 1}{\exp(Pe_{\mathrm{e,w}}) - 1} \tag{4.67}$$

$$\beta^i_{\mathrm{e,w}} = Pe_{\mathrm{e,w}} \frac{\exp(Pe_{\mathrm{e,w}})/2}{\exp(Pe_{\mathrm{e,w}}) - 1} \tag{4.68}$$

$$Pe_{\mathrm{e,w}} = \frac{\Psi_{\mathrm{e,w}}}{\Lambda_{\mathrm{e,w}}} u^* \Delta z^* \tag{4.69}$$

Rewriting the discretized fluid energy equation for the internal volumes in Eq. (4.56) gives:

$$A_{\mathrm{w}} = \Psi_{\mathrm{w}} u^*_{\mathrm{w}} (0.5 + \alpha^i_{\mathrm{w}}) + \beta^i_{\mathrm{w}} \frac{\Lambda_{\mathrm{w}}}{\Delta z^*}$$

$$A_{\mathrm{e}} = -\Psi_{\mathrm{e}} u^*_{\mathrm{e}} (0.5 - \alpha^i_{\mathrm{e}}) + \beta^i_{\mathrm{e}} \frac{\Lambda_{\mathrm{e}}}{\Delta z^*}$$

$$B_{\mathrm{p}} = S_{\mathrm{c}} \Delta z^* + \frac{\Delta z^*}{\Delta t^*} \theta^o_{\mathrm{f,P}}$$

$$A_{\mathrm{p}} = A_{\mathrm{w}} + A_{\mathrm{e}} + \frac{\Delta z^*}{\Delta t^*} - S_{\mathrm{p}} \Delta z^*$$

and:

$$S_{\mathrm{p}} = -Nu_{\mathrm{dh}} Fo_{\mathrm{f}}$$

$$S_{\mathrm{c}} = Nu_{\mathrm{dh}} Fo_{\mathrm{f}} \theta_{\mathrm{s}} + \frac{Br}{Pr} \left| g(t^*) u^* \right| + \dot{q}^*_{\mathrm{csg}}$$

The boundary conditions for the fluid phase depend on the direction of the fluid flow. For convenience, if $u^* > 0$, then at $z^* = 0$ (cold boundary) an inlet boundary condition is used with $\theta_{\mathrm{f}} = \theta_{\mathrm{C}} = 0$, and at $z^* = 1$ an outflow boundary condition, $\frac{\partial \theta_{\mathrm{f}}}{\partial z^*}(t^*, z^* = 1) = 0$, is applied. On the other hand, if $u^* < 0$, an inlet boundary condition is applied at $z^* = 1$ (hot boundary) with $\theta_{\mathrm{f}} = \theta_{\mathrm{H}} = 1$ and an outflow boundary condition is set at $z^* = 0$ with $\frac{\partial \theta_{\mathrm{f}}}{\partial z^*}(t^*, z^* = 0) = 0$ (MALISKA, 2004). Using fictitious volumes to implement the boundary conditions, the matrix coefficients are given by:

- if $u^* > 0$ - cold blow:

Cold or West boundary volume:	Hot or East boundary volume:
$A_{\mathrm{w}} = 0$	$A_{\mathrm{w}} = 1$
$A_{\mathrm{e}} = 0$	$A_{\mathrm{e}} = 0$
$B_{\mathrm{p}} = \theta_{\mathrm{C}} = 0$	$B_{\mathrm{p}} = 0$
$A_{\mathrm{p}} = 1$	$A_{\mathrm{p}} = 1$

- if $u^* < 0$ - hot blow:

Cold or West boundary volume:	Hot or East boundary volume:
$A_{\mathrm{w}} = 0$	$A_{\mathrm{w}} = 0$
$A_{\mathrm{e}} = 1$	$A_{\mathrm{e}} = 0$
$B_{\mathrm{p}} = 0$	$B_{\mathrm{p}} = \theta_{\mathrm{H}} = 1$
$A_{\mathrm{p}} = 1$	$A_{\mathrm{p}} = 1$

The final form of the discretized energy equation for the solid phase is:

$$\frac{\Delta z^*}{\Delta t^*} \theta_{\mathrm{s,P}} = \left(\Lambda_{\mathrm{e}} \left. \frac{\partial \theta_{\mathrm{s}}}{\partial z^*} \right|_{\mathrm{e}} - \Lambda_{\mathrm{w}} \left. \frac{\partial \theta_{\mathrm{s}}}{\partial z^*} \right|_{\mathrm{w}} \right) + (S_{\mathrm{p}} \theta_{\mathrm{s,P}} + S_{\mathrm{c}}) \Delta z^* + \frac{\Delta z^*}{\Delta t^*} \theta^{\mathrm{o}}_{\mathrm{s,P}} \tag{4.70}$$

The Central Difference Scheme (CDS) was used as the interpolating function for the diffusion terms. Thus:

$$\left.\frac{\partial \theta_{\mathrm{s}}}{\partial z^*}\right|_{\mathrm{e}} = \left(\frac{\theta_{\mathrm{s,E}} - \theta_{\mathrm{s,P}}}{\Delta z^*}\right) \tag{4.71}$$

$$\left.\frac{\partial \theta_{\mathrm{s}}}{\partial z^*}\right|_{\mathrm{w}} = \left(\frac{\theta_{\mathrm{s,P}} - \theta_{\mathrm{s,W}}}{\Delta z^*}\right) \tag{4.72}$$

Rewriting the discretized solid energy equation for the internal volumes in Eq. (4.56) gives:

$$A_{\mathrm{w}} = \frac{\Lambda_{\mathrm{w}}}{\Delta z^*}$$

$$A_{\mathrm{e}} = \frac{\Lambda_{\mathrm{e}}}{\Delta z^*}$$

$$B_{\mathrm{p}} = S_{\mathrm{c}} \Delta z^* + \frac{\Delta z^*}{\Delta t^*} \theta^o_{\mathrm{s,P}}$$

$$A_{\mathrm{p}} = A_{\mathrm{w}} + A_{\mathrm{e}} + \frac{\Delta z^*}{\Delta t^*} - S_{\mathrm{p}} \Delta z^*$$

and:

$$S_{\mathrm{p}} = -BiFo_{\mathrm{s}}$$

$$S_{\mathrm{c}} = BiFo_{\mathrm{s}} \theta_{\mathrm{f}} + \dot{q}^*_{\mathrm{MCE}}$$

The boundary conditions for the solid phase are: $\frac{\partial \theta_{\mathrm{s}}}{\partial z^*}(t^*, z^* = 0) = \frac{\partial \theta_{\mathrm{s}}}{\partial z^*}(t^*, z^* = 1) = 0$. The boundary matrix coefficients are determined by energy balances on the solid phase boundaries. The coefficients are identical to the ones presented above, with the following changes: $A_{\mathrm{w}} = 0$ to Cold or West boundary volume; $A_{\mathrm{e}} = 0$ to Hot or East boundary volume.

To accelerate the numerical convergence, linear temperature profiles, i.e., $\theta_{f,s}(z^* = 0) = 0$ and $\theta_{f,s}(z^* = 1) = 1$ were assumed as initial conditions for the fluid and solid energy equations. The solver was a line-by-line Tri-Diagonal Matrix Algorithm (TDMA). This solver, also known as the Thomas Algorithm, was chosen as it does not require an iterative processes, such as other known methods (Jacobi or Gauss-Seidel elimination).

The fluid and solid energy equations are solved coupled. This means that at any given time, the fluid equation is solved first, and its solution is used to solve the solid energy equation before returning to the fluid domain with a new solution for the solid phase. This procedure is repeated until the convergence criteria are satisfied. Fig. 4.7 presents the coupled solution routine.

After the solution of the momentum equation, the cycle starts at $t^* = 0$ with the initial condition. A blow is identified as cold or hot, and, for every time step, the internal loop of the energy equations are solved until the convergence criterion of 10^{-6} is satisfied for both θ_f and θ_s. In all iterations, the fluid and solid properties are recalculated based on the previous θ_f and θ_s solution. If the convergence criterion is satisfied, the next time step is solved. After all time steps are solved, the cycle convergence is verified, which consists of comparing the solutions $\theta_{\mathrm{f,s}}(t)$ from the current (ς) and previous ($\varsigma - 1$) cycles with the convergence criterion as follows:

$$\left|\theta_{\mathrm{f,s}}(z^*, t^*)|_\varsigma - \theta_{\mathrm{f,s}}(z^*, t^*)|_{\varsigma-1}\right| < 10^{-6} \tag{4.73}$$

If the convergence criterion is not satisfied, the solver returns to the beginning of the cycle, but using the previous temperature fields as initial conditions. This procedure is repeated until all convergence criteria are respected.

4.5.3 Void Volume

The implementation of the energy equation for the fluid in the void volume, Eq. (4.12), is similar to that for the fluid in the porous medium, for which the fully implicit scheme was used. Table 4.3 identifies the generic variables in the void volume energy equation.

Table 4.3 – Variables in the void volume model.

φ	Γ	Ψ	Λ	$S = S_\mathrm{p}\varphi + S_\mathrm{c}$
$\theta_\mathrm{f}^{\mathrm{vv}}$	1	$\frac{Re_{\mathrm{max}}^{\mathrm{vv}}}{Re_\omega^{\mathrm{vv}}\zeta^{\mathrm{vv}}}$	$\frac{1}{PrRe_\omega^{\mathrm{vv}}\zeta^{\mathrm{vv}2}}$	0

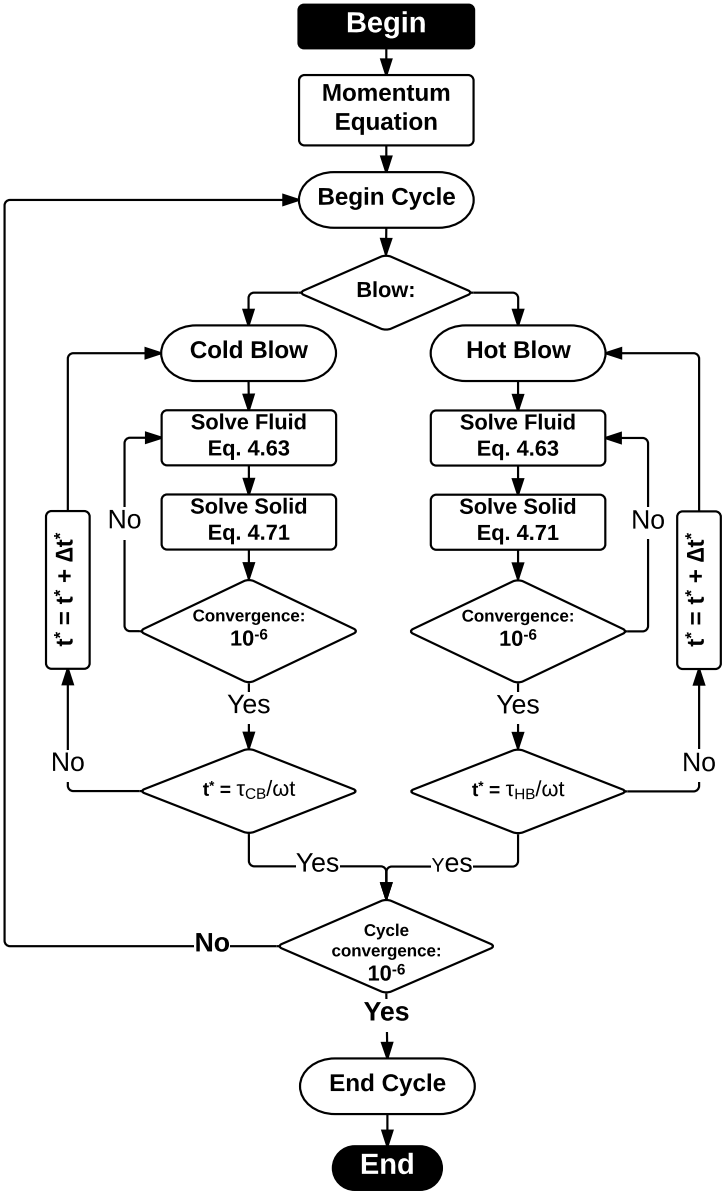

Figure 4.7 – Solver routine for the energy equations.

The final form of the discretized energy equation for the fluid is given by:

$$\frac{\Delta z^*_{\mathrm{vv}}}{\Delta t^*}\theta^{\mathrm{vv}}_{\mathrm{f,P}} = -\left(\Psi_{\mathrm{e}}u^*_{\mathrm{e}}\theta^{\mathrm{vv}}_{\mathrm{f,e}} - \Psi_{\mathrm{w}}u^*_{\mathrm{w}}\theta^{\mathrm{vv}}_{\mathrm{f,w}}\right) + \left(\Lambda_{\mathrm{e}}\frac{\partial\theta^{\mathrm{vv}}_{\mathrm{f}}}{\partial z^*}\bigg|_{\mathrm{e}} - \Lambda_{\mathrm{w}}\frac{\partial\theta^{\mathrm{vv}}_{\mathrm{f}}}{\partial z^*}\bigg|_{\mathrm{w}}\right) + \frac{\Delta z^*_{\mathrm{vv}}}{\Delta t^*}\theta^{\mathrm{vv,o}}_{\mathrm{f,P}} \tag{4.74}$$

The WUDS was also used as the interpolation function for the advection and diffusion terms. The WUDS coefficients were calculated as described earlier for the energy equation in the porous medium. Rewriting the discretized fluid energy equation for the internal volumes of the void volume in Eq. (4.56) gives:

$$A_{\mathrm{w}} = \Psi_{\mathrm{w}}u^*_{\mathrm{w}}(0.5+\alpha^i_{\mathrm{w}}) + \beta^i_{\mathrm{w}}\frac{\Lambda_{\mathrm{w}}}{\Delta z^*_{\mathrm{vv}}}$$

$$A_{\mathrm{e}} = -\Psi_{\mathrm{e}}u^*_{\mathrm{e}}(0.5-\alpha^i_{\mathrm{e}}) + \beta^i_{\mathrm{e}}\frac{\Lambda_{\mathrm{e}}}{\Delta z^*_{\mathrm{vv}}}$$

$$B_{\mathrm{p}} = \frac{\Delta z^*_{\mathrm{vv}}}{\Delta t^*}\theta^{\mathrm{vv,o}}_{\mathrm{f,P}}$$

$$A_{\mathrm{p}} = A_{\mathrm{w}} + A_{\mathrm{e}} + \frac{\Delta z^*_{\mathrm{vv}}}{\Delta t^*}$$

Eq. (4.74) is solved for the cold and hot void volumes. However, the boundary conditions are different, depending on the blow direction. Using fictitious volumes to implement the boundary conditions, the matrix coefficients are calculated as explained below.

- If $u^* > 0$ - cold blow: The fluid coming from the cold reservoir enters the cold void volume, flows through the regenerator and through the hot void volume, up to the hot reservoir.

On the cold side, the fluid coming from the cold reservoir enters the cold void volume and the fluid exiting this void volume enters the regenerator. Thus, at $z^* = -L^*_{\mathrm{vv}}$, an inlet boundary condition is applied, in which $\theta^{\mathrm{C,vv}}_{\mathrm{f}} = \theta_{\mathrm{C}} = 0$. At $z^* = 0$, an outflow boundary condition is applied, i.e., $\frac{\partial\theta^{\mathrm{C,vv}}_{\mathrm{f}}}{\partial z^*} = 0$. Here, $L^*_{\mathrm{vv}} = L_{\mathrm{vv}}/L_{\mathrm{Reg}}$. The matrix coefficients are defined as follows:

West boundary volume:	East boundary volume:
$A_\mathrm{w} = 0$	$A_\mathrm{w} = 1$
$A_\mathrm{e} = 0$	$A_\mathrm{e} = 0$
$B_\mathrm{p} = \theta_\mathrm{C} = 0$	$B_\mathrm{p} = 0$
$A_\mathrm{p} = 1$	$A_\mathrm{p} = 1$

On the hot side, the fluid leaving the regenerator enters the hot void volume and flows towards the hot reservoir. Thus, at $z^* = 1$, an inlet boundary condition is applied, in which $\theta_\mathrm{f}^{\mathrm{H,vv}} = \theta_\mathrm{f}|_{z^*=1}$. At $z^* = 1 + L_\mathrm{vv}^*$, an outflow boundary condition is applied, i.e., $\frac{\partial \theta_\mathrm{f}^{\mathrm{H,vv}}}{\partial z^*} = 0$. The matrix coefficients are, therefore:

West boundary volume:	East boundary volume:
$A_\mathrm{w} = 0$	$A_\mathrm{w} = 1$
$A_\mathrm{e} = 0$	$A_\mathrm{e} = 0$
$B_\mathrm{p} = \theta_\mathrm{f}\|_{z^*=1}$	$B_\mathrm{p} = 0$
$A_\mathrm{p} = 1$	$A_\mathrm{p} = 1$

- If $u^* < 0$ - hot blow: The fluid coming from the hot reservoir enters the hot void volume, flows through the regenerator and through the cold void volume, down to the cold reservoir.

On the hot side, at $z^* = 1 + L_\mathrm{vv}^*$, an inlet boundary condition is applied, in which $\theta_\mathrm{f}^{\mathrm{H,vv}} = \theta_\mathrm{H} = 1$. At $z^* = 1$, an outflow boundary condition is applied, i.e., $\frac{\partial \theta_\mathrm{f}^{\mathrm{H,vv}}}{\partial z^*} = 0$. The matrix coefficients are given by:

West boundary volume:	East boundary volume:
$A_\mathrm{w} = 0$	$A_\mathrm{w} = 0$
$A_\mathrm{e} = 1$	$A_\mathrm{e} = 0$
$B_\mathrm{p} = 0$	$B_\mathrm{p} = \theta_\mathrm{H} = 1$
$A_\mathrm{p} = 1$	$A_\mathrm{p} = 1$

On the cold side, at $z^* = 0$, an inlet boundary condition is applied, in which $\theta_\mathrm{f}^{\mathrm{C,vv}} = \theta_\mathrm{f}|_{z^*=0}$. At $z^* = -L_\mathrm{vv}^*$, an outflow boundary condition is set, i.e., $\frac{\partial \theta_\mathrm{f}^{\mathrm{C,vv}}}{\partial z^*} = 0$. The matrix coefficients are given by:

West boundary volume:	East boundary volume:
$A_{\mathrm{w}} = 0$	$A_{\mathrm{w}} = 0$
$A_{\mathrm{e}} = 1$	$A_{\mathrm{e}} = 0$
$B_{\mathrm{p}} = 0$	$B_{\mathrm{p}} = \theta_{\mathrm{f}}\vert_{\mathrm{z}^* = 0}$
$A_{\mathrm{p}} = 1$	$A_{\mathrm{p}} = 1$

The initial condition for the fluid in the cold void volume is the temperature of the cold reservoir, $\theta_{\mathrm{f}}^{\mathrm{Cvv}} = \theta_{\mathrm{C}} = 0$. For the hot void volume, the initial condition is the temperature of the hot reservoir, $\theta_{\mathrm{f}}^{\mathrm{Hvv}} = \theta_{\mathrm{H}} = 1$. The TDMA was also used in the void volume solver. As explained earlier, the main impact of the void volume on the regenerator behavior is the change of the inlet temperature during the cold and hot blows, which means that, when the void volumes are taken into account, the boundary conditions for Eq. (4.62), originally presented in Section 4.5.2, have to be updated. Hence, when the void volumes are considered, the new boundary conditions for the energy equation of the fluid phase are given by:

- For $u^* > 0$ - cold blow:

Cold or West boundary volume:	Hot or East boundary volume:
$A_{\mathrm{w}} = 0$	$A_{\mathrm{w}} = 1$
$A_{\mathrm{e}} = 0$	$A_{\mathrm{e}} = 0$
$B_{\mathrm{p}} = \theta_{\mathrm{f}}^{\mathrm{Cvv}}\vert_{\mathrm{z}^* = 0}$	$B_{\mathrm{p}} = 0$
$A_{\mathrm{p}} = 1$	$A_{\mathrm{p}} = 1$

- For $u^* < 0$ - hot blow:

Cold or West boundary volume:	Hot or East boundary volume:
$A_{\mathrm{w}} = 0$	$A_{\mathrm{w}} = 0$
$A_{\mathrm{e}} = 1$	$A_{\mathrm{e}} = 0$
$B_{\mathrm{p}} = 0$	$B_{\mathrm{p}} = \theta_{\mathrm{f}}^{\mathrm{Hvv}}\vert_{\mathrm{z}^* = 1}$
$A_{\mathrm{p}} = 1$	$A_{\mathrm{p}} = 1$

4.5.4 Casing Heat Transfer

The energy equations for the casing heat transfer modeling, Eqs. (4.17) and (4.18), were also discretized using a fully implicit scheme. Table

4.4 identifies the generic variables of the 2-D energy equations for the casing and air gap layers.

Table 4.4 – Variables in the casing heat transfer model.

φ	Γ	Λ_y	Λ_z	$S = S_p\varphi + S_c$
θ_{wall}	1	$\frac{\alpha}{\omega e^2}\Big\|_y$	$\frac{\alpha}{\omega L_{Reg}^2}\Big\|_z$	0
θ_{air}	1	$\frac{\alpha}{\omega e^2}$	$\frac{\alpha}{\omega L_{Reg}^2}$	$\frac{\dot{q}_{air}}{\rho c_p\|_{air}\omega\Delta T_{Hex}}$

The discretized energy equations for the air gap and casing layers are given by:

$$\frac{\Delta y^*\Delta z^*}{\Delta t^*}\theta_{(wall,air)} = \left(\Lambda_{y^*}\frac{\partial\theta_{(wall,air)}}{\partial y^*}\bigg|_n - \Lambda_{y^*}\frac{\partial\theta_{(wall,air)}}{\partial y^*}\bigg|_s\right)\Delta z^* + \left(\Lambda_{z^*}\frac{\partial\theta_{(wall,air)}}{\partial z^*}\bigg|_e - \Lambda_{z^*}\frac{\partial\theta_{(wall,air)}}{\partial z^*}\bigg|_w\right)\Delta y^* + \frac{\Delta y^*\Delta z^*}{\Delta t^*}\theta^o_{(wall,air)} + S_c \tag{4.75}$$

Following the same procedure presented for the other numerical equations in which the CDS interpolation scheme was used, the coefficients of the internal volumes of Eq. (4.56) for the air gap and casing layers are given by:

$$A_w = \Lambda_w\frac{\Delta y^*}{\Delta z^*}$$

$$A_e = \Lambda_e\frac{\Delta y^*}{\Delta z^*}$$

$$A_s = \Lambda_s\frac{\Delta z^*}{\Delta y^*}$$

$$A_n = \Lambda_n\frac{\Delta z^*}{\Delta y^*}$$

$$B_p = \frac{\Delta y^*\Delta z^*}{\Delta t^*}\theta^o_{(wall,air)P} + S_c$$

$$A_p = A_w + A_e + A_s + A_n + \frac{\Delta y^*\Delta z^*}{\Delta t^*}$$

Regarding the boundaries conditions for both layers, the west and east boundaries are $\left.\frac{\partial\theta(t^*,z^*=0)}{\partial z^*}\right|_{(\text{wall,air})} = \left.\frac{\partial\theta(t^*,z^*=1)}{\partial z^*}\right|_{(\text{wall,air})} = 0$. In the casing layer, the south wall is in contact with the porous medium, thus a convective boundary condition is used, $q''_{\text{wall}} = h_{\text{wall}}(T_{\text{f}} - T_{\text{wall}}|_{(\text{y}^*=0)})$. The north wall and the south air boundaries are in contact, hence the boundary conditions is simply the heat flux continuity: $k_{\text{y}}\left.\frac{\partial T}{\partial y}\right|_{\text{wall}} = k\left.\frac{\partial T}{\partial y}\right|_{\text{air}}$. Due to the large thermal mass of the magnetic circuit, this is assumed to be in thermal equilibrium with the surrounding air. Thus, the north boundary condition of the air layer was set as a prescribed temperature at θ_{amb}. Therefore, the matrix coefficients for the boundaries are presented below, with the fictitious volumes considered at each end.

West wall boundary:	West air boundary:
$A_{\text{w}} = 0$	$A_{\text{w}} = 0$
$A_{\text{e}} = 1$	$A_{\text{e}} = 1$
$A_{\text{s}} = 0$	$A_{\text{s}} = 0$
$A_{\text{n}} = 0$	$A_{\text{n}} = 0$
$B_{\text{p}} = 0$	$B_{\text{p}} = 0$
$A_{\text{p}} = 1$	$A_{\text{p}} = 1$

East wall boundary:	East air boundary:
$A_{\text{w}} = 1$	$A_{\text{w}} = 1$
$A_{\text{e}} = 0$	$A_{\text{e}} = 0$
$A_{\text{s}} = 0$	$A_{\text{s}} = 0$
$A_{\text{n}} = 0$	$A_{\text{n}} = 0$
$B_{\text{p}} = 0$	$B_{\text{p}} = 0$
$A_{\text{p}} = 1$	$A_{\text{p}} = 1$

South wall boundary:	South air boundary:
$A_{\text{w}} = 0$	$A_{\text{w}} = 0$
$A_{\text{e}} = 0$	$A_{\text{e}} = 0$
$A_{\text{s}} = -(1/2) + \frac{(k_{\text{y}}/e)\|_{\text{wall}}}{h_{\text{wall}}}$	$A_{\text{s}} = 0$
$A_{\text{n}} = 0$	$A_{\text{n}} = -1$
$B_{\text{p}} = \theta_{\text{f}}$	$B_{\text{p}} = 2\left(\frac{(k/e\|_{\text{air}})\theta_{\text{air}} + (k_{\text{y}}/e\|_{\text{wall}})\theta_{\text{wall}}}{(k/e\|_{\text{air}}) + (k_{\text{y}}/e\|_{\text{wall}})}\right)$
$A_{\text{p}} = (1/2) + \frac{(k_{\text{y}}/e)\|_{\text{wall}}}{h_{\text{wall}}}$	$A_{\text{p}} = 1$

North wall boundary:	North air boundary:
$A_{\mathrm{w}} = 0$	$A_{\mathrm{w}} = 0$
$A_{\mathrm{e}} = 0$	$A_{\mathrm{e}} = 0$
$A_{\mathrm{s}} = -1$	$A_{\mathrm{s}} = -1$
$A_{\mathrm{n}} = 0$	$A_{\mathrm{n}} = 0$
$B_{\mathrm{p}} = 2\left(\frac{(k/e\|_{\mathrm{air}})\theta_{\mathrm{air}}+(k_{\mathrm{y}}/e\|_{\mathrm{wall}})\theta_{\mathrm{wall}}}{(k/e\|_{\mathrm{air}})+(k_{\mathrm{y}}/e\|_{\mathrm{wall}})}\right)$	$B_{\mathrm{p}} = 2\theta_{\mathrm{amb}}$
$A_{\mathrm{p}} = 1$	$A_{\mathrm{p}} = 1$

The linear temperature distribution used as initial condition in the porous solid and fluid flow equations were also adopted in the casing and air gap models. The TDMA was used, but with an additional convergence loop for the y direction. Thus, convergence is obtained when two successive iterations satisfy the following criterion:

$$\left|\theta_{(\mathrm{wall,air})}(t^*, y^*, z^*)|_i - \theta_{(\mathrm{wall,air})}(t^*, y^*, z^*)|_{i-1}\right| < 10^{-6} \tag{4.76}$$

where i is the current iteration and $i-1$ is the previous iteration. The casing heat transfer model is solved coupled with the fluid and solid porous medium energy equations, as will be detailed in the next section.

4.5.5 Complete Regenerator Simulation Routine

The complete regenerator routine is presented in Fig. 4.8. The solver starts with the solution of the momentum equation. After, the passive and AMR solvers can be selected and solved independently. Each calculation procedure is presented in detail as follows:

- Passive regenerator:

The routine is divided between the cold and hot blows. In the cold blow routine, the cold void volume energy equation is computed and its solution is used as the west boundary condition in the regenerator fluid phase model. Then, the internal fluid-solid energy equations are solved coupled and the fluid exiting the regenerator is used as the west boundary condition in the hot void volume. In the hot blow routine, the hot void volume energy equation is computed and its solution is used as the east boundary condition in the regenerator fluid phase model. Then, the internal fluid-solid energy equations are solved coupled and

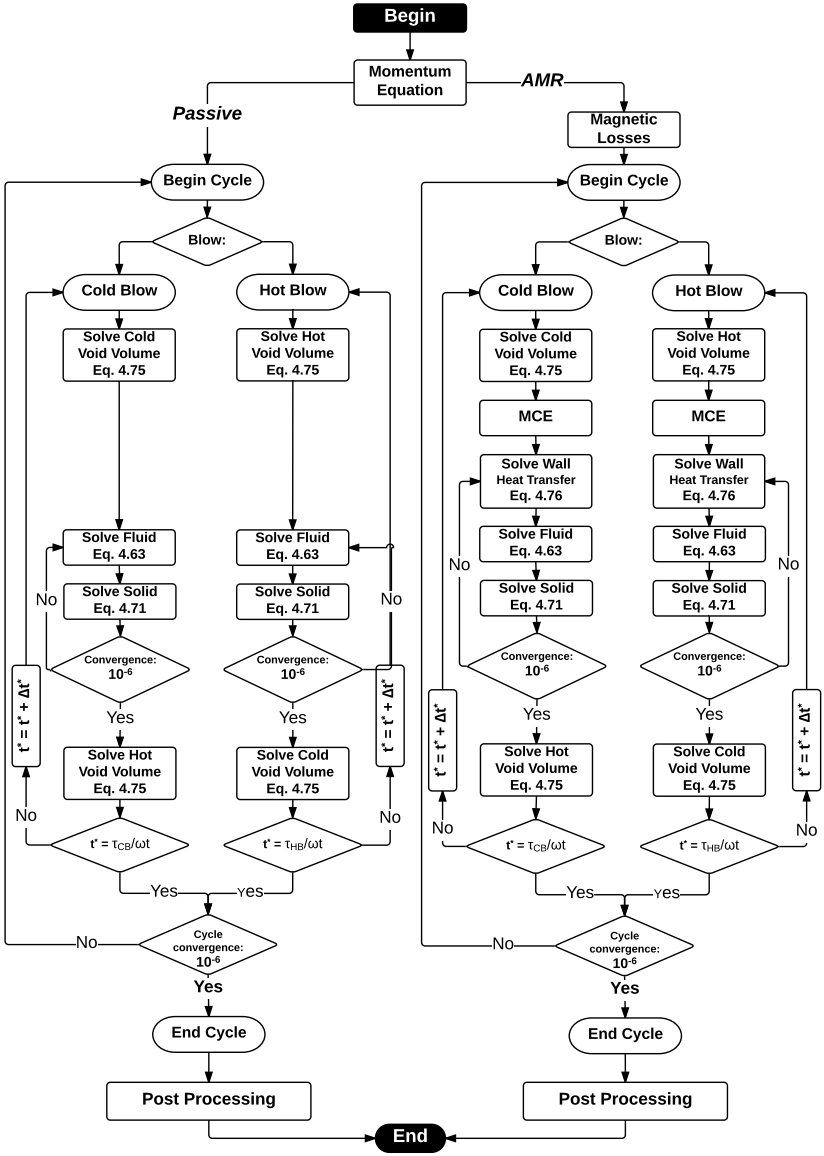

Figure 4.8 – Passive and active magnetic regenerator final solver routine.

the fluid exiting the regenerator is used as the east boundary condition in the cold void volume. The procedure is repeated for each time step until convergence is achieved. After that, the following parameters are calculated: thermal effectiveness, pressure drop, pumping power and entropy generation per unit volume (to be defined in Sections 5.2 and 7.1).

- Active magnetic regenerator:

The routine starts with the evaluation of magnetic losses. Later, it is also divided between the cold and hot blows. In the cold blow routine, the cold void volume energy equation is calculated and its solution is used as the west boundary condition for the regenerator fluid phase model. Then, the MCE and $\dot{q}^*_{\mathrm{csg}}$ are computed and incorporated in the solid and fluid energy equations, respectively. Next, the fluid exiting the regenerator is used as the west boundary condition for the hot void volume. The hot blow routine is similar. The procedure is repeated for each time step until convergence is achieved. After that, the following parameters are calculated: cooling capacity, regenerator temperature span, pressure drop, pumping power and entropy generation per unit volume (to be defined in Sections 6.3 and 7.1).

4.6 Numerical Mesh and Convergence Evaluation

An evaluation of the numerical mesh was performed based on differences between converged results for different mesh sizes and the overall computing time associated with each mesh. Four different meshes were evaluated: the temporal mesh, the porous medium z-direction mesh, the void volume z-direction mesh and the casing heat transfer y-direction mesh.

The porous medium heat transfer model was used to evaluate the temporal and the porous medium z-direction meshes together. In this analysis, four different mesh sizes were investigated, as shown in Table 4.5.

As presented in Table 4.5, the mesh sizes double with each mesh number. For both the passive and AMR regenerators, the mesh evaluation

Table 4.5 – Porous medium heat transfer model meshes.

Mesh	Temporal mesh	z-direction mesh
1	90	50
2	180	100
3	360	200
4	720	400

was performed based on the results for several different operating conditions, but only three cases were selected for the present discussion. As shows in Table 4.6, Cases 1, 2 and 3 have different regenerator lengths and cycle frequencies to test the sensitivity of these parameters with respect to the temporal and spatial mesh sizes. The remaining variables of the packed bed of spheres regenerator, i.e., mass flow rate, particle diameter, porosity, and cold and hot reservoirs temperatures, were kept constant.

Table 4.6 – Simulations cases used in the mesh evaluation.

Case	Length [mm]	frequency [Hz]
1	50	2
2	100	2
3	100	0.5

For passive regenerators, the mesh evaluation was made based on the thermal effectiveness, ϵ. Table 4.7 shows the results for the mesh evaluation for passive regenerators for $D_{\mathrm{h,Reg}} = 25$ mm, $d_{\mathrm{p}} = 1$ mm, $\varepsilon = 0.36$, $\dot{m} = 50$ kg/h, $T_{\mathrm{H}} = 320$ K and $T_{\mathrm{C}} = 280$ K. In Table 4.7, the variable $\Delta = 100 \times (\epsilon_{\mathrm{n}} - \epsilon_{\mathrm{n\text{-}1}})/\epsilon_{\mathrm{n}}$ is the effectiveness difference between two consecutive meshes, i.e., n and $n-1$. t is the total computational time for each case.

Table 4.7 – Mesh evaluation for passive regenerators.

Mesh	Case 1			Case 2			Case 3		
	ϵ	Δ[%]	t[s]	ϵ	Δ[%]	t[s]	ϵ	Δ[%]	t[s]
1	0.951	-	12	0.970	-	43	0.950	-	18
2	0.958	0.7	51	0.976	0.7	177	0.961	1.2	61
3	0.960	0.3	212	0.979	0.3	743	0.967	0.6	234
4	0.961	0.1	718	0.981	0.1	2790	0.970	0.3	857

The results for passive regenerator show that there is some improvement in the effectiveness results when the mesh is refined. However,

when the computational time, t, is evaluated, it can be concluded that the improvement in the effectiveness is minor when compared with the increasing computational cost. This means that Mesh 3 provides the best compromise. The passive regenerator mesh evaluation can also be evaluated in terms of the ideal regenerator solution available in Dragutinovic and Baclic (1998). Fig. 4.9 shows plots of the regenerator effectiveness as a function of the NTU for the different meshes. The parameters of the matrix simulated in this analysis are as follows: $D_{\mathrm{h,Reg}} = 25$ mm, $L_{\mathrm{Reg}} = 100$ mm, $d_{\mathrm{p}} = 1$ mm, $\varepsilon = 0.36$, $f = 1$ Hz, $T_{\mathrm{H}} = 320$ K and $T_{\mathrm{C}} = 280$ K. The mass flow rate was varied from 10 to 200 kg/h. These results led to the same conclusion i.e., that Mesh 3 appears to be the best option. The ideal regenerator simplification and model are presented and discussed in more details in Section 4.7.1.

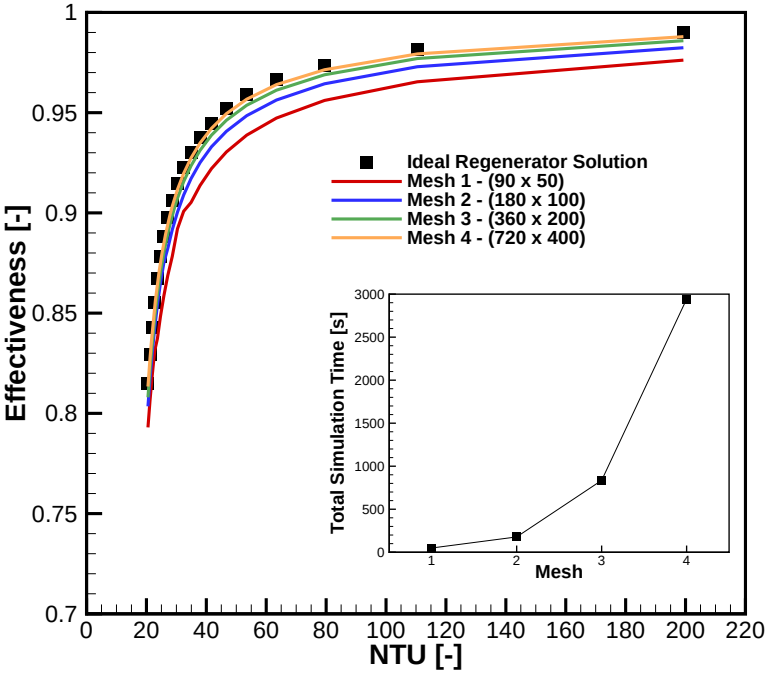

Figure 4.9 – Mesh evaluation for passive regenerators and comparison with the ideal regenerator solution.

For AMRs, the mesh evaluation was carried out based on the cooling capacity, $\dot{Q}$. Table 4.8 shows the mesh evaluation for the following

parameters: $D_{\mathrm{h,Reg}} = 25$ mm, $d_{\mathrm{p}} = 1$ mm, $\varepsilon = 0.36$, $\dot{m} = 50$ kg/h, $T_{\mathrm{H}} = 300$ K and $\Delta T_{\mathrm{Hex}} = 10$ K. The instantaneous magnetic flux density was varied between 0 and 1 T. In Table 4.8 the variable $\Delta = 100 \times (\dot{Q}_{\mathrm{n}} - \dot{Q}_{\mathrm{n\text{-}1}})/\dot{Q}_{\mathrm{n}}$ is the cooling capacity difference between two consecutive meshes, i.e., n and $n-1$.

Table 4.8 – Mesh evaluation for AMRs.

Mesh	Case 1			Case 2			Case 3		
	$\dot{Q}$[W]	Δ[%]	t[s]	$\dot{Q}$[W]	Δ[%]	t[s]	$\dot{Q}$[W]	Δ[%]	t[s]
1	12.2	-	57	15.5	-	190	10.9	-	58
2	14.2	14.4	217	17.1	9.1	808	14.3	23.8	218
3	15.2	6.6	987	17.8	3.7	3979	16.5	12.8	791
4	15.7	3.0	2889	18.0	1.2	11168	17.3	4.9	2441

The results in Table 4.8 show that the AMR solution is more sensitive to the mesh size. Nevertheless, they also indicate that Mesh 3 is the most appropriate option because a more refined mesh (Mesh 4) increases significantly the total computational time, especially when the void volume and casing heat transfer models are solved. Moreover, the benefit of using Mesh 4 is only a 4.9% improvement over Mesh 3, for the worst case (Case 3).

An evaluation of the void volume z-direction and casing heat transfer y-direction meshes was also carried out. In order to evaluate the void volume mesh, several simulations were undertaken varying the void volume size and the z-direction mesh size between 10 and 200 volumes. The temporal mesh had 360 time steps and the porous medium spatial mesh had 200 volumes. Here, only one void volume mesh analysis is presented, whose results were obtained considering the simulation conditions from Case 3 in Table 4.8, i.e., $D_{\mathrm{h,Reg}} = 25$ mm, $L_{\mathrm{Reg}} = 100$ mm, $d_{\mathrm{p}} = 1$ mm, $\varepsilon = 0.36$, $f = 0.5$ Hz, $\dot{m} = 50$ kg/h. For the passive regenerator tests, $T_{\mathrm{H}} = 320$ K and $T_{\mathrm{C}} = 280$ K, while for the AMR simulations $T_{\mathrm{H}} = 300$ K and $\Delta T_{\mathrm{Hex}} = 10$ K. The instantaneous magnetic flux density was varied between 0 and 1 T. Also, a void volume fraction of 15% was used.

The results shown in Table 4.9 demonstrate that the passive regenerator solution is less sensitive to the void volume mesh size when compared to the AMR solution. Additionally, the refining of the mesh size did not increase significantly the computational time. Therefore, a z-direction mesh of 100 finite volumes was selected for the void volume.

Table 4.9 – Mesh evaluation of the void volume model.

Mesh	Passive			AMR		
	ϵ	Δ[%]	t[s]	$\dot{Q}$[W]	Δ[%]	t[s]
10	0.955	-	216	13.9	-	827
50	0.948	0.73	240	9.9	29.3	864
100	0.948	0.09	255	9.2	6.2	931
200	0.947	0.04	278	9.0	3.0	1051

Regarding the casing heat transfer model, the y-direction wall mesh was also evaluated based on several simulations. Considering the same conditions of Case 3, i.e., $D_{\mathrm{h,Reg}} = 25$ mm, $d_{\mathrm{p}} = 1$ mm, $\varepsilon = 0.36$, $\dot{m} = 50$ kg/h, $T_{\mathrm{H}} = 300$ K and $\Delta T_{\mathrm{Hex}} = 10$ K, a G10 casing with a 2-mm wall thickness and an air gap of 1 mm was simulated. These wall thickness and air gap dimensions are in agreement with the actual AMR apparatus discussed in this thesis. The temporal mesh had 360 time steps and the porous medium spatial mesh had 200 volumes. According to the results, the air layer did not require a refined mesh, so only 5 finite volumes were used. On the other hand, the wall in contact with the porous medium, where the temperature and flow velocities are changing continuously, requires a more refined mesh due to the transient heat transfer between the porous matrix and the wall. Hence, the y-direction wall mesh was evaluated for 10, 20 and 40 volumes.

Table 4.10 presents the results of the mesh study for the casing heat transfer modeling. Based on these results a y-direction mesh with 20 finite volumes was selected. In addition, the results in Table 4.10 shows that the increase in the total simulation time when the casing heat transfer model is included in the model cannot be neglected.

Table 4.10 – Mesh evaluation to wall heat transfer model.

Mesh	1 wall		
	$\dot{Q}$[W]	Δ[%]	t[s]
10	14.723	-	1566
20	14.718	0.03	2063
40	14.717	0.01	3013

In summary, the following mesh characteristics were selected as the best compromise between accuracy and computational time for both passive and active regenerators:

- Temporal mesh: 360 time steps;
- Regenerator z-direction mesh: 200 finite volumes;
- Void volume z-direction mesh: 100 finite volumes;
- Casing y-direction mesh: 20 finite volumes;

In general words, for the AMR simulations a more refined mesh would be the best option. However, when the void volume and casing heat transfer models are considered, the computational time increases significantly. Thus, smaller meshes are more appropriate for comparisons with the experimental data and the generation of results in the optimization routine. The latter requires a significant number (around 10k) of simulated scenarios.

4.7 Initial Model Verification

The initial model validation is discussed in this section. First, the ideal passive regenerator model is presented and compared with Dragutinovic and Baclic (1998). The following parameters were changed: spheres size, operating frequency, plates thickness and porosity of the parallel plate regenerator. Next, it is demonstrated that the built-in and discrete implementations of the MCE give the same cooling capacity, when a refined data set of the magnetocaloric properties are available.

4.7.1 Ideal Passive Regenerator Model

To simulate the ideal regenerator behavior the simplifications discussed in Section 2.5 were implemented in the numerical model. This first verification is an important step to evaluate the iterative routine solver and also the mesh sensitivity analysis presented previously.

The first comparison between the ideal regenerator model and the numerical results considers a packed bed of spheres with different particle sizes, i.e., $d_\mathrm{p} = 0.5$ mm, $d_\mathrm{p} = 0.8$ mm, $d_\mathrm{p} = 1$ mm and $d_\mathrm{p} = 2$ mm. The operating conditions were: $D_\mathrm{h,Reg} = 25$ mm, $L_\mathrm{Reg} = 100$ mm, $\varepsilon = 0.36$, $f = 1$ Hz, $T_\mathrm{H} = 320$ K and $T_\mathrm{C} = 280$ K. The mass flow rate was varied between 10 and 200 kg/h. Fig. 4.10 plots the regenerator effectiveness as a function of the NTU, which varies from 5 to 750. A

good agreement between the Dragutinovic and Baclic (1998) solution and the numerical model was verified, with a maximum deviation of about 1.5%.

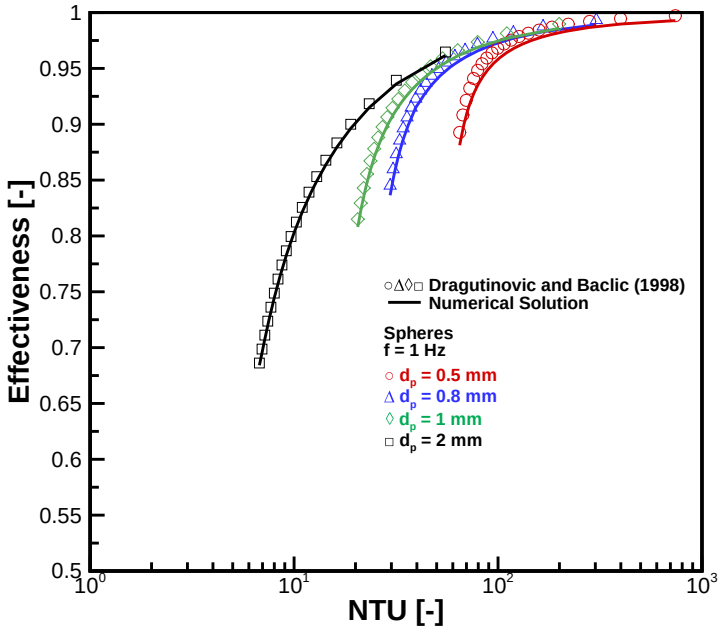

Figure 4.10 – Effectiveness vs. NTU for spheres packed bed matrix with different particle sizes. Comparison of numerical modeling results with the Dragutinovic and Baclic (1998) solution for ideal passive regenerators.

The second comparison considers a packed bed of spheres operating at different frequencies, i.e., 0.25, 0.5, 1 and 2 Hz. The particle diameter was kept fixed at 1 mm. The remaining operating conditions were the same as in the first comparison. Fig. 4.11 plots the regenerator effectiveness as a function of the NTU between 20 and 200. The results showed a good agreement between the Dragutinovic and Baclic (1998) solution and the numerical model, with a maximum deviation of about 1.5%.

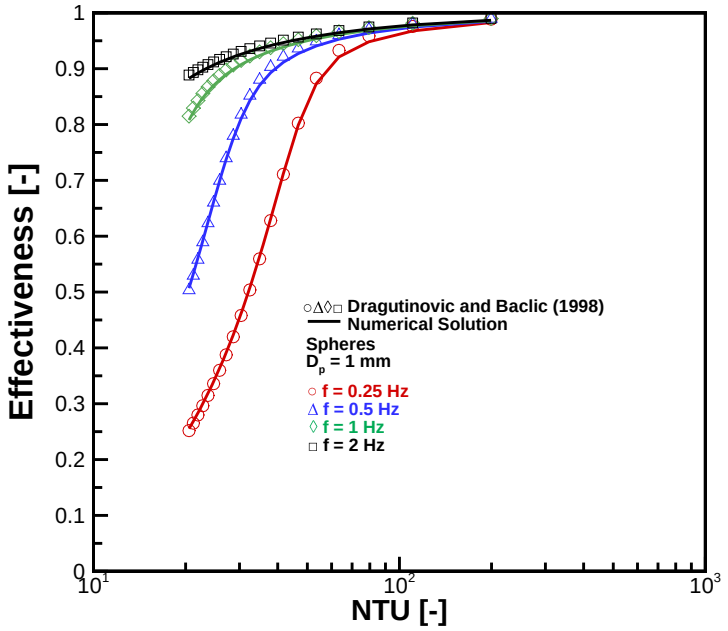

Figure 4.11 – Effectiveness vs. NTU for spheres packed bed matrix with different operating frequencies. Comparison of numerical modeling results with the Dragutinovic and Baclic (1998) solution for ideal passive regenerators.

The third comparison considers a parallel plate matrix with a constant porosity of $\varepsilon = 0.36$ and different plate thickness, e_{PP}, of 0.25, 0.5, and 1 mm. The other operating conditions were as follows: square sectional area with $W_{\mathrm{Reg}} = 13$ mm, $L_{\mathrm{Reg}} = 91$ mm, $f = 1$ Hz, $T_{\mathrm{H}} = 320$ K and $T_{\mathrm{C}} = 280$ K. The mass flow rate was ranged from 10 to 200 kg/h. Fig. 4.12 plots the regenerator effectiveness as a function of the NTU, which varies from 1 to 110. The results showed a good agreement between the Dragutinovic and Baclic (1998) solution and the numerical model, with a maximum deviation of about 1.0%.

Finally, the fourth comparison considers a parallel plate matrix with a constant plate thickness of $e_{\mathrm{PP}} = 0.25$ mm and variable porosity of 0.2, 0.36 and 0.5. The other operating conditions were the same as in the third comparison. Fig. 4.13 shows plots of the regenerator effectiveness as a function of the NTU, which varies between 1 and 300. The results showed a good agreement with the Dragutinovic and

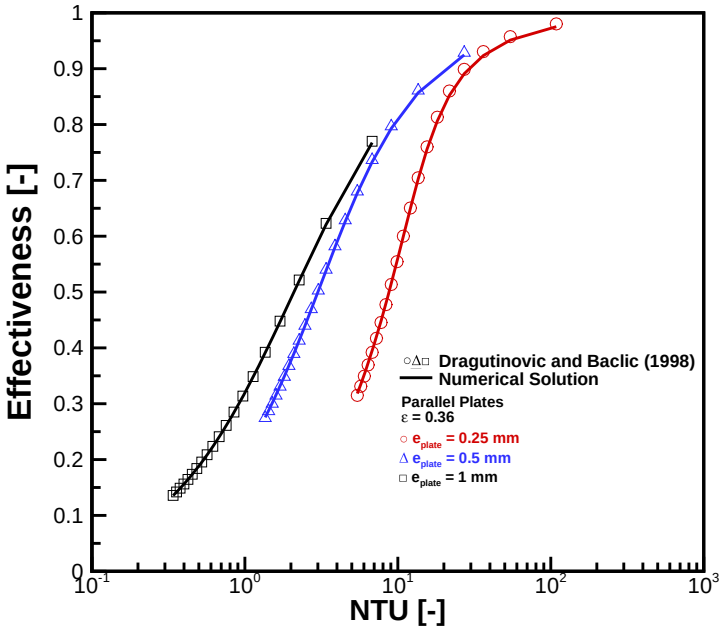

Figure 4.12 – Effectiveness vs. *NTU* for parallel plates matrix with different plate thickness. Comparison of numerical modeling results with the Dragutinovic and Baclic (1998) solution for ideal passive regenerators.

Baclic (1998) solution, with a maximum deviation of about 1.0%.

As presented in Figs. 4.10, 4.11, 4.12 and 4.13, all comparisons between the numerical model and the ideal regenerator solution of Dragutinovic and Baclic (1998) were in very good agreement. This means that the coupled solution of the energy equations for the fluid and solid phases was executed correctly, the convergence tolerances were satisfactorily selected and the solver iterative routine was successfully implemented. Therefore, it is believed that the inclusion in the numerical model of non-idealities such as the time-dependent properties and mass flow rate, axial heat conduction and viscous dissipation will result in physically consistent behavior that will not depend on the numerical implementation.

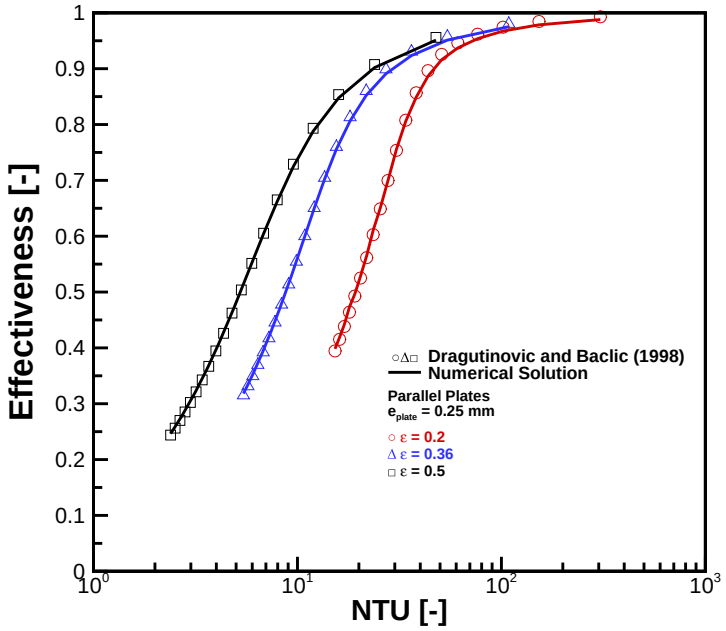

Figure 4.13 – Effectiveness vs. *NTU* for parallel plates matrix with different porosities. Comparison of numerical modeling results with the Dragutinovic and Baclic (1998) solution for ideal passive regenerators.

4.7.2 Validation of the MCE Implementation

The validation of the MCE implementation is an important step before running the final AMR simulations. This section compares the two different types of MCE implementation, discussed in Section 4.4.1, namely the discrete and the built-in methods subjected to a continuous sinusoidal magnetic flux density waveform between 0 and 1 T. The regenerator matrix dimensions are: $D_{\mathrm{h,Reg}} = 25$ mm, $L_{\mathrm{Reg}} = 100$ mm, $d_{\mathrm{p}} = 1$ mm and $\varepsilon = 0.36$. The hot reservoir temperature was kept constant at $T_{\mathrm{H}} = 300$ K, while the reservoir temperature span was allowed to vary. Five different operating conditions were evaluated, changing the operating frequency and the mass flow rate. The utilization changed as a consequence. Table 4.11 shows the simulation conditions of each case.

Fig. 4.14 shows the numerical results for the five cases, in which the con-

Table 4.11 – Operating conditions of the simulated cases to compare the different MCE implementations.

Case	f [Hz]	$\dot{m}$ [kg/h]
1	0.5	9.3
2	0.5	18.7
3	0.5	28.0
4	1	37.3
5	1	56.0

tinuous line correspond to the results of the discrete approach and the open circles are for the built-in approach. As expected, when a refined data set of the magnetocaloric properties are available, both approaches have to return about the same converged results for the cooling capacity, even when a continuous magnetic flux density variation is imposed. These results lead to the conclusion that both MCE approaches were successfully implemented in the AMR modeling. However, the discrete approach was selected for the AMR evaluation performed in this thesis.

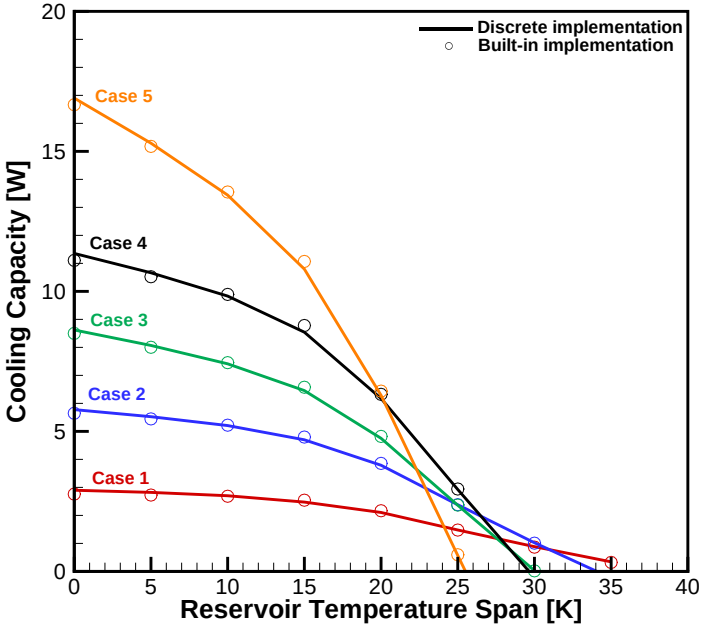

Figure 4.14 – Comparison between the discrete and built-in implementation of the MCE.

4.8 RegSim Development

The numerical model, *RegSim - Regenerator Simulator*, was written in Delphi 7. The user interface was divided in different palettes to enable easy understanding of the type of regenerator being simulated, selection of materials and heat transfer fluid, operating parameters and losses modeling. The *RegSim* interface is shown in Fig. 4.15. The simulator enables the following features:

- Selection of the problem to be solved, i.e., momentum equation only, single blow regenerator, passive regenerator or AMR;
- Selection of four different regenerator matrix geometries, namely, spheres, pins, parallel plates and micro-channels;
- Selection of three different fluid flow waveforms: instantaneous, sinusoidal and trapezoidal, which is characteristic of rotary valves;
- Selection of five different applied magnetic field waveforms: instantaneous, sinusoidal, rectified sinusoidal (used in the present thesis), trapezoidal and rotor-stator.
- Selection of different operating conditions, defined in terms of the reservoir temperatures, operating frequencies and mass flow rates;
- Selection of the losses models to simulate: casing heat transfer, void volume and magnetic losses.

Also, the interface enables selecting ranges of several parameters to be simulated. For example, if the mass flow rate needs to be varied between 10 and 100 kg/h, in intervals of 10 kg/h, these can be directly input via the user interface so that the simulations will run sequentially. This is very important in the simulations carried out in the optimization procedure.

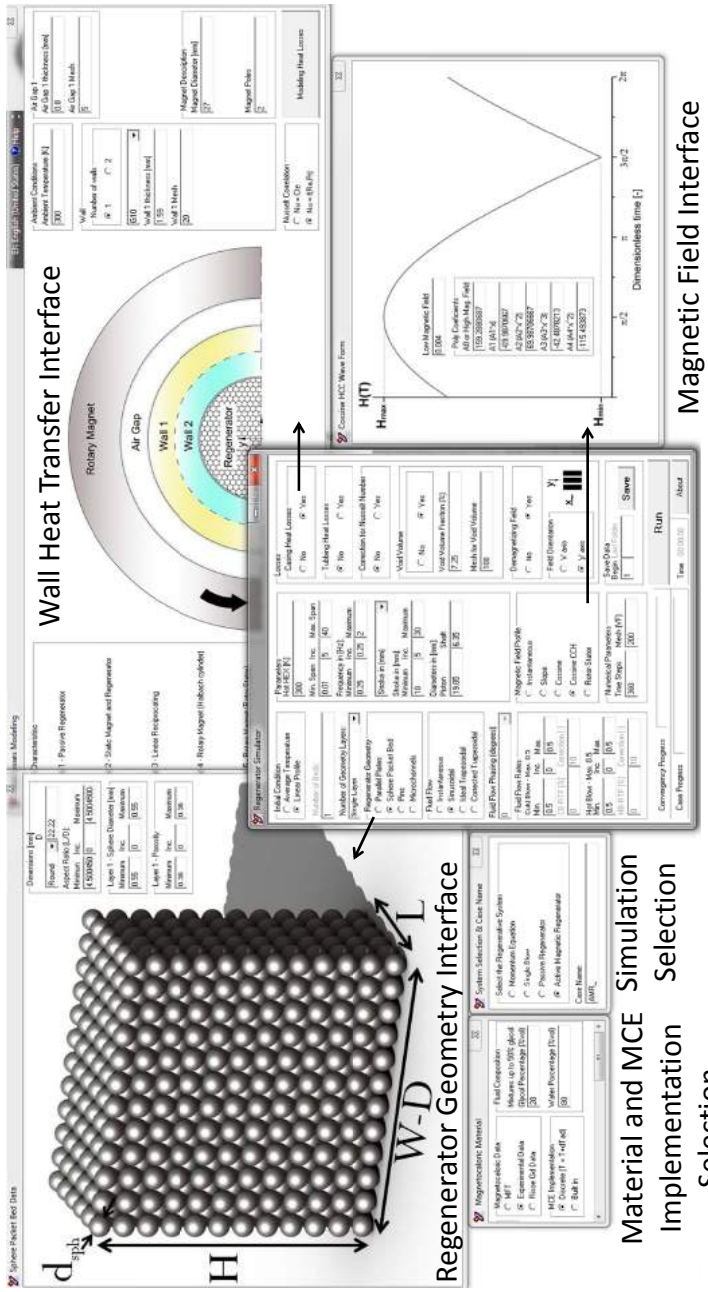

Figure 4.15 – *RegSim - Regenerator Simulator* interface.

5 Passive Thermal Regenerators

The study of passive regenerator is the basis to understand the heat transfer, fluid flow and losses in the regenerative matrix. Additionally, the experience acquired with the instrumentation and transient measurements during the passive experiments was valuable to define the AMR experimental procedure. The present chapter shows the experimental and numerical evaluation of passive thermal regenerators, starting with the time dependent measurements of temperature, pressure drop and mass flow rate. Next, the data regression and the metrics used to evaluate the numerical and experimental results are presented. The comparison between the data and numerical results is presented at the end of the chapter.

5.1 Time-Dependent Measurements

The time-dependent measurements performed by different transducers are used to calculate the time-average values that characterize the main system variables. As explained in Chapter 3, in all transient measurements, a total of 5 cycles with 300 data points per cycle were used to evaluate the time-average metrics. The transient measurements are explained next.

5.1.1 Temperature Measurements

A passive regenerator test starts with the regenerator at a given initial condition and the setting of the temperatures of the two thermal

reservoirs. The hot and cold reservoirs were kept at 320 and 280 K, respectively, in all tests. The ambient temperature was at 300 ± 2 K. Fig. 5.1 shows a typical evolution of the temperature at the cold (T_{CE}) and hot (T_{HE}) ends, and the internal temperatures at different positions (T_{i1}, T_{i2}, T_{i3}, T_{i4} and T_{i5}). Having started at around 300 K, the temperatures reach the periodically developed regime in a few minutes. It is possible to observe the symmetry between the cold and hot sides of the regenerator, which is a consequence of the well balanced operating conditions, i.e., equal blow periods and blow-average mass flow rates.

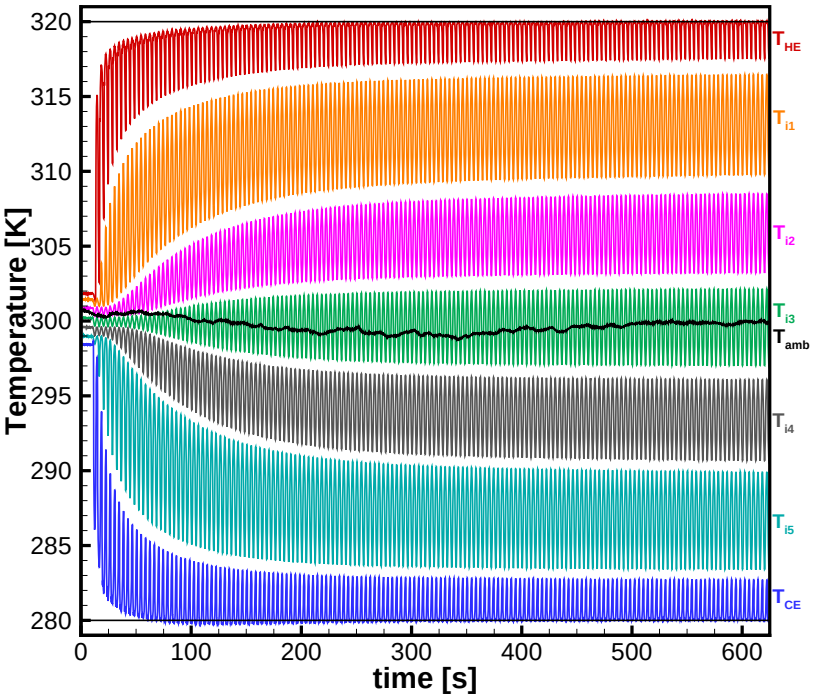

Figure 5.1 – Time-dependent temperature evolution in the passive experimental tests.

In the periodically developed regime, the last five cycles of the total sampling interval are selected to evaluate the time-average metrics. Fig. 5.2 shows the last five cycles for four different tests, as presented in Table 5.1. Additionally, Fig. 5.3 shows the temperature profiles in these tests immediately after the hot blow (open symbols) and immediately after the cold blow (solid symbols).

Table 5.1 – Geometry and operating conditions of the experimental tests to evaluate the time-dependent temperature measurements.

Test	Casing	d_p [mm]	ϕ	f [Hz]	NTU[-]	V_{pump} [cm^3]
Test#1	#3	0.5	0.23	0.25	≈ 650	5.07
Test#2	#4	1	1.43	0.25	≈ 40	13.90
Test#3	#3	1	0.62	1	≈ 28	13.90
Test#4	#1	1	1.25	1	≈ 14	13.90

The conditions of Test #1, Fig. 5.2(a), result in a high thermal effectiveness. T_{i1} and T_{i5} never get close to the reservoirs temperatures, T_H and T_C, which gives rise to almost linear temperature profiles at the end of the blows, as seen in Fig. 5.3. Also, the internal temperature readings have sinusoidal shapes with small temperature amplitudes (of the order of 5 K), which are typical of high effectiveness, as a result of high NTU matrices and low utilization conditions.

Conversely, the conditions of Test #2, Fig. 5.2(b), are those of a low effectiveness regenerator. Now, only the middle probe, T_{i3}, has a perfect sinusoidal behavior, but with a large amplitude approaching 40 K. In this case, T_{i1} and T_{i2} reach T_H at the end of the cold blow and, symmetrically, T_{i4} and T_{i5} reach T_C at the end of the hot blow. As a result, the temperature profiles at the end of the blows are no longer linear, and there is a significant penetration of the constant temperature of the reservoirs into the matrix, due to the large displaced fluid volumes in the blows associated with a large utilization factor. In this case, close to 30% of the regenerator length, closer to the reservoirs, attain the reservoir temperature after each blow. As a consequence, the outlet blow time-dependent temperature also presents a large amplitude, which is typical of low effectiveness, resulted from low NTU matrices and large utilization conditions.

Tests #3 and #4, Figs. 5.2(c) and (d), were carried out to compare two matrices at the same operating conditions (frequency and superficial velocity), but with different values of utilization and NTU, since the Casing #1 has only half the volume of Casing #3. As expected, the results show clearly the effects of utilization and interstitial heat transfer area on the regenerator performance, since the results for Casing #3 are in much better agreement with the behavior expected for a high effectiveness matrix than Casing #1.

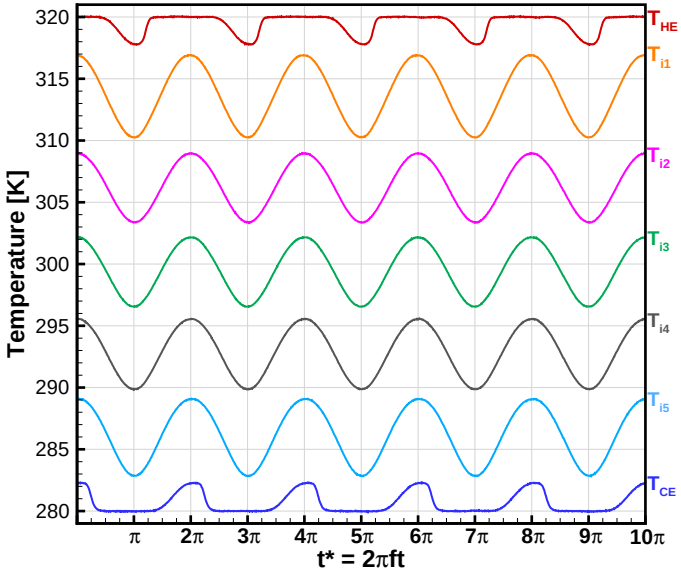
Temperature [K]
320
315
310
305
300
295
290
285
280
π
2π
3π
4π
5π
6π
7π
8π
9π
10π
t* = 2πft
T_HE
T_i1
T_i2
T_i3
T_i4
T_i5
T_CE

(a)

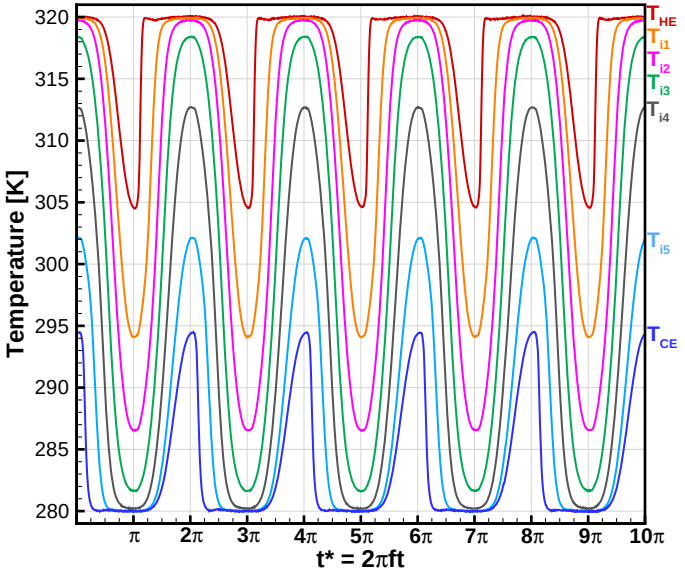
Temperature [K]
320
315
310
305
300
295
290
285
280
π
2π
3π
4π
5π
6π
7π
8π
9π
10π
t* = 2πft
T_HE
T_i1
T_i2
T_i3
T_i4
T_i5
T_CE

(b)

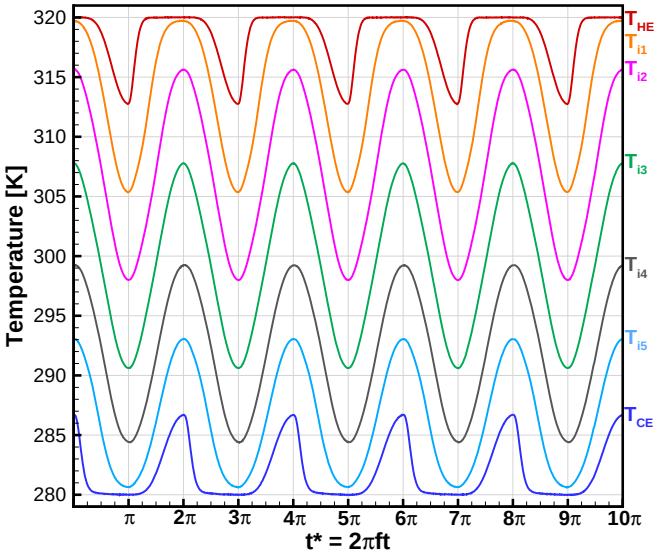

(c)

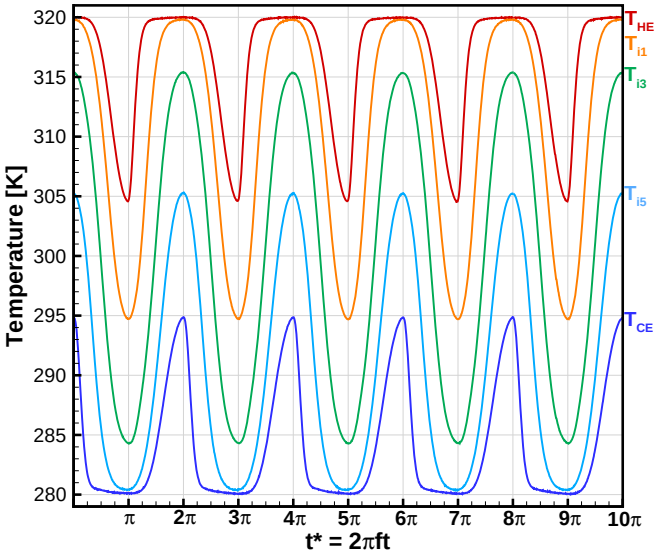

(d)

Figure 5.2 – Time-dependent temperature measurements: (a) Test#1; (b) Test#2; (c) Test#3; (d) Test#4.

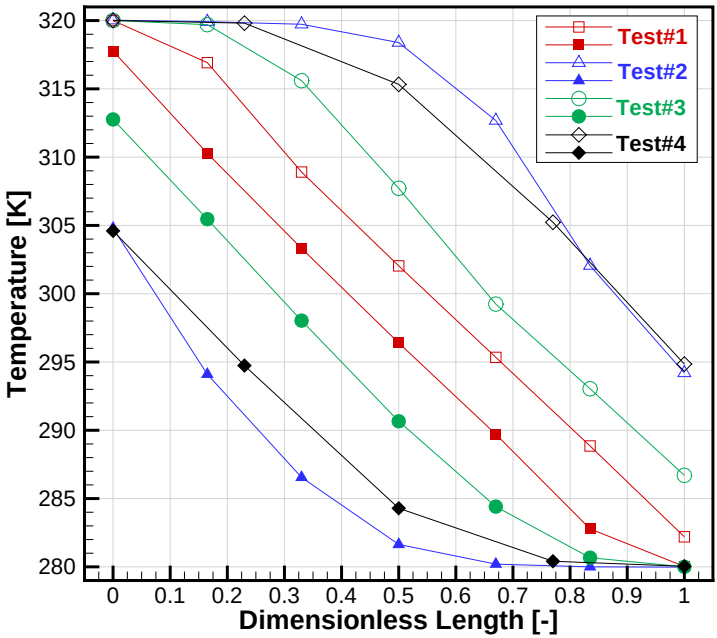

Figure 5.3 – Axial temperature profiles after the hot blow (open symbols) and after the cold blow (solid symbols). Conditions are presented in Table 5.1.

Fig. 5.4 shows the time-dependent temperature at the regenerator hot end during two consecutive cycles. The tests were conducted with Casing #3 with 1-mm spheres. While Fig. 5.4(a) is for a constant utilization of approximately 0.62 and variable frequency, Fig. 5.4(b) is for a constant frequency of 0.5 Hz and variable utilization.

For a fixed utilization, Fig. 5.4(a), the fluid displaced volume does not change with frequency. However, the average fluid velocity and the mass flow rate increase with frequency because the fluid volume is displaced faster through the porous medium. The mass flow rate results in a lower NTU, which causes the temperature of the fluid exiting the regenerator to reach lower and lower values at the end of the cold blow as the frequency increases. With a fixed displaced volume, the reservoir temperature penetration is very little affected by the frequency, as seen in Fig. 5.5(a), which shows the longitudinal temperature profiles at the end of the blows for the fixed utilization condition.

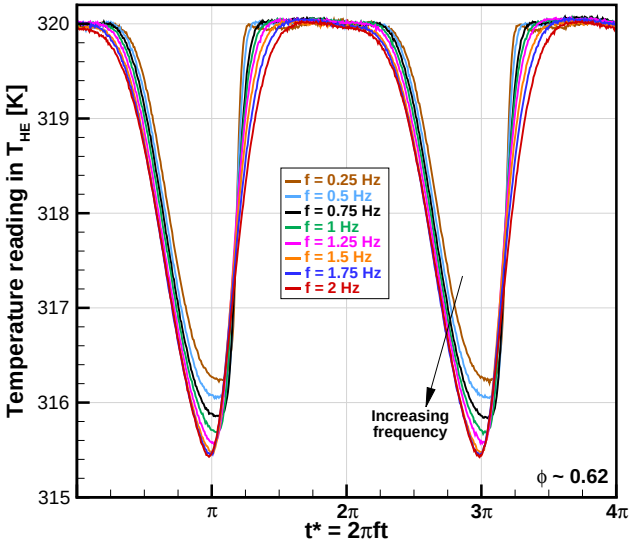

(a)

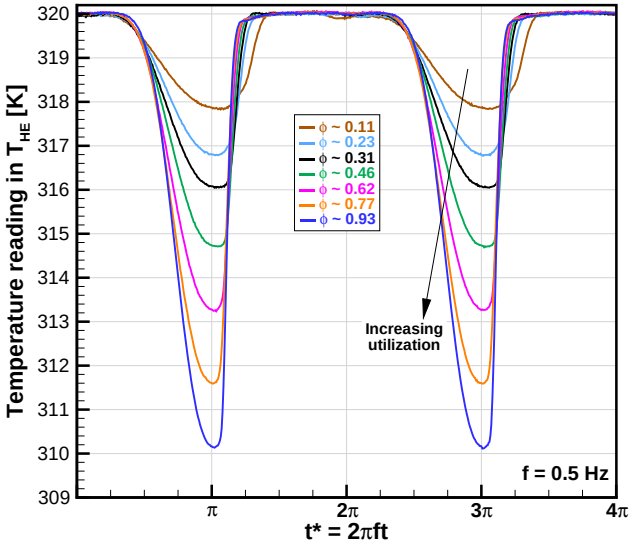

(b)

Figure 5.4 – Time-dependent temperature behavior at the hot end: (a) Constant utilization (≈ 0.62) and variable frequency; (b) Constant frequency (0.5 Hz) and variable utilization.

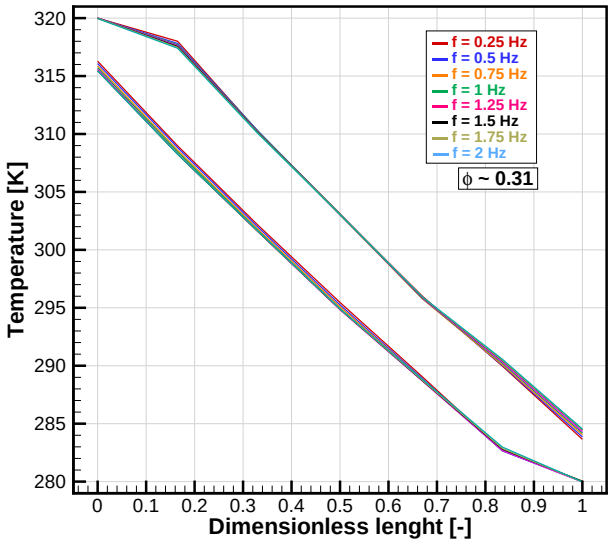

(a)

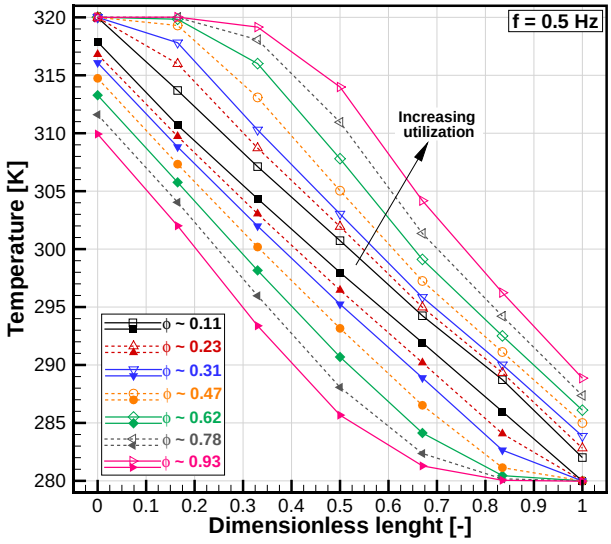

(b)

Figure 5.5 – Axial temperature profiles after the hot blow (open symbols) and after the cold blow (solid symbols): (a) Constant utilization (≈ 0.31) and variable frequency; (b) Constant frequency (0.5 Hz) and variable utilization.

For the condition of Fig. 5.4(b), increasing the utilization for a constant frequency means displacing a larger fluid volume through the matrix in the same period of time. This, at the same time as it enhances the interstitial heat transfer coefficient, it also increases the reservoir temperature penetration in the matrix as a result of a higher utilization. The latter effect can be perceived quite clearly in Fig. 5.5(b), which shows the axial temperature profiles becoming more deviated from the linear behavior as the utilization increases. It is clear from Figs. 5.4(b) and 5.5(b) that the increase in utilization reduces significantly the effectiveness of the regenerator.

5.1.2 Mass Flow Rate Measurement

The mass flow rate is varied when the frequency or utilization are changed. Fig. 5.6 shows the transient response of the Coriolis mass flow meter. Fig. 5.6(a) is for a constant utilization of approximately 0.62 and a variable frequency, and Fig. 5.6(b) is for a constant frequency of 0.25 Hz and a variable utilization.

As explained in Chapter 3, the Coriolis mass flow meter is not capable of measuring fast transients. Ideally, during the cold blow period, the flow rate measured by the cold-side MFM should be the first top half of the sinusoidal flow waveform, while the flow rate given by the hot-side MFM should be zero. During the hot blow, the behavior should be the opposite, i.e., the cold-side MFM should read zero flow, while the hot-side MFM should give the last bottom half of the flow waveform (see Fig. 3.15). This behavior is somewhat followed at low frequencies (0.25 and 0.5 Hz), as can be seen in Fig. 5.6(a), but fails at frequencies above 0.75 Hz, since the flow rate measurements no longer go to zero during the opposite blows. It should be mentioned that the mass flow rate measurements are not in phase with the other transient measurements, with the dephasing increasing with the frequency. In Fig. 5.6(a), however, the dephasing has been corrected.

At higher operating frequencies, the transient measurement do not reach the maximum instantaneous (peak) flow rate or the zero flow rate due to second-order (time constant) effects in the flow meters. However, the blow-average mass flow rate is still calculated with reasonable accuracy, as can be seen in Fig. 5.7. This figure shows the experimental blow-average mass flow rate as a function of the reference average mass flow rate calculated by Eq. (3.1). The results shown in this figure

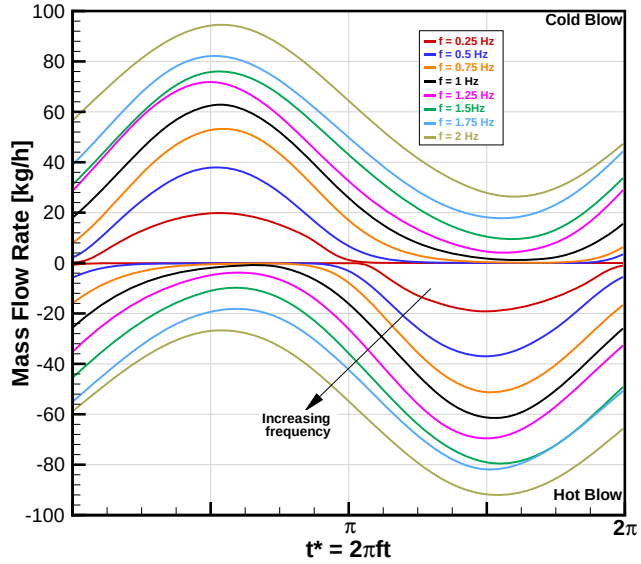
Cold Blow
f = 0.25 Hz
f = 0.5 Hz
f = 0.75 Hz
f = 1 Hz
f = 1.25 Hz
f = 1.5Hz
f = 1.75 Hz
f = 2 Hz
Increasing frequency
Hot Blow
Mass Flow Rate [kg/h]
t* = 2πft

(a)

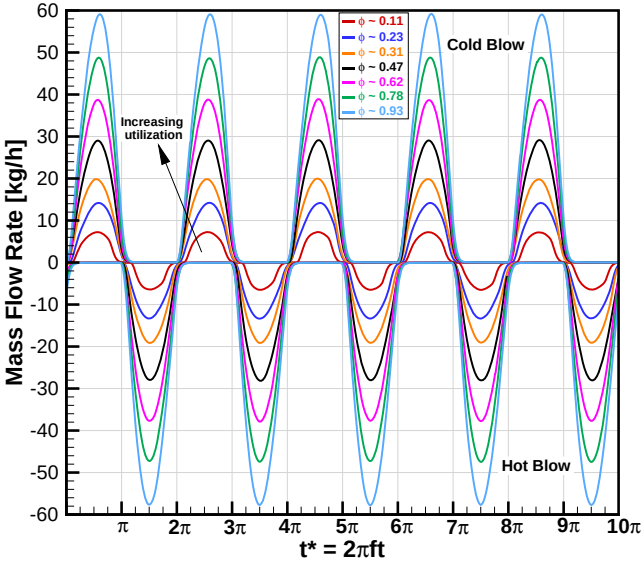
ϕ ~ 0.11
ϕ ~ 0.23
ϕ ~ 0.31
ϕ ~ 0.47
ϕ ~ 0.62
ϕ ~ 0.78
ϕ ~ 0.93
Cold Blow
Increasing utilization
Hot Blow
Mass Flow Rate [kg/h]
t* = 2πft

(b)

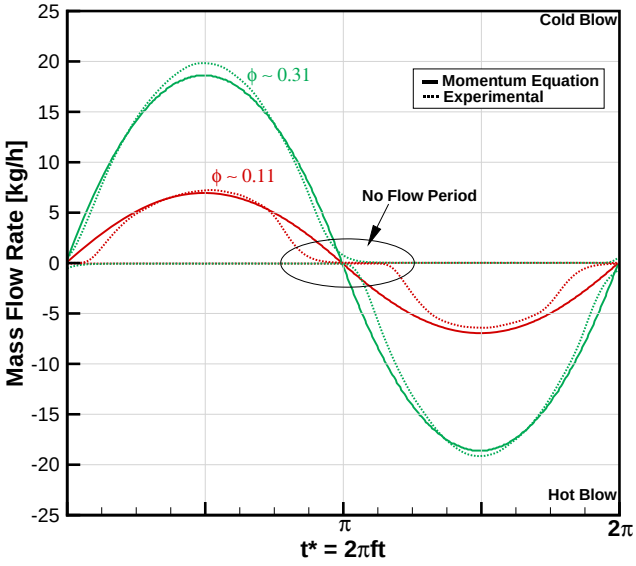

(c)

Figure 5.6 – Time-dependent mass flow rate measurements: (a) Constant utilization (≈ 0.62) and variable frequency; (b) Constant frequency (0.25 Hz) and variable utilization; (c) Detail of the no flow period.

were obtained with Casing #3 using 1-mm spheres. A good agreement is observed between the cold (solid symbols) and hot (open symbols) blow-average mass flow rates. The deviations between the experimental data and the reference curve are of the order of the experimental uncertainty, which were observed to increase with frequency. For this reason, the reference value (calculated based on the system frequency and the piston displacement) was used to determine parameters such as the NTU, Re_{dp}, friction factor and pumping power. The data trend presented in Fig. 5.7 was observed in all other test conditions.

At low frequencies the time-dependent mass flow rate measurements are in agreement with the expected sinusoidal waveform. Fig. 5.6(b) shows the measurements for different utilizations at a constant frequency of 0.25 Hz. This enables identifying the no flow period for $\phi \approx 0.11$, shown in greater detail in Fig. 5.6(c). The no flow period occurs when a small amount of fluid is pumped using pump PP42.5 with strokes between

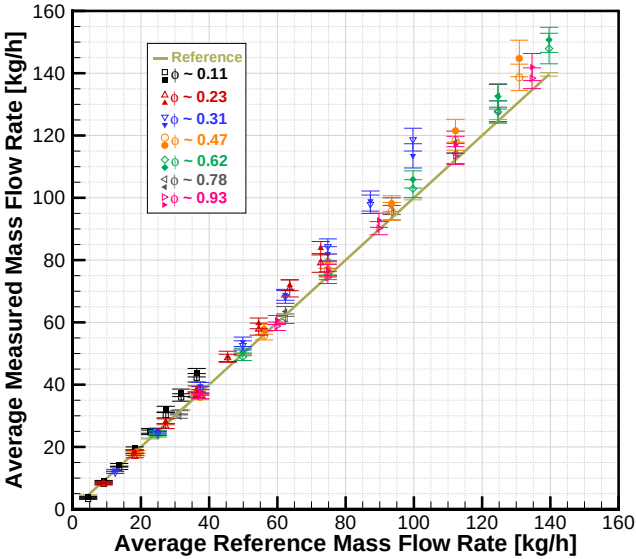

Figure 5.7 – Experimental blow-averaged mass flow rate as a function of the reference mass flow rate. The solid symbols correspond to the cold blow and the open symbols are related to the hot blow measurements.

10 and 20 mm, i.e., small displaced volumes. Fig. 5.6(c) compares the experimental and numerically determined mass flow rates for pumps PP42.5 ($\phi \approx 0.11$) and PP122.5 ($\phi \approx 0.31$), both with $s_k = 10$ mm. The numerical results show a perfect sinusoidal waveform. Deviations such as those shown in Fig. 5.6(c) can lead to differences between the modeling and experimental results, which will be explained later.

5.1.3 Pressure Drop Measurements

Fig. 5.8 shows the last five cycles of the time-dependent total pressure drop for two different tests. Fig. 5.8(a) is for a constant utilization of approximately 0.62 and a variable frequency, and Fig. 5.8(b) is for a constant frequency of 0.5 Hz with a variable utilization. Again, these figures refer to Casing #3 with 1-mm spheres. The results show clearly the sinusoidal waveform characteristic of double effect pumps. At low mass flow rates, the influence of the check valves is small, given that there is little distortion of the sinusoidal profiles. However, the no flow

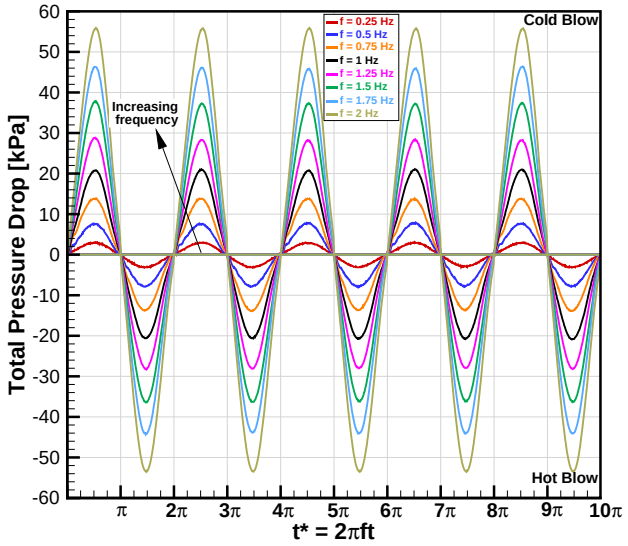

(a)

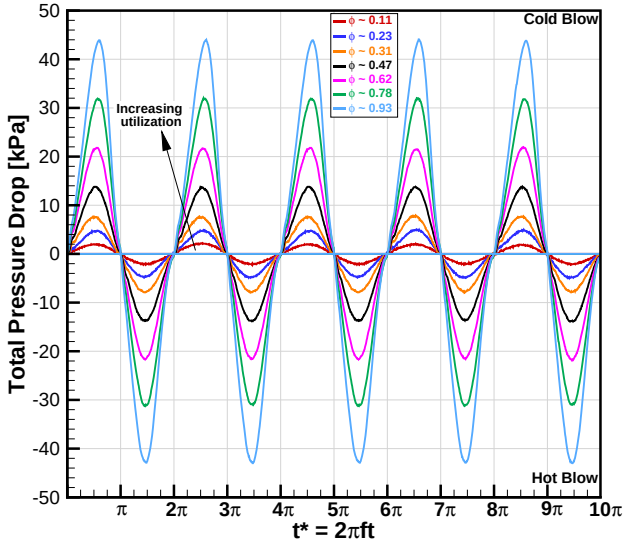

(b)

Figure 5.8 – Time-dependent total pressure drop measurements: (a) Constant utilization (≈ 0.62) and variable frequency; (b) Constant frequency (0.5 Hz) and variable utilization.

periods are not captured in great detail, since two absolute pressure transducers were used to measure the pressure drop instead of a differential pressure transducer. This usually increases the experimental uncertainties.

As expected, the mass flow rate changes when frequency or utilization are changed. Thus, when either one is increased keeping the other constant, the peak of the total pressure drop increases. As will be shown further ahead, these results will be used to determine the cycle-averaged porous medium pressure drop by subtracting the average pressure drop in the tubing from the blow-average total pressure drop.

5.2 Performance Metrics and Data Regression

The passive regenerator evaluation is carried out in terms of the ϵ-NTU relationship, which represents the thermal performance of the matrix, and of the pressure drop, friction factor and pumping power as a function of the Reynolds number, which quantify the viscous losses. Based on these metrics, the regenerative matrices can be compared.

The data regression to calculate the effectiveness is based on the time-dependent temperature measurements at the hot, T_{HE}, and cold, T_{CE}, ends. All tests were carried out under balanced flow conditions (SCHMIDT; WILLMOTT, 1981; ACKERMANN, 1997), i.e., $\dot{m}c_{\mathrm{p,f}}|_{\mathrm{CB}} = \dot{m}c_{\mathrm{p,f}}|_{\mathrm{HB}}$. Thus, the effectiveness can be defined only as a function of the temperatures:

- Cold blow - measured at the hot end ($T_{HE}(t)$):

$$\epsilon_{\mathrm{CB}} = \frac{1}{\varsigma}\sum_{i=1}^{\varsigma}\left[\frac{\left(\frac{1}{\tau/2}\int_0^{\tau/2} T_{\mathrm{HE}}(t)dt\right) - T_{\mathrm{C}}}{T_{\mathrm{H}} - T_{\mathrm{C}}}\right] \tag{5.1}$$

- Hot blow - measured at the cold end ($T_{CE}(t)$):

$$\epsilon_{\mathrm{HB}} = 1 - \frac{1}{\varsigma}\sum_{i=1}^{\varsigma}\left[\frac{\left(\frac{1}{\tau/2}\int_{\tau/2}^{\tau} T_{\mathrm{CE}}(t)dt\right) - T_{\mathrm{C}}}{T_{\mathrm{H}} - T_{\mathrm{C}}}\right] \tag{5.2}$$

where τ is the cycle period and $\varsigma = 5$ is the number of cycles used in the data regression. To correct for oscillations in the temperature readings, the reservoir temperatures were calculated as the averages of the inlet constant temperatures (see Fig. 5.2). In all cases, $T_{\mathrm{H}} = 320 \pm 0.15$ K and $T_{\mathrm{C}} = 280 \pm 0.15$ K. The differentiation between the two definitions of effectiveness, i.e., of the cold blow (measured at the hot end) and of the hot blow (measured at the cold end), is an important one because even when the regenerator operates under balanced flow conditions, the effectivenesses defined by Eqs. (5.1) and (5.2) may not be the same, generating an effectiveness imbalance, β_ϵ, defined as (SCHMIDT; WILLMOTT, 1981):

$$\beta_\epsilon = \frac{\epsilon_{CB}}{\epsilon_{HB}} \tag{5.3}$$

An effectiveness imbalance greater or smaller than unity can be associated with different physical phenomena (axial heat conduction, temperature-dependent properties), which may act independently or combined (TREVIZOLI *et al.*, 2014). Also, the imbalance may be attributed to a bad regenerator assembly, as will be explained below.

The blow-averaged (hot and cold) mass flow rate, $\overline{\dot{m}}$, is calculated by:

$$\overline{\dot{m}} = \frac{1}{\varsigma}\sum_{i=1}^{\varsigma}\left(\frac{1}{\tau/2}\int_0^{\tau}\dot{m}(t)dt\right) \tag{5.4}$$

Analogously, the blow-averaged total pressure drop, $\overline{\Delta P}_{\mathrm{tot}}$, is defined by:

- Cold blow - $\Delta P_{\mathrm{CB}}(t) = P_{\mathrm{H,out}}(t) - P_{\mathrm{C,in}}(t)$:

$$\overline{\Delta P}_{\mathrm{tot,CB}} = \frac{1}{\varsigma}\sum_{i=1}^{\varsigma}\left(\frac{1}{\tau/2}\int_0^{\tau/2}\Delta P_{\mathrm{CB}}(t)dt\right) \tag{5.5}$$

- Hot blow - $\Delta P_{\mathrm{HB}}(t) = P_{\mathrm{C,out}}(t) - P_{\mathrm{H,in}}(t)$:

$$\overline{\Delta P}_{\mathrm{tot,HB}} = \frac{1}{\varsigma}\sum_{i=1}^{\varsigma}\left(\frac{1}{\tau/2}\int_{\tau/2}^{\tau}\Delta P_{\mathrm{HB}}(t)dt\right) \tag{5.6}$$

The blow-averaged total pressure drop is composed by the porous medium and the tubing average pressure drops. The tubing pressure drop, $\overline{\Delta P}_{\mathrm{tub}}$, includes the tubing itself, T- and Y-junctions and the empty regenerator housing. The porous medium average pressure drop is the actual frictional loss through the porous medium, $\overline{\Delta P}$, and is the quantity used in the comparison with the modeling results. Thus:

$$\overline{\Delta P} = \overline{\Delta P}_{\mathrm{tot}} - \overline{\Delta P}_{\mathrm{tub}} \tag{5.7}$$

$\overline{\Delta P}_{\mathrm{tub}}$ varies according to the geometry of the regenerator housing. For instance, Casing #1 has the same housing diameter, but a shorter housing length and a longer tubing length compared with Casing #3. Casing #4 has a smaller housing diameter, but the same housing and tubing lengths as Casing #3. Thus, for a precise determination of the porous medium average pressure drop, $\overline{\Delta P}_{\mathrm{tub}}$ was experimentally evaluated via single (unidirectional) blow tests performed on all regenerator housings under variable mass flow rates between 10 and 180 kg/h.

The friction factor, f_{D}, is a non-dimensional form of the pressure drop. For porous media, it can be calculated as follows, using the blow-averaged pressure drop as follows (KAVIANY, 1995):

$$f_{\mathrm{D}} = \frac{\varepsilon^3}{1-\varepsilon}\frac{d_{\mathrm{p}}}{\rho_{\mathrm{f}} u^2}\frac{\overline{\Delta P}}{L_{\mathrm{Reg}}} \tag{5.8}$$

The blow-averaged pumping power required to overcome the viscous losses of the fluid through the porous medium, $\overline{\dot{W}}_{\mathrm{pump}}$, is given by:

$$\overline{\dot{W}}_{\mathrm{pump}} = \frac{\overline{\dot{m}}}{\rho_{\mathrm{f}}}\overline{\Delta P} \tag{5.9}$$

Since the regenerator operates at balanced conditions, it is expected, as will be seen, that $\overline{\Delta P}_{\mathrm{HB}} \approx \overline{\Delta P}_{\mathrm{CB}}$, $f_{\mathrm{D,HB}} \approx f_{\mathrm{D,CB}}$ and $\overline{\dot{W}}_{\mathrm{pump,HB}} \approx \overline{\dot{W}}_{\mathrm{pump,CB}}$.

All time integrations presented in this section were performed numerically using the extended Simpson's rule (PRESS *et al.*, 2007):

$$\int_{t_0}^{t_{N-1}} f(t)dt = \delta t\left[\frac{3}{8}f_0 + \frac{7}{6}f_1 + \frac{23}{24}f_2 + f_3 + f_4 + \cdots + f_{N-5} + f_{N-4} + \frac{23}{24}f_{N-3} + \frac{7}{6}f_{N-2} + \frac{3}{8}f_{N-1}\right] + O\left(\frac{1}{N^4}\right) \quad (5.10)$$

where N is the total number of points used to calculate the numerical integral and δt is the time increment. N was equal to 300 for cycle-averaged variables and 150 points for blow-averaged variables.

5.2.1 Uncertainty Analysis

The experimental uncertainties were evaluated based on the procedures presented in INMETRO (2003) and Holman (2006). The metrics were calculated based on experimental measurements of independent variables, such as temperature, pressure and mass flow rate. Thus, the uncertainty of a dependent variable R (u_R) is a combination of the uncertainties of each independent variable ($u_{x1}, u_{x2}, u_{x3}, ..., u_{xn}$). Thus:

$$u_R = \left[\left(\frac{\partial R}{\partial x_1}u_{x1}\right)^2 + \left(\frac{\partial R}{\partial x_2}u_{x2}\right)^2 + \cdots + \left(\frac{\partial R}{\partial x_n}u_{xn}\right)^2\right]^{1/2} \quad (5.11)$$

For instance, the total blow-averaged pressure drop is a function of the instantaneous pressure and time measurements, $\overline{\Delta P}_{\text{tot}} = \text{f}(\Delta P(t), t)$ as shown in Eqs. (5.5) and (5.6). Thus, the uncertainty related with $\overline{\Delta P}_{\text{tot}}$ is calculated by:

$$u_{\Delta P tot} = \left[\left(\frac{\partial \overline{\Delta P}_{\text{tot}}}{\partial \Delta P(t)}u_{\Delta P(t)}\right)^2 + \left(\frac{\partial \overline{\Delta P}_{\text{tot}}}{\partial t}u_t\right)^2 + \left(\frac{\sigma_{sd}}{\sqrt{\varsigma}}\right)^2\right]^{1/2} \quad (5.12)$$

where $u_{\Delta P(t)} = f(P_{\text{out}}, P_{\text{in}})$ and σ_{sd} is the standard deviation calculated from the averaged values of $\overline{\Delta P}_{\text{tot}}$ obtained in each of the five cycles:

$$\sigma_{sd} = \sqrt{\sum_{i=1}^{\varsigma} \left(\frac{\Delta P_{\mathrm{tot,i}} - \overline{\Delta P}_{\mathrm{tot}}}{\varsigma - 1} \right)^2} \tag{5.13}$$

Additionally, the numerical integration is a summation ($R = \sum a_{\mathrm{i}} x_{\mathrm{i}}$) and the uncertainty of such a function is given by (HOLMAN, 2006):

$$u_R = \left[\sum \left(\frac{\partial R}{\partial x_1} u_{x1} \right)^2 \right]^{1/2} = \left[\sum (a_{\mathrm{i}} u_{x1})^2 \right]^{1/2} \tag{5.14}$$

Thus, substituting Eq. (5.14) in Eq. (5.12) gives:

$$u_{\Delta P tot} = \left[\left(\frac{\overline{\Delta P}_{\mathrm{tot}}}{\tau} u_\tau \right)^2 + \left(\frac{\overline{\Delta P}_{\mathrm{tot}}}{\delta t} u_{\delta t} \right)^2 + \left(\frac{2}{\tau \delta t} u_\tau u_{\delta t} (\overline{\Delta P}_{\mathrm{tot}})^2 \right) + (2\tau\delta t)^2 \sum (a_{\mathrm{i}} u_{\Delta P(t)})^2 + \left(\frac{\sigma_{sd}}{\sqrt{\varsigma}} \right)^2 \right]^{1/2} \tag{5.15}$$

where u_τ and $u_{\delta t}$ are the uncertainties of the cycle frequency (or period) and the time increment, respectively. These time uncertainties were calculated based on the error associated with the frequency calculation from the linear potentiometer and on the stepper motor resolution. The time increment, δt, is the same used in the numerical integration using Eq. (5.10). The third term in Eq. (5.15) results from the fact that there is a correlation between τ and δt, so their uncertainties are also correlated. Finally, a_{i} are the coefficients in the extended Simpson rule.

Similar procedures to evaluate experimental uncertainties were performed for all variables that required numerical integration. Variables that did not require numerical integration, such as β_ϵ, $\overline{\Delta P}$ (porous media pressure drop) and f_{D}, had their uncertainties directly evaluated by Eq. (5.11).

Finally, the expanded uncertainty (U_R) is calculated by:

$$U_R = t_s u_R \tag{5.16}$$

where t_s is the Student's t-distribution calculated based on the effective number of degrees of freedom and on the confidence level.

The expanded uncertainties of the experimental measurements were presented in Table 3.10. These were obtained from either calibration or from manufacturer's catalog in the following manner: (i) if U_R was evaluated from calibration, a normal distribution is assumed, with a 95% confidence level and infinite degrees of freedom. Hence, $u_R = U_R/2$; (ii) if U_R was evaluated from catalog information, as suggested by INMETRO (2003), a rectangular distribution is assumed with 68% confidence interval and, thus, $u_R = U_R/\sqrt{3}$.

5.3 Experimental Results

5.3.1 Reproducibility of the Experimental Results

The reproducibility of the experiments was verified by means of a procedure consisting of the following steps:

1. Disassembling of the passive apparatus and removal of the regenerative matrix from the housing;

2. Rebuilding of the regenerative matrix, following the step-by-step procedure described in Appendix B for the packed bed of spheres;

3. Reassembling of the passive apparatus, including all the instrumentation;

4. Execution of 32 experimental tests varying the utilization and the operating frequency;

The procedure was repeated three times by two different operators (PVT and GFP), as presented in Table 5.2. Casing #3 and 1-mm diameter spheres with a porosity of 0.363 ± 0.005 were used as the regenerative matrix. Assembly #1 was the first experimental evaluation of the passive system, for which the operator PVT was involved in the assembling itself and in running tests. In Assembly #2, a second operator (GFP) performed the same procedure as in Assembly #1. In a third test, Assembly #3, conducted by operator PVT, the hot and

Table 5.2 – Reproducibility tests.

Assembly	Hot and cold reservoirs	Operator
Assembly#1	as designed	PVT
Assembly#2	as designed	GFP
Assembly#3	inverted	PVT

cold reservoirs were inverted in order to verify the thermal symmetry of the apparatus.

Fig. 5.9 shows the reproducibility tests results for the porous medium pressure drop, $\overline{\Delta P}$, as a function of Re_{dp} for the three assemblies presented in Table 5.2. Fig. 5.9 also shows the numerical results for $\overline{\Delta P}$. A good agreement is observed between the experimental and numerical results, with similar trends for all assemblies. The deviations observed for some individual points are of the order of the experimental uncertainties, which was about 2.5 kPa for all experimental points. The uncertainty of Re_{dp} is about 1%.

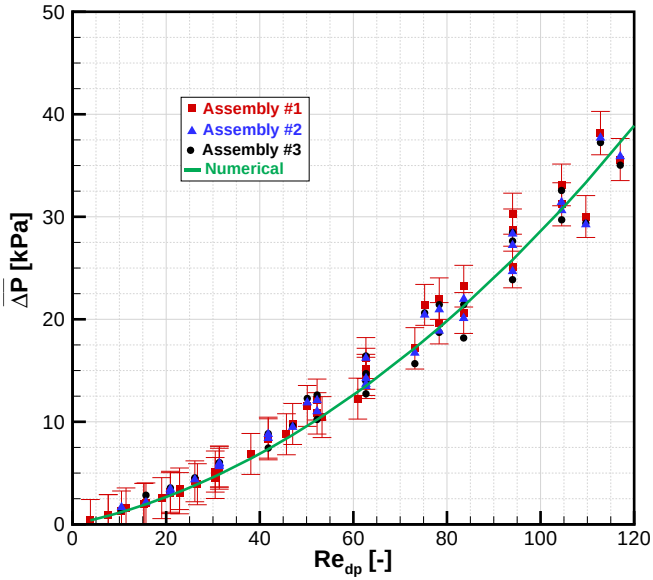

Figure 5.9 – Reproducibility tests: $\overline{\Delta P}$ as a function of Re_{dp} and comparison with the numerical model.

Fig. 5.10 shows the reproducibility tests results of the thermal effectiveness, ϵ, as a function of NTU. The results show a good reproducibility, with very similar trends for all assemblies. The experimental uncertainty for the effectiveness was within 1.5 to 2.5% for all experimental points, and NTU had an uncertainty of about 2.5%.

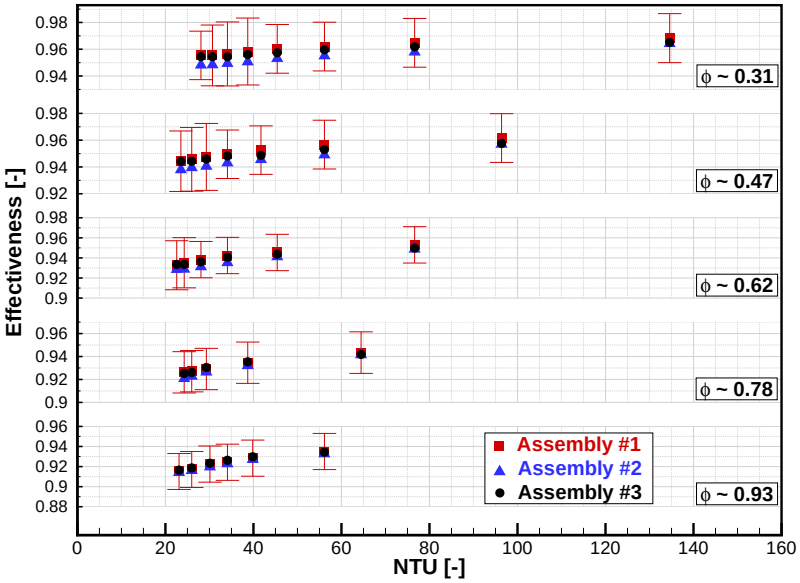

Figure 5.10 – Reproducibility tests: ϵ as a function of NTU.

5.3.2 Effectiveness Imbalance

An effectiveness imbalance greater or smaller than unity can be associated with different physical phenomena (axial heat conduction, temperature dependent properties), which may act independently or combined. The imbalance may also be caused by poor assembling of the packed bed, such as porosities higher than 36% or an axially variable porosity. Trevizoli *et al.* (2014) presented some results for the effectiveness imbalance for three different matrices composed by stainless steel, lead and gadolinium spheres. They identified a severe effectiveness imbalance in the lead and gadolinium passive regenerators. This was attributed to axial heat conduction effects and, in the case of Gd, also to the specific heat capacity variation with temperature.

Contrary to Gd, the thermophysical properties of stainless steel are not strongly dependent on temperature. As an example of the small impact on the effectiveness, Fig. 5.11 shows the results for the effectiveness imbalance as a function of NTU for Casing #3 for spheres sizes of 0.5 and 1 mm.

Therefore, since all the passive regenerator experiments are highly reproducible, and have only been performed using stainless steel matrices, the effectiveness imbalance is expected to be around unity for all cases in this thesis. Hence, the effectiveness results will be represented either by the cold or hot blow effectiveness, since they are always very similar.

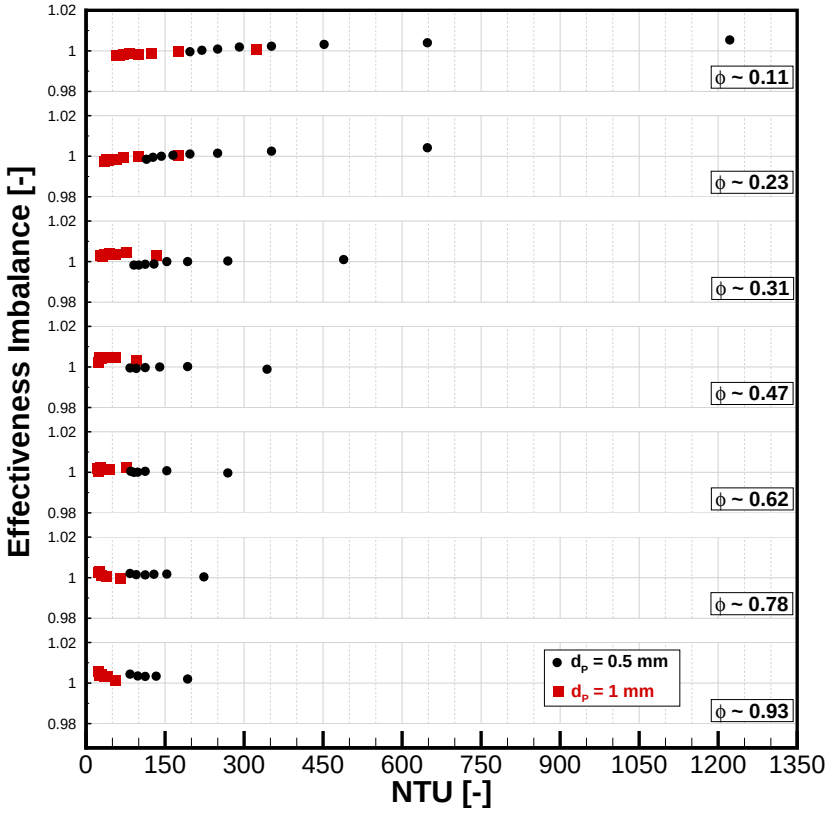

Figure 5.11 – Effectiveness imbalance as a function of NTU for Casing #3 with 0.5 and 1-mm stainless steel spheres.

5.3.3 Packed Bed Regenerator

5.3.3.1 Pressure Drop and Pumping Power

The blow-averaged porous medium pressure drop - calculated according to Eq. (5.7) - is shown in Fig. 5.12 as a function of Re_{dp} for three different spheres sizes (0.5, 0.8 and 1 mm diameter) and Casings #1 to #4. As expected for packed bed porous media, the pressure drop exhibits a linear trend at low Re_{dp}, which is typical of the Stokes flow regime at which Darcy's law is valid. At higher velocities, the pressure drop deviates from Darcy's law and a parabolic behavior is observed with respect to Re_{dp} (inertial regime).

For all casings, $\overline{\Delta P}$ is inversely proportional to the particle size. Also, Re_{dp} extends over longer ranges as the particle diameter increases. The following remarks can be made considering a constant sphere diameter:

1. For Casings #1, #2 and #3, both the superficial velocities and the Re_{dp} ranges are the same, since the housing diameter is identical in these casings. Therefore, the increase observed in $\overline{\Delta P}$ is due to the increasing housing length, as $\overline{\Delta P}$ increases linearly with the regenerator length;

2. Casings #3 and #4 have the same regenerator length, but the housing diameter is different. Thus, the superficial velocity for Casing #4 is higher than in Casing #3 and, as a consequence, the Re_{dp} range is longer for Casing #4. As a result, for identical operating conditions, i.e., displaced volume and frequency, Casing #4 exhibits a higher $\overline{\Delta P}$ associated with a higher Re_{dp}.

The blow-averaged pumping power as a function of Re_{dp} is shown in Fig. 5.13. As expected, for a given Re_{dp}, the highest values of $\overline{\dot{W}}_{\mathrm{pump}}$ are related to the smaller particle diameters. Comparing the different regenerator housings for a constant sphere diameter, the following considerations can be made:

1. For Casings #1, #2 and #3, if the mass flow rate is the same, then Re_{dp} is also the same, but the utilization is different. This means that $\overline{\dot{W}}_{\mathrm{pump}}$ only changes with $\overline{\Delta P}$. In this situation, Casing #3 presented the highest $\overline{\dot{W}}_{\mathrm{pump}}$ because of its longer regenerator length;

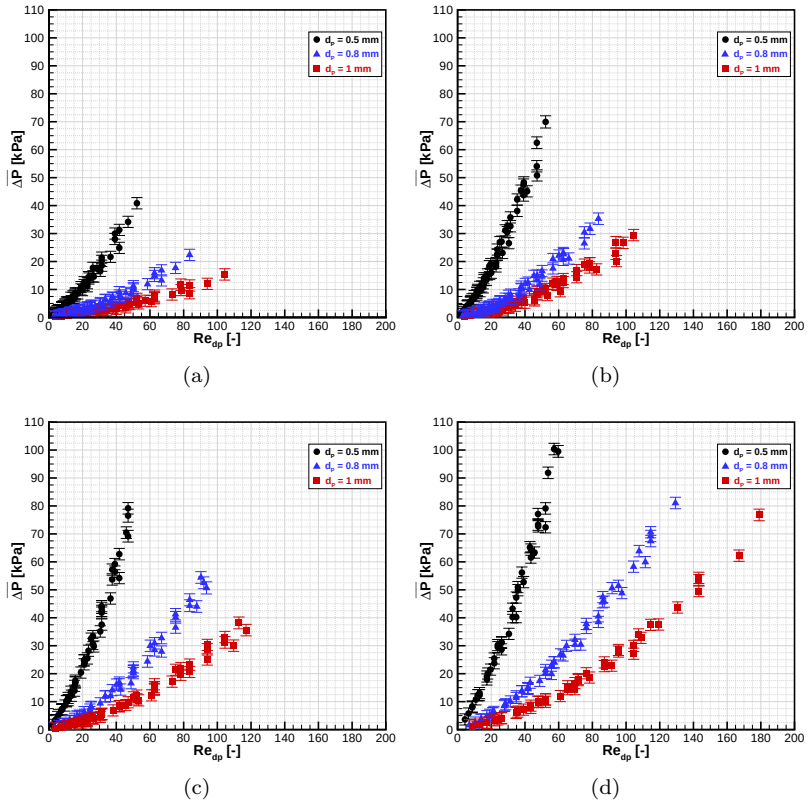

Figure 5.12 – $\overline{\Delta P}$ for packed bed regenerators as a function of Re_{dp} for sphere sizes of 0.5, 0.8 and 1 mm: (a) Casing #1; (b) Casing #2; (c) Casing #3; (d) Casing #4.

2. Comparing Casings #3 and #4: (i) for a fixed Re_{dp}, Casing #3 has a higher $\overline{\dot{W}}_{\mathrm{pump}}$ because of the higher mass flow rate. For example, for a particle diameter of 0.5 mm and $Re_{\mathrm{dp}} = 40$, both casings have a $\overline{\Delta P}$ of about 50 kPa. However, since Casing #3 operates with a higher mass flow rate, it has a higher $\overline{\dot{W}}_{\mathrm{pump}}$; (ii) for identical operating, i.e., displaced volume and operating frequency, Casing #4 has a clearly higher $\overline{\dot{W}}_{\mathrm{pump}}$ due to the higher $\overline{\Delta P}$ and Re_{dp}.

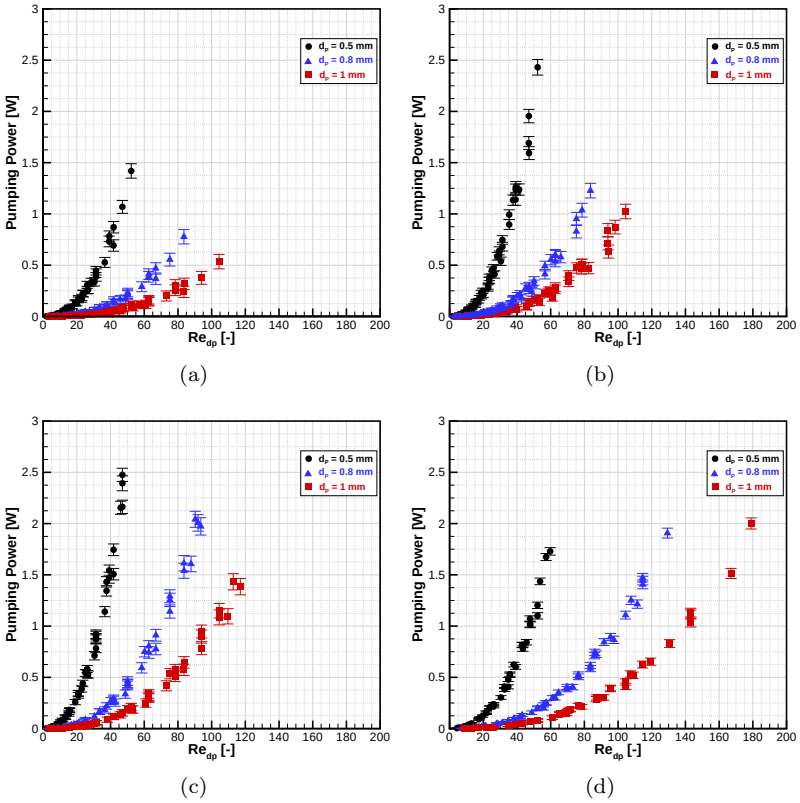

Figure 5.13 – $\overline{\dot{W}}_{\text{pump}}$ for packed bed regenerators as a function of Re_{dp} for spheres sizes of 0.5, 0.8 and 1 mm: (a) Casing #1; (b) Casing #2; (c) Casing #3; (d) Casing #4.

5.3.3.2 Effectiveness: Effect of the Sphere Diameter

Figs. 5.14 to 5.17 present the experimental thermal effectiveness as a function of NTU for different values of sphere sizes and utilization, for Casings #1 to #4, respectively. The uncertainty bars for the effectiveness are not plotted to allow a better visualization of the results. However, the uncertainties for ϵ are between 1.5% and 2.5%.

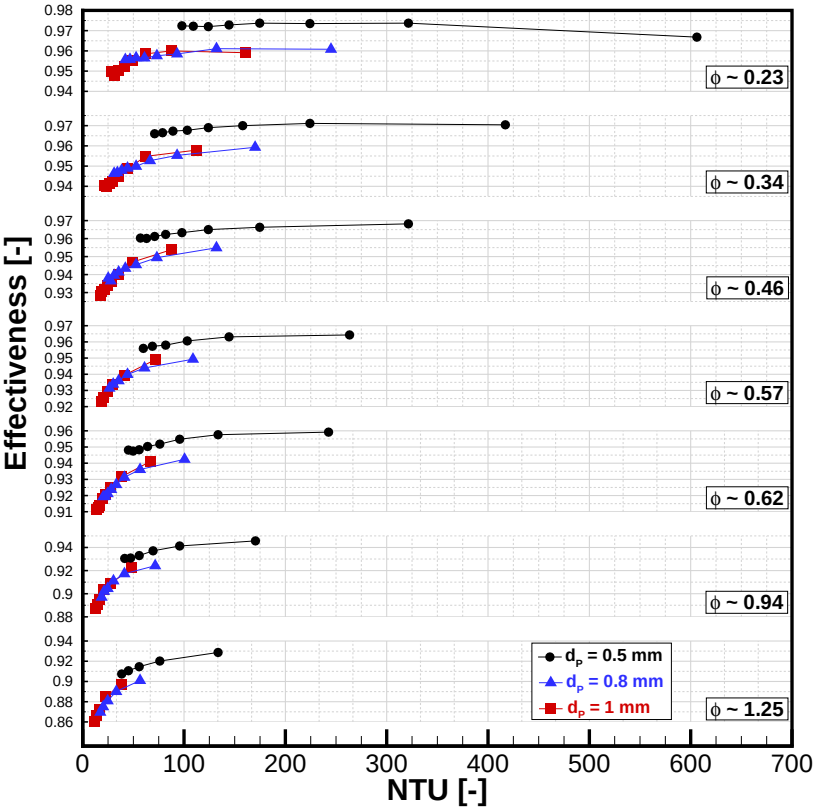

Figure 5.14 – Casing #1: ϵ as a function of NTU for different values of sphere size and utilization.

Regarding the experimental NTU ranges, the following remarks can be made:

1. For a fixed utilization, considering different sphere sizes, the NTU range is longest for the smallest sphere diameter because of the largest interstitial heat transfer area;

2. For a fixed particle size and a fixed utilization, the NTU decreases with the increasing mass flow rate. The higher values of NTU are for the lower operating frequencies, which for a constant utilization means a lower mass flow rate. In other words, increasing the operating frequency decreases the NTU;

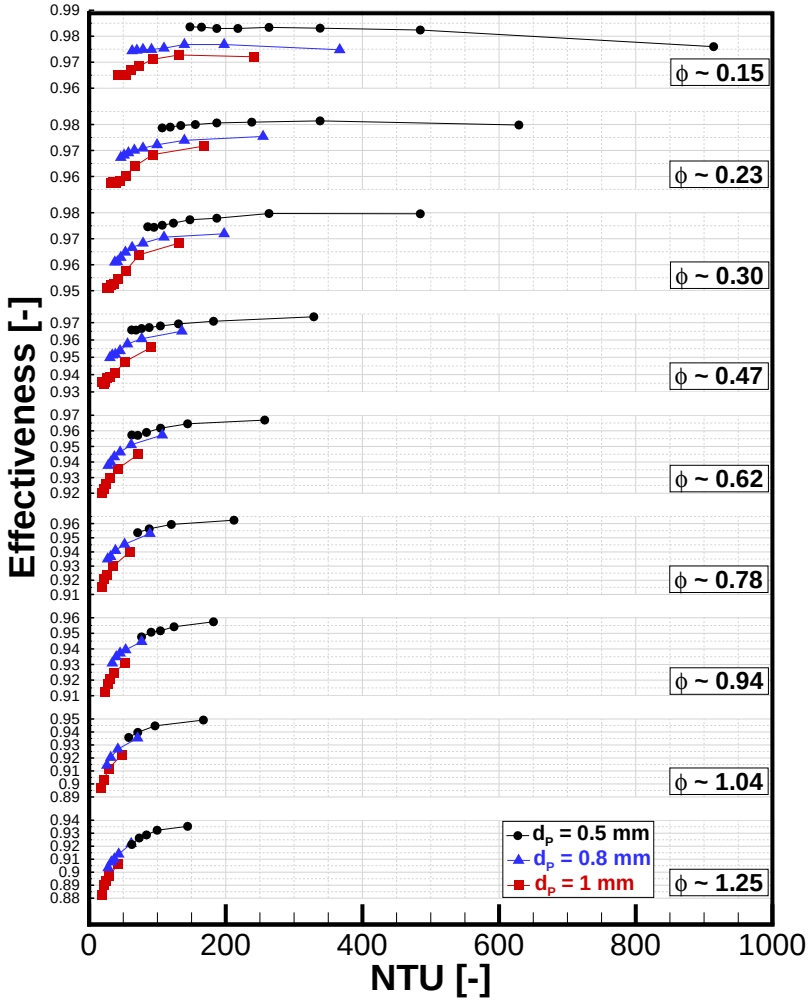

Figure 5.15 – Casing #2: ϵ as a function of NTU for different values of sphere size and utilization.

3. For a constant particle size and different utilizations, the NTU decreases when ϕ increases due to the increasing mass flow rate;

4. Casing #3 has the highest NTU due to its capacity to house a large mass of regenerative material. On the other hand, Casing #4 has the smallest NTU.

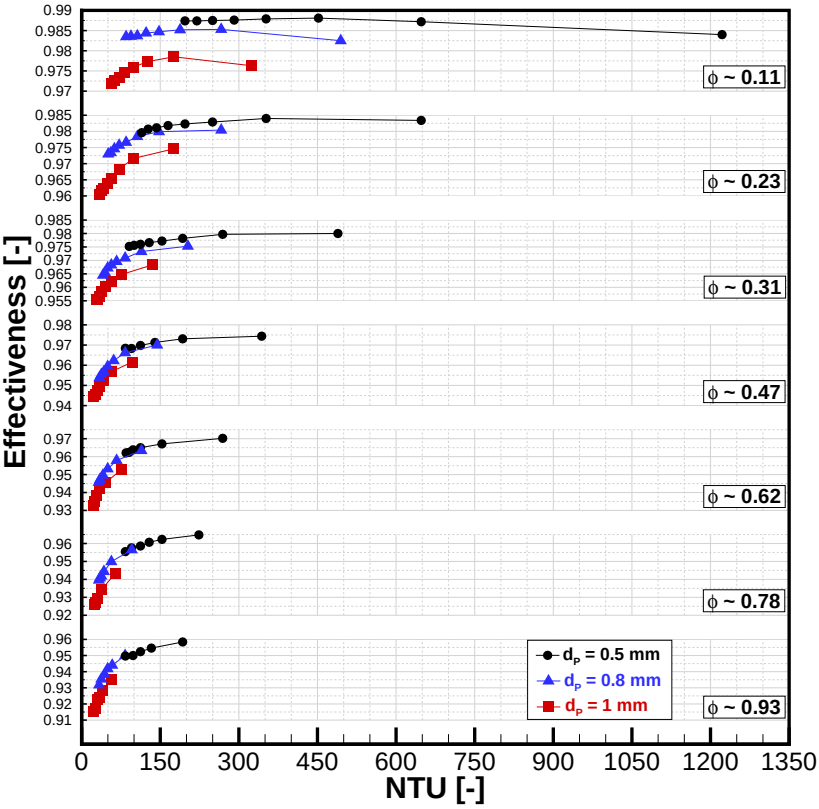

Figure 5.16 – Casing #3: ϵ as a function of NTU for different values of sphere size and utilization.

As far as the thermal effectiveness results are concerned, the following comments can be made:

1. For a fixed utilization and different sphere sizes, the effectiveness improves for the smaller particle diameters, which is associated with the larger heat transfer surface area and NTU. Thus, 0.5-mm sphere matrices presented the highest ϵ-NTU combinations, with the effectiveness approaching 98% to 99%;

2. For a fixed particle size and different utilizations, the effectiveness range decreases with increasing utilization due to a reduction of the NTU;

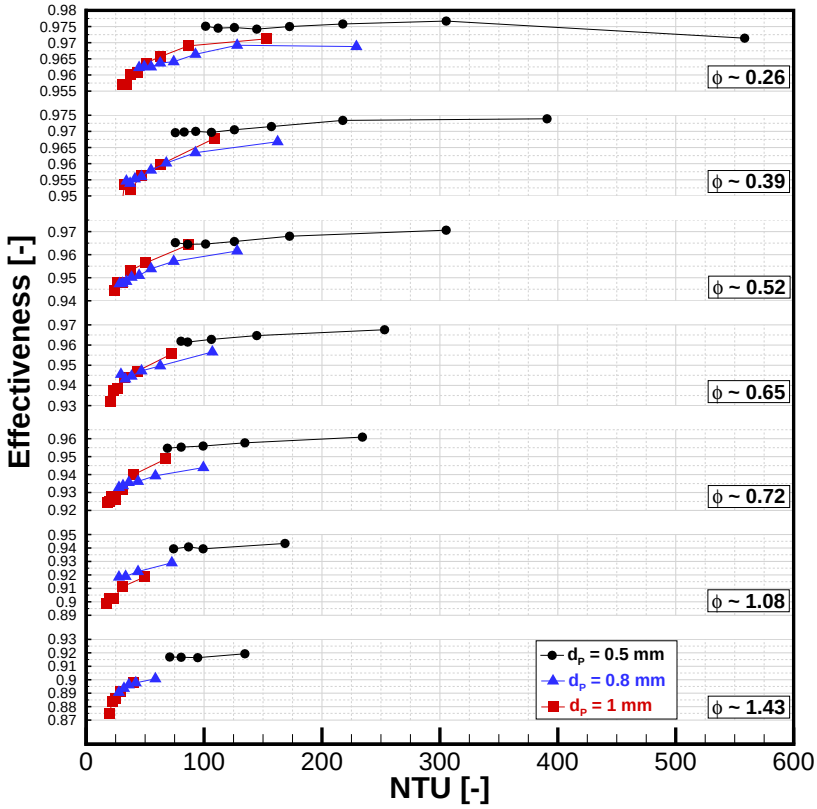

Figure 5.17 – Casing #4: ϵ as a function of NTU for different values of sphere size and utilization.

3. For a fixed particle size and a fixed utilization, in general, the effectiveness increases with increasing NTU;

4. For small utilizations the effectiveness may not increase with the NTU due to the influence of axial heat conduction. In these cases, the low mass flow rate - resulting from a small pumped volumes and low frequencies - gives rise to low superficial velocities that result in small interstitial heat transfer coefficients. Thus, the interphase convection and axial conduction heat fluxes are comparable in magnitude, reducing the effectiveness associated with the regenerator and even increasing the NTU. This is more visible for the smallest sphere diameter, 0.5 mm, for which

the effectiveness is approximately constant or decreases as NTU increases. For the 1-mm spheres, the effectiveness first increases with the NTU, but later decreases, as the axial heat conduction becomes more important. In addition, the effect of axial heat conduction is more noticeable as the casing length becomes shorter, like in Casing #1.

5. The differentiation between the effectivenesses related to the three sphere sizes becomes more evident at low utilizations and larger values of NTU. As the NTU decreases, the results for the three sphere sizes tend to converge into a single ϵ-NTU curve, but the 0.5-mm spheres always have higher ϵ-NTU values when compared with the other particle diameters.

In an evaluation specifically for the smallest pumped volume (2.53 cm^3), which corresponded to the smallest utilization for each casing, the following effectiveness ranges were found:

- Casing#1: $\phi \approx 0.23 - 94.5\% < \epsilon < 97.5\%$;
- Casing#2: $\phi \approx 0.15 - 96.5\% < \epsilon < 98.5\%$;
- Casing#3: $\phi \approx 0.11 - 97\% < \epsilon < 98.5\%$;
- Casing#4: $\phi \approx 0.26 - 95.5\% < \epsilon < 97.5\%$;

For Casings #1, #2 and #3, the superficial velocity and Re_{dp} are the same for a given particle diameter. In this case, the differences in effectiveness are related to the different utilization values for the three matrices. Also, the shorter matrices are more susceptible to axial heat conduction losses. Nevertheless, the effectiveness values are of the same order, but the shorter matrices have lower viscous losses. Comparing Casings #1 and #4, the ϵ-NTU and the utilization ranges are approximately the same. However, in Casing #4 the axial heat conduction is less important, but the viscous losses are higher than in Casing #1.

5.3.3.3 Effectiveness: Effect of Regenerator Housing Dimensions

Figs. 5.18 to 5.20 show the effectiveness as a function of NTU for the different regenerator housings considering nearly constant utilizations, for the sphere diameters of 0.5, 0.8 and 1 mm, respectively. In this case, to fix the utilization, different fluid volumes were pumped considering the different regenerator sizes. For example, for $\phi \approx 0.23$, in Casings #1 and #4, the displaced volume was 2.53 cm^3, while for Casings #2 and #3 it was 3.80 cm^3 and 5.07 cm^3, respectively. Hence, for the smaller regenerators, in terms of the total matrix mass, always a smaller amount of fluid was displaced to achieve about the same utilization.

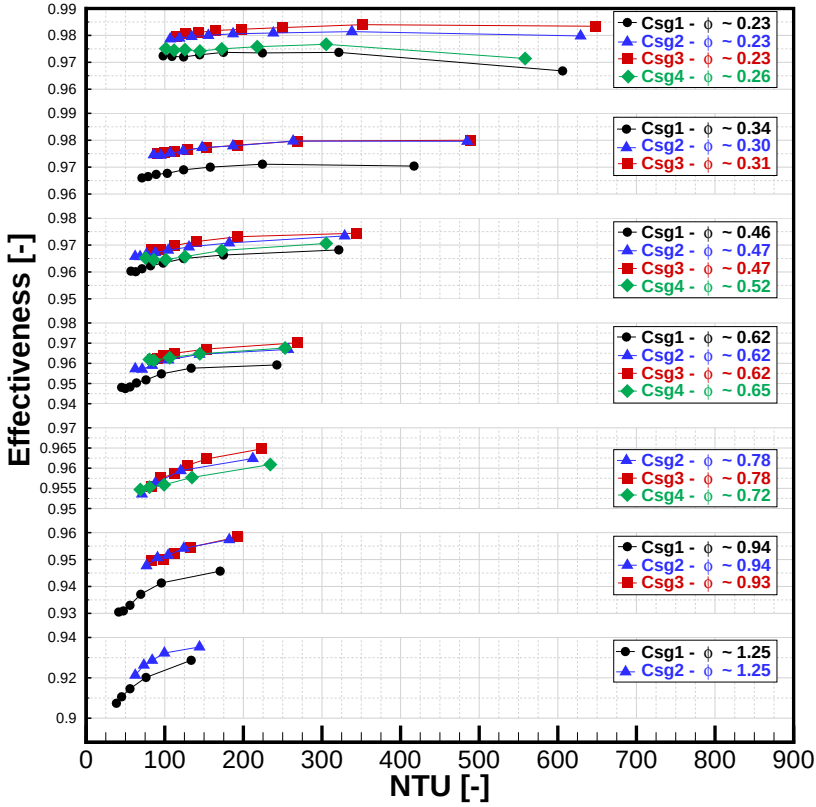

Figure 5.18 – $d_p = 0.5$ mm: ϵ as a function of NTU for different regenerator casings.

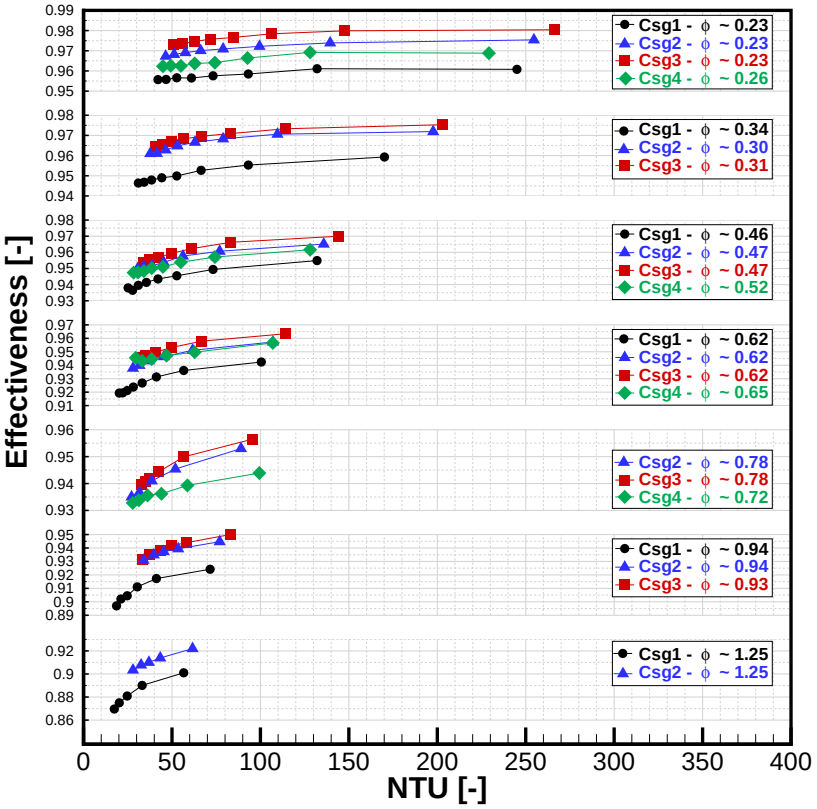

Figure 5.19 – $d_p = 0.8$ mm: ϵ as a function of NTU for different regenerator casings.

In an ideal regenerator, for a fixed utilization and independently of the housing size, the results would lead to the same ϵ-NTU curve. However, when losses are taken into account, a more in-depth evaluation is required to understand the differences between the regenerators:

1. Casing #1 always presented the smallest effectiveness values because of: (i) the axial conduction losses, that become more pronounced for the smaller particle diameters and utilizations; (ii) its smaller NTU given that this casing has the smallest total heat transfer area;

2. Casing#2, #3 and #4, presented very similar results. Only for the smallest utilization, Casing #4 indicated some significant axial conduction losses associated for the smaller spheres sizes (0.5 and 0.8 mm).

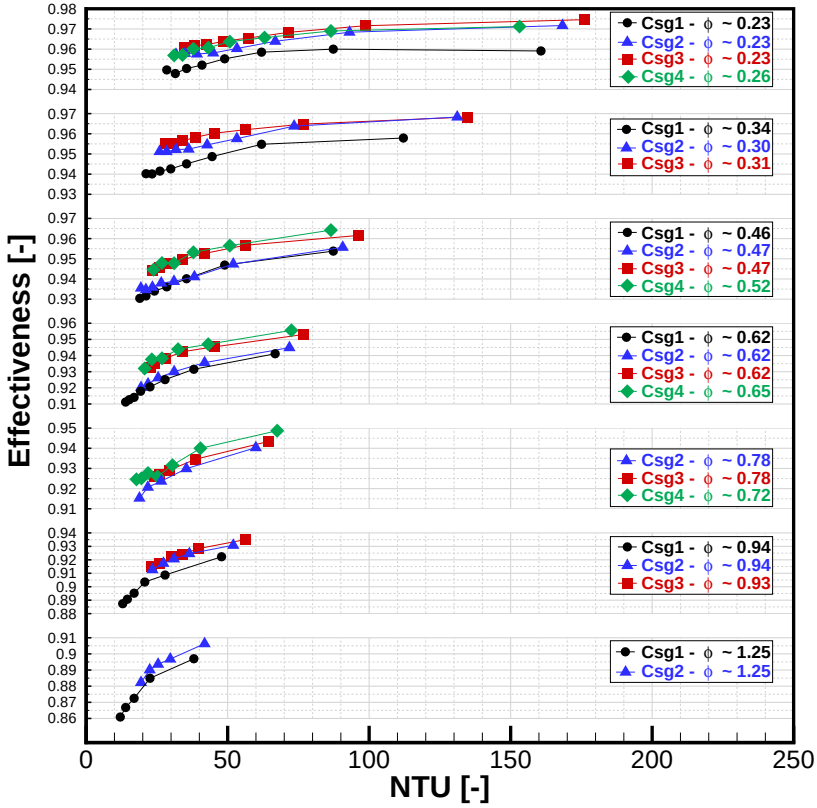

Figure 5.20 – $d_p = 1$ mm: ϵ as a function of NTU for different regenerator casings.

5.3.3.4 General Conclusions About the Packed Bed Regenerators

The results presented in this section for: (i) identical regenerator housing and different spheres sizes and (ii) identical sphere size and different housing dimensions, lead to the following conclusions:

1. All matrices presented exhibited high values of effectiveness, which is a typical feature of oscillating flow packed bed regenerators (SCHMIDT; WILLMOTT, 1981; ACKERMANN, 1997). The smallest values were found for Casing #1 with a sphere diameter of 1 mm and $\phi \approx 1.25$;

2. Smaller particle diameters are associated with the highest ϵ-NTU values, but are more susceptible to axial heat conduction losses at small utilizations, and higher viscous losses at high flow rates;

3. The smallest aspect ratio regenerator housing, Casing #1, for a fixed utilization, was the least effective matrix, but presented the lowest viscous losses;

4. Casing #4, the highest aspect ratio matrix, was directly compared with Casings #2 and #3. However, no significant effectiveness improvement was verified. Additionally, Casing #4 was the worst casing in terms of viscous losses;

5. Casings #2 and #3 were the most thermally effective matrices, showing a very good agreement with each other at the highest values of ϵ-NTU for a fixed utilization. However, Casing #2 presented lower viscous losses than Casing #3 because of its shorter length.

In conclusion, with regard to the thermal effectiveness, axial conduction and viscous losses, high aspect ratio regenerators do not seem to be the best configuration. On the other hand, too short regenerators may increase the axial conduction losses and are associated with the smallest NTU ranges. Moreover, there seems to be an optimal relationship between d_{p}, $D_{\mathrm{h,reg}}$ and L_{Reg} for a given operating condition dictated by the mass flow rate and frequency, that guarantees a high effectiveness with minimal axial heat conduction and viscous losses, as will be discussed later.

5.3.4 Pins, Plates and Spheres: A Regenerative Matrix Comparison

Fig. 5.21 shows the pressure drop and pumping power associated with the different passive matrix geometries presented in Table 3.8. As discussed previously, the different matrices were designed to have approximately the same particle diameter and porosity so that the porous medium hydraulic diameter and the heat transfer area are approximately the same for all geometries. The following remarks can be made about the results shown in Fig. 5.21:

1. At low Reynolds number, in the viscous (Darcian) regime, the differences in pressure drop or pumping power among the three geometries are minimal;

2. As expected, the plates present a linear pressure drop as a function of the Reynolds number, characteristic of the Darcian flow regime;

3. The packed bed of spheres shows the highest viscous losses, especially at higher velocities, where the microscopic inertial forces become more significant;

4. The pressure drop of the pin array also presents a quadratic dependence on the Reynolds number, however, it is clear that the microscopic inertial force is weaker when compared with the packed bed of spheres;

5. For the pumping power, at the same Re_{dp}, the parallel plate regenerator has the lowest viscous losses, while the bed of spheres shows the worst pumping power performance among the three geometries.

Fig. 5.22 shows the behavior of ϵ as a function of NTU and utilization for the three matrix geometries. Based on these results, the following conclusions can be drawn:

1. Since the total heat transfer area is approximately the same for all geometries, for a given mass flow rate, the NTU depends only on the interstitial convective heat transfer coefficient;

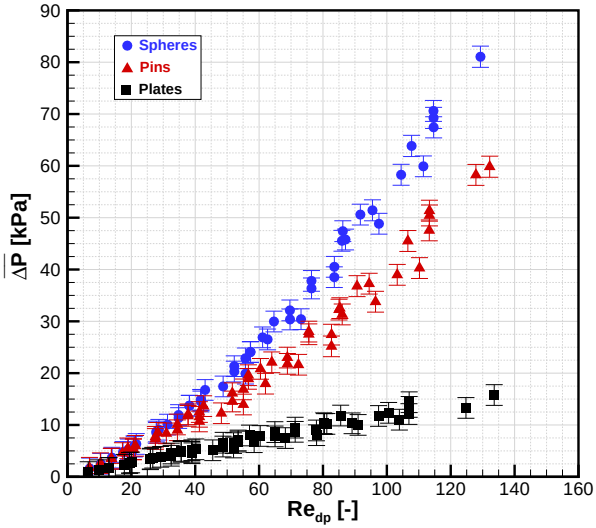

(a)

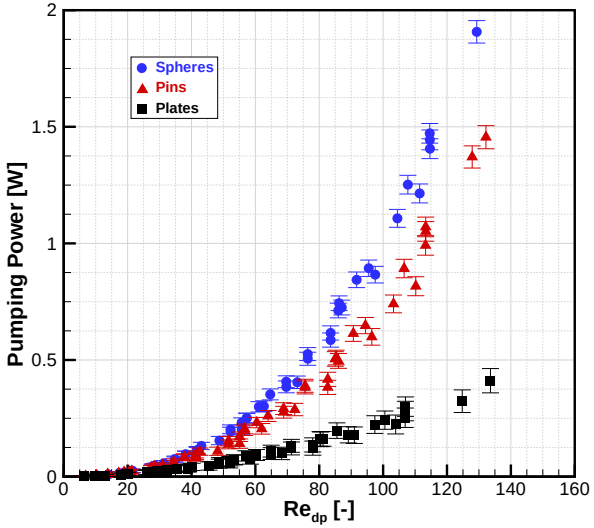

(b)

Figure 5.21 – Viscous losses of the different matrix geometries: (a) $\overline{\Delta P}$ as a function of Re_{dp}; (b) $\overline{\dot{W}}_{\mathrm{pump}}$ as a function of Re_{dp}.

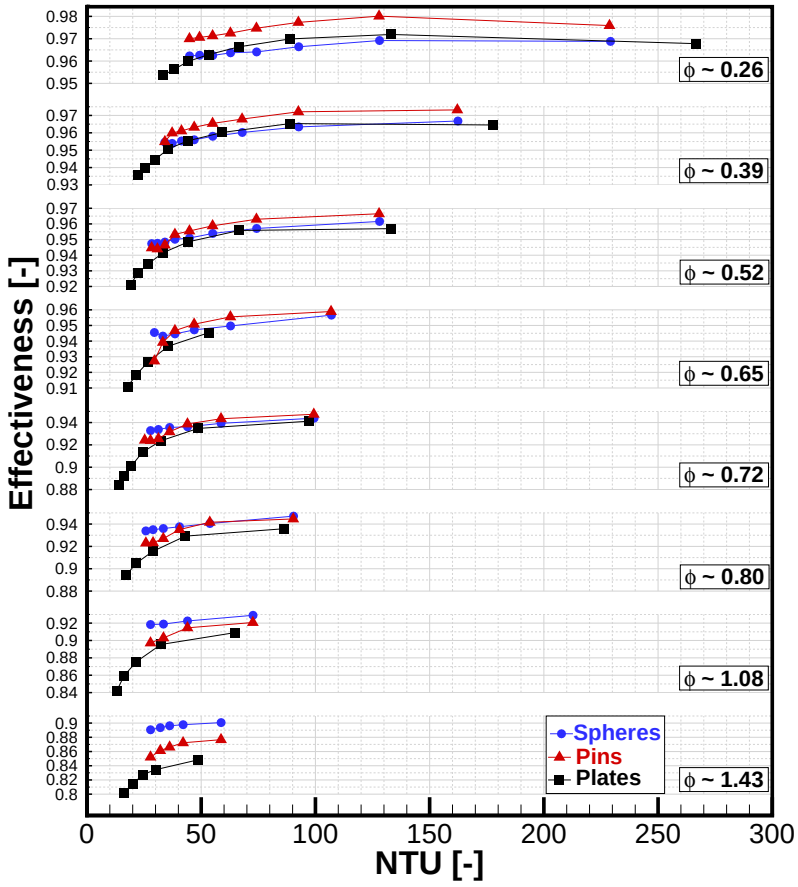

Figure 5.22 – ϵ as a function of NTU and utilization for different regenerator geometries.

2. At the smallest values of utilization: (i) the parallel plate geometry encompasses a broader range of NTU because its convective heat transfer coefficient is constant (disregarding the entrance effects) and, at some operating conditions, is higher than the convective coefficient of the remaining geometries; (ii) the pin array matrix exhibited a slightly higher effectiveness, which can be associated with the smaller axial heat conduction losses characteristic of this matrix. It is worth pointing out that there is no point of contact between adjacent pins, which reduces the importance of

heat conduction in the matrix;

3. For intermediate values of utilization, the thermal performance of all matrices is very similar, especially for $NTU > 25$, which corresponds to the smallest mass flow rates or superficial velocities. Considering the same operating conditions, the values of NTU for the parallel plate geometry cover wider ranges for each utilization, but these ranges decrease faster than in the other geometries, due to the approximately constant convection heat transfer coefficient;

4. At the highest values of utilization, the thermal performance of the packed bed of spheres is better than that of the other geometries. The parallel plates showed the worst performance at these operating conditions. This may be associated with the high interstitial heat transfer coefficients for pins and spheres, and to the fluid mixing due induced by the tortuosity of the packed bed.

With regard to the thermal-hydraulic behavior of the different matrix geometries, it can be concluded that, at the smallest flow rates, where the viscous losses are similar for all matrices, the pin array showed the best performance since it is less affected by axial heat conduction. On the other hand, all geometries presented, in general, equivalent thermal performances (ϵ-NTU), with the parallel plates being characterized by the smallest viscous losses. For the highest values of utilization, the packed spheres showed the best thermal performance, but at the expense of the highest values of pressure drop and pumping power.

5.4 Numerical Results

5.4.1 Packed Bed Regenerator

Fig. 5.23 presents comparisons between experimental data and numerical results for $\overline{\Delta P}$ as a function of Re_{dp} for different sphere sizes and regenerator housings.

The numerical results predicted the experimental data very well, with deviations of the order of the experimental uncertainties ($\pm$ 2.5 kPa). The sensitivity of the experimental results with respect to the particle

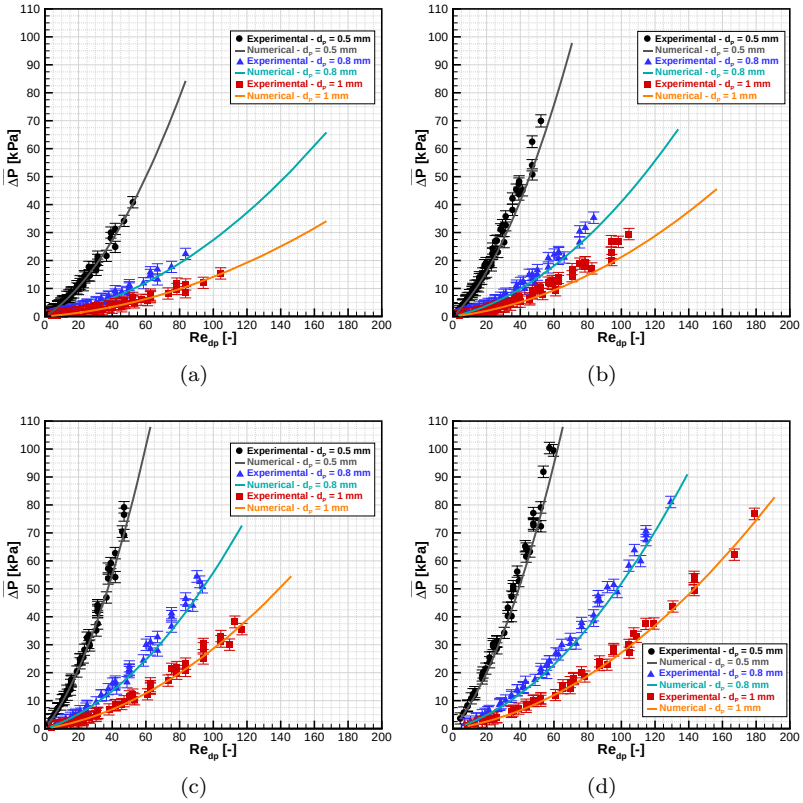

Figure 5.23 – Comparison between the numerical results and the experimental data: $\overline{\Delta P}$ as a function of Re_{dp} for packed beds with spheres of different sizes: (a) Casing #1; (b) Casing #2; (c) Casing #3; (d) Casing #4.

size and regenerator dimensions, i.e., length and diameter, was reproduced satisfactorily by the model, which leads to the conclusion that the closure relationships for the permeability and constant proposed by (ERGUN, 1952) are valid for the present experimental conditions.

Other important conclusions can be drawn regarding the friction factor. If the permeability and Ergun constant are valid for the regenerative matrix, the friction factor should depend only on Re_{dp}, independently of the particle diameter, housing dimensions or operating condition.

Fig. 5.24 contains all results for $\overline{\Delta P}$ shown in Fig. 5.23, in the non-dimensional form of the friction factor as a function of Re_{dp}.

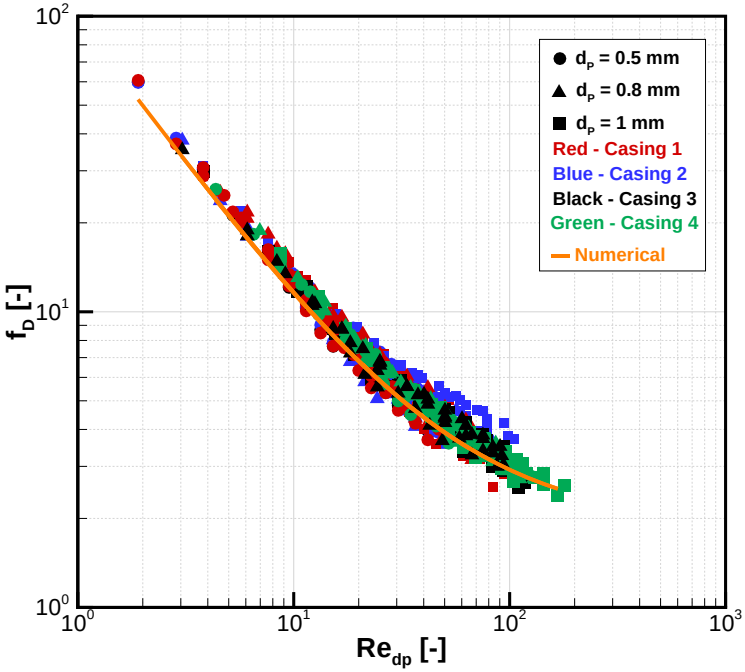

Figure 5.24 – Comparison between the numerical results and the experimental data: f_{D} as a function of Re_{dp} for packed beds of spheres.

The f_{D} as a function of Re_{dp} experimental data exhibited the expected trend: (i) all the results collapsed into a single curve; (ii) as explained before, at low Re_{dp}, where Darcy's law is valid, a linear trend is observed; (iii) as Re_{dp} increases, the f_{D} trend deviates from the linear behavior. The numerical prediction is in a good agreement with the experimental results.

Figs. 5.25 to 5.33 compare the numerical results and experimental data for ϵ as a function of NTU for different values of utilization, spheres sizes, and regenerator housing dimensions. The numerical results are presented for two situations: (i) considering the existence of the void volume - solid blue lines; (ii) disregarding the void volume - dotted black lines. The caption of each figure describes the conditions of the comparison between the numerical model and the experimental data.

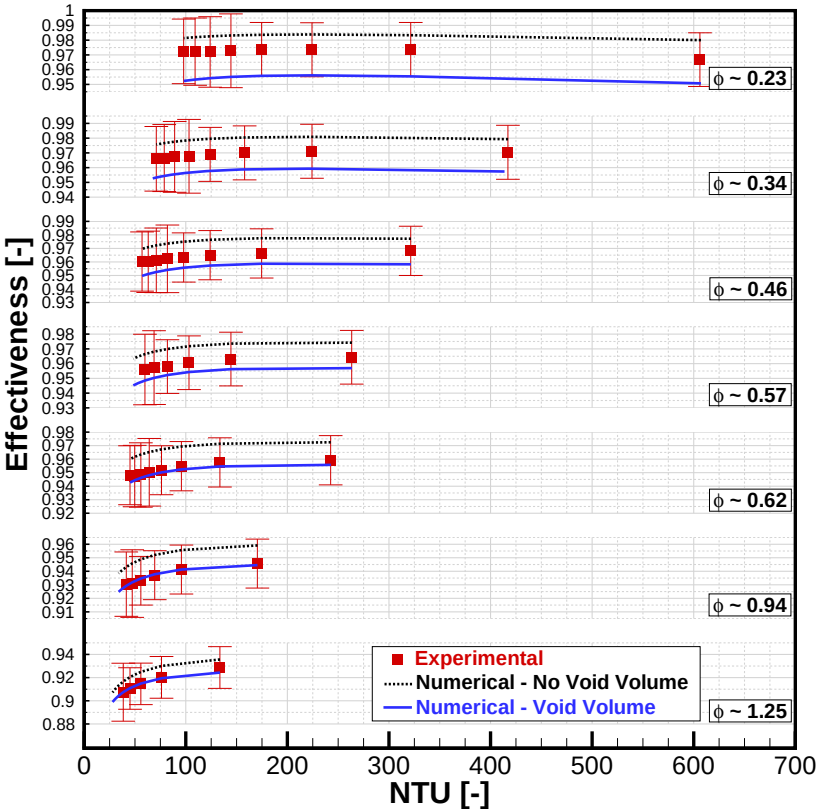

Figure 5.25 – Comparison between the numerical results and the experimental data: ϵ as a function of NTU for Casing #1 and $d_{\mathrm{p}} = 0.5$ mm.

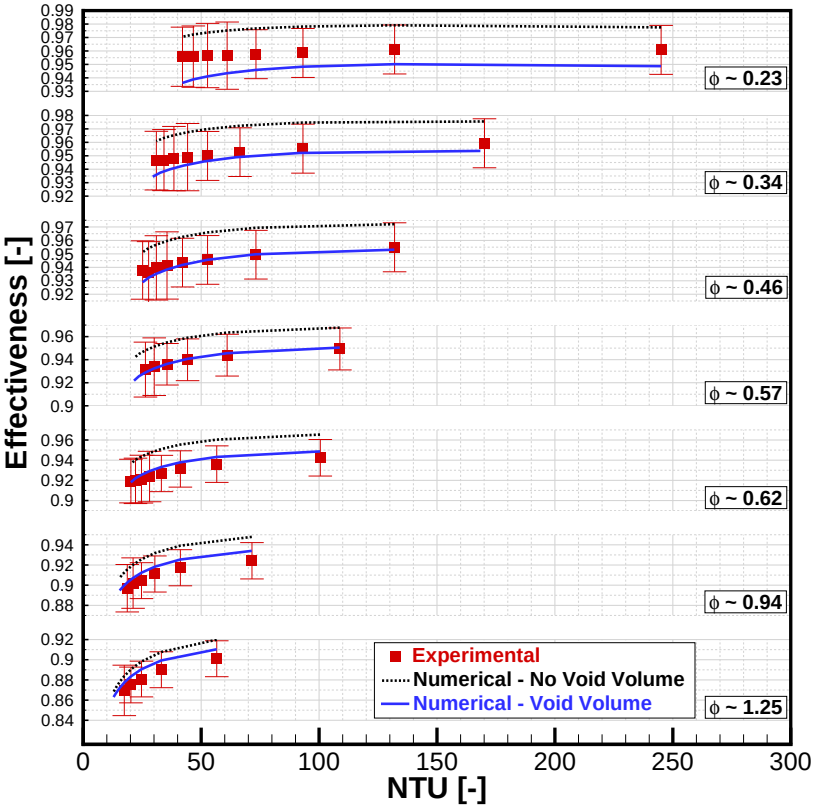

Figure 5.26 – Comparison between the numerical results and the experimental data: ϵ as a function of NTU for Casing #1 and $d_p = 0.8$ mm.

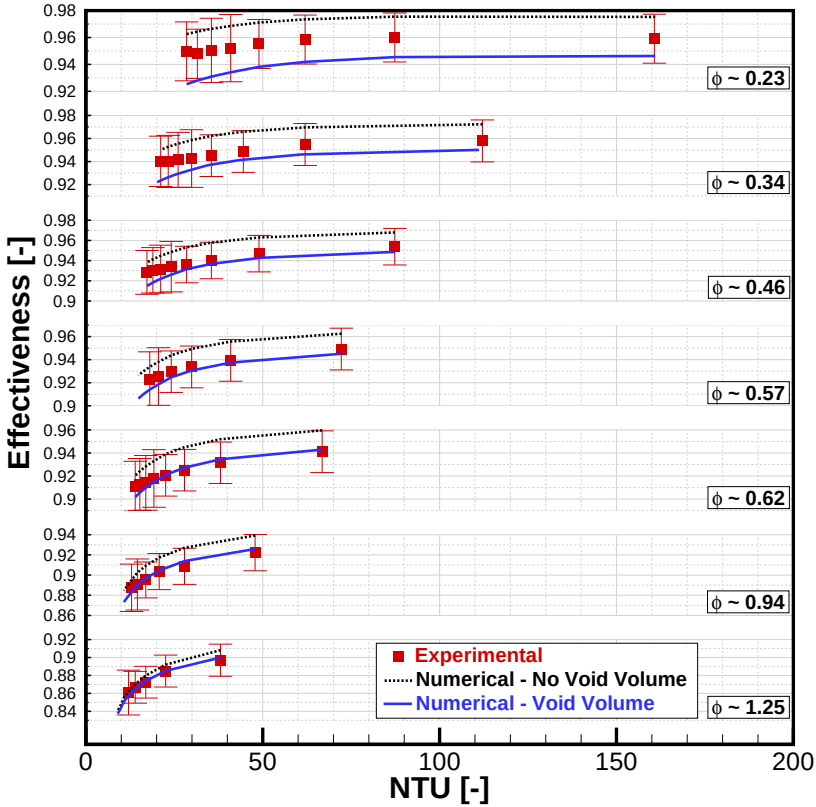

Figure 5.27 – Comparison between the numerical results and the experimental data: ϵ as a function of NTU for Casing #1 and $d_{\mathrm{p}} = 1$ mm.

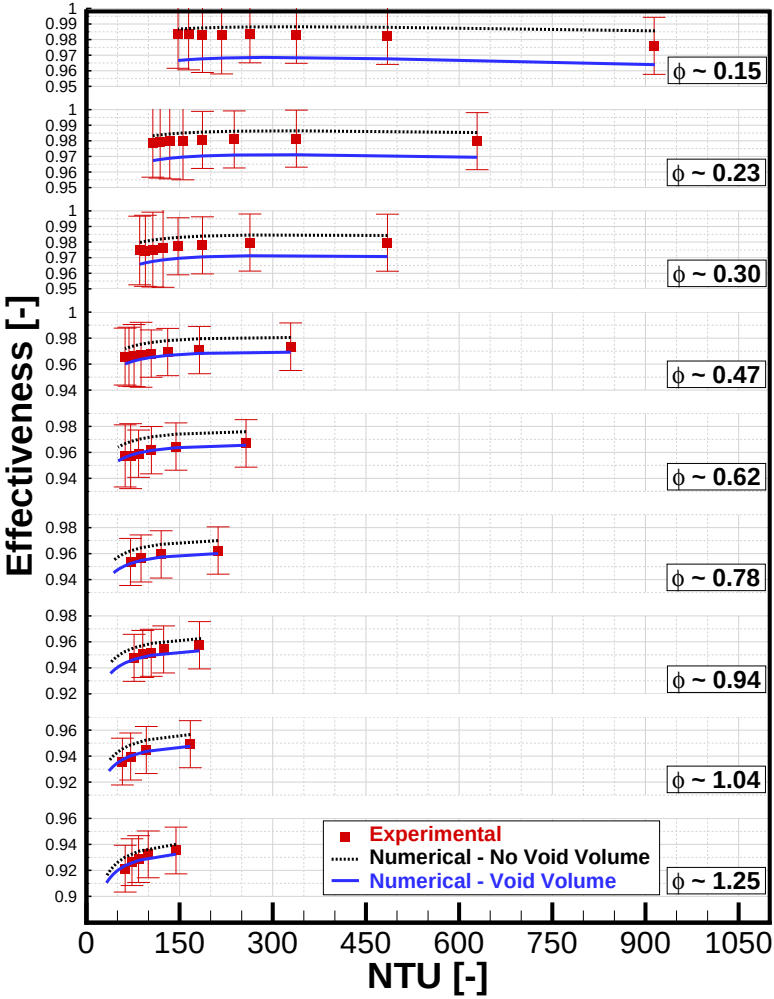

Figure 5.28 – Comparison between the numerical results and the experimental data: ϵ as a function of NTU for Casing #2 and $d_{\mathrm{p}} = 0.5$ mm.

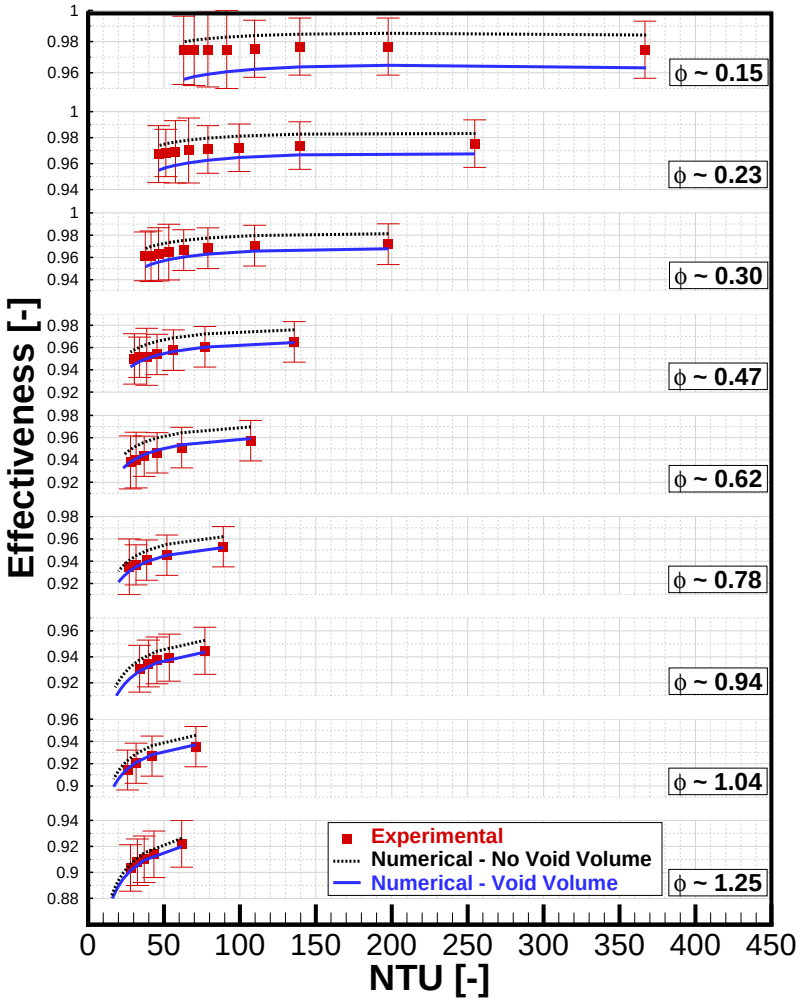

Figure 5.29 – Comparison between the numerical results and the experimental data: ϵ as a function of NTU for Casing #2 and $d_p = 0.8$ mm.

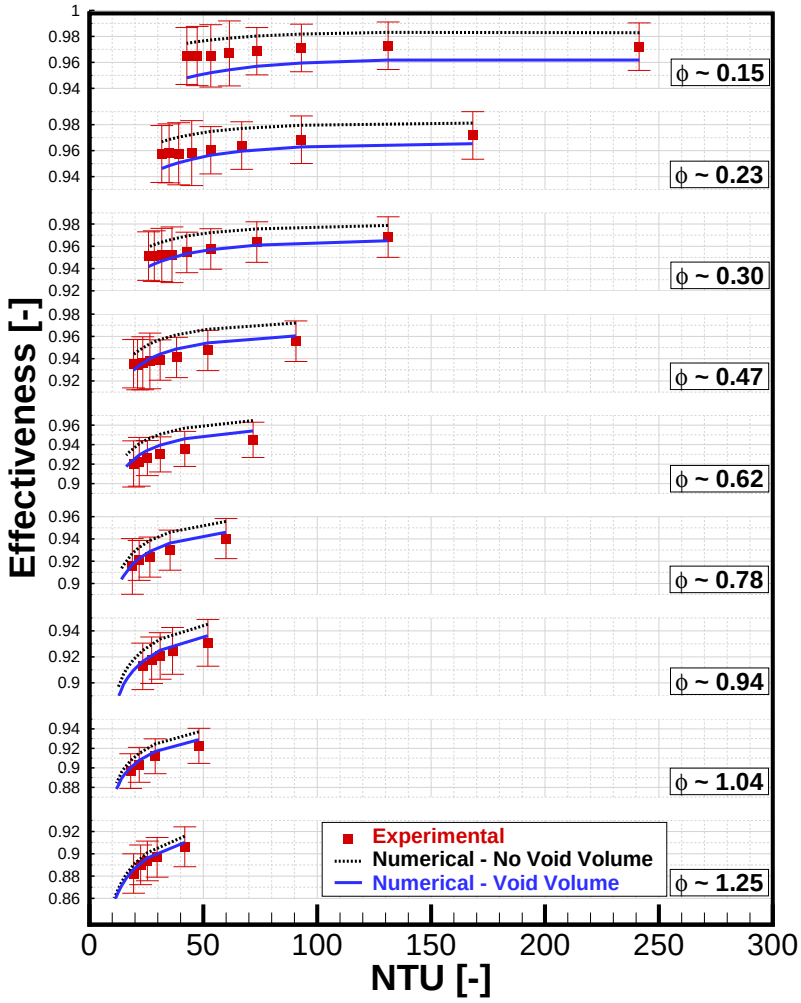

Figure 5.30 – Comparison between the numerical results and the experimental data: ϵ as a function of NTU for Casing #2 and $d_{\mathrm{p}} = 1$ mm.

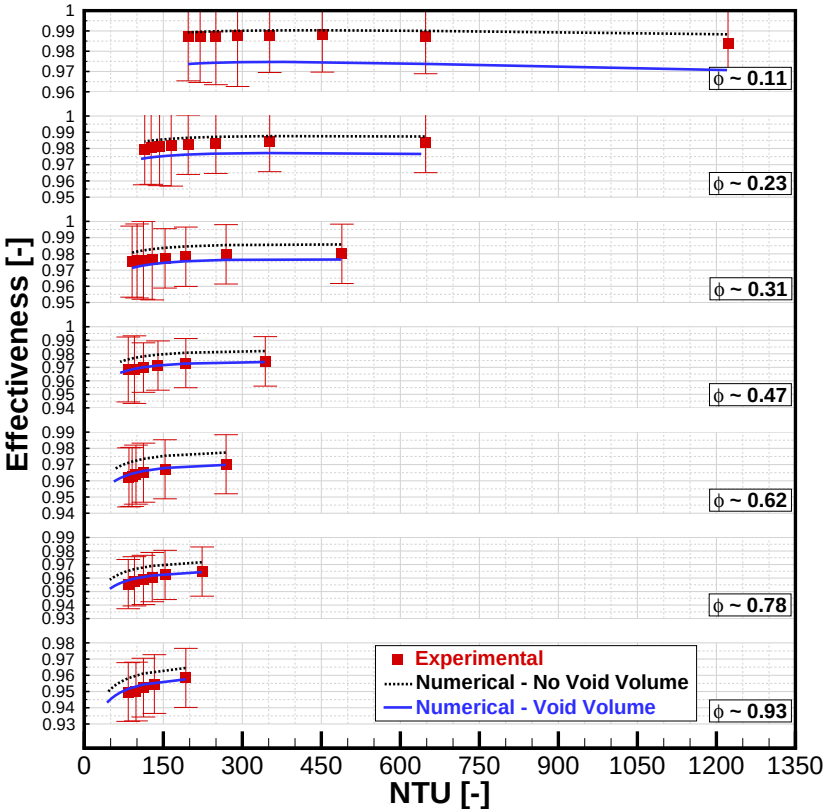

Figure 5.31 – Comparison between the numerical results and the experimental data: ϵ as a function of NTU for Casing #3 and $d_{\mathrm{p}} = 0.5$ mm.

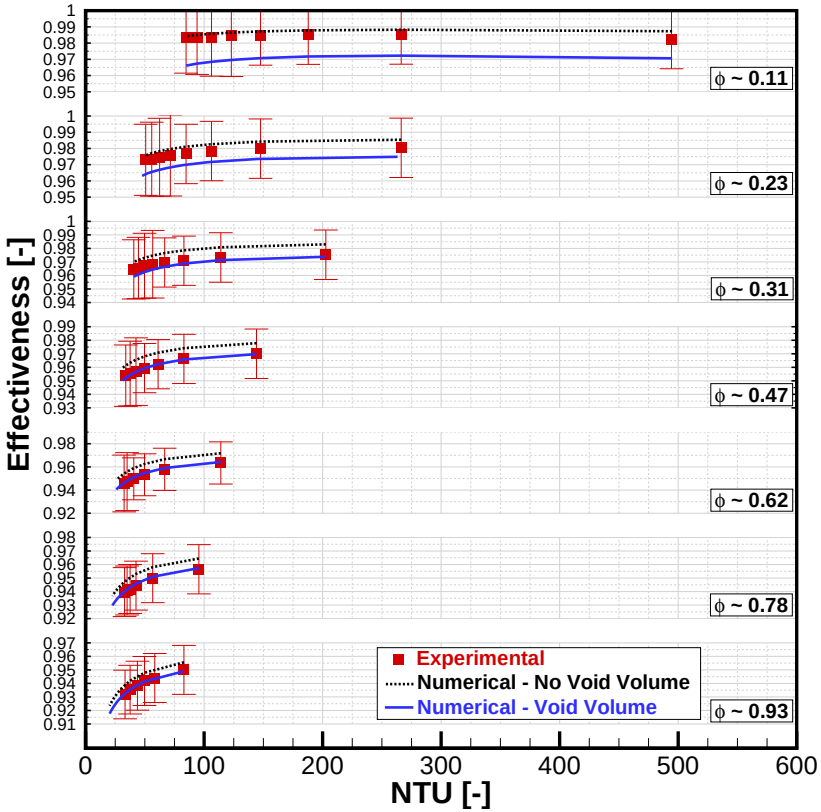

Figure 5.32 – Comparison between the numerical results and the experimental data: ϵ as a function of NTU for Casing #3 and $d_p = 0.8$ mm.

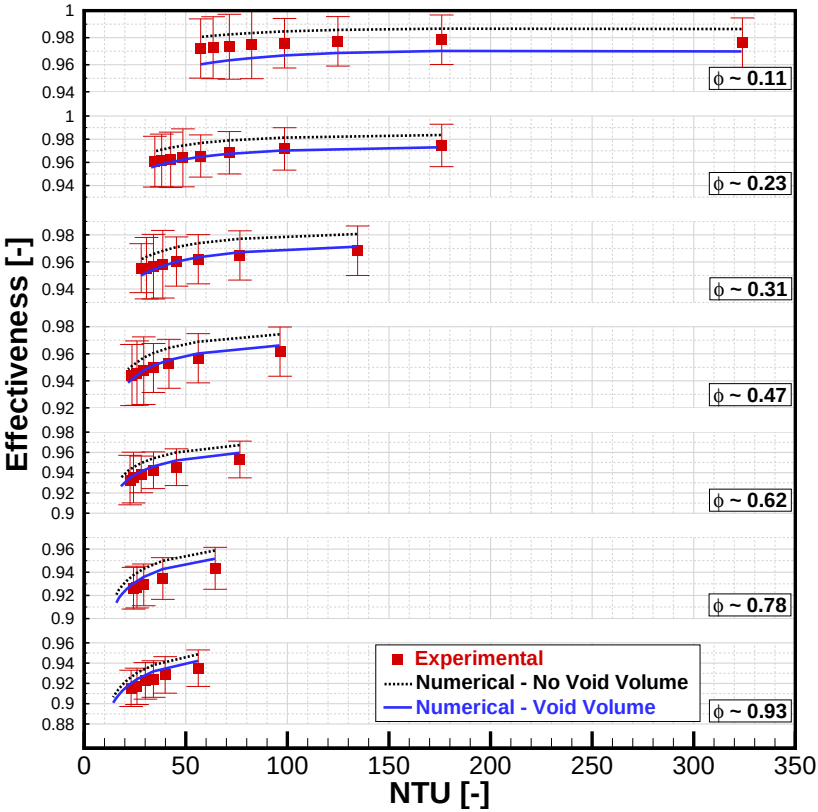

Figure 5.33 – Comparison between the numerical results and the experimental data: ϵ as a function of NTU for Casing #3 and $d_{\mathrm{p}} = 1$ mm.

Firstly, the discussion will be based on the results for Casings #1, #2 and #3. Casing #4 followed basically the same general trends of the other casings. However, its results, particularly for $d_p = 0.8$ mm, will be discussed later, in the context of a direct comparison with the parallel plate and pin array geometries.

The simulations that did not take the void volume model into account always overestimated the experimental results. On the other hand, the simulations that considered this type of leakage loss were in much better agreement with the experimental data. In particular, the following comments can be made: (i) for all cases, the experimental and numerical ϵ-NTU results presented the same trend; (ii) The model was able to reproduce the sensitivity of the experimental data with respect to the sphere size and housing dimensions; (iii) the differences between the simulations with and without the void volumes are greater at small values of utilization (small pumped volumes). This was somewhat expected, since a considerable fraction of the pumped volume becomes trapped in the void space. As the displaced volume is increased, this fraction is reduced and the penalties associated with the void volume become less important.

For a more specific evaluation, Fig. 5.34 shows comparisons between the experimental and numerical time-dependent temperature results with ($\vartheta \neq 0$) and without ($\vartheta = 0$) the void volumes evaluated at the cold and hot ends. The results are for Casing #3, $d_p = 0.8$ mm, $\phi \approx 0.467$ and different operating frequencies.

When no void volume is considered, the model predicts that the returning fluid stream will be at the reservoir temperature followed by an abrupt variation of the temperature signal. In the case of the hot end, if $t^* > \pi$ the inlet stream is at 320 K. This is different from the actual experimental temperature measurement shown in Fig. 5.34. On the other hand, when the void volume is considered, the returning fluid stream is firstly at the temperature of the fluid trapped in the void space and, only later, at the reservoir temperature. The fluid trapped in the hot-side void volume is at a temperature lower than that of the hot reservoir because it does not interact thermally with the reservoir. Thus, the time-dependent temperature signal from the model including the void volumes deviates from the zero void volume results, and a larger amplitude of the temperature signal is observed, which results in a lower thermal effectiveness. This behavior of the mathematical model agrees well with the experimental measurements and confirms

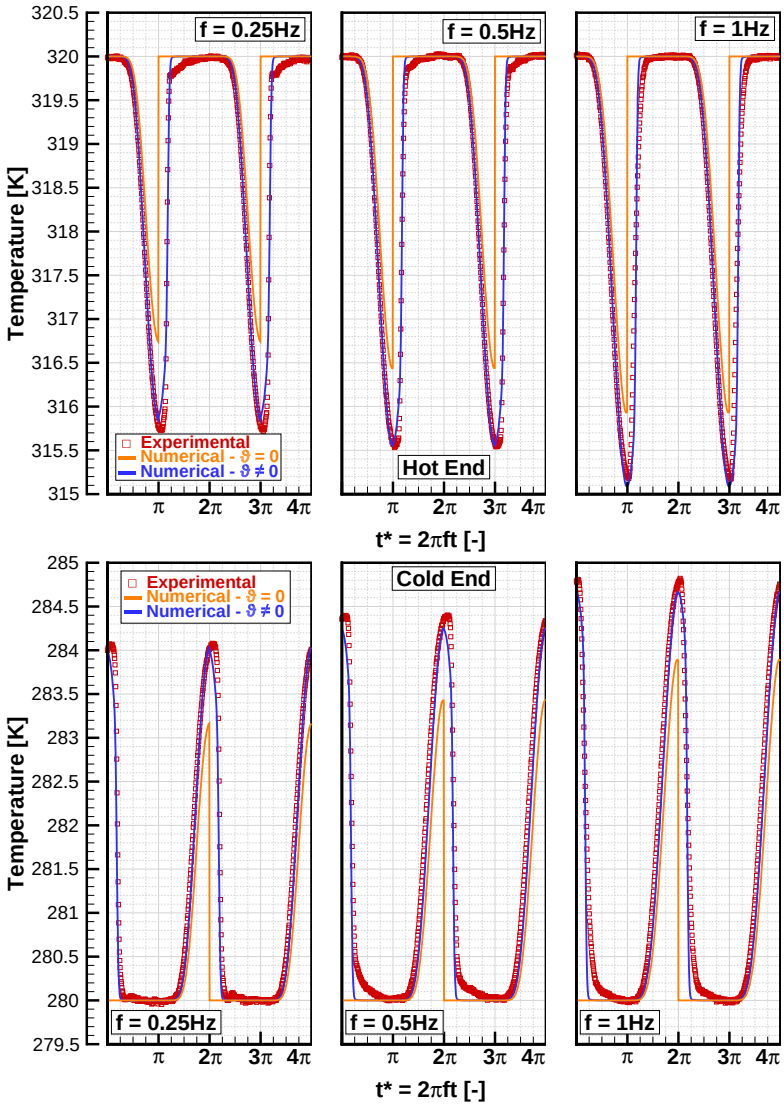

Figure 5.34 – Comparison of the experimental and numerical time-dependent temperatures with ($\vartheta \neq 0$) and without ($\vartheta = 0$) the void volumes for Casing #3, $d_p = 0.8$ mm, $\phi \approx 0.467$ and different operating frequencies; at the hot end (top) and at the cold end (bottom).

the suitability of the numerical modeling of the void volume, for describing with good precision the actual behavior of the time-dependent temperature and the thermal effectiveness in real regenerators.

Fig. 5.35 presents comparisons between the experimental and numerical (with void volume) time-dependent temperatures at the hot end as a function of the utilization. As can be seen, the model does a good job at predicting the experimental data for the high values of utilization. However, the model under-predicts the temperatures for the lowest utilizations (0.11 and 0.23). It is believed that this underestimation of the experimental results can be caused by the no flow period associated with the small pumped volumes. As seen in Fig. 5.6(c), the no flow period was significant for the flow conditions.

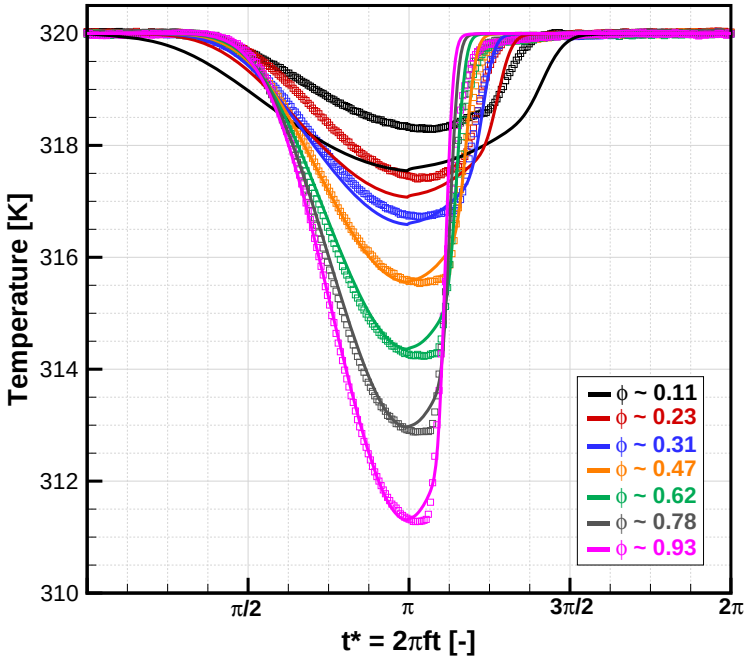

Figure 5.35 – Prediction of the time-dependent experimental temperature by the numerical model (continuous lines) considering the void volume for Casing #3, $d_p = 0.8$ mm, $f = 0.5$ Hz and different values of utilization.

As seen in this section, the numerical model with the void volume was capable of reproducing the thermal effectiveness for intermediate and

high values of utilization with deviations of the order of 1%. For low utilizations, the deviations were as large as 2%, but still below the experimental uncertainty range.

Figs. 5.36 to 5.40 show the axial temperature profiles (as a function of the dimensionless length, z^*) after the cold blow (solid symbols) and after hot blow (open symbols), for different regenerator housing dimensions and spheres sizes. In each figure, different utilizations are presented considering a single value of frequency (fixed at 0.5 Hz). The different conditions related to each figure are presented in their captions. In general, the model captures the sensitivity of the temperature profiles with respect to the experimental parameters for all cases, just with some local deviations. At low utilizations, the temperature profiles follow almost linear trends, while for higher values of utilization, a significant penetration of the constant temperature of the reservoirs into the matrix is observed. In this case, it is important to highlight that the model captures with a good precision the constant temperature penetration region, including the position of the thermal front.

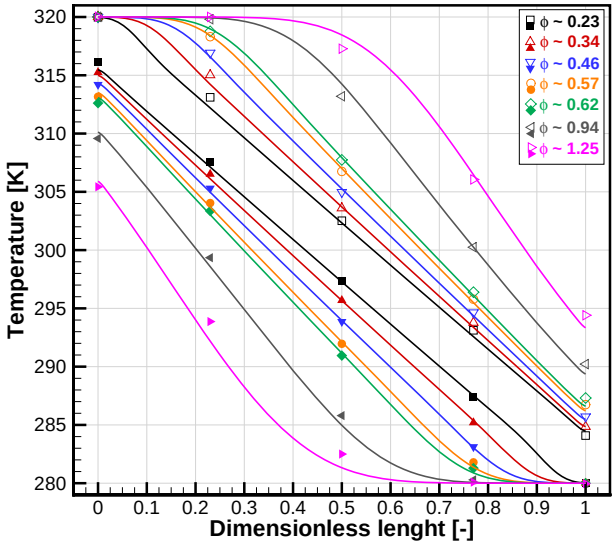

Figure 5.36 – Experimental and numerical temperature profiles for Casing #1, $f = 0.5$ Hz and $d_p = 0.8$ mm.

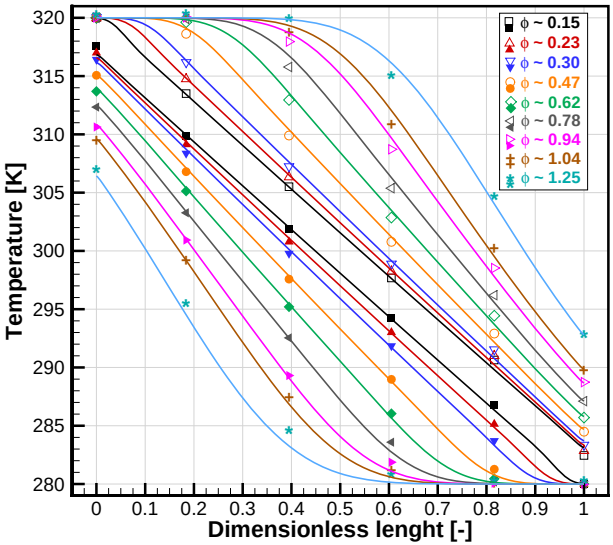

Figure 5.37 – Experimental and numerical temperature profiles for Casing #2, $f = 0.5$ Hz and $d_p = 0.8$ mm.

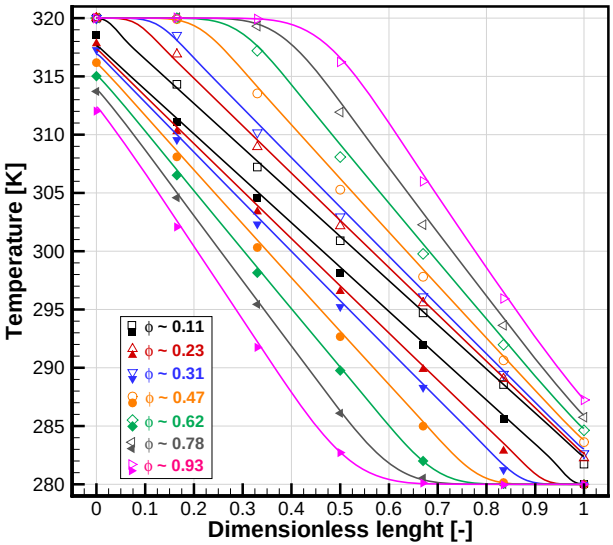

Figure 5.38 – Experimental and numerical temperature profiles for Casing #3, $f = 0.5$ Hz and $d_p = 0.5$ mm.

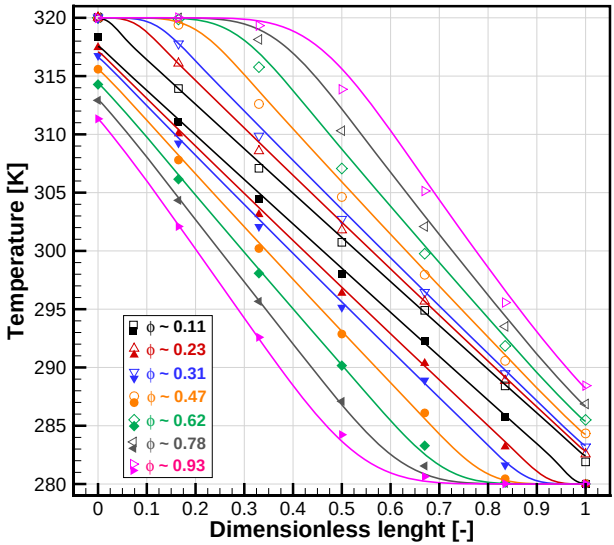

Figure 5.39 – Experimental and numerical temperature profiles for Casing #3, $f = 0.5$ Hz and $d_p = 0.8$ mm.

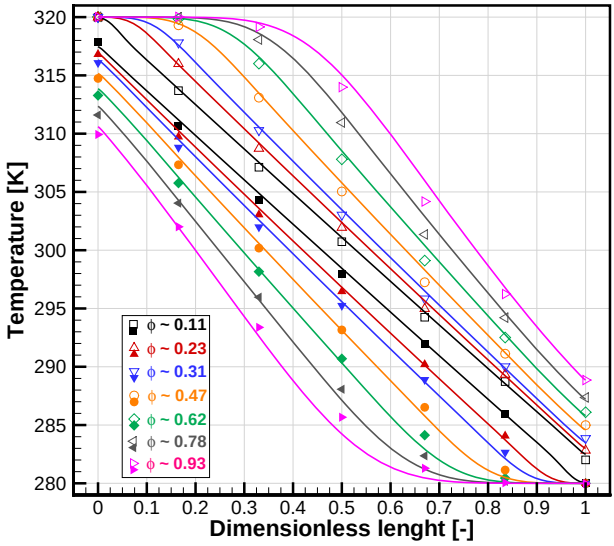

Figure 5.40 – Experimental and numerical temperature profiles for Casing #3, $f = 0.5$ Hz and $d_p = 1$ mm.

5.4.2 Pin, Plate and Sphere Matrices

Fig. 5.41 presents a comparison between the experimental and numerical results for $\overline{\Delta P}$ as a function of Re_{dp}. Fig. 5.42 shows the results for f_{D} as a function of Re_{dp} for the three different regenerator geometries: 0.8-mm spheres, parallel plates and pin arrays.

The numerical results show a generally good agreement with the experimental data. Regarding the spheres and pin array matrices, the model captured the very similar behavior of these two geometries: (i) at low Re_{dp}, Darcy regime, the $\overline{\Delta P}$ and f_{D} for the pins are both sightly higher than those for the bed of spheres, which can be due to the lower permeability of the pins porous medium. (ii) at high Re_{dp}, the microscopic inertial force of the pin array is weaker compared with that of the bed of spheres. This way, the suitability of the closure relationships for the permeability and Ergun constant for parallel plates and pin arrays is also verified.

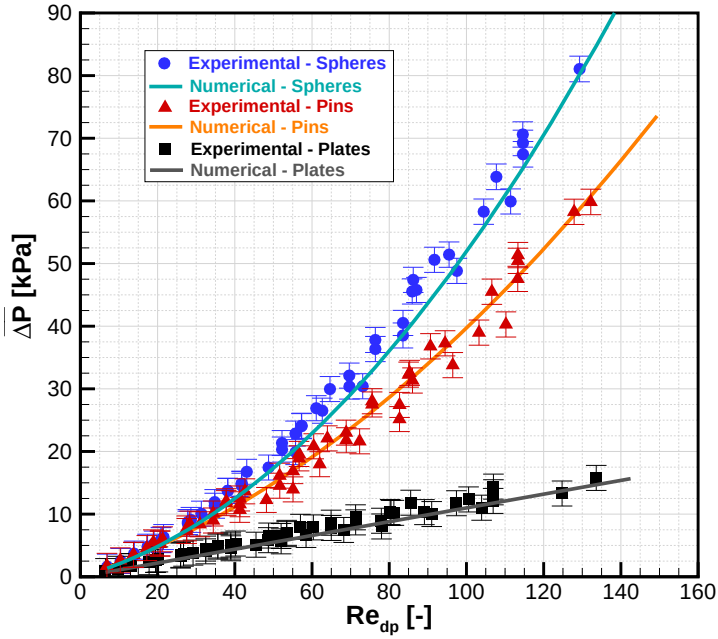

Figure 5.41 – Comparison between the numerical results and the experimental data: $\overline{\Delta P}$ as a function of Re_{dp} for different matrix geometries.

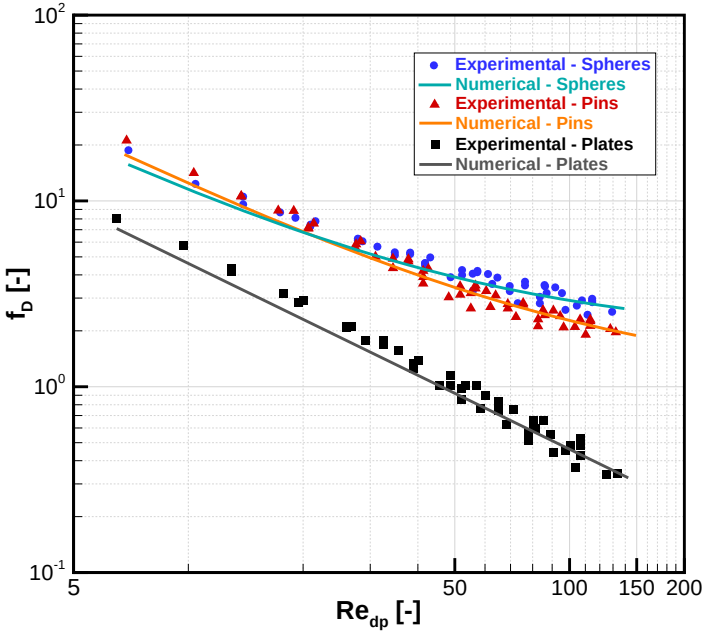

Figure 5.42 – Comparison between the numerical results and the experimental data: f_D as a function of Re_{dp} to different matrix geometries.

Figs. 5.43 to 5.45 show comparisons between the numerical model and the experimental data for ϵ as a function of NTU and utilization for the three basic geometries (0.8-mm spheres, plates and pins).

As expected, the numerical results for the packed spheres presented a good agreement with the experimental data. The model also represented fairly well the effectiveness results for the parallel plate and pin matrices. The following general comments can be made: (i) for low utilizations the numerical results underestimated the experimental data, which can be associated with the no flow period, but the general trend of the ϵ-NTU relationship is picked up by the model; (ii) as the utilization increases, the model describes well the experimental values and the ϵ-NTU curve trend. On the other hand, for the largest values of the utilization, the model for plates and pins overestimates the experimental data. In summary, the majority of modeling results agreed fairly well with the experimental data, with deviations of the order of 2 to 3% for the lowest and highest utilization values.

The good agreement between the experimental data and numerical results leads to the following conclusions: (i) the parallel plates and pin arrays were successfully assembled based on the procedure presented in Appendix B, and flow maldistribution, common in parallel plate geometries, was not verified; (ii) the model may have some limitations at high mass flow rates and high utilizations; (iii) but the closure relations used for parallel plates and pin arrays seemed to have been satisfactorily selected.

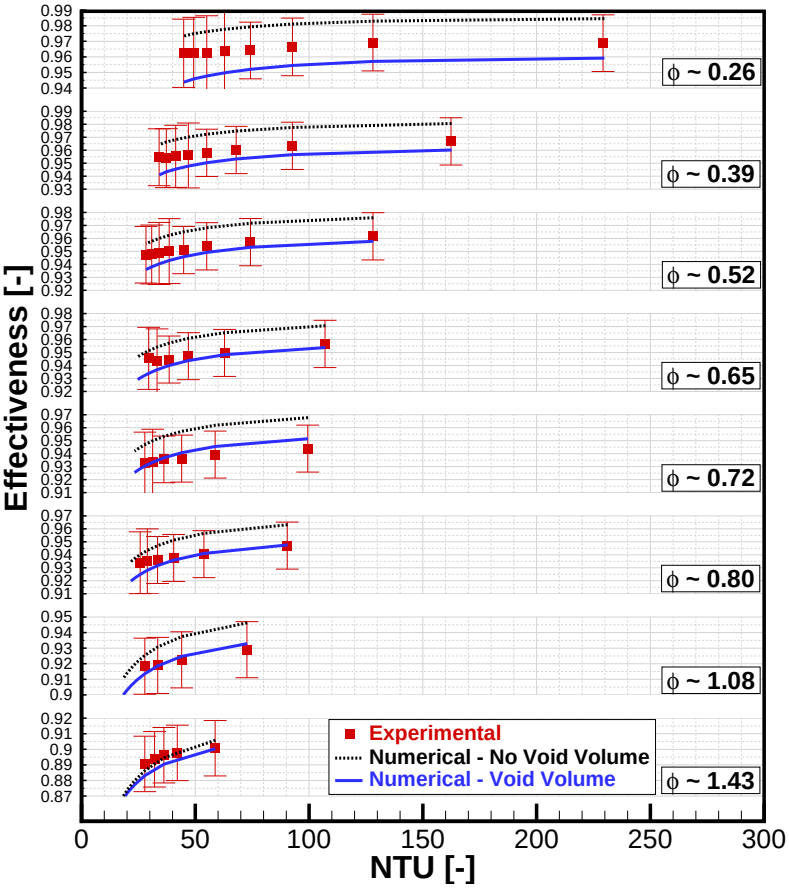

Figure 5.43 – Comparison between the numerical results and the experimental data: ϵ as a function of NTU for the packed bed regenerator - Casing #4 and $d_p = 0.8$ mm.

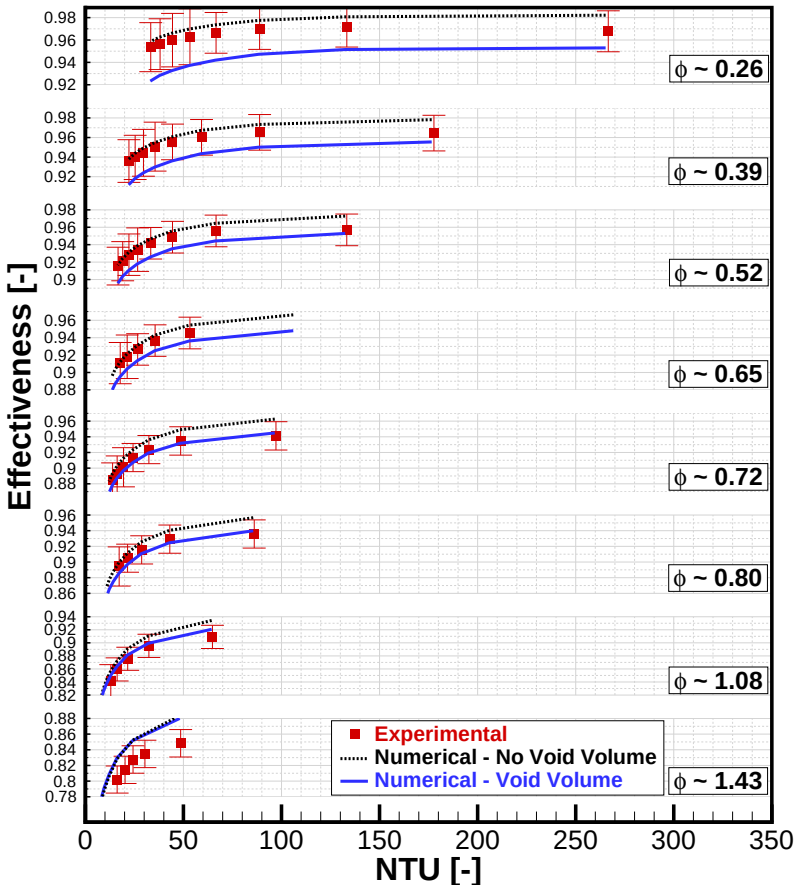

Figure 5.44 – Comparison between the numerical results and the experimental data: ϵ as a function of NTU for the parallel plate regenerator.

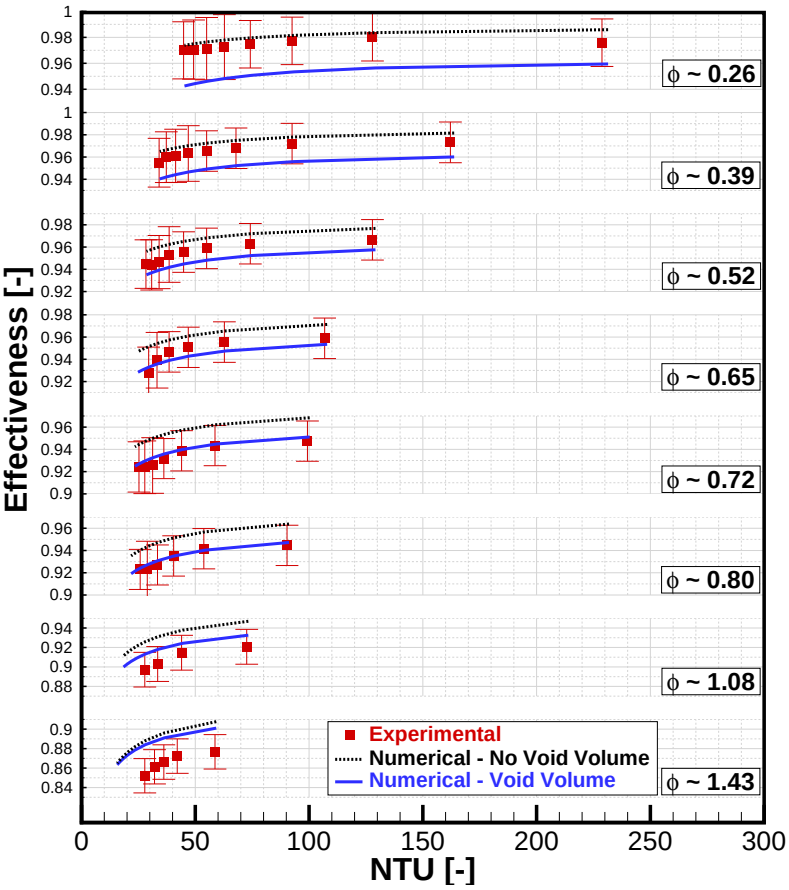

Figure 5.45 – Comparison between the numerical results and the experimental data: ϵ as a function of NTU for the pin array regenerator.

5.5 Void Volume and Inlet Flow Maldistribution

The presence of a void volume imposes changes on the boundary conditions for the thermal balance in the regenerator matrix that are responsible for decreasing the heat transfer effectiveness. Hence, it becomes intuitive that the regenerator performance improves as the void volume becomes smaller and, in a limiting situation, a regenerator without void volumes will have the best performance. Fig. 5.46 shows the numerical results for ϵ as a function of NTU for Casing #1 with 1-mm spheres and different void volumes fractions, as presented in Tab. 3.6. The numerical results somehow reproduced the expected behavior: (i) by decreasing the void volume size the effectiveness has improved, approaching the results for the zero void volume regenerator; (ii) by increasing the utilization, the void volume impact is reduced because the fraction of the total pumped volume trapped in the void space becomes smaller.

In order to characterize experimentally the results shown in Fig. 5.46, experimental tests were performed using the same porous matrix, but changing the R-T adapter to decrease the void volume size, as presented in Fig. 3.18 and Table 3.6. 1-mm spheres were used in the tests carried out using Casings #1, #2 and #3. The results for ϵ as a function of NTU for these casings are presented in Figs. 5.47 to 5.49.

Considering the same regenerator housing used in the numerical model, Fig. 5.46, the experimental results shown in Fig. 5.47 exhibit an opposite behavior, i.e., by decreasing the void volume size, the regenerator effectiveness is reduced. The same behavior was observed in Casing #2. In Casing #3, the effectiveness reduction was smaller, but definitely no improvement of the effectiveness was observed, as predicted by the model.

The reduction of the regenerator effectiveness can be explained by a maldistribution of the inlet flow through the regenerator. When the void volume is reduced, the diverging angle of the inlet R-T adapter becomes smaller, approaching the shape of a sudden expansion. Thus, with the abrupt variation in cross sectional area, like in R-T Adapter #3, an abrupt change in average flow velocity is produced. As a result, a flow recirculation region is created inside the matrix, near the inlet. The fluid in this recirculation region does not interact effectively with the inlet stream, which acts as an internal void space that reduces the

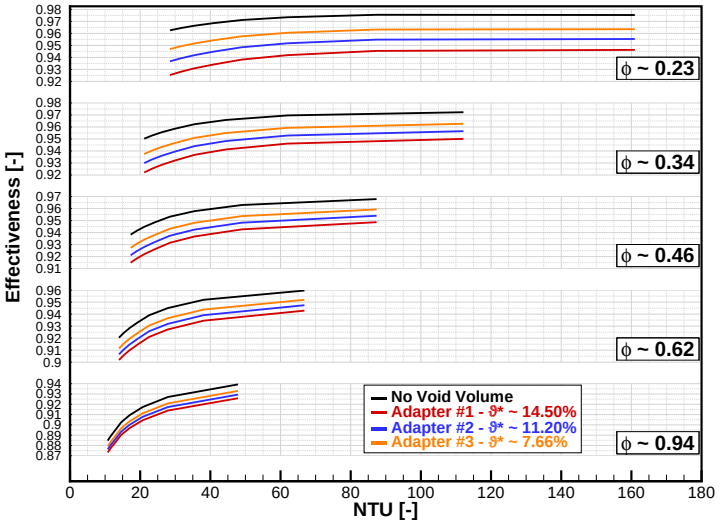

Figure 5.46 – Numerical results for ϵ as a function of NTU for Casing #1 with 1-mm spheres and different void volume fractions.

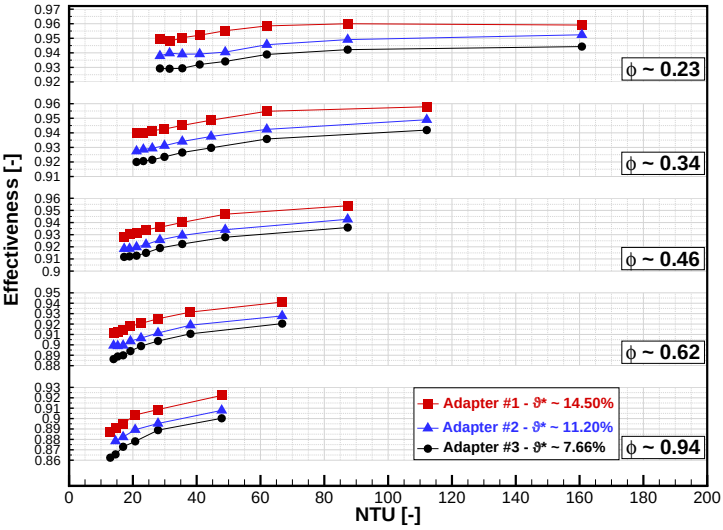

Figure 5.47 – Casing #1 experimental results for ϵ as a function of NTU for different void volume sizes.

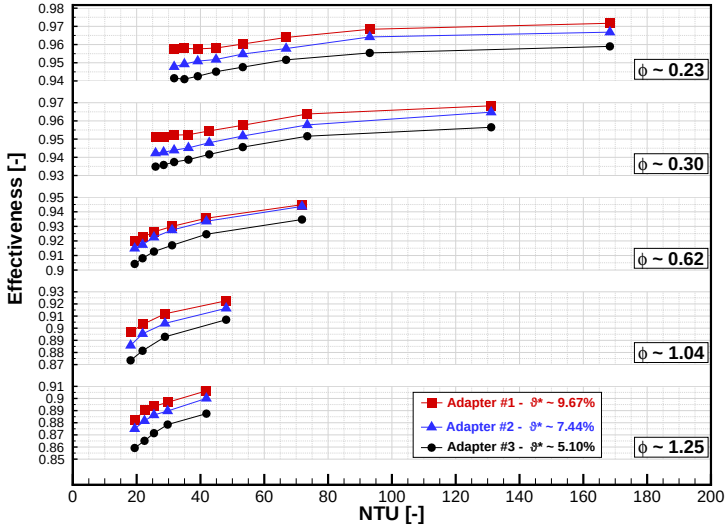

Figure 5.48 – Casing #2 experimental results for ϵ as a function of NTU for different void volume sizes.

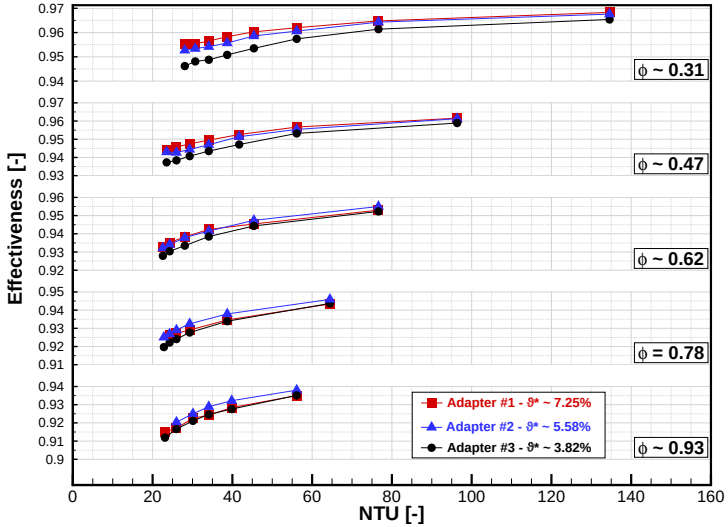

Figure 5.49 – Casing #3 experimental results for ϵ as a function of NTU for different void volume sizes.

total heat transfer area and the effective thermal mass of the matrix. As a result, the heat transfer effectiveness decreases. Also, the void region creates internal gradients in the transverse direction. The 1-D model approach is not capable of simulating these losses because they involve two-dimensional effects related to the fluid flow and heat transfer.

The inlet flow maldistribution imposes heavier penalties on shorter matrices, such as Casing #1, as the length fraction of the recirculation region is larger. In longer matrices, such as Casing #3, the influence of the flow maldistribution is smaller, as can be seen in Fig. 5.49. However, this was not sufficient to improve the performance in comparison with a regenerator with a larger void volume.

There still remains the question about what the results would be if a zero void volume regenerator was evaluated. Lozano (2015) proposed a regenerator housing with a round rectangular cross sectional area, in which the inlet and outlet streams are different, as can be seen in Fig. 3.19. This geometry guarantees a zero void volume but the inlet flow tubing is similar to R-T Adapter #3. Using this casing geometry (Casing #7), two different packed bed matrices were characterized experimentally, one with 0.5 and another with 1 mm spheres. The results for the two spheres are presented in Figs. 5.50 and 5.51, respectively. The experimental results are compared with the numerical model considering a zero void volume. Fig. 5.52 presents the experimental results for $\overline{\Delta P}$ as a function of Re_{dp} for Casing #7 and a comparison with the numerical model.

As can be seen in Figs. 5.50 and 5.51, there are considerable differences, as high as 7%, between the numerical and experimental effectiveness results. These discrepancies in the thermal effectiveness can also be attributed to the inlet flow maldistribution. The design of Casing #7 gave rise to recirculation regions near the flow inlet, creating a large thermally inactive region, which reduced the effective heat transfer area, also creating internal temperature gradients transversal to the flow direction. In addition, due to the two-dimensional nature of the flow, the one-dimensional momentum equation does not adequately represent this regenerator configuration. As a result, the variation of $\overline{\Delta P}$ with Re_{dp} was under-predicted by the model. In summary, the design geometry chosen for Casing #7, albeit having a zero void volume, deteriorated the regenerator thermal performance and increased the viscous losses.

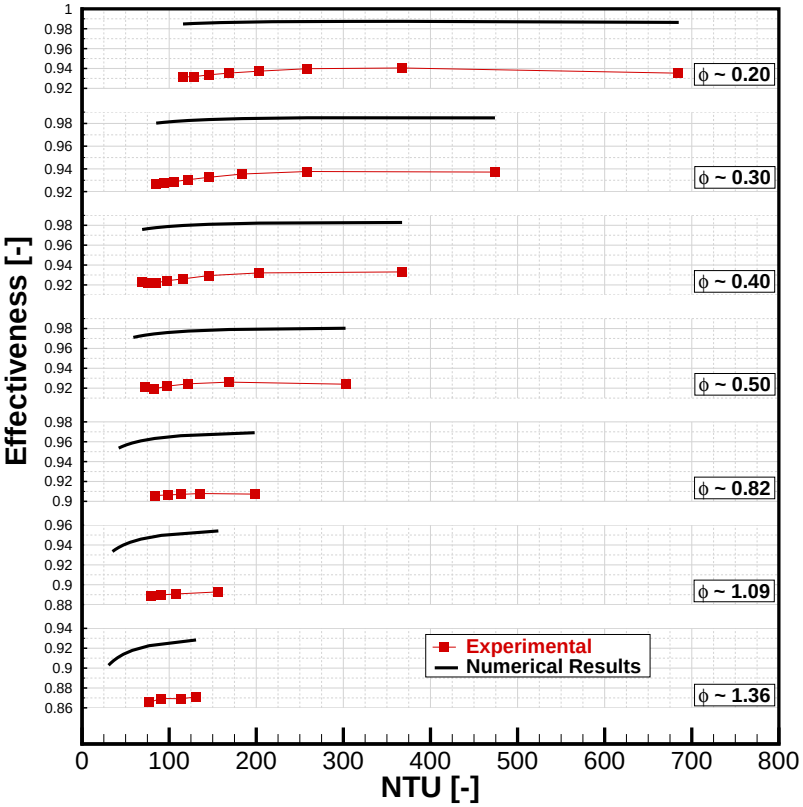

Figure 5.50 – Experimental data and numerical results for ϵ as a function of NTU for the zero void volume regenerator: Casing #7 with 0.5-mm spheres.

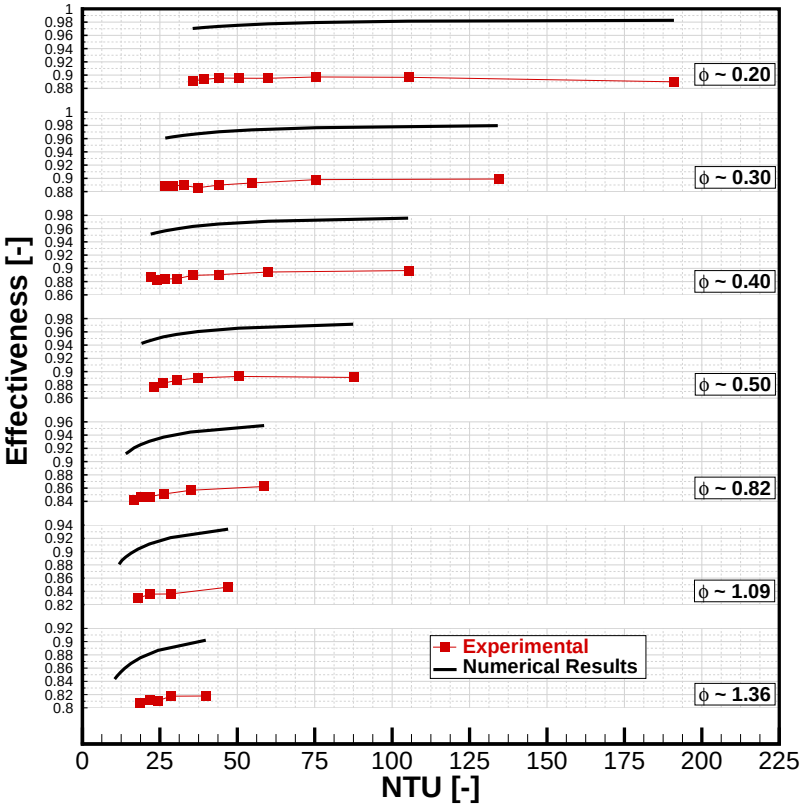

Figure 5.51 – Experimental data and numerical results for ϵ as a function of NTU for the zero void volume regenerator: Casing #7 with 1-mm spheres.

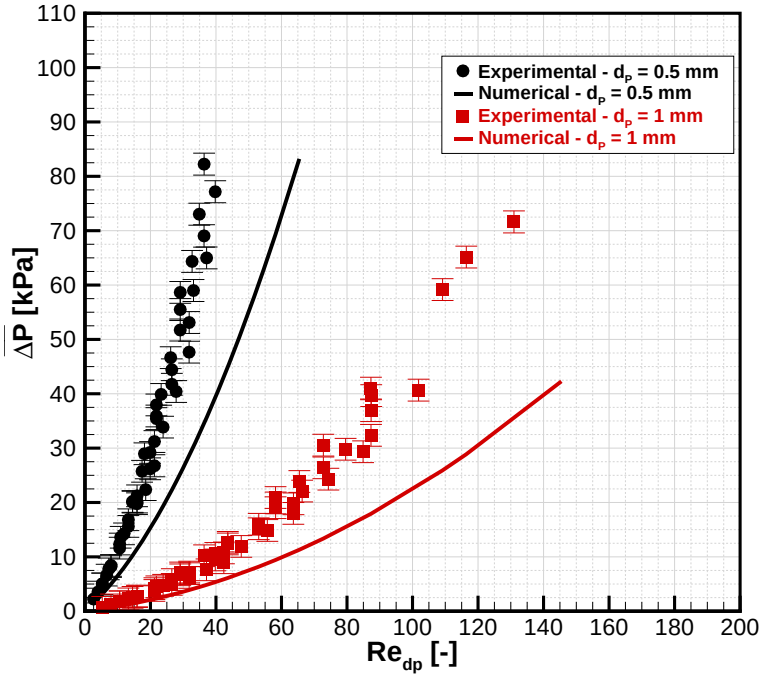

Figure 5.52 – Experimental data and numerical results for $\overline{\Delta P}$ as a function of Re_{dp} for the zero void volume regenerator.

6 Active Magnetic Regenerators

The present chapter discusses the experimental and numerical evaluations of active magnetic regenerators, starting with some preliminary results, for which the influence of the ambient and magnet temperature on the regenerator temperature span is quantified. Next, the time-dependent measurements, the performance metrics and the uncertainty analysis required for the data regression are presented. Later, the results for the AMR performance metrics are discussed based on experimental results for a sphere packed bed matrix. The experimental data are compared with the numerical results, where the different types of losses are identified. Finally, comparisons are made between the parallel plate, pin array and packed bed geometries based on the performance metrics for AMRs.

6.1 Preliminary Tests

Before starting the description of the main results and the evaluation of the AMR performance, a preliminary experimental characterization was carried out. In these tests, the cold side of the AMR apparatus was modified (see Fig. 3.4), in which the entire cold side instrumentation, including the pressure transducers, mass flow meter, cold heat exchanger and heater, was replaced by a single tube in which only temperature readings were performed. The single tube linked directly the cold end of the regenerator to the double effect pump. Thus, the fluid that exits the cold end of the regenerator during the hot blow is trapped in the tubing and returns to the regenerator in the cold blow. In other words, the single tubing acts as a void volume.

In the preliminary tests, no thermal load is applied (zero load condition), so the maximum regenerator temperature span is achieved at each particular operating condition. Fig. 6.1 shows a typical temperature measurement obtained in a preliminary test.

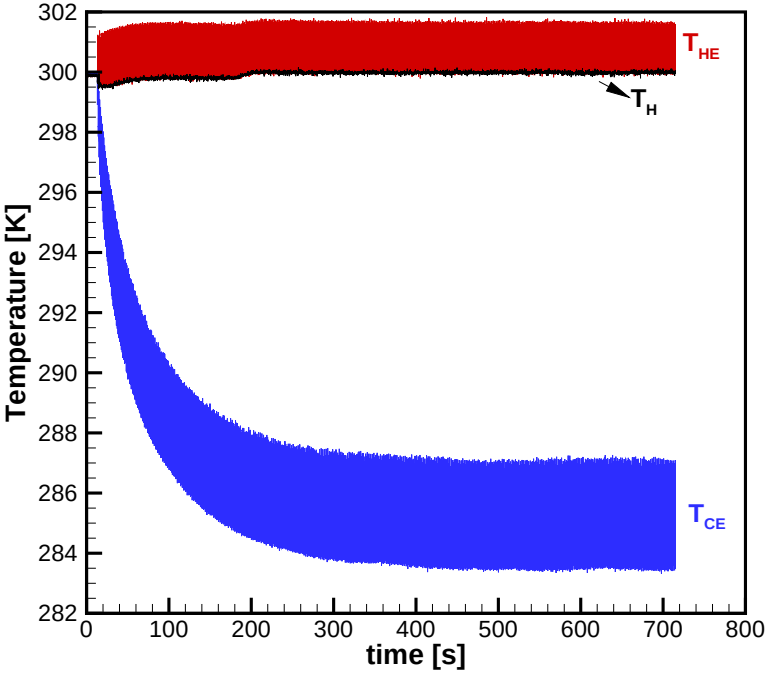

Figure 6.1 – Typical time-dependent temperature evolution during the AMR preliminary tests.

The no-load tests were performed for different temperatures of the hot reservoir, between 290 K and 315 K, in steps of 5 K. The results of the preliminary tests are presented in terms of ΔT_{Reg} as a function of T_{H} for two different frequencies: 0.25 and 0.5 Hz, as shown in Fig. 6.2. The experiments were performed at the ambient temperatures, T_{Amb}, of 293 and 300 K. In all tests, after setting the temperature of the room, the measurements started only after 24 hours to ensure thermal equilibrium between the magnetic circuit and the ambient.

The results presented in Fig. 6.2 in general agreed with those by other authors (TURA; ROWE, 2011; ARNOLD *et al.*, 2014). Based on the preliminary no-load tests, the following remarks can be made:

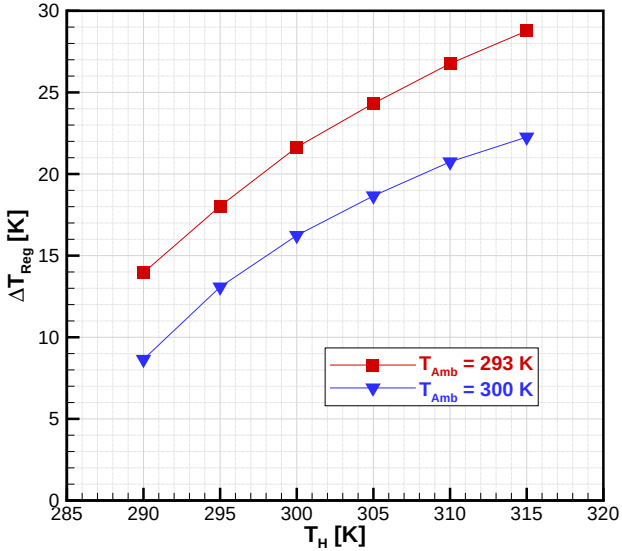

(a)

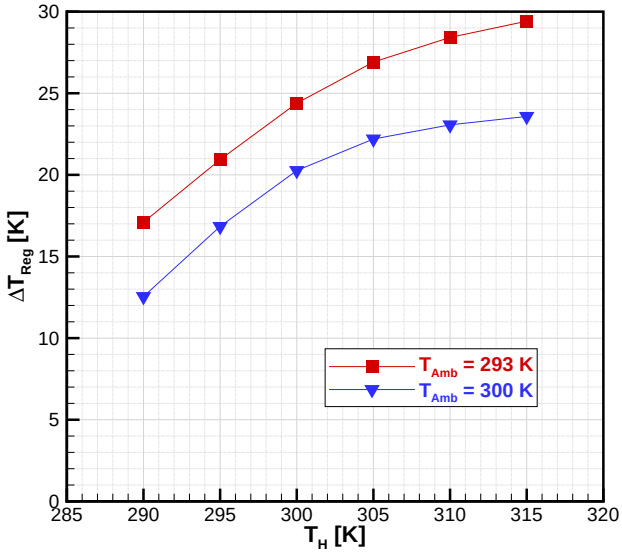

(b)

Figure 6.2 – ΔT_{Reg} as a function of T_{H}: (a) $f = 0.25$ Hz; (b) $f = 1$ Hz.

1. In Fig. 6.1, the outlet temperature at the cold end, T_C, has a large amplitude as a result of the single tubing acting as void volume. As discussed in Sections 5.4 and 5.5 the void volumes impose variable temperature boundary conditions at the regenerator ends that, in the case of the zero load AMR tests, are not strictly adiabatic due to the thermal interaction of the void volume with the ambient at the cold end;

2. Due to a less effective thermal insulation of the active regenerators, the ambient and the magnetic circuit temperatures have a significant influence on ΔT_{Reg}. This influence can be understood as a parasitic heat gain, or a parasitic heat loss, depending on the temperatures of the hot and cold ends of the regenerator;

3. Considering the axial temperature profile in the regenerator, the region along which the temperature inside the regenerator is below the magnetic circuit temperature experiences a heat gain. Conversely, the region along which the temperature is above the magnetic circuit temperature experiences a heat loss. If the heat gain surpasses the heat loss, the magnetic circuit acts toward reducing ΔT_{Reg}. Otherwise, if the heat loss wins, the magnetic circuit helps to cool down the matrix, increasing ΔT_{Reg};

4. For the conditions in Fig. 6.2, as T_H is increased, ΔT_{Reg} becomes larger for two different reasons: (i) the decrease with temperature of the (negative) adiabatic temperature change for demagnetization (MCE), which reaches a minimum coming from the ferromagnetic phase at around 295 K, and increases at a slower rate for higher temperatures, in the paramagnetic phase (TREVIZOLI *et al.*, 2011); (ii) the change from a net heat gain case (considering the whole length of the regenerator), to a net heat loss case, as the length of the heat gain region is reduced and T_C approaches T_{Amb}.

Therefore, to perform experiments that truly evaluate the AMR performance, it is important to avoid conditions in which the heat loss to magnetic circuit "improve" the regenerator performance. Therefore, in all experimental tests, the following temperature equilibrium condition will be considered: $T_H = T_{Amb} = T_{Mag}$. This condition is one of heat gain, which deteriorates the AMR performance, but is more realistic from the point of view of a real magnetic cooling application. Finally, as in the passive regenerator experiments, the temperature equilibrium

condition was such that $T_{\mathrm{H}} = T_{\mathrm{Amb}} = 300$ K in all experiments presented in this thesis.

6.2 Time-Dependent Measurements

The time-dependent measurements performed by the different transducers were used in the calculation of the time-average values needed to compute the performance metrics. The same instrumentation and DAQ used in the passive experiments were used in the AMR tests. Also, the same strategy to evaluate the time-average variables was applied, in which 300 experimental points per cycle and a total of five cycles are considered in the calculations. The time-dependent measurements are explained next.

6.2.1 Temperature Measurements

An AMR test starts with a zero thermal load applied on the heater. The temperatures of the hot reservoir and of the ambient were kept at 300 K (temperature equilibrium condition). As the test progresses, the temperature at the cold end of the regenerator, T_{CE}, decreases and the compensation temperatures, $T_{\mathrm{CH\text{-}out}}$ and $T_{\mathrm{Heater\text{-}in}}$, are adjusted so as to match the time-average temperature of the fluid that exits the regenerator at the cold end, $\overline{T}_{\mathrm{CE}}$. When this condition is reached (with a safety margin of +0.1 K), the periodically developed regime is assumed and the data are saved considering 300 points per cycle. In the following test, the heater is turned on and, again, $T_{\mathrm{CH\text{-}out}}$ and $T_{\mathrm{Heater\text{-}in}}$ are adjusted to match the new $\overline{T}_{\mathrm{CE}}$ temperature, and a new periodically developed condition is established. This procedure was repeated until the maximum thermal load condition, at which $\Delta T_{\mathrm{Hex}} = T_{\mathrm{H}} - T_{\mathrm{C}} \approx 0$. Fig. 6.3 shows the five cycles of the time-dependent temperature measurements during the periodically developed regime for different thermal loads, considering the operating condition of $f = 0.5$ Hz and $\phi \approx 0.41$.

Some remarks are in order regarding the experimental procedure:

- The objective of the temperature compensation is to find the condition at which $T_{\mathrm{CH\text{-}out}} = T_{\mathrm{Heater\text{-}in}} = \overline{T}_{\mathrm{CE}}$. During a test, two different situations can occur while the bath temperature

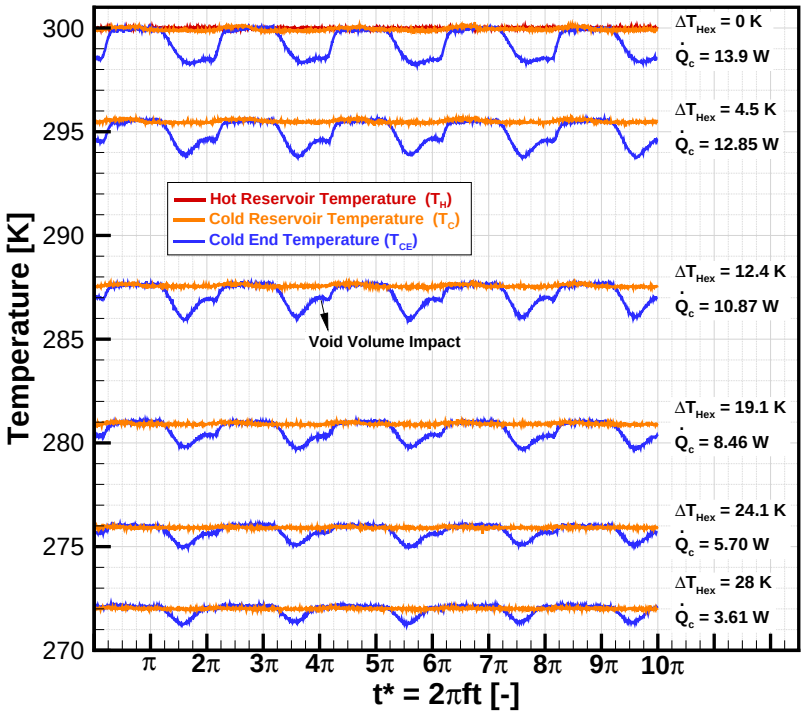

Figure 6.3 – Time-dependent temperature measurements at the periodically developed regime for different thermal loads at the operating condition of $f = 0.5$ Hz and $\phi \approx 0.41$ for Spheres#3 geometry (Casing #3 and $d_p = 0.55$ mm).

is adjusted: (i) if $T_{\text{Heater-in}}$ (and $T_{\text{CH-out}}$) is greater than $\overline{T}_{\text{CE}}$, the temperature of the thermal bath has to be reduced; (ii) if $T_{\text{Heater-in}}$ (and $T_{\text{CH-out}}$) is lower than $\overline{T}_{\text{CE}}$, the temperature of the bath has to be raised. To perform a reliable characterization, if situation (i) exists, then the thermal bath is adding some heat to the regenerator, which can be interpreted as an additional thermal load. On the other hand, if situation (ii) is verified, then the thermal bath is artificially increasing the AMR cooling capacity, what is not physically consistent with the actual AMR performance. To avoid the situation (ii) a safety margin of +0.1 K was included in the temperature compensation. In this case, the safety margin of +0.1 K represents an additional heat input

that has to be included in the experimental procedure to calculate the cooling capacity that will be explained in Section 6.3;

- In the tests where the heater is turned off, because of the temperature safety margin and mainly due to the heat gain from the ambient through the cold side tubing, the zero thermal load condition is never truly satisfied. For example, in Fig. 6.3 for the test in which the heater was switched off, ΔT_{Hex} and the cooling capacity were calculated at 28 K and 3.61 W, respectively, which can be attributed mainly to the heat gain from the ambient. In this case, the ambient temperature was 300 K and T_{C} was approximately 272 K. Clearly, the higher ΔT_{Hex}, the higher the heat gain from the ambient;

- In Fig. 6.3, there is an indication of the void volume impact on the time-dependent temperature measurements. In the AMR tests the void volume plays the same role as in the passive regenerators. Its impact on the AMR performance will be discussed in Section 6.5.2.

6.2.2 Torque Measurements

Fig. 6.4 shows the last five cycles of the time-dependent total torque measurements. Fig. 6.4(a) presents the results for different values of ΔT_{Hex}, considering $f = 0.5$ Hz and $\phi \approx 0.41$, as in Fig. 6.3. Fig. 6.4(b) presents the results for different utilizations, considering $f = 0.5$ Hz and $\Delta T_{\mathrm{Hex}} = 0$. The results resemble a sinusoidal waveform, with superposed high frequency oscillations that are related to the magnetic circuit torque contribution. The magnetic circuit torque characterization is discussed in greater detail in Appendix A.

Since the magnetic circuit and the pumping system are driven by a single motor, the total torque is a combination of four different contributions: (i) the torque of the magnetic circuit without the regenerator (see Appendix A), (ii) the pumping system torque, (iii) the magnetic interaction torque and (iv) the torque associated with the mechanical losses. The magnetic interaction torque is the reversible part of the torque, which can be positive or negative depending on the magnetic attraction. The positive values are related to the torque necessary to remove the magnetic field from the regenerator bed, which corresponds to the demagnetization process. On the other hand, the negative part

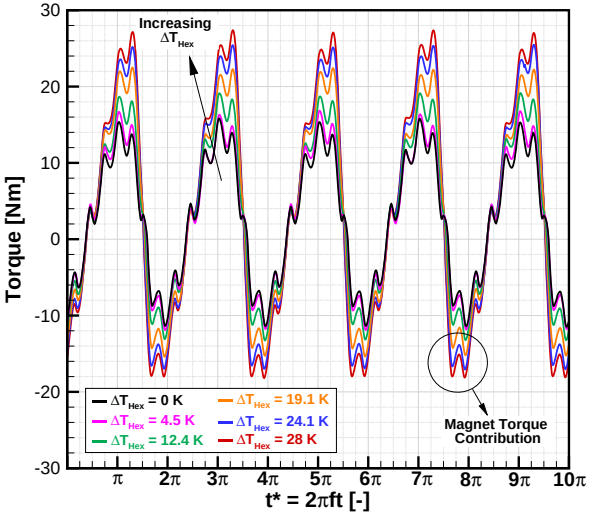

(a)

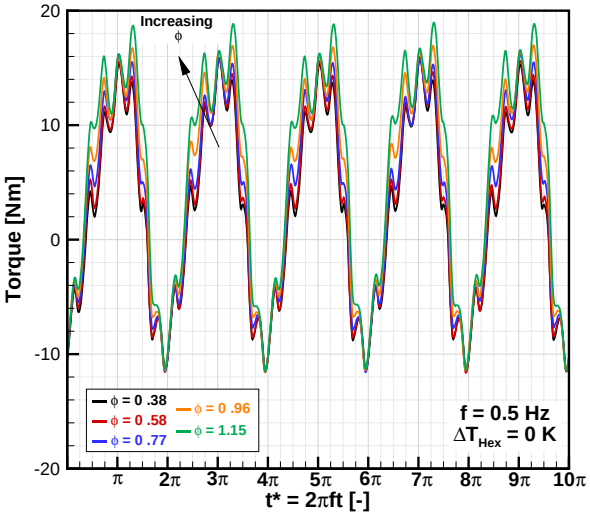

(b)

Figure 6.4 – Time-dependent total torque measurements: (a) Variable ΔT_{Hex} for $f = 0.5$ Hz and $\phi \approx 0.41$; (b) Variable utilization for $f = 0.5$ Hz and $\Delta T_{\mathrm{Hex}} = 0$.

is related to the application of the magnetic field on the regenerator bed during the magnetization process. The pumping torque is an irreversible contribution, i.e., always positive. As a result, the positive peaks and the negative valleys of the total torque are not symmetric.

In Fig. 6.4(a), since the utilization and frequency are constant, the increase in the total torque is just related to the increasing ΔT_{Hex}. As ΔT_{Hex} becomes higher, the temperature of the cold reservoir is reduced. For a fixed hot reservoir temperature, the fraction of the regenerator that is in the ferromagnetic phase increases. This increases the magnetic attraction and the torque necessary to rotate the magnet becomes higher. Also, but to a lower extent, the pumping system torque also increases as the working fluid becomes more viscous due to the temperature reduction. Fig. 6.4(b) shows the influence of the pumping system torque, considering $\Delta T_{\mathrm{Hex}} = 0$. In this case, the magnetic interaction torque is the same for all utilizations. As the utilization is increased, the total torque becomes higher because of the viscous losses.

6.2.3 Influence of the Oscillating Torque on the Pressure Drop and Mass Flow Rate

The drivers for the pumping system and magnetic circuit are linked by the bevel gear boxes and are driven by the same stepper motor. As a result, the oscillating torque from the magnetic circuit interferes with the flow velocity. Fig. 6.5 shows the influence of the oscillating torque on the instantaneous mass flow rate (for PP#122.5 and s_k = 10 mm), and on the instantaneous total pressure drop (for PP#122.5 and s_k = 10 and 20 mm), respectively. The measurements performed in AMRs are compared with those carried out in passive regenerators. The differences in mass flow rate and pressure drop can be attributed to the oscillating torque and to the fluid properties, since the water-glycol mixture is more dense and more viscous than pure water and, hence, the peak of the mass flow rate and pressure drop are higher for the AMRs.

The instantaneous mass flow rate, Fig. 6.5(a), is less sensitive to the torque oscillations due to the second-order measurement effects (time constant) of the Coriolis mass flow meters, but some influences are visible and indicated by the arrows. The impact on the instantaneous pressure drop is more visible, indicating some significant variations of

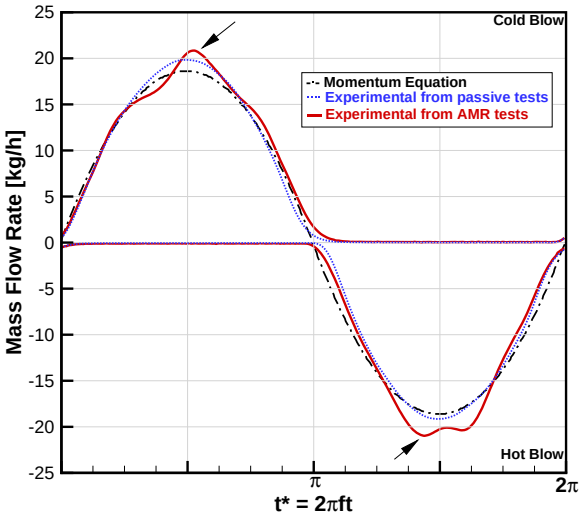

(a)

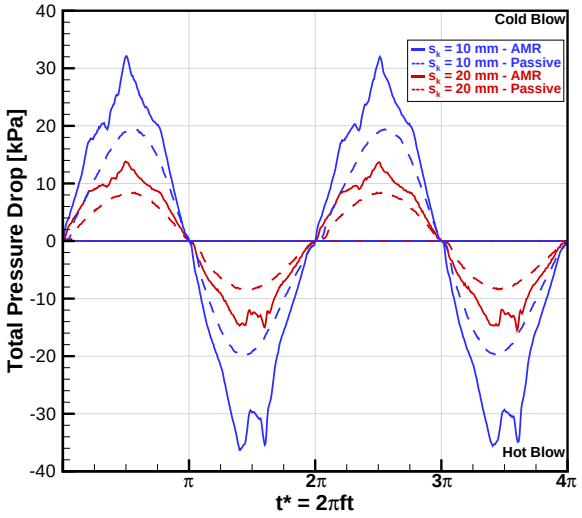

(b)

Figure 6.5 – Oscillating torque influences on the: (a) Instantaneous mass flow rate for PP#122.5 and $s_k = 10$ mm; (b) Instantaneous total pressure drop for PP#122.5 and $s_k = 10$ and 20 mm.

the instantaneous flow velocity. Also, the variations in flow velocity are not perfectly symmetric.

It is important to mention that, although the instantaneous velocities in the hot and cold blows are not symmetric, in terms of the cycle-average values, the AMR still operates under balanced flow conditions, as the amount of pumped fluid (and the utilization factor) is fixed for both blows. The blow period did not present significant variations either (lower than 5%). Despite the variation in the instantaneous value, the time-average mass flow rate is still in good agreement with the reference value, as explained in Section 5.1.2. Thus, the time-average value will be used in the performance metrics analysis explained next.

6.3 Performance Metrics and Data Regression

The AMR performance metrics are related to the cycle-average cooling capacity and the total cycle-average power input to drive the magnetic circuit and pumping system. Fig. 6.6 shows a schematic representation of the main variables of a generic magnetic refrigerator.

Based on the schematic diagram in Fig. 6.6 there are finite temperature differences associated with the hot, ΔT_{H}, and cold, ΔT_{C}, reservoirs. These temperature differences are necessary due to finite heat transfer areas in each heat exchanger, which make their thermal effectiveness lower than unity. The temperature differences in the figure are defined as follows:

$$\Delta T_{\mathrm{C}} = T_{\mathrm{C}} - \overline{T}_{\mathrm{CE}} \tag{6.1}$$

$$\Delta T_{\mathrm{H}} = T_{\mathrm{H}} - \overline{T}_{\mathrm{HE}} \tag{6.2}$$

$$\Delta T_{\mathrm{Hex}} = T_{\mathrm{H}} - T_{\mathrm{C}} \tag{6.3}$$

$$\Delta T_{\mathrm{Reg}} = \overline{T}_{\mathrm{HE}} - \overline{T}_{\mathrm{CE}} \tag{6.4}$$

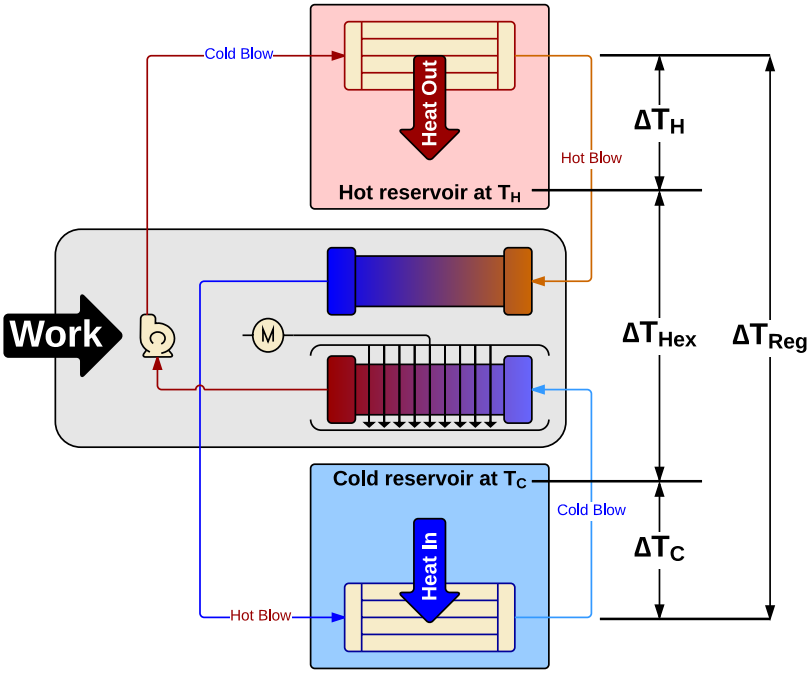

Figure 6.6 – Schematic representation of the main variables of a generic magnetic refrigerator.

where ΔT_{Reg} is the regenerator temperature span, which is always greater than the thermal reservoir temperature span, ΔT_{Hex}. $\overline{T}_{\text{HE}}$ and $\overline{T}_{\text{CE}}$ are the time-average temperatures of the fluid exiting the regenerator at the hot and cold ends, respectively. These are calculated by:

$$\overline{T}_{\text{HE}} = \frac{1}{\varsigma}\sum_{i=1}^{\varsigma}\left[\frac{1}{\tau/2}\int_{0}^{\tau/2} T_{\text{HE}}(t)dt\right] \tag{6.5}$$

$$\overline{T}_{\text{CE}} = \frac{1}{\varsigma}\sum_{i=1}^{\varsigma}\left[\frac{1}{\tau/2}\int_{\tau/2}^{\tau} T_{\text{CE}}(t)dt\right] \tag{6.6}$$

and the reservoir temperatures are determined by:

$$\overline{T}_{\mathrm{H}} = \frac{1}{\varsigma}\sum_{i=1}^{\varsigma}\left[\frac{1}{\tau/2}\int_{\tau/2}^{\tau} T_{\text{HR-in}}(t)dt\right] \tag{6.7}$$

$$\overline{T}_{\mathrm{C}} = \frac{1}{\varsigma}\sum_{i=1}^{\varsigma}\left[\frac{1}{\tau/2}\int_{0}^{\tau/2} T_{\text{Heater-out}}(t)dt\right] \tag{6.8}$$

where $\varsigma = 5$ is the number of cycles employed in the data regression. $T_{\text{HR-in}}$ is the temperature read by the probe located between the hot heat exchanger and the hot regenerator end and, similarly $T_{\text{Heater-out}}$ is the temperature read by the probe located at the heater end and assumed as the cold reservoir temperature (see Fig. 3.4). The integrations were performed numerically using the extended Simpson rule (Eq. (5.10)). Fig. 6.7 shows the time-dependent temperature measurements of T_{H}, T_{C}, T_{HE} and T_{CE} for two different situations: (i) an intermediate thermal load test, Fig. 6.7(a), and (ii) a maximum thermal load test, Fig. 6.7(b).

The intermediate thermal load test situation is associated with a specific operating condition characterized by positive (non-zero) values of cooling capacity and ΔT_{Hex}. The maximum load test, on the other hand, is defined by $\Delta T_{\mathrm{Hex}} = 0$ and $\Delta T_{\mathrm{Reg}} > 0$. In this case, if $\Delta T_{\mathrm{Reg}} = 0$ is considered for the condition of maximum cooling capacity, there will be a thermodynamic inconsistency regarding the operation of the refrigeration system, as the temperatures of the thermal reservoirs will be inverted, i.e., $T_{\mathrm{H}} < T_{\mathrm{C}}$.

The instantaneous cooling capacity, $\dot{Q}_{\mathrm{C}}$, is calculated by:

$$\dot{Q}_{\mathrm{C}} = \dot{m}(t)c_{\mathrm{p,f}}(T_{\mathrm{C}} - T_{\mathrm{CE}}(t)) \tag{6.9}$$

and the cycle-average cooling capacity, $\overline{\dot{Q}}_{\mathrm{C}}$, is determined by:

$$\overline{\dot{Q}}_{\mathrm{C}} = \frac{1}{\tau}\int_{0}^{\tau/2} \dot{m}(t)c_{\mathrm{p,f}}(T_{\mathrm{C}} - T_{\mathrm{CE}}(t))dt \tag{6.10}$$

Eqs. (6.9) and (6.10) are used in the numerical model to evaluate the AMR cooling capacity. Also, Eqs. (6.4), (6.5) and (6.6) are used to cal-

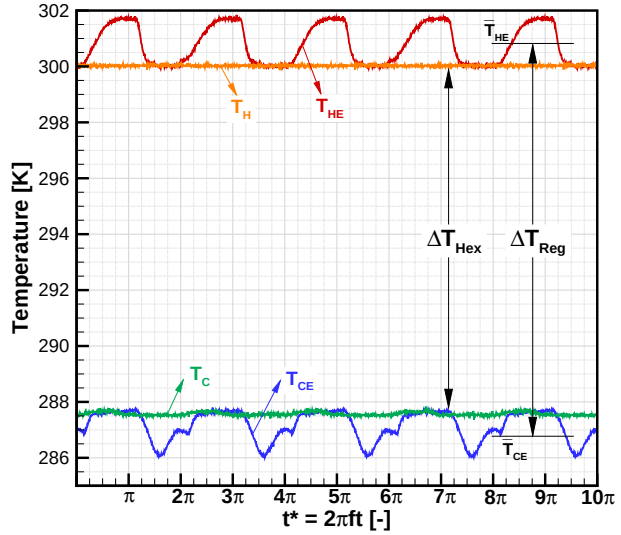

(a)

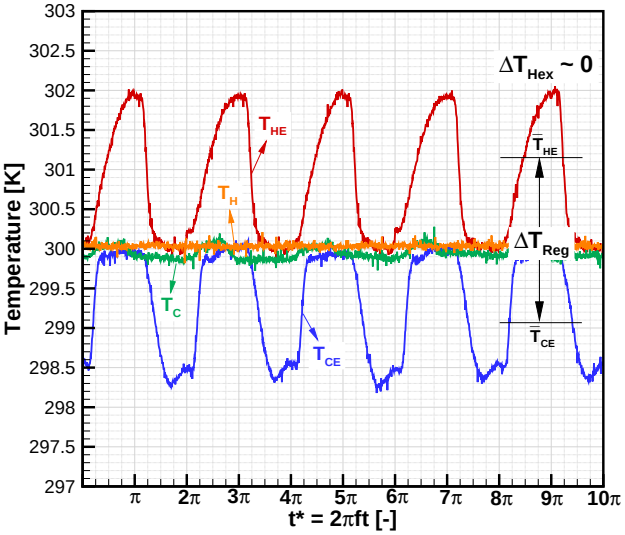

(b)

Figure 6.7 – Time-dependent measurements of T_{H}, T_{C}, T_{HE} and T_{CE}: (a) Intermediate thermal load test; (b) Maximum thermal load test.

culate ΔT_{Reg}, considering a single cycle. ΔT_{Hex} is used directly as the temperature boundary conditions of the numerical simulation. However, due to the existence of oscillating torque and second-order effects in the Coriolis mass flow meter, the experimental determination of $\dot{m}(t)$ may be subjected to a few inconsistencies at some conditions. To eliminate this problem, the experimental cycle-average cooling capacity was calculated by:

$$\overline{\dot{Q}}_{\mathrm{C}} = \frac{1}{2}\overline{\dot{m}} c_{\mathrm{p,f}} (T_{\mathrm{C}} - \overline{T}_{\mathrm{CE}}) \tag{6.11}$$

where $\overline{\dot{m}}$ is the reference mass flow rate, T_{C} is given by Eq. (6.8) and $\overline{T}_{\mathrm{CE}}$ by Eq. (6.6). The factor (1/2) accounts for the discontinuity of the cycle, i.e., the hot blow period is half the total period.

The experimental evaluation of $\overline{\dot{Q}}_{\mathrm{C}}$ proposed in this thesis is different from those usually encountered in the literature (KITANOVSKI *et al.*, 2015). Generally, the electrical heater power is used to emulate a thermal load. However, since one of the main objectives of the experimental analysis is to compare and validate the numerical model, the use of Eq. (6.11) is more appropriate, since the calculation is based on the same parameters ($\dot{m}$ and T_{CE}) derived from the numerical results (Eq. (6.10)). The main advantage of this procedure is that Eq. (6.11) returns the 'actual cooling potential' of the AMR, which takes into account all the thermal loads imposed on the regenerator, including the electrical heater power input and the heat gain from external sources, such as the ambient and the safety margin used in the cold heat exchanger temperature compensation explained previously.

On the other hand, this kind of experimental evaluation is more susceptible to experimental uncertainties, as will be explained in more details and quantified in the next section. Because of this, an additional evaluation of $\overline{\dot{Q}}_{\mathrm{C}}$ was performed and used to verify the consistency of the calculation. Thus:

$$\overline{\dot{Q}}_{\mathrm{C,ver}} = \overline{\dot{m}} c_{\mathrm{p,f}} (T_{\mathrm{Heater\text{-}out}} - \overline{T}_{\mathrm{Heater\text{-}in}}) \tag{6.12}$$

where $\overline{\dot{Q}}_{\mathrm{C,ver}}$ is the heat load applied by the heater, which includes the Joule heating by the electrical heater and the heat gain from the ambient through the heater control volume.

The cycle-average total power, $\overline{\dot{W}}$, needed to perform the magnetic flux density variation and the oscillating fluid flow is calculated by:

$$\overline{\dot{W}} = 2\pi f_{\mathrm{M}} \overline{\Gamma} \tag{6.13}$$

where $\overline{\Gamma}$ is the cycle-average total torque and f_{M} is the stepper motor frequency, which is half the AMR operating frequency. As explained previously, the instantaneous torque measurement, Γ(t), already accounts for four torque contributions, namely the magnetic circuit torque, the pumping torque, magnetic interaction torque and mechanical losses. $\overline{\Gamma}$ is calculated by:

$$\overline{\Gamma} = \frac{1}{\varsigma} \sum_{i=1}^{\varsigma} \left(\frac{1}{\tau} \int_0^{\tau} \Gamma(t) dt \right) \tag{6.14}$$

The coefficient of performance, COP, is defined as:

$$COP = \frac{\overline{\dot{Q}}_{\mathrm{C}}}{\overline{\dot{W}}} \tag{6.15}$$

and the second-law efficiency, $\eta_{2\mathrm{nd}}$, as:

$$\eta_{2\mathrm{nd}} = \frac{COP}{COP_{\mathrm{id}}} \tag{6.16}$$

where the ideal, or Carnot, coefficient of performance, COP_{id}, is given by:

$$COP_{\mathrm{id}} = \frac{T_{\mathrm{C}}}{T_{\mathrm{H}} - T_{\mathrm{C}}} \tag{6.17}$$

6.3.1 Uncertainty Analysis

The experimental uncertainties related to the AMR performance metrics were evaluated according to the methodology presented in Section

5.2.1. Eqs. (5.11), (5.14) and (5.16) were used to compute the combined and the expanded uncertainties. The values of the calculated expanded uncertainties are described together with the results.

Regarding the uncertainties of the cycle-average cooling capacity and, consequently, the COP and the second-law efficiency, $\overline{\dot{Q}}_{\mathrm{C}}$ is calculated based on the temperature difference between the time-average temperatures T_{C} and $\overline{T}_{\mathrm{CE}}$ ($\Delta T_{\mathrm{C}} = T_{\mathrm{C}} - \overline{T}_{\mathrm{CE}}$). Depending on the value of $\overline{\dot{Q}}_{\mathrm{C}}$ and $\dot{m}$, the absolute value of the temperature difference ΔT_{C} can be of the order of the experimental uncertainty of ΔT_{C}. The uncertainty associated with ΔT_{C} is approximately 0.3 K. As a result, the uncertainty evaluated for $\overline{\dot{Q}}_{\mathrm{C}}$ is on same order of the absolute value of $\overline{\dot{Q}}_{\mathrm{C}}$.

However, the points mentioned below ensure that the proposed experimental evaluation of $\overline{\dot{Q}}_{\mathrm{C}}$ is robust and reliable:

1. All experimental tests were performed using the same calibrated temperature probes. The calibration procedure, described in Chapter 3, was carefully performed and utilized a recently calibrated standard thermometer;

2. The assembly and measurements with the temperature probes were performed following the procedure developed for the passive regenerators, which was demonstrated to be physically consistent through comparisons with the numerical model. Based on this previous experience, one can ensure that the temperature measurements in the AMR were successfully performed;

3. Although the absolute value of ΔT_{C} is of the order of 0.3 K, the time-dependent measurement of T_{CE} presented a continuous behavior with an amplitude always larger than 0.5 K. In addition, a very good reproducibility was observed considering the five cycles used in the calculation of the average temperature values. This means a small standard deviation for the five cycles;

4. In all experimental results presented in this thesis, the differences between $\overline{\dot{Q}}_{\mathrm{C}}$ and $\overline{\dot{Q}}_{\mathrm{C,ver}}$ were smaller than the related uncertainties, with $\overline{\dot{Q}}_{\mathrm{C}}$ always slightly larger than $\overline{\dot{Q}}_{\mathrm{C,ver}}$. This is justified by the temperature safety margin used in the cold heat exchanger temperature compensation.

6.4 Reproducibility of the Experimental Results

As in the passive regenerator experimental characterization, the first evaluation of the AMR performance focuses on the experimental reproducibility of the results. These experimental tests were repeated three times by three different operators (PVT, ATN and GFP). The Spheres #3 geometry (see Table 3.9) were used as the regenerative matrix. Assembly #1 was evaluated first by operator PVT. Later, Assemblies #2 and #3 were tested by operators ATN and GFP, respectively, following the same procedure used by PVT.

Fig. 6.8 shows the reproducibility of the results for $\overline{\dot{Q}}_{\mathrm{C}}$ as a function of ΔT_{Hex} considering three different operating conditions: (i) $\phi \approx 0.41$ and $f = 0.25$ Hz, (ii) $\phi \approx 0.41$ and $f = 0.5$ Hz, (iii) $\phi \approx 1.23$ and $f = 0.25$ Hz. The results showed a very good reproducibility, with the same trend being observed for all assemblies. The experimental uncertainty for ΔT_{Hex} was evaluated at 0.3 K. Regarding the uncertainty of $\overline{\dot{Q}}_{\mathrm{C}}$, the following comments can be made:

- For $\phi \approx 0.41$ and $f = 0.25$ Hz, the uncertainty was estimated at 1.5 W, with the lowest $\overline{\dot{Q}}_{\mathrm{C}}$ being around 2.6 W and the maximum $\overline{\dot{Q}}_{\mathrm{C}}$ being close to 7.5 W;
- For $\phi \approx 0.41$ and $f = 0.5$ Hz, the uncertainty was estimated at 3.0 W, with the lowest $\overline{\dot{Q}}_{\mathrm{C}}$ being around 3.6 W and the maximum $\overline{\dot{Q}}_{\mathrm{C}}$ being close to 14.0 W;
- For $\phi \approx 1.23$ and $f = 0.25$ Hz, the uncertainty was estimated at 4.5 W, with the lowest $\overline{\dot{Q}}_{\mathrm{C}}$ being around 5.3 W and the maximum $\overline{\dot{Q}}_{\mathrm{C}}$ being 20.1 W.

Considering the three cases above, the uncertainty related to the maximum $\overline{\dot{Q}}_{\mathrm{C}}$ is around 20%. As $\overline{\dot{Q}}_{\mathrm{C}}$ decreases, ΔT_{C} also decreases since the mass flow rate is fixed. As a result, the uncertainty related to $\overline{\dot{Q}}_{\mathrm{C}}$ approaches 90% of the calculated $\overline{\dot{Q}}_{\mathrm{C}}$. In both situations, the calculated uncertainties are considerably large. However, based on the discussion from the previous section and on the good reproducibility of

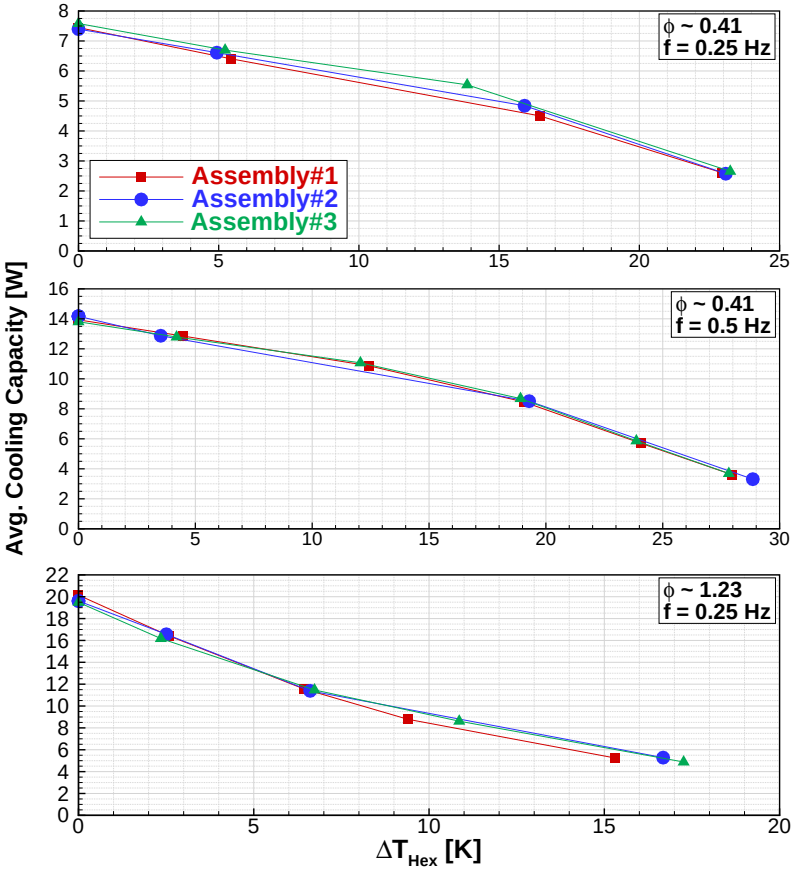

Figure 6.8 – Reproducibility tests for $\overline{\dot{Q}}_{\mathrm{C}}$ as a function of ΔT_{Hex}.

the results presented in Fig. 6.8, one can conclude that the experimental procedure and evaluation were successfully carried out, considering the robust instrumentation, measurements and data regression.

6.5 Spheres Packed Bed Regenerator

This section presents the experimental and numerical results for the AMR identified as Spheres #3 in Table 3.9, which contains 0.55-mm Gd spheres assembled as a packed bed in the Casing #3 housing. In the present analysis, this will be considered the reference AMR geometry.

6.5.1 Experimental Results

6.5.1.1 Characteristic Curves

The cooling capacity, $\overline{\dot{Q}}_{\mathrm{C}}$, as a function of the temperature span, ΔT_{Hex}, is known as the cooling system characteristic (or performance) curve. Fig. 6.9 shows the characteristic curves for Spheres #3 as a function of utilization for frequencies of 0.25, 0.5 and 1 Hz. T_{H} was kept at 300 K. The curves were generated increasing the thermal load from a minimum value up to the maximum value, for which $\Delta T_{\mathrm{Hex}} \approx 0$. As already discussed, the true zero-load condition cannot be evaluated because of the external heat gain. However, it can be inferred from extrapolations of the performance curves.

The results in Fig. 6.9 show that $\overline{\dot{Q}}_{\mathrm{C}}$ varies approximately linearly with ΔT_{Hex}. However, for some utilizations, as ΔT_{Hex} increases (and $\overline{\dot{Q}}_{\mathrm{C}}$ decreases), some deviations in the linear trend are seen. This change in behavior of the system curve can be attributed to: (i) the temperature and magnetic flux density dependence on the specific heat and MCE; (ii) the reversibility of the MCE; (iii) the void volume influence on the AMR performance, as will be explained in Section 6.5.2.

Regarding the differences between ΔT_{Hex} and ΔT_{Reg}, Fig. 6.10 shows $\overline{\dot{Q}}_{\mathrm{C}}$ as a function of the two temperature spans, ΔT_{Hex} and ΔT_{Reg}, for $\phi \approx 0.38$ and different frequencies. From these results, it is possible to verify that the differences between ΔT_{Hex} and ΔT_{Reg} go from approximately 1 K, for the smallest values of $\overline{\dot{Q}}_{\mathrm{C}}$, to around 2 K for the maximum values of $\overline{\dot{Q}}_{\mathrm{C}}$. This result strengthens the justification for choosing $\Delta T_{\mathrm{Hex}} \approx 0$ for the experimental definition of the maximum $\overline{\dot{Q}}_{\mathrm{C}}$; alternatively if $\Delta T_{\mathrm{Reg}} \approx 0$ was set as the maximum cooling capacity condition, then ΔT_{Hex} would be negative, which is against the purpose of a refrigeration system.

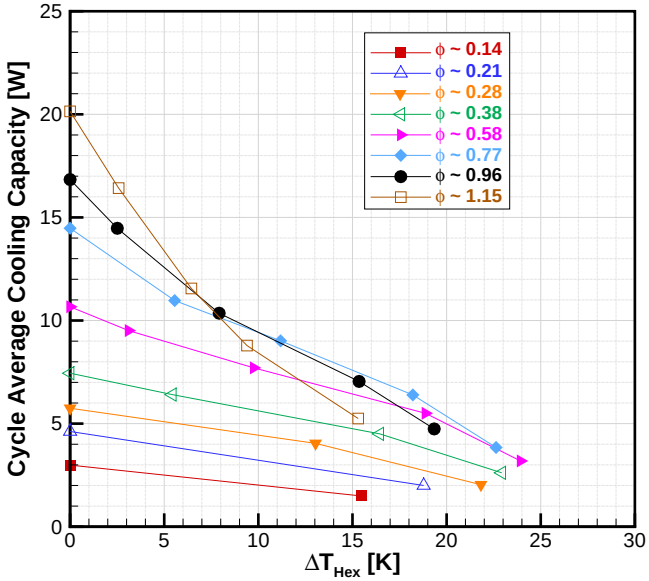
Cycle Average Cooling Capacity [W]
ΔT_Hex [K]
ϕ ~ 0.14
ϕ ~ 0.21
ϕ ~ 0.28
ϕ ~ 0.38
ϕ ~ 0.58
ϕ ~ 0.77
ϕ ~ 0.96
ϕ ~ 1.15

(a)

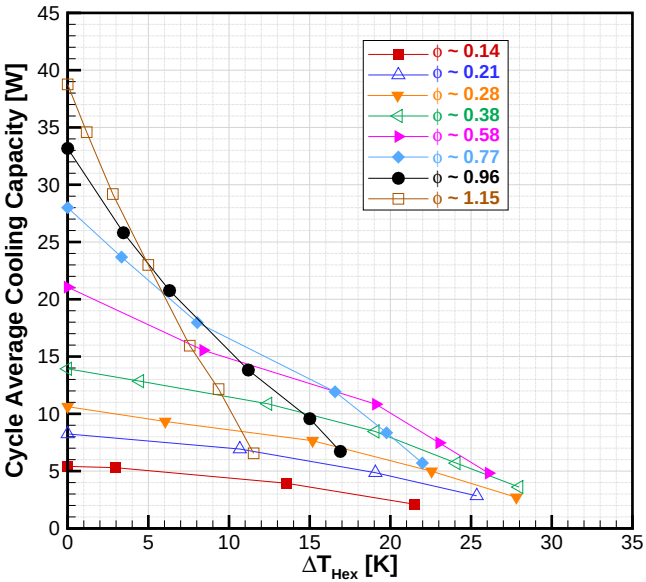
Cycle Average Cooling Capacity [W]
ΔT_Hex [K]
ϕ ~ 0.14
ϕ ~ 0.21
ϕ ~ 0.28
ϕ ~ 0.38
ϕ ~ 0.58
ϕ ~ 0.77
ϕ ~ 0.96
ϕ ~ 1.15

(b)

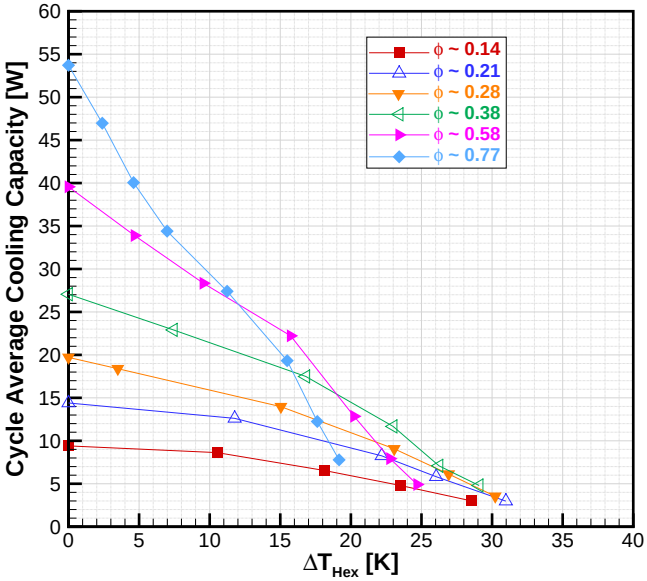

(c)

Figure 6.9 – $\overline{\dot{Q}}_C$ as a function of ΔT_{Hex} for $T_H = 300$ K and a range of utilization factors: (a) $f = 0.25$ Hz; (b) $f = 0.5$ Hz; (c) $f = 1$ Hz.

6.5.1.2 Total Power (Work) Analysis

Like the torque, the total power consumed by the system is composed by four contributions: (i) the power to drive the magnetic circuit without the regenerator; (ii) the pumping power; (iii) the power to overcome the magnetic interaction with the regenerator; (iv) the power to overcome the mechanical losses. Since there is no relationship between the magnetic circuit and mechanical loss contributions and the variable regenerator temperature span or the utilization factor[1], to simplify the analysis, the total power will be divided in only two contributions:

$$\overline{\dot{W}} = \overline{\dot{W}}_{Mag} + \overline{\dot{W}}_{pump} \tag{6.18}$$

where $\overline{\dot{W}}_{Mag}$ is the magnetic portion of the total cycle average power

[1]The magnetic circuit torque increases slightly with frequency, as will be shown in Appendix A.

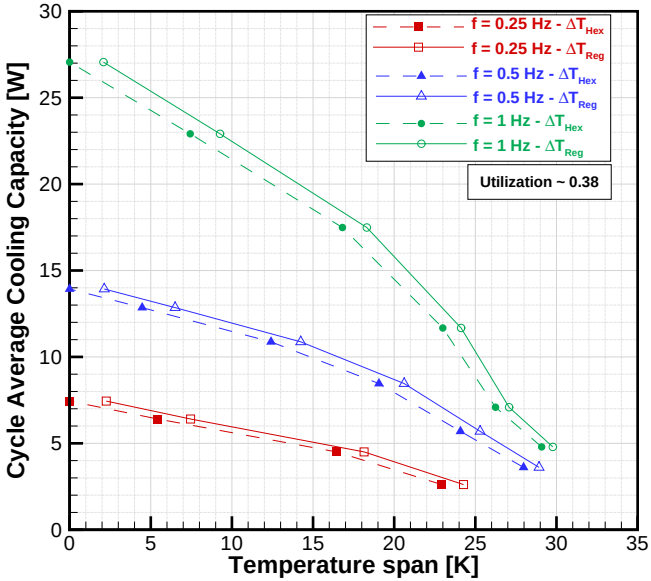

Figure 6.10 – $\overline{\dot{Q}}_{\mathrm{C}}$ as a function of ΔT_{Hex} and ΔT_{Reg}, for $\phi \approx 0.38$ and different frequencies (0.25, 0.5 and 1 Hz).

that comprises the magnetic circuit and the magnetic interaction with the regenerator, while $\overline{\dot{W}}_{\mathrm{pump}}$ is the portion of the total cycle average power responsible for generating the oscillatory fluid flow in the system, including the regenerator and the tubing. For simplicity the power required to overcome the mechanical losses is included in the pumping power. The thermodynamic magnetic power is comparatively small and it is already accounted for in $\overline{\dot{W}}_{\mathrm{Mag}}$.

Fig. 6.11 shows in detail the magnetic and pumping contributions to the total power as a function of the cold reservoir temperature, T_{C}, for three different utilization factors (0.28, 0.38 and 0.58) and two operating frequencies (0.5 and 1 Hz). The uncertainties related to the cycle average power are of the order of 5% . An analysis of the results leads to the following conclusions:

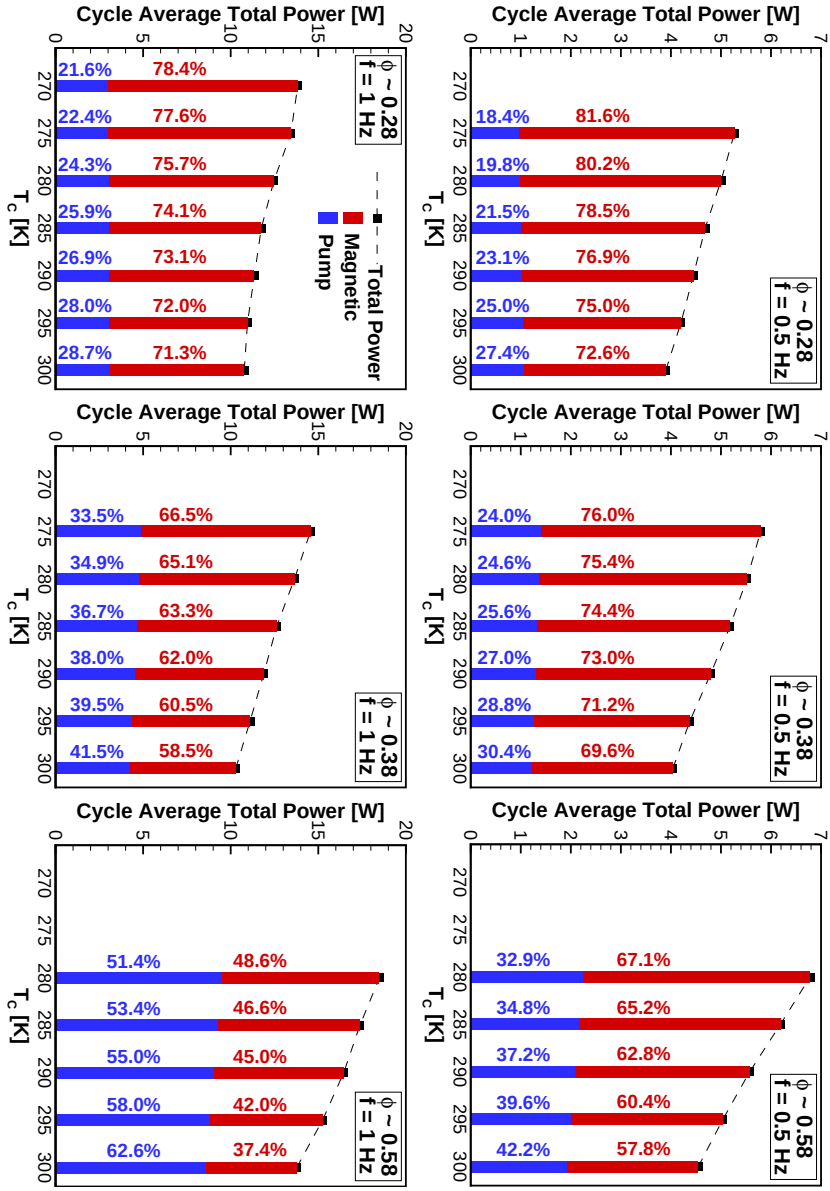

Figure 6.11 – $\overline{\dot{W}}$ as a function of T_C for different utilization factors (0.28, 0.38 and 0.58) and frequencies (0.5 and 1 Hz).

1. As T_C is reduced with the increasing temperature span for $T_H = 300$ K, the cycle average total power increases mainly due to the increase of the magnetic interaction, as the magnetic material becomes more ferromagnetic. Also, a small increase in the pumping contribution is verified, given the increase in fluid viscosity as the fluid becomes colder;

2. By increasing the utilization for a fixed frequency, $\overline{\dot{W}}_{pump}$ becomes higher. For example, for $\phi \approx 0.28$, $f = 0.5$ Hz and $T_C = 280$ K, the contributions of $\overline{\dot{W}}_{Mag}$ and $\overline{\dot{W}}_{pump}$ are 80.2% and 19.8%, respectively. On the other hand, for $\phi \approx 0.58$, $f = 0.5$ Hz and $T_C = 280$ K, the contribution of $\overline{\dot{W}}_{pump}$ is increased to 32.9% and that of $\overline{\dot{W}}_{Mag}$ is reduced to 67.1%. Since T_C and T_H are fixed and the absolute value of $\overline{\dot{W}}_{Mag}$ is about the same, the increase in the total power is due to an increase in $\overline{\dot{W}}_{pump}$ resulting from a larger pressure drop and higher mass flow rate. The same conclusions can be extended to all values of T_C and to the frequency of 1 Hz;

3. By increasing the frequency, the contribution of $\overline{\dot{W}}_{pump}$ is also increased due to the larger pressure drop and higher mass flow rate. For example, for $\phi \approx 0.58$, $f = 0.5$ Hz and $T_C = 280$ K, the contributions of $\overline{\dot{W}}_{Mag}$ and $\overline{\dot{W}}_{pump}$ are 67.1% and 32.9%. However, for $\phi \approx 0.58$, $f = 1$ Hz and $T_C = 280$ K, the contribution of $\overline{\dot{W}}_{pump}$ is increased to 51.4% and that of $\overline{\dot{W}}_{Mag}$ is reduced to 48.6%, taking into account the additional increase in the magnetic circuit torque. Thus, the increase in the total power, when the frequencies of 0.5 Hz and 1 Hz are compared, is mainly due to the increase in $\overline{\dot{W}}_{pump}$. The same conclusions can be extended to all values of T_C and to the other utilizations.

In conclusion, the magnetic interaction contribution is more significant for the smaller values of T_C and ϕ. On the other hand, as the mass flow rate is increased, by changing the utilization or the operating frequency, the pumping power becomes more important and, in some cases, is the main component of the total power.

6.5.1.3 AMR Performance Analysis

The AMR performance analysis is based on the behavior of $\overline{\dot{Q}}_C$, COP and η_{2nd} as a function of ϕ for different lines of constant ΔT_{Hex}, as shown in Figs. 6.12 to 6.14. Separate figures are used for different frequencies, namely 0.25, 0.5 and 1 Hz. For the Spheres #3 bed, ΔT_{Hex} ranges from 5 to 25 K. The main advantage of having ΔT_{Hex} as a parameter in the plots is the existence of a single ideal coefficient of performance, COP_{id}, for each line. This facilitates the interpretation of the results from a thermodynamic efficiency point of view.

It is important to mention that the values of $\overline{\dot{Q}}_C$ that correspond to a given target value of ΔT_{Hex} were evaluated using interpolating functions ($R^2 > 0.99$) of the experimental data shown in the system characteristic curves of Fig. 6.9. The use of the interpolating functions has a negligible influence on the experimental uncertainty discussed in Sections 6.3.1 and 6.4.

In the cooling capacity curves, Fig. 6.12, as the value of ΔT_{Hex} increases, $\overline{\dot{Q}}_C$ decreases and, depending on the target ΔT_{Hex}, it is possible to observe a peak of $\overline{\dot{Q}}_C$ for a given utilization. For $\Delta T_{Hex} = 0$ and 5 K, the peak of $\overline{\dot{Q}}_C$ is outside the experimental utilization range. For safety reasons, at $f = 1$ Hz, it was not possible to perform measurements at the highest utilizations due to the high pressure drop in the regenerator.

Taking the curve for $\Delta T_{Hex} = 10$ K as an example, the following remarks can be made:

- For 0.25 Hz, a peak $\overline{\dot{Q}}_C$ of approximately 9.5 W (48.6 W/kg) is observed in the range $0.8 < \phi < 1$;
- For 0.5 Hz, a peak $\overline{\dot{Q}}_C$ of approximately 16.5 W (84.5 W/kg) is found at $\phi \approx 0.77$;
- For 1 Hz the highest value of $\overline{\dot{Q}}_C$ for $\Delta T_{Hex} = 10$ K is around 29.2 W (149.5 W/kg), and the peak is outside the utilization range.

In terms of the specific cooling capacity (in W/kg) for $\Delta T_{Hex} = 10$ K, the results are on the same order of magnitude as those from other published works, as presented in Table 2.2.

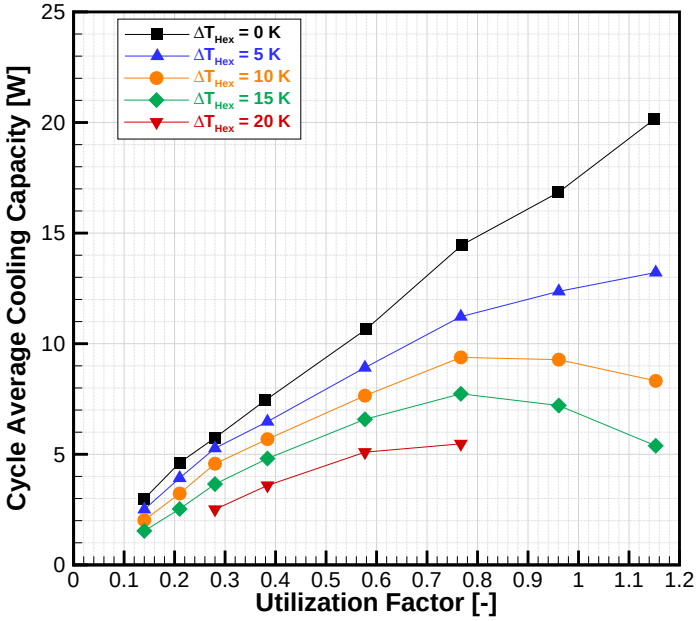
ΔT_Hex = 0 K
ΔT_Hex = 5 K
ΔT_Hex = 10 K
ΔT_Hex = 15 K
ΔT_Hex = 20 K
Cycle Average Cooling Capacity [W]
Utilization Factor [-]
0
5
10
15
20
25
0 0.1 0.2 0.3 0.4 0.5 0.6 0.7 0.8 0.9 1 1.1 1.2

(a)

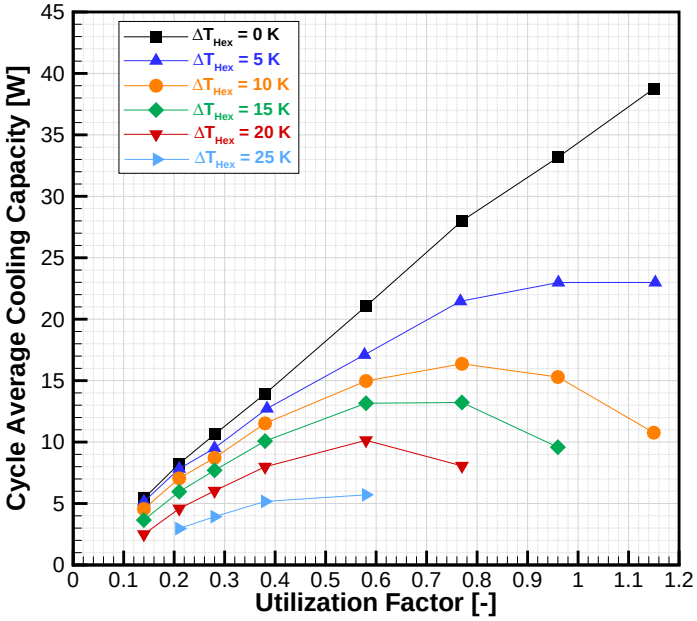
ΔT_Hex = 0 K
ΔT_Hex = 5 K
ΔT_Hex = 10 K
ΔT_Hex = 15 K
ΔT_Hex = 20 K
ΔT_Hex = 25 K
Cycle Average Cooling Capacity [W]
Utilization Factor [-]
0
5
10
15
20
25
30
35
40
45
0 0.1 0.2 0.3 0.4 0.5 0.6 0.7 0.8 0.9 1 1.1 1.2

(b)

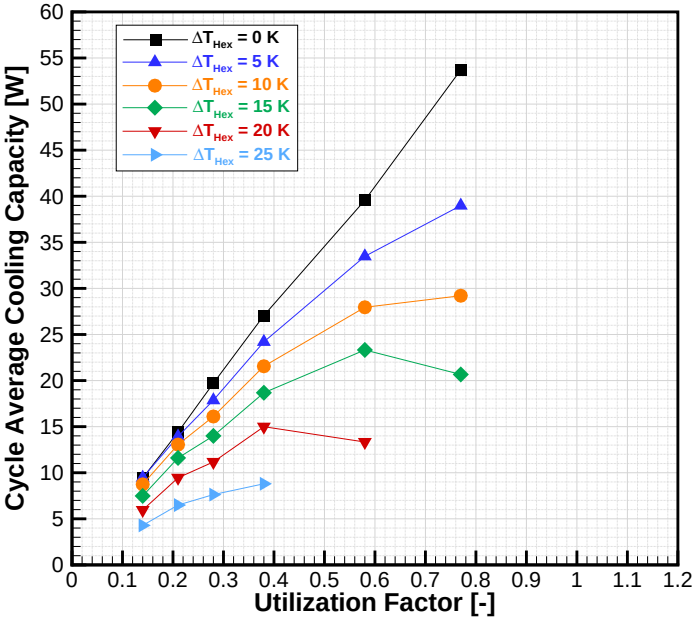

(c)

Figure 6.12 – $\overline{\dot{Q}}_C$ as a function of ϕ for $T_H = 300$ K and different ΔT_{Hex}: (a) $f = 0.25$ Hz; (b) $f = 0.5$ Hz; (c) $f = 1$ Hz.

In the COP curves, Fig. 6.13, COP increases as the T_{Hex} decreases, owing to the reduction of $\overline{\dot{Q}}_C$ (Fig. 6.12) and the increase in $\overline{\dot{W}}$ (Fig. 6.11). As a result, for a fixed T_{Hex}, the COP peaks at a certain utilization. Taking the curve for $\Delta T_{Hex} = 10$ K as an example, the following remarks can be made:

- For 0.25 Hz, a peak COP of approximately 3.4 is observed at $\phi \approx 0.77$;
- For 0.5 Hz, a peak COP of approximately 2.7 is found at $\phi \approx 0.58$;
- For 1 Hz, a peak COP of approximately 1.8 is expected at $0.38 < \phi < 0.58$.

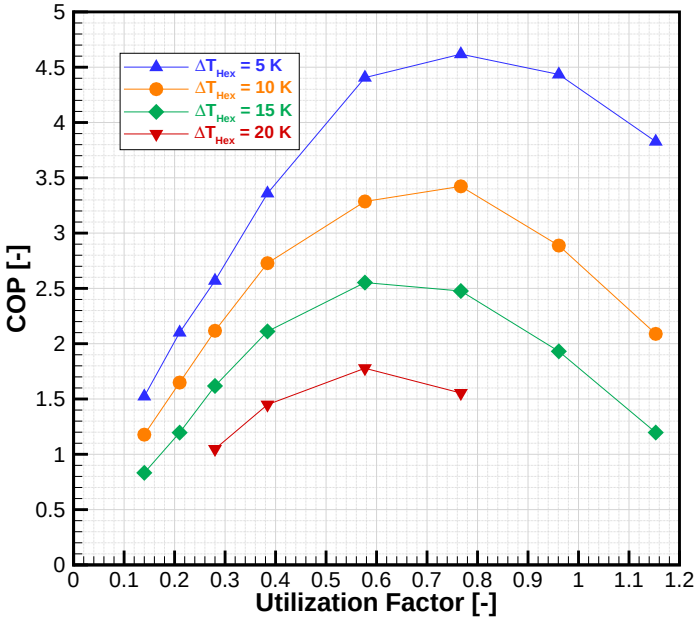
ΔT_Hex = 5 K
ΔT_Hex = 10 K
ΔT_Hex = 15 K
ΔT_Hex = 20 K
COP [-]
Utilization Factor [-]
0
0.5
1
1.5
2
2.5
3
3.5
4
4.5
5
0.1
0.2
0.3
0.4
0.5
0.6
0.7
0.8
0.9
1
1.1
1.2

(a)

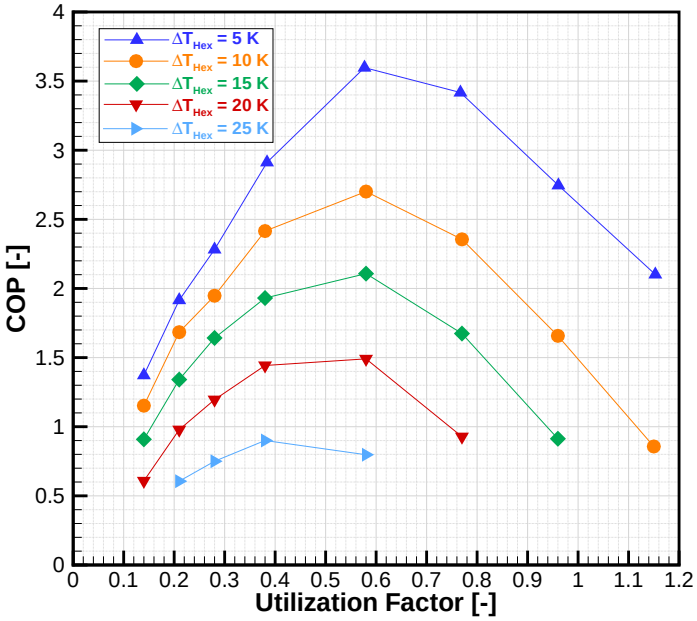
ΔT_Hex = 5 K
ΔT_Hex = 10 K
ΔT_Hex = 15 K
ΔT_Hex = 20 K
ΔT_Hex = 25 K
COP [-]
Utilization Factor [-]
0
0.5
1
1.5
2
2.5
3
3.5
4
0.1
0.2
0.3
0.4
0.5
0.6
0.7
0.8
0.9
1
1.1
1.2

(b)

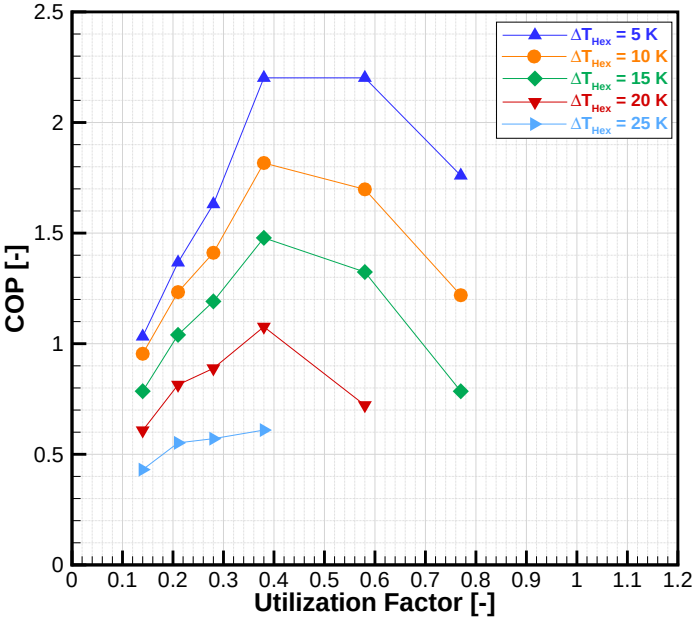

(c)

Figure 6.13 – COP as a function of ϕ for $T_{\mathrm{H}} = 300$ K and different ΔT_{Hex}: (a) $f = 0.25$ Hz; (b) $f = 0.5$ Hz; (c) $f = 1$ Hz.

The smallest frequency presented the highest COP, since $\overline{\dot{W}}$ is directly proportional to the motor frequency. Moreover, as the frequency increases, both $\overline{\dot{Q}}_{\mathrm{C}}$ and $\overline{\dot{W}}$ increase, since the penalties associated with the viscous losses become more significant as the superficial flow velocity is raised, requiring a larger total power to drive the AMR. In terms of the utilization factor, the peaks of the COP and $\overline{\dot{Q}}_{\mathrm{C}}$ do not necessarily coincide, as a result of the steeper increase in $\overline{\dot{W}}$ as ϕ increases. In summary, as ϕ or f increase, the COP becomes more sensitive to the viscous losses.

The behavior of the second-law efficiency with respect to utilization and ΔT_{Hex} is presented in Fig. 6.14. The lines of constant ΔT_{Hex} correspond to fixed values of COP_{id}, which decrease as ΔT_{Hex} increases. From a thermodynamic efficiency standpoint, the best operating conditions for each ΔT_{Hex} are clearly identified for each frequency in Fig. 6.14. Some general quantitative remarks can be made as follows:

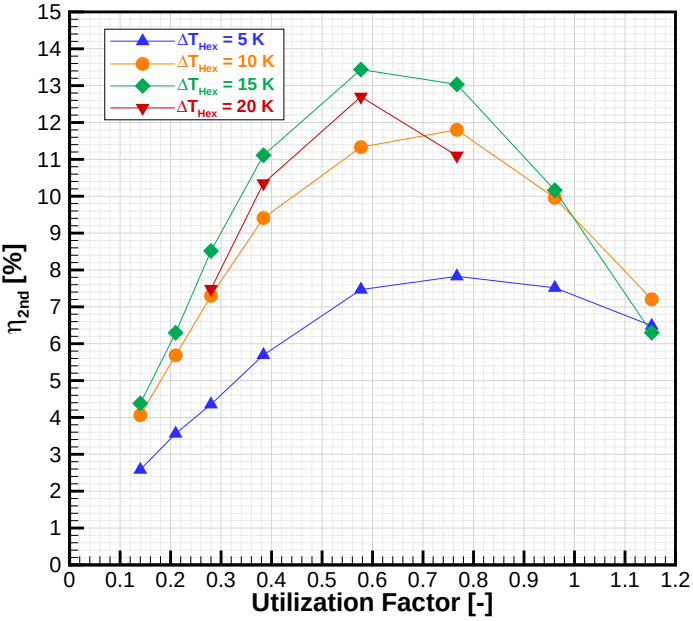
ΔT_Hex = 5 K
ΔT_Hex = 10 K
ΔT_Hex = 15 K
ΔT_Hex = 20 K
η_2nd [%]
Utilization Factor [-]

(a)

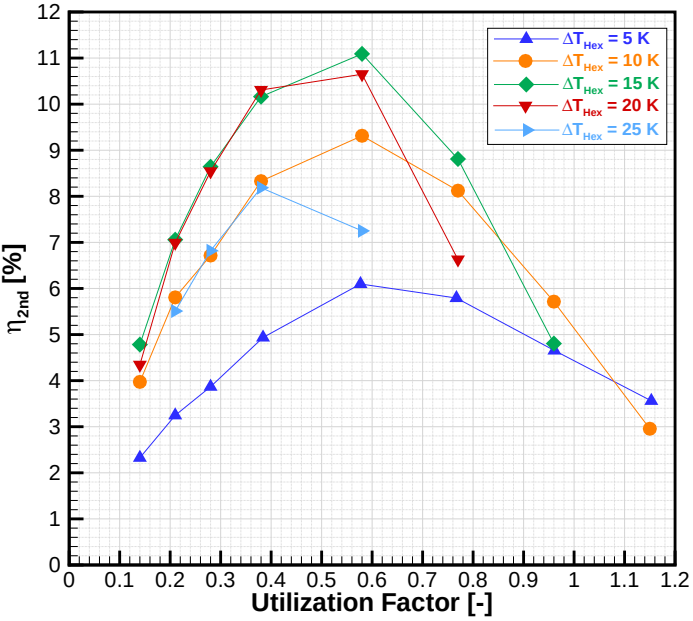
ΔT_Hex = 5 K
ΔT_Hex = 10 K
ΔT_Hex = 15 K
ΔT_Hex = 20 K
ΔT_Hex = 25 K
η_2nd [%]
Utilization Factor [-]

(b)

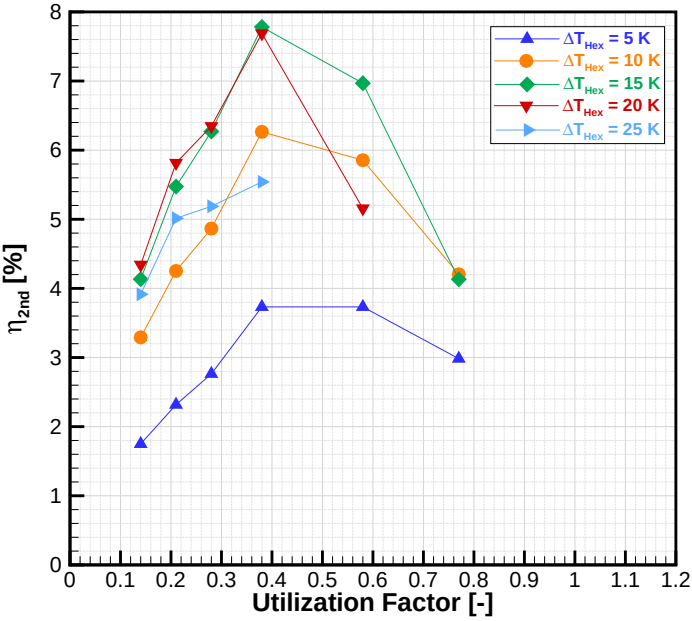

(c)

Figure 6.14 – η_{2nd} as a function of ϕ for $T_H = 300$ K and different ΔT_C: (a) $f = 0.25$ Hz; (b) $f = 0.5$ Hz; (c) $f = 1$ Hz.

- For 0.25 Hz, a peak η_{2nd} of approximately 13% is observed at $\phi \approx 0.58$ for $\Delta T_{Hex} = 15$ and 20 K. For $\Delta T_{Hex} = 15$ K, $\overline{\dot{Q}}_C \approx 7$ W (35.8 W/kg) and $COP \approx 2.5$;
- For 0.5 Hz a peak η_{2nd} of approximately 11% is observed at $\phi \approx 0.58$ for $\Delta T_{Hex} = 15$ and 20 K. For $\Delta T_{Hex} = 15$ K, $\overline{\dot{Q}}_C \approx 13$ W (66.6 W/kg) and $COP \approx 2.1$;
- For 1 Hz a peak η_{2nd} of approximately 7.9% is observed at $\phi \approx 0.38$ for $\Delta T_{Hex} = 15$ and 20 K. For $\Delta T_{Hex} = 15$ K, $\overline{\dot{Q}}_C \approx 19$ W (97.3 W/kg) and $COP \approx 1.5$;

Although peaks in second-law efficiency can be identified for each operating condition, direct comparisons between curves for the same ΔT_{Hex} at different frequencies must be made cautiously, as the cooling capacity is not the same. However, it is clear that the tests with the Spheres

#3 AMR assembled in Casing #3 with 0.55-mm spheres resulted in more thermodynamically efficient conditions for ΔT_{Hex} around 15 and 20 K. For temperature spans smaller than these, although the COP is the highest (see Fig. 6.13), COP_{id} is much higher. For the largest ΔT_{Hex} of 25 K, COP_{id} is lower, but the system COP is already too low due to a combination of a low cooling capacity and a high total power, which increases mainly due to a higher magnetic attraction of the ferromagnetic phase, as seen in Fig. 6.11. At intermediate values of ΔT_{Hex}, the effects are counterbalanced. It should be mentioned that, for a given ΔT_{Hex}, the value of utilization that gives the maximum $\eta_{2\mathrm{nd}}$ also gives the maximum COP. This is because COP_{id} is constant for a given ΔT_{Hex}.

The occurrence of maximum second-law efficiencies for ΔT_{Hex} between 15 and 20 K reflects one of the main limitations of current AMR systems, for which the best performance in terms of $\eta_{2\mathrm{nd}}$ is not compatible with the high cooling capacity/large temperature span operation typical of commercially available cooling systems. On the contrary, (i) for the highest attainable cooling capacities, the temperature span was small and the lowest values of $\eta_{2\mathrm{nd}}$ were found; (ii) for the highest temperature span, both the cooling capacity and the COP were low, which reduced $\eta_{2\mathrm{nd}}$.

Although they are out of the scope of this thesis, some reflections and guidelines to improve the performance of AMR systems equipped with standard magnetocaloric materials are in order, given the experience accumulated in this study:

1. The use of higher operating frequencies increases the cooling capacity, but does not necessarily increase the temperature span. Moreover, it increases the viscous losses. Also, as shown in the results, increasing the motor frequency reduces the system COP. A more appropriate approach would be to increase the AMR frequency keeping a lower motor operating frequency, for example, using a magnetic circuit with 2 or more magnetic poles;

2. The arrangement of regenerators in parallel increases the cooling capacity due to the larger mass of magnetocaloric material and guarantees a continuous cycle. However, this configuration does not increase the temperature span and adds to the complexity of the combined design of the AMR and flow distribution system. Therefore, if this design is not performed carefully, the cooling

system may not perform adequately in terms of COP and ΔT_{Hex};

3. The arrangement of regenerators in series (e.g., cascade) can improve the system temperature span, but does not increase the cooling capacity. In addition, this arrangement usually requires a larger total power to overcome the viscous losses.

Figs. 6.15 and 6.16 present the maximum values of ΔT_{Hex} and $\overline{\dot{Q}}_{\mathrm{C}}$, respectively, as a function of frequency and utilization. The maximum $\overline{\dot{Q}}_{\mathrm{C}}$ was obtained directly for the condition $\Delta T_{\mathrm{Hex}} = 0$. However, the maximum ΔT_{Hex} could not be characterized experimentally because, even when the electrical heater was not in operation, the zero thermal load condition cannot be truly obtained because of the heat gain from the ambient. This way, the maximum ΔT_{Hex} was determined from an extrapolation/interpolation of the system curves (Fig. 6.9). The uncertainty of this extrapolation was estimated at 2 K.

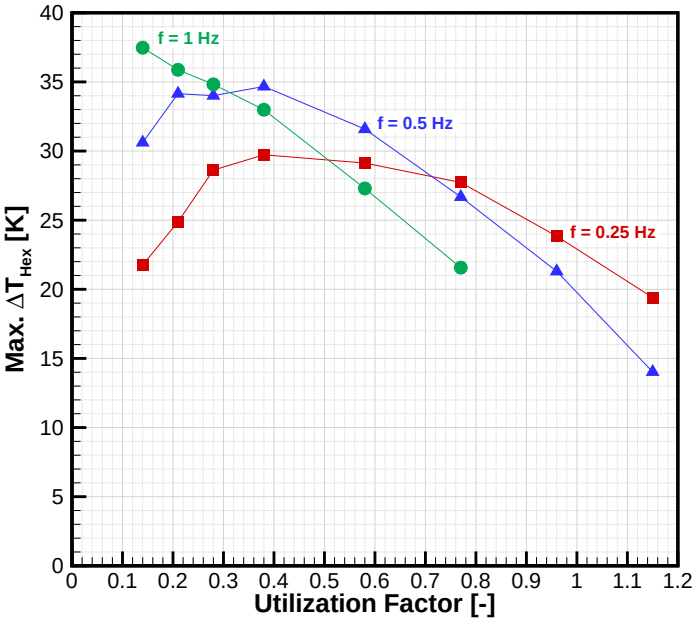

Figure 6.15 – Maximum ΔT_{Hex} as a function of ϕ for $T_{\mathrm{H}} = 300$ K and different operating frequencies.

The results for the maximum ΔT_{Hex} share some of the characteristic

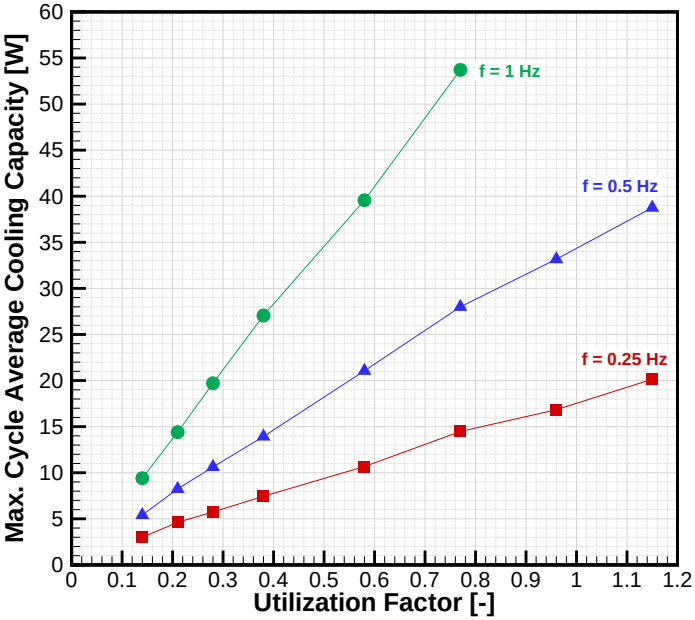

Figure 6.16 – Maximum $\overline{\dot{Q}}_{\mathrm{C}}$ as a function of ϕ for $T_{\mathrm{H}} = 300$ K and different operating frequencies.

trends reported by other authors in the literature (NIELSEN *et al.*, 2009; TUSEK *et al.*, 2011) where, depending on the frequency, a peak can be identified. The following quantitative features can be obtained from Fig. 6.15 as follows:

- For 0.25 Hz, a peak close to 30 K was found at $\phi \approx 0.38$;
- For 0.5 Hz, a peak close to 35 K seems is likely in the range $0.21 < \phi < 0.38$;
- For 1 Hz, no peak was observed and a maximum ΔT_{Hex} of 37.5 K was found at $\phi \approx 0.14$;

Taking the $f = 0.25$ Hz curve as an example, for $\phi > 0.38$, the regenerator effectiveness decreases with the reduction of the NTU due to the increasing mass flow rate, and, as a result, ΔT_{Hex} decreases. On the other hand, for $\phi < 0.38$, the tendency is for the regenerator effectiveness to increase due to the increase in NTU, however, due to

thermal losses, ΔT_{Hex} decreases. In this situation, two types of losses are the most important: (i) the axial heat conduction that reduces the regenerator effectiveness at small values of utilizations, as discussed in Chapter 5; (ii) the casing heat gain. As will be shown in Section 6.5.2, the casing heat gain is the most significant thermal loss at low frequencies, because the AMR cooling capacity is usually small. As the frequency increases, the peak of ΔT_{Hex} is shifted to small values of ϕ because, the magnitude of the axial heat conduction is reduced and, as the AMR cooling capacity increases, the relative importance of the casing heat gain decreases.

Regarding the behavior of the maximum $\overline{\dot{Q}}_{\mathrm{C}}$, it increases with the utilization for all frequencies and the peaks, if any, are out of the utilization range. In this case, the axial heat conduction is negligible and the casing heat gain is very small. However, as will be explained in detail in Section 6.5.2, the void volume has an important influence on the maximum cooling load. The maximum cooling capacities were obtained at the highest utilizations tested. For each frequency, namely, 0.25, 0.5 and 1 Hz, these were equal to 20.1, 38.8 and 53.7 W, respectively. The corresponding specific cooling capacities were equal to 103, 198.7 and 275 W/kg, respectively.

6.5.2 Numerical Results and Losses Analyses

This section will present and discuss the numerical results for the Spheres #3 AMR. Simulations were performed with and without the terms responsible for the different types of losses in the numerical model, for the same ranges of frequency, utilization and ΔT_{Hex} explored in the experiments. It is worth mentioning that the simulations labeled as without losses already take into account the axial heat conduction, viscous dissipation and the demagnetization losses, as these are intrinsic to AMR regenerators. To be consistent with the experiments, in the simulations including losses, $T_{\mathrm{Amb}} = T_{\mathrm{Mag}} = T_{\mathrm{H}} = 300$ K. More specifically, the following loss terms are considered:

1. Casing heat gain (CHG): this loss corresponds to the heat transfer from the external environment (i.e., the magnetic circuit) to the regenerative matrix;

2. Non-uniformity of the magnetic field (MF): this loss corresponds to non-uniformities (i.e., density reductions) of the axial profile

of the magnetic flux density due to edge effects in the magnetic circuit. The axial profile of the magnetic flux density was experimentally characterized and was presented in Fig. 3.12(b);

3. Void volume (VV): these are leakage losses, already discussed in detail in Chapter 5, in the context of passive regenerators. Similar effects are expected here.

Fig. 6.17 shows a comparison between the numerical results and experimental data for $\overline{\dot{Q}}_{\mathrm{C}}$ as a function of ΔT_{Hex} for different values of utilization (0.38, 0.58 and 0.77) and frequency (0.25, 0.5 and 1 Hz). The numerical simulations were performed considering: (i) no losses; (ii) with CHG loss; (iii) with CHG+MF losses; (iv) with CHG+MF+VV losses. This enables the evaluation of the impact of each loss on the AMR performance and, clearly, as the losses are included in the simulation, the numerical results get closer to the experimental data, showing a very good agreement for all the operating conditions.

The model without losses over-predict the data for virtually all conditions, with the deviations increasing with the increase of ΔT_{Hex}, as the zero thermal load conditions are approached. These deviations can be justified based on the thermal losses in the AMR, especially the casing heat gain. A first remark in support of the casing heat gain as the main thermal loss in an AMR system is the behavior near the point of maximum cooling capacity, at which the no-loss model results and the experimental data are very close. At this condition, $\Delta T_{\mathrm{Hex}} \approx 0$ K (i.e., $T_{\mathrm{Amb}} \approx T_{\mathrm{H}} \approx T_{\mathrm{C}}$), thus, the casing heat gain is small and its influence on the $\overline{\dot{Q}}_{\mathrm{C}}$ is negligible.

When the casing heat gain is included in the simulations, the numerical results in Fig. 6.17 show an impressive reduction of the AMR performance curve, especially near the maximum temperature span. For example, for $\phi \approx 0.38$ and $f = 0.25$ Hz, a reduction of approximately 13 K is observed for ΔT_{Hex} at zero load. In addition, the following observations can be made regarding the simulations including the CHG thermal loss:

- For a fixed frequency, as the utilization factor is increased, the impact of the CHG on the $\overline{\dot{Q}}_{\mathrm{C}}$ *vs.* ΔT_{Hex} curves is reduced. For example, for $\phi \approx 0.77$ and $f = 0.25$ Hz, the no-loss maximum ΔT_{Hex} is 37 K and, considering the CHG loss, the maximum ΔT_{Hex} is close to 30 K, i.e., a reduction of 7 K;

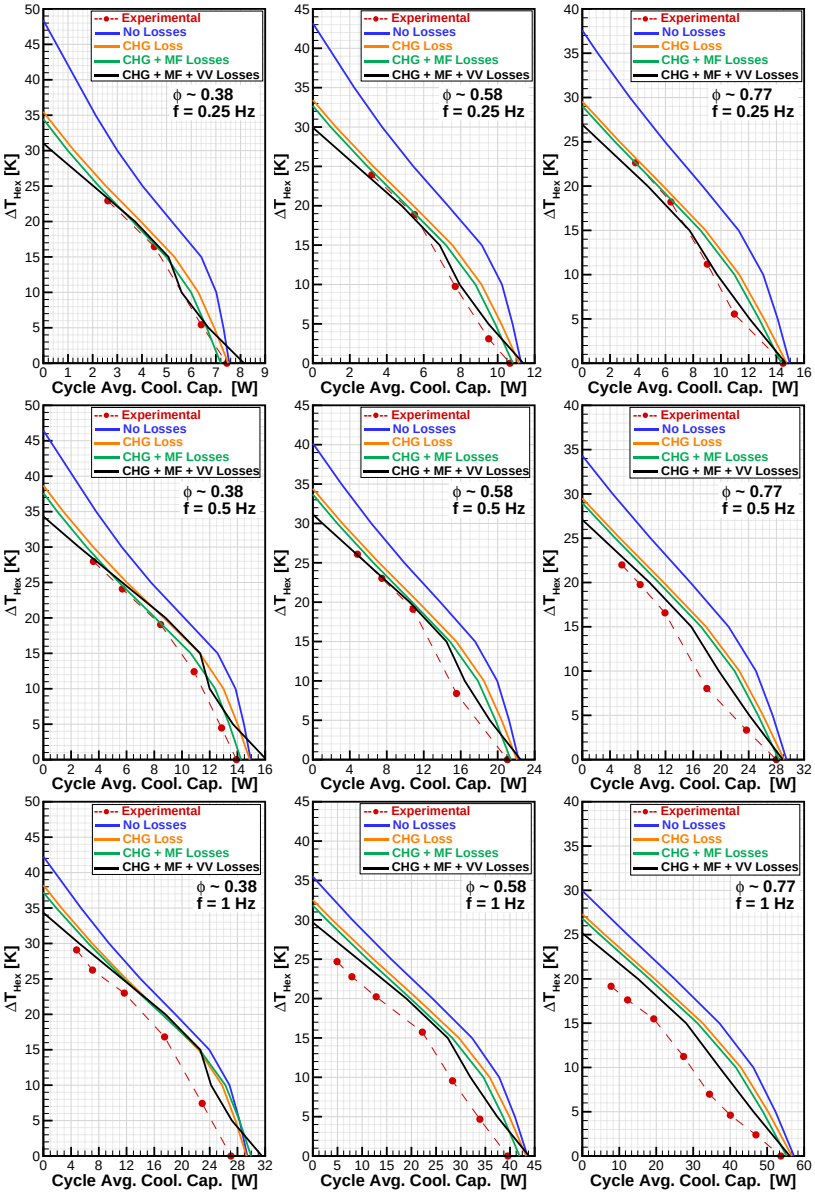

Figure 6.17 – Comparison between the numerical model and experimental data for $\overline{\dot{Q}}_{\mathrm{C}}$ as a function of ΔT_{Hex} for different values of utilization and frequency, considering different types of losses.

- For a fixed utilization (e.g., $\phi \approx 0.38$), increasing the frequency also reduces the impact of the CHG on the $\overline{\dot{Q}}_{\mathrm{C}}$ *vs.* ΔT_{Hex} curves. For example, for $\phi \approx 0.38$ and $f = 1$ Hz, the no loss maximum ΔT_{Hex} is 42 K and, considering the CHG loss, the maximum ΔT_{Hex} is close to 38 K, representing a reduction of 4 K.

To substantiate this analysis, Fig. 6.18 shows the cycle average casing heat gain for the discrete finite volumes, i.e., volume 1 to volume 200, along the axial direction. Fig. 6.18(a) shows the results for different values of ΔT_{Hex} for $\phi \approx 0.38$ and $f = 0.25$ Hz. Fig. 6.18(b) shows the effect of the operating frequency for $\phi \approx 0.38$ and $\Delta T_{\mathrm{Hex}} = 25$ K. At last, Fig. 6.18(c) shows the influence of the utilization factor for $\Delta T_{\mathrm{Hex}} = 25$ K and $f = 0.25$ Hz.

In Fig. 6.18, volume 1 is close to the regenerator hot end and volume 200 is next to the cold end. In the simulations, the magnetic circuit was assumed to be in thermal equilibrium with the ambient at 300 K, which is the temperature of the hot reservoir. As a result, the volumes closer to the hot end present a negative heat gain. In other words, this portion of the regenerator is at a higher temperature than the magnetic circuit (remember that $T_{\mathrm{HE}} > T_{\mathrm{H}}$), and the AMR transfers heat to the Halbach magnets. As the regenerator becomes colder, the heat gain increases up to a maximum at the cold end. These results show how important it was to be strict about the thermal equilibrium condition of $T_{\mathrm{Amb}} = T_{\mathrm{Mag}} = T_{\mathrm{H}}$ discussed in Section 6.1, so that the CHG always reduces the AMR performance, which is a more realistic condition in terms of applications of cooling systems.

Considering a single finite volume, at a given time-step, the CHG is responsible for a small amount of heat being added to the energy balance, whose main effects can be summarized as follows:

- During the hot period of the cycle (i.e., magnetization and cold blow) the amount of heat entering the colder part of the regenerator is combined with the positive MCE and the enthalpy fluxes (in and out), resulting in a new thermal condition. Part of the CHG modifies the temperature profiles at the end of the hot period, and the remainder is released at the hot reservoir and in the hotter part of the regenerator;
- During the cold period of the cycle (i.e., demagnetization and hot blow) the MCE is negative. Thus, a fraction of the MCE is

consumed by the CHG. This, together with the enthalpy fluxes, yields a new thermal condition in the volume. As a result, the cooling capacity decreases, as part of the refrigerating effect is counterbalanced by the heat gained from the external environment.

In Fig. 6.18(a), for fixed values of utilization and frequency, by increasing ΔT_{Hex}, the casing heat gain in a given volume increased. In terms of the cycle-average cooling capacity, Table 6.1 shows the reduction of $\overline{\dot{Q}}_{\text{C}}$ as ΔT_{Hex} increases. For $\Delta T_{\text{Hex}} = 25$ K, the reduction in $\overline{\dot{Q}}_{\text{C}}$ was 1.49 W, which represented 37% of the AMR potential (no loss) cooling capacity.

Table 6.1 – Impact of the casing heat gain on the cycle average cooling capacity for different values of ΔT_{Hex}, for $\phi \approx 0.38$ and $f = 0.25$ Hz.

ΔT_{Hex} [K]	No losses [W]	CHG [W]	Variation [W]
5	7.31	6.93	0.37 (5.1%)
15	6.41	5.32	1.09 (17.0%)
25	4.03	2.54	1.49 (37.0%)

In Fig. 6.18(b), by increasing the operating frequency, for fixed values of utilization and ΔT_{Hex}, the casing heat gain in a given volume increases. As discussed in Chapter 5, since the regenerator temperature profiles did not have substantial variations with frequency, in this case, the change in the total casing heat gain is quite small, which is related to the increasing wall heat transfer coefficient with frequency (see Section 4.3.6). In terms of the cycle average cooling capacity, presented in Table 6.2, increasing the frequency causes a reduction of the percentage decrease in $\overline{\dot{Q}}_{\text{C}}$ compared with the no-loss cooling capacity.

Table 6.2 – Impact of the casing heat gain on the cycle average cooling capacity for different values of f, for $\phi \approx 0.38$ and ΔT_{Hex} of 25 K.

f [Hz]	No losses [W]	CHG [W]	Variation [W]
0.25	4.03	2.54	1.49 (37.0%)
0.5	7.76	6.02	1.74 (22.4%)
1	14.02	11.92	2.09 (14.9%)

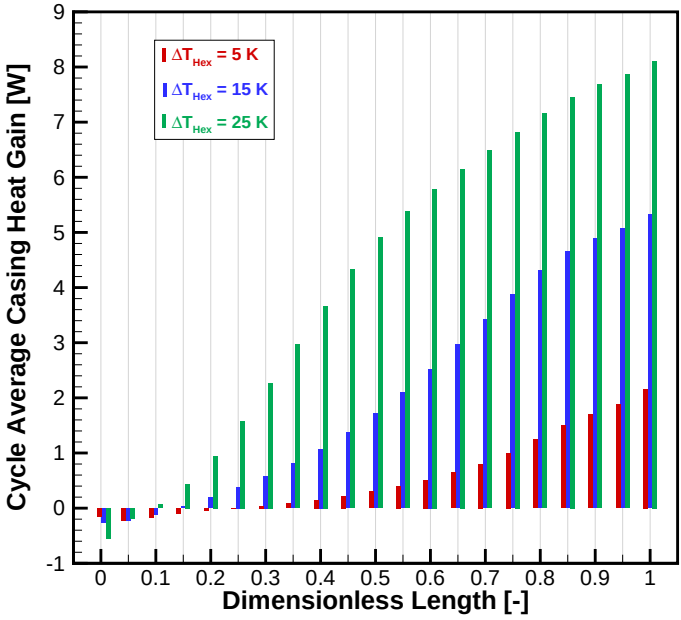
ΔT_Hex = 5 K
ΔT_Hex = 15 K
ΔT_Hex = 25 K
Cycle Average Casing Heat Gain [W]
Dimensionless Length [-]
9
8
7
6
5
4
3
2
1
0
-1
0
0.1
0.2
0.3
0.4
0.5
0.6
0.7
0.8
0.9
1

(a)

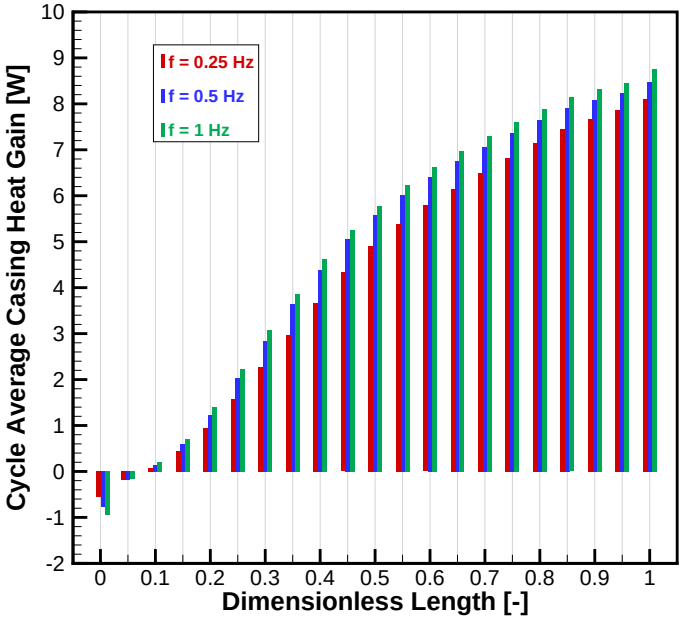
f = 0.25 Hz
f = 0.5 Hz
f = 1 Hz
Cycle Average Casing Heat Gain [W]
Dimensionless Length [-]
10
9
8
7
6
5
4
3
2
1
0
-1
-2
0
0.1
0.2
0.3
0.4
0.5
0.6
0.7
0.8
0.9
1

(b)

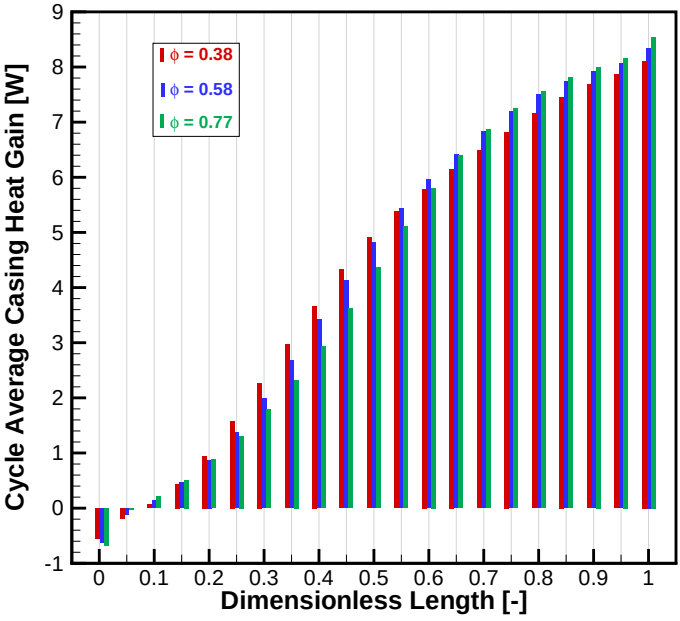

(c)

Figure 6.18 – Cycle average casing heat gain at different regenerator positions (finite volumes) for: (a) Different ΔT_{Hex} for $\phi \approx 0.38$ and $f = 0.25$ Hz; (b) Different operating frequencies for $\phi \approx 0.38$ and $\Delta T_{\text{Hex}} = 25$ K; (c) Different utilization factors for $f = 0.25$ Hz and $\Delta T_{\text{Hex}} = 25$ K.

Increasing the utilization factor for a fixed frequency and ΔT_{Hex}, Fig. 6.18(c), causes a somewhat different effect on the casing heat gain in a given volume. In this case, as ϕ increases and the effectiveness decreases, different temperature profiles are established along the regenerator. As a result, the local heat gain presents a high dependence on the local temperature difference (at each finite volume) and on the increasing heat transfer coefficient due to the higher mass flow rate. In turn, the cycle average cooling capacity, presented in Table 6.3, showed that increasing ϕ increases the penalties with respect to the no loss cooling capacity.

All the results and discussions presented above clearly show that the casing heat gain changes the local thermal equilibrium along the regenerative matrix and reduces the refrigerating effect of the AMR.

Table 6.3 – Impact of the casing heat gain on the cycle average cooling capacity for different values of ϕ, for $f = 0.25$ Hz and ΔT_{Hex} of 25 K.

ϕ [-]	No losses [W]	CHG [W]	Variation [W]
0.38	4.03	2.54	1.49 (37.0%)
0.58	5.44	3.27	2.17 (39.9%)
0.77	5.96	2.70	3.27 (54.8%)

Therefore, in cases where the cooling capacity is small, i.e., for low utilization factors and low frequencies, the penalties associated with the casing heat gain are more pronounced because the magnetic refrigerating effect required to counterbalance the casing heat gain is on the same order of the cooling capacity, especially for large ΔT_{Hex}.

This discussion supports the differences observed in the maximum temperature span between the model without losses and the experimental data. Considering $f = 0.25$ Hz and $\phi \approx 0.38$, while the experiments gave the smallest maximum ΔT_{Hex}, Fig. 6.15, the zero-loss model gave the highest maximum ΔT_{Hex} for all conditions, Fig. 6.17. However, when the casing heat gain is included in the simulations, a reduction of the potential cooling capacity of the order of 3 W is already sufficient to reduce the maximum temperature span to 35 K, as shown in Fig. 6.17.

When the non-uniformity in the magnetic field (MF) is incorporated in the model (CHG+MF losses), the local magnetic field is reduced, which causes an almost uniform decrease in the characteristic curves. The consideration of an axial magnetic flux density profile is important for the local demagnetization loss, which depends on the applied magnetic flux density and the local temperature of the regenerator matrix.

Finally, the inclusion of the void volume (VV) losses modifies even further the trends of the $\overline{\dot{Q}}_{\text{C}}$ *vs.* ΔT_{Hex} curves, improving considerably the prediction of the experimental results. The following remarks can be made based on an analysis of the results considering the CHG+MF+VV losses in Fig. 6.17:

1. For $\Delta T_{\text{Hex}} > 15$ K, the characteristic curves exhibit a fairly linear trend, but with a different inclination in comparison with the simulated cases in which the VV was not included;

2. For $\Delta T_{\text{Hex}} < 15$ K, all characteristic curves show a clear deviation from the linear trend;

3. For $\Delta T_{\mathrm{Hex}} = 0$, the numerical results with the CHG+MF+VV losses gave higher values of the maximum $\overline{\dot{Q}}_{\mathrm{C}}$.

To facilitate the interpretation of the points explained above, Fig. 6.19 presents a comparison between the numerical results and the experimental data for the time-dependent temperatures at the hot and cold ends for different operating conditions. Fig. 6.19(a) shows results for different ΔT_{Hex} and Fig. 6.19(b) for $\Delta T_{\mathrm{Hex}} \approx 0$. The following remarks can be made:

1. The AMR model showed good predictions of the time-dependent temperatures at the hot and cold ends;

2. Comparing the experimental and numerical results for T_{HE} and T_{CE}, it is clearly seen that they are not symmetric, i.e., the peak of T_{HE} has a smooth round shape, while T_{CE} has a sharp valley. This behavior is caused by the angular (or time) dependence of the magnetic flux density in Nested Halbach cylinders (see Figs 3.10 and 3.15). During the hot cycle ($0 \leq t^* \leq 180^{\mathrm{o}}$) the magnetic flux density varies smoothly and during the cold cycle ($180^{\mathrm{o}} \leq angle \leq 360^{\mathrm{o}}$) a sharp change is observed. The MCE resulting from this magnetic field variation clearly has an impact on the temperature of the fluid leaving the regenerator bed at T_{HE} and T_{CE};

3. The discontinuities caused by the void volume on the time-dependent temperature are clearly visible, such as for T_{CE} at $t^* \approx 0$.

As in passive regenerators, the existence of void volumes on each side of the AMR alters the temperature boundary conditions of the regenerator thermal balance. However, contrary to the passive regenerator case, the void volume influence on the temperature boundary conditions can sometimes improve the AMR performance.

To explain how the void volume influences the AMR performance, it is necessary to understand the behavior of the T_{C} data (green open square symbols) in Fig. 6.19. If the values of T_{CE} corresponding to the fluid trapped in the void volume are below T_{C}, then the fluid returns to the regenerator at a temperature lower than that of the cold reservoir.

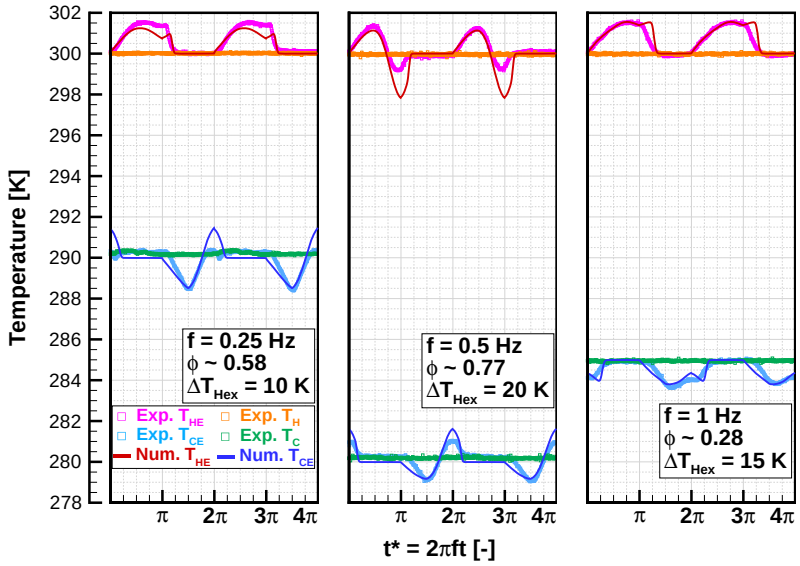

(a)

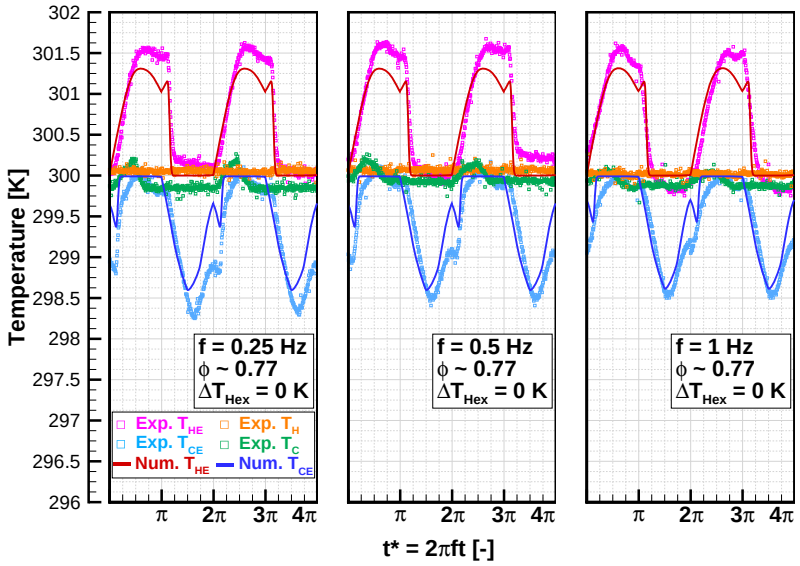

(b)

Figure 6.19 – Comparison between the numerical results and experimental data for the time-dependent temperatures at different operating conditions: (a) Different ΔT_{Hex}; (b) $\Delta T_{\mathrm{Hex}} \approx 0$.

As a result, it helps to cool down the matrix during the cold blow. This was the case for the maximum $\overline{\dot{Q}}_{\mathrm{C}}$ conditions shown in Fig. 6.19(b), which explains the improvement of the maximum $\overline{\dot{Q}}_{\mathrm{C}}$ observed when the void volume is included in the simulations.

On the other hand, if the values of T_{CE} corresponding to the fluid trapped in the void volume are above T_{C}, as in some cases of Fig. 6.19(a), the fluid that returns to the regenerator is warmer than the cold reservoir, which reduces the cooling capacity of the AMR. This explains the reduction of the maximum ΔT_{Hex} when the void volume was included on the simulations. The intermediate points of the $\overline{\dot{Q}}_{\mathrm{C}}$ *vs.* ΔT_{Hex} curves can represent one of these two situations. However, it should be noted that the temperature of the fluid exiting the regenerator is extremely dependent on the void volume size, operating parameters, thermophysical and magnetocaloric properties of the regenerative material, and regenerator effectiveness.

Fig. 6.20 presents a comparison between the numerical results including the CHG+MF+VV losses and the experimental data for $\overline{\dot{Q}}_{\mathrm{C}}$ as a function of ϕ and ΔT_{Hex}. Each plot corresponds to a different frequency. The following remarks can be made:

1. For $f = 0.25$ Hz, the numerical results are in very good agreement with the experimental data for all values of utilization. A maximum deviation of 3 W was found for the largest value of utilization;

2. For $f = 0.5$ and 1 Hz, the numerical results reproduced the experimental trends quite well. However, for some values of ΔT_{Hex}, the model overestimates the experimental cooling capacity, for which a maximum deviation of 9 W was observed at high values of utilization;

3. For some ΔT_{Hex} at the smallest utilizations, especially for $f = 0.5$ and 1 Hz, the numerical results overestimated the cooling capacity by as much as 10 W;

4. The model predicted quite accurately the maximum values of $\overline{\dot{Q}}_{\mathrm{C}}$ at $\Delta T_{\mathrm{Hex}} = 0$.

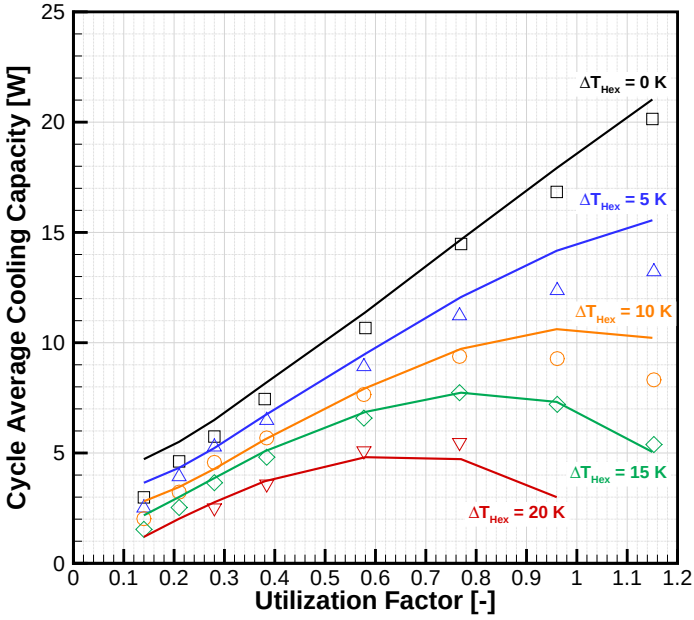
Cycle Average Cooling Capacity [W]
Utilization Factor [-]
ΔT_Hex = 0 K
ΔT_Hex = 5 K
ΔT_Hex = 10 K
ΔT_Hex = 15 K
ΔT_Hex = 20 K

(a)

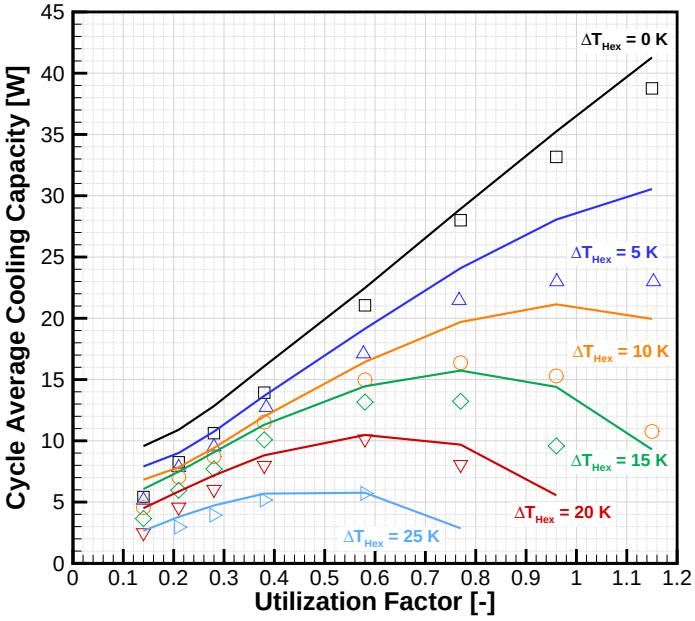
Cycle Average Cooling Capacity [W]
Utilization Factor [-]
ΔT_Hex = 0 K
ΔT_Hex = 5 K
ΔT_Hex = 10 K
ΔT_Hex = 15 K
ΔT_Hex = 20 K
ΔT_Hex = 25 K

(b)

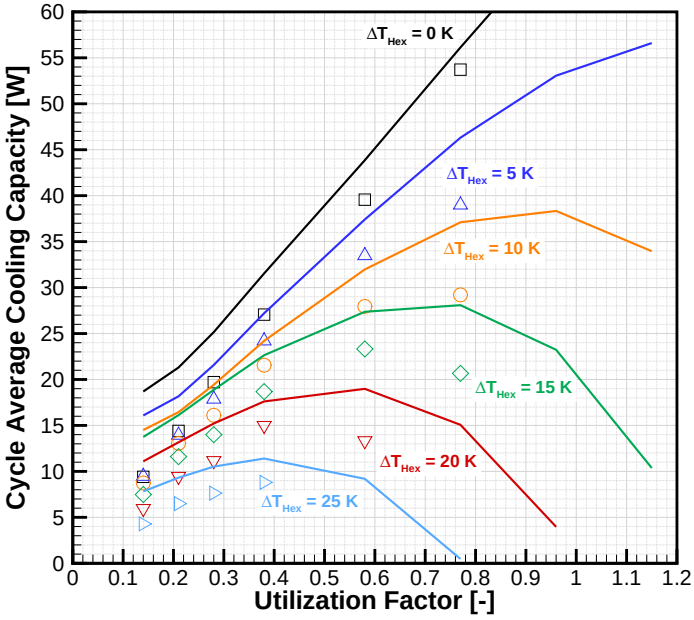

(c)

Figure 6.20 – Numerical results (solid lines) and experimental data (open symbols) for $\overline{\dot{Q}}_C$ as a function of ϕ for $T_H = 300$ K and different ΔT_{Hex}: (a) $f = 0.25$ Hz; (b) $f = 0.5$ Hz; (c) $f = 1$ Hz.

Regarding item 2, the largest differences between the model and the data was observed for $\Delta T_{Hex} = 10$ and 15 K. This is exactly the region where the void volume has a major impact on the AMR performance and the $\overline{\dot{Q}}_C$ *vs.* ΔT_{Hex} curves deviate from their linear behavior (see Fig. 6.17). Possibly, if the experimental tests were performed with a better resolution, i.e., using smaller cooling capacity steps in the region $5 < \Delta T_{Hex} < 15$ K, the agreement could be improved.

Regarding item 3, this corresponds to the same operating condition in the passive regenerator tests in which a no flow period was verified for smallest pumped volumes (see Sections 5.1.2 and 5.4). However, contrary to what has been observed for passive regenerators results, in the AMR tests a smaller mass flow rate reduces the cooling capacity, which explains the over prediction of the numerical results.

Fig. 6.21 shows comparisons between the experimental data and numerical results for the maximum ΔT_{Hex} as a function of ϕ for the three frequencies. The numerical results are presented for two situations: (i) without losses and (ii) with the CHG+MF+VV losses. As mentioned in Section 6.5.1.3, it is quite common in the literature to attribute the reduction of the maximum ΔT_{Hex} at small ϕ to axial heat conduction in the matrix (NIELSEN *et al.*, 2011; TUSEK *et al.*, 2011). However, the model without losses already takes into account axial heat conduction in the fluid and solid phases. As can be seen, the no-loss numerical results severely overestimate the experimental data. Clearly, the dependence of the maximum ΔT_{Hex} on the utilization factor results from a combination of different losses in the AMR, axial heat conduction being one of them. The incorporation of the casing heat gain, magnetic flux density non-uniformity and void volume losses improves significant the prediction of the experimental data for ΔT_{Hex} as a function of the utilization factor. An analysis of the numerical results revealed that the casing heat gain was the main contributing factor to the reduction of the AMR performance in the present experiments. Based on the analysis presented in this section, the following recommendations can be made regarding the design of AMR systems:

1. A systematic evaluation/quantification of the thermal-hydraulic and magnetic losses is a powerful tool to improve AMR design;

2. The inclusion of the different types of losses in numerical models for AMR systems is of paramount importance. Without them, a robust and reliable analysis of the results is not possible;

3. The thermal insulation of the AMR is an important additional parameter to be taken into account in the design and evaluation of AMRs. This way, possible design strategies could involve the optimization of the AMR cross sectional area together with the thermal insulation thickness, so that the reduction of the sectional area can be compensated by a better thermal insulation of the regenerator assembly.

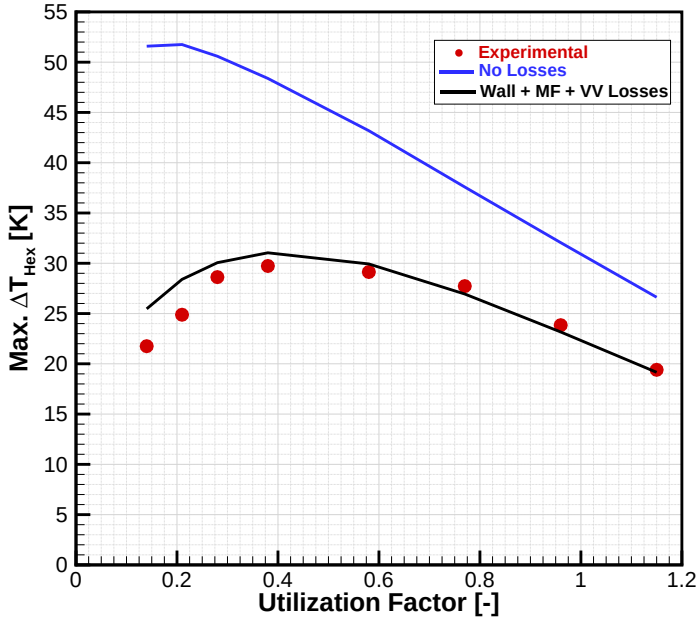
Experimental
No Losses
Wall + MF + VV Losses
Max. ΔT_Hex [K]
Utilization Factor [-]
0
5
10
15
20
25
30
35
40
45
50
55
0
0.2
0.4
0.6
0.8
1
1.2

(a)

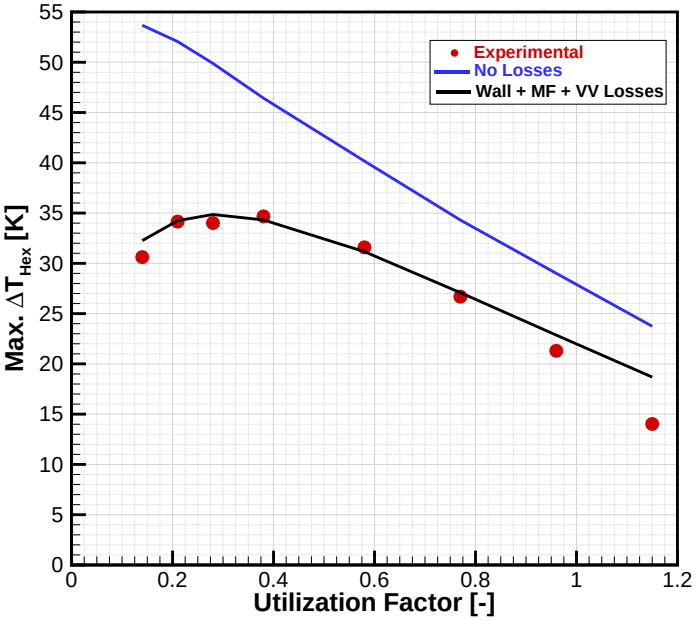
Experimental
No Losses
Wall + MF + VV Losses
Max. ΔT_Hex [K]
Utilization Factor [-]
0
5
10
15
20
25
30
35
40
45
50
55
0
0.2
0.4
0.6
0.8
1
1.2

(b)

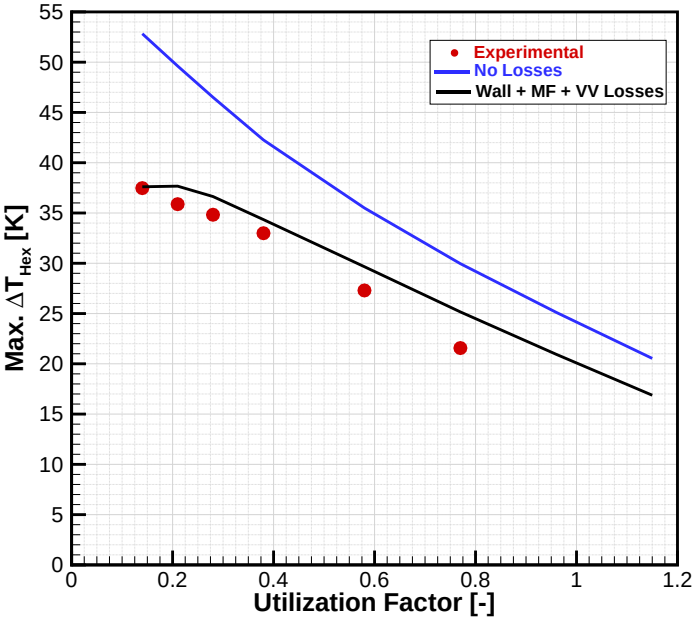

(c)

Figure 6.21 – Numerical results (solid lines) and experimental data (symbols) for ΔT_{Hex} as a function of ϕ for $T_{\mathrm{H}} = 300$ K: (a) $f = 0.25$ Hz; (b) $f = 0.5$ Hz; (c) $f = 1$ Hz.

6.6 Performance Assessment of Different Matrix Geometries

This section presents comparisons of the AMR performance for three Gd matrices: (i) Spheres #4, which consists of a packed bed of 0.78-mm Gd spheres assembled in Casing #4, (ii) Plates #5 and (iii) Pins #6. The geometric properties and characteristics of these matrices are presented in Table 3.9. The performance analysis is based on the behavior of $\dot{Q}_{\mathrm{C}}$, COP and $\eta_{2\mathrm{nd}}$ as a function of ϕ for different values of ΔT_{Hex}. In the present analysis, ΔT_{Hex} was varied from 3 to 18 K, in steps of 3 K. As in the experimental analysis for the Spheres #3 matrix, interpolating functions were used to transform the characteristic curves into curves of $\dot{Q}_{\mathrm{C}}$ as a function of ϕ, having ΔT_{Hex} as a parameter.

The experimental uncertainties associated with the measurements in all geometries evaluated in this section are similar to those for the Spheres #3 tests.

As in the passive regenerator experiments, the three matrix geometries have approximately the same equivalent particle diameter and porosity. The results for the cooling capacity as a function of utilization for $f =$ 0.25, 0.5 and 1 Hz, are shown in Figs. 6.22 to Fig. 6.24. Figs. 6.25 to Fig. 6.27 show the results for the COP as a function of ϕ for $f =$ 0.25, 0.5 and 1 Hz. Figs. 6.28 to 6.30 present the results for $\eta_{2\text{nd}}$ as a function of ϕ for $f = 0.25$, 0.5 and 1 Hz.

Before starting the performance analysis, it is important to mention that, since the void volume size is about the same for the three regenerators, its impact on the AMR performance comparison can be disregarded. Also, the gadolinium used to manufacture the spheres and the pins and plates came from different suppliers, and there is no information regarding the purity or the magnetocaloric properties of the samples. Thus, the performance analysis does not take into account any difference regarding the MCE of the samples. Therefore, the following comparisons take into consideration the effectiveness of the regenerative matrix, the demagnetization factor and the casing heat gain.

The parameters associated with the demagnetization factor, namely $N_{\text{D,geo}}$, $N_{\text{D,csg}}$ and N_{D} (see Eq. (4.49)) are presented in Table 6.4. Although a single plate or pin presents a much smaller $N_{\text{D,geo}}$ compared with a single sphere, the value of $N_{\text{D,csg}}$ counterbalances the overall demagnetization factor. As a result, the difference between the maximum and minimum N_{D} is of the order of 0.11, with the pin array presenting the lowest overall demagnetizing factor.

Table 6.4 – Demagnetizing factors for the different AMR matrices.

Matrix	$N_{\text{D,geo}}$ [-]	$N_{\text{D,csg}}$ [-]	N_{D} [-]
Spheres #4	0.330	0.466	0.417
Pins	0.020	0.470	0.302
Plates	0.033	0.470	0.313

The cooling capacity results in Figs. 6.22 to Fig. 6.24 reveal that, for all operating frequencies, the parallel plate AMR presented a poorer performance when compared with the remaining geometries. Only at the smallest utilization $\overline{\dot{Q}}_{\text{C}}$ for this geometry was comparable to the

results for pins and spheres, which is consistent with the thermal effectiveness results for the passive geometries shown in Section 5.3.4. Since the demagnetization factor for the plate geometry is smaller than for the packed bed of spheres and very close to that for the pin array, the poorer AMR performance cannot be attributed to magnetic losses, so the casing heat gain appears to be the main contributing factor to the comparatively low cycle-average cooling capacity. In the plate geometry, there is a large fraction of the matrix area in direct contact with the ABS casing, i.e., the two sides and the continuous base. This certainly contributes a lot to increasing the casing heat gain.

The pin and packed sphere matrices exhibited similar cooling capacity performances. For a fixed ΔT_{Hex}, the packed bed has a slightly higher cooling capacity, especially for $f = 1$ Hz. This is also in agreement with the passive regenerator effectiveness results. On the other hand, since the pin array has a smaller demagnetizing factor than the packed bed, it may be that the heat gain is higher in the pin array matrix than in the packed bed. As in the plate matrix, the pin array also has a continuous base in contact with the ABS housing, which can increase the heat gain. Somehow, the demagnetizing field and the casing heat gain effects counterbalance each other, and both geometries present similar performances curves. Only for $f = 1$ Hz, it seems that the casing heat gain for the pins is higher than the effect of the demagnetizing field for the packed bed, which seems to agree with the discussion in Section 6.5.2.

Before addressing the results for the COP as a function of the utilization, Figs. 6.25 to Fig. 6.27, it is important to observe that: (i) since the total mass of Gd in the three regenerators is approximately the same, and since the AMR performance is evaluated at a fixed T_{C}, the variation of $\overline{\dot{W}}_{\mathrm{Mag}}$ can be neglected when the three matrices are compared; (ii) from the passive regenerator results, the three matrices presented different values of pressure drop, with the parallel plate regenerator presenting the lowest and the packed bed the highest pumping power. Thus, for a fixed T_{C}, the total power can be compared among the different geometries only in terms of the pumping power contribution.

The parallel plate regenerator presents the smallest values of $\overline{\dot{W}}$ due to the smallest viscous losses. However, its performance is the poorest in comparison with the other matrices, resulting in the smallest COP. On the other hand, since the pumping power for the pin array is smaller than in the packed bed, the COP for the pins is a bit higher than for

the spheres, especially at higher values of ΔT_{Hex} and lower frequencies (0.25 and 0.5 Hz). For $f = 1$ Hz the pin and packed sphere geometries present basically the same results for the COP.

As expected, the second-law efficiency, Figs. 6.28 to Fig. 6.30, follows similar trends as the COP, with the pin array showing slightly higher values of $\eta_{2\mathrm{nd}}$ for 0.25 and 0.5 Hz, while for 1 Hz, the pins and spheres presented very similar results. Taking the frequency of 0.5 Hz as an example, the following remarks can be made:

1. For the parallel plates, a peak $\eta_{2\mathrm{nd}}$ of approximately 3% was observed for a ΔT_{Hex} of 9 K and $\phi \approx 0.32$, $\overline{\dot{Q}}_{\mathrm{C}} \approx 3.5$ W (40 W/kg) and COP of 0.9;

2. For the packed bed of spheres, a peak $\eta_{2\mathrm{nd}}$ of approximately 5% was observed for ΔT_{Hex} of 12 K and 15 K and $\phi \approx 0.5$. Considering $\Delta T_{\mathrm{Hex}} = 12$ K, $\overline{\dot{Q}}_{\mathrm{C}} \approx 5.5$ W (65.6 W/kg) with a COP of about 1.2;

3. For the pin array, a peak $\eta_{2\mathrm{nd}}$ of approximately 5.5% was observed for ΔT_{Hex} of 12 K and 15 K and $\phi \approx 0.5$. Considering $\Delta T_{\mathrm{Hex}} = 12$ K, $\overline{\dot{Q}}_{\mathrm{C}} \approx 5.25$ W (58.5 W/kg) with a COP of about 1.4;

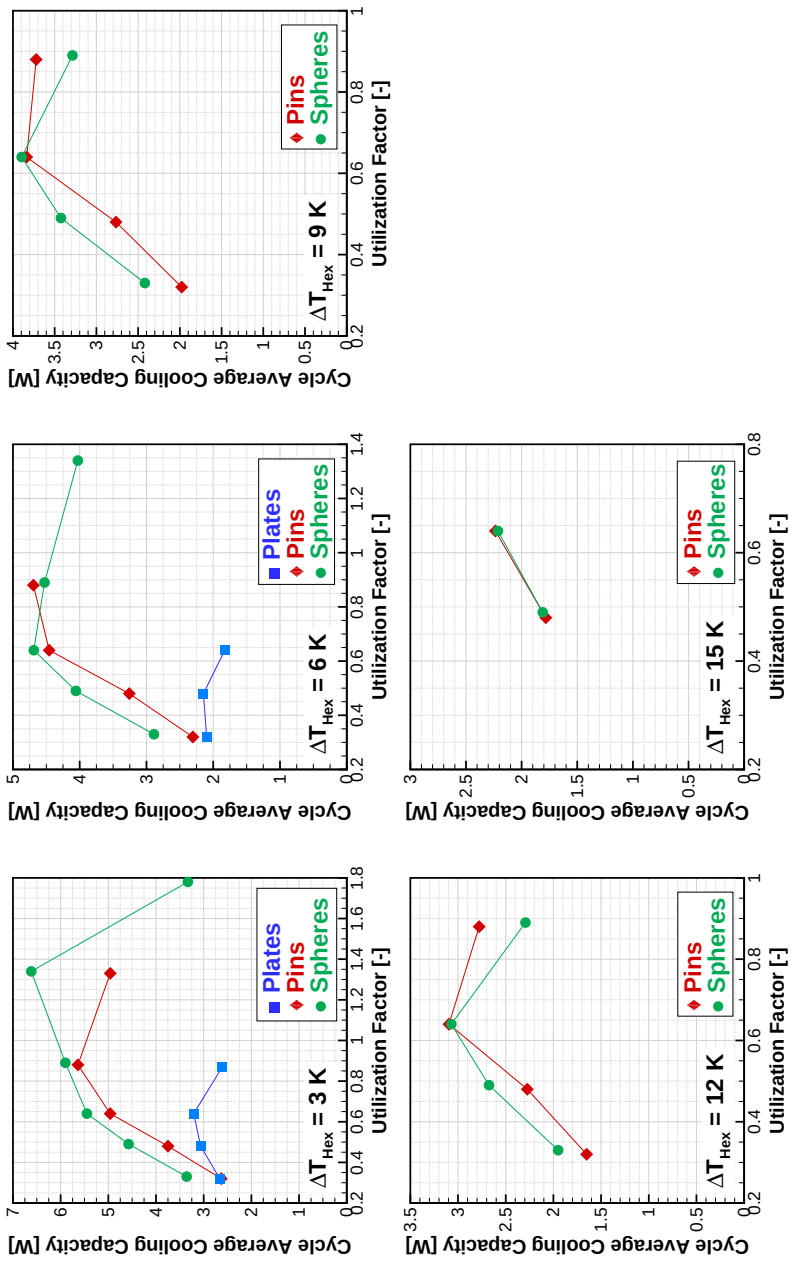

Figure 6.22 – $\overline{\dot{Q}}_{\mathrm{C}}$ as a function of ϕ for the three matrix geometries: $f = 0.25$ Hz, $T_{\mathrm{H}} = 300$ K and different ΔT_{Hex}.

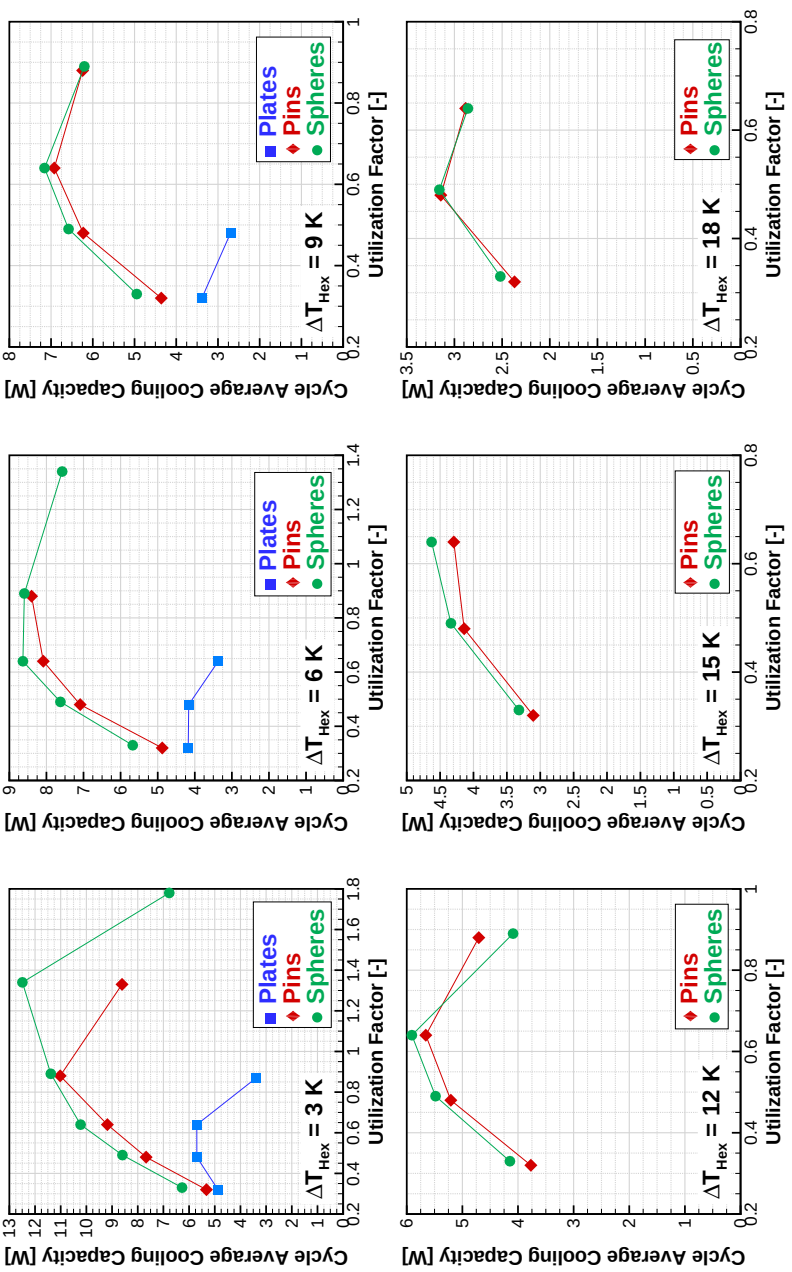

Figure 6.23 – $\overline{\dot{Q}}_{\mathrm{C}}$ as a function of ϕ for the three matrix geometries: $f = 0.5$ Hz, $T_{\mathrm{H}} = 300$ K and different ΔT_{Hex}.

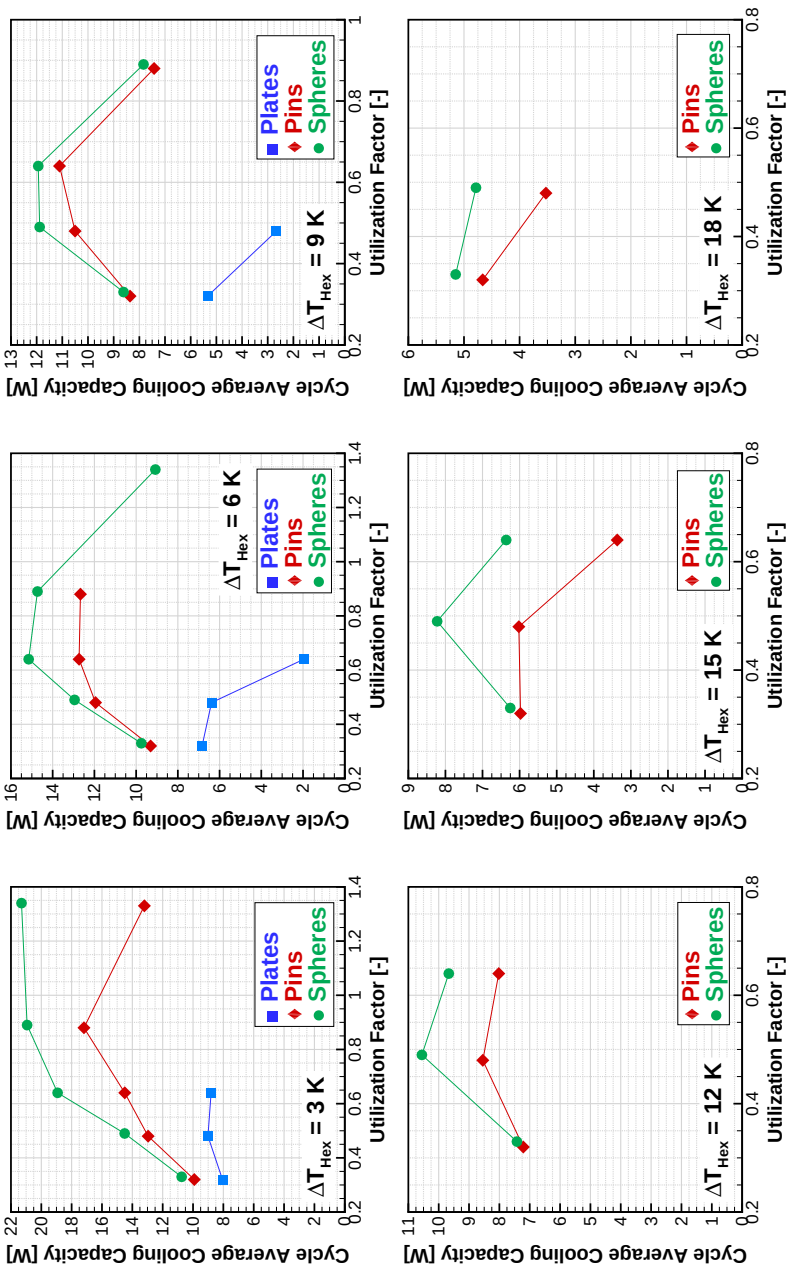

Figure 6.24 – $\overline{\dot{Q}}_{\mathrm{C}}$ as a function of ϕ for the three matrix geometries: $f = 1$ Hz, $T_{\mathrm{H}} = 300$ K and different ΔT_{Hex}.

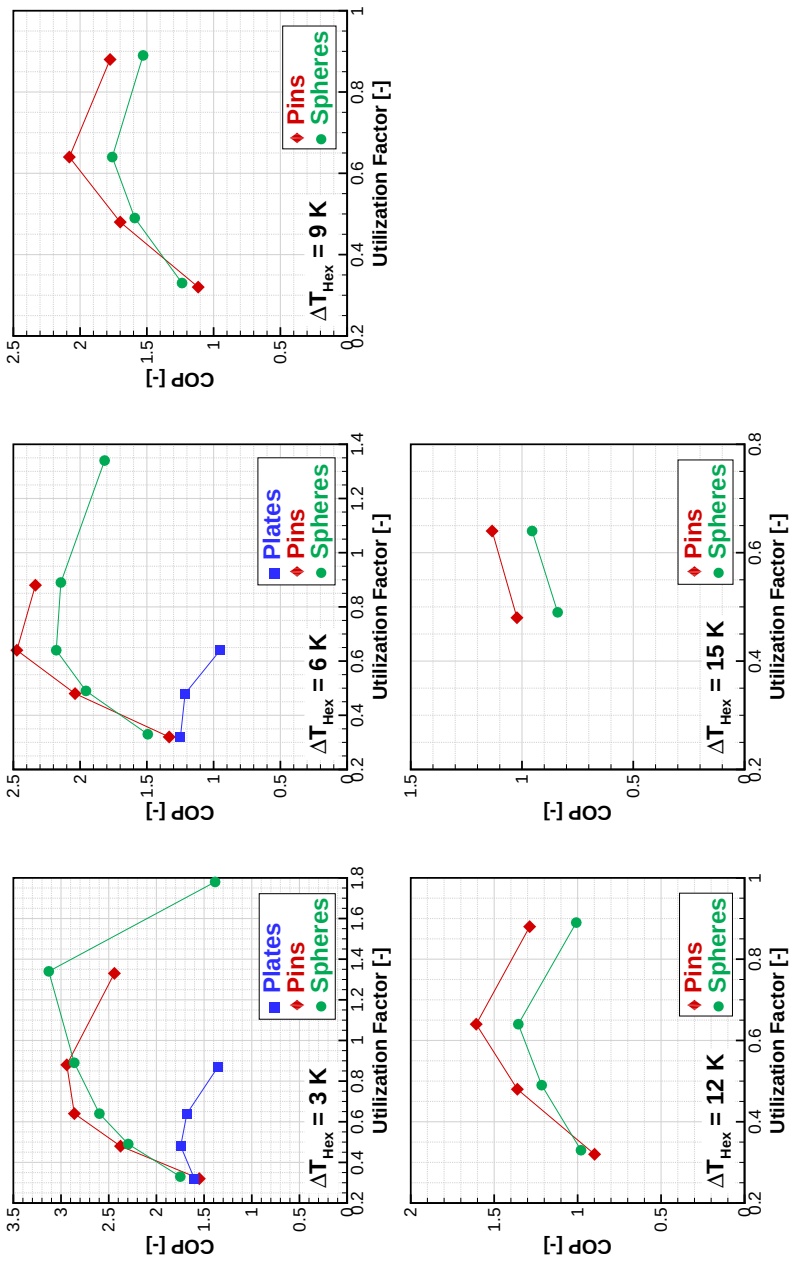

Figure 6.25 – COP as a function of ϕ for the three matrix geometries: $f = 0.25$ Hz, $T_{\mathrm{H}} = 300$ K and different ΔT_{Hex}.

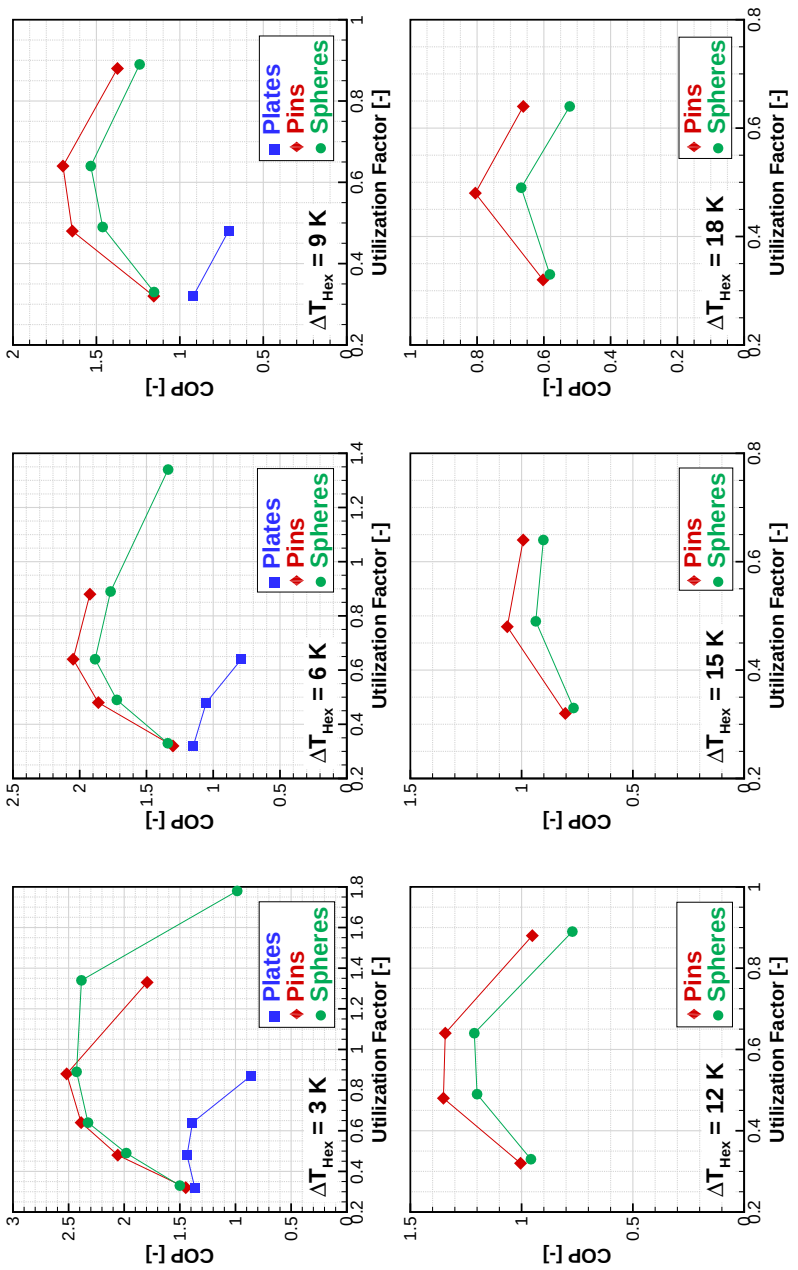

Figure 6.26 – COP as a function of ϕ for the three matrix geometries: $f = 0.5$ Hz, $T_{\mathrm{H}} = 300$ K and different ΔT_{Hex}.

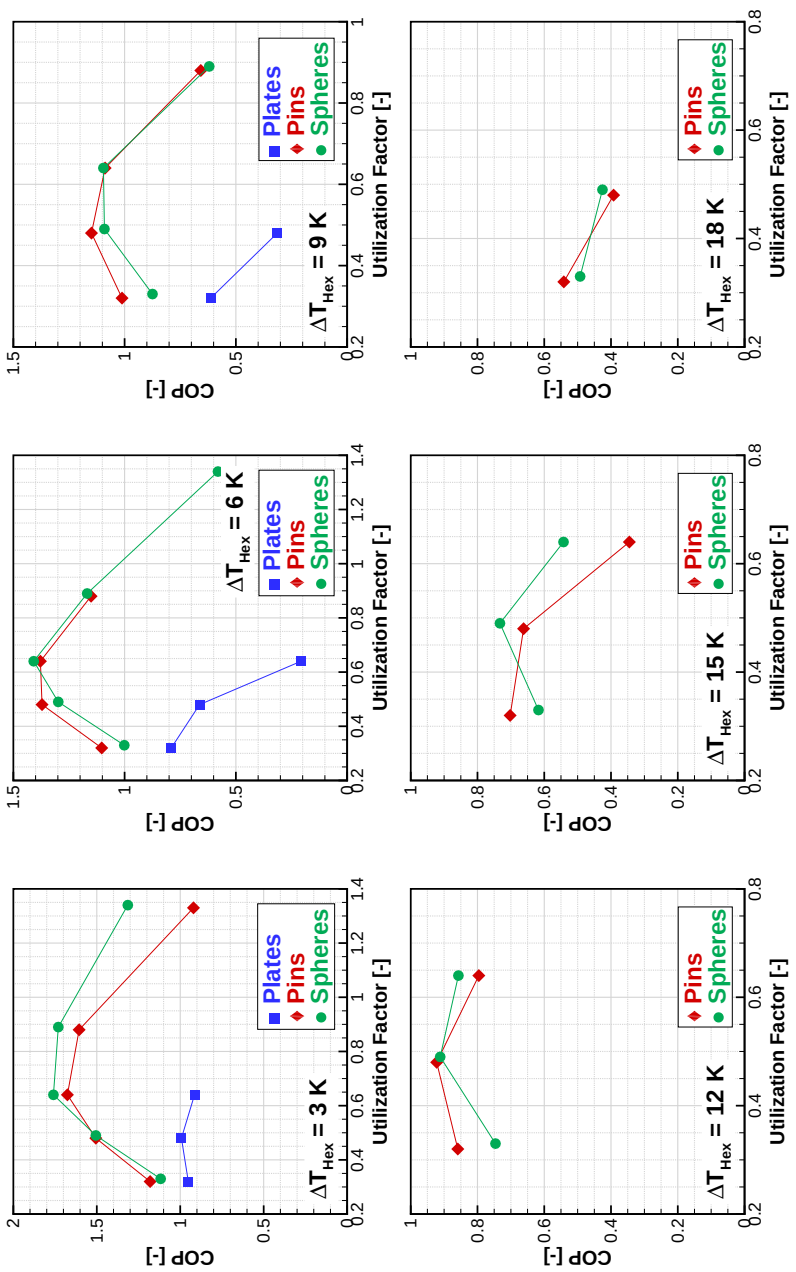

Figure 6.27 – COP as a function of ϕ for the three matrix geometries: $f = 1$ Hz, $T_{\mathrm{H}} = 300$ K and different ΔT_{Hex}.

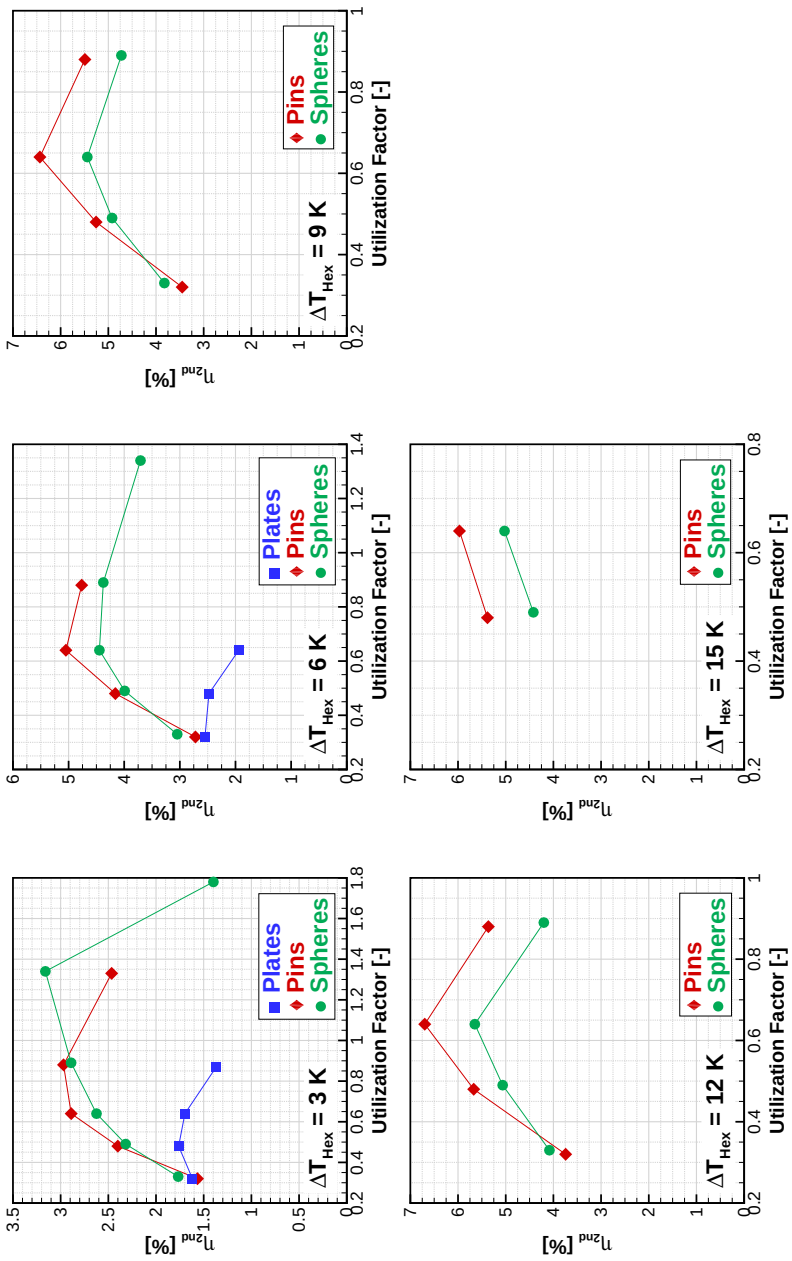

Figure 6.28 – $\eta_{2\mathrm{nd}}$ as a function of ϕ for the three matrix geometries: $f = 0.25$ Hz, $T_{\mathrm{H}} = 300$ K and different ΔT_{Hex}.

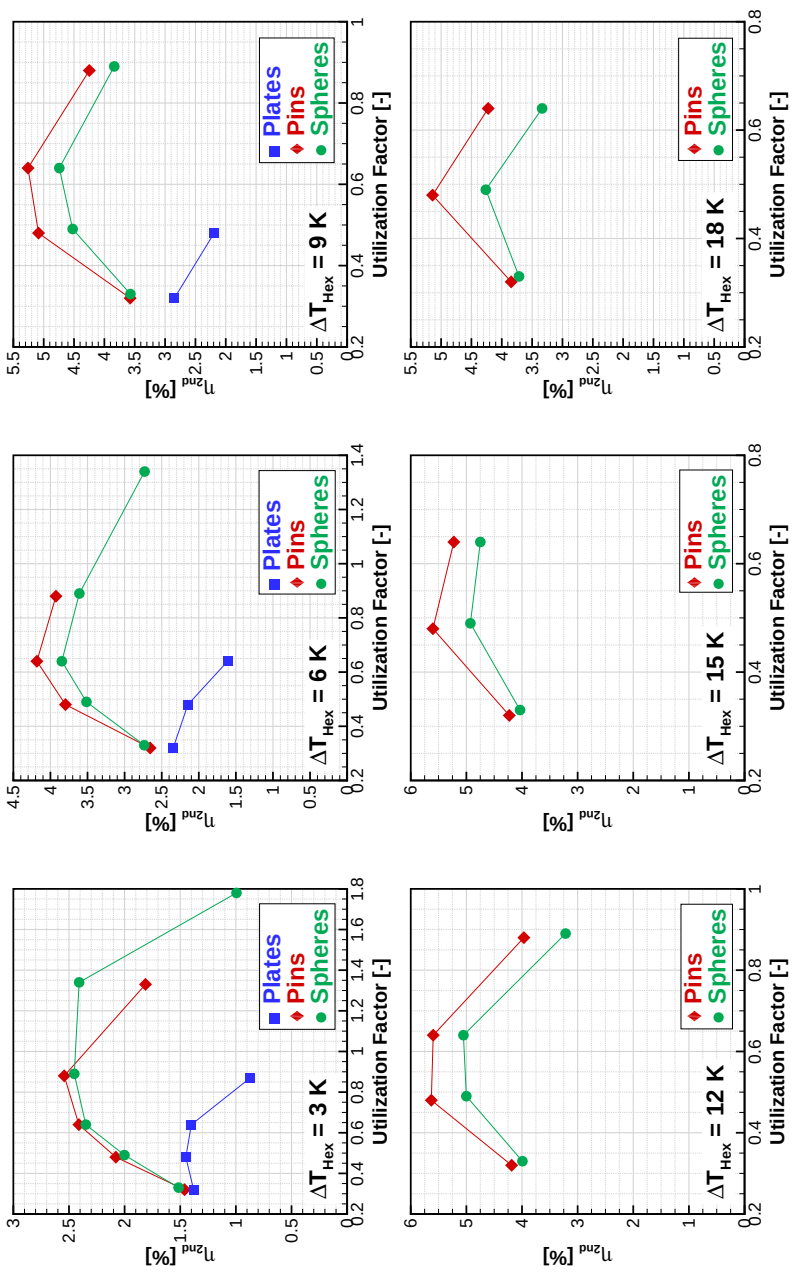

Figure 6.29 – $\eta_{2\mathrm{nd}}$ as a function of ϕ for the three matrix geometries: $f = 0.5$ Hz, $T_{\mathrm{H}} = 300$ K and different ΔT_{Hex}.

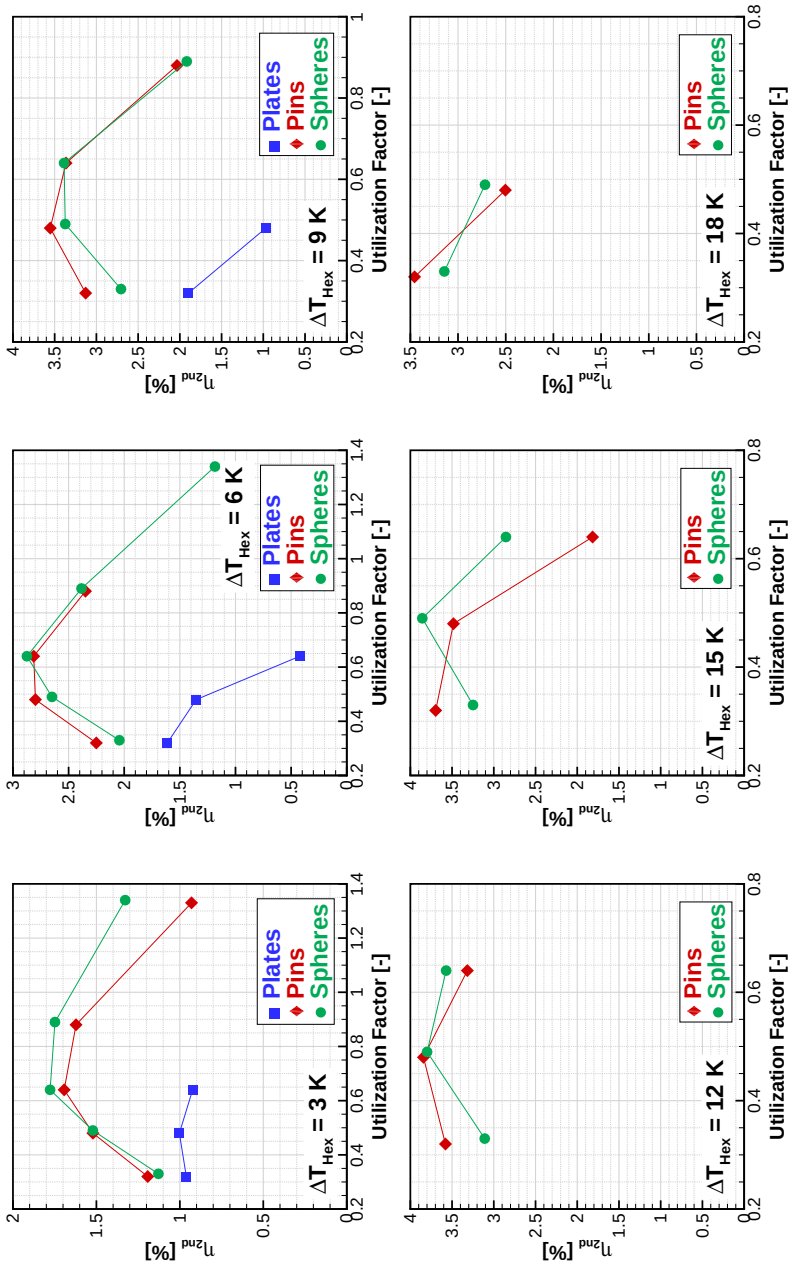

Figure 6.30 – $\eta_{2\mathrm{nd}}$ as a function of ϕ for the three matrix geometries: $f = 1$ Hz, $T_{\mathrm{H}} = 300$ K and different ΔT_{Hex}.

Fig. 6.31 presents a comparison between the AMR regenerator geometries regarding the maximum ΔT_{Hex} as a function of ϕ for the different frequencies of 0.25, 0.5 and 1 Hz. As performed for Spheres #3, the maximum ΔT_{Hex} was determined from an extrapolation/interpolation of the system curves. The trends are somewhat similar to those for Spheres#3, allowing the following remarks to be made:

1. For all the geometries, the points of maximum ΔT_{Hex} are found at small utilization factors. This corroborates the assumption that the regenerators assembled in Casings #4, #5 and #6 have lower casing heat gains because of their better thermal insulation, owing to the additional ABS housing, compared with Casing #3;

2. For all the frequencies, the points of maximum temperature span for the parallel plate geometry were always lower than for the remaining geometries. This supports the argument of a larger casing heat gain for the plates geometry.

All geometries showed their best performance, in terms of the maximum ΔT_{Hex}, at a frequency of 0.5 Hz. These results are supported by the following points: (i) at this frequency, the regenerator effectiveness is higher than at 1 Hz; (ii) as shown in item (1) above, the casing heat gain is smaller for Casings #4, #5 and #6 than for Casing #3 (used in Spheres #3). In the case of Spheres #3, this matrix also presented a higher effectiveness at 0.5 Hz, however, since the casing heat gain presents a larger impact on the regenerator performance, the frequency of 1 Hz showed a higher maximum ΔT_{Hex}.

Regarding the utilization factor, for $f = 0.25$ and 0.5 Hz, comparing the pins and spheres matrices, it is observed that for small ϕ the pins presented a larger maximum ΔT_{Hex}, while for $\phi > 1$ the packed spheres matrix had a higher maximum ΔT_{Hex}. This result can be attributed first to the higher effectiveness (smaller axial heat conduction loss) and lower demagnetizing loss of the pin array geometry at low utilizations and high temperature spans. As the utilization increases and the temperature span decreases, the spheres packed bed thermal performance improves, given the reduction of the axial heat condition and demagnetizing losses, and due to a better effectiveness of this matrix at high utilizations. For $f = 1$ Hz, both geometries presented the same values of maximum ΔT_{Hex} which can be attributed to the higher heat gain for the pin array, as explained previously in this section.

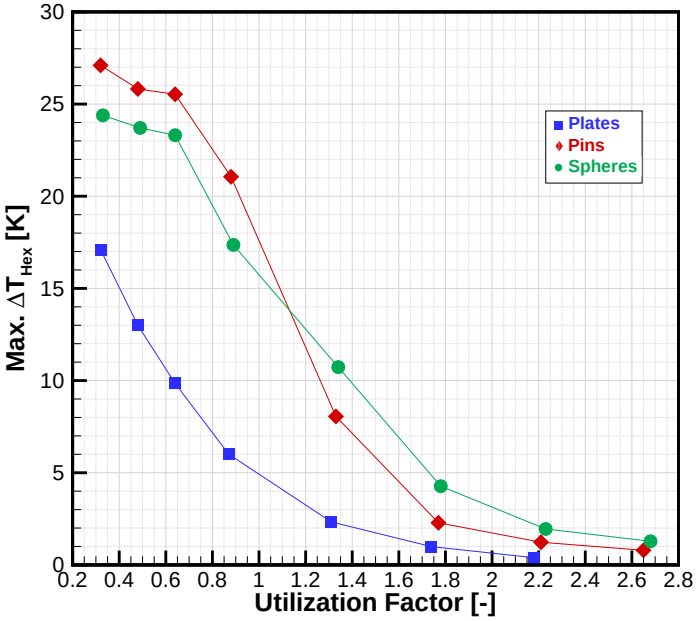
Plates
Pins
Spheres
Max. ΔT_Hex [K]
Utilization Factor [-]
0
5
10
15
20
25
30
0.2
0.4
0.6
0.8
1
1.2
1.4
1.6
1.8
2
2.2
2.4
2.6
2.8

(a)

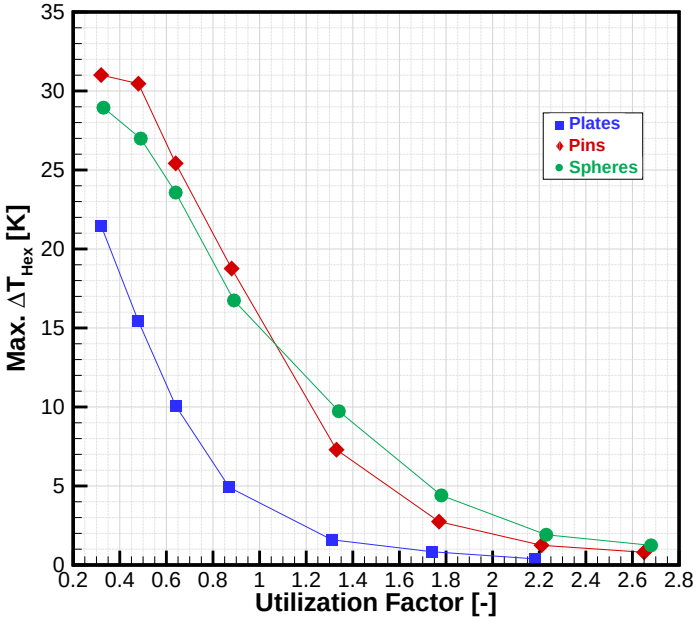
Plates
Pins
Spheres
Max. ΔT_Hex [K]
Utilization Factor [-]
0
5
10
15
20
25
30
35
0.2
0.4
0.6
0.8
1
1.2
1.4
1.6
1.8
2
2.2
2.4
2.6
2.8

(b)

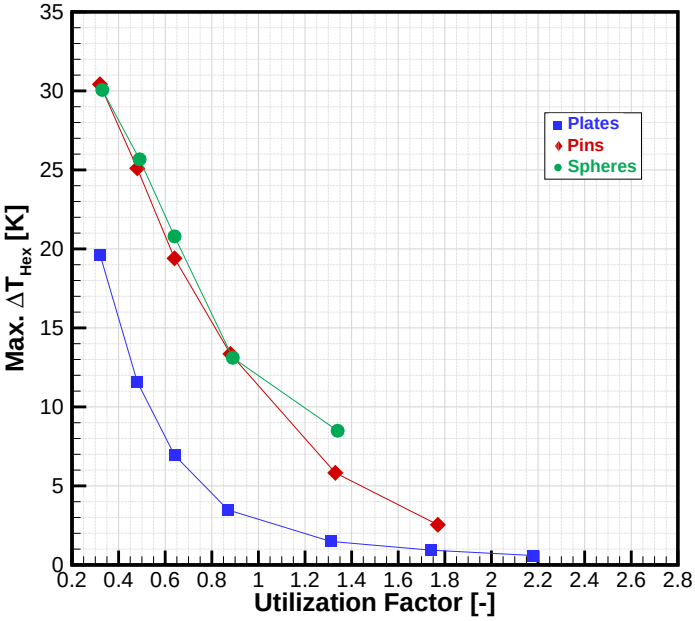

(c)

Figure 6.31 – Comparison of the maximum ΔT_{Hex} as a function of ϕ for each AMR regenerator geometry and $T_{\text{H}} = 300$ K: (a) $f = 0.25$ Hz; (b) $f = 0.5$ Hz; (c) $f = 1$ Hz.

Fig. 6.32 makes a comparison of the maximum $\overline{\dot{Q}}_{\text{C}}$ as a function of the utilization factor for all regenerative matrices, for the three frequencies. In general, the results presented the expected trend, i.e., with a distinct peak at some operating conditions. As expected, the peaks of maximum $\overline{\dot{Q}}_{\text{C}}$ for the three geometries at the three frequencies is observed in the range $1 \leq \phi \leq 2$. Moreover, in terms of the maximum $\overline{\dot{Q}}_{\text{C}}$, the spheres regenerator presented a better performance, especially at higher utilizations, where this geometry is the most thermally effective in terms of heat transfer. Also, at $T_{\text{H}} = 300$ K and zero span, the axial heat conduction and the demagnetizing effects are lower, contributing to a better performance of the spheres packed beds.

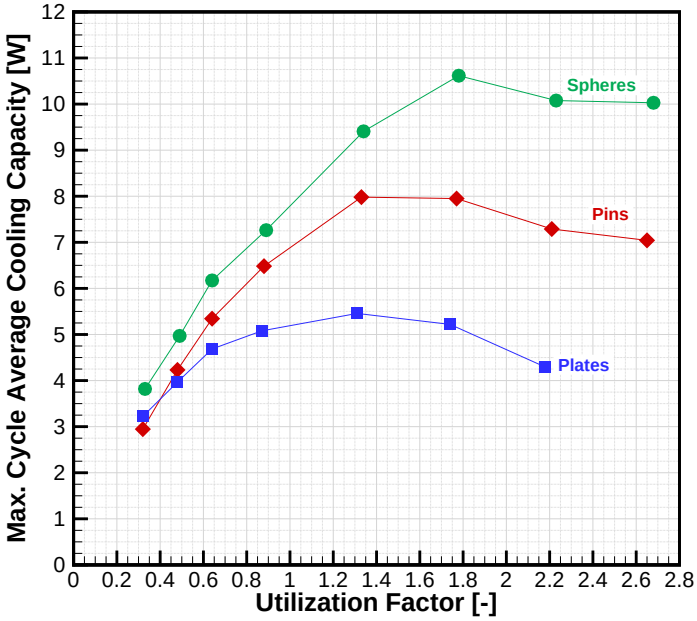
Max. Cycle Average Cooling Capacity [W]
Utilization Factor [-]
Spheres
Pins
Plates
0
1
2
3
4
5
6
7
8
9
10
11
12
0 0.2 0.4 0.6 0.8 1 1.2 1.4 1.6 1.8 2 2.2 2.4 2.6 2.8

(a)

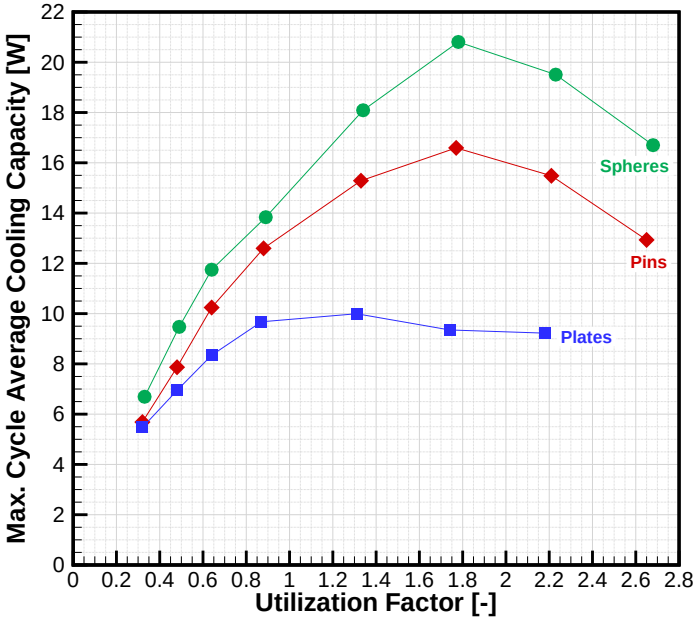
Max. Cycle Average Cooling Capacity [W]
Utilization Factor [-]
Spheres
Pins
Plates
0
2
4
6
8
10
12
14
16
18
20
22
0 0.2 0.4 0.6 0.8 1 1.2 1.4 1.6 1.8 2 2.2 2.4 2.6 2.8

(b)

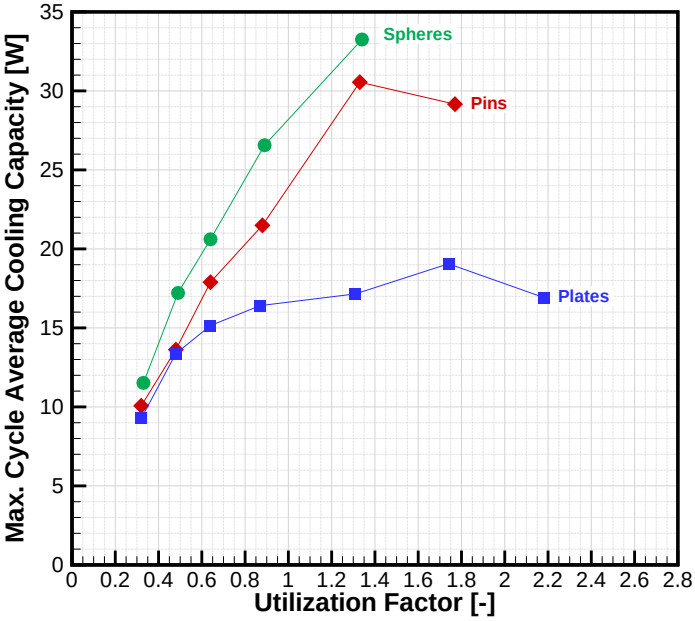

(c)

Figure 6.32 – Comparison of the maximum $\overline{\dot{Q}}_{\mathrm{C}}$ as a function of ϕ for each AMR regenerator geometry and $T_{\mathrm{H}} = 300$ K: (a) $f = 0.25$ Hz; (b) $f = 0.5$ Hz; (c) $f = 1$ Hz.

In conclusion, the pin array and the packed bed of spheres are the most promising regenerative geometries for magnetic refrigeration. If, on the one hand, the packed bed presented slightly higher cooling capacities, on the other hand, the pin array had lower penalties associated with the viscous losses and, as a consequence, a little higher values of COP and $\eta_{2\mathrm{nd}}$. However, considering the manufacturing of the regenerator, the packed bed of spheres is by far the best option for applications in AMRs. The WEDM technique employed to fabricate the pin array is still time consuming and expensive to be considered for large scale production.

7 Optimization of Thermal Regenerators

The thermodynamic efficiencies of regenerative cooling cycles are directly linked to the heat transfer effectiveness and viscous losses in the regenerator. In a heat exchanger, there must be good thermal contact between the fluid and solid phases, but the latter should offer a small resistance to the fluid flow. These conflicting requirements are often equalized using thermal optimization. A regenerator can be designed for optimal performance according to the Entropy Generation Minimization (EGM) method (BEJAN, 1996). In active magnetic regenerators, the structure and geometry of the solid matrix have to be optimized to reduce the thermal, viscous and magnetic losses and achieve the desired operating conditions of temperature span, cooling capacity and cycle efficiency.

The present chapter advances a performance analysis of thermal passive and active magnetic regenerators based on the Entropy Generation Minimization (EGM) theory. The cycle-average entropy generation contributions are due to: axial heat conduction, fluid friction and interstitial heat transfer. It is important to notice that, in the cases where the magnetocaloric effect is reversible and does not present irreversibilities like magnetic and thermal hysteresis, there is no additional (i.e., magnetic) contribution to the cycle-average entropy generation. The influences of parameters such as the mass flow rate, operating frequency, regenerator cross sectional area, housing aspect ratio, utilization factor and particle diameter are evaluated according to the following performance evaluation criteria (PEC): variable geometry (**VG**) and fixed face (cross-section) area (**FA**).

7.1 Entropy Generation Model

In a thermal regenerator, entropy is generated due to heat transfer and viscous dissipation. Selecting a control volume containing the solid and fluid phases of the porous media, as presented in Fig. 7.1, the macroscopic entropy balance is given by (STEIJAERT, 1999):

$$\left.\frac{dS}{dt}\right|_{\mathrm{CV}} = \left.\frac{dS}{dt}\right|_{\mathrm{s}} + \left.\frac{dS}{dt}\right|_{\mathrm{f}} \tag{7.1}$$

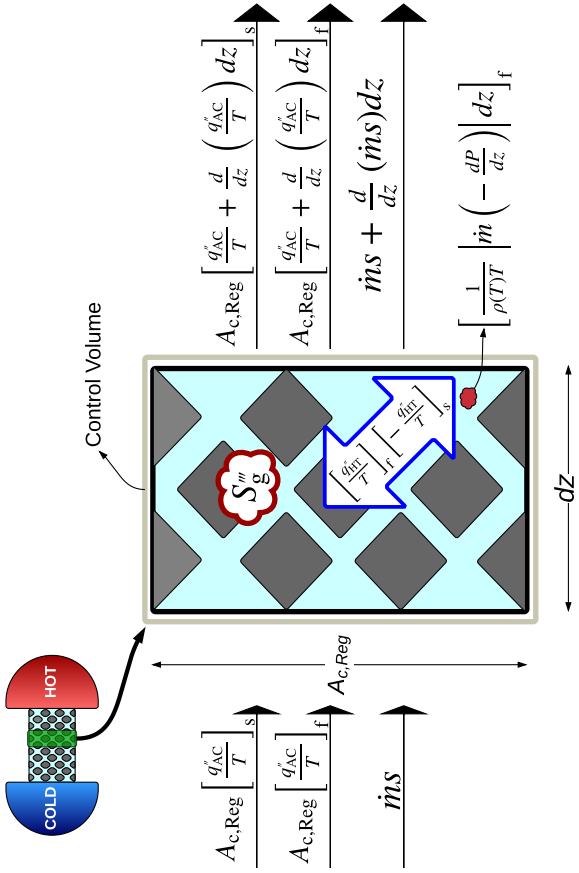

Figure 7.1 – Entropy generation model.

The rate of entropy change in a control volume containing both the solid and fluid phases is given by (STEIJAERT, 1999):

$$\left.\frac{dS}{dt}\right|_{\mathrm{CV}} = -A_{\mathrm{c,Reg}}\left[\frac{d}{dz}\left(\frac{q''_{\mathrm{AC}}}{T}\right)dz\right]_{\mathrm{s}} - A_{\mathrm{c,Reg}}\left[\frac{d}{dz}\left(\frac{q''_{\mathrm{AC}}}{T}\right)dz\right]_{\mathrm{f}} + \dot{m}\frac{ds}{dz}dz + S'''_{\mathrm{g}}A_{\mathrm{c,Reg}}dz \tag{7.2}$$

where the first and second terms on the right are changes in entropy rate due to axial conduction heat transfer in the solid and fluid. The third term is the rate of entropy change associated with the fluid flow into and out of the control volume. The fourth term is the rate of entropy generation in the control volume, and S''' is local rate of entropy generation per unit volume during a cycle. The rates of entropy change in the fluid and solid phases are given by (STEIJAERT, 1999):

$$\left.\frac{dS}{dt}\right|_{\mathrm{f}} = -\frac{A_{\mathrm{c,Reg}}}{T_{\mathrm{f}}}\left[\frac{q''_{\mathrm{AC}}}{dz}dz\right]_{\mathrm{f}} + \frac{q''_{\mathrm{HT}}}{T_{\mathrm{f}}}A_{\mathrm{c,Reg}}dz + \dot{m}\frac{ds}{dz}dz + \frac{1}{\rho_{\mathrm{f}}(T)T_{\mathrm{f}}}\left|\dot{m}\left(-\frac{dP}{dz}\right)\right|dz \tag{7.3}$$

$$\left.\frac{dS}{dt}\right|_{\mathrm{s}} = -\frac{A_{\mathrm{c,Reg}}}{T_{\mathrm{s}}}\left[\frac{dq''_{\mathrm{AC}}}{dz}dz\right]_{\mathrm{s}} - \frac{q''_{\mathrm{HT}}}{T_{\mathrm{s}}}A_{\mathrm{c,Reg}}dz \tag{7.4}$$

where

$$q''_{\mathrm{AC,f}} = -(k_{\mathrm{f}}^{\mathrm{eff}} + \rho_{\mathrm{f}}(T)c_{\mathrm{p,f}}(T)D_{||})\left.\frac{dT}{dz}\right|_{\mathrm{f}} \tag{7.5}$$

$$q''_{\mathrm{AC,s}} = -k_{\mathrm{s}}^{\mathrm{eff}}\left.\frac{dT}{dz}\right|_{\mathrm{s}} \tag{7.6}$$

$$q''_{\mathrm{HT}} = h(z)\beta(T_{\mathrm{s}} - T_{\mathrm{f}}) \tag{7.7}$$

Thus, replacing Eqs. (7.2) to (7.4) in Eq. (7.1) and using the heat fluxes defined above (Eqs. (7.5) to (7.7)), the local rate of entropy generation per unit volume is given by:

$$S_{\mathrm{g}}^{'''} = \frac{h(z)\beta(T_{\mathrm{s}} - T_{\mathrm{f}})^2}{T_{\mathrm{s}}T_{\mathrm{f}}} + \frac{(k_{\mathrm{f}}^{\mathrm{eff}} + \rho_{\mathrm{f}}(T)c_{\mathrm{p,f}}(T)D_{||})}{T_{\mathrm{f}}^2}\left(\left.\frac{dT}{dz}\right|_{\mathrm{f}}\right)^2 + \frac{k_{\mathrm{s}}^{\mathrm{eff}}}{T_{\mathrm{s}}^2}\left(\left.\frac{dT}{dz}\right|_{\mathrm{s}}\right)^2 + \frac{1}{T_{\mathrm{f}}}\left|u\left(-\frac{dP}{dz}\right)\right| \tag{7.8}$$

where the first term on the right is the entropy generation rate per unit volume due to interphase heat transfer with a finite temperature difference. The second and third terms are the entropy generation rates due to axial conduction in the fluid and solid matrix, and the fourth term is the entropy generation rate per unit volume due to viscous friction. The cycle-average entropy generation in the regenerator, S_{g}, is defined as:

$$S_{\mathrm{g}} = A_{\mathrm{c,Reg}} \int_0^L \int_0^\tau S_{\mathrm{g}}^{'''}\, dt\, dz \tag{7.9}$$

S_{g} (in [J/K]) will be used as the objective function to be minimized in the regenerator optimization. Also, Eq. (7.8) is used to calculate the local rate of entropy generation per unit volume in passive and active magnetic regenerators. In cases where the magnetocaloric effect is reversible, such as in materials with a continuous magnetic transition (e.g., gadolinium), the local rate of entropy generation due to the MCE is directly included in the interphase heat transfer. In this case, the ΔT_{ad} resulting from the external magnetic flux density variation creates a finite temperature difference between the solid and fluid phases. Otherwise, if irreversibilities are present, such as magnetic and thermal hysteresis, additional terms have to be included in Eq. (7.8) to compute these irreversibilities. However, these will not be necessary in the present thesis, as Gd is the magnetocaloric material being considered.

7.2 Optimization of Passive Oscillating-Flow Regenerators

This section presents and discusses the results for the optimization of passive oscillating-flow regenerators. The analysis considers packed bed matrices composed by stainless steel spheres of different sizes. To the fluid phase was considered as pure water.

7.2.1 Performance Evaluation Criteria for Passive Regenerators

The EGM calculations were carried out based on the PEC of Webb and Kim (WEBB; KIM, 2005). The first criterion is of Variable Geometry (**VG**), for which the regenerator housing cross sectional area, or the housing diameter, $D_{\mathrm{h,Reg}}$, and the length, L_{Reg}, are allowed to vary, keeping a constant housing volume. The second criterion is of Fixed Face Area (**FA**), where the regenerator housing cross sectional area is kept constant and the regenerator length can vary, thus changing also the housing volume. For reasons that will be discussed later, the Fixed Geometry (**FG**) criterion was not evaluated for passive regenerators. The baseline (reference) housing geometry has the following geometric characteristics: $D_{\mathrm{h,Reg}} = 25$ mm and $\zeta = 2$, where $\zeta = L_{\mathrm{reg}}/D_{\mathrm{h,Reg}}$ is the aspect ratio of the regenerator housing. Thus, the baseline regenerator housing volume is 24.544 cm^3, and the ranges of the variables explored in the analysis are presented in Table 7.1. A flow chart of the various scenarios is shown in Fig. 7.2. The operating conditions (i.e., frequency and mass flow rates) and ranges of geometric parameters evaluated were chosen so as to be consistent with figures currently encountered in active magnetic regenerators (YU *et al.*, 2010; NIELSEN *et al.*, 2011).

Table 7.1 – Ranges of the geometric variables for each PEC of the passive regenerator optimization.

PEC	$D_{\mathrm{h,Reg}}$ [mm]	ζ	Housing volume [cm^3]	d_{p} [mm]
VG	12.5 - 75	16 - 0.074	24.544	0.2 - 2
FA	25	1 - 8	12.272 - 98.175	0.2 - 2

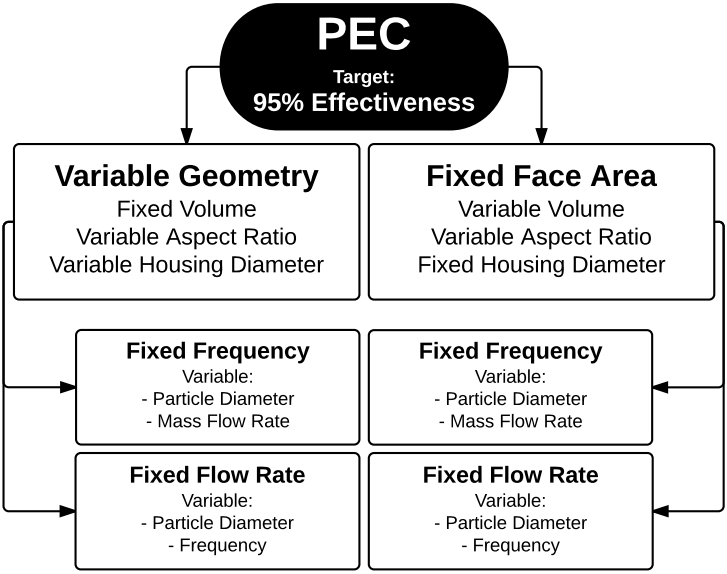

Figure 7.2 – Flow chart of the various scenarios evaluated in the simulations for the passive regenerator optimization.

As can be seen from Table 7.1, all the possible $D_{\mathrm{h,Reg}}$ and ζ combinations in the **VG** criterion result in a fixed housing volume of 24.544 cm^3. The particle diameter is varied from 0.2 to 2 mm, for each possible combination. In the **FA** criterion, $D_{\mathrm{h,Reg}}$ is fixed at 25 mm, while ζ is changed from 1 to 8. The particle diameter is also varied from 0.2 to 2 mm for each possible combination.

For each combination of $D_{\mathrm{h,Reg}}$, ζ and d_{p} in each PEC, simulations were carried out considering two different scenarios. In the first scenario, the frequency was kept constant at 1 Hz and the mass flow rate was varied from 40 to 100 kg/h (steps of 10 kg/h) for the **VG** PEC and from 100 to 300 kg/h (steps of 25 kg/h) for the **FA** PEC, as presented in Table 7.2. In the second scenario, the frequency was varied from 1 to 4 Hz (steps of 0.5 Hz) and the mass flow rate was kept constant at 60 kg/h for the **VG** PEC and at 250 kg/h for the **FA** PEC, as presented in Table 7.3.

As defined previously, the regenerator effectiveness is a measure of the rate at which heat is transferred between the fluid and solid phases in

Table 7.2 – Constraints of the regenerator analysis for the **VG** and **FA** PEC for a fixed frequency and a variable mass flow rate in the passive regenerator optimization.

Variable	Value or range	Units
ε	0.36	-
T_{H}	283	K
T_{C}	323	K
ϵ	0.95	-
f	1	Hz
VG - $\dot{m}$	40 - 100 ($\Delta\dot{m} = 10$)	kg/h
VG - ϕ	0.40 - 0.99	-
FA - $\dot{m}$	100 - 300 ($\Delta\dot{m} = 25$)	kg/h
FA - ϕ	Variable (0.25 - 5.95)	-

Table 7.3 – Constraints of the regenerator analysis for the **VG** and **FA** PEC for a fixed mass flow rate and a variable frequency in the passive regenerator optimization.

Variable	Value or range	Units
ε	0.36	-
T_{H}	283	K
T_{C}	323	K
ϵ	0.95	-
f	1 - 4 ($\Delta f = 0.5$)	Hz
VG - $\dot{m}$	60	kg/h
VG - ϕ	0.60 - 0.15	-
FA - $\dot{m}$	250	kg/h
FA - ϕ	Variable (4.96 - 0.15)	-

a given blow (SCHMIDT; WILLMOTT, 1981). In the **VG** and **FA** PEC, a fixed regenerator effectiveness is equivalent to a fixed heat transfer rate when the temperatures of the reservoirs and the frequency *or* the mass flow rate are fixed (Tables 7.2 and 7.3). In the present analyses, a target value for ϵ was set at **95%** (performance constraint).

In the **VG** cases, for fixed values of frequency, mass flow rate and utilization, the regenerator effectiveness will change as a result of changes in $D_{\mathrm{h,Reg}}$ and ζ (which are reciprocal because of the constant housing

volume constraint) or d_p. Changes in cross-section area affect the fluid superficial velocity, the particle Reynolds number (which is also affected by d_p) and the magnitude of the axial heat conduction. The surface area per unit volume is directly affected by the particle diameter. In the **FA** cases, the interstitial heat transfer coefficient is only a function of d_p, since the superficial velocity is constant for a given mass flow rate. On the other hand, the interstitial area changes with both d_p and ζ. The utilization factor decreases with increasing ζ, which contributes to achieving higher values of regenerator effectiveness due to the larger thermal mass of the solid phase.

It should be noted that the Fixed Geometry (**FG**) PEC (WEBB; KIM, 2005), i.e., that in which *both* the regenerator length and cross-section area are kept fixed, could not be evaluated given the present constraints because fixing a value of ϵ in this case does not necessarily correspond to a fixed cycle-average heat transfer rate.

7.2.2 PEC Numerical Implementation

Each operating condition is defined by a set of constraints specified according to Table 7.2 (variable mass flow rate) or Table 7.3 (variable frequency). For a specific operating condition, the ranges of the geometric variables (e.g., housing and particle diameters and aspect ratio) are chosen according to each PEC (**VG** or **FA**), as shown in Table 7.1. For each point in the range associated with a given PEC, the momentum and energy equations are solved numerically and the cycle-average entropy generation is calculated.

For each scenario of the **VG** PEC (i.e., variable frequency or variable mass flow rate), discrete data points were selected in the housing diameter and particle diameter ranges shown in Table 7.1 (incremental steps of 5 mm for $D_{h,Reg}$ and 0.1 mm for d_p), resulting in 266 independent cases. Similarly, for the **FA** PEC, the aspect ratio range was divided in incremental steps of 0.5 (plus the 0.1 mm steps for d_p), resulting in 342 cases for the variable frequency and variable mass flow rate scenarios. In total, 9196 different simulations were performed for the **VG** and **FA** PEC. The searches for the points of minimum entropy generation were refined further by means of 4th-order (or less) polynomial interpolations ($R^2 > 0.9999$), which guaranteed the stability of the numerical solutions and a better resolution (finer than 0.5 mm for $D_{h,Reg}$, 0.05 for ζ and 0.01 mm for d_p) for the minimum S_g value at a reasonable

computational cost.

7.2.3 Entropy Generation-Effectiveness Contour Maps

As the numerical convergence is obtained for the momentum and energy equations for a specific case (defined by values of frequency, mass flow rate and geometric parameters associated with each PEC), the regenerator configurations that yield the desired value of hot-blow effectiveness can be identified. To illustrate this, Fig. 7.3 presents the results for the **VG** PEC with $\dot{m} = 60$ kg/h and frequencies of 1 and 3 Hz. Fig. 7.4, in turn, presents the results for the **FA** PEC with $\dot{m} = 250$ kg/h and frequencies of 1 and 3 Hz. Lines of constant S_g (red lines) are plotted together with lines of constant effectiveness (blue lines), as a function of the particle diameter and housing diameter for the **VG** PEC (Fig. 7.3), and particle diameter and housing aspect ratio for the **FA** PEC (Fig. 7.4).

As can be seen from Figs. 7.3 and 7.4, the target value of $\epsilon = 95\%$ (blue solid line) can be achieved with different combinations of d_p and $D_{h,Reg}$ or ζ, with f and $\dot{m}$ being held constant for each PEC. According to the **VG** PEC with $\dot{m} = 60$ kg/h and $f = 1$ Hz, Fig. 7.3(a), $\epsilon = 95\%$ can be achieved with small values of d_p in the 0.2 to 1.3 mm range and small housing diameters (12.5 to 58 mm), yielding values of ζ between 0.16 and 16. Following the line of constant hot-blow effectiveness of 95%, different values of S_g can be achieved with a minimum at around $d_p = 1.07$ mm and $D_{h,Reg} = 17.23$ mm. As the operating frequency is increased, Fig. 7.3(b), the minimum S_g for $\epsilon = 95\%$ is shifted to larger values of d_p, yielding other combinations of $D_{h,Reg}$ and ζ.

For the **FA** PEC with $\dot{m} = 250$ kg/h and $f = 1$ Hz, Fig. 7.4(a), the minimum S_g for $\epsilon = 95\%$ was identified in the vicinity of $d_p = 0.59$ mm, with an aspect ratio of around 5.12. As expected, for other frequencies the minimum S_g range changes and $\epsilon = 95\%$ is achieved with other combinations of d_p, $D_{h,Reg}$ and ζ, as presented in Fig. 7.4(b).

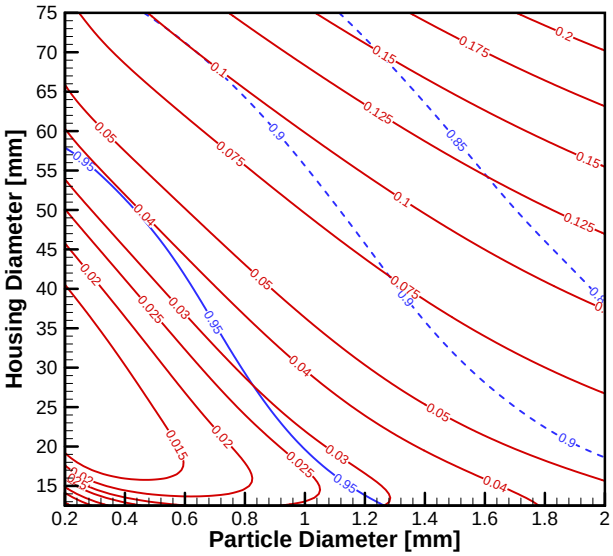

(a)

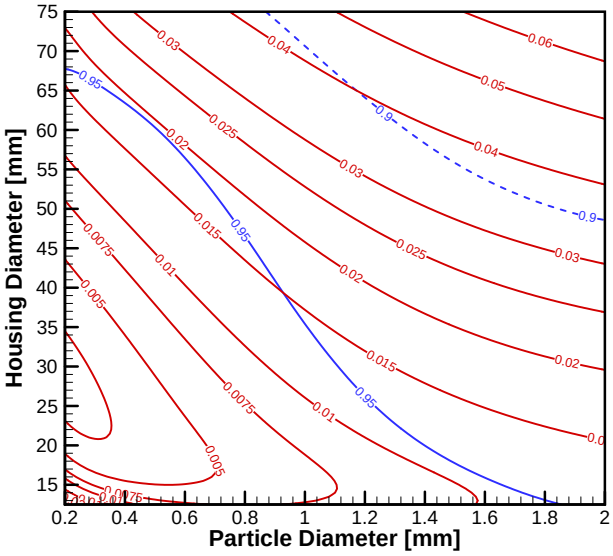

(b)

Figure 7.3 – Lines of constant effectiveness (blue lines) and S_g (red lines) as a function of d_p and $D_{h,Reg}$ for the **VG** PEC for $\dot{m} = 60$ kg/h and frequencies of (a) 1 Hz; (b) 3 Hz.

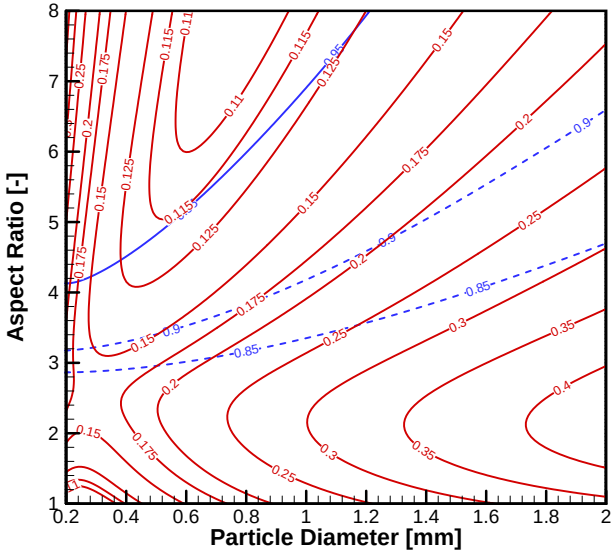

(a)

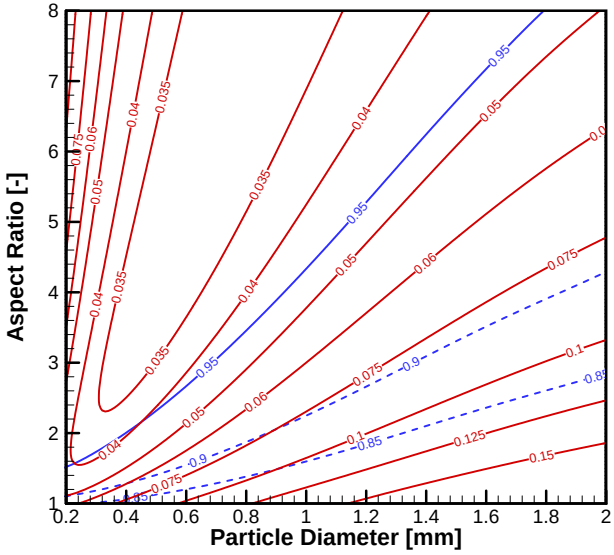

(b)

Figure 7.4 – Lines of constant effectiveness (blue lines) and S_g (red lines) as a function of d_p and ζ for the **FA** PEC for $\dot{m} = 250$ kg/h and frequencies of (a) 1 Hz; (b) 3 Hz.

7.2.4 Individual Contributions to the Total Entropy Generation

This section illustrates the behavior of the three sources of entropy generation (interstitial heat transfer, axial conduction and viscous dissipation) for two regenerators with the same housing volume, but very distinct values of housing diameter and aspect ratio, as seen in Table 7.4. In these two cases, the particle diameter is varied between 0.2 and 2 mm. The flow rate was 60 kg/h and the frequency was 1 Hz in both cases. However, it must be noted that the hot-blow effectiveness is not the same for the two simulated cases, as illustrated in Fig. 7.5.

Table 7.4 – Parameters of the case study on the contributions to the total entropy generation.

Case	$D_{h,Reg}$ [mm]	ζ	d_p [mm]
Case 1	12.5	16	0.2-2
Case 2	75	0.074	0.2-2

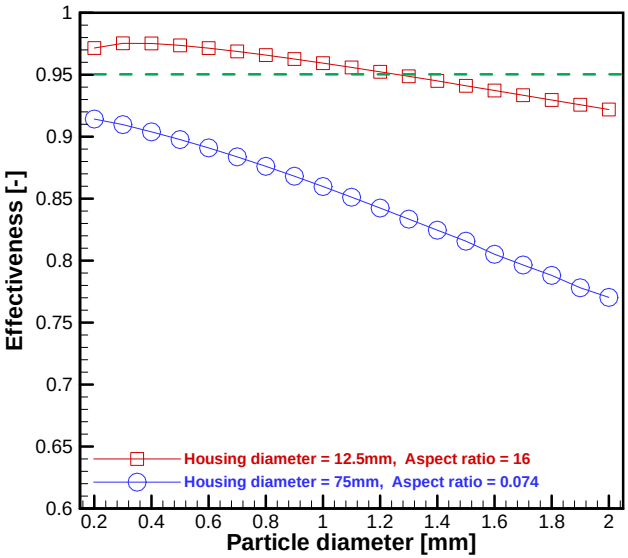

Figure 7.5 – Effectiveness as a function of the particle diameter for Cases 1 and 2 at 60 kg/h and 1 Hz.

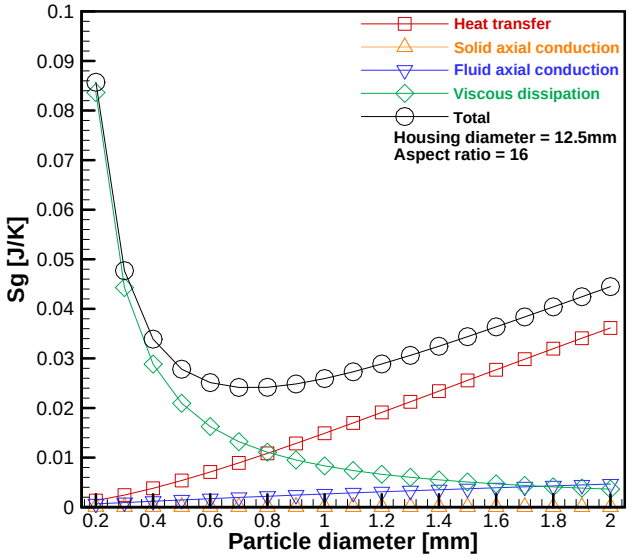

(a)

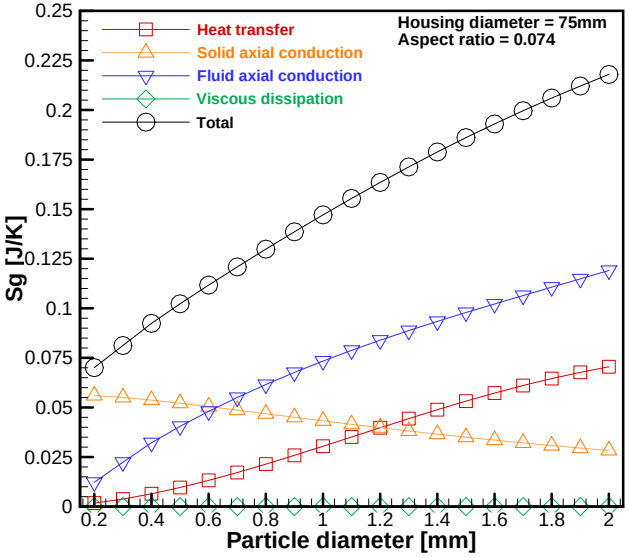

(b)

Figure 7.6 – Entropy generation due to each contribution: (a) Case 1: $D_h = 12.5$ mm and $\zeta = 16$; (b) Case 2: $D_h = 75$ mm and $\zeta = 0.074$.

Fig. 7.6 shows the total entropy generation and the individual contributions as a function of the particle diameter for Cases 1 and 2 of Table 7.4. Case 1, Fig. 7.6(a), is a thin (small housing diameter) and long regenerator. As expected, the axial heat conduction contribution is very small and the total entropy generation is basically a combination of viscous dissipation (because of the long matrix length and the high superficial velocity) and interstitial heat transfer. For small particle diameters, viscous dissipation is the main source of entropy because of the large values of pressure drop. As the particle diameter increases, the pressure drop decreases but the interstitial heat transfer becomes less effective. As a result, the entropy generated due to a finite temperature difference between the solid and the fluid becomes more important. A local minimum S_g at a particle diameter of around 0.7 mm can be verified. However, at this point of minimum entropy generation, the effectiveness is slightly higher than the desired performance constraint of 95% effectiveness (see Fig. 7.5).

Case 2, Fig. 7.6(b), illustrates an opposite situation, i.e., a large-diameter short regenerator, for which the contributions of axial heat conduction are expected to be more important because of the low superficial velocity and the short regenerator length. The total entropy generation in Case 2 is a combination of the entropy production by axial heat conduction and interstitial heat transfer. As shown in Fig. 7.6(b), for small particle diameters, axial heat conduction in the solid is the main source of entropy generation. As the particle diameter increases, interstitial heat transfer is poorer and the dispersion axial conduction in the fluid phase becomes more important. In this case, the target effectiveness of 95% is not achieved. It can be concluded, therefore, that this is a poor regenerator matrix, with low effectiveness and larger S_g values when compared with Case 1.

7.2.5 Variable Geometry (VG) Evaluation Criteria

7.2.5.1 Fixed Frequency

In this section, the results for the **VG** PEC at a fixed frequency and variable mass flow rate are presented as a function of changes in the geometric parameters. To exemplify the analysis, Fig. 7.7 shows the variation of S_g as a function of d_p, $D_{h,Reg}$ and ζ, for a mass flow rate of 60 kg/h and a frequency of 1 Hz. These results are for a constant

effectiveness of 95%, as demonstrated in Fig. 7.3(a).

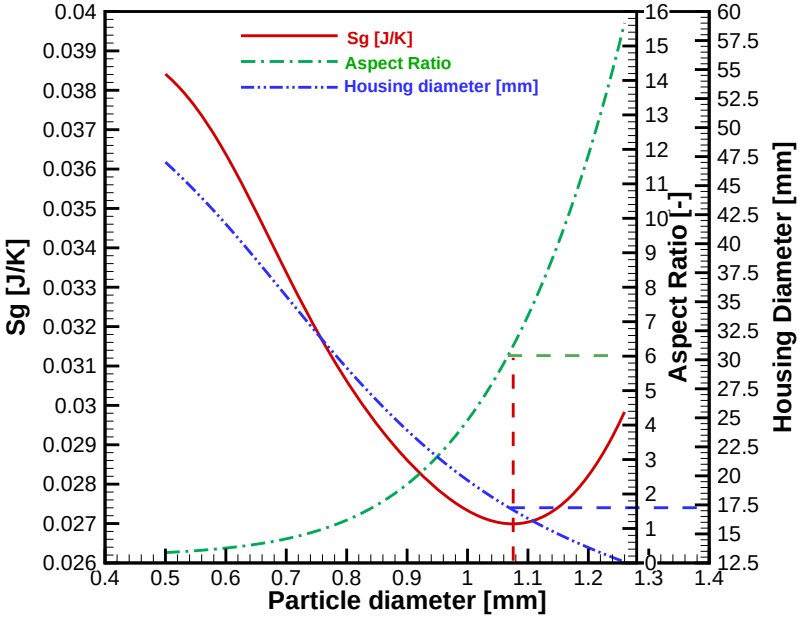

Figure 7.7 – Entropy generation in the **VG** PEC, for a mass flow rate of 60 kg/h and $f = 1$ Hz, at a constant effectiveness of 95%.

As can be seen in Fig. 7.7, a minimum S_g is clearly achieved. The dashed lines indicate the optimal values of d_p, $D_{h,Reg}$ and ζ - 1.07 mm, 17.23 mm and 6.11, respectively - that result in an effectiveness of 95% with a minimum entropy production. Repeating the analysis for the other mass flow rates (see Table 7.2) gives the optimal combinations of d_p, $D_{h,Reg}$ and ζ that guarantee a hot-blow effectiveness of 95%. The results for the **VG** PEC for a fixed frequency and variable mass flow rates are further illustrated in Fig. 7.8. A summary of the conditions associated with the points of minimum S_g is presented in Table 7.5. In addition to the values of the utilization factor, ϕ, the particle Reynolds number, $Re_{dp} = ud_p/\nu_f$, the number of transfer units, $NTU = hA_{HT}/\dot{m}c_{p,f}$ are presented. The individual contributions to the total entropy at the minimum, $S_{g,min}$, due to interstitial heat transfer with a finite temperature difference, $S_{g,HT}$, axial conduction in the solid, $S_{g,SAC}$, axial conduction in the fluid, $S_{g,FAC}$, and viscous dissipation, $S_{g,VD}$, are presented in Table 7.6.

Table 7.5 – Minimum S_{g} parameters for the **VG** PEC for $\epsilon = 95\%$, at a fixed frequency of 1 Hz and flow rates between 40 and 100 kg/h.

$\dot{m}$ [kg/h]	ϕ [-]	$Re_{d_{\mathrm{p}}}$ [-]	NTU [-]	d_{p} [mm]	$D_{\mathrm{h,Reg}}$ [mm]	ζ [-]	$S_{\mathrm{g,min}}$ [J/K]
40	0.397	148.3	20.0	1.66	13.610	12.396	0.01971
50	0.496	115.4	23.0	1.32	15.386	8.579	0.02360
60	0.595	89.5	26.6	1.07	17.227	6.113	0.02704
70	0.695	75.6	31.2	0.89	18.460	4.968	0.02997
80	0.794	61.0	37.9	0.73	19.900	3.965	0.03210
90	0.893	43.8	48.4	0.58	22.206	2.854	0.03343
100	0.992	31.1	66.2	0.45	24.468	2.133	0.03377

Table 7.6 – Individual contributions to the total entropy at the minimum, $S_{\mathrm{g,min}}$, for the **VG** PEC for $\epsilon = 95\%$, at a fixed frequency of 1 Hz and flow rates between 40 and 100 kg/h.

$\dot{m}$ [kg/h]	$S_{\mathrm{g,HT}}$ [J/K] (%)	$S_{\mathrm{g,SAC}}$ [J/K] (%)	$S_{\mathrm{g,FAC}}$ [J/K] (%)	$S_{\mathrm{g,VD}}$ [J/K] (%)
40	0.01569 (79.6)	0.00007 (0.3)	0.00304 (15.4)	0.00091 (4.6)
50	0.01829 (77.5)	0.00011 (0.5)	0.00404 (17.1)	0.00115 (4.9)
60	0.02029 (75.0)	0.00019 (0.7)	0.00519 (19.2)	0.00137 (5.0)
70	0.02171 (72.4)	0.00027 (0.9)	0.00615 (20.5)	0.00184 (6.1)
80	0.02215 (69.0)	0.00039 (1.2)	0.00721 (22.5)	0.00235 (7.3)
90	0.02146 (64.2)	0.00069 (2.0)	0.00873 (26.1)	0.00259 (7.7)
100	0.01948 (57.7)	0.00107 (3.2)	0.01009 (29.9)	0.00313 (9.3)

A more in-depth evaluation of the results in Fig. 7.8 and Tables 7.5 and 7.6 reveals that for $\dot{m} = 40$ kg/h the optimal region involves bigger particle diameters, with larger values of $Re_{d_{\mathrm{p}}}$. As the interstitial heat transfer is less effective (lower NTU and higher $S_{\mathrm{g,HT}}$) and the viscous losses are smaller for bigger particle diameters, long regenerative matrices with smaller housing diameters are required in order to achieve the 95% regenerator effectiveness, giving rise to the lowest contributions of axial conduction in the fluid and solid. On the other hand, for $\dot{m} = 100$ kg/h the optimal region involves small particle diameters, larger housing diameters and smaller values of aspect ratio. Since at high mass flow rates and small particle diameters the viscous losses become more important (see the $S_{\mathrm{g,VD}}$ column), a big housing diameter is required to decrease the superficial velocity, which results in shorter matrices.

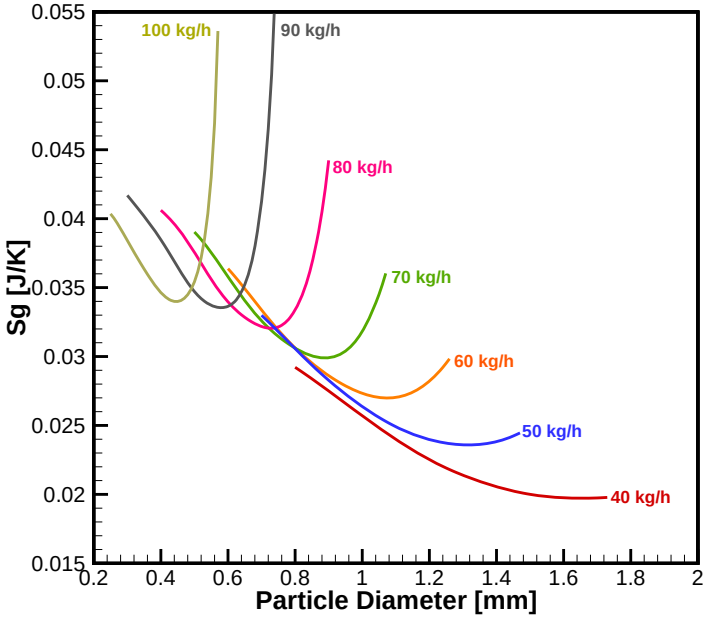
0.055
0.05
0.045
0.04
0.035
0.03
0.025
0.02
0.015
Sg [J/K]
0.2
0.4
0.6
0.8
1
1.2
1.4
1.6
1.8
2
Particle Diameter [mm]
100 kg/h
90 kg/h
80 kg/h
70 kg/h
60 kg/h
50 kg/h
40 kg/h

(a)

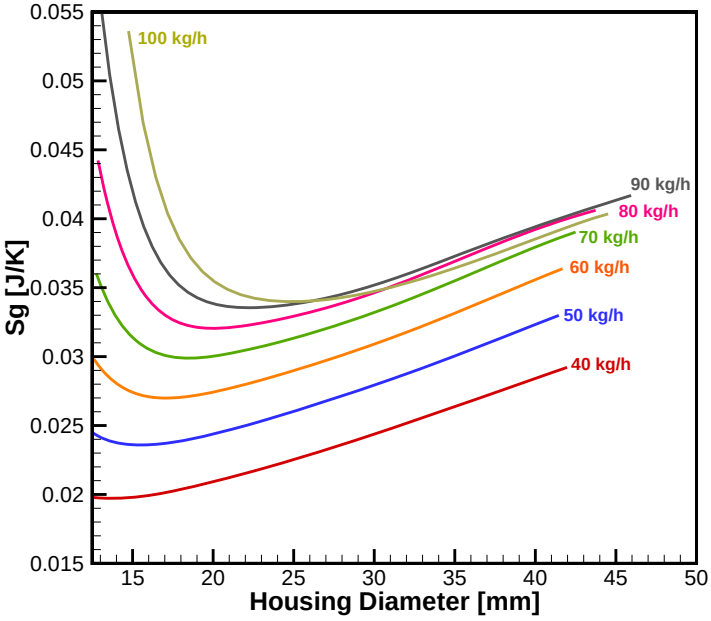
0.055
0.05
0.045
0.04
0.035
0.03
0.025
0.02
0.015
Sg [J/K]
15
20
25
30
35
40
45
50
Housing Diameter [mm]
100 kg/h
90 kg/h
80 kg/h
70 kg/h
60 kg/h
50 kg/h
40 kg/h

(b)

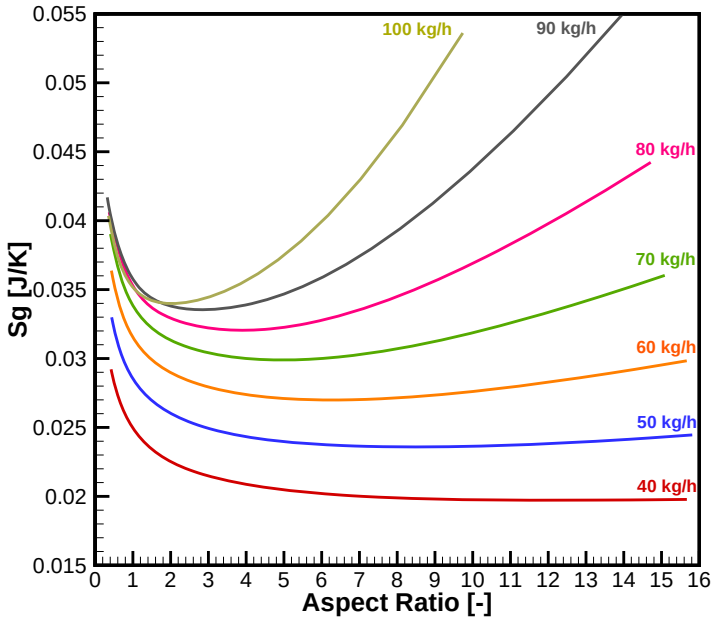

(c)

Figure 7.8 – Minimum entropy analysis for the **VG** PEC for $\epsilon = 95\%$, frequency of 1 Hz and variable flow rates in the range of 40-100 kg/h: (a) S_g as a function of d_p; (b) S_g as a function of $D_{h,Reg}$; (c) S_g as a function of ζ.

Nevertheless, smaller particle diameters are necessary to enhance the interstitial heat transfer and guarantee an optimal performance of the regenerator, increasing NTU and decreasing $S_{g,HT}$. As a result, the axial conduction contributions become more important since the spheres size becomes smaller and the superficial velocity decreases (see the $S_{g,SAC}$ and $S_{g,FAC}$ columns).

In summary, $S_{g,HT}$ was found to be the main contribution (in %) to the total entropy generation for the **VG** PEC at a fixed frequency (although its importance decreases with flow rate as the NTU increases). The second largest contribution is $S_{g,FAC}$, which increases with the flow rate since the matrices becomes shorter and the velocity decreases with increasing housing diameters. The $S_{g,SAC}$ and $S_{g,VD}$ contributions are less important to $S_{g,min}$, with $S_{g,VD}$ increasing with flow rate as a result of the decrease in particle diameter.

7.2.5.2 Fixed Mass Flow Rate

The results for the **VG** PEC at a fixed mass flow rate and variable frequency (see Table 7.3) are presented as a function of changes in $D_{\mathrm{h,Reg}}$, ζ and d_{p} for a constant effectiveness of 95%. The analysis discussed in Fig. 7.7 enabled the construction of diagrams to quantify the effect of frequency and geometric parameters on the cycle-average entropy generation for $\epsilon = 95\%$, as illustrated in Fig. 7.9. In general, the regions of minimum S_{g} with respect to d_{p}, $D_{\mathrm{h,Reg}}$ and ζ become wider as the frequency increases. A summary of the conditions leading to the minimum S_{g} results is presented in Table 7.7 and the individual contributions to the total entropy at the minimum, $S_{\mathrm{g,min}}$, in Table 7.8.

Table 7.7 – Minimum S_{g} parameters for the **VG** PEC for $\epsilon = 95\%$, at a fixed mass flow rate of 60 kg/h and frequencies between 1 and 4 Hz.

f [Hz]	ϕ [-]	$Re_{d_{\mathrm{p}}}$ [-]	NTU [-]	d_{p} [mm]	$D_{\mathrm{h,Reg}}$ [mm]	ζ [-]	$S_{\mathrm{g,min}}$ [J/K]
1.0	0.595	89.5	26.6	1.07	17.227	6.113	0.02704
1.5	0.397	121.3	19.8	1.31	16.373	7.120	0.02032
2.0	0.298	139.4	17.8	1.42	15.903	7.770	0.01565
2.5	0.238	154.5	16.1	1.52	15.630	8.185	0.01277
3.0	0.198	175.2	14.6	1.64	15.246	8.818	0.01079
3.5	0.170	193.1	12.8	1.78	15.127	9.029	0.00933
4.0	-	-	-	-	-	-	-

Table 7.8 – Individual contributions to the total entropy at the minimum, $S_{\mathrm{g,min}}$, for the **VG** PEC for $\epsilon = 95\%$, at a fixed mass flow rate of 60 kg/h and frequencies between 1 and 4 Hz.

f [Hz]	$S_{\mathrm{g,HT}}$ [J/K] (%)	$S_{\mathrm{g,SAC}}$ [J/K] (%)	$S_{\mathrm{g,FAC}}$ [J/K] (%)	$S_{\mathrm{g,VD}}$ [J/K] (%)
1.0	0.02029 (75.0)	0.00019 (0.7)	0.00519 (19.2)	0.00137 (5.0)
1.5	0.01586 (78.0)	0.00009 (0.5)	0.00347 (17.1)	0.00091 (4.5)
2.0	0.01229 (78.6)	0.00006 (0.4)	0.00258 (16.5)	0.00072 (4.6)
2.5	0.01005 (78.7)	0.00004 (0.3)	0.00210 (16.4)	0.00058 (4.5)
3.0	0.00847 (78.5)	0.00003 (0.3)	0.00178 (16.5)	0.00051 (4.7)
3.5	0.00726 (77.8)	0.00003 (0.3)	0.00163 (17.5)	0.00041 (4.4)
4.0	-	-	-	-

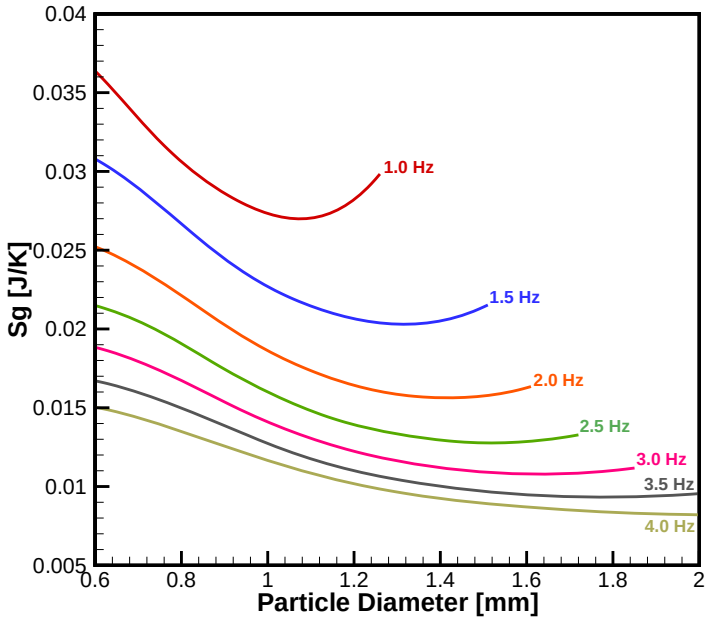
0.04
0.035
0.03
0.025
0.02
0.015
0.01
0.005
Sg [J/K]
1.0 Hz
1.5 Hz
2.0 Hz
2.5 Hz
3.0 Hz
3.5 Hz
4.0 Hz
0.6
0.8
1
1.2
1.4
1.6
1.8
2
Particle Diameter [mm]

(a)

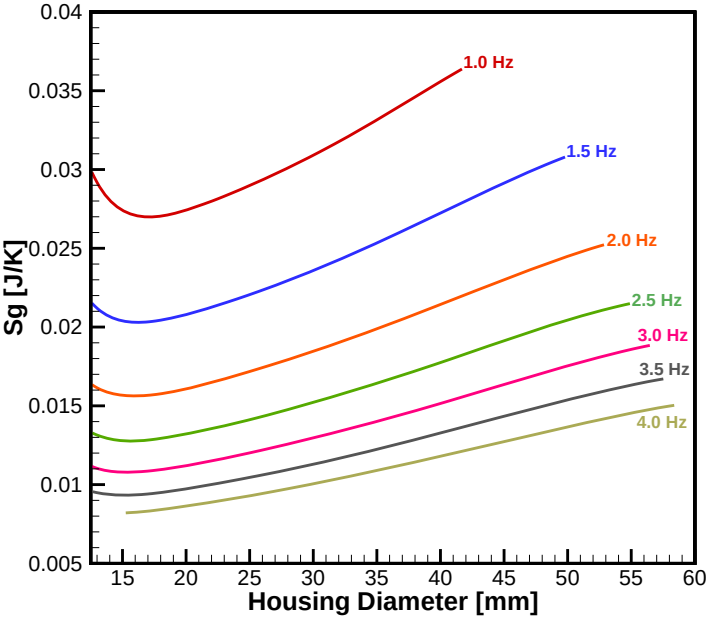
0.04
0.035
0.03
0.025
0.02
0.015
0.01
0.005
Sg [J/K]
1.0 Hz
1.5 Hz
2.0 Hz
2.5 Hz
3.0 Hz
3.5 Hz
4.0 Hz
15
20
25
30
35
40
45
50
55
60
Housing Diameter [mm]

(b)

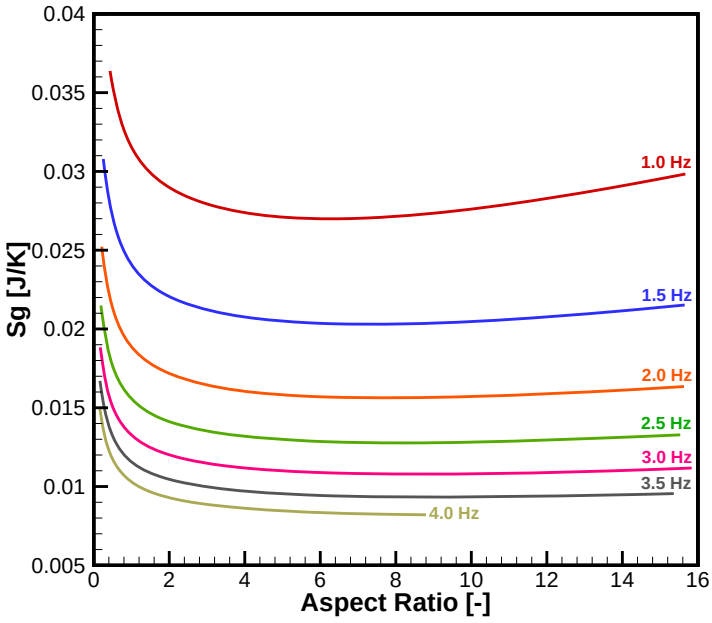

(c)

Figure 7.9 – Minimum entropy analysis for the **VG** PEC for $\epsilon = 95\%$, fixed mass flow rate of 60 kg/h and variable frequencies in the range of 1-4 Hz: (a) S_g as a function of d_p; (b) S_g as a function of $D_{h,Reg}$; (c) S_g as a function of ζ.

An analysis of the results in Fig. 7.9 and Tables 7.7 and 7.8 reveals that for $f = 1.0$ Hz the optimal region involves smaller particle diameters, which guarantee values of NTU that are sufficiently large to achieve 95% effectiveness. In turn, larger housing diameters and shorter matrices are needed to decrease the superficial velocity and reduce the viscous losses, which leads to significant axial conduction contributions to $S_{g,min}$. On the other hand, for $f = 3.5$ Hz the optimal region involves bigger particle diameters, smaller housing diameters and larger values of the aspect ratio. Since the utilization factor decreases with increasing frequency, bigger particle diameters, i.e., larger solid thermal mass, are sufficient to guarantee 95% effectiveness, even at lower values of the NTU. In general, at the highest frequencies, the effectiveness is higher than 95% due to the small values of the utilization factor. Thus, longer regenerators are required to produce sufficiently large heat transfer areas and decrease the axial conduction losses. As

a consequence, the housing diameter decreases.

It should be noted in Table 7.7 that for $f = 4.0$ Hz, a minimum S_g was not found within the ranges of the simulated parameters. A comparison between the contributions of each term (in %) for the variable frequency (Table 7.8) and variable mass flow rate (Table 7.6) cases shows that these are much more sensitive to variations in flow rate for a fixed frequency.

7.2.6 Fixed Face Area (FA) Evaluation Criteria

7.2.6.1 Fixed Frequency

This section presents the results for the **FA** PEC for a fixed frequency and variable mass flow rate as a function of ζ and d_p. As mentioned above, $D_{h,Reg}$ is constant and kept fixed at 25 mm (see Table 7.2). Again, the results are illustrated for a target effectiveness of 95%. The **FA** PEC is further explored in Fig. 7.10, which shows S_g as a function of d_p and ζ for mass flow rates ranging from 100 to 300 kg/h. Table 7.9 summarizes the parameters associated with the optimal conditions for each mass flow rate. Table 7.10 shows the individual contributions to the total entropy at the minimum, $S_{g,min}$.

As can be seen from the results, for $\dot{m} = 100$ kg/h the minimum S_g is associated with a small particle diameter ($d_p = 0.21$ mm) and a short matrix ($\zeta = 1.674$), while for $\dot{m} = 300$ kg/h the minimum S_g was observed at a bigger particle diameter ($d_p = 0.80$ mm) and a longer matrix ($\zeta = 7.003$). As the mass flow rate is increased (increasing the superficial velocity and Re_{dp}), the advection term becomes more important in the energy equation and the value of NTU is decreased. Therefore, a longer regenerator (i.e., a larger interstitial area and a lower utilization factor) is required to keep the effectiveness at 95%. However, as ζ increases, a larger particle diameter is needed to compensate for the entropy generated due to the viscous dissipation.

For the **FA** PEC at a fixed frequency, $S_{g,HT}$ and $S_{g,VD}$ are the main contributions (in %) to the total entropy generation. As the mass flow rate increases, NTU decreases and ζ increases, making the heat transfer less effective (higher $S_{g,HT}$) and, even for increasing particle diameters, the viscous dissipation becomes more important. Also, the $S_{g,FAC}$ and $S_{g,SAC}$ contributions were found to be significant at lower mass flow

rates, i.e., lower superficial velocities and shorter matrices.

Table 7.9 – Minimum S_g parameters for the **FA** PEC for $\epsilon = 95\%$, at a fixed frequency of 1 Hz and variable flow rates between 100 and 300 kg/h.

$\dot{m}$ [kg/h]	ϕ [-]	Re_{d_p} [-]	NTU [-]	d_p [mm]	$D_{h,Reg}$ [mm]	ζ [-]	$S_{g,min}$ [J/K]
100	1.186	13.9	214.1	0.21	25.0	1.674	0.02615
125	1.178	20.7	164.4	0.25	25.0	2.106	0.03616
150	1.149	29.8	127.3	0.30	25.0	2.591	0.04787
175	1.114	41.7	99.5	0.36	25.0	3.119	0.06167
200	1.070	56.9	79.3	0.43	25.0	3.709	0.07752
225	1.027	74.5	66.6	0.50	25.0	4.350	0.09547
250	0.969	97.7	55.5	0.59	25.0	5.120	0.11562
275	0.910	125.6	47.3	0.69	25.0	6.000	0.13825
300	0.850	158.9	41.2	0.80	25.0	7.003	0.16363

Table 7.10 – Individual contributions to the total entropy at the minimum, $S_{g,min}$, for the **FA** PEC for $\epsilon = 95\%$, at a fixed frequency of 1 Hz and variable flow rates between 100 and 300 kg/h.

$\dot{m}$ [kg/h]	$S_{g,HT}$ [J/K] (%)	$S_{g,SAC}$ [J/K] (%)	$S_{g,FAC}$ [J/K] (%)	$S_{g,VD}$ [J/K] (%)
100	0.00797 (30.5)	0.00180 (6.9)	0.00761 (29.1)	0.00877 (33.5)
125	0.01254 (34.7)	0.00141 (3.9)	0.00879 (24.3)	0.01342 (37.1)
150	0.01839 (38.4)	0.00109 (2.3)	0.00983 (20.5)	0.01856 (38.8)
175	0.02582 (41.9)	0.00086 (1.4)	0.01086 (17.6)	0.02412 (39.1)
200	0.03465 (44.7)	0.00069 (0.9)	0.01177 (15.2)	0.03042 (39.2)
225	0.04382 (45.9)	0.00055 (0.6)	0.01246 (13.1)	0.03863 (40.5)
250	0.05462 (47.2)	0.00044 (0.4)	0.01307 (11.3)	0.04749 (41.1)
275	0.06615 (47.8)	0.00036 (0.3)	0.01355 (9.8)	0.05819 (42.1)
300	0.07828 (47.8)	0.00029 (0.2)	0.01394 (8.5)	0.07112 (43.5)

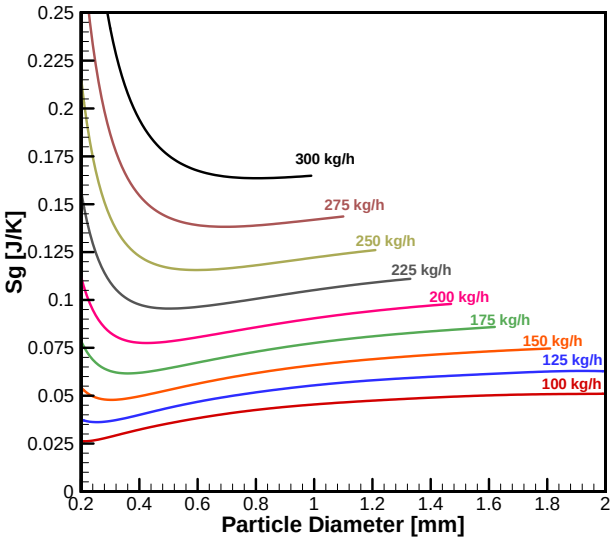

(a)

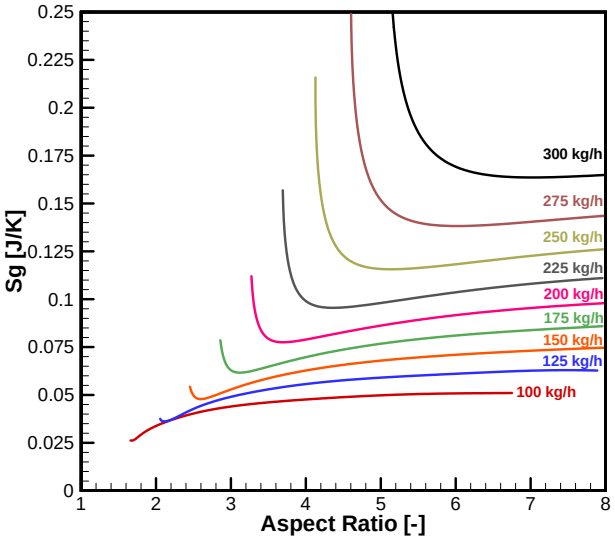

(b)

Figure 7.10 – Minimum entropy analysis for the **FA** PEC for $\epsilon = 95\%$, fixed frequency of 1 Hz and variable mass flow rates in the range of 100-300 kg/h: (a) S_g as a function of d_p; (b) S_g as a function of ζ.

7.2.6.2 Fixed Mass Flow Rate

This section presents the results for the **FA** PEC for a fixed mass flow rate of 250 kg/h and variable frequency between 1 and 4 Hz. Again, changes in ζ and d_p are evaluated along the line of 95% effectiveness (see Table7.3). Fig. 7.11 shows the behavior of S_g as a function of d_p and of ζ and Table 7.11 summarizes the optimal parameters for each frequency. Table 7.12 presents the individual contributions to the total entropy at the minimum, $S_{g,min}$.

Table 7.11 – Minimum S_g parameters for the **FA** PEC for $\epsilon = 95\%$, at a fixed mass flow rate of 250 kg/h and variable frequency between 1 and 4 Hz.

f [Hz]	ϕ [-]	Re_{d_p} [-]	NTU [-]	d_p [mm]	$D_{h,Reg}$ [mm]	ζ [-]	$S_{g,min}$ [J/K]
1.0	0.969	97.7	55.5	0.59	25.0	5.120	0.11562
1.5	0.988	74.5	56.9	0.45	25.0	3.349	0.07723
2.0	0.977	62.9	58.0	0.37	25.0	2.539	0.05752
2.5	0.970	54.6	58.7	0.33	25.0	2.047	0.04630
3.0	0.959	49.7	58.2	0.30	25.0	1.724	0.03874
3.5	0.945	46.3	57.0	0.28	25.0	1.500	0.03336
4.0	0.928	44.7	54.1	0.27	25.0	1.337	0.02945

Table 7.12 – Individual contributions to the total entropy at the minimum, $S_{g,min}$, for the **FA** PEC for $\epsilon = 95\%$, at a fixed mass flow rate of 250 kg/h and variable frequency between 1 and 4 Hz.

f [Hz]	$S_{g,HT}$ [J/K] (%)	$S_{g,SAC}$ [J/K] (%)	$S_{g,FAC}$ [J/K] (%)	$S_{g,VD}$ [J/K] (%)
1.0	0.05462 (47.2)	0.00044 (0.4)	0.01307 (11.3)	0.04749 (41.1)
1.5	0.03623 (46.9)	0.00046 (0.6)	0.01031 (13.4)	0.03022 (39.1)
2.0	0.02648 (46.0)	0.00045 (0.8)	0.00841 (14.6)	0.02218 (38.6)
2.5	0.02105 (45.5)	0.00044 (1.0)	0.00736 (15.9)	0.01744 (37.7)
3.0	0.01761 (45.4)	0.00043 (1.1)	0.00657 (17.0)	0.01414 (36.5)
3.5	0.01525 (45.7)	0.00042 (1.3)	0.00596 (17.9)	0.01172 (35.1)
4.0	0.01383 (47.0)	0.00041 (1.4)	0.00554 (18.8)	0.00967 (32.8)

As seen from Table 7.11, for $f = 1$ Hz the minimum S_g was found at a relatively large particle diameter ($d_p = 0.59$ mm) and a large aspect ratio ($\zeta = 5.120$), while for $f = 4$ Hz the minimum S_g was found at a smaller particle size ($d_p = 0.27$ mm) and a shorter matrix length ($\zeta = 1.337$).

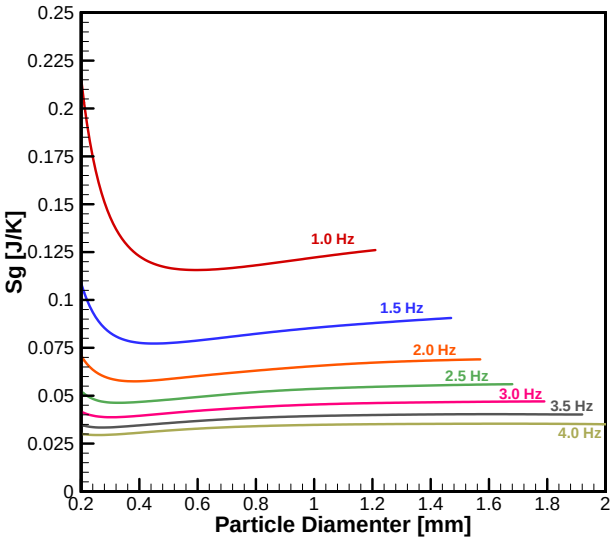

(a)

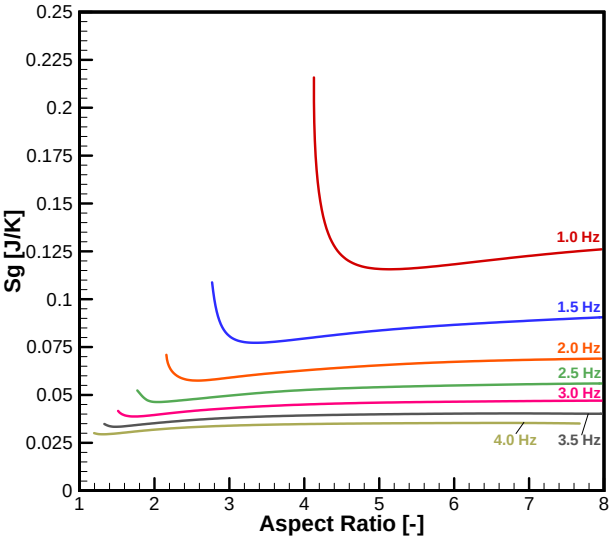

(b)

Figure 7.11 – Minimum entropy analysis for the **FA** PEC for $\epsilon = 95\%$, fixed mass flow rate of 250 kg/h and variable frequencies in the range of 1-4 Hz: (a) S_g as a function of d_p; (b) S_g as a function of ζ.

A different trend is observed when the results in this section are compared with the variable mass flow rate cases. As the frequency increases, the utilization factor decreases due to the shorter blow period. Nevertheless, the matrix length also decreases, reducing the thermal mass of the solid phase and the total interstitial area. As a result, the utilization factor and NTU do not present significant variations with frequency, which result in a nearly constant contribution (in %) of $S_{g,HT}$ to $S_{g,min}$. At small frequencies $S_{g,VD}$ was higher even for bigger particle diameters due to the large value of the matrix length. On the other hand, higher frequencies need shorter matrix lengths and smaller particle diameters, which increases the penalty associated with axial heat conduction ($S_{g,FAC}$ and $S_{g,SAC}$).

7.3 Optimization of Active Magnetic Regenerators

The results for the optimization of active magnetic regenerators are discussed in this section. The simulations were carried out considering packed bed matrices composed by gadolinium spheres of different sizes. Eq. (7.8) was applied to calculate the local rate of entropy generation. The properties of pure water were assumed for the fluid phase. For simplicity, the magnetic flux density variation is described by a step function, with minimum and maximum flux densities of 0 and 1.5 T.

7.3.1 Performance Evaluation Criteria for AMRs

The PEC used in the AMR optimization were the same used in the passive regenerator optimization: the Variable Geometry (**VG**) and the Fixed Face Area (**FA**) (WEBB; KIM, 2005). The ranges of the variables explored in the analysis are presented in Table 7.13 and the flow chart of the various scenarios is in Fig. 7.2. The performance constraint of an AMR optimization is the cycle-average cooling capacity at a fixed temperature difference between the hot and cold reservoirs. This constraint corresponds to a fixed cycle-average heat transfer rate at the cold heat exchanger, independently of the matrix size/mass and operating conditions. In the present analysis, a cycle-average cooling capacity, $\overline{\dot{Q}}_c$, of **20 W per regenerator** is considered, for a temperature span $\Delta T_{Hex} = \mathbf{15\ K}$.

Table 7.13 – Ranges of the geometric variables for each PEC in the AMR optimization.

PEC	$D_{\mathrm{h,Reg}}$ [mm]	ζ	Housing volume [cm^3]	d_{p} [mm]
VG	12.5 - 50	16 - 0.25	24.544	0.3 - 2
FA	25	1 - 8	12.272 - 98.175	0.3 - 2

As in the passive regenerator optimization procedure, for the **VG** and **FA** PEC, for each combination of $D_{\mathrm{h,Reg}}$, ζ and d_{p}, the simulations were carried out considering two different scenarios. In the first scenario, the frequency was kept fixed at 1 Hz and the mass flow rate was varied from 40 to 100 kg/h (steps of 10 kg/h) for the **VG** PEC and from 50 to 200 kg/h (steps of 25 kg/h) for the **FA** PEC. In the second scenario, the frequency was varied from 1 to 4 Hz (steps of 0.5 Hz) and the mass flow rate was kept constant at 60 kg/h for the **VG** PEC and at 200 kg/h for the **FA** PEC.

For each scenario of the **VG** PEC, discrete data points were selected in the housing diameter and particle diameter ranges shown in Table 7.13. The incremental steps were 2.5 mm for the range $12.5 \leq D_{\mathrm{h,Reg}} \leq 30$ mm, 5 mm for $30 \leq D_{\mathrm{h,Reg}} \leq 50$ mm and 0.1 mm for d_{p}, which resulted in 216 independent cases for each designed mass flow rate or frequency. Similarly, for the **FA** PEC, the aspect ratio range was divided in incremental steps of 0.5, plus the 0.1-mm steps for d_{p}, resulting in 270 cases for the variable frequency and variable mass flow rate scenarios for each designed mass flow rate or frequency. In total, 6804 different simulations were performed for the two PEC. As in the passive regenerator simulations, the searches for the points of minimum entropy generation were refined further using 4th-order (or less) polynomial interpolations ($R^2 > 0.9999$) to guarantee the stability of the numerical solutions and provide a better resolution (finer than 0.5 mm for $D_{\mathrm{h,Reg}}$, 0.05 for ζ and 0.01 mm for d_{p}) for the minimum S_{g} value at a reasonable computational cost.

7.3.2 Entropy Generation Cycle-Average Cooling Capacity Contour Maps

As the numerical convergence is obtained for a specific set of simulated parameters associated with a PEC, the AMR configurations that yield

the desired value of $\overline{\dot{Q}}_c$ can be identified. As illustrated previously in the passive regenerators optimization, Fig. 7.12 presents the contour maps for the **VG** PEC with $\dot{m} = 60$ kg/h and frequencies of 1 and 4 Hz. Fig. 7.13 shows the contour maps for the **FA** PEC with $\dot{m} = 200$ kg/h and frequencies of 1 and 4 Hz. Lines of constant S_g (red lines) are plotted together with lines of constant $\overline{\dot{Q}}_c$ (blue lines), as a function of the particle diameter and housing diameter for the **VG** PEC (Fig. 7.12) and particle diameter and housing aspect ratio for the **FA** PEC (Fig. 7.13).

From Figs. 7.12 and 7.13, it can be seen that the target value of $\overline{\dot{Q}}_c = 20$ W per regenerator (blue solid line) can be achieved with different combinations of d_p and $D_{h,Reg}$ or ζ, with different frequencies and flow rates for each PEC. For the **VG** PEC with $\dot{m} = 60$ kg/h and $f = 1$ Hz, Fig. 7.12(a), $\overline{\dot{Q}}_c = 20$ W per regenerator can be achieved with values of d_p between 0.5 and 1.4 mm and housing diameters between 12.5 and 50 mm, which correspond to values of ζ between 0.25 and 16. In this case, the minimum value of S_g that guarantees a value of $\overline{\dot{Q}}_c = 20$ W per regenerator was found around $d_p = 1.2$ mm and $D_{h,Reg} = 20$ mm. For the 4 Hz operating frequency, Fig. 7.12(b), the minimum S_g is shifted to larger values of d_p, yielding other combination of $D_{h,Reg}$ and ζ.

For the **FA** PEC with $\dot{m} = 200$ kg/h and $f = 1$ Hz, Fig. 7.13(a), the minimum S_g for $\overline{\dot{Q}}_c = 20$ W per regenerator was identified in the vicinity of $d_p = 1.1$ mm, with an aspect ratio around 4. As expected, for other frequencies the minimum S_g range changes and $\overline{\dot{Q}}_c = 20$ W per regenerator is achieved with other combinations of d_p and ζ, as presented in Fig. 7.13(b).

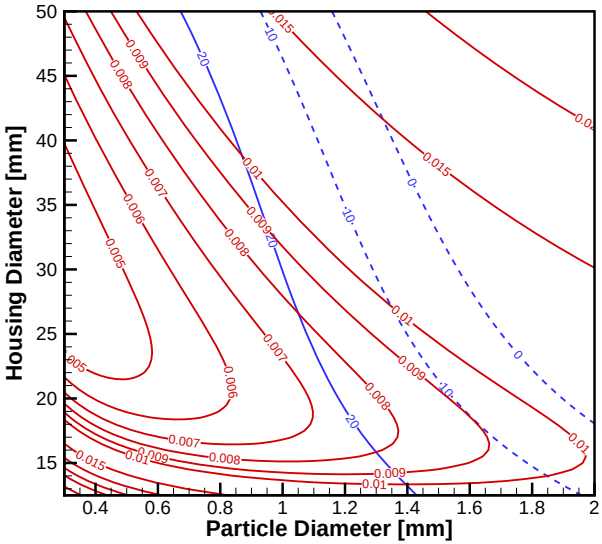

(a)

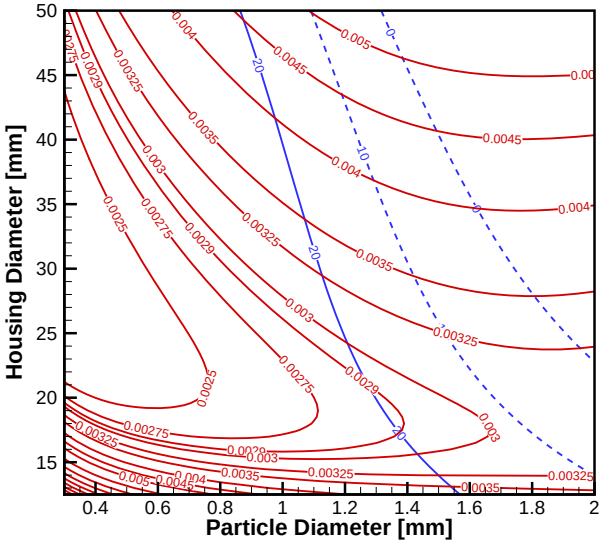

(b)

Figure 7.12 – Lines of constant $\overline{\dot{Q}}_c$ (blue lines) and S_g (red lines) as a function of d_p and $D_{h,Reg}$ for the **VG** PEC with $\dot{m} = 60$ kg/h and frequencies of (a) 1 Hz; (b) 4 Hz.

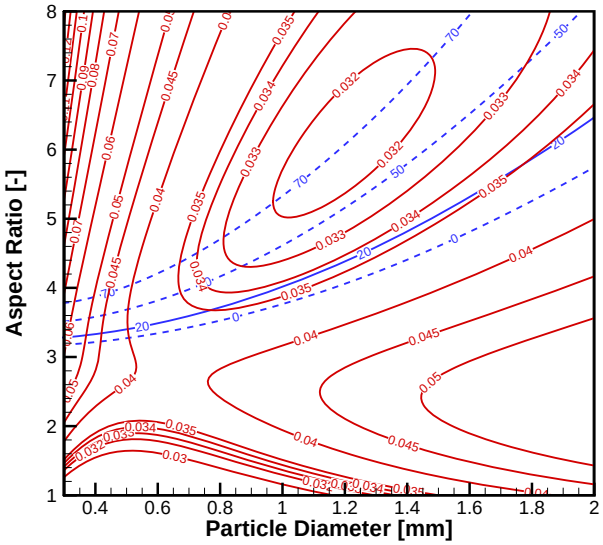

(a)

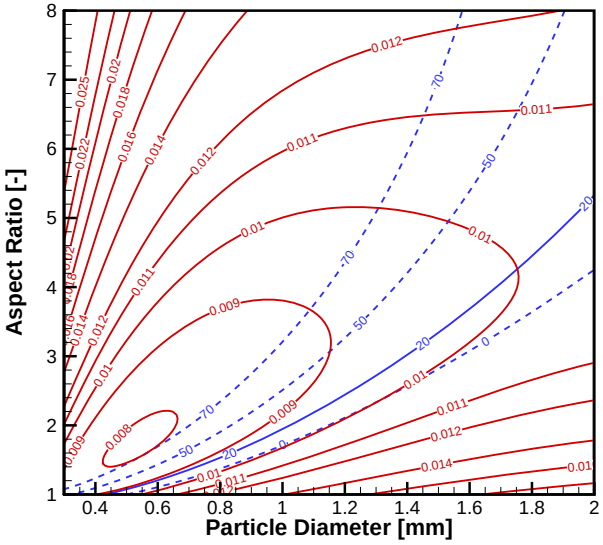

(b)

Figure 7.13 – Lines of constant $\overline{\dot{Q}}_c$ (blue lines) and S_g (red lines) as a function of d_p and ζ for the **FA** PEC with $\dot{m} = 200$ kg/h and frequencies of (a) 1 Hz; (b) 4 Hz.

7.3.3 Variable Geometry (VG) Evaluation Criteria

7.3.3.1 Fixed Frequency

This section describes the results for the **VG** PEC at a fixed frequency and variable mass flow rate. Performing the same evaluation presented in Fig. 7.7 for passive regenerators, it is possible to find the optimal combinations of d_p, $D_\mathrm{h,Reg}$ and ζ that guarantee a $\overline{\dot{Q}}_\mathrm{c} = 20$ W per regenerator at $\Delta T_\mathrm{Hex} = 15$ K. The results are shown in Fig. 7.14. A summary of the conditions associated with the points of minimum S_g is presented in Table 7.14, which also presents the values of the utilization, ϕ, and the total demagnetization factor, $N_\mathrm{D,total}$ (calculated from Eq. (4.49)), which depends only on $D_\mathrm{h,Reg}$ and ζ since the porosity of the regenerator is constant. The individual contributions to the total entropy at the minimum, $S_\mathrm{g,min}$, due to interstitial heat transfer with a finite temperature difference, $S_\mathrm{g,HT}$, axial conduction in the solid, $S_\mathrm{g,SAC}$, axial conduction in the fluid, $S_\mathrm{g,FAC}$, and viscous dissipation, $S_\mathrm{g,VD}$, are presented in Fig. 7.15.

Table 7.14 – Minimum S_g parameters for the **VG** PEC for $\overline{\dot{Q}}_\mathrm{c} = 20$ W per regenerator and $\Delta T_\mathrm{Hex} = 15$ K, at a fixed frequency of 1 Hz and flow rates between 40 and 100 kg/h.

$\dot{m}$ [kg/h]	d_p [mm]	$D_\mathrm{h,Reg}$ [mm]	ζ [-]	$N_\mathrm{D,total}$ [-]	ϕ [-]	NTU [-]	$S_\mathrm{g,min}$ [J/K]
40	1.07	18.217	5.169	0.412	0.505	17.3	0.00414
50	1.2	19.030	4.535	0.408	0.631	11.0	0.00580
60	1.18	19.966	3.926	0.404	0.757	9.5	0.00741
70	1.1	21.000	3.375	0.399	0.884	9.4	0.00897
80	0.99	22.120	2.887	0.393	1.010	10.1	0.01046
90	0.86	23.426	2.431	0.385	1.136	11.9	0.01183
100	0.71	25.167	1.960	0.375	1.262	15.7	0.01298

Before starting the analysis of the results, it is important to remember how $\overline{\dot{Q}}_\mathrm{c}$ is defined:

$$\overline{\dot{Q}}_\mathrm{c} = \overline{\dot{m}} c_\mathrm{p,f} (T_\mathrm{C} - \overline{T}_\mathrm{CE}) \tag{7.10}$$

where $\overline{\dot{m}}$ is the average mass flow rate and $\overline{T}_\mathrm{CE}$ is the average temperature of the fluid exiting the regenerator at the cold end. Also, $T_\mathrm{C} - \overline{T}_\mathrm{CE}$ is the temperature difference at the cold reservoir, ΔT_c.

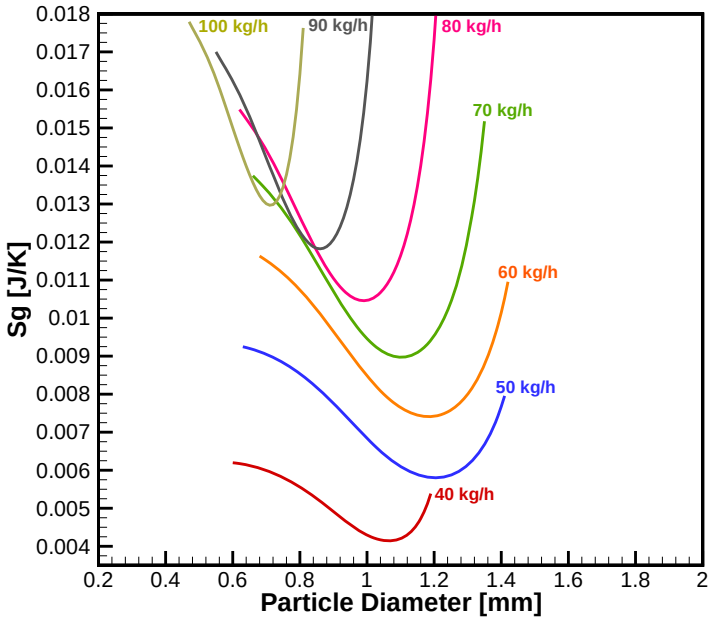
100 kg/h
90 kg/h
80 kg/h
70 kg/h
60 kg/h
50 kg/h
40 kg/h
Sg [J/K]
Particle Diameter [mm]
0.018
0.017
0.016
0.015
0.014
0.013
0.012
0.011
0.01
0.009
0.008
0.007
0.006
0.005
0.004
0.2
0.4
0.6
0.8
1
1.2
1.4
1.6
1.8
2

(a)

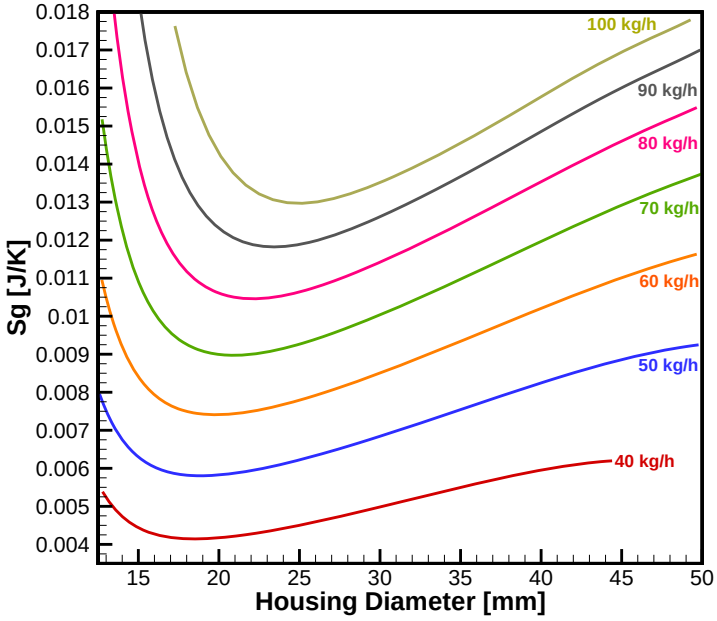
100 kg/h
90 kg/h
80 kg/h
70 kg/h
60 kg/h
50 kg/h
40 kg/h
Sg [J/K]
Housing Diameter [mm]
0.018
0.017
0.016
0.015
0.014
0.013
0.012
0.011
0.01
0.009
0.008
0.007
0.006
0.005
0.004
15
20
25
30
35
40
45
50

(b)

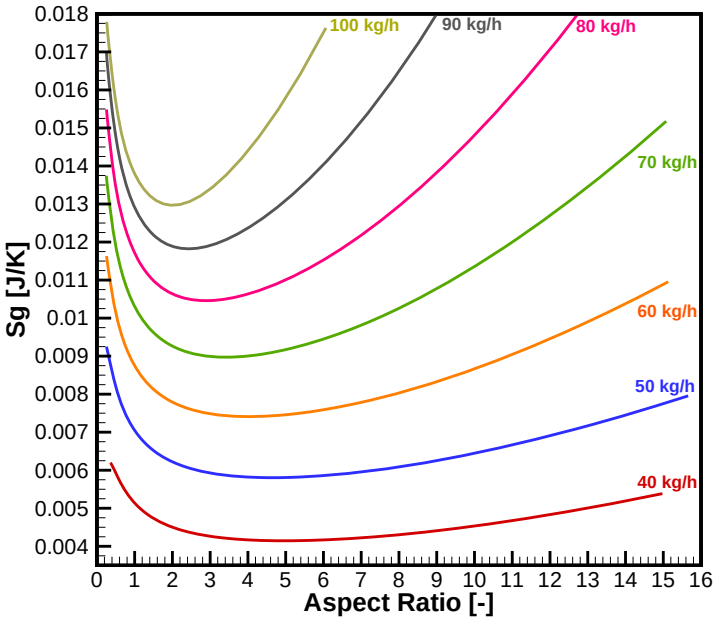

(c)

Figure 7.14 – Minimum entropy analysis for the **VG** PEC for $\overline{\dot{Q}}_c$ = 20 W per regenerator and ΔT_{Hex} = 15 K, at a frequency of 1 Hz and variable flow rates in the range of 40-100 kg/h: (a) S_g as a function of d_p; (b) S_g as a function of $D_{h,Reg}$; (c) S_g as a function of ζ.

An evaluation of the results in Figs. 7.14 and 7.15 and Table 7.14 reveals that for the smallest mass flow rate, $\dot{m}$ = 40 kg/h, to achieve the performance constraint of $\overline{\dot{Q}}_c$ = 20 W per regenerator, a larger ΔT_c is necessary, which is associated with a lower average temperature $\overline{T}_{CE}$ (the reservoir temperature is fixed). To achieve a lower $\overline{T}_{CE}$ a higher ϵ-NTU matrix is necessary, which is guaranteed by the smallest utilization, smaller particle size (compared with 50-70 kg/h) and a longer matrix with a smaller $D_{h,Reg}$, corresponding to higher superficial velocities. This optimum scenario is confirmed by the smallest absolute value of $S_{g,HT}$, meaning a high effectiveness heat transfer. However, the use of a smaller particle size increased slightly the penalties associated with the viscous dissipation.

As the mass flow rate is increased up to 70 kg/h, the optimal region

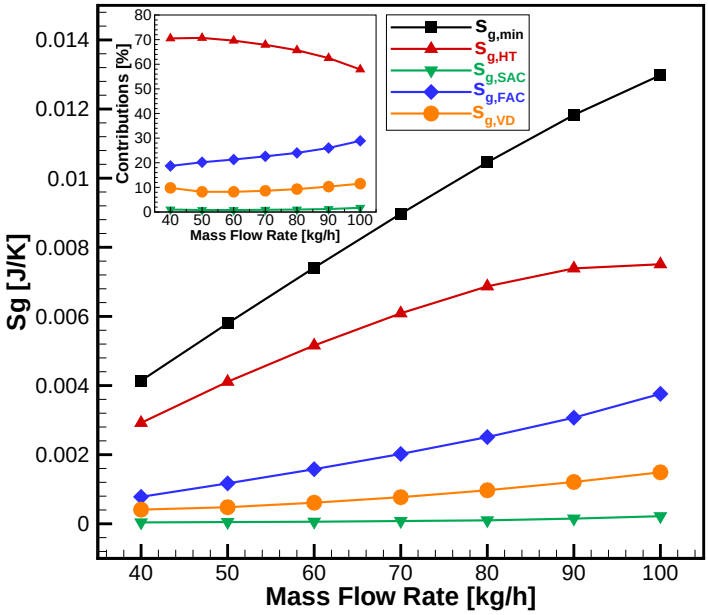

Figure 7.15 – Individual contributions to the total entropy at the minimum, $S_{g,min}$, for the **VG** PEC for $\overline{\dot{Q}}_c = 20$ W per regenerator and $\Delta T_{Hex} = 15$ K, at a fixed frequency of 1 Hz and flow rates between 40 and 100 kg/h.

shifts to bigger particle diameters, larger housing diameters and shorter aspect ratios (see Table 7.14). Although the NTU is low, the small absolute values of utilization still result in a high effectiveness and a large ΔT_c, which when multiplied by the low flow rate guarantees the 20-W constraint. This trend persists until a minimum NTU is found for $\dot{m} = 70$ kg/h.

For mass flow rates higher than 70 kg/h, lower values of ΔT_c are sufficient to guarantee the 20-W constraint. However, the increase of the utilization needs to be compensated with a larger NTU in order to achieve the 15 K of span. Hence, the optimal conditions involve small particle diameters, large housing diameters and small values of aspect ratio. Since at high mass flow rates and small particle diameters the viscous losses become more important, a big housing diameter is required to decrease the superficial velocity, which results in shorter matrices.

Nevertheless, smaller particle diameters are necessary to enhance the interstitial heat transfer, increasing NTU and decreasing $S_{\mathrm{g,HT}}$ (in %). However, as the regenerator effectiveness decreases with the increasing utilization, the absolute value of $S_{\mathrm{g,HT}}$ increases with $\dot{m}$. With shorter matrices, the axial conduction contributions ($S_{\mathrm{g,FAC}}$) become more important (in %) since the spheres size becomes smaller and the superficial velocity decreases. $S_{\mathrm{g,VD}}$, also increases with the mass flow rate and the decreasing on the particle size. The contribution of $S_{\mathrm{g,SAC}}$ is small, around 1%.

Regarding the demagnetization factor, for a constant temperature difference between the thermal reservoirs, a bigger $N_{\mathrm{D,total}}$ means a smaller effective magnetic field, H_{eff}, (Eq. (4.47)) and a smaller ΔT_{ad}. To compensate the reduction of the MCE, a higher effectiveness regenerator is required. However, for the cases evaluated here, the variations in $N_{\mathrm{D,total}}$ were little and, for the relatively small temperature difference of 15 K used as a constraint, these effects were of secondary importance to the MCE when the different optimum dimensions were compared.

It has been shown in this section that the optimal configurations for $f = 1$ Hz and several mass flow rates are related to small housing diameters (between 18 and 25 mm). Thus, the magnetic circuit size can be estimated considering a permanent magnet built in a Halbach cylinder array, for which the magnetic flux density, B, inside the bore of an infinite cylinder is given by (BJØRK *et al.*, 2008):

$$B = B_{\mathrm{rem}} \ln\left(\frac{D_{\mathrm{e}}}{D_{\mathrm{i}}}\right) \tag{7.11}$$

where B_{rem} is the remanence of the magnet grade, D_{e} is the external and D_{i} the internal diameters of the cylinder. Considering $B = 1.5$ T, $B_{\mathrm{rem}} = 1.4$ T for a $Nd_2Fe_{14}B$ magnet grade (BAKKER-MAGNETICS, 2014), $D_{\mathrm{i}} = D_{\mathrm{h,Reg}}$ and $L_{\mathrm{mag}} = L_{\mathrm{Reg}} = \zeta D_{\mathrm{h,Reg}}$, the optimum regenerator dimensions for each flow rate lead to the ideal Halbach cylinder dimensions presented in Table 7.15.

The results show that the smaller mass flow rates require smaller diameters and longer magnets, while the higher flow rates are related to bigger diameters and shorter magnets. However, the total volume of permanent magnet necessary to create a flux density of 1.5 T in the bore of the Halbach cylinder is about the same for all cases. Therefore,

Table 7.15 – Ideal Halbach cylinder dimensions considering the optimized parameters according to the **VG** PEC for a frequency of 1 Hz and flow rates between 40 and 100 kg/h.

$\dot{m}$ [kg/h]	D_{i} [mm]	D_{e} [mm]	L_{mag} [mm]	$Volume$ [cm^3]
40	18.217	53.185	94.164	233.7
50	19.030	55.559	86.301	233.8
60	19.966	58.292	78.387	233.7
70	21.000	61.310	70.875	233.8
80	22.120	64.580	63.860	233.7
90	23.426	68.393	56.949	233.8
100	25.157	73.447	49.308	233.4

in terms of the minimum entropy generated (less irreversibility), using the smallest mass flow rate possible is recommended since it achieves the performance constraint with a more efficient AMR design.

7.3.3.2 Fixed Mass Flow Rate

The results for the **VG** PEC at a fixed mass flow of 60 kg/h rate and variable frequencies, between 1 and 4 Hz, are presented as a function of changes in $D_{\mathrm{h,Reg}}$, ζ and d_{p} for a constant $\overline{\dot{Q}}_{\mathrm{c}} = 20$ W per regenerator at $\Delta T_{\mathrm{Hex}} = 15$ K, as illustrated in Fig. 7.16. A summary of the conditions that lead to the minimum S_{g} results is presented in Table 7.7 and the individual contributions to the total entropy at the minimum, $S_{\mathrm{g,min}}$, are shown in Fig. 7.17.

Table 7.16 – Minimum S_{g} parameters for the **VG** PEC for $\overline{\dot{Q}}_{\mathrm{c}} = 20$ W per regenerator at $\Delta T_{\mathrm{Hex}} = 15$ K, at a fixed mass flow rate of 60 kg/h and frequencies between 1 and 4 Hz.

f [Hz]	d_{p} [mm]	$D_{\mathrm{h,Reg}}$ [mm]	ζ [-]	$N_{\mathrm{D,total}}$ [-]]	ϕ [-]	NTU [-]	$S_{\mathrm{g,min}}$ [J/K]
1	1.18	19.966	3.926	0.404	0.757	9.5	0.00741
1.5	1.35	19.096	4.488	0.408	0.505	7.3	0.00549
2	1.39	19.043	4.525	0.408	0.379	6.9	0.00446
2.5	1.39	18.962	4.584	0.409	0.303	6.9	0.00383
3	1.38	18.923	4.612	0.409	0.253	7.0	0.00339
3.5	1.36	18.810	4.696	0.409	0.216	7.2	0.00309
4	1.33	18.752	4.739	0.409	0.189	7.5	0.00288

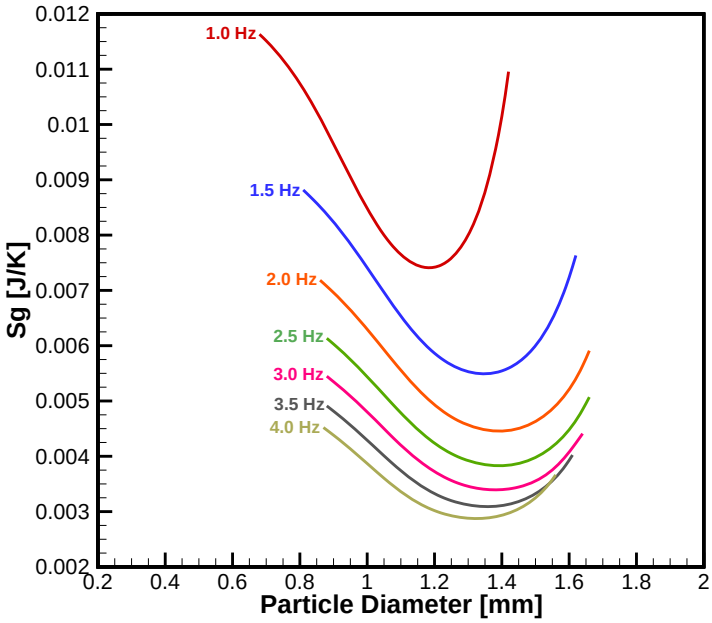
1.0 Hz
1.5 Hz
2.0 Hz
2.5 Hz
3.0 Hz
3.5 Hz
4.0 Hz
Sg [J/K]
Particle Diameter [mm]
0.012
0.011
0.01
0.009
0.008
0.007
0.006
0.005
0.004
0.003
0.002
0.2
0.4
0.6
0.8
1
1.2
1.4
1.6
1.8
2

(a)

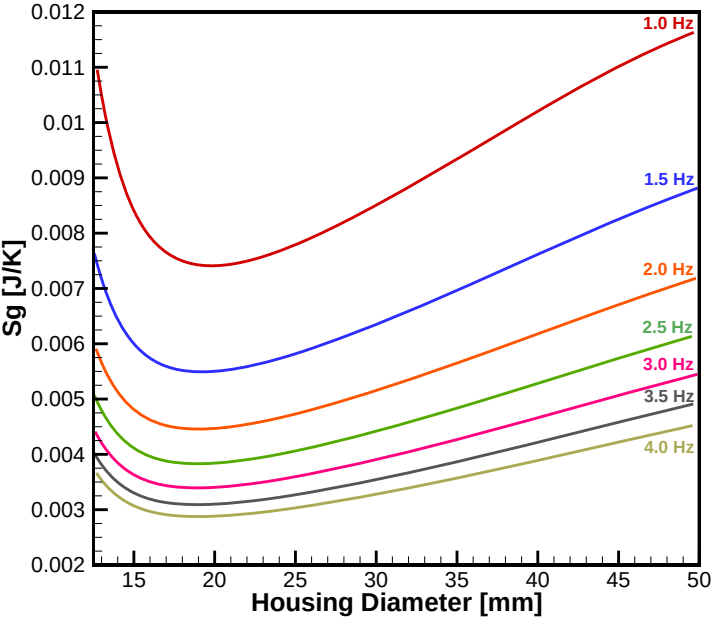
1.0 Hz
1.5 Hz
2.0 Hz
2.5 Hz
3.0 Hz
3.5 Hz
4.0 Hz
Sg [J/K]
Housing Diameter [mm]
0.012
0.011
0.01
0.009
0.008
0.007
0.006
0.005
0.004
0.003
0.002
15
20
25
30
35
40
45
50

(b)

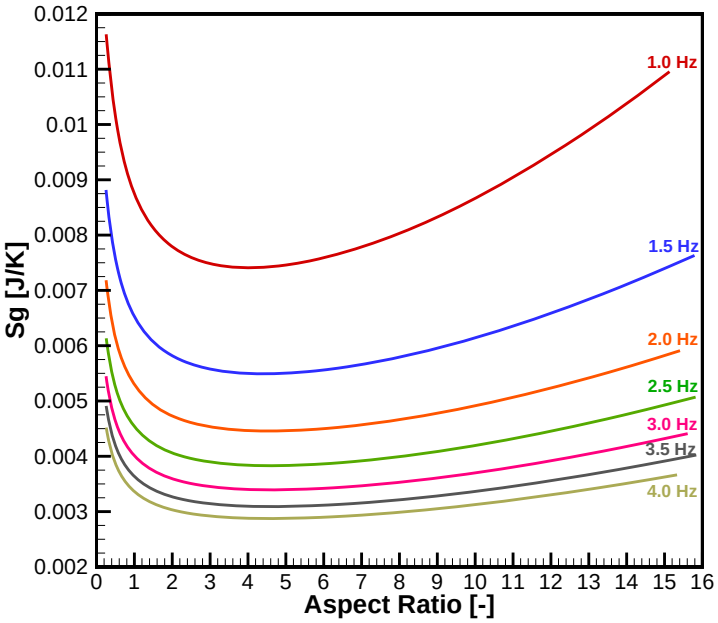

(c)

Figure 7.16 – Minimum entropy analysis for the **VG** PEC for $\overline{\dot{Q}}_c = 20$ W per regenerator at $\Delta T_{Hex} = 15$ K, fixed mass flow rate of 60 kg/h and variable frequencies in the range of 1-4 Hz: (a) S_g as a function of d_p; (b) S_g as a function of $D_{h,Reg}$; (c) S_g as a function of ζ.

In this scenario, with a fixed mass flow rate, ΔT_c is also constant in order to achieve the performance constraint of $\overline{\dot{Q}}_c = 20$ W per regenerator. As a result, the regenerator effectiveness is approximately constant and the output parameters vary according to the frequency/utilization. Regarding $N_{D,total}$, the results show that it is also approximately constant. The results in Figs. 7.16 and 7.17 and Table 7.16 show that for $f = 1.0$ Hz the optimal region involves comparatively smaller particle diameters, meaning a larger NTU for a higher utilization. Hence, larger housing diameters and shorter matrices are needed to decrease the superficial velocity and reduce the viscous losses, which leads to a more significant axial conduction contribution to $S_{g,min}$.

By increasing the frequency and reducing the utilization, the heat transfer is enhanced, which decreases the absolute values of $S_{g,HT}$, as seen in

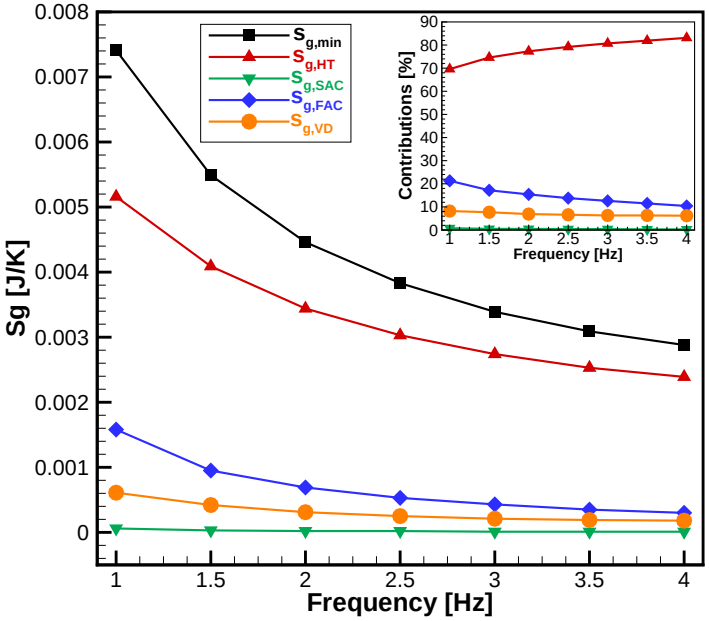

Figure 7.17 – Individual contributions to the total entropy at the minimum, $S_{\mathrm{g,min}}$, for the **VG** PEC for $\dot{\overline{Q}}_{\mathrm{c}} = 20$ W per regenerator at $\Delta T_{\mathrm{Hex}} = 15$ K, at a fixed mass flow rate of 60 kg/h and frequencies between 1 and 4 Hz.

Fig. 7.17. Also, the individual contributions of axial heat conduction and viscous dissipation at the minimum are reduced. As seen in Table 7.16, the longer matrices cause reductions in $S_{\mathrm{g,FAC}}$ and $S_{\mathrm{g,SAC}}$, and bigger particle diameters are responsible for the reduction in $S_{\mathrm{g,VD}}$.

The optimum values encountered for $D_{\mathrm{h,Reg}}$, ζ and d_{p} did not present significant variations with the frequency, and, as a result, the variation in the NTU was also small. As seen in Fig. 7.17, the contributions of $S_{\mathrm{g,SAC}}$ are almost negligible, while $S_{\mathrm{g,HT}}$ dominates the total $S_{\mathrm{g,min}}$. In conclusion, the operation of an AMR at a higher frequency reduces the level of irreversibility in the AMR, as $S_{\mathrm{g,min}}$ decreases with frequency. The optimized points at $\dot{m} = 60$ kg/h and f between 1 and 4 Hz are associated with small housing diameters, around 19 mm, and aspect ratios of approximately 4.5. Regarding the magnetic circuit size, as in the previous case (fixed mass flow rate), all of the optimized conditions had virtually the same total volume of permanent magnet to generate

a 1.5-T variation in magnetic flux density.

7.3.4 Fixed Face Area (FA) Evaluation Criteria

7.3.4.1 Fixed Frequency

This section presents the results for the **FA** PEC for a fixed frequency of 1 Hz and variable mass flow rate, between 50 and 200 kg/h, as a function of ζ and d_{p}. As mentioned previously, $D_{\mathrm{h,Reg}}$ is constant and kept fixed at 25 mm. Again, the results are illustrated for a target $\overline{\dot{Q}}_{\mathrm{c}} = 20$ W per regenerator at $\Delta T_{\mathrm{Hex}} = 15$ K. The **FA** PEC is further explored in Fig. 7.18, which shows S_{g} as a function of d_{p} and ζ. Table 7.17 summarizes the parameters associated with the optimal conditions for each mass flow rate. Fig. 7.10 shows the individual contributions to the total entropy at the minimum, $S_{\mathrm{g,min}}$.

Table 7.17 – Minimum S_{g} parameters for the **FA** PEC for $\overline{\dot{Q}}_{\mathrm{c}} = 20$ W per regenerator at $\Delta T_{\mathrm{Hex}} = 15$ K, at a fixed frequency of 1 Hz and variable flow rates between 50 and 200 kg/h.

$\dot{m}$ [kg/h]	d_{p} [mm]	$D_{\mathrm{h,Reg}}$ [mm]	ζ [-]	$N_{\mathrm{D,total}}$ [-]	ϕ [-]	NTU [-]	$S_{\mathrm{g,min}}$ [J/K]
50	0.33	25.0	1.005	0.334	1.256	72.8	0.00477
75	0.3	25.0	1.311	0.352	1.445	76.7	0.00788
100	0.38	25.0	1.737	0.368	1.453	47.3	0.01173
125	0.49	25.0	2.195	0.381	1.438	28.9	0.01635
150	0.63	25.0	2.704	0.390	1.401	18.0	0.02171
175	0.82	25.0	3.326	0.398	1.328	11.23	0.02768
200	1.07	25.0	4.129	0.405	1.223	7.181	0.03433

For $\dot{m} = 50$ kg/h, the minimum S_{g} configuration is out of the range of the particle diameter and aspect ratio. The values in Table 7.17 refer to the minimum value found (at the end of the interval). Thus, the $\dot{m}$ = 50 kg/h condition is not included in following analysis.

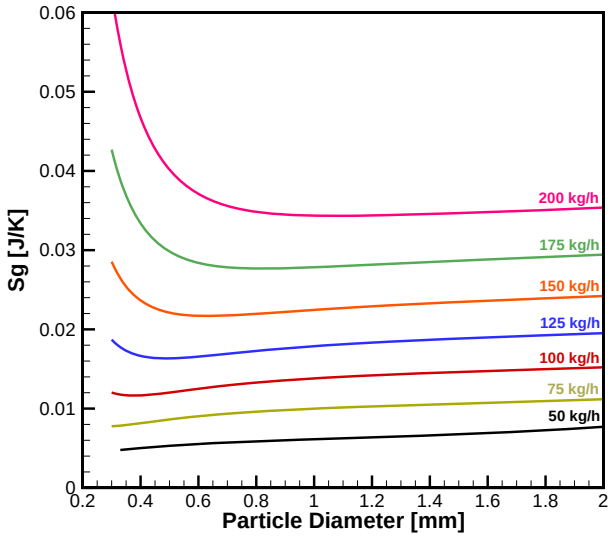

(a)

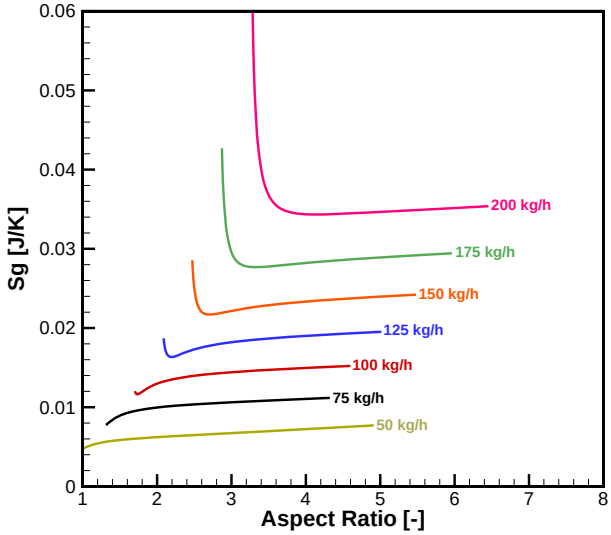

(b)

Figure 7.18 – Minimum entropy analysis for the **FA** PEC for $\overline{\dot{Q}}_c = 20$ W per regenerator at $\Delta T_{Hex} = 15$ K, fixed frequency of 1 Hz and variable mass flow rates in the range of 50-200 kg/h: (a) S_g as a function of d_p; (b) S_g as a function of ζ.

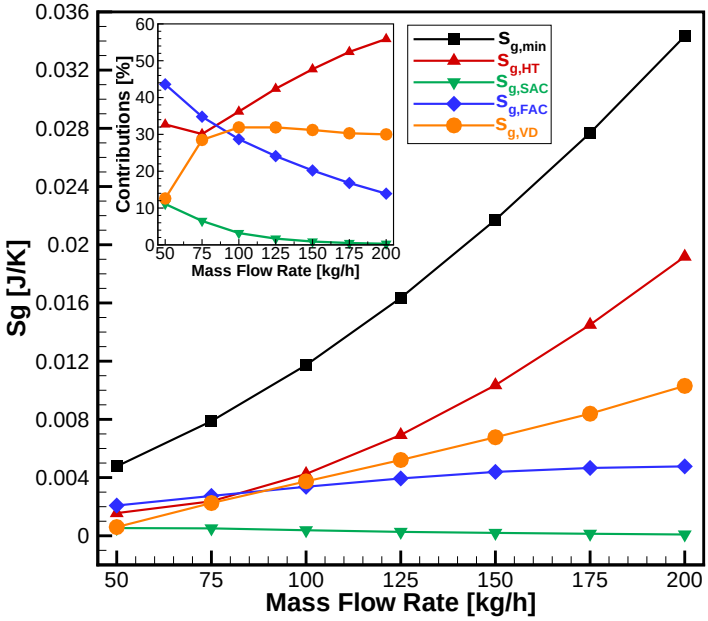

Figure 7.19 – Individual contributions to the total entropy at the minimum, $S_{\mathrm{g,min}}$, for the **FA** PEC for $\dot{\overline{Q}}_{\mathrm{c}} = 20$ W per regenerator at $\Delta T_{\mathrm{Hex}} = 15$ K, fixed frequency of 1 Hz and variable mass flow rates in the range of 50-200 kg/h.

For $\dot{m} = 75$ kg/h, the minimum S_{g} is associated with the smallest particle diameter, that corresponds to a large heat transfer area. Such a high ϵ-NTU matrix is required to achieve the cooling capacity target by increasing ΔT_{c}, which results in comparatively small value of $S_{\mathrm{g,HT}}$ (see Fig. 7.19). However, a shorter matrix is necessary to cut the viscous dissipation contribution, but ends up increasing the penalties associated with the axial heat conduction. In this case, the $S_{\mathrm{g,HT}}$, $S_{\mathrm{g,VD}}$ and $S_{\mathrm{g,FAC}}$ have around the same weight (in % and absolute values) to the total S_{g}.

Increasing the mass flow rate, the minimum S_{g} is shifted to bigger particle diameters and longer matrices. As the mass flow rate is increased, ΔT_{c} becomes smaller, and less effective matrices are necessary, which raises $S_{\mathrm{g,HT}}$. Therefore, the use of bigger particle sizes compensates the increasing superficial velocities and the effect of longer matrices on the viscous dissipation contribution, which increases in terms of its

absolute value but not in relative terms (%). Longer matrices help to reduce the impact of the axial conduction. The increase of $N_{\mathrm{D,total}}$ is also small for the optimized dimensions.

As in the passive regenerator optimization for the **FA** PEC at a fixed frequency, $S_{\mathrm{g,HT}}$ and $S_{\mathrm{g,VD}}$ are the main contributions (in %) to the total entropy generation. As the mass flow rate increases, NTU decreases and ζ increases, making the heat transfer less effective (higher $S_{\mathrm{g,HT}}$) and, even though the particle diameter that minimizes the entropy generation increases, the viscous dissipation becomes more important. Also, the $S_{\mathrm{g,FAC}}$ and $S_{\mathrm{g,SAC}}$ contributions were found to be significant at lower mass flow rates, i.e., lower superficial velocities and shorter matrices.

Regarding the optimum regenerator and magnet dimensions, an external diameter $D_{\mathrm{e}} = 73$ mm was encountered for the ideal Halbach cylinder. Obviously, the amount of magnet material required to generate the 1.5 T flux density change increases linearly with the optimized regenerator length. In this case, in terms of the total minimum entropy generated, using the lowest mass flow rate possible means a more efficient AMR design, which coincides with the smallest ideal magnetic circuit size (short Halbach cylinders).

7.3.4.2 Fixed Mass Flow Rate

This section presents the results for the **FA** PEC for a fixed mass flow rate of 200 kg/h and variable frequency between 1 and 4 Hz. Again, the results are illustrated for a target $\overline{\dot{Q}}_{\mathrm{c}} = 20$ W per regenerator at $\Delta T_{\mathrm{Hex}} = 15$ K. Fig. 7.20 shows the behavior of S_{g} as a function of d_{p} and ζ. Table 7.18 summarizes the optimal parameters for each frequency. Fig. 7.21 presents the individual contributions to the total entropy at the minimum, $S_{\mathrm{g,min}}$.

As in the **VG** PEC, for a constant mass flow rate, the ΔT_{c} that satisfies the performance constraint of $\overline{\dot{Q}}_{\mathrm{c}} = 20$ W per regenerator is also fixed. Hence, in the **FA** PEC for a constant mass flow rate, the effectiveness changes only a little to compensate the small variations of $N_{\mathrm{D,total}}$ and, thus, minor differences in the utilization factor and NTU are observed when compared with the **FA** PEC to a constant frequency.

For $f = 4$ Hz, the minimum S_{g} configuration is out of the range of the particle diameter and aspect ratio. The values in Table 7.18 refer to

Table 7.18 – Minimum S_g parameters for the **FA** PEC for $\overline{\dot{Q}}_c = 20$ W per regenerator at $\Delta T_{Hex} = 15$ K, at a fixed mass flow rate of 200 kg/h and variable frequency between 1 and 4 Hz.

f [Hz]	d_p [mm]	$D_{h,Reg}$ [mm]	ζ [-]	$N_{D,total}$ [-]	ϕ [-]	NTU [-]	$S_{g,min}$ [J/K]
1	1.07	25	4.129	0.405	1.223	7.2	0.03433
1.5	0.86	25	2.788	0.391	1.207	7.5	0.02307
2	0.69	25	2.044	0.377	1.235	8.5	0.01750
2.5	0.62	25	1.658	0.366	1.219	8.6	0.01416
3	0.52	25	1.335	0.353	1.261	9.8	0.01196
3.5	0.51	25	1.185	0.345	1.217	9.0	0.01035
4	0.5	25	1.070	0.338	1.180	8.5	0.00916

the minimum value found (at the end of the interval). Thus, this case was not included in the analysis.

Since ϵ is approximately constant, this AMR optimization scenario is quite similar to the passive regenerator optimization. For $f = 1$ Hz, the minimum S_g was found for a big particle diameter and a large aspect ratio, while for $f = 3.5$ Hz, the minimum S_g was characterized by a small particle size and a short matrix length. As the frequency is increased, the utilization factor decreases due to the shorter blow period. Nevertheless, the matrix length also decreases, reducing the thermal mass of the solid phase and the total interstitial area. Consequently, the utilization factor and the NTU did not present significant variations with frequency, resulting in a nearly constant contribution (in %) of $S_{g,HT}$ to $S_{g,min}$, as can be seen in Fig. 7.21. At low frequencies $S_{g,VD}$ was large even for bigger particle diameters due to the large value of the matrix length. On the other hand, higher frequencies can sustain shorter matrix lengths and smaller particle diameters, but this increases (in %) the penalty associated with axial heat conduction in the fluid, $S_{g,FAC}$. $S_{g,SAC}$ presented a minor contribution to $S_{g,min}$.

In the present scenario, the total minimum entropy generation was observed at the higher operating frequencies. As in the **FA** PEC for a fixed frequency and variable mass flow rate, the more efficient AMR design dimensions, found at the higher frequencies, require the smallest ideal magnetic circuit size due to their shorter aspect ratios.

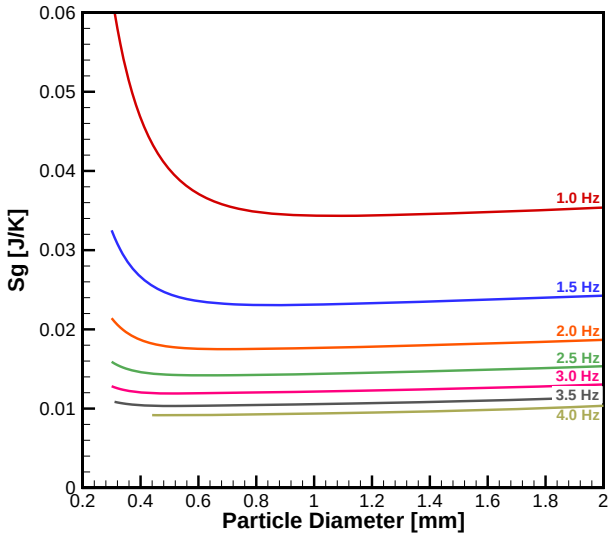

(a)

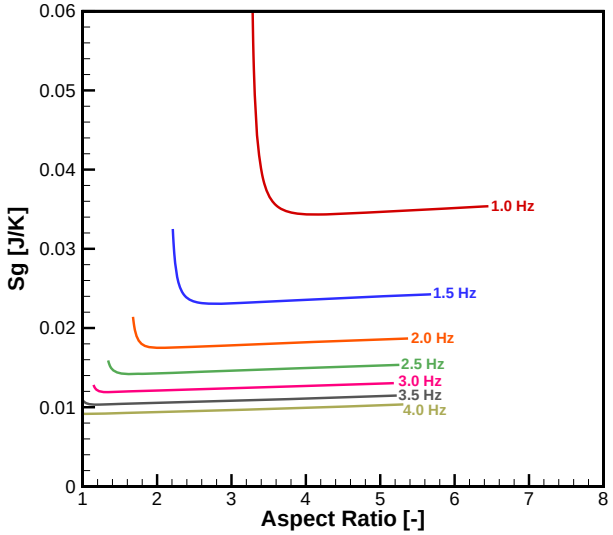

(b)

Figure 7.20 – Minimum entropy analysis for the **FA** PEC for $\overline{\dot{Q}}_c = 20$ W per regenerator at $\Delta T_{Hex} = 15$ K, fixed mass flow rate of 200 kg/h and variable frequencies in the range of 1-4 Hz: (a) S_g as a function of d_p; (b) S_g as a function of ζ.

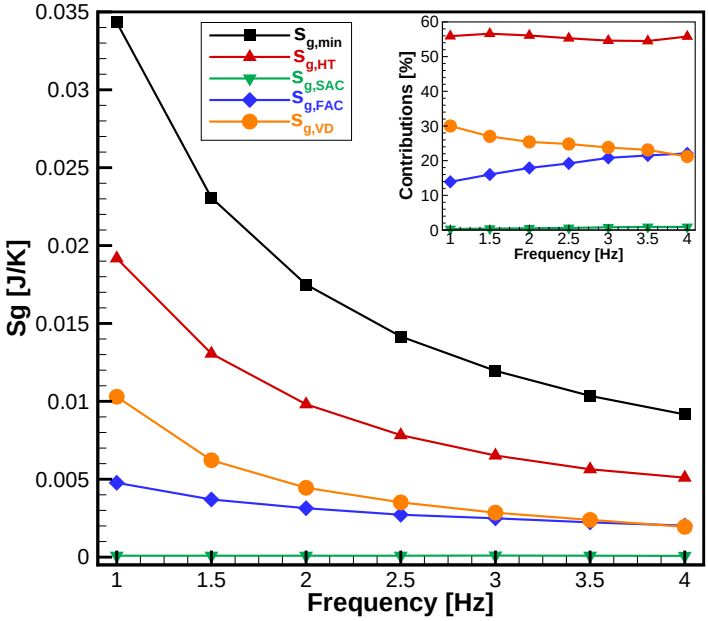

Figure 7.21 – Individual contributions to the total entropy at the minimum, $S_{\mathrm{g,min}}$, for the **FA** PEC for $\overline{\dot{Q}}_{\mathrm{c}} = 20$ W per regenerator at $\Delta T_{\mathrm{Hex}} = 15$ K, at a fixed mass flow rate of 200 kg/h and variable frequency between 1 and 4 Hz.

8 Final Considerations

The work presented in this thesis dealt with the experimental and numerical evaluation of the fluid flow, heat transfer and thermo-magnetic phenomena in thermal regenerators for magnetic cooling applications around room temperature. As proposed initially, an experimental apparatus was designed and built, as well an 1D transient numerical model was developed to accomplish the objectives of this work. Also, different porous media matrices were used as thermal regenerators. Information regarding the heat transfer effectiveness, viscous, thermal and magnetic losses, and performance as a cooling system were evaluated by means of the experimental and numerical approaches.

The passive regenerator study was fundamental to understand the heat transfer and viscous losses in regenerative matrices using a liquid as a heat transfer agent. Firstly, the experience gained along the experimental testing of the passive regenerators related to the instrumentation and regression of the experimental data was crucial for the development of a robust experimental procedure to evaluate the performance of passive and magnetic regenerators.

By using different sizes of spheres and different regenerator casing dimensions it was possible to verify the sensitivity of the experimental and numerical results when operating parameters were changed, e.g., operating frequency and utilization factor. The results for packed beds of spheres corroborated the expectation that small particle diameter spheres guarantee the highest thermal effectivenesses, at the expense of higher viscous losses. In terms of the casing dimensions, matrices with bigger aspect ratios have a high effectiveness as found for Casings #3 and #4. However, for Casing #4 (smaller cross sectional area and higher superficial velocities), the penalties associated with the viscous losses were more pronounced. On the other hand, for a fixed cross sectional area (Casings #1, #2 and #3), higher effectivenesses were found

for the regenerators with larger thermal mass. Nevertheless, the results showed that the improvement of the effectiveness by increasing the regenerator aspect ratio was little when compared with the increasing of the viscous losses.

Comparing different matrix geometries, the results showed that, in terms of the thermal effectiveness, the geometries behaved were very similarly, with the pin arrays presenting a better performance at low utilization and the packed beds performing better at high utilizations. The parallel plate geometry presented a more limited performance because of the axial heat conduction and approximately constant interstitial heat transfer coefficient.

In addition, the results showed that a good regenerator design also has to take into account an optimum balance between the void volume size and the inlet flow distribution in the regenerative matrix. As a recommendation, the void volume has to be as smaller as possible, without restricting the fluid flow at the entrance region. This way, square and round regenerator cross sectional areas are less susceptible to maldistribution effects on the fluid flow.

The numerical model, including the void volume modeling, was successfully implemented and was capable of reproducing the experimental results for all the operating conditions. The model was able to reproduce with good precision the variation on the inlet fluid stream temperature due to the void volumes, and captured the axial heat conduction in situations where the diffusion heat transfer is on the same order as the advection heat transfer.

With respect to the thermodynamic performance of active regenerators, the results for Spheres #3 exposed one of the main limitations of state of the art in AMR research, namely the inability to achieve high cooling capacities together with large temperature spans between the reservoirs. For regenerators composed by Gd spheres, the second-law efficiency was maximum for 15 and 20-K temperature spans.

Comparing different matrix geometries, the results showed a similar performance for the pin arrays and spheres packed beds in terms of the cooling capacity and coefficient of performance. While the spheres bed had a higher cooling capacity due to a higher thermal effectiveness, especially at high utilizations, the pins had a higher COP because of the lower viscous losses. Again, the parallel plate geometry presented several limitations due to the approximately interstitial constant heat

transfer coefficient and possibly due to a higher heat gain through the regenerator casing. In this scenario, if manufacturing limitations are considered, the spheres packed beds are certainly the most promising geometry for applications in AMR coolers.

The AMR numerical model, including the different external losses, i.e., casing heat gain, magnetic field axial profile and void volume, was capable of reproducing the experimental data with good precision. Therefore, the satisfactory performance of the methodology in simulating passive and active regenerators, demonstrated that the 1D approach can be used as a tool to design optimum regenerators.

This way, a robust methodology combining the Entropy Generation Minimization and the Performance Evaluation Criteria (PEC) was proposed. The variable geometry (**VG**) and fixed face area (**FA**) PEC were implemented aiming at optimizing passive regenerators for a target effectiveness of 95%, and AMRs for a target condition of 20-W cooling capacity at 15-K temperature span. The results presented optimum combinations of casing diameter, aspect ratio and sphere diameter, for specified values of mass flow rate and operating frequency.

The study indicated possible directions for the AMR performance, such as: (i) the optimization of the casing dimensions and matrix geometry to reduce the penalties associated with heat transfer and viscous dissipation; (ii) the optimization of the regenerator cross sectional area with respect to the reduction of the regenerative mass at the expense of a better thermal insulation.

8.1 Recommendations to Future Works

Based on the advances presented in this thesis some important recommendations for future works can be listed as follows:

1. Replace the double effect pump by a rotary valve system and perform experimental tests using the same operating conditions as presented for the Spheres #3 regenerator. This will allow comparisons between the different pumping systems in terms of the AMR performance;

2. Use different rotary valve gaskets to evaluate experimentally the synchronization of the magnetic and fluid flow profiles in order to

find the best operating condition of the AMR;

3. Validate the numerical model in terms of the synchronization of the magnetic and fluid flow profiles and perform the optimization of the fluid flow periods;

4. Expand the magnetocaloric materials properties library and implement a multi-layer regenerator routine in the numerical model to evaluate the performance improvement reported in the literature;

5. Perform experimental tests with different magnetocaloric materials, assembling the new materials in a multi-layer configuration;

6. Validate the numerical model with respect to the multi-layer experimental tests;

7. Use the optimization expertise to optimize the multi-layer configuration in terms of the Curie Temperature and the length of each layer;

8. Include in the EGM model the entropy generated by the heat transfer through the regenerator casing. This modified model, associated with the PECs, will allow the optimization between the reduction of the regenerator cross sectional area at the expense of improving the thermal insulation;

9. Evaluate the applicability of lumped models to describe the heat transfer in the casing region, given that such models are less computationally demanding.

References

ACKERMANN, R. A. *Cryogenic Regenerative Heat Exchangers*. New York: Plenum Press, 1997.

AHARONI, A. Demagnetizing factors for rectangular ferromagnetic prisms. *Journal of Applied Physics*, v. 83, p. 3432–3434, 1998.

ARNOLD, D. S.; TURA, A.; RUEBSAAT-TROTT, A.; ROWE, A. Design improvements of a permanent magnet active magnetic refrigerator. *International Journal of Refrigeration*, v. 37, p. 99–105, 2014.

AWAD, M. M.; MUZYCHKA, Y. S. Thermodynamic optimization. In: _____. [S.l.]: INTECH, 2012. cap. 1, p. 3–52.

BAHL, C. R. H.; NIELSEN, K. K. The effect of demagnetization on the magnetocaloric properties of gadolinium. *Journal of Applied Physics*, v. 105, p. 013916(1–5), 2009.

BAHL, C. R. H.; PETERSEN, T. F.; PRYDS, N.; SMITH, A. A versatile magnetic refrigeration test device. *Review of Scientific Instruments*, v. 79, p. 093906(1–7), 2008.

BAKKER-MAGNETICS. [S.l.], 2014. Available from Internet: <http://www.bakkermagnetics.com/>.

J A Barclay and W A Steyert. *Active Magnetic Regenerator*. 1982.

US-Patent 4332135.

BEJAN, A. Entropy generation minimization. In: _____. [S.l.]: CRC Press, 1995.

BEJAN, A. *Entropy Generation Minimization: The Method of Thermodynamic Optimization of Finite-Size Systems and Finite-Time Processes*. [S.l.]: CRC Press, 1996.

BJORK, R. *Designing a magnet for magnetic refrigeration*. PhD Thesis (PhD) — Risoe DTU, 2010.

BJØRK, R. The ideal dimensions of a Halbach cylinder of finite length. *Journal of Applied Physics*, v. 109, p. 13915(1–6), 2011.

BJØRK, R.; BAHL, C. R. H.; SMITH, A.; PRYDS, N. Optimization and improvement of Halbach cylinder design. *Journal of Applied Physics*, v. 104, p. 13910(1–9), 2008.

BJØRK, R.; BAHL, C. R. H.; SMITH, A.; PRYDS, N. Comparison of adjustable permanent magnetic field sources. *Journal of Magnetism and Magnetic Materials*, v. 322, p. 3664–3671, 2010.

BJØRK, R.; BAHL, C. R. H.; SMITH, A.; CHRISTENSEN, D. V.; PRYDS, N. An optimized magnet for magnetic refrigeration. *Journal of Magnetism and Magnetic Materials*, v. 322, p. 3324–3328, 2010.

BJØRK, R.; BAHL, C. R. H.; SMITH, A.; PRYDS, N. Review and comparison of magnet designs for magnetic refrigeration. *International Journal of Refrigeration*, v. 33, p. 437–448, 2010.

BJØRK, R.; SMITH, A.; BAHL, C. R. H. Analysis of the magnetic

field, force and torque for two-dimensional Halbach cylinders. *Journal of Magnetism and Magnetic Materials*, v. 322, p. 133–141, 2010.

BLOCH, F.; CUGAT, O.; MEUNIER, G. Innovating approaches to the generation of intense magnetic fields: Design and optimization of a 4 tesla permanent magnet flux source. *IEEE Transactions on Magnetics*, v. 34, p. 2465–2468, 1998.

BROWN, G. V. Magnetic heat pumping near room temperature. *Journal of Applied Physics*, v. 47, p. 3673–3680, 1976.

BRÜCK, E.; TEGUS, O.; THANH, D. T. C.; TRUNG, N. T.; BUSCHOW, K. H. J. A review on Mn based materials for magnetic refrigeration: structure and properties. *International Journal of Refrigeration*, v. 31, p. 763–770, 2008.

BURDYNY, T. *Simplified Modeling of Active Magnetic Regenerators*. Master Dissertation (Master) — University of Victoria, 2012.

CHA, J. S.; GHIAASIAAN, S. M.; KIRKCONNELL, C. S. Oscillatory flow in microporous media applied in pulse-tube and stirling-cycle cryocooler regenerators. *Experimental Thermal and Fluid Science*, v. 32, p. 1264–1278, 2008.

CHEN, Y.; LUO, W.; DAI, W. Heat transfer characteristics of oscillating flow regenerator filled with circular tubes or parallel plates. *Cryogenics*, v. 47, p. 40–48, 2007.

COEY, J. M. D. Permanent magnet applications. *Journal of Magnetism and Magnetic Materials*, v. 248, p. 441–456, 2002.

COEY, J. M. D. *Magnetism and magnetic materials*. [S.l.]: Cambridge University Press, 2010.

COMSOL Multiphysics. [S.l.], 2011. Available from Internet: <http://www.comsol.com/>.

DAN´KOV, S. Y.; TISHIN, A. M.; PECHARSKY, V. K.; GSCHNEIDNER JR., K. A. Magnetic phase transitions and the magnetothermal properties of gadolinium. *Physical Review B*, v. 57, p. 3478–3490, 1998.

DAS, S. K.; SAHOO, R. K. Thermodynamic optimization of regenerators. *Cryogenics*, v. 31, p. 862–868, 1991.

DAS, S. K.; SAHOO, R. K. Second law analysis of a cyclic regenerator in presence of longitudinal heat conduction in matrix. *Heat and Mass Transfer*, v. 34, p. 395–403, 1999.

de BOER, P. C. T. Thermodynamic analysis of the basic pulse-tube refrigerator. *Cryogenics*, v. 34, p. 669–711, 1994.

de BOER, P. C. T. Analysis of basic pulse-tube refrigerator with regenerator. *Cryogenics*, v. 35, p. 547–553, 1995.

de WAELE, A. T. A. M.; STEIJAERT, P. P.; GIJZEN, J. Thermodynamical aspects of pulse tubes. *Cryogenics*, v. 37, p. 313–324, 1997.

DEGROOT, C. T.; STRAATMAN, A. G. Numerical analysis of heat and mass transfer in porous media. In: _____. [S.l.]: Spinger, 2012. cap. 6, p. 153–180.

DINESEN, A. R. *Magnetocaloric and magnetoresistive properties of* $La_{0.67}Ca_{0.33-x}Sr_xMnO_3$. PhD Thesis (PhD) — Technical University of Denmark, 2004.

DRAGUTINOVIC, G. D.; BACLIC, B. S. *Operation of Counterflow Regenerators, Computational Mechanics Publications*. [S.l.]: Billerica, 1998.

EDM-TECHNOLOGIES. [S.l.], 2013. Available from Internet: <http://www.edmtechnologies.net/>.

ENGELBRECHT, K. *A numerical model of an active magnetic regenerator refrigerator with experimental validation*. PhD Thesis (PhD) — University of Winsconssin-Madison, 2008.

ENGELBRECHT, K.; ERIKSEN, D.; BAHL, C. R. H.; BJÃ¸RK, R.; GEYTI, J.; LOZANO, J. A.; NIELSEN, K. K.; SAXILD, F.; SMITH, A.; PRYDS, N. Experimental results for a novel rotary active magnetic regenerator. *International Journal of Refrigeration*, v. 35, p. 1498–1505, 2012.

ENGELBRECHT, K.; NIELSEN, K. K.; PRYDS, N. An experimental study of passive regenerator geometries. *International Journal of Refrigeration*, v. 34, p. 1817–1822, 2011.

ERGUN, S. Fluid flow through packed collumn. *Chemical Engineering Progress*, v. 48, p. 89–94, 1952.

ERIKSEN, D.; ENGELBRECHT, K.; BAHL, C. R. H.; BJÃ¸RK, R.; NIELSEN, K. K.; INSINGA, A. R.; PRYDS, N. Design and experimental tests of a rotary active magnetic regenerator prototype. *International Journal of Refrigeration*, In Press, 2015.

FRISCHMANN, M.; ENGELBRENCHT, K.; NELLIS, G.; KLEIN, S. Heat transfer coefficient in a packed sphere regenerator for use in active magnetic regenerative refrigeration. In: *Proceedings in International Refrigeration and Air Conditioning Conference at Purdue*. [S.l.: s.n.], 2008.

GEDEON, D.; WOOD, J. G. *Oscillating-Flow Regenerator Test Rig: Hardware and Theory with Derived Correlations for Screens and Felts.* [S.l.], 1996.

GIROTTO, S.; MINETTO, S.; NEKSA, P. Commercial refrigeration system using CO_2 as the refrigerant. *International Journal of Refrigeration*, v. 27, p. 717–723, 2004.

GOSNEY, W. B. *Principles of Refrigeration.* [S.l.]: Cambridge University Press, 1982.

GSCHNEIDNER JR., K. A.; PECHARSKY, V. K. Thirty years of near room temperature magnetic cooling: Where we are today and future prospects. *International Journal of Refrigeration*, v. 31, p. 945–961, 2008.

GSCHNEIDNER JR., K. A.; PECHARSKY, V. K.; BRÜCK, E.; DUIJN, H. G. M.; LEVIN, E. M. Comment on direct measurement of the giant adiabatic temperature change in $Gd_5Ge_2Si_2$. *Physical Review Letters*, v. 85, p. 4190–4190, 2000.

GSCHNEIDNER JR., K. A.; PECHARSKY, V. K.; TSOKOL, A. O. Recent developments in magnetocaloric materials. *Reports on Progress in Physics*, v. 68, p. 1479–1539, 2005.

HADLEY, G. R. Thermal conductivity of packed metal powder. *International Journal of Heat and Mass Transfer*, v. 29, p. 909–920, 1986.

HASHIMOTO, T.; KUZUHARA, T.; SAHASHI, M.; INOMATA, K.; TOMOKIYO, A.; YAYAMA, H. New application of complex magnetic materials to he magentic refrigerant in an Ericsson magnetic refrigerator. *Journal of Applied Physics*, v. 62, p. 3873–3878, 1987.

HAUSEN, H. *Heat Trasfer in Counterflow, Parallel-Flow and Cross-Flow*. New York: McGraw-Hill Co, 1983.

HIRANO, N.; NAGAYA, S.; OKAMURA, T.; KAWANAMI, T.; WADA, H. Development of room temperature magnetic refrigerator in japan. In: *Proceedings in 4th International Conference on Magnetic Refrigeration at Room Temperature (THERMAG IV)*. Baotou, China: [s.n.], 2010.

HOLMAN, J. P. *Experimental Methods for Engineers*. Eighth. New York: McGraw-Hill, 2006.

IBRAHIM, M. B.; Tew Jr, R. C. *Stirling Convertor Regenerators*. [S.l.]: CRC Press, 2012.

INMETRO. *Guia para a Expressão da Incerteza de Medição*. 2003.

JACOBS, S.; AURINGER, J.; BOEDER, A.; KOMOROWSKI, J. C. aand L.; LEONARD, J.; RUSSEK, S.; ZIMM, C. The performance of a large-scale rotary magnetic refrigerator. *International Journal of Refrigeration*, v. 37, p. 84–91, 2014.

JACOBS, S.; ZIMM, C. Modeling magnetic refrigeration. In: *Delft Days on Magnetocalorics*. Delft, The Netherlands: [s.n.], 2008.

JU, Y.; JIANG, Y.; ZHOU, Y. Experimental study of the oscillating flow characteristics for a regenerator in a pulse tube cryocooler. *Cryogenics*, v. 38, p. 649–656, 1998.

JU, Y.; SHEN, Q. Comparative study of oscillating flow characteristics of cryocooler regenerator at low temperatures. *Frontiers of Energy and Power Engineering in China*, v. 3, p. 80–84, 2009.

KAVIANY, M. *Principles of Heat Transfer in Porous Media*. Second. [S.l.]: Springer, 1995.

KITANOVSKI, A.; EGOLF, P. W. Thermodynamics of magnetic refrigeration. *International Journal of Refrigeration*, v. 29, p. 3–21, 2006.

KITANOVSKI, A.; TUSEK, J.; TOMC, U.; PLAZNIK, U.; OZBOLT, M.; POREDOS, A. *Magnetocaloric Energy Conversion: From Theory to Applications*. [S.l.]: Springer International Publishing, 2015.

KLEIN, S. A. *Engineering* E*quation* S*olver (*EES*)* P*rofessional* V*ersion*. 2013. V9.339, F-Chart Software, Madison, WI.

KNAUF, S. M.; NELLIS, G.; KLEIN, S. Experimental determination of flow and heat transfer correlations for passive regenerators. In: *Proceedings in International Refrigeration and Air Conditioning Conference at Purdue*. [S.l.: s.n.], 2008.

KOCH, D. L.; BRADY, J. F. Dispersion in fixed beds. *Journal of Fluid Mechanics*, v. 154, p. 399–427, 1985.

KRANE, R. J. A second law analysis of the optimum design and operation of thermal energy storage systems. *International Jounal of Heat and Mass Transfer*, v. 30, p. 43–57, 1987.

KREITH, F. *The CRC Handbook of Thermal Engineering*. [S.l.]: CRC Press, 2000.

KUPPAN, T. *Heat exchanger design handbook*. [S.l.]: Marcel Dekker, Inc, 2000.

KUWAHARA, F.; SHIROTA, M.; NAKAYAMA, A. A numerical study of interfacial convective heat transfer coefficient in two-energy equation model for convection in porous media. *International Journal of Heat and Mass Transfer*, v. 44, p. 1153–1159, 2001.

LEE, G. T.; KANG, B. H.; LEE, J. H. Effectiveness enhancement of a thermal regenerator in an oscillating flow. *Applied Thermal Engineering*, v. 18, p. 653–660, 1998.

LI, C. H.; FINLAYSON, B. A. Heat transfer in packed beds - a reevaluation. *Chemical Engineering Science*, v. 32, p. 1055–1066, 1977.

LI, P.; GONG, M.; WU, J. Geometric optimization of an active magnetic regenerative refrigerator via second-law analysis. *Journal of Applied Physics*, v. 104, p. 103536(1–9), 2008.

LOZANO, J. A. *Designing a rotary magentic refrigerator*. PhD Thesis (PhD) — Federal University of Santa Catarina, 2015.

LOZANO, J. A.; CAPOVILLA, M. S.; Barbosa Jr., J. R. Development of a novel rotary magentic regenerator. *Submited to International Journal of Refrigeration*, 2015.

MACDONALD, I. F.; EL-SAYED, M. S.; MOW, K.; DULLIEN, F. A. Flow through porous media - ergun equation revisited. *Industrial and Engineering Chemistry Fundamentals*, v. 18, p. 199–208, 1979.

MALISKA, C. R. *Transferência de Calor e Mecânica dos Fluidos Computacional*. 2. ed. [S.l.]: LTC, 2004.

MARCONNET, A. *Predicting Regenerator Performance with a Single-Blow Experiment*. Master Dissertation (Master) — University of Wisconsin Madison, 2007.

MHÍOCHÁIN, T. R. N.; WEAIRE, D.; MCMURRY, S. M.; COEY, J. M. D. Analysis of torque in nested magnet cylinders. *Journal of Applied Physics*, v. 86, p. 6412–6424, 1999.

MONFARED, B.; FURBERG, R.; PALM, B. Magnetic vs. vapour-compression household refrigerators: A preliminary comparative life cycle assessment. *International Journal of Refrigeration*, v. 42, p. 69–76, 2014.

MORRISH, A. *The Physical Principles of Magnetism*. [S.l.]: John Wiley & Sons, Inc., 1965.

NAKAYAMA, A.; KUWAHARA, F. Numerical modeling of convective heat transfer in porous media using microscopic structures. In: _____. [S.l.]: Taulor & Francis e-Library, 2005. cap. 10, p. 441–448.

NAM, K.; JEONG, S. Novel flow analysis of regenerator under oscillating flow with pulsating pressure. *Cryogenics*, v. 45, p. 368–379, 2005.

NAM, K.; JEONG, S. Development of parallel wire regenerator for cryocoolers. *Cryogenics*, v. 46, p. 278–287, 2006.

NELLIS, G.; KLEIN, S. *Heat Transfer*. [S.l.]: Cambridge University Press, 2009.

NICKOLAY, M.; MARTIN, H. Improved approximation for the Nusselt number for hydrodynamically developed laminar flow between parallell plates. *International Journal of Heat and Mass Transfer*, v. 45, p. 3263–3266, 2002.

NIELD, D. A.; BEJAN, A. *Convection in Porous Media*. 3a. ed. [S.l.: s.n.], 2006.

NIELSEN, K. K. *Numerical modeling and analysis of the active magnetic regenerator*. PhD Thesis (PhD) — Technical University of Denmark, 2010.

NIELSEN, K. K.; BAHL, C. R. H.; SMITH, A. Constraints on the adiabatic temperature change in magnetocaloric materials. *Physical Review B*, v. 81, p. 054423(1–5), 2010.

NIELSEN, K. K.; BAHL, C. R. H.; SMITH, A.; BJØRK, R.; PRYDS, N.; HATTEL, J. Detailed numerical modeling of a linear parallel-plate active magnetic regenerator. *International Journal of Refrigeration*, v. 32, p. 1478–1486, 2009.

NIELSEN, K. K.; BAHL, C. R. H.; SMITH, A.; ; ENGELBRECHT, K.; OLSEN, U. L.; PRYDS, N. The influence of non-magnetocaloric properties on the AMR performance. In: *Proceeding in 5th International Conference on Magnetic Refrigeration at Room Temperature (THERMAG V)*. Grenoble, France: [s.n.], 2012.

NIELSEN, K. K.; BARBOSA JR., J. R.; TREVIZOLI, P. V. Numerical analysis of a linear reciprocating active magnetic regenerator. In: *Proceeding in 4th International Conference on Magnetic Refrigeration at Room Temperature (THERMAG IV)*. Baotou, China: [s.n.], 2010.

NIELSEN, K. K.; TUSEK, J.; ENGELBRECHT, K.; SCHOPFER, S.; KITANOVSKI, A.; BAHL, C. R. H.; SMITH, A.; PRYDS, N.; POREDOS, A. Review on numerical modeling of active magnetic regenerators for room temperature applications. *International Journal of Refrigeration*, v. 34, p. 603–616, 2011.

NUMAZAWA, T.; MATSUMOTO, K.; YANAGISAWA, Y.; NAKAGOME, H. A modeling study on the geometry of active magnetic regenerator. *AIP Conference Proceedings*, v. 1434, p. 327–342, 2012.

OKAMURA, T.; YAMADA, K.; HIRANO, N.; NAGAYA, S. Performance of a room-temperature rotary magnetic refrigerator. *International Journal of Refrigeration*, v. 29, p. 1327–1331, 2006.

OLIVEIRA, P. A.; TREVIZOLI, P. V.; BARBOSA JR., J. R.; PRATA, A. T. A 2D hybrid model of the fluid flow and heat transfer in a reciprocating active magnetic regenerator. *International Journal of Refrigeration*, v. 35, p. 98–114, 2012.

OZBOLT, M.; KITANOVSKI, A.; TUSEK, J.; POREDOS, A. Electrocaloric refrigeration: Thermodynamics, state of the art and future perspectives. *International Journal of Refrigeration*, v. 40, p. 174–188, 2014.

PALLARES, J.; GRAU, F. X. A modification of a nusselt number correlation for forced convection in porous media. *International Communications in Heat and Mass Transfer*, v. 37, p. 1187–1190, 2010.

PATANKAR, S. V. *Numerical Heat Transfer and Fluid Flow*. [S.l.]: Hemisphere Publishing Corporation, 1980.

PECHARSKY, V. K.; GSCHNEIDNER JR., K. A. Giant magnetocaloric effect in $Gd_5Ge_2Si_2$. *Physical Review Letters*, v. 78, p. 4494–4497, 1997.

PECHARSKY, V. K.; GSCHNEIDNER JR., K. A. Tunable magnetic regenerator alloys with a giant magnetocaloric effect for magnetic refrigeration from 20 to 290 k. *Applied Physics Letters*, v. 70, p. 3299–3301, 1997.

PECHARSKY, V. K.; GSCHNEIDNER JR., K. A. Magnetocaloric effect from indirect measurements: magnetization and heat capacity. *Journal of Applied Physics*, v. 86, p. 565–575, 1999.

PECHARSKY, V. K.; GSCHNEIDNER JR., K. A. Advanced magnetocaloric materials: What does the future hold? *International Journal of Refrigeration*, v. 29, p. 1239–1249, 2006.

PECHARSKY, V. K.; GSCHNEIDNER JR., K. A.; PECHARSKY, A. O.; TISHIN, A. M. Thermodynamics of the magnetocaloric effect. *Physical Review B*, v. 64, p. 144406(1–13), 2001.

PETERSEN, T. F. *Numerical modelling and analysis of a room temperature magnetic refrigeration system*. Master Dissertation (Master) — Technical University of Denmark, 2007.

PETERSEN, T. F.; ENGELBRECHT, K.; BAHL, C. R. H.; ELMEGAARD, B.; PRYDS, N.; SMITH, A. Comparison between a 1D and a 2D numerical model of an active magnetic regenerative refrigerator. *Journal of Physics D: Applied Physics*, v. 41, p. 105002(1–8), 2008.

PRESS, W. H.; TEUKOLSKY, S. A.; VETTERLING, W. T.; FLANNERY, B. P. *Numerical Recipes: The Art of Scientific Computing*. [S.l.]: Cambridge University Press, 2007.

QUINTARD, M.; WHITAKER, S. Transport in ordered and disordered porous media: volume-averaged equations, closure problems and comparison with experiment. *Chemical Engineering Science*, v. 48, p. 2537–2564, 1993.

ROWE, A.; DIKEOS, A.; TURA, A. Experimental studies of a near room temperature magnetic refrigeration. In: EGOLF, P. W. (Ed.). *Proceedings 1st International Conference on Magnetic Refrigeration at Room Temperature*. Montreux, SWI: [s.n.], 2005.

ROWE, A.; TURA, A.; DIKEOS, J.; CHAHINE, R. Near room temperature magnetic refrigeration. In: *Proceedings in International*

Green Energy Conference. Ontario, Canada: [s.n.], 2005.

RUSSEK, S. L.; ZIMM, C. B. Potential for cost effective magnetocaloric air conditioning systems. *International Journal of Refrigeration*, v. 29, p. 1366–1373, 2006.

SATO, M.; ISHII, Y. Simple and approximate expressions of demagnetizing factors of uniformly magnetized rectangular rod and cylinder. *Journal of Applied Physics*, v. 66, p. 983–985, 1989.

SCARPA, F.; TAGLIAFICO, G.; TAGLIAFICO, L. A. Control optimization in experiments for the heat transfer assessment of saturated packed bed regenerators. *International Journal of Heat and Mass Transfer*, v. 55, p. 6944–6950, 2012.

SCHMIDT, F. W.; WILLMOTT, A. J. *Thermal Energy Storage and Regeneration*. [S.l.]: Hemisphere Publishing Co., 1981.

SCHOPFER, S. *Experimental and Numerical determination of thermohydraulic properties of regenerators subject to oscillating flow*. Master Dissertation (Master) — University of Victoria, 2010.

SHAH, R. K.; SEKULIĆ, D. P. *Fundamentals of Heat Exchanger Design*. [S.l.]: John Wiley & Sons, 2003.

SIDDIKOV, B. M.; WADE, B. A.; SCHULTZ, D. H. Numerical simulation of the active magnetic regenerator. *Computers and Mathematics with Applications*, v. 49, p. 1525–1538, 2005.

SIMON, T. W.; SEUME, J. R. *A survey of oscillationg flow in Stirling engine heat exchargers*. [S.l.], 1988.

SMAÏLI, A.; CHAHINE, R. Composite materials for Ericsson-like magnetic refrigeration cycle. *Journal of Applied Physics*, v. 81, p. 824–829, 1997.

SMITH, A. Who discovered the magnetocaloric effect? *The European Physical Journal H*, v. 38, p. 507–517, 2013.

SMITH, A.; BAHL, C. R. H.; BJØRK, R.; ; ENGELBRECHT, K.; PRYDS, K. K. N. N. Materials challenges for high performance magnetocaloric refrigeration devices. *Advanced Energy Materials*, v. 2, p. 1288–1318, 2012.

SMITH, A.; NIELSEN, K. K.; CHRISTENSEN, D. V.; BAHL, C. R. H.; BJØRK, R.; HATTEL, J. The demagnetizing field of a nonuniform rectangular prism. *Journal of Applied Physics*, v. 107, p. 103910(1–8), 2010.

STEIJAERT, P. P. *Thermodynamical aspects of pulse-tube refrigerators*. PhD Thesis (PhD) — Technical University of Eindhoven, 1999.

STEYERT, W. A. Magnetic refrigerations for use at room temperature and below. *Journal of Physique*, v. 8, p. 1598–1604, 1978.

TAMAYOL, A.; WONG, K. W.; BAHRAMI, M. Effects of fiber orientation on flow properties of fibrous porous structures at moderate reynolds number. In: *Proceedings (CD) of the 3rd International Conference on Porous Media and its Applications in Science and Engineering*. Montecatini, Italy: [s.n.], 2010.

TERUEL, F. E.; RIZWAN-UDDIN. Characterization of a porous medium employing numerical tools: Permeability and pressure-drop from darcy to turbulence. *International Journal of Heat and Mass Transfer*, v. 52, p. 5878–5888, 2009.

TISHIN, A. M.; SPICHKIN, Y. I. *The magnetocaloric effect and its applications*. [S.l.]: IoP Istitute of Physics Puclishing, 2003.

TREVIZOLI, P. V.; BARBOSA JR., J. R.; FERREIRA, R. T. S. Experimental evaluation of a Gd-based linear reciprocating active magnetic regenerator test apparatus. *International Journal of Refrigeration*, v. 34, p. 1518–1526, 2011.

TREVIZOLI, P. V.; BARBOSA JR., J. R.; OLIVEIRA, P. A. de; CANESIN, F. C.; FERREIRA, R. T. S. Assessment of demagnetization phenomena in the performance of an active magnetic regenerator. *International Journal of Refrigeration*, v. 35, p. 1043–1054, 2012.

TREVIZOLI, P. V.; BARBOSA JR., J. R.; TURA, A.; ROWE, A. Modeling of thermo-magnetic phenomena in active magentic regenerators. In: *Proceedings of the ASME 2013 Summer Heat Transfer Conference (HT 2013)*. Minneapolis, USA: [s.n.], 2013.

TREVIZOLI, P. V.; BARBOSA JR., J. R.; TURA, A.; ARNOLD, D.; ROWE, A. Modeling of thermo-magnetic phenomena in active magnetic regenerators. In: *Proceedings of the of the ASME 2013 Summer Heat Transfer Conference*. HT 2013 Minneapolis, USA: [s.n.], 2013.

TREVIZOLI, P. V.; BARBOSA JR., J. R.; TURA, A.; ARNOLD, D.; ROWE, A. Modeling of thermo-magnetic phenomena in active magnetocaloric regenerators. *Journal of Thermal Science and Engineering Applications*, v. 6, p. 031016, 2014.

TREVIZOLI, P. V.; LIU, Y.; TURA, A.; ROWE, A.; BARBOSA JR., J. R. An apparatus to measure heat transfer and viscouss losses in thermal regenerators. In: *Proceedings of the 8th Conference on Experimental Heat Transfer, Fluid Mechanics and Thermidynamics*. Lisbon, Portugal: [s.n.], 2013.

TREVIZOLI, P. V.; LIU, Y.; TURA, A.; ROWE, A.; BARBOSA JR., J. R. Experimental assessment of the thermal-hydraulic performance of packed-sphere oscillating-flow regenerators using water. *Experimental Thermal and Fluid Science*, v. 57, p. 324–334, 2014.

TREVIZOLI, P. V.; LOZANO, J. A.; PEIXER, G. F.; BARBOSA JR., J. R. Design of nested Halbach cylinder arrays for magnetic refrigeration applications. *Journal of Magnetism and Magnetic Materials*, v. 395, p. 109–122, 2015.

TURA, A. *Active Magnetic Regenerator Experimental Optimization*. Master Dissertation (Master) — University of Victoria, 2005.

TURA, A.; ROWE, A. Permanent magnet magnetic refrigerator design and experimental characterization. *International Journal of Refrigeration*, v. 34, p. 628–639, 2011.

TUSEK, J.; KITANOVSKI, A.; PREBIL, I.; POREDOS, A. Dynamic operation of an active magnetic regenerator (AMR): Numerical optimization of a packed-bed AMR. *International Journal of Refrigeration*, v. 34, p. 1507–1517, 2011.

UNITED NATIONS. *United Nations Climate Change*. 2015. Available from Internet: <www.unfccc.int>.

WAKAO, N.; KAGUEI, S. *Heat and mass transfer in packed beds*. New York: Gordon and Breach Science, 1982.

WEBB, R. L.; KIM, N. H. *Principles of Enhanced Heat Transfer*. Second. [S.l.]: Taylor & Francis, 2005.

WHITAKER, S. Forced convection heat transfer correlations for flow in pipes, past flat plates, single cylinders, single spheres, and for

flow in packed beds and tube bundles. *AIChE Journal*, v. 18(2), p. 361–371, 1972.

WHITAKER, S. *Fundamental principles of heat transfer*. [S.l.]: Krieger Publishing Company, 1983.

YAZDCHI, K.; SRIVASTAVA, S.; LUDING, S. Microstructural effects on the permeability of periodic fibrous porous media. *International Journal of Multiphase Flow*, v. 37, p. 956–966, 2011.

YU, B.; LIU, M.; EGOLF, P. W.; KITANOVSKI, A. A review of magnetic refrigerator and heat pump prototypes built before the year 2010. *International Journal of Refrigeration*, v. 13, p. 1029–1066, 2010.

YU, B. F.; GAO, Q.; ZHANG, B.; MENG, X. Z.; CHEN, Z. Review on research of room temperature magnetic. *International Journal of Refrigeration*, v. 26, p. 622–636, 2003.

ZHAO, T.; CHENG, P. Oscillatory heat transfer in a pipe subjected to a laminar reciprocating flow. *ASME Journal of Heat Transfer*, v. 118, p. 592–598, 1996.

ZHAO, T. S.; CHENG, P. Heat transfer in oscillatory flows. In: *Annual Review of Heat Transfer*. [S.l.]: Begell House, 1998.

ZIMM, C.; BOEDER, A.; CHELL, J.; STERNBERG, A.; FUJITA, A.; FUJIEDA, S.; FUKAMICHI, K. Design and performance of a permanent-magnet rotary refrigerator. *International Journal of Refrigeration*, v. 29, p. 1302–1306, 2006.

APPENDIX A

Nested Halbach Cylinder Design

The present appendix shows the optimization routine proposed to design optimum Nested Halbach Cylinders (NHC) magnetic circuits as proposed by Trevizoli *et al.* (2015).

A.1 Modeling

A.1.1 Analytical Modeling

A.1.1.1 Basic Equations

In the analytical model of the NHC configuration, the magnetic flux density generated at the core of each cylinder is evaluated independently. The fundamental expression to quantify the magnetic flux density at the center of a finite length non-segmented Halbach cylinder, B_{fin}, is given by (BJØRK *et al.*, 2010d; COEY, 2002):

$$B_{\text{fin}} = B_{\text{rem}}\left[\ln\left(\frac{D_{\text{e}}}{D_{\text{i}}}\right) + \frac{(L/2)}{2}\left(\frac{1}{\sqrt{(L/2)^2+(D_{\text{i}}/2)^2}} - \frac{1}{\sqrt{(L/2)^2+(D_{\text{e}}/2)^2}}\right) - \ln\left(\frac{(L/2)+\sqrt{(L/2)^2+(D_{\text{e}}/2)^2}}{(L/2)+\sqrt{(L/2)^2+(D_{\text{i}}/2)^2}}\right)\right] \tag{A.1}$$

where B_{rem} is the magnitude of the remanent flux density of the permanent magnet, L is the length of the Halbach cylinder, and D_{e} and D_{i} are the external and internal diameters of the cylinder, respectively. In Eq. (A.1), it follows that if $L \to \infty$, then $B_{\text{fin}} \to B_{\text{inf}} = B_{\text{rem}} \ln(D_{\text{e}}/D_{\text{i}})$, where B_{inf} is the magnetic flux density at the center of an infinite non-segmented Halbach cylinder.

Due to fabrication restrictions, the magnet cylinder has to be divided into n segments with specific remanent flux density orientations (see Fig. 3.6 for an example of an 8-segment NHC). The magnetic flux density at the center of a finite length Halbach cylinder with n segments is given by (COEY, 2002; BJØRK *et al.*, 2008):

$$B_{\text{HC}} = B_{\text{fin}}\left[\frac{\sin(2\pi/n)}{(2\pi/n)}\right] \tag{A.2}$$

where n is the number of segments. Naturally, if $n \to \infty$ and the remanent flux density changes continuously for each segment, then $B_{\text{HC}} \to B_{\text{fin}}$ (BJØRK *et al.*, 2008). Therefore, in the design procedure, the analytical expression given by Eq. (A.2) is used to calculate the magnetic flux densities at the center of the external ($B_{\text{HC,E}}$) and internal ($B_{\text{HC,I}}$) cylinders.

A.1.1.2 Parameters and Constraints

The magnetic circuit is designed in accordance with the regenerator dimensions. Parameters such as the regenerator diameter, length and mass have a direct effect on the magnetic field intensities and field volume. The following input parameters are required in the proposed

design procedure:

- The inner diameter of the internal magnet, $D_{\mathrm{i,I}}$, which is directly related to the regenerator housing diameter;

- The air gap between the magnet arrays, ℓ_{gap}. This parameter determines the inner diameter of the external magnet, $D_{\mathrm{i,E}}$. The smaller the air gap the higher the magnetic field intensity at the NHC core. However, as pointed out by Arnold *et al.* (2014), small air gaps intensify the interaction between the fringing fields of the internal and external magnets, increasing the torque needed to rotate the system;

- Number of Halbach segments, n. Tura and Rowe (2011) compared a 16-segment NHC with an 8-segment NHC and observed a reduction of about 7% in the maximum magnetic flux density. Manufacturing costs have to be considered in the selection of this parameter;

- Magnet grade. This determines the remanent flux density, B_{rem}, and intrinsic coercivity, H_{cj}, of each magnet. While B_{rem} is directly proportional to the resultant magnetic flux density, Eq. (A.2), H_{cj} controls the operating stability of the NHC. As will be seen, the internal Halbach cylinder must be manufactured with a high coercivity magnet grade (small B_{rem}), to avoid magnetization reversal.

To determine the outer diameter of the inner magnet, $D_{\mathrm{e,I}}$, Bjørk (2011) derived an ideal ratio between the outer and inner diameters of an infinite non-segmented Halbach cylinder, $D_{\mathrm{e,I}}/D_{\mathrm{i,I}}$, of 2.219. In the present analysis, the range of values to find $D_{\mathrm{e,I}}$ was set around this optimum as follows:

$$2.15 \leq \frac{D_{\mathrm{e,I}}}{D_{\mathrm{i,I}}} \leq 2.25 \tag{A.3}$$

The inner diameter of the external magnet, $D_{\mathrm{i,E}}$, is calculated by simply adding the air gap, ℓ_{gap}:

$$D_{\mathrm{i,E}} = D_{\mathrm{e,I}} + 2\ell_{\mathrm{gap}} \tag{A.4}$$

To determine the outer diameter of the external magnet, $D_{\mathrm{e,E}}$, Bjørk *et al.* (2010a) proposed the following design relationship for NHCs:

$$0.8 \leq \frac{D_{\mathrm{e,I}}/D_{\mathrm{i,I}}}{D_{\mathrm{e,E}}/D_{\mathrm{i,E}}} \leq 1 \tag{A.5}$$

At this point, in the present method, the diameters of the internal and external magnets are known, but the lengths of the magnet cylinders are not. In the interest of weight, cost and manufacturability, Tura and Rowe (2011) suggest that the ratio of the external diameter and the length of the external cylinder, $D_{\mathrm{e,E}}/L_{\mathrm{E}}$ should be close to unity. This leads to the following design constraint:

$$0.8 \leq \frac{D_{\mathrm{e,E}}}{L_{\mathrm{E}}} \leq 1.2 \tag{A.6}$$

In order to minimize the stray field gradient out of the magnet and, at the same time, maintain a high average magnetic flux density at the maximum position (see Fig. 3.7), the following constraint has been used to determine the length of the internal magnet (BJØRK *et al.*, 2010a):

$$0.8 \leq \frac{L_{\mathrm{I}}}{L_{\mathrm{E}}} \leq 1 \tag{A.7}$$

A.1.1.3 Design Procedure

In the NHC design procedure, the parameter ranges given by Eqs. (A.3), (A.5), (A.6) and (A.7) are divided into 21 increments each, resulting in $21^4 = 194{,}481$ possible magnet configurations. For a set of input parameters, namely, $D_{\mathrm{i,I}}$, ℓ_{gap}, n and magnet grade, Eq. (A.2) is applied to calculate the magnetic flux densities at the centers of the external and internal cylinders, $B_{\mathrm{HC,E}}$ and $B_{\mathrm{HC,I}}$, for each possible magnet configuration. Then, the maximum and minimum magnetic flux densities for the nested configuration, $B_{\max}$ and $B_{\min}$, are simply calculated by:

$$B_{\max} = B_{\mathrm{HC,E}} + B_{\mathrm{HC,I}} \tag{A.8}$$

$$B_{\min} = |B_{\mathrm{HC,E}} - B_{\mathrm{HC,I}}| \tag{A.9}$$

Bjørk *et al.* (2010b) proposed the following figure of merit to characterize permanent magnet designs for magnetic refrigeration,

$$\Lambda_{\text{cool}} = \left(\langle B_{\text{high}} \rangle^{2/3} - \langle B_{\text{low}} \rangle^{2/3} \right) \frac{\vartheta_{\text{Field}}}{\vartheta_{\text{Magnet}}} \tau^* \tag{A.10}$$

where $\langle B_{\text{high}} \rangle$ is the volumetric average high magnetic flux density, $\langle B_{\text{low}} \rangle$ is the volumetric average low magnetic flux density, ϑ_{Field} is the total volume where the magnetic field is applied, $\vartheta_{\text{Magnet}}$ is the volume of permanent magnet raw material, for instance, $Nd_2Fe_{14}B$, and τ^* is the fraction of the cycle period during which the magnet is used. Λ_{cool} quantifies the potential of a magnetic circuit for magnetic refrigeration applications. An ideal magnet for an AMR prototype should guarantee a high magnetic field variation (higher magnetocaloric effect), a large volume of generated magnetic field (larger density of magnetocaloric material), must be used during most of the cycle time (ideally in a continuous cycle) and, equally important, use a small amount of permanent magnet (to reduce cost).

The Λ_{cool} figure of merit, Eq. (A.10), is calculated for each NHC configuration and used as the main parameter to determine the optimal NHC dimensions, i.e., those which result in the highest magnetic flux density variation for the lowest possible amount of raw magnet material. However, the analytical model gives the magnetic flux density at a single point (the center of the magnets), which is assumed to be close to the volume average. The magnetic field volume, ϑ_{Field}, is calculated considering the internal magnet diameter and the regenerator maximum length, since this is the useful volume of magnetic field. The fraction of the cycle period, τ^*, was assumed equal to 0.5, which is typical of NHC arrays (BJØRK *et al.*, 2010c).

Additional constraints were adopted to rule out poor performance configurations and select the candidates with more desirable characteristics. These are as follows:

1. $\mu_0 H_{\text{min}} < 0.1$ T, or as close as possible to 0 T (BJØRK *et al.*, 2010d);
2. $\Lambda_{\text{cool}} \geq 0.025$, since $\Lambda_{\text{cool}} \approx 0.03$ was reported by Bjørk *et al.* (2010c) for typical NHC configurations.

A.1.2 COMSOL Multiphysics Modeling

The optimal NHC configuration designed according to the analytical procedure was numerically simulated using COMSOL Multiphysics (v. 4.2, AC/DC Module, Magnetic Fields, No Currents formulation). The magnetostatic formulation, where the electric currents are negligible, is modeled using the magnetic scalar potential (V_{m}) defined as $\vec{H} = -\nabla V_{\mathrm{m}}$. Substituting the constitutive relation for permanent magnets ($\vec{B} = \mu_0 \mu_{\mathrm{r}} \vec{H} + \vec{B}_{\mathrm{rem}}$) into the Gauss's law for magnetism ($\nabla \cdot \vec{B} = 0$), and by employing the magnetic scalar potential, the model becomes $-\nabla \cdot (\mu_0 \mu_{\mathrm{r}} \nabla V_{\mathrm{m}} - \vec{B}_{\mathrm{rem}}) = 0$ (COMSOL..., 2011).

3-D simulations were performed to compute the magnetic flux density profile along the axial z-direction, including the center of the magnet. As will be discussed later, the analytical model corrects $\vec{B}$ at the center of the magnet for finite length effects according to Eq. (A.1), but does not calculate the axial magnetic flux density profile and how this profile is influenced by end effects, which are crucial to the determination of the final length of the internal array. The 3-D simulations were carried out using a mesh of about 1.63 million tetrahedral elements with an average element quality of 0.835. A conjugated gradient solver was employed with a convergence tolerance of 10^{-6}.

2-D simulations were carried out to evaluate the magnetization reversal in the external and internal arrays and the energy product, BH, of the permanent magnets. The 2D simulations used a mesh with 87443 quadrilateral elements with an average element quality of 0.985. The input parameters in the 2-D and 3-D simulations were the magnet remanent flux density and the magnet relative permeability, μ_{r}, which was set to 1.05.

A.2 Experimental Analysis

The optimal NHC array was manufactured (Bakker Magnetics B.V.) and experimental measurements were performed to validate the design procedure and characterize the main parameters of the magnetic circuit. Magnetic flux density measurements were carried out using a LakeShore 425 model gaussmeter coupled to a transverse probe (model HMMT-6J04-VF). Using a purpose-built 3-D Cartesian probe traversing system, the probe was positioned at the center line of the magnet,

$x = y = 0$ (see Fig. A.1), and traversed from one end of the magnet structure to the other along the center line. At each z-position, the NHC was rotated at a frequency of 0.25 Hz and the instantaneous magnetic flux density was acquired at a sampling rate of 60 Hz. The experimental uncertainty of the magnetic flux density was evaluated at 1% of the measured value. As illustrated in Fig. A.1, both the x and y-components of the magnetic flux density vector were measured, which enabled the evaluation of both the magnitude and direction of $\vec{B}$.

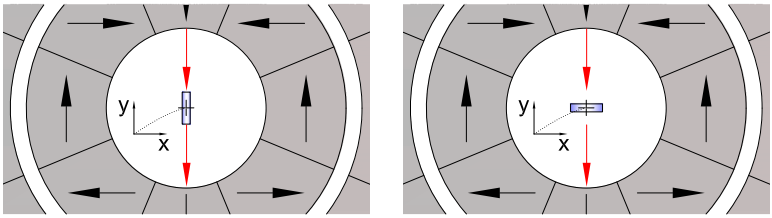

(a) (b)

Figure A.1 – Illustration of the probe position to measure magnetic flux density components: (a) Measurement of the B_x component. (b) Measurement of the B_y component.

Torque measurements were carried out using a torque transducer (HBM model T22) with a full-scale reading of 20 N m. Time dependent torque measurements were performed at variable magnet operating frequencies, f, between 0.25 Hz and 1.5 Hz. The sampling rate was changed from 75 Hz (at $f = 0.25$ Hz) to 450 Hz (at $f = 1.5$ Hz) so as to measure 300 experimental data points per cycle. The experimental uncertainty of the torque was estimated at 0.6% of the measured value.

A.3 Results and Discussions

A.3.1 Design Procedure Results

A basic prerequisite of the NHC array is that a high magnetic field intensity must be generated along the entire regenerator length. In the present AMR test device, the maximum regenerator length was set at 100 mm. Therefore, the NHC array must be longer than the

regenerator to minimize the influence of magnet end effects on the regenerator performance. The other design input parameters are as follows:

- $D_{\mathrm{i,I}} = 27.0$ mm, which is enough to accommodate a 25.4-mm OD G10 fiberglass tube used as the regenerator housing;
- $\ell_{\mathrm{gap}} = 3.0$ mm, following the recommendations of Arnold *et al.* (2014);
- $n = 8$ magnet segments to balance cost and performance.

The $Nd_2Fe_{14}B$ sintered magnet grade properties selected for the internal and external magnets are presented in Table A.1 (BAKKER-MAGNETICS, 2014). The choice of two different magnet grades for the inner and outer magnets was based on experience gained through numerical analysis using COMSOL. Although grades with a higher remanence (which are associated with lower coercivities) resulted higher magnetic flux densities, they were more prone to magnetization reversal. After trying a few grade combinations, it was verified that the one presented in Table 1 did not reverse the magnetization and imposed a small penalty on the magnetic flux density at the maximum position.

Table A.1 – $Nd_2Fe_{14}B$ sintered magnet grade properties (BAKKER-MAGNETICS, 2014).

Cylinder	Magnet grade	B_{rem}[1][T]	H_{cj}[2][kA/m]
External	N50M	1.41	1114
Internal	N42UH	1.30	1989

[1] The minimum value of the remanent flux density presented in BAKKER-Magnetics (2014) was used.

[2] The value of H_{cj} at 293 K was chosen since the application is at near room temperature conditions.

Application of the design procedure with the above parameters and conditions resulted in a number of possible dimensions for the NHC array that satisfied the minimum magnetic flux density and the Λ_{cool} constraints. The selected configuration also satisfied compactness criteria of maximum dimensions for $D_{\mathrm{e,E}}$ and L_{E} of 140.0 mm and 130.0 mm, respectively. Rounding up the values for manufacture simplicity,

Table A.2 – Dimensions of the NHC array obtained from the analytical design procedure.

Internal Magnet			External Magnet		
$D_{\mathrm{i,I}}$ (mm)	$D_{\mathrm{e,I}}$ (mm)	L_{I} (mm)	$D_{\mathrm{i,E}}$ (mm)	$D_{\mathrm{e,E}}$ (mm)	L_{E} (mm)
27.0	58.0	115.0	64.0	135.0	130.0

Table A.3 – Magnetic flux densities and Λ_{cool} results for the NHC array obtained from the analytical design procedure.

$B_{\mathrm{HC,E}}$ (T)	$B_{\mathrm{HC,I}}$ (T)	B_{max} (T)	B_{min} (T)	ΔB (T)	Λ_{cool}
0.890	0.894	1.784	0.004	1.780	0.025

the selected dimensions of the NHC array are presented in Table A.2. The results for B_{max}, B_{min} and Λ_{cool} are presented in Table A.3.

The numerical results for B_{max}, B_{min} and Λ_{cool} at the center of the magnet obtained from the 3D numerical simulations using COMSOL Multiphysics are presented in Table A.4. These were generated with the same input parameters, magnet grade properties and dimensions obtained from the analytical model.

Table A.4 – Analytical and 3D COMSOL Multiphysics results for the center of the NHC magnet array.

Model	B_{max} (T)	B_{min} (T)	ΔB (T)	Λ_{cool}
Analytical	1.784	0.004	1.780	0.025
COMSOL 3D	1.741	0.006	1.735	0.024

As can be seen, the results obtained with the 3D numerical model (COMSOL..., 2011) tend to be more conservative, but a very good agreement is observed between the analytical design procedure and the 3D COMSOL results. This indicates that the analytical method can be used to design NHC arrays.

Fig. A.2 illustrates the magnetic flux density in the x-y plane at the center of the magnet array ($z = 0$). Both the maximum, Fig. A.2(a), and the minimum, Fig. A.2(b), magnetic flux densities are homogeneously distributed in the magnet core. This is an important result from the point of view of the validity of the analytical model, which is concerned only with the flux density at the center point of the magnet

array.

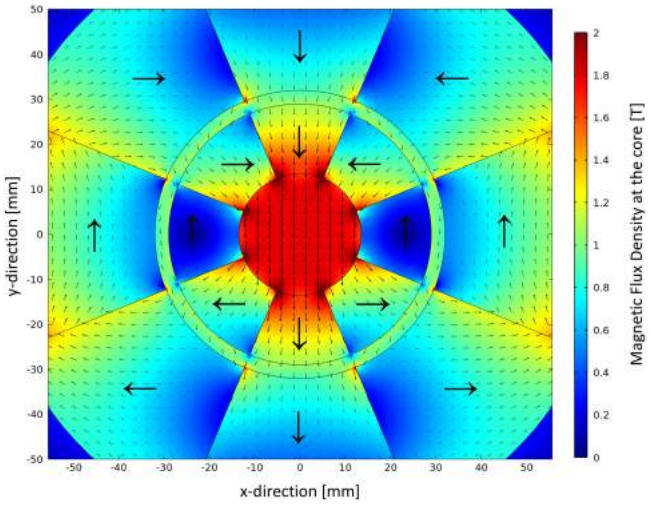

(a)

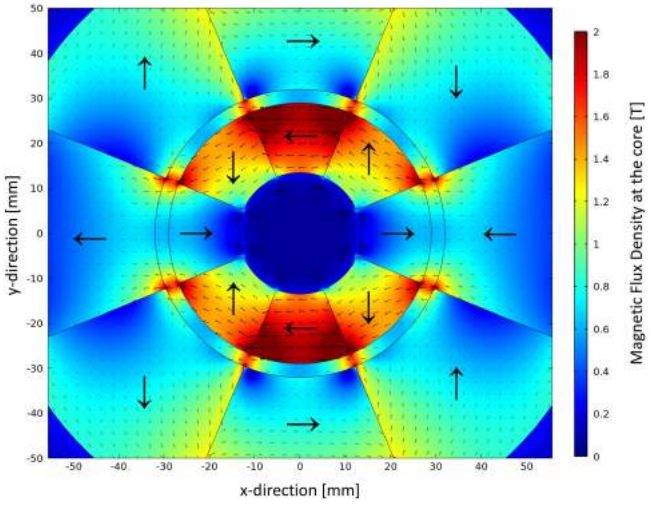

(b)

Figure A.2 – Magnetic flux density distribution in the x-y plane at the center of the magnet array ($z = 0$): (a) Maximum flux density magnet position; (b) Minimum flux density magnet position.

The analytical design procedure indicates that any value of internal magnet length in the range $100 \leq L_{\mathrm{I}} \leq 130$ mm satisfies the constraints imposed on Λ_{cool} and does not generate significant deviations in the maximum and minimum magnetic flux densities, as shown in Table A.5. To demonstrate that $L_{\mathrm{I}} = 115$ mm is a suitable length, 3-D COMSOL simulations were performed and the magnetic flux density along the axial direction was evaluated for three different values of L_{I}. The results are presented in Fig. A.3 and in Table A.5. It should be noted that in Fig. A.3 the magnetic flux density is plotted along the length of the regenerator only, i.e., 100 mm. The following remarks can be made regarding the internal magnet length selection:

1. $L_{\mathrm{I}} = 100$ mm. The internal magnet and the regenerator have the same length. As seen in Fig. A.3, as the edge of the magnet is approached, a significant reduction of B_{max} is observed. This reduces the z-averaged maximum magnetic field applied on the regenerator in comparison with the other magnet lengths;

2. $L_{\mathrm{I}} = 130$ mm. This length gives the smallest reduction of B_{max} close to the ends of the regenerator and, consequently, the highest average magnetic field. However, it represents an increase of 30% in the internal magnet volume, which increases the cost of the system and slightly reduces Λ_{cool};

3. $L_{\mathrm{I}} = 115$ mm. This length constitutes a good compromise in terms of cost and performance. While end effects do not reduce significantly the local and z-averaged values of B_{max} when compared to $L_{\mathrm{I}} = 130$ mm, this length actually represents a better use of $Nd_2Fe_{14}B$ because of the smaller amount of material and higher Λ_{cool}.

A.3.2 Magnetization Reversal and Energy Product (BH) Analysis

Halbach cylinders can generate in their core fairly high magnetic flux densities, $\vec{B}$, of the order of 2.0 T. Nevertheless, $\vec{B}$ is mainly limited by the intrinsic coercivity of the magnet grade, H_{cj}. Physically, once the reverse component of the magnetic field, $\vec{H}$, reaches a value higher than H_{cj}, a localized reversal of the direction of the magnetization is created, giving rise to an additional opposite internal field in the magnet. As a

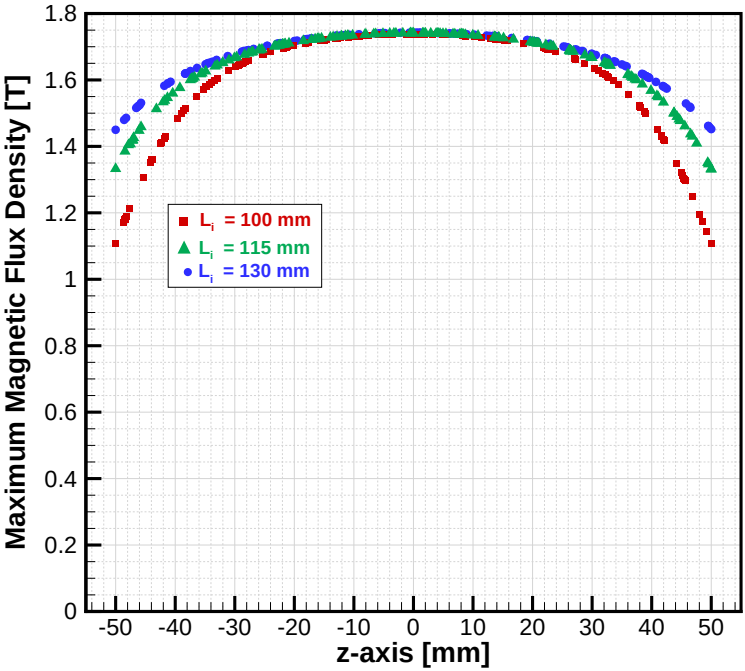

Figure A.3 – Magnetic flux density at the maximum position along the axial z-direction for different values of the internal magnet length.

result, the magnet will find a new equilibrium point, but with a lower $\vec{B}$ (BJØRK *et al.*, 2008; BLOCH *et al.*, 1998).

An evaluation of the reverse field has been performed based on the 2-D COMSOL simulation results, according to the following criterion:

$$\left(\mu_0 H_{\mathrm{cj}} + \mu_0 \vec{H} \cdot \frac{\vec{B}_{\mathrm{rem}}}{|\vec{B}_{\mathrm{rem}}|} \right) \geq 0 \tag{A.11}$$

where H_{cj} and $\vec{B}_{\mathrm{rem}}$ are the magnetic grade properties (Table A.1) and $\vec{B}_{\mathrm{rem}}$ follows the remanence orientation of each segment (Fig. 3.6) (BJØRK *et al.*, 2008). Thus, if the criterion imposed by Eq. (A.11) is locally violated, then a localized reversal of the direction of the magnetization is possible. Fig. A.4 shows the results of a magnetization reversal analysis of the NHC array considering the maximum and min-

Table A.5 – Results of the design procedure for different lengths of the internal magnet.

L_{I} (mm)	Results	$B_{\max}$ (T)	$B_{avg}{}^{*}$ (T)	$B_{\min}$ (T)	Λ_{cool}
100	Analytical	1.781	-	0.008	0.025
	COMSOL	1.738	1.550	0.009	0.024
115	Analytical	1.784	-	0.004	0.025
	COMSOL	1.741	1.631	0.006	0.024
130	Analytical	1.786	-	0.003	0.024
	COMSOL	1.742	1.667	0.003	0.023

$^{(*)}$ B_{avg} is the z-averaged $B_{\max}$.

imum magnetic flux densities positions (see Fig. 3.6).

According to Fig. A.4, neither at the maximum magnetic flux density magnet position, Fig. A.4(a), nor at the minimum magnetic flux density magnet position, Fig. A.4(b), a reversal field was verified in the selected NHC array. The gray arrows indicate the orientation of the remanent flux density of each segment. Hence, one can conclude that the present NHC array will operate safely.

The energy product, BH, of the permanent magnet in the magnetic circuit was evaluated by means of the 2-D COMSOL numerical simulation as the norm product of the components of $\vec{B}$ and $\vec{H}$ parallel to $\vec{B}_{\mathrm{rem}}$ as follows (BJORK, 2010):

$$BH = \left| \vec{B} \cdot \frac{\vec{B}_{\mathrm{rem}}}{|\vec{B}_{\mathrm{rem}}|} \right| \left| \vec{H} \cdot \frac{\vec{B}_{\mathrm{rem}}}{|\vec{B}_{\mathrm{rem}}|} \right| \tag{A.12}$$

The BH results of Eq. (A.12) are presented in Fig. A.5 to illustrate quantitatively the performance of the magnet design and draw attention to the regions where the use of $Nd_2Fe_{14}B$ is less effective. Figs. A.5(a) and A.5(b) present the energy product of the magnets at the maximum and minimum magnetic flux density positions, respectively. Table A.6 summarizes the BH product evaluated separately for each magnet cylinder.

The external magnet operates with a high energy product most of the time, particularly the segments with a remanent flux density parallel to the x-axis, at the maximum magnetic field position. On the other hand, the segments with a remanent flux density parallel to y-axis have a lower average energy, and a reasonable area with low energy operation. One

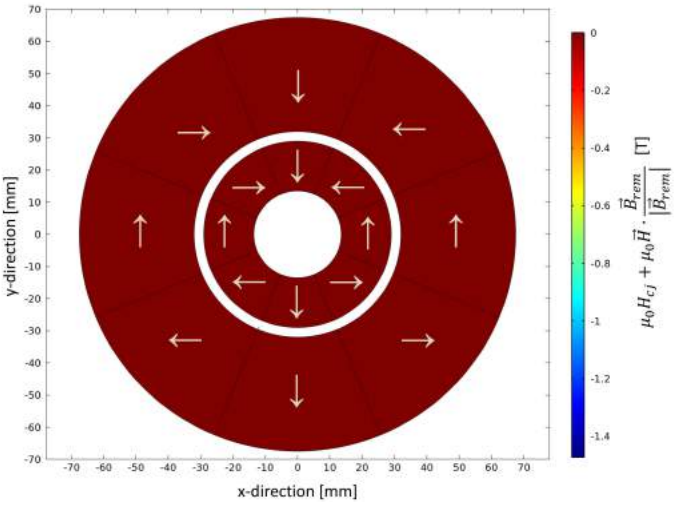

(a)

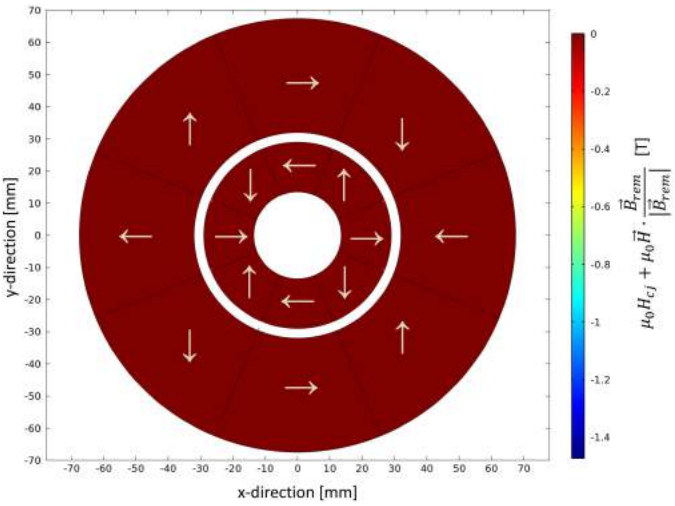

(b)

Figure A.4 – Magnetization reversal analysis: (a) Maximum magnetic field position; (b) Minimum magnetic field position. The gray arrows represent the remanent flux density orientation of each segment.

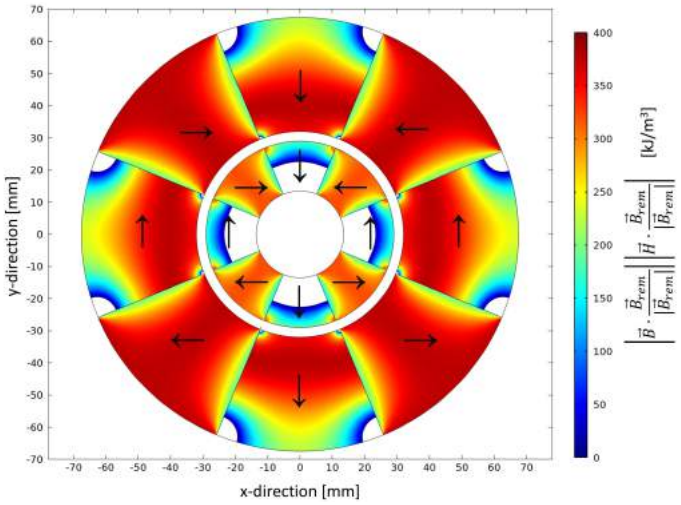

(a)

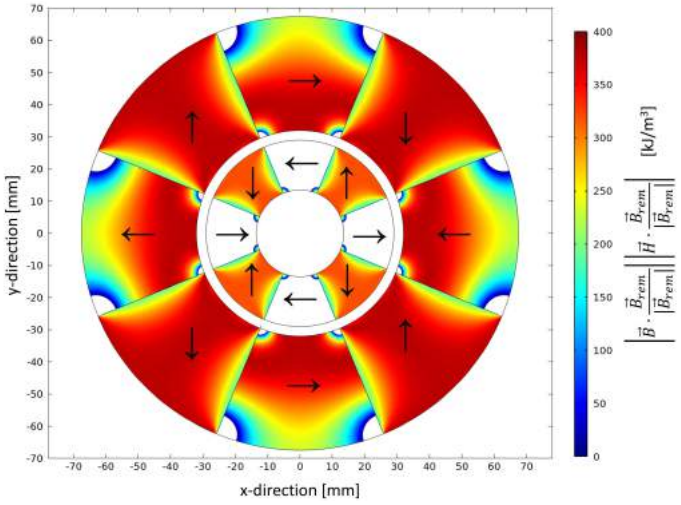

(b)

Figure A.5 – Energy product of the permanent magnet array: (a) Maximum magnetic flux density magnet position; (b) Minimum magnetic magnetic flux density magnet position. The black arrows indicate the remanent flux density of each segment.

Table A.6 – Energy product BH (in kJ/m^3) calculated from the 2-D COMSOL simulations of the external and internal magnet arrays.

Array	Magnet grade $BH_{\max}$	Max. $\vec{B}$ position $BH_{\max}$	Min. $\vec{B}$ position $BH_{\max}$
External	N50M - 382-398	376.7	376.7
Internal	N42UH - 318-334	302.2	302.2

possible improvement might be to replace some of these low energy regions in the external cylinder by a soft magnetic material, i.e. iron, which would save raw magnet material and help to concentrate the magnetic flux lines.

Conversely, the internal magnet operates most of the time with a low energy product, especially when the remanent flux densities of the segments are aligned with those in the external magnet. This constitutes a considerable volume of $Nd_2Fe_{14}B$ whose potential energy is not used effectively. A more specific evaluation of the behavior of the BH product of the internal magnet can be made based on Fig. A.6, which allows the following remarks:

- For the segments in position S1 in Fig. A.6, the resulting magnetic field $\vec{H}$ (represented by gray arrows) has the same direction of the remanent flux density (represented by the purple arrows). This results in a magnetization of the permanent magnet in segments S1 due to the high magnetic field generated by the external magnet array in the same direction of the remanent flux density of the internal segment;

- For the segments in position S2, the resulting magnetic field $\vec{H}$ (gray arrows) has an opposite direction in relation to the remanent flux density (purple arrows). This results in a reversal magnetic field in segments S2 (see Eq. (A.11)) which can lead to a magnetization reversal if the intrinsic coercivity is not properly selected.

It can be concluded that in the present NHC design, replacement of the raw magnet material by soft magnetic material in the low energy region of the internal magnet is not an option since the flux density generated by the internal array is continuously added to and subtracted from the flux density generated by the external array so as to achieve the

high and low magnetic flux densities in the core. Thus, the internal magnet must operate at a low energy to allow the desired magnetic field variation in a fixed volume region. This explains why Λ_{cool} is comparatively low in this type of magnet system. Additionally, the results for the magnetization reversal and the energy product (BH) reinforce the idea that the magnet grade has to be carefully selected for the NHC configuration.

A.3.3 Nested Halbach Cylinder Final Design

A photograph of the final NHC design built according to the dimensions presented in Tab. A.2 is presented in Fig. A.7. As mentioned before, despite the more complex bearing structure and motion system, the counter rotating configuration was preferred. Moreover, this design requires the motor to operate at lower angular velocities and higher torques. Also, since one of the objectives of the AMR test apparatus is to evaluate experimentally regenerative geometries, such as parallel plates and staggered arrays of pins, a fixed direction of the magnetic flux density vector guarantees structural stability of the regenerator geometry. Fig. A.8 presents a $y - z$ cutaway view of the final magnet design, showing the bearing structure designed for the counter rotation of the magnets.

Fig. A.9 shows the NHC motion system. A stepper motor (Kalatec Nema 34, model KML-HT34-487) coupled to a 15:1 reduction gearbox is employed to achieve high torques. The stepper motor is controlled by a driver (Applied Motion model ST10), which guarantees a precise operating speed and frequency control. The torque transducer (HBM model T22) is assembled between the reduction and spiral bevel gearboxes. The spiral bevel gearbox (Tandler STD00-EA-III, 1:1) was found to be a suitable and compact solution to counter rotate the magnets; the torque imposed by the stepper motor is transmitted by the bevel gears to two independent shafts that rotate in opposite directions. Two sets of pulleys and belts are used to connect the spiral bevel gearbox and the magnets.

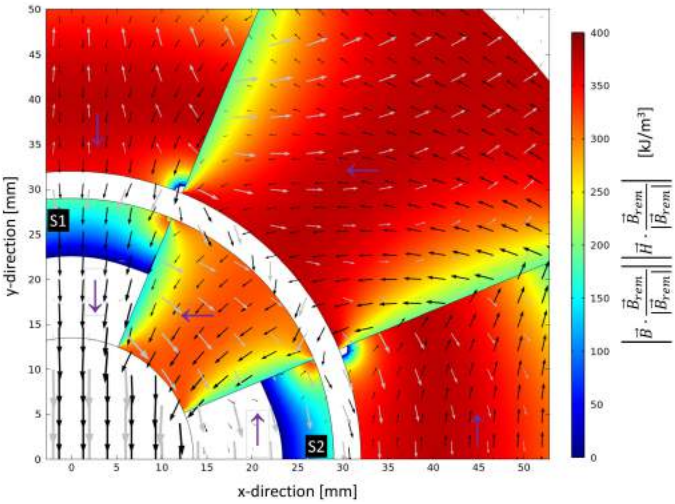

(a)

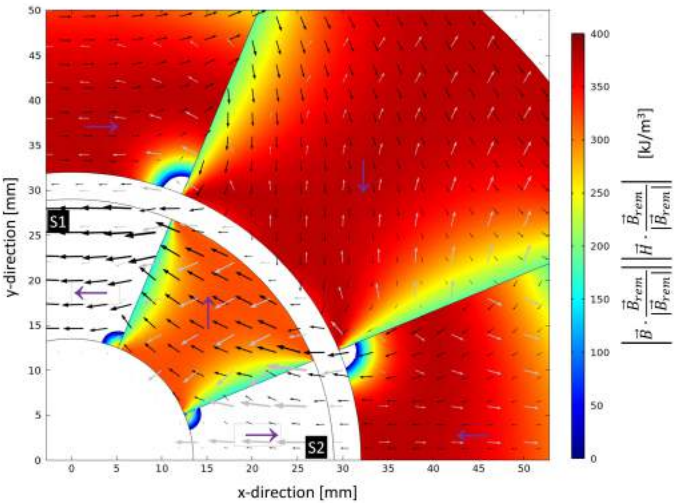

(b)

Figure A.6 – Energy product analysis of the internal magnet: (a) Maximum magnetic field position; (b) Minimum magnetic field position. The black arrows indicate the remanent flux density of each segment.

Figure A.7 – Nested Halbach Cylinder magnetic circuit built according to the dimensions obtained from the proposed design procedure.

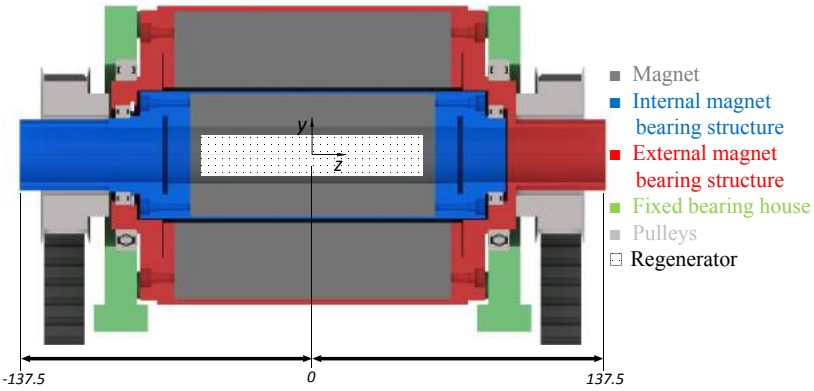

Figure A.8 – $y-z$ cutaway view of the NHC design showing the bearing structure to enable the counter rotation of the external and internal magnets. Dimensions in mm.

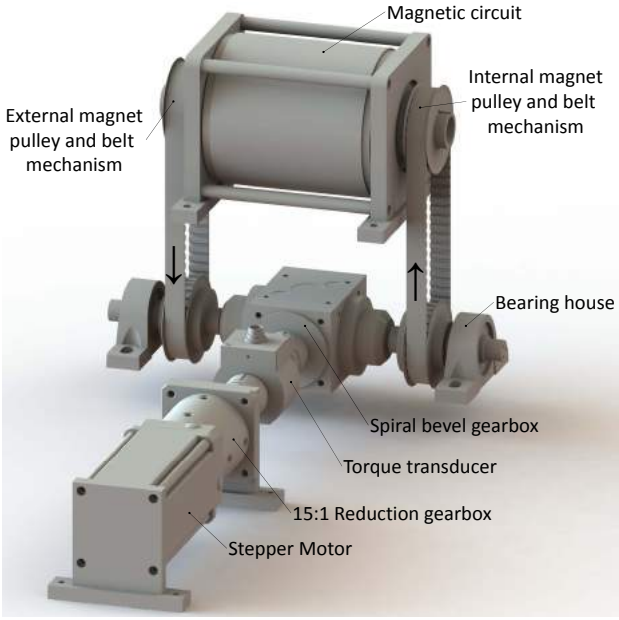

Figure A.9 – Motion system designed and constructed to counter rotate the magnets in the NHC array.

A.3.4 Experimental Results

Fig. A.10 presents the experimental results of the magnetic flux density along the center line ($x = y = 0$) of the NHC array (between $z = 0$ and 137.5 mm) as a function of the rotating angle of the internal cylinder. It should be noted from Fig. 3.7(b) that in the counter rotating configuration the two cylinders are dephased by 180°, so the rotating angle of the external cylinder has a negative sign. Figs. A.10(a) and (b) show the results for the y- and x-components, respectively. The resultant of the magnetic flux density vector and its direction (i.e., the angle θ of the resultant with the vertical y axis) are shown in Figs. A.10(c) and (d), respectively. The solid lines represent the measurement stations inside the NHC array where the regenerator is located ($-50 \leq z \leq 50$ mm). The dotted lines correspond to stations outside the regenerator region surrounded by the bearing structure (see Fig. A.8). Ideally, the x-component should be equal to zero, and the resultant should be equal to the y-component ($\theta = 0$).

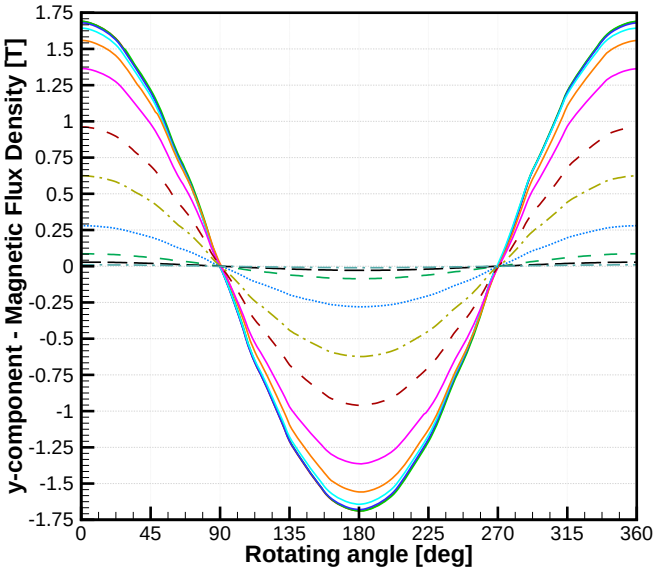
y-component - Magnetic Flux Density [T]
Rotating angle [deg]
1.75
1.5
1.25
1
0.75
0.5
0.25
0
-0.25
-0.5
-0.75
-1
-1.25
-1.5
-1.75
0
45
90
135
180
225
270
315
360

(a)

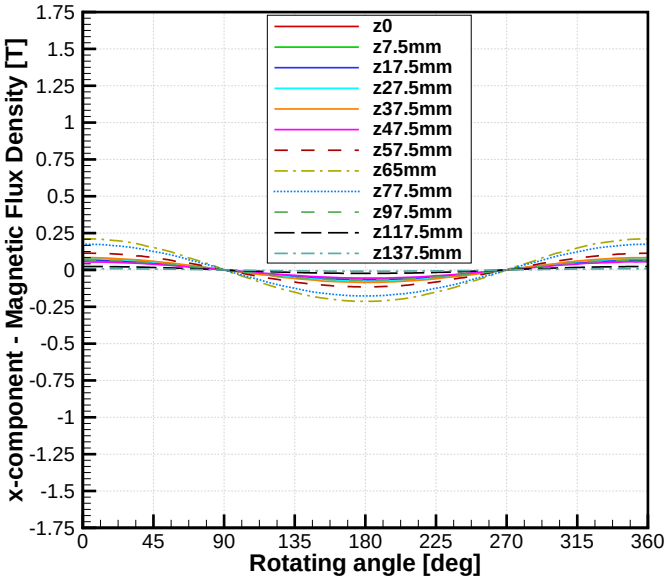
x-component - Magnetic Flux Density [T]
Rotating angle [deg]
z0
z7.5mm
z17.5mm
z27.5mm
z37.5mm
z47.5mm
z57.5mm
z65mm
z77.5mm
z97.5mm
z117.5mm
z137.5mm
1.75
1.5
1.25
1
0.75
0.5
0.25
0
-0.25
-0.5
-0.75
-1
-1.25
-1.5
-1.75
0
45
90
135
180
225
270
315
360

(b)

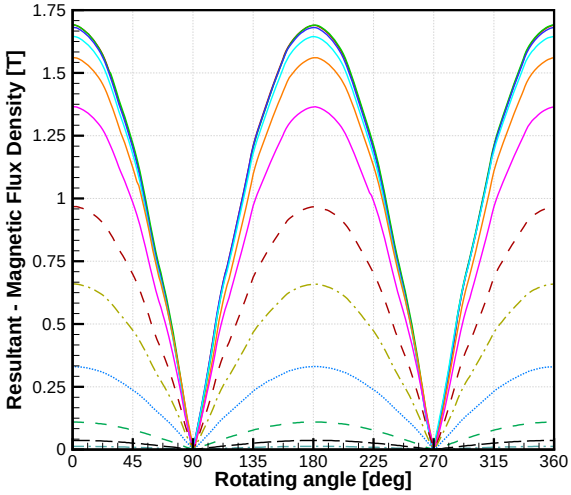

(c)

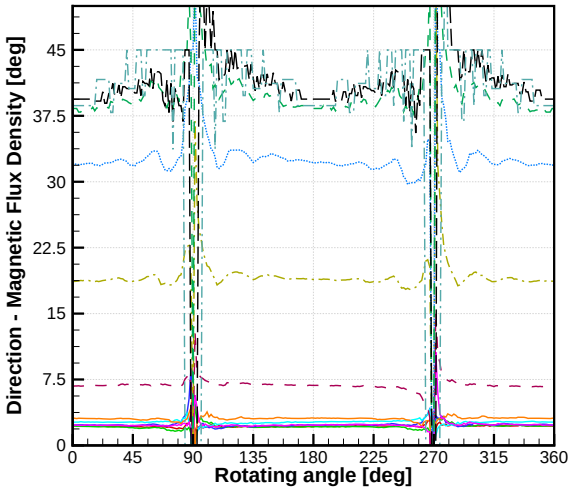

(d)

Figure A.10 – Experimental magnetic flux density vector measurements at different positions along the z axis as a function of the rotating angle of the inner magnet. (a) y-component; (b) x-component; (c) Resultant; (d) Angle of the resultant with the vertical direction. The legend presented in figure (b) is the same for the other figures.

As can be seen from Fig. A.10, in the regenerator region (solid lines), the x-component is close to zero, which makes the resultant magnetic flux density very close to the measured y-component. θ changes very little in this region. On the other hand, outside the NHC array ($z \rightarrow$ 137.5 mm), the x-component increases and the y-component decreases, reducing the absolute magnetic flux density to around zero. This causes θ to increase, showing a residual magnetic flux density outside the magnets.

Fig. A.11 shows the axial profiles of the maximum magnetic flux density components (x and y), the resultant and the vector direction (θ). The dark gray region represents the external and internal cylinder arrays, and the light gray region the stainless steel support structure. In the regenerator region ($-50 \leq z \leq 50$ mm), the magnetic flux density is higher than 1.3 T and θ is approximately 2.5°. As expected, θ does not vary with the rotating angle. Outside the cylinder arrays, the magnetic field decreases continuously to 0 T at $z = 137.5$ mm and the vector magnetic flux density changes its direction between $7.5 < \theta < 45^o$.

A comparison between the analytical, 3-D COMSOL simulation and the experimental results for the magnetic flux density is presented in Table A.7. As can be seen, $B_{\max}$ is over-predicted by approximately 3.0% by the numerical analysis and by approximately 5.5% by the analytical procedure, which can be applied to design NHC arrays for AMR systems at a negligible computational cost. Equally negligible are the differences in the predictions of Λ_{cool}.

Table A.7 – Comparison of the analytical, 3-D COMSOL simulation and experimental results for the magnetic flux density and figure of merit at the center of the magnet for the constructed NHC system.

Model	$B_{\max}$ (T)	$B_{\min}$ (T)	ΔB (T)	Λ_{cool}
Analytical	1.784	0.004	1.780	0.025
COMSOL 3D	1.741	0.006	1.735	0.024
Experimental	1.690	0.004	1.686	0.023

Fig. A.12 compares the 3-D COMSOL simulations and the experimental results of the magnetic flux density as a function of the axial distance in the regenerator region ($-50 \leq z \leq 50$ mm). Fig. A.12(a) presents the magnetic flux density variation with the rotating angle for different z positions and Fig. A.12(b) shows the maximum magnetic flux density

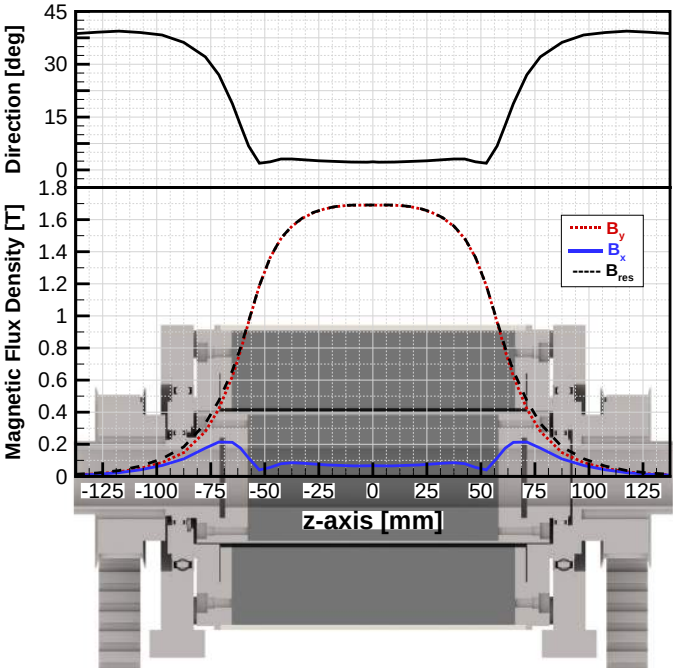

Figure A.11 – Magnitude of the components, resultant and direction of the magnetic flux density at the maximum field position along the z-axis.

along the z-axis. The agreement between the 3-D COMSOL numerical model and the experimental data is very encouraging and seems to reinforce the validity of the proposed analytical procedure to design NHC arrays. The experimental z-averaged magnetic flux density over the regenerator region was 1.61 T, which corresponds to an experimental Λ_{cool} based on averaged values of 0.023.

The results of torque measurements at different operating frequencies are presented in Fig. A.13. The time dependent torque data present characteristic oscillations which are due to magnet segmentation of the magnets, as discussed by other authors (ARNOLD *et al.*, 2014; MHÍOCHÁIN *et al.*, 1999). When the angular frequency is increased, the amplitude of the oscillation decreases due to the inertia of the magnets. On the other hand, as seen in Fig. A.13(b), the average cycle torque increases linearly with the operating frequency.

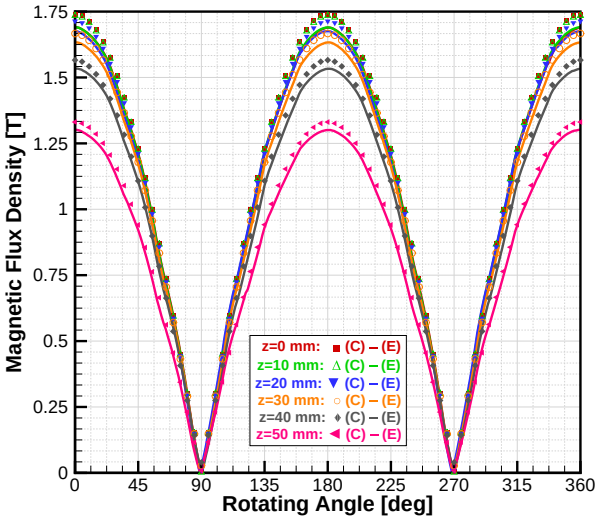

(a)

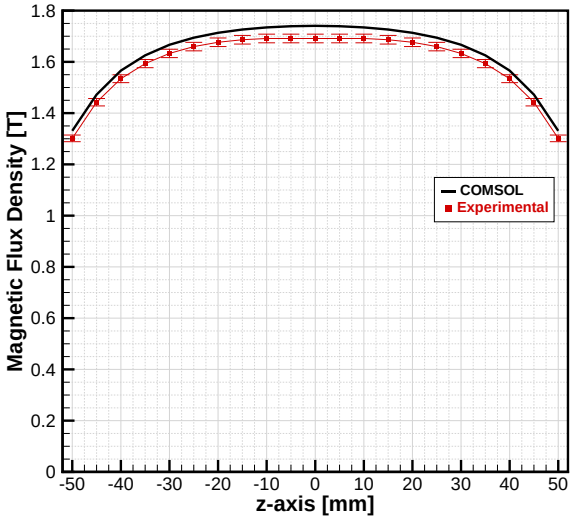

(b)

Figure A.12 – Comparison between the 3-D COMSOL simulation results and the experimental data for the magnetic flux density: (a) As a function of the rotating angle for different axial positions; (b) Axial variation of the maximum magnetic flux density.

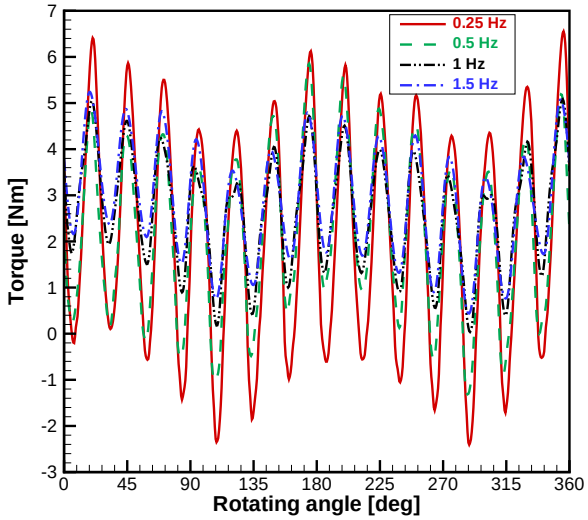

(a)

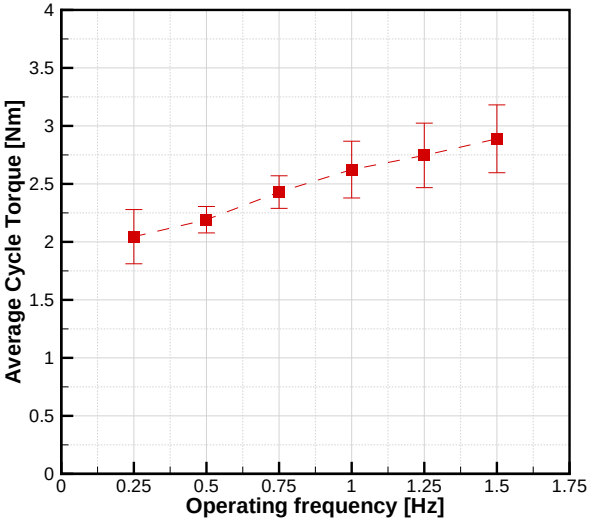

(b)

Figure A.13 – Torque measurements: (a) Torque as a function of the rotating angle at different frequencies; (b) Average cycle torque as a function of the operating frequency.

APPENDIX B

Assembly of the Regenerative Matrices

B.1 Assembly of Packed Bed Matrices

The steps of the assembly of the packed bed matrices, presented in Fig. B.1, were performed as follows:

1. A specified amount of spheres is weighted and the initial mass is recorded;
2. A R-T adapter is mounted at the bottom of the regenerator housing and the casing is held in place by a benchtop vise;
3. A stainless steel end screen, mesh 80, is inserted in the regenerator, on top of the R-T adapter. The screen holds the spheres inside the housing and is carefully assembled so as to remain perpendicular to the center line of the casing. Otherwise, a different bed length or volume is calculated, resulting in a wrong estimate of the porosity;
4. From the initial amount of weighted spheres, small samples are collected and carefully spilled into the regenerator housing;
5. Using a pestle, the spheres are compacted in the housing;
6. Steps (4) and (5) are repeated until the housing is filled up with spheres;

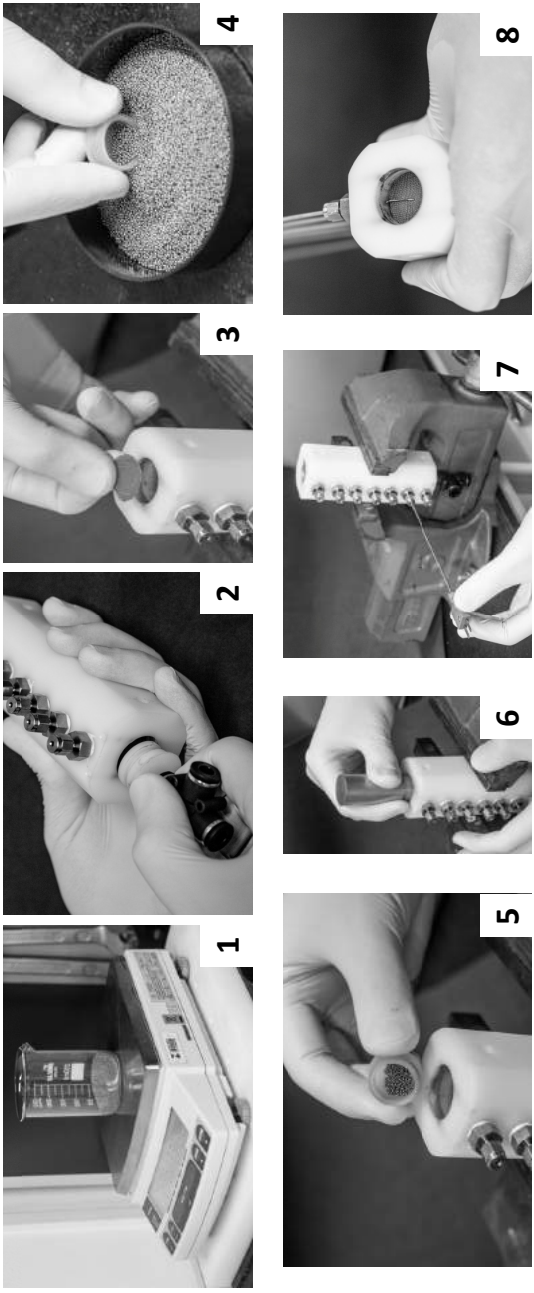

Figure B.1 – Steps of the assembly of the packed bed matrix.

7. When the packed spheres reach a thermocouple feed-through, a temperature probe is inserted and positioned at the center of the housing. The uncertainty related with the temperature probe axial position was evaluated at 2 mm;

8. When the regenerator is completely filled, another stainless steel end-screen is placed at the top end. Next, the temperature probes T_{CE} and T_{HE} are assembled and carefully positioned at the ends of the matrix. The top R-T adapter is connected, sealing the matrix.

9. Finally, the excess amount of spheres are weighted and the porosity of the matrix is calculated based on the total mass of material used and the volume of the matrix.

B.2 Assembly of Parallel-Plate and Pin Array Matrices

The steps of the assembly of the parallel plate and pin array matrices are presented in Fig. B.2. This procedure was used in both the stainless steel and Gd matrices. The steps are described next:

1. The five pieces of parallel plates are aligned and 0.13-mm thick polymer plates are inserted into the channels to guarantee their alignment without obstruction – see Fig. B.3(a);

2. A similar procedure is carried out for the pin array. However, the polymer plates are positioned at 45° to guarantee the alignment of the pieces – see Fig. B.3(b);

3. After the alignment, the pieces are glued (using an epoxy glue) on a polymer sheet;

4. And a steel weight is carefully placed on top of the assembly to guarantee a good contact with the polymer sheet;

5. This procedure is repeated for all the sides of the matrix, until the five pieces are securely combined into a single matrix;

6. The regenerator matrix is inserted into the ABS housing;

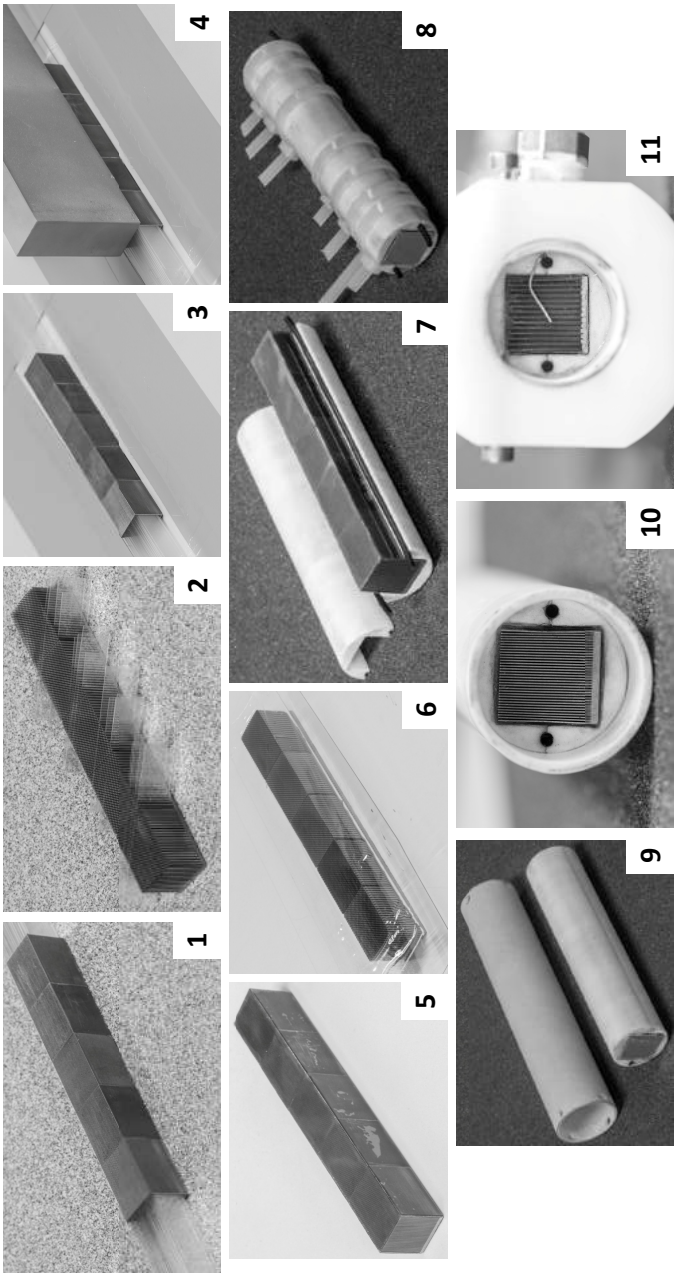

Figure B.2 – Steps of the assembly of the parallel plate and pin array matrices.

7. The regenerator is glued (using an epoxy glue) to the ABS housing. This is important to avoid flow channeling between the regenerator geometry and the ABS housing;

8. The ABS housing is cleaned with isopropyl alcohol, and assembled into the G10 casing. This process was designed with a tight tolerance between the external ABS diameter and the internal G10 diameter to avoid flow channeling/leakage;

9. Finally, the temperature probes and the R-T adapters are connected.

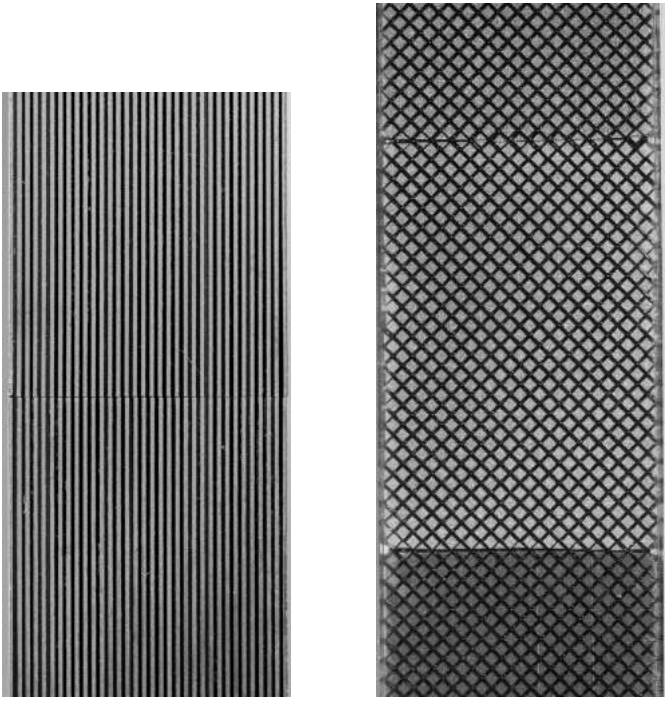

(a) (b)

Figure B.3 – (a) Detail in the alignment of the parallel plates geometry; (b) Detail in the alignment of the pins array geometry.

APPENDIX C

Nusselt Number Correlation for Packed Beds of Spheres

The interstitial convective heat transfer coefficient for a packed bed of spheres used in the present thesis was calculated using the Nusselt number correlation of (PALLARES; GRAU, 2010). This correlation was preferred to more traditional ones (WHITAKER, 1972; WAKAO; KAGUEI, 1982), because it is valid for porosities between 0.2 and 0.9 and for a wide range of Prandtl numbers (KUWAHARA *et al.*, 2001). The results discussed along the thesis are such that the particle Reynolds numbers lie between 1 and 500, which for water ($Pr \approx 6$) correspond to $(Re_{dp}^{0.6} Pr^{1/3})^2$ between 2 and 6 $\times 10^3$. However, the majority of the data in the present experimental data and simulations are for $Re_{dp} < 150$, or $(Re_{dp}^{0.6} Pr^{1/3})^2 < 1350$, which is exactly the range where the Wakao and Kaguei (1982) correlation exhibits the largest discrepancy with respect to experimental data (PALLARES; GRAU, 2010). Finally, comparing Wakao and Kaguei (1982) and Pallares and Grau (2010) correlations against the experimental data presented in this thesis, Pallares and Grau (2010) exhibited a better reproduction of the experimental data, as showed in Fig. C.1 that compares the experimental and numerical results, using those Nusselt correlations, for the effectiveness as a function of the frequency to Casing#3 and two particle sizes, Fig. C.1(a) $d_\mathrm{p} = 0.5$ mm and Fig. C.1(b) $d_\mathrm{p} = 0.8$ mm. Wakao and Kaguei (1982) correlation, in general, underestimated the experimental values. The same conclusion can be addressed to the other casings and particle sizes presented in this thesis.

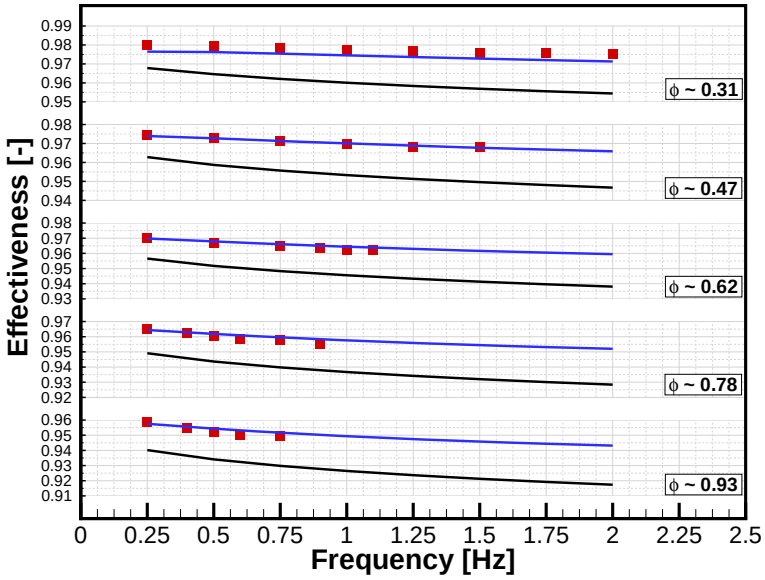

(a)

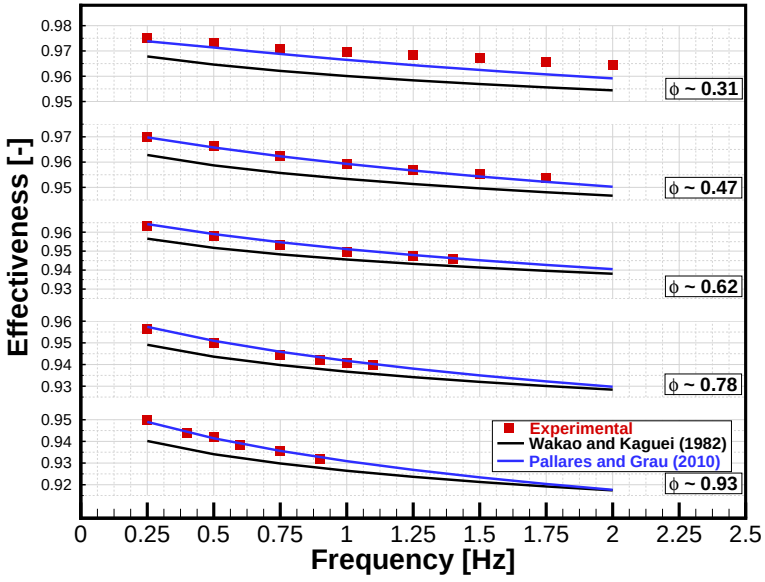

(b)

Figure C.1 – Effectiveness as a function of frequency for Casing #3: (a) $d_p = 0.5$ mm; (b) $d_p = 0.8$ mm.